

Engineering Materials

Evgeny N. Barkanov
Andrei Dumitrescu
Ivan A. Parinov *Editors*

Non-destructive Testing and Repair of Pipelines

 Springer

Engineering Materials

The “Engineering Materials” series provides topical information on innovative, structural and functional materials and composites with applications in optical, electrical, mechanical, civil, aeronautical, medical, bio and nano engineering. The individual volumes are complete, comprehensive monographs covering the structure, properties, manufacturing process and applications of these materials. This multidisciplinary series is devoted to professionals, students and all those interested in the latest developments in the Materials Science field.

More information about this series at <http://www.springer.com/series/4288>

Evgeny N. Barkanov · Andrei Dumitrescu
Ivan A. Parinov
Editors

Non-destructive Testing and Repair of Pipelines



 Springer

Editors

Evgeny N. Barkanov
Institute of Materials and Structures
Riga Technical University
Riga
Latvia

Ivan A. Parinov
Mathematics, Mechanics and Computer
Sciences Institute
Southern Federal University
Rostov-on-Don
Russia

Andrei Dumitrescu
Petroleum-Gas University of Ploiesti
Ploiești
Romania

ISSN 1612-1317

Engineering Materials

ISBN 978-3-319-56578-1

DOI 10.1007/978-3-319-56579-8

ISSN 1868-1212 (electronic)

ISBN 978-3-319-56579-8 (eBook)

Library of Congress Control Number: 2017937123

© Springer International Publishing AG 2018, corrected publication 2018

This work is subject to copyright. All rights are reserved by the Publisher, whether the whole or part of the material is concerned, specifically the rights of translation, reprinting, reuse of illustrations, recitation, broadcasting, reproduction on microfilms or in any other physical way, and transmission or information storage and retrieval, electronic adaptation, computer software, or by similar or dissimilar methodology now known or hereafter developed.

The use of general descriptive names, registered names, trademarks, service marks, etc. in this publication does not imply, even in the absence of a specific statement, that such names are exempt from the relevant protective laws and regulations and therefore free for general use.

The publisher, the authors and the editors are safe to assume that the advice and information in this book are believed to be true and accurate at the date of publication. Neither the publisher nor the authors or the editors give a warranty, express or implied, with respect to the material contained herein or for any errors or omissions that may have been made. The publisher remains neutral with regard to jurisdictional claims in published maps and institutional affiliations.

Printed on acid-free paper

This Springer imprint is published by Springer Nature

The registered company is Springer International Publishing AG

The registered company address is: Gewerbestrasse 11, 6330 Cham, Switzerland

Preface

Transmission pipeline systems have supreme significance for an effective functioning of the petroleum industry, providing European market with energy resources: crude oil, natural gas, liquid petroleum products, and liquefied natural or petroleum gas. Taking into account the long life of such pipeline networks and the present situation, with over 20% of the large-diameter pipelines having exhausted their lifetime, an important task at the present moment becomes safeguarding the reliability for these transmission systems. In such a context, pipeline maintenance activities (comprising inspection and repair) are very important. Many studies have proven that among the main reasons of steel pipeline failures are the volumetric surface defects (VSDs, also named local metal loss defects), generated by corrosion and/or erosion processes and by this way considerably decreasing the pipeline strength and expected lifetime.

The present book is devoted to a provision of efficient and safe operations of transmission pipelines by improvement of existing and development of new methods for the detection (by means of non-destructive techniques, based on low-frequency ultrasonic testing with directional waves) and repair (using advanced composite materials systems) of VSDs, generated in the pipelines. These studies are performed in order to bring the efficiency of damaged sections up to the level of the undamaged pipeline. The combination of both research directions mentioned above is, in our opinion, important since the increased technological opportunities of long-range ultrasonic testing promote a more efficient application of composite repair technologies, which are developed taking into account an assessment of the stress–strain state in the VSD areas of in-service repaired pipelines.

The activities of transporting petroleum, natural gas and petroleum products are services that must be provided continuously. As a consequence, the present-day maintenance strategies require that the inspection and technological repair procedures normally used should be applied without removing the pipelines from service. In such conditions, the pipe repair systems, based on composite materials (that are analysed in the present book), are more and more often used, because they have a

good economic efficiency. They considerably increase the remaining life of the repaired pipelines and they do not require welding operations (implied by using another repair methods, which require special precautions, when performed on pipelines under pressure).

In order to ensure efficient and safe operation of existing transmission pipelines, operating companies routinely inspect the pipes. The methods normally used to such a purpose, like for instance “smart pigs”, are sufficiently expensive, require significant reconstruction and have, in some cases, an insufficient sensitivity. As an alternative, the application of long-range ultrasonic testing and phased array technologies, studied in Chapter “[Long-Range Ultrasonic and Phased Array Technologies](#)”, contributes to the increase of the functional capability of non-destructive testing, namely range of test, defect detection, positioning and sizing capabilities.

Aiming at the development of recommendations for an application of the long-range ultrasonic and phased array technologies for pipeline diagnostics, different types of generated and received guided ultrasonic waves, their interaction with discontinuities and directional properties of ultrasonic antenna array are analysed. An accurate characterisation of damaged area detected in the transmission pipeline by the long-range ultrasonic waves is carried out using the wavelet transform and inverse techniques. The vibration-based damage detection (VBDD) techniques, based on the changes in the dynamic characteristics of a structure caused by the defect, are also analysed for steel pipeline systems. The localization of impact damage in thin-walled composite structure using variance-based continuous wavelet transform technique is investigated, and the defects identification method in pipeline systems, based on a combination of finite element method and artificial neural networks, is proposed.

The methods for the assessment of the pipeline areas, requiring maintenance works, are performed. The remaining strength of a transmission pipeline on which VSDs have been detected (using the results of non-destructive testing) are analysed and compared in Chapter “[T- and L-Types of Long-Range Guided Waves for Defect Detection](#)”, with the help of several case studies. The VSDs are characterised, the criteria and procedures, defined by the norms presently used, are discussed, focusing on the assessment of the remaining strength factor and residual life of damaged pipelines. The procedures for the evaluation of the possible interaction between several adjacent VSDs are also discussed and compared.

Different types of materials (polymeric fillers, fibre reinforced materials and polymeric adhesives) are studied in Chapter “[Directional Properties of Ultrasonic Antenna Array](#)” in their application to advanced composite repair systems. After reviewing the properties of such materials, the methods of enhancing the strength of adhesion interaction between the composite wrap/sleeve, used for repair and the steel pipe, are analysed. The mechanical properties of composite materials are characterised by both fracture methods (used to determine also dynamic characteristics) and non-destructive techniques (impulse excitation and inverse technique,

based on low-frequency vibrations, laser-induced ultrasound, used to define elastic properties), demonstrating the efficiency of the developed procedures and the reliability of the obtained results.

The existing technologies using advanced polymeric composite materials systems for the reinforcement of pipelines with VSDs are analysed and compared in Chapter “[Interaction of Low-Frequency Guided Waves with Discontinuities](#)”, using information from the manufacturers of such repair systems, the pipeline operating companies and the experience of the authors. The technologies, based on composite materials, used for pipelines coating to ensure their protection against corrosion, are also present, together with repair methods for such coatings. The design methods, applied for the definition of the characteristic dimensions (thickness and length) of the composite wraps/sleeves, used in the repair systems, are also compared and a new design procedure is proposed by the authors.

Many standards dealing with the composite repair systems are based on simplified approaches and do not take into account the complex stress–strain state in the damaged areas. Consequently, several analytical and numerical procedures, presented in Chapter “[Vibration-Based Damage Detection of Steel Pipeline Systems](#)”, are developed for the detailed assessment of the stress–strain state in the repaired VSD areas. The recovery, by applying advanced composite repair systems, of the carrying capacity of pipeline sections with local corrosion damage is also analysed, using the finite elements method, considering also the case of pipes with two interacting VSDs. Several analytical models, developed to model the contact interaction between the steel pipe and the composite wrap, are also described. An optimisation methodology, based on the planning of experiments and response surface technique, is developed for the composite repair systems considerably reducing the required computational expenses.

An experimental programme (comprising full-scale hydraulic tests of pipes under inner pressure, up to bursting), developed and performed by the authors, aiming at studying the reinforcement effects of a repair system using composite materials for a damaged transmission pipeline, is described in Chapter “[Localization of Impact Damage in Thin-Walled Composite Structure Using Variance-Based Continuous Wavelet Transform](#)”. Validation of the developed numerical models and estimation of the composite repair efficiency is made, based on the results of such a programme.

The topics discussed and the solutions formulated in this book will be interesting and useful for a wide audience, namely for students and researchers studying and developing effective non-destructive techniques and advanced composite materials repair systems for transmission pipelines, as well as for the providers or manufacturers of the components of such techniques and repair systems and for the engineers designing, planning and executing maintenance activities for different pipelines belonging to the transmission systems of hydrocarbons or of other fluids.

The authors would like to express their gratitude to the European Commission for the financial support of their research work under FRAMEWORK7 programme,

Marie Curie action, contract no. PIRSES-GA-2012-318874, project “Innovative Non-destructive Testing and Advanced Composite Repair of Pipelines with Volumetric Surface Defects (INNOPIPES)”.

Riga, Latvia
Ploiești, Romania
Rostov-on-Don, Russia
March 2017

Evgeny N. Barkanov
Andrei Dumitrescu
Ivan A. Parinov

*The original version of the book was revised:
Incorrect author names have been corrected.
The erratum to the book is available at
https://doi.org/10.1007/978-3-319-56579-8_28*

Contents

Part I Non-destructive Testing of Transmission Pipelines	
Long-Range Ultrasonic and Phased Array Technologies	3
Y.N. Mirchev, A.R. Alexiev, A.L. Shekero and S.N. Bukharov	
T- and L-Types of Long-Range Guided Waves for Defect Detection . . .	15
A. Tatarinov, Evgeny N. Barkanov, E. Davydov and M. Mihovski	
Directional Properties of Ultrasonic Antenna Array	31
Y.N. Mirchev, A.L. Shekero and V.V. Kozhushko	
Interaction of Low-Frequency Guided Waves with Discontinuities	45
A.A. Nasedkina, A.R. Alexiev and J. Malachowski	
Vibration-Based Damage Detection of Steel Pipeline Systems	63
A.A. Lyapin, Y.Y. Shatilov and A.A. Lyapin, Jr.	
Localization of Impact Damage in Thin-Walled Composite Structure Using Variance-Based Continuous Wavelet Transform	73
R. Janeliukstis, S. Rucevskis, M.A. Sumbatyan and A. Chate	
Identification of Defects in Pipelines Through a Combination of FEM and ANN	91
A.N. Soloviev, Giang D.T. Nguen, P.V. Vasiliev and A.R. Alexiev	
Dynamic Properties of Thin-Walled Structures Under Changing Pressure Conditions in the Contact Fluid	107
M.A. Sumbatyan, Evgeny N. Barkanov and A.E. Tarasov	
Part II Volumetric Surface Defects in Transmission Pipelines	
Characterisation of Volumetric Surface Defects	117
Andrei Dumitrescu, Gh. Zecheru and A. Diniță	

Assessment of the Remaining Strength Factor and Residual Life of Damaged Pipelines 137
 Gh. Zecheru, Andrei Dumitrescu, P. Yukhymets, A. Gopkalo and M. Mihovski

Assessment of Interacting Volumetric Surface Defects 153
 M.I. Chebakov, Gh. Zecheru and V.A. Chebanenko

Part III Materials Used for the Composite Repair Systems of Transmission Pipelines

Review on Materials for Composite Repair Systems 169
 V.P. Sergienko, S.N. Bukharov, E. Kudina, C.M. Dusescu and I. Ramadan

Techniques for Non-destructive Material Properties Characterisation 191
 Evgeny N. Barkanov, M. Wesolowski, P. Akishin and M. Mihovski

Characterization of Elastic Properties of Metals and Composites by Laser-Induced Ultrasound 209
 V.V. Kozhushko, V.P. Sergienko, Y.N. Mirchev and A.R. Alexiev

Experimental Characterization of Composite Material Properties 227
 P. Yukhymets, R.I. Dmytriienko, I. Ramadan and S.N. Bukharov

Part IV Technologies Used for the Composite Repair Systems of Transmission Pipelines

Comparative Analysis of Existing Technologies for Composite Repair Systems 241
 E. Kudina, S.N. Bukharov, V.P. Sergienko and Andrei Dumitrescu

Design of Composite Repair Systems 269
 Gh. Zecheru, Andrei Dumitrescu, A. Diniță and P. Yukhymets

Part V Simulation of Advanced Composite Repair Systems of Transmission Pipelines

Finite Element Stress Analysis of Pipelines with Advanced Composite Repair 289
 A. Diniță, I. Lambrescu, M.I. Chebakov and Gh. Dumitru

Finite-Element Modeling of a Repaired Pipeline Containing Two Volumetric Surface Defects 311
 M.I. Chebakov, R.D. Nedin and A.A. Lyapin

Assessment of the Reinforcement Capacity of Composite Repair Systems for Pipelines with Interacting Defects 321
 I. Lambrescu, V.A. Chebanenko, D.V. Gusakov and A.V. Morgunova

Modeling of the Contact Interaction Between Steel Pipe and Composite Bandage 339
 I. Lvov and D.A. Beschtnikov

Experimental and Numerical Research of Renovated Pipeline Prototype with Surface Defect 353
 Evgeny N. Barkanov, I. Lvov and D.A. Beschtnikov

Analytical Modeling of the Damaged Zone of Pipelines Repaired with Composite Materials Systems. 369
 A.S. Skaliukh, M.I. Chebakov and Andrei Dumitrescu

Optimal Design of Composite Repair Systems of Transmission Pipelines. 387
 Evgeny N. Barkanov, I. Lvov and P. Akishin

Part VI Testing of Advanced Composite Repair Systems of Transmission Pipelines

Development of an Experimental Programme for Industrial Approbation 401
 Gh. Zecheru, Andrei Dumitrescu, P. Yukhymets and R.I. Dmytriienko

Inner Pressure Testing of Full-Scale Pipe Samples. 417
 R.I. Dmytriienko, S.M. Prokopchuk and O.L. Paliienko

Effectiveness Assessment of Composite Repair Systems 431
 R.I. Dmytriienko, O.L. Paliienko, P. Yukhymets, I. Lvov and O. Marusenko

Errata to: Non-destructive Testing and Repair of Pipelines E1
 Evgeny N. Barkanov, Andrei Dumitrescu and Ivan A. Parinov

Index 449

Contributors

P. Akishin Riga Technical University, Riga, Latvia

A.R. Alexiev Institute of Mechanics of Bulgarian Academy of Sciences, Sofia, Bulgaria

Evgeny N. Barkanov Riga Technical University, Riga, Latvia

D.A. Beschelnikov National Technical University, Kharkiv Polytechnical Institute, Kharkiv, Ukraine

S.N. Bukharov V.A. Belyi Metal Polymer Research Institute of National Academy Science of Belarus, Gomel, Belarus

A. Chate Riga Technical University, Riga, Latvia

M.I. Chebakov I.I. Vorovich Institute of Mathematics, Mechanics and Computer Science, Southern Federal University, Rostov-on-Don, Russia

V.A. Chebanenko I.I. Vorovich Institute of Mathematics, Mechanics and Computer Science, Southern Federal University, Rostov-on-Don, Russia; Southern Scientific Center of Russian Academy of Science, Rostov-on-Don, Russia

E. Davydov E.O. Paton Electric Welding Institute, Kiev, Ukraine

A. Diniță Petroleum-Gas University of Ploiesti, Ploiești, Romania

R.I. Dmytrienko E.O. Paton Electric Welding Institute, Kiev, Ukraine

Andrei Dumitrescu Petroleum-Gas University of Ploiesti, Ploiești, Romania

Gh. Dumitru Petroleum-Gas University of Ploiesti, Ploiești, Romania

C.M. Dusescu Petroleum-Gas University of Ploiesti, Ploiești, Romania

A. Gopkalo G.S. Pisarenko Institute for Problem of Strength, Ukrainian National Academy of Sciences, Kiev, Ukraine

D.V. Gusakov I.I. Vorovich Institute of Mathematics, Mechanics and Computer Science, Southern Federal University, Rostov-on-Don, Russia

R. Janeliukstis Riga Technical University, Riga, Latvia

V.V. Kozhushko V.A. Belyi Metal Polymer Research Institute of National Academy Science of Belarus, Gomel, Belarus

E. Kudina V.A. Belyi Metal Polymer Research Institute of National Academy of Sciences of Belarus, Gomel, Belarus

I. Lambrescu Petroleum-Gas University of Ploiesti, Ploiești, Romania

I. Lvov National Technical University, Kharkiv Polytechnical Institute, Kharkiv, Ukraine

A.A. Lyapin Don State Technical University, Rostov-on-Don, Russia; I.I. Vorovich Institute of Mathematics, Mechanics and Computer Science, Southern Federal University, Rostov-on-Don, Russia

A. A. Lyapin Jr. I.I. Vorovich Institute of Mathematics, Mechanics and Computer Sciences, Southern Federal University, Rostov-on-Don, Russia

J. Malachowski Military University of Technology, Warsaw, Poland

O. Marusenko National Technical University, Kharkiv Polytechnic Institute, Kharkiv, Ukraine

M. Mihovski Institute of Mechanics of Bulgarian Academy of Science, Sofia, Bulgaria

Y.N. Mirchev Institute of Mechanics of Bulgarian Academy of Sciences, Sofia, Bulgaria

A.V. Morgunova I.I. Vorovich Mathematics, Mechanics and Computer Sciences Institute, Southern Federal University, Rostov-on-Don, Russia

A.A. Nasedkina I.I. Vorovich Institute of Mathematics Mechanics and Computer Science, Southern Federal University, Rostov-on-Don, Russia

R.D. Nedin I.I. Vorovich Institute of Mathematics, Mechanics and Computer Science, Southern Federal University, Rostov-on-Don, Russia

Giang D.T. Nguen Viet Nam Maritime University, Haiphong, Vietnam

O.L. Paliienko E.O. Paton Electric Welding Institute, Kiev, Ukraine

S.M. Prokopchuk E.O. Paton Electric Welding Institute, Kiev, Ukraine

I. Ramadan Petroleum-Gas University of Ploiesti, Ploiești, Romania

S. Rucevskis Riga Technical University, Riga, Latvia

V.P. Sergienko V.A. Belyi Metal Polymer Research Institute of National Academy of Sciences of Belarus, Gomel, Belarus

- Y.Y. Shatilov** Don State Technical University, Rostov-on-Don, Russia
- A.L. Shekero** E.O. Paton Electric Welding Institute of NASU, Kiev, Ukraine
- A.S. Skaliukh** I.I. Vorovich Institute of Mathematics Mechanics and Computer Science, Southern Federal University, Rostov-on-Don, Russia
- A.N. Soloviev** Don State Technical University, Rostov-on-Don, Russia; I.I. Vorovich Institute of Mathematics, Mechanics and Computer Science, Southern Federal University, Rostov-on-Don, Russia
- M.A. Sumbatyan** I.I. Vorovich Institute of Mathematics, Mechanics and Computer Science, Southern Federal University, Rostov-on-Don, Russia
- A.E. Tarasov** I.I. Vorovich Institute of Mathematics, Mechanics and Computer Science, Southern Federal University, Rostov-on-Don, Russia
- A. Tatarinov** Riga Technical University, Riga, Latvia
- P.V. Vasiliev** Don State Technical University, Rostov-on-Don, Russia
- M. Wesolowski** Riga Technical University, Riga, Latvia
- P. Yukhymets** E.O. Paton Electric Welding Institute, Ukrainian National Academy of Sciences, Kiev, Ukraine
- Gh. Zecheru** Petroleum-Gas University of Ploiesti, Ploiești, Romania

Part I
Non-destructive Testing of Transmission
Pipelines

Long-Range Ultrasonic and Phased Array Technologies

Y.N. Mirchev, A.R. Alexiev, A.L. Shekero and S.N. Bukharov

Abstract Extensive knowledge is required for proper use of phased array technology with long-range ultrasonic technique (LRUT) and subsequent interpretation of the results in connection with the study of the interaction of low-frequency ultrasonic waves with discontinuities in pipelines. This chapter presents the basic operation principles of the phased array technology, as well as physical processes of spreading of low-frequency ultrasonic waves in pipes. An attempt is performed at summarizing the advantages and shortcomings of pipelines' control with low-frequency ultrasonic waves, using phased array technology. Advantages, shortcomings, applications, and limitations of the method are present. Sensitivity of the method is analyzed to discontinuity and constituents of the pipeline.

Keywords Long-range ultrasonic technique (LRUT) · Phased array technology · Active/synthetic focusing · Longitudinal/torsional modes · Flexural mode · Dispersion curves

1 Introduction

Seventy percent of the total volume of the control in the petrochemical industry plants are the pipelines. A major problem is corrosion under insulation of pipelines, used to transport oil and chemical products. To ensure the safe operation of pipelines in service is necessary to give them an assessment of their condition.

Y.N. Mirchev (✉) · A.R. Alexiev
Institute of Mechanics of Bulgarian Academy of Science, Sofia, Bulgaria
e-mail: mirchev@imbm.bas.bg

A.L. Shekero
E.O. Paton Electric Welding Institute of NASU, Kiev, Ukraine

S.N. Bukharov
V.A. Belyi Metal Polymer Research Institute of National
Academy Science of Belarus, Gomel, Belarus

According to the results of the assessment is passed on to repair the pipeline with new technologies and materials, in order to increase the time for safe operation.

Primary data are necessary to assess the condition of the pipeline in operation, from which the basic is information about deviations from documented requirements for wall thickness (volume surface discontinuities). A basic requirement for reducing the risk of accidents is tracking the wall thickness of the pipeline at 100% of its volume, for the possible shortest time. Providing these requirements for audit, integrity of pipelines requires globally in recent years, the application of low-frequency ultrasonic waves, using phased array technology. Besides, in spite of its profitability, the method is preferable to other methods of pipelines' control, because it possesses more development opportunities. With its application, processes and subsequent processing were developed from the recorded signals by phased array technology [1, 2] and the use of technology to actively focusing of the emitted signal in a specific area of testing pipeline [3]. Its use, together with developed techniques, requires considerable knowledge of the operating principle of phased arrays and clarity of the results, obtained in the form of two-dimensional images.

2 Application of Phased Array Technology to Control Pipelines with Long-Range Ultrasound Technique

The application of this method is carried out with waves of Lamb, taking into account the peculiarities of their spreading at possible longest distances in the pipe material.

The development of this method is possible, since about 10 years ago with the development of phased array technology and the use of new materials for the production of sensors [4]. The wave propagation at a longer distance into the tube material is achieved using a phased array antenna technology with sensors operating at low frequencies.

In practice, a significant portion of the manufactured equipment emits and receives the ultrasonic waves with piezo-elements, using echo pulse method and operating on the frequency range of 10–100 kHz. The use of this frequency range facilitates the contactless transmission of ultrasonic waves from the probes in the material, and vice versa, by applying a certain pressure between them. Probes are installed in the array in the form of a ring, which is controlled by multiplexer with software and a laptop computer to display the results of controls in the A-scan and 2D-images in type of C-scan (top view). The number of probes in the phased array is determined so that the Nyquist criterion is met for the corresponding pipeline diameter. Part of the elements work, as emitting simultaneously and are grouped in separate channels of the ultrasound systems.

Emitted ultrasonic waves propagate in both directions of the phased array, along the pipe length. The waves reflect from the pipe end, the welded joints,

and variations of the thickness of the tube wall. Changing the thickness must be big enough to be able to adopt a reflected signal from this region, which is bigger than the noises. Assessment of the signals does not perform by the method of conventional dimensions, but by relative change of the reflecting surface with respect to the wall thickness of the pipe.

The control scope is determined by artificial reflector, located at a distance, where the screen registers reflected signal. During the control, antenna array is moved twice a defined control scope with a little overlap. Depending on many factors, such as diameter and thickness of the tube wall, the tube material and the frequency of the wave control range can reach up to 50 m. For torsional mode T(0, 1), orientation values of the control range are present in Table 1, depending on the pipeline condition.

Minimum number of channels accepted in practice for optimum performance of ultrasound system is equal to 8. An exemplary embodiment of the circuit with grouping of elements in the channels is shown in Fig. 1 [5]. Probes of each channel form a virtual aperture of the antenna array, that according to their excitation emit different in shape and amplitude ultrasound field. All virtual apertures of the antenna array work in a given sequence or simultaneously to achieve different shapes and sizes of spread fields in a desired area of the controlled pipeline.

The active focusing of an antenna array is implemented with electronic delay of each separate element in the separate virtual aperture of phased array antenna. The active focusing allows the increase of the ability of reliable assessment of the damage, achieving a concentration of energy of emitted ultrasonic field in a specific area of the controlled pipeline, to obtain a better sensitivity of the useful to noise signal. Once determined the distance from the antenna array to a desired area, for control in the pipeline focuses the emitted beam of each virtual aperture along the circumference of the tube and assayed conduit section for each separate virtual aperture. This sets the virtual amount of change in the section of pipe in its lap.

Table 1 Typical test range for different test pipe configuration

Test condition	Typical range of test (m)
Clean, straight pipe	50–182
Clean, wool insulated pipe	40–175
Minor corrosion	20–50
Significant corrosion	15–30
Kevlar wrapped	30–182
Spun epoxy coating	30–50
Well-packed earth	15–30
Thin, hard bitumen tape of 2.5 mm	5–25
Thick, soft bitumen tape >2.5 mm	2–8
Well-bounded concrete wall	1–2
Grout-lined pipe	10–30
Loosely bonded concrete wall	2–8

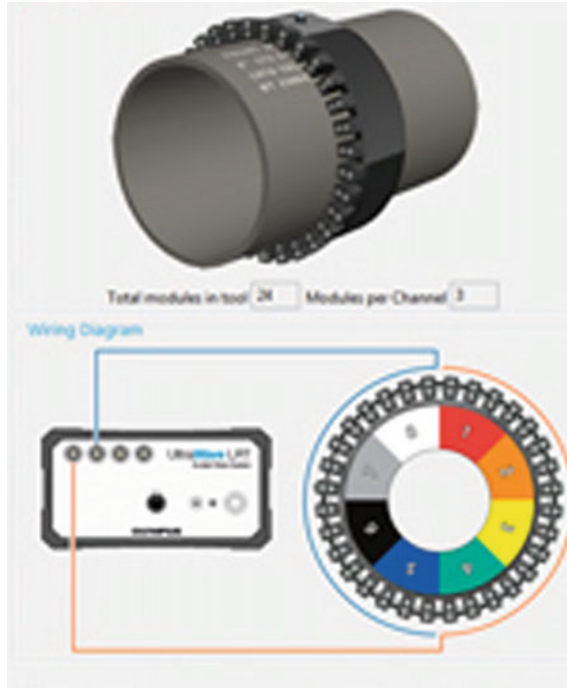


Fig. 1 Antenna array with eight channel

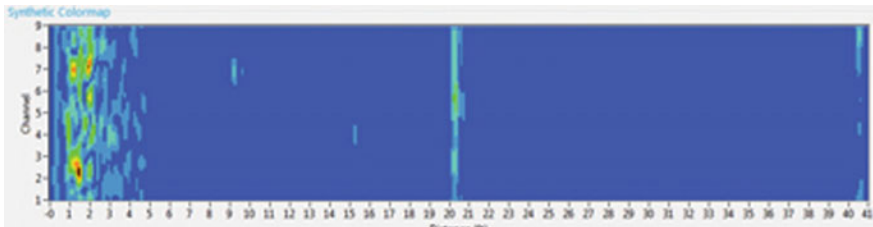


Fig. 2 Synthetic focusing aperture technique provides an unrolled pipe view (C-scan)

Synthetic focusing is a program for post-processing of the received data signal. This treatment is applied after being held control of the collected data and additional analysis is conducted and presented in the form of a virtual picture of the extended pipeline with two-dimensional C-scan image, shown in Fig. 2 [5]. It is obtained from the phase velocity of the accepted mode and is held on single working frequency. The most used synthetic focusing methods are common source method (CSM), synthetic aperture focusing technique (SAFT) [1], and total focusing method (TFM) [2].

3 Pipe Types Modes and Dispersion Curves

Existing modes in tube and in plates are almost identical except for low frequencies. The following nomenclature was adopted, recording their $X(n, m)$, to explain the differences in the modes of distributed ultrasonic waves in pipes. Here X represents one of the three types of mode longitudinal L and torsional T axially symmetric or flexural F , axially nonsymmetrical. The value of the symbol n represents the harmonious movement of the particles with respect to the circumference of the pipe and the figure, presented with m gives serial number of mode, as in Lamb waves in the plate. Axially symmetric modes possess always zero of the symbol n and the flexural not axial symmetrical modes possess different bigger than zero values of that symbol. It is schematically represented in Fig. 3, the difference between the longitudinal axial symmetrical mode and flexural not axially symmetric modes with $n = 1, 2$ and 3.

The longitudinal modes $L(0, m)$ (Fig. 3, left diagram) possess displacements U_r and U_z , without angular displacements U_θ and are similar to Lamb waves in a plate. Modes $L(0, 1)$ and $L(0, 2)$ overlap, respectively modes A_0 and S_0 of waves of Lamb in a plate. Torsion axially symmetrical mode $T(0, m)$ has only angular displacement U_θ and is similar to the horizontally polarized transverse mode SH in plates. Mode $T(0, 1)$ overlaps with mode SH_0 of Lamb waves in a plate. The other group not axially symmetric modes that exist in pipes are flexural modes $F(n, m)$ (Fig. 3, right three schemes). Flexural modes pass into longitudinal L or torsional T modes at higher frequencies. For example, at a higher frequency mode $F(n, 1)$ goes to $L(0, 1)$, $F(n, 2)$ in $T(0, 1)$, and $F(n, 3)$ in $L(0, 2)$. Their motion is along the three components r, z and θ . To illustrate the defined movements in a pipe, geometry is presented in Fig. 4 of a pipe in a cylindrical coordinate system, at which the material particles vibrate together with distributed ultrasonic waves in a pipe for different modes.

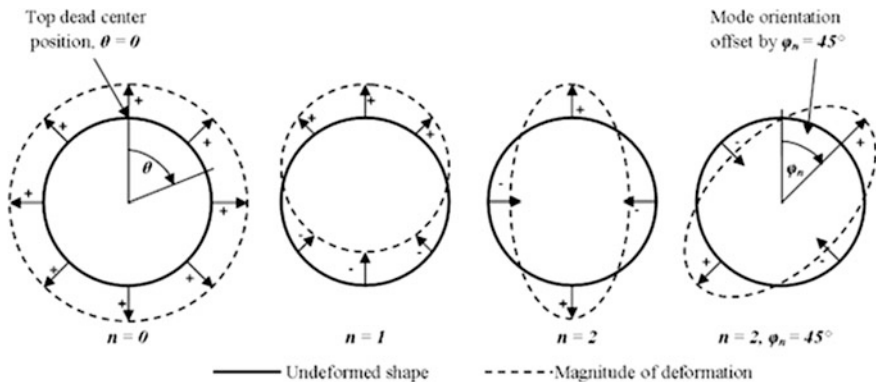


Fig. 3 Pipe deformation depending on n

Dispersion curves are an essential tool for optimum mode and frequency selection to detect discontinuity in the test object. We conducted calculations for a pipe with a diameter of 323 mm and a wall thickness of 9.5 mm steel at speed of longitudinal and transverse wave: $C_l = 5900$ m/s and $C_t = 3260$ m/s, respectively. The results for their phase velocity $C_{ph}(f)$, depending on the frequency are present in Fig. 5 in the form of dispersion curves.

As seen from the dispersion curves, many modes are observed, for which their speed is a function of frequency. This can make interpretation of the monitoring controlled results quite complicated. That is why, it is important for pipeline with known geometric dimensions must be selected properly probes, their location on the pipe and the control scheme. The objective of the work, presented in this paper, is getting a stable signal (A-scan) that can be interpreted correctly by choosing the mode from the dispersion curves in the frequency range of operation of the probes. It corresponds to the following requirements: (i) ultrasonic waves propagate with only one single mode in the testing volume; (ii) this mode has as little as possible dispersion and (iii) there is a focus of ultrasonic waves in a desired direction of controlled volume. All mentioned requirements meet the fundamental torsional

Fig. 4 Geometry of pipe in cylindrical coordinates

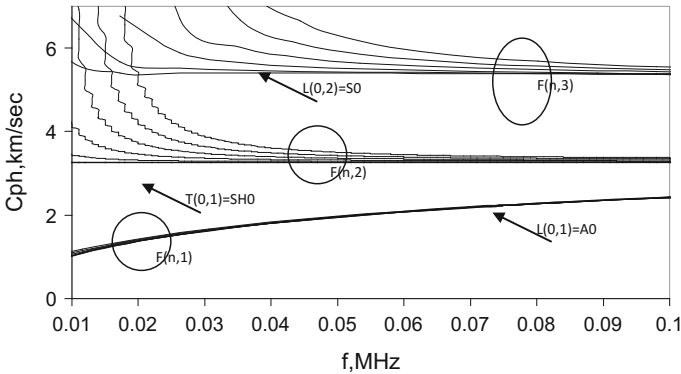
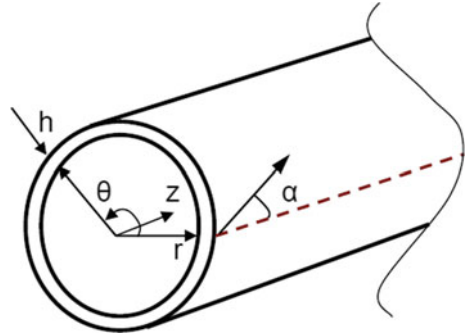


Fig. 5 Dispersion curves for phase velocity in pipe

mode $T(0, 1)$, which has been used recently most often for pipelines testing. It propagates without dispersion of speed from frequency, is axisymmetric, that makes it easy for excitation and reception. Another advantage of this mode is that it is not affected by the presence of liquid from any part of the tube wall. Maintaining excitation bandwidth of mode $T(0, 1)$, less than that of $T(0, 2)$, makes relatively easy the emission of a single mode $T(0, 1)$.

4 Method Application and Restriction

The main application of the method is to control the pipelines. There are number of European projects, performed in recent years with the aim to improve the technology at controlling equipments of industry, including in this number the pipelines, as LRUCM [6], INNOPIPES [7], SHIPINSPECTOR [8], MONITORAIL [9], and others. Improvement of the method aims for application in shipbuilding and ship maintenance for control of large sheets of liner shipping, in railway infrastructure at the control of rails, in energetic at controlling heat exchangers, in construction at control of lighting columns and bridge ropes.

LRUT represents a new rapid screening tool for pipelines. It can examine large volumes of material from a single location for short time and therefore, has the following benefits: (i) reduction in the costs of gaining access to the pipes for inspection; (ii) avoidance of removal and reinstatement of insulation or coatings (where present), except for the area on which the transducers are mounted; (iii) the ability to inspect inaccessible areas, such as at clamps and sleeved or buried pipes; (iv) the whole pipe wall is tested, thereby achieving a 100% examination. A shortcoming of the method is reduced sensitivity to small changes in the thickness and probability of their detection is smaller as compared with the conventional approaches to measuring deviations in the pipe wall thickness.

The limitations of the method are related to the following features of manufacture, installation, and operation of the controlled pipeline: geometry and components, insulation, fluid content in the pipeline, the pipeline status of noise around the pipeline and others. Figure 6 presents the influence of some of the designed peculiarities and exploitation of the pipeline on the distance of the action of the ultrasonic waves along the pipeline [10].

The geometry of the pipeline, when tested with this method significantly affects the distance of the action of ultrasonic waves along the pipeline length. The method is more effective, when the constituent parts of the conduit are at a greater distance from one another. The flanges of the pipeline determine the end of the controlled section. Other components such as valves, elbows, welded supports, and welded sections between the pipes greatly reduce the scope of control along the pipeline length. The greater part of the energy, distributed by ultrasound waves in the pipeline, is reflected by them. More significantly, the reflection from pipe components has torsional according to longitudinal axially symmetrical modes.

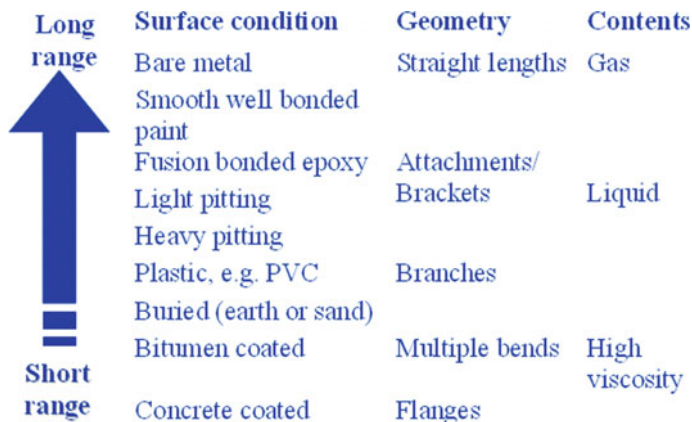


Fig. 6 Pipe configuration influencing on range test

Coverage like bitumen, polyethylene and others is a factor for increasing the attenuation of ultrasonic waves, distributed in such a pipeline. In such a case, it is possible that the converters are used with lower operating frequencies. Another embodiment of the pipeline coating is, when it is hidden under the ground or concrete. Then, ultrasound waves of some modes are passing in soil or in concrete and distributed energy of ultrasound waves is significantly weakened. Contents of gas or viscoelastic fluids in the controlled pipeline do not affect the ultrasonic wave, propagating in it. Viscoelastic fluids or corrosive deposits substantially reduce the size of the scope of the distributed ultrasonic waves in the walls of the conduit. Depending on the polarization of the ultrasound waves, the influence of viscoelastic fluids can be neglected. For this purpose, the mode with transverse polarization of the ultrasound waves is used in the direction of their propagation. Such a mode is torsion axially symmetrical mode $T(0, 1)$.

The noise from the surrounding working machines is usually in the low-frequency range, which operates under control with LRUT. This fact can compromise the test results and obtain false statements about the controlled pipeline. Status of the controlled pipelines also possesses an influence on the size of the length of the sections, controlled by them. State of the pipeline with 10–20% in the wall thickness reduction of the general corrosion significantly reduces the size of the length of the controlled section. When the total corrosion is more pronounced and displayed through the wall thickness of around and above 40%, it is impossible to continue a monitoring the section of the pipeline after the damage, due to the corrosion. In this case, the arrays are placed after the corroded surface of the pipeline in order to continue the control after the corroded area. Depending on the manufacturing specifics, construction and operation of the pipeline, the appropriate working mode and frequency were selected, because the selection took into account the sensitivity of mode orientation, type and size of demanded discontinuities.

5 Method Sensitivity to Discontinuities and to Pipelines Components

The sensitivity of the method to detect changes in the thickness or the integral parts of the pipeline is influenced by the following factors: (i) type, location, and size of reflectors, (ii) transformation of the emitted mode into another type mode after impact, (iii) selection of mode and operating frequency. All reflectors in pipelines can be classified as symmetric and asymmetric. Figure 7 shows classification of types of reflectors in the pipeline. Indicated discontinuities and geometry peculiarities of pipeline structure are the reflectors of ultrasonic guided waves, propagating along pipe centreline.

Welded joints, flanges, supports, branch pipes etc., location of which in the pipeline is known and determined by specification, can be referred to symmetric reflectors. Defective areas of the pipes, caused, as a rule, by damages of pipe wall cross section, due to corrosion and erosive wear of pipe wall, can be referred to the asymmetric ones. Corrosion damages in pipe wall is oriented along the pipe circumference, as well as along pipe longitudinal axis. They can be located on external and internal surfaces, however, cannot be found by results of LRUT. The damages, caused by erosive wear of the pipe wall, orient along the pipe longitudinal axis and located at internal surface. In practice, when tested with low-frequency ultrasonic waves, the corrosive damages with 5–10% of cross-section area (CSA) are detected in respect to CSA of the pipeline, spaced along the axis of the tube from the probe, for tubes with diameters from 50.8 to 609.6 mm [11].

Transformation of the spreading mode after reflection in another type influences the coefficient of reflection, depending on the type, location, and size of the reflectors. The potential transformed modes depend on the degree of asymmetry or the location of the discontinuity, circumferentially of the pipe. For example, if it is spread by axial symmetrical mode and is reflected by axial symmetrical components of the pipeline, then only axially symmetrical modes are reflected. In the other case, when the constituent parts of the pipeline, mounted thereon are not axially

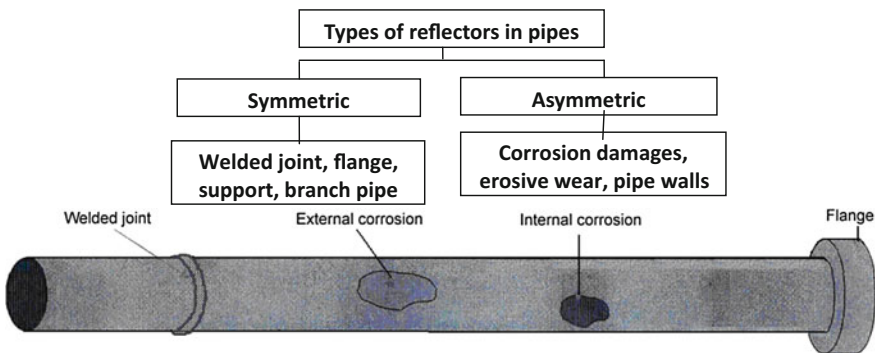


Fig. 7 Classification of reflectors in pipelines

symmetrical and/or there is area along it with developed general corrosion, then they reflect the emitted mode with transformed no axially symmetric flexural modes $F(n, m)$. Echo signals from the symmetric reflectors are reference signals for detection of the asymmetric reflectors.

The most common transformed modes are $F(1, 3)$ and $F(2, 3)$ in emission of mode $L(0, 2)$ and reflected by the no axially symmetric damages, caused by general corrosion. They possess similar ultrasound velocities in the pipeline with mode $L(0, 2)$. Figure 8 presents a coefficient of reflectance of mode $L(0, 2)$ and transformed modes $F(1, 3)$ and $F(2, 3)$ of the reflector of trough notch type, covering a sector of the circumference of a tube with a diameter of 76.2 mm. In the pipe, mode $L(0, 2)$ is emitted on an operating frequency of 70 kHz. The pipeline perimeter is present in % of circumference [12, 13].

The location of discontinuity, circumferentially to the quarter of the circumference of the conduit, gives almost the same amplitude values of the reflected by it modes $L(0, 2)$ and $F(1, 3)$. This fact can be used to conclude that the discontinuity comprises less than $\frac{1}{4}$ the size of the pipeline circumference. The same effect is observed, when working with mode $T(0, 1)$, because here the transformed mode at the reflection is $F(1, 2)$.

The sensitivity of the method to a reflector type notch is a function of frequency, but different from that of Rayleigh attenuation. A study of this function was performed by Demma [14]. Reflection coefficients are for mode $T(0, 1)$ of the initial rectangular notch, along the entire circumference of the pipe diameter $D = 76.2$ mm and wall thickness $t = 5.5$ mm. The axial size of the rectangular notch is not considered. The results are present in Fig. 9.

It is seen in Fig. 9 that with reduction in frequency reduces the coefficient of reflection. The most significant differences of coefficients of reflection for different frequencies at the same depth of the notch are observed for depths 50–80% of the wall thickness. Notch depth less than 10% of the thickness of the wall is almost impossible for registration.

Fig. 8 Reflection coefficient of notch circumferential extend

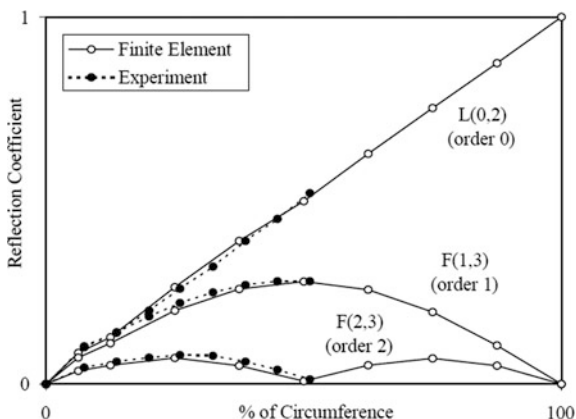
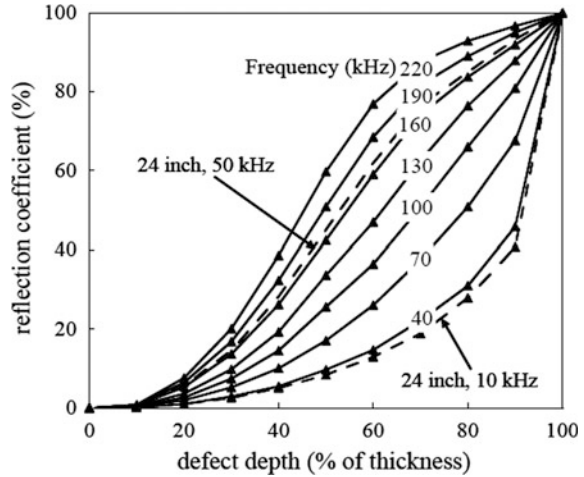


Fig. 9 Reflection coefficient of notch depth



In [14], the coefficient of reflection of mode T(0.1) is investigated for rectangular notch in a tube and it is proved, that it is expected finding out such a reflector with dimensions, corresponding to 2% of the CSA of new, not exploited pipe, when its axial size is approximately 25% of the mode wavelength. The reliability of detection can be enhanced by using focused targeting of the emitted field.

For bigger sensitivity, a higher operating frequency is used, which reduces the range of LRUT testing in the pipeline. For example, for control of the pipeline at a distance up to 5 m in a single placement of the arrays, an ultrasonic system may be used with an operating frequency up to 0.5 MHz and sometimes up to 1 MHz.

6 Conclusion

The possibilities of the method are present for control of pipelines with its advantages and limitations. Criteria are present for choosing an appropriate mode for control with the aim of easier interpretation of the obtained results. A dispersion curve is built up for a pipe with diameter $D = 323$ mm and thickness $t = 9.5$ mm, which are defined according to a given criteria for the most appropriate mode for control T(0, 1). The similarity of pipe modes is analyzed with modes of Lamb waves in the plate.

An approach to classify types of reflectors is present. The classified reflectors are used to explain the transformation of mode after reflection from them. The influence of the transformation on the sensitivity of the method is present by a coefficient of reflection from trough rectangular notch of the mode $L(0, 2)$. Coefficients of reflectance of the transformed modes $F(1, 3)$ and $F(2, 3)$ are substantially smaller than that of mode $L(0, 2)$ for a reflector trough notch with more than 50% CSA. When CSA is near 100%, the coefficient of reflection of the transformed modes tends to zero, which means, that there is no transformation of the emitted mode.

The frequency dependence coefficient of reflection of a rectangular notch around the circumference of the pipe of torsional mode $T(0, 1)$, indicates, that reliably can be recorded a signal from the notch with a depth of more than 10% of the wall thickness of the pipe. At the notch depth of 50–80% of the wall thickness, the differences in the coefficient of reflection increase at a same depth on the wall and different frequencies.

References

1. J. Davies, F. Simonetti, M. Lowe, P. Cawley, Review of synthetically focused guided wave imaging techniques with application to defect sizing, in *Review of Progress in Quantitative NDE*, vol. 25, ed. by D.O. Thompson, D.E. Chimenti (American Institute of Physics, Melville, New York, 2006), p. 142
2. C. Holmes, B. Drinkwater, P. Wilcox, Post-processing of the full matrix of ultrasonic transmit–receive array data for non-destructive evaluation. *NDT E Int.* **38**(8), 701 (2005)
3. J. Li, J.L. Rose, Natural Beam focusing of non-axisymmetric guided waves in large-diameter pipes. *Ultrasonics* **44**, 35 (2006)
4. P. Jackson, P. Mudge, I. Daniel, Pipeline Corrosion Control: a historical perspective and a guided wave approach to the future. in *Proceeding of the 2nd South-East European IIV International Congress Welding, High-tech Technology in 21st Century, Pipeline Welding: Current Topic of the Region Sofia*, Bulgaria, 21–24 Oct 2010, 118
5. <http://www.olympus-ims.com/en/ultrawave/>. UltraWave LRT, OLYMPUS
6. http://cordis.europa.eu/result/rcn/52049_en.html. project LRUCM
7. http://cordis.europa.eu/project/rcn/104754_en.html. project INNOPIPES
8. http://cordis.europa.eu/result/rcn/58383_en.html. project SHIPINSPECTOR
9. http://cordis.europa.eu/publication/rcn/16190_en.html. project MONITRAIL
10. J. Heerings, N. Trimbom, A. den Herder, Inspection effectiveness and its effect on the integrity of pipework, in *9th European Conference NDT*, www.ndt.net. e-Journal & Exhibition of Nondestructive Testing, Berlin, Germany, Sept 2006
11. P. Cawley, M.J.S. Lowe, F. Simonetti, C. Chevalier, A.G. Roosenbrand, The variation of the reflection coefficient of extensional guided waves in pipes from defects as a function of defect depth, axial extent, circumferential extent and frequency. *Proc. Inst. Mech. Eng. Part C J. Mech. Eng. Sci.* **43**, 216 (2002)
12. M.J.S. Lowe, D.N. Alleyne, P. Cawley, The mode conversion of a guided wave by a part circumferential notch in a pipe. *ASME J. Appl. Mech.* **65**, 649 (1998)
13. D.N. Alleyne, M.J.S. Lowe, P. Cawley, The reflection of guided waves from circumferential notches in pipes. *ASME J. Appl. Mech.* **65**, 635 (1998)
14. A. Demma, P. Cawley, M.J.S. Lowe, A.G. Roosenbrand, B. Pavlakovic, The reflection of guided waves from notches in pipes: a guide for interpreting corrosion measurements. *NDT E Int.* **37**, 167 (2004)

T- and L-Types of Long-Range Guided Waves for Defect Detection

A. Tatarinov, Evgeny N. Barkanov, E. Davydov and M. Mihovski

Abstract Despite technical advancement and wide industrial application, long-range ultrasonic testing (LRUT) has several bottlenecks, which restrict its abilities and complicate the data interpretation. Particularly, these are related to simultaneous presence along with the main used torsional wave (T-wave) of other wave modes, including longitudinal (L-wave) and flexural (F-wave) ones. The latter are considered as unwanted components, but on the other hand could be a source of additional useful information. The purpose of this study was to use small-scaled models of pipes with simulated defects of different kind to demonstrate some possibilities of signals contrasting for a selected wave mode and sensitivity of T- and L-waves in assessment of these defects. Ultrasonic testing was performed by a specially designed laboratory setup, comprising a data acquisition unit with a waveform generator and an amplifier/digitizer circuitry allowing switching in turn between several transducers pairs. An array of magnetostrictive transducers located stepwise along tubes was arranged, where switching between T- and L-wave excitation modalities was done by changing orientation of the static magnetic field. Experiments were done on thin-walled tubes with diameters of 10 and 45 mm, applying ultrasonic tone-burst pulses with carrying frequency of 125 kHz. Contrast of echo responses from defects for switched in turn T- or L-waves was enhanced by signals processing based on time-shifting of signals from several distantly located transducers along the tube to known time delays for the certain type of wave and further multiplication of the signals amplitudes. The demonstrated efficiency of the approach was in discerning of small defects on the background of parasite components and improved contrasting of large defects. Modeling of several types of defects such as pitting, crevice, and stress corrosion was done by means of mechanical tools. The study showed that different responsiveness of T- and

A. Tatarinov (✉) · E.N. Barkanov
Riga Technical University, Riga, Latvia
e-mail: alta2003@apollo.lv

E. Davydov
E.O. Paton Electric Welding Institute, Kiev, Ukraine

M. Mihovski
Institute of Mechanics of Bulgarian Academy of Science, Sofia, Bulgaria

L-waves to these defects could be a basis for combined use of both modes to characterize the type of defect, depth of penetration through the tube's wall, and expansion along the length. Comparison of T-wave and L-wave responses in the same tube filled by air and water showed that liquid filling not only increased attenuation of the both propagating waves, but also caused significant transformation of echo pattern of L-wave having dispersive nature, while T-wave was more stable. Thus, use of L-wave in LRUT should account for pipes filling by liquid contents.

Keywords Long-range ultrasonic testing (LRUT) · Torsional wave (T-wave) · Longitudinal wave (L-wave) · Corrosion · Modeling · Magnetostrictive transducers

1 Introduction

Application of guided waves in long-range ultrasonic testing (LRUT) of pipelines has a several decade history of research and commercial implementation. From early works in 1970–1990s [1–3], interest to the subject grew and resulted in numerous research papers devoted to theoretical foundation and demonstration of feasibility of the technology [4–7]. The advanced LRUT techniques provided by such manufacturers as Guide Wave Analysis, Guided Ultrasonics Limited, Olympus, Plant Integrity, and others found application in oil and gas industry, as well as in other branches for structural health monitoring of main and technological pipes. Recently issued International Standard ISO 18211:2016 “Nondestructive testing—Long-range inspection of above-ground pipelines and plant piping using guided wave testing with axial propagation” sets definitions and standards for LRUT instrumentation, data collection, and interpretation [8].

In contrast to traditional ultrasonic flaw detection using bulk waves at megahertz frequencies and testing regions in the close vicinity to transducers, LRUT operates with low frequency guided waves, typically in the 30–200 kHz range, traveling long distances along a pipe as a waveguide without sufficient loss of energy. Diagnostic ranges of commercial systems are estimated by tens and even hundreds of meters depending on conditions. Pulse-echo responses from all targets on the way are collected, including reflections from small defects that may be quite weak. The important peculiarity of LRUT is its ability to sense defects that are much smaller (in best resolution cases from 1 to 3% of the pipe's cross-section) than the ultrasonic wavelength, which much exceeds the thickness of pipe's wall and is comparable or even exceeds the pipe's diameter.

Basically, three types of waves propagate in pipes as prolonged hollow thin-walled cylinders: longitudinal (L-wave), torsional (T-wave), and flexural (F-wave), shown schematically in Fig. 1. Although many acoustical modes of different orders are possible, in reality only a few of them are observed in practice.

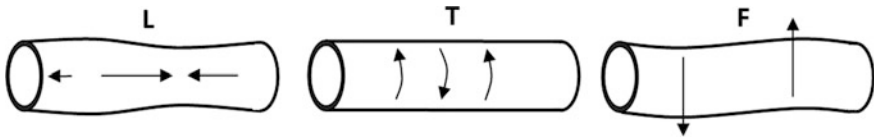


Fig. 1 Schematic illustration of longitudinal (L), torsional (T), and flexural (F) waves in pipes

L-wave or $L(0, 1)$ mode is the fastest wave having similarity to the zero-symmetric Lamb wave S_0 in plates and axisymmetric waves in rods [9]. It is a highly dispersive wave with a strong dependence of the velocity on frequency. T-wave, $T(0, 1)$ mode has the shear origin and its velocity is the same as of the shear wave SH_0 . It has no geometric dispersion, i.e., its velocity is invariant of frequency at any geometrical parameters of a pipe. It is the main advantage of T-wave in LRUT, since its pulses being short and not spreading by distance provide the best axial resolution. Moreover, because of the constancy of T-wave's velocity in pipes made of a certain metal, the distance scale is unambiguously established from the time scale allowing localization of a target along the pipe. F-wave may exist in the form of $F(1, 1)$ mode, which velocity is lower than that of T-wave and depends on the relation of its geometrical parameters to ultrasonic wavelength. Its analogs are flexural or non-axisymmetric waves in rods. This wave is not commonly used in LRUT due to a very dispersive character and a lower sensitivity; however, it is present in echograms as an unwanted component. Dispersion curves for phase and group velocities of different modes of L-, T-, and F-waves are calculated analytically for pipes of a known diameter, wall thickness, and material type. Some examples of such dispersion curves for description of certain pipes are present in the related works [10, 11].

Since its first introduction, the LRUT technology achieved significant progress [12]. Particularly, the achievements included: (i) understanding T- and L-waves, ability of choosing the wave modes and use them at different frequencies to obtain information about the size of a defect; (ii) reducing the size of a detected defect to 3–5% of the pipe's cross-section area; and (iii) introduction of focusing by the length that allowed circumferential location of defects at middle range distances.

At the same time, diagnostic capabilities of LRUT are limited by a number of factors, part of which are hardly overcome due physical reasons and another part represent technical challenges. These factors comprise: (i) sharp damping of ultrasonic signals in pipes buried in sand [13], insulated by plastics and immured in concrete that dramatically reduces the diagnostic range; (ii) energy absorption in fluid filled pipes leading to the same consequences [14]; (iii) difficulty of results interpretation due to multimode propagation and mode conversion at reflection targets (welds, defects) causing false detections; insufficient axial and lateral resolution; (iv) presence of a dead zone; (v) poor ability for detection after the first large target due to signal damping accompanied by the modes conversion and (vi) poor recognition of small pitting defects that impose a serious risk of pipe failure. The testing hardware still remains heavy and complicated requiring labor and time for installation.

The above-mentioned suggests that there is still a room for further improvement of the technology. The purpose of the presented study was to conduct a series of laboratory experiments on small-scaled models of pipes introducing an array of circumferential transducers along the length of a tube. The aims were to demonstrate enhancement of contrast in detection of small defects using a plurality of signals from the array allowing elimination of unwanted modes and to show differences in responses of T- and L-waves from defects of different types. Effect of water filling was also shown.

2 Experimental Setup

To conduct modeling experiments on a smaller scale, a laboratory ultrasonic measurement setup schematically shown in Fig. 2 was constructed. An ultrasonic data acquisition unit comprised a programmable waveform generator with an output amplification circuitry, an input amplifier-digitizer circuitry, and a microprocessor managing data transfer to a computer for processing. Experiments were performed on duralumin tubes with diameters of 10 and 45 mm and wall thicknesses of 1 and 2 mm, respectively, in which defects of different types were simulated artificially by means of mechanical tools. Total lengths of the tubes were 2.5–3 m, corresponding to several dozen of feet in pipes with the natural scale, if to consider the length-to-diameter ratios. Accordingly, the applied ultrasonic wavelengths, time ranges for signals recording, and sizes of ultrasonic transducers were scaled proportionally.

To have a possibility of the selection between the shear and longitudinal acoustic modes purposefully, the magnetostriction principle of ultrasound generating and

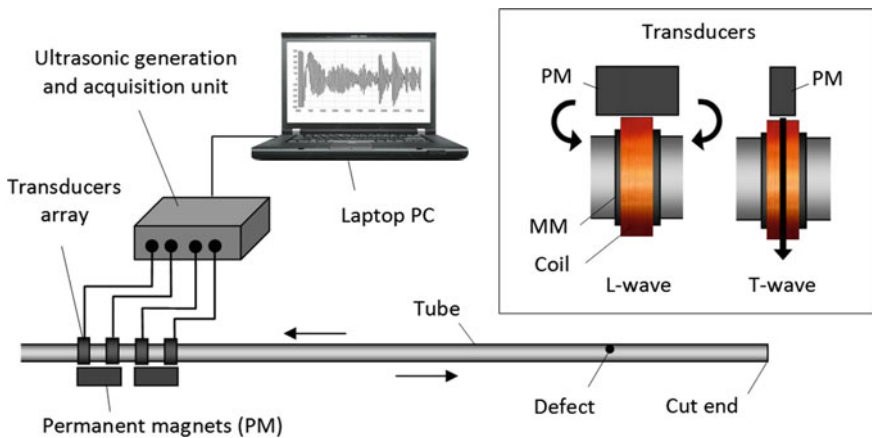


Fig. 2 Experimental setup and layout of transducers arrangement for excitation of L- and T-waves. *MM* Magnetostrictive metal; *thick arrows* show orientation of static magnetic field

receiving was applied. The method called as EMAT (electromagnetic acoustic transducer) is routinely applied in LRUT as an alternative to the piezoelectric transducers arrays and featured by relative simplicity, lightweight and cost efficiency of the transducer's part [15, 16]. Joule–Villary and Wiedemann effects are utilized to generate respectively longitudinal and torsional waves in tubes. In the first case, the vector of electromagnetic induction of time alternating or oscillating magnetic field is orientated parallel to the same of static magnetic field applied to the magnetostrictive material. In the second case, the vectors of alternating and static magnetic fields are orientated perpendicularly to each other. As the testing tubes in experiments were not ferromagnetic to provide actions of EMAT by itself, 7 mm wide strips of magnetostrictive materials—permenedur (iron and cobalt alloy) and nickel were stiffly glued around the tubes by epoxy. The alternating magnetic field was induced in copper wire coils with number of turns 40 wound over the magnetostrictive strips. The static magnetic field was applied by permanent ferrite magnets of rectangular shape sizes $15 \times 10 \times 5 \text{ mm}^3$ put over the coils parallel or perpendicularly to the wire wound, depending on the desirable wave mode, and held by the magnetic force. Four magnetostrictive transducers were arranged along the tube with a step of 25 mm.

Ultrasonic signals were excited by electrical tone-burst pulses applied to the coils. The waveforms were 2-period of sine at a frequency of 125 kHz enveloped by Gauss function and amplified to a voltage of 140 V peak to peak. The acquisition parameters for received signals were as follows: sampling rate of 30 Msps, dynamic range of 10-bit, time frame of 30 ks or about 1 ms in time scale. To acquire signals from different pairs of transducers, the pairs were switched correspondingly. The technical problems to overcome were, first, a low level of signals caused by much weaker ultrasonic outcome of magnetostrictive transducers than of piezoceramic ones and noisiness of acquired signals due to external electromagnetic interferences. The first problem was solved by application of an additional 40 dB preamplifier and electrical matching of the transducers by series connection of capacitors in the excitation and receiving circuits in order to reach resonances in the electrical oscillatory circuits at the applied ultrasonic frequency. To eliminate signals noisiness, the transducers were shielded by grounded foil housings and signals averaging at 256 times.

To observe acoustic modes propagating in the tube at two orientations of the permanent magnet and to determine its velocities, axial profiling by an external piezoelectric transducer with the same work frequency of 125 kHz was undertaken. The coupling was semi-solid plasticine mass permitting reception of both compression and shear oscillations. The resulting hodographs in Fig. 3 show simultaneous presence of all three wave modes—longitudinal (L-wave), torsional (T-wave) and flexural (F-wave) at the both excitation modalities. However, turning of the permanent magnet orientation from L-wave to T-wave helped the relative exaggeration of the torsional mode on the background of other modes. The hodographs demonstrate evidently the lowest dispersion of T-wave signals and no virtual spreading by the distance that beneficially differs from L- and F-waves. The approximate estimates of ultrasound velocities, determined by the hodographs, were

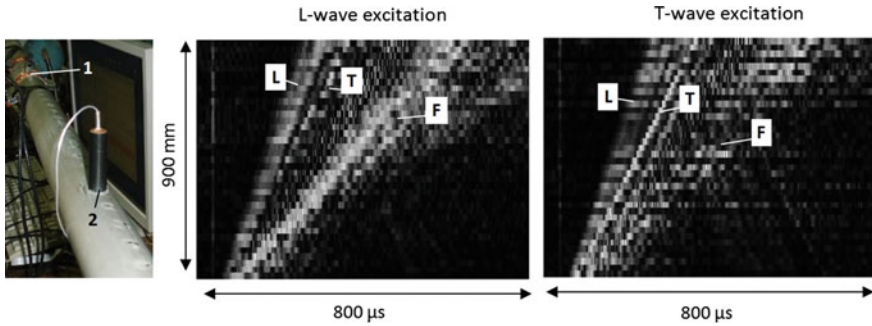


Fig. 3 Ultrasonic profiling of tube: 1 fixed magnetostrictive transducer; 2 piezoelectric receiver traveling stepwise along tube (*left picture*) and time–distance graphs showing hodographs of *L*-, *T*-, and *F*- wave modes at *L*- and *T*-wave excitation modalities

4900 m/s for L-wave, 3150 m/s for T-wave, and 1950 m/s for F-wave. The value for T-wave corresponded well to the known tabulated values for the duralumin, while values for L-wave (lower than the bulk longitudinal velocity in duralumin 6400 m/s) and F-wave were determined by the material and geometrical parameters of the tube and influenced by the geometrical dispersion effects.

3 Enhancement of Contrast in Detection of Small Defects

Enhancement of contrast of helpful pulse-echo signals on the background of parasite signals is important to discern small defects and improve data interpretation. Parasite signals relate to accompanying acoustic modes, for example, L- and F-waves when tested in T-mode. The accompanying modes can occur due to mode conversion upon the reflection of T-wave from a certain target or multiple targets in a pipe. The parasite signals propagate at different velocities resulting in a complex interference pattern of the echo response. The most confusing case is the interference between the helpful signal from a small defect with the parasite wave signal from a larger target (weld, edge, support, another defect) having a larger amplitude. The main advantage of T-wave is absence of dispersion and ability to propagate over long distances without spreading that provides the best resolution of detection. However, due to the fact that T-wave velocity being equal to the same of shear wave is about twice lower than that of the L-wave, the first arriving parasite L-wave can mask the later arriving T-wave. Despite success in designing of special ultrasonic arrays for prevailing generation of T-waves, the problem of wave modes conversion at a target remains in effect.

Mathematical processing of several received signals from an array of transducers set at some distance along the pipe is a possible approach to enhance signals propagating only with a known velocity in one direction and scatter all other

signals. Processing of a combination of signals recorded by an array of transducers along a tube included application of corresponding time offsets and further multiplication of the amplitudes. The multiplication procedure was adopted to get equal contributions from all transducer pairs. Algebraic summation would not be appropriate because dissimilarity of bonding and damping of signals passed under glued sensors caused sharp differences of the signal amplitudes in different pairs requiring complicated normalizing. The processing algorithm is presented in Fig. 4. Raw signals from six possible combinations of transducers (including three pairs, two alternating input, and output variants) were recorded and digitized. Time offset or bringing all signals to a common start time applied delays of T-wave propagation between the pairs. The velocity was experimentally predetermined as 3150 m/s corresponding to the shear velocity in duralumin. The differences in distances between pairs were 0, 25, and 50 mm that corresponded to 0, 8, and 16 μs in time domain. Taking into account that the wave period at 125 kHz was 8 μs , the signal offsets were comparable and larger than the wavelength. Region of interest was determined in time scale in order to avoid residuals of excitation and unwanted components from farer zones. Amplitudes of 6 time-shifted signals in the region of interest were multiplied. The resulting signal or the product of multiplication was rectified, enveloped by a linear smoothening and displayed. The same procedure was performed also for L-mode applying the corresponding time offsets.

The test object was a 2.5 m duralumin tube with OD = 10 mm, ID = 8 mm, and wall thickness of 1 mm. The array of four transducers was placed approximately in the middle. Two defects simulating pitting corrosion were compared: (i) small defect—a single 0.9 mm diameter through hole in the wall (about 3% of the cross-section area) and (ii) large defects—8 symmetric holes of the same diameter distributed upon the same cross-section (about 24% of the area). The tube's cut end was taken as the reference reflection. The distances from the transducer's array to the defects and the tube's end cut were 92.5 and 105 cm.

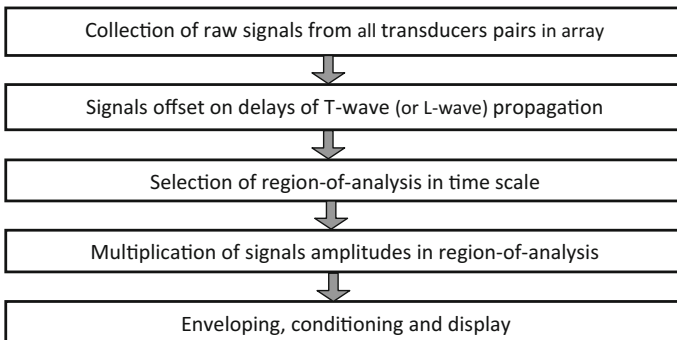


Fig. 4 Diagram of signals processing

Examples of raw signals from an individual transducer pairs and processed echo signals from the plurality of all pairs in the array for T- and L-waves in small and large defects are present in left plots in Figs. 5 and 6. Since the tested length of tube was rather short, echograms obtained by individual pairs of transducers are densely saturated by many interfering signals, where it is difficult to discern separate echo components and understand its origin. Obviously, these are reflections from the both tube's cut ends, defects, and transducers themselves traveling back and forth

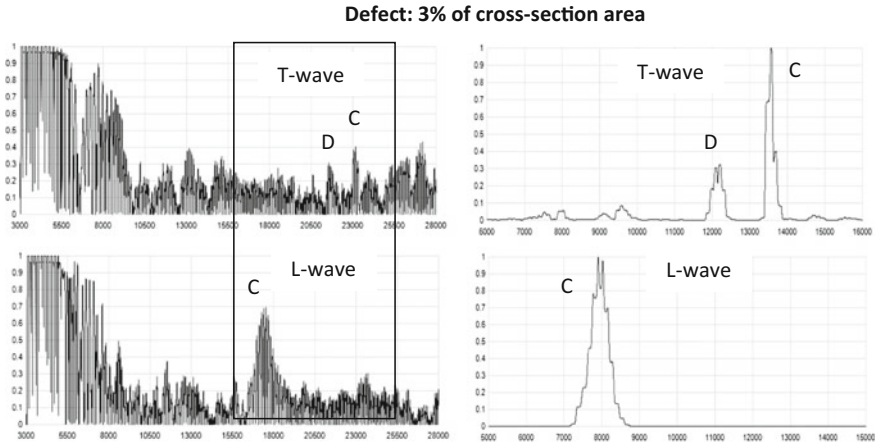


Fig. 5 T- and L-wave responses in the case of small defect (3% of cross-section): *left plots* represent examples of raw signals from a single transducers pairs; *right plots* represent processed signals from all array of transducers in the selected region of analysis marked by rectangle: *D* and *C* are echo peaks from defect and tube's cut end

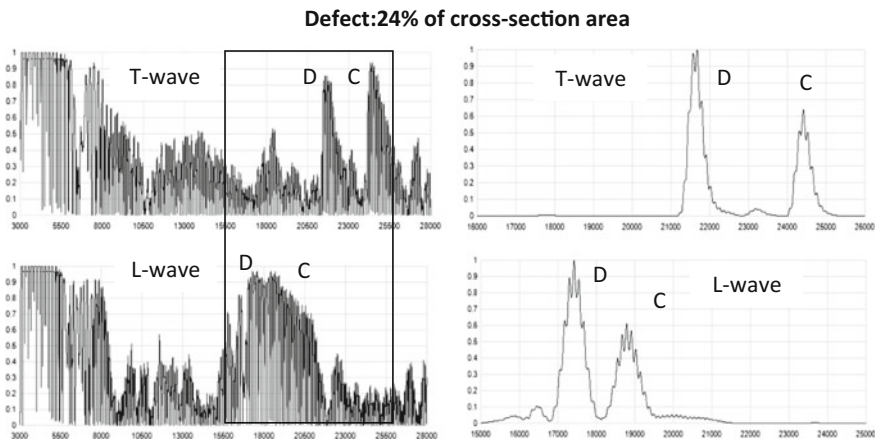


Fig. 6 T- and L-wave responses in the case of large defect (24% of cross-section); indications are the same as in Fig. 5

the tube with different velocities due to relation to different acoustic modes. Locations of responses from defect and tube’s end cut can be predicted by real knowledge of the distances and T- and L-waves’ velocity. In the case of the large defect, the echo response from it is quite pronounced and the defect can be detected simply by applying a threshold exceeding the average noise level in the region of analysis. However, it is problematic for revealing the small single defect, the response from which is within the average level of acoustic noise and is masked by the latter.

The resulting signals after processing all combinations in the array are present in right plots of Figs. 5 and 6. The amplitudes were normalized by the maximum in the region of analysis. The processing really exaggerated propagation of the helpful signals in selected testing modality and damped all other modes. The reflections from the defect and tube’s cut end increased substantially and dominated over parasite modes and reflections coming from the opposite direction along the tube. In the case of small defect, the weak reflection of T-wave from the single defect became prominent on the background, but smaller than reflection of from the tube’s end cut. In the case of the large multiple-hole defect, the T-wave reflection from the defect dominated over reflection from the tube’s end cut and became absolute over completely suppressed parasite signals. The similar effects were observed for L-wave with the difference that echo pulses of L-wave were more diffuse. In the case of small defect, no L-wave reflection from the defect was observed, while the same of T-wave was quite notable. A defect area of 3% of the cross-section is usually considered as a cut point of resolution for LRUT systems in its real application. The applied processing approach showed an opportunity to lower the resolution threshold in certain cases. Comparison of T- and L-wave responses from a defect may help understanding its size.

Visual comparison of raw and processed signals is shown in Fig. 7 as B-scans, where a line corresponds to a signal in the time scale and brightness codes the amplitude. All signals are present at the same settings of signals conditioning and

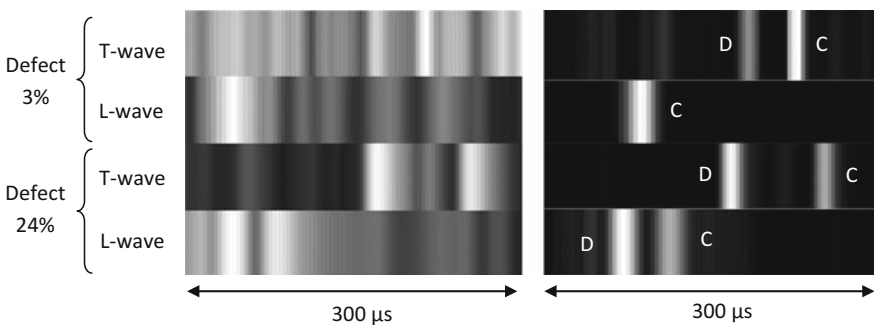


Fig. 7 B-scan presentation of T- and L-wave responses comparing raw (*left*) and processed (*right*) signals in the same region of analysis and at the same contrast of imaging: *D* and *C* are echoes from defect and cut end

imaging contrasting. In raw signals, only the large multiple-hole defect can be surely detected, while the response from small single-hole defect is masked by parasite signals. In the processed signals, only helpful information remained that are responses from small and large defects and the tube's end cut. In the current study, the problem of setting thresholds was solved by normalizing the signals in the presence of a constant target that was the tube's cut end serving as the reference for relative comparison of the amplitudes of responses from the defects. In practice, it can be solved by other reference targets, for instance welds.

Summing, the complex processing proved it helpfulness for the contrast enhancement in LRUT, especially valuable in the case of small defects. Increase of number of transducers in the array can increase the resolution of detection, at one hand, since the more multiplication factors act, the higher is the product, increasing the resolution between the desired modes and parasite signals. On the other hand, this increase is limited by the attenuating action of stiffly glued transducers themselves that damp the propagated guided waves within the array's area. An optimal solution can be obtained experimentally for certain cases.

4 Comparison of T- and L-Modes in Detection of Through and Surface Defects

The aim of this part was modeling different kinds of defects such as pitting corrosion, surface corrosion, and axial cracking observing T- and L-waves responses in each case. Relatively successful attempts to estimate pitting corrosion by guided waves was performed in circumferential testing of pipes at short distances [17]. Although there are some approaches to characterize size and length of defects using L- and T-modes at different wavelengths [5], there is no or almost no practice to identify the type of defect, to describe its expansion by the pipe's depth quantitatively based on the combination of waves. However, a possibility of using a combination of T- and L-waves can be grounded by different intensity of responses of these waves from defects of different geometry.

As mentioned above, a transformed pulse-echo from a defect due to the modes conversion contains longitudinal, torsional, and flexural waves propagating with different velocities and scattering over distance differently. The amplitude ratios between the mentioned modes may vary and be dependent on diverse factors. The difficulty of assessment is caused by spreading of the reflected pulse over the pipe's cross-section by propagation from a local defect along the pipe over a long distance. Another difficulty is the presence of hardly accounted factors of the measurement technology that may overbear effects related to the defect type, for example, uniformity of gluing of magnetostrictive strips to the tube and uniformity of application of the static magnetic field to magnetostrictive transducers.

Although the above-described approach of enhancement signals contrasting was practical for localization of small defects, it came out problematic to use this

processing for comparison of energetic parameters of signals due to distortion and damping of signals passing under transducers in the array. That is why a modified algorithm was applied where locations of defects in the time scale were determined using the contrasting procedure, but energetic characteristics of echo responses from the defects were determined from signals obtained by the nearest transducers pair. The energetic parameter I_d —intensity of the echo from the defect was calculated as the amplitudes integral of the rectified signal in a constant length time “window” around the echo peak. The echo from the tube’s cut end was chosen as the reference reflection, since the size of that target was constant during the experiment, and the corresponding parameter I_c for the echo from the cut end determined. The necessity of the reference reflection was caused by inability to provide a precise reproducibility of the static magnetic field during turning the magnets orientation and, consequently, to provide ideally the same level of excitation of the transducers. A relative value—the ratio of signal integrals of defect and cut end I_d/I_c size was determined to characterize the relative amount of reflected and transmitted energy of ultrasonic pulse interacting with the defect.

Pitting corrosion. Pitting corrosion was modeled by drilling thin through holes in the tube’s wall. In practice, it is the most dangerous type of corrosion manifesting as thin through holes developing across the wall and resulting in leaking. Four stages of the corrosion developments were modeled by gradual doubling the number of through holes symmetrically arranged upon the same cross-section of the tube: 1, 2, 4, and 8. The corresponding metal loss or total defect area S was about 3, 6, 12, and 24% of the tube’s cross-section area or 1.2, 2.5, 5, and 10% of the volume if to account the cylindrical shape of defects. Amplitude integrals for T-wave and L-wave echoes were determined for the zones of defects I_d and the tube’s cut end I_c . The plots of the ratios I_d/I_c dependencies on the total area of defects or metal loss S for T- and L-waves based on the data of four modeled stages are depicted in Fig. 8.

The experimental data showed different character of I_d/I_c dependencies on S for T- and L-waves. The dependence for L-wave has a more linear character, but the

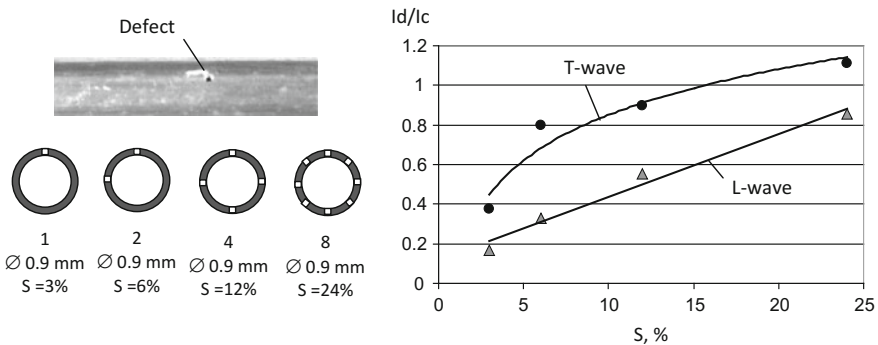


Fig. 8 Model of pitting corrosion and plot of dependence of parameter I_d/I_c on total area of defects S for T- and L-waves

same for T-wave is a strongly nonlinear one with a sharp increment at small values of S . A possible explanation could be that the echo response of L-wave is closer to a laminar character, where the intensity of echo is linearly proportional to the area of reflection, while the T-wave response having the torsional origin is more sensitive to breaking of the cross-section continuity and disruption of its closed circle conducting the torsional mode. Nonlinearity and uneven character of the parameter I_d/I_c in Fig. 8 is explained not only by measurement errors but also by dispersion and spreading of ultrasonic pulses on multiple defects resulting in broad tailing that is seen, for examples, in signals presented in Fig. 6.

Crevice corrosion. In this case, the defects involved only a surface part of the tube's wall penetrating it maximally to a half of the thickness, thus not breaking the entire cross-section. It was considered as a simulation of crevice corrosion that may have similar mechanisms to pitting corrosion but having a less severe form with a more shallow penetration of the tube's wall. Two types of defects were inserted by fine milling: (i) a small notch with a diameter of 2.5 mm and a depth of 0.5 mm and (ii) a prolonged groove along the tube. The groove was 60 mm long, 2.5 mm wide, and 0.3 mm deep. The intensity of T- and L-waves reflections from the defects were normalized by the same from the tube cut end by calculating the parameter I_d/I_c . The result presented in Fig. 9 showed the following findings. Both T-wave and L-wave recognized the single notch (i), but the T-wave's response was much more pronounced than of L-wave. A shallower groove modeling surface corrosion produces a detectable response only by L-wave while the T-wave response remains at the noise level. These data correspond to results described above on modeling pitting corrosion that showed increased sensitivity of T-wave to small defects deeper penetrating the wall. L-wave is more capable to reveal prolonged shallow defects. A combined data on T- and L-waves reflections may help to reveal the type of defect and characterize its expansion upon the wall depth.

Stress corrosion. Stress corrosion cracking occurring in a corrosive environment under tensile stress results in growth of circumferential and longitudinal cracks in pipes. Developing of longitudinal cracks was modeled by axial thin cutting through the entire wall thickness produced by a circular abrasive disk. The length of cutting varied from 10 mm that is comparable to less than a half of ultrasonic wavelength to

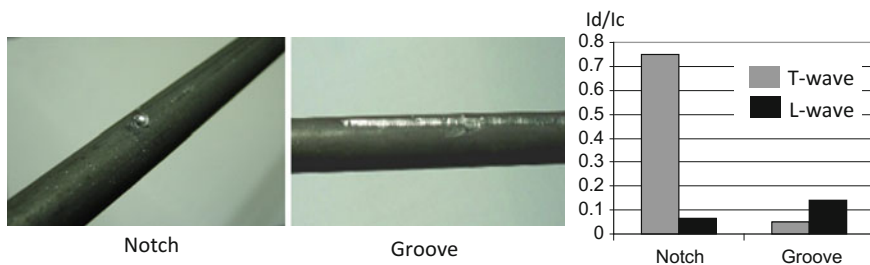


Fig. 9 Models of crevice corrosion and graphical comparison of parameter I_d/I_c in notch and groove types of defects for T- and L-waves

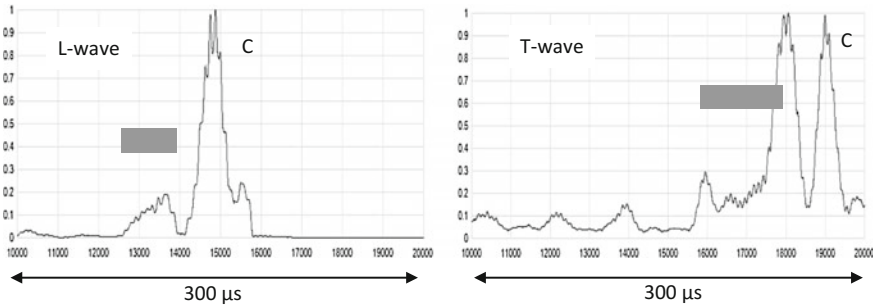


Fig. 10 T- and L-wave echo signals from 110 mm axial thin cutting of tube’s wall mimicking longitudinal crack; signals are normalized by amplitude of cut end echo (C); echo responses from axial cutting are marked by rectangles

110 mm or about 4 wavelengths. Both L- and T-wave modes were sensitive to such kind of defects, where short cuts generated single short echoes, but prolonged cuts comparable by the length to 1.5–2 ultrasonic wavelengths and larger generated two pronounced echoes—from the beginning and end points of the cuts. Figure 10 illustrates the example with the longest 110 mm cutting where responses of both T- and L-waves are present. As the reference reflection, the tube’s cut end was taken. The similar regularities manifested as for other above-mentioned defects, particularly, T-wave reflection signals are relatively greater than the same of L-wave. It can be explained by the fact that the cutting disturbed the continuity of the section’s circle that affected the torsional wave stronger but captured only a small area of the tube’s cross-section that had a relatively little effect on the longitudinal or compression wave. Reflection pulses of T-wave from the ends of cutting were lesser dispersed and shorter than of L-wave, producing sharper discerning of the cutting boundaries.

5 Influence of Liquid Filling

The influence of liquid filling was demonstrated by comparing ultrasonic echo signals for switched in turn for T-wave and L-wave modes in an empty or air-filled tube and in the same tube filled with water. The tube’s cut ends were similarly sealed in the empty and water-filled conditions to make the results comparable. The targets along the tube were the tube’s cut end and a drilled hole simulating a defect located closer to the glued magnetostrictive transducers.

The recorded signals shown in Fig. 11 exhibited obvious differences in the obtained echo patterns for both modes. First, water filling acted as a damper causing a higher attenuation of the reflected signals propagated in the tube due to leakage of ultrasound into water due to a lower differences of impedances between the tube and the medium than in the case of air. Reduction of the echo intensities was by about 1.5 times for T-wave and by more than 2 times for L-wave. Due to a higher

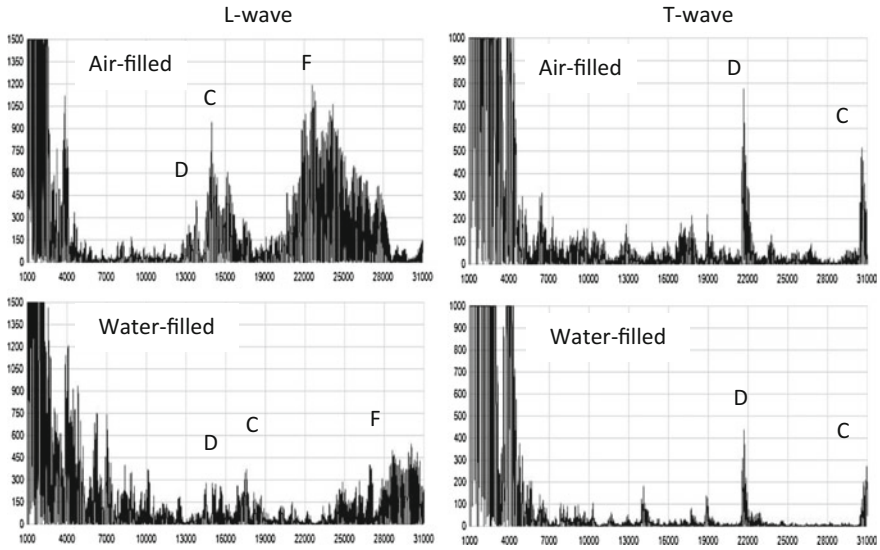


Fig. 11 Illustrations of influence of water filling on T- and L-wave signals in tube: *D* is echo from defect; *C* is echo from cut end; *F* is echo related to F-mode. Signals were obtained at the same settings

degree of damping of longitudinal and flexural modes, the echogram of T-wave in the water-filled tube cleared up from parasite echoes of L- and F-modes and thus the reflections of T-wave from the targets became more contrast in comparison to the empty case, despite lowered amplitudes. The T-wave responses remained practically unchanged in the time scale, while both L-wave and F-wave echoes were delayed. Reduction of velocities of the later modes can be explained by increase of the bulk mass or density of the oscillating system due to water content occurring without increase of its stiffness.

The findings confirmed the necessity to take into account water filling when setting the ranging scale based on the propagation time for different acoustic modes. Variations of the physical properties such as viscosity and density of different liquids and of the same liquid, for instance, under the effect of temperature are capable to affect the velocities. In this view, the most consistent T-wave has an obvious superiority to be used in pipes with liquid fillings.

6 Conclusion

Application of time-shifting and multiplication of echo responses from several transducers arranged stepwise along the length of a pipe can significantly enhance the contrast of desired acoustic modes and damp parasite signals related to other modes that result from the signal conversion or reflections from the opposite

direction. This is an effective measure to increase efficacy of LRUT. Advancement of data processing may include sweeping of the time-shifting in order to account variations of the velocities for different acoustic modes and introduction of calibration for individual pairs of transducers to compensate dissimilarities and attenuation.

Combined use of both T- and L-waves can provide additional information about the type and size of a detected defect, particularly of its development by the depth of the tube's wall and expansion along the length. The study has demonstrated a potential of such approaches based on specific ratios of T- and L-wave responses, however, additional studies are required to investigate quantitative relationships for different types of defects.

Filling the pipe with liquid contents not only creates an increased attenuation of propagating waves, but causes significant transformation of echo patterns, especially of L-waves having dispersive nature, while T-wave keeps stability. In LRUT of pipes filled by liquid contents, the certain type of liquid and its condition should be accounted.

References

1. W. Mohr, P. Holler, IEEE Trans. Ultrason. Ferroelectr. Freq. Control **23**(5), 369 (1976)
2. J.J. Ditri, J. Acoust. Soc. Am. **96**, 3769 (1994)
3. D.N. Alleyne, P. Cawley, IEEE Trans. Ultrason. Ferroelectr. Freq. Control **39**(3), 381 (1992)
4. P. Mudge, Insight **43**, 74 (2001)
5. A. Demma, P. Cawley, M.J.S. Lowe, A.G. Roosenbrand, B. Pavlakovic, NDT Int **37**, 167 (2004)
6. J.L. Rose, Key Eng. Mater. **270**, 14 (2004)
7. M. Sheard, A. McNulty, Insight **43**, 79 (2001)
8. BS ISO 18211:2016. *Non-destructive testing. Long-range inspection of above-ground pipelines and plant piping using guided wave testing with axial propagation* (2016)
9. I.A. Viktorov, *Rayleigh and Lamb Waves* (Plenum Press, New York, 1967)
10. J. Zemanek, J. Acoust. Soc. Am. **51**, 265 (1972)
11. D.N. Alleyne, T. Vogt, P. Cawley, Insight **51**(7), 373 (2009)
12. J.R. Rose, Mater. Eval. **68**(5), 495 (2010)
13. E. Leinov, J.S. Michael, M.J.S. Lowe, P. Cawley, J. Sound Vib. **347**, 96 (2015)
14. H. Sato, H. Ogiso, Jpn. J. Appl. Phys. **53**, 07KC13 (2014)
15. S. Vinogradov, Mater. Eval. **67**, 333 (2009)
16. P. Sun, X. Wu, J. Xu, L. Li, Sensors **14**, 1544 (2014)
17. K. Shivaraj, K. Balasubramaniam, C.V. Krishnamurthy, R. Wadhwan, J. Pressure Vessel Technol. **130**(2), 021502 (2008)

Directional Properties of Ultrasonic Antenna Array

Y.N. Mirchev, A.L. Shekero and V.V. Kozhushko

Abstract Proper using of long-range ultrasonic (LRUT) technique for different test pipe configuration, and test conditions according to the technical task requires comprehensive knowledge of ultrasonic field generated by ultrasonic phased antenna array. This chapter shows results calculated for ultrasonic beam spreading by antenna array in pipe and receiving its reflection from the pipe wall edge. The results show influence of antenna array with different characteristics to directional properties of ultrasonic field. The calculations of the ultrasonic fields are carried out using numerical method based on principles of Huygens and Fermat. In any point of interest in researched area, it is calculated interference of waves emitted from all elements of the phased antenna array. The results are present in type of distance and circumference amplitude curves for point source located at the center of the active group replacing the antenna array. Any point of interest on pipe wall edge is also present as secondary source of spherical waves by point spread function. Directional properties of active focused and unfocused ultrasonic antenna array are studied for torsional mode $T(0, 1)$ emitted in pipe. Possibilities to use the antenna array focusing technology in pipeline testing by LRUT technique are discussed.

Keywords Long-range ultrasonic technique (LRUT) • Torsional mode • Active and synthetic focusing techniques • Dynamic distance focusing (DDF) • Phased antenna array • Focal law • Distance and circumferential amplitude curves • Full width at half maximum (FWHM)

Y.N. Mirchev (✉)

Institute of Mechanics of Bulgarian Academy of Science, Sofia, Bulgaria
e-mail: mirchev@imbm.bas.bg

A.L. Shekero

E.O. Paton Electric Welding Institute of NASU, Kiev, Ukraine

V.V. Kozhushko

V.A. Belyi Metal Polymer Research Institute of National
Academy Science of Belarus, Gomel, Belarus

© Springer International Publishing AG 2018

E.N. Barkanov et al. (eds.), *Non-destructive Testing and Repair of Pipelines*,
Engineering Materials, DOI 10.1007/978-3-319-56579-8_3

1 Introduction

Insufficient sensitivity of LRUT technique to different types of reflectors is general shortcoming of its application for pipeline testing. The application of phased antenna array with define number of channels depends on test pipe configuration to generate ultrasonic fields of various directional properties of increased sensitivity to specific types of reflectors in pipelines.

The impact on the amplitude sensitivity of the method to specific types of reflectors is determined by directional properties of ultrasonic fields emitted by phased antenna array and depends on the following factors: (i) nominal frequency and number of elements in antenna array, (ii) type of pipe mode, (iii) geometry, configuration, and material of test pipe.

In this chapter, the ability of phased antenna arrays is studied to emit low-frequency ultrasonic fields of various directional properties for torsional mode $T(0, 1)$ in pipeline. Gain coefficient is defined for active focusing antenna array technique and focusing range to gain coefficient equal to 1.

2 Basic Principles and Methods for Theoretical Calculation of Ultrasonic Phased Antenna Array Fields

Emitting ultrasonic waves by one element probe and reflecting them by artificial reflectors are ruled by various laws in dependence on the value of parameter ka , where k is the wave number given by $k = \frac{2\pi}{\lambda}$, a is a characteristic dimension of emitting probe or reflector [1].

In the discussed cases here of ultrasonic wave emitted by one element in antenna array and one reflector, for parameter $ka > 1$, the calculations are present by Green function. Each element of the phased antenna array is considered as point source of spherical ultrasonic wave, according to principle of Huygens. Ultrasonic waves emitted by all elements of the antenna array in the pipe are summed up and present as one ultrasonic field. Directional properties of ultrasonic field is generally affected by position of elements on pipeline surface and presence or absence of focal law with electronic time delay of pulses generated by elements. Using various algorithms of synthetic focusing technique, it is possible to present amplitude of ultrasonic fields in each point of interest in investigated area. Limitations of investigated area are given by geometrical form of area of different acoustic characteristics compared to the medium, where ultrasonic waves propagate. Kirchhoff approximation can be used for reflections from known area with different acoustic characteristics, as known area being replaced by point source. Emitting and reflecting from such an area is present by point spread function [2–4].

To illustrate a wave propagated, reflected, and received in pipeline, a two-dimensional matrix algorithm is used to show a reconstruction of the pipe under test. The rows and columns of the matrix give the location of propagated

waves in circumference la and along Z-axis on the pipe, respectively. Variations of amplitude of the summary wave are listed in it.

Steps of the algorithm are as follows: (i) selection of acoustical medium and properties of propagated impulse (emitted signal); (ii) considering the geometry of investigated object with coordinate system and position of array elements and reflectors; (iii) studying propagation patterns of ultrasonic waves of known properties in tested object; (iv) application of method for reconstruction of the area of object bounded in two-dimensional image.

In literature sources, the techniques, used to generate two-dimensional images of investigated area, are: common source method (CSM) (see Fig. 1a), synthetic aperture focusing technique (SAFT) (see Fig. 1b) [2, 5] and total focusing method (TFM) or full capture matrix (see Fig. 1c) [6]. Each element in active group works as transmitter and receiver as indicated in Fig. 1 by Tr or Re, respectively.

In this chapter, CSM and SAFT are applied to form ultrasonic field transmitted, reflected and received by all elements of an active group of a phased antenna array. Active group is a number of elements transmitting under one focal law that are controlled by one channel of the ultrasonic unit.

Focal law is the electronic delay that establishes the directional properties of an ultrasonic field transmitted by one active group. A directional property of ultrasonic field of one active group is built by using one active focal law (electronically set time delay) and many synthetic focusing laws. For active group with focusing distance, aspiring to infinity, focal law of electronic time delay, aspiring to 0, generates unfocused ultrasonic field. The focused ultrasonic field is generated by elements in active group with electronic time delay different from 0. The change of electronic time delay in order to achieve focusing at specified distances along the axis of propagated waves is possible in some ultrasonic systems, using function, named dynamic distance focusing (DDF) technique.

Synthetic focusing aperture of an active group is given by synthetic time delay for the position of each element related to any point of tested area. Forming of synthetic focusing apertures for any point of tested area, with or without the presence of reflectors, gives a two-dimensional image of the area by FMC. This technique or SAFT is used in phased array equipment as farther processing of

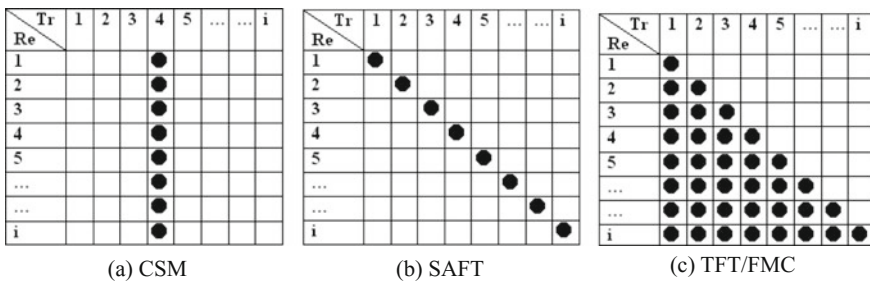


Fig. 1 Synthetic focusing techniques

accumulated data to produce images (A-, B-, E-, or C-scans). To save time in data processing, SAFT is used more frequently to build two-dimensional images of the tested object.

3 Numerical Method and Initial Data

To construct one-dimensional image, the scan algorithm is used with following sequence: (i) selection of properties for acoustic medium (material) and propagated waves (emitted pulse); (ii) defining geometry of investigated object with coordinate system and position of array elements and reflectors; (iii) selection of methods and principles presenting propagated waves in object; (iv) application of synthetic focusing techniques for reconstruction of object bounded area in two-dimensional (B-, E- or C-scan) or one-dimensional (distance or circumference amplitude curves) images.

The case when the pipe has a radius much larger than the thickness of the wall is investigated. Then cylindrical contour of the pipe is neglected for spreading waves and it can be replaced by a plate having dimensions equal to the additional circumference number and the length of the pipe [2, 7].

Scheme of investigated pipe and phased antenna array as one active group is shown in Fig. 2. The active group has length la and Na number of elements with pitch $p = \frac{la}{Na}$, arranged in linear phased array mounted in antenna array collar attached to the circumference of the outer surface of the pipe with diameter D , thickness h and length H . Number of elements corresponds to the Nyquist criteria.

Additional requirement to pipe boundary conditions is specified and shown on the scheme with letters $A-A$ and $A'-A'$. The properties of ultrasonic beam at the pipe boundary $A-A$ are equal to those at the $A'-A'$. Fulfilling this requirement means that there are no interruptions in the calculation of the ultrasonic beam for the analogous plate. Zero order and two additional extra wave paths of the pipe, marked with dashed line and $H_{i,r}$ are shown in Fig. 2. This approach eliminates the restriction on propagation of waves in the pipe of the contour, marked with a black solid line. To calculate all possible extra wave paths in the pipe, it is necessary to include sufficient number of extra wave paths according to initial data.

The operation of ultrasonic antenna array is studied as one active group in one channel of ultrasonic system, when all elements transmit applying one focal law. A possible active group in one channel is equal to its number of elements n . Acoustic Z -axis of each active group begins from its central position, equal to half-length of la from first element closest to the end of active group. Amplitude of ultrasonic field in any point of interest S_r is given by interference of the sequence of emitted waves by the individual elements in the antenna array due to the selected focal law. The shortest path between center of the active group $O_n(Y)$ and center of the reflector $S_r(Y, Z)$ is taken as reference wave path for calculation of synthetic delay time. Active group and reflectors are replaced by point sources $O_n(Y)$ and

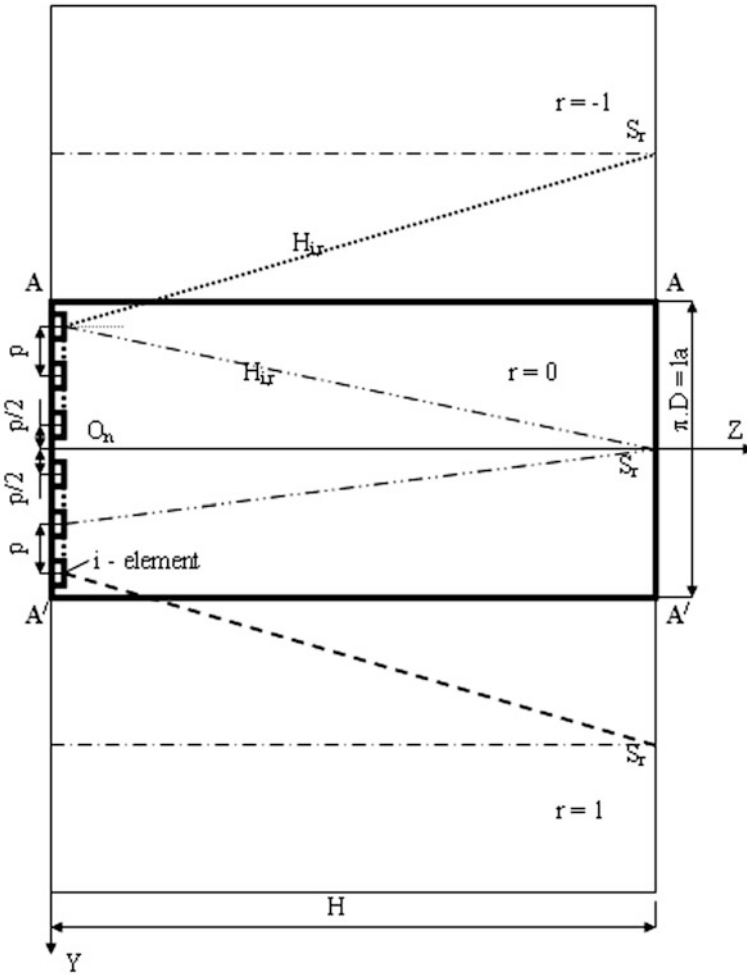


Fig. 2 Geometry of unrolled pipe, antenna array and extra wave path as plate analog

$S_r(Y, Z)$, respectively. The position of point source can be any other in the investigated area than that shown in Fig. 2.

In this chapter, the ultrasonic field transmitted, reflected, and received for each element in one active group of phased antenna array is present as one-domain scan with distance or circumference amplitude curves, using CSM and SAFT. Active group is the number of elements pulsed by one focal law, controlled by one channel of ultrasonic systems. Study of maximum reflected amplitude received by antenna array elements is carried out by calculation of active group used with number n in channel with position of its center (point source $O_n(Y)$) laying on acoustic axis (perpendicular) of reflecting surface. Reconstruction of pipe with reflector in

two-dimensional scan (C-scan) for one focal law is performed by calculation of synthetic focused apertures of all active groups. If ultrasonic equipment has 1 channel with 32 elements, 32 ultrasonic fields are calculated, because one field is considered for each point of interest in investigated area.

All the calculations are carried out for the case shown in Fig. 2 for torsional mode T(0, 1) propagating in material of pipe with constant ultrasonic velocity $C = 3260$ m/s. In the theoretical modeling, mode transformation after reflection is not considered. The pipe dimensions are: diameter $D = 323.9$ mm; thickness $h = 9.5$ mm; length $H = 2.2$ m.

The calculations are performed for pulse-echo method. In investigated area, the propagated ultrasonic waves are considers as sine wave with shape close to bell pulse, illustrated by the following equation:

$$A(t) = A_0 e^{j\omega_0(t-t_0) - \beta^2 \omega_0^2 (t-t_0)^2}, \quad (1)$$

where A_0 is the maximum amplitude of transmitted pulse (accepted condition: $A_0 = 1$), e is a Euler's number, $\omega_0 = 2 \cdot \pi f_0$ is the circular nominal frequency, f_0 is the nominal frequency, t is the time for propagating wave, $\beta = \frac{0.265}{m}$ is a coefficient defining impulse shape and length, m is the number of impulse oscillations at the amplitude $A = 0.5 A_0$ (in this chapter $m = 1$), $t_0 = \frac{H(Z)}{C}$ is the time of wave propagation on distance $H(Z)$ with velocity C , j is a imaginary unit, k is a wave number.

Ultrasonic beam $I_{PA}^{Na}(Z)$ transmitted in pipe by one active group as part of antenna array is given as

$$I_{PA}^{Na}(Z) = \sum_{i=1}^{Na} \sum_r \left[T_{i,r}^{PA}(Z) \cdot A_{i,r}^{PA}(\Delta t_{i,r}) \right], \quad (2)$$

where

$$T_{i,r}^{PA}(Z) = \frac{Z}{H_{i,r}(Z) \cdot \sqrt{H_{i,r}(Z)}}, \quad (3)$$

$$A_{i,r}^{PA}(\Delta t_{i,r}) = e^{j\omega_0[t - (t_0 + \Delta t_{i,r})] - \beta^2 \omega_0^2 [t - (t_0 + \Delta t_{i,r})]^2}, \quad (4)$$

$$\Delta t_{i,r}(Y, Z) = \Delta t_{i,r}^{NF}(Y, Z) + \Delta t_{i,r}^{AF}(Y, Z), \quad (5)$$

$$\Delta t_{i,r}^{NF}(Y, Z) = \frac{H_{i,r}(Y, Z) - O_n(Y)S_r(Y, Z)}{C}, \quad (6)$$

$$\Delta t_{i,r}^{AF}(Y, Z) = -\frac{H_{i,r}(Y, Z) - O_n(Y)F_{i,r}(Y, Z)}{C}, \quad (7)$$

$$H_{i,r}(Y, Z) = \sqrt{Z^2 + \left[p \left(i - n - \frac{1}{2} \right) + rla - S_r(Y) \right]^2}, \quad (8)$$

$T_{i,r}^{PA}(Z)$ is a angular coefficient of ultrasonic beam spreading. Increasing the spreading angle leads to a reduction of amplitude. Change of ultrasonic beam due to absorption and scattering in investigated medium is not considered. $A_{i,r}^{PA}(\Delta t_{i,r})$ is the wave transmitted by element i in active group n for extra path wave r , with overall delay time $\Delta t_{i,r}(Y, Z)$ of wave propagating on distance $H_{i,r}(Y, Z)$. Delay time $\Delta t_{i,r}^{NF}(Y, Z)$ is considered according to time $t_0 = \frac{O_n S_r}{C}$. Z is the shortest path from center of antenna array to center of reflecting area. Delay time $\Delta t_{i,r}^{AF}(Y, Z)$ is electronically set delay time for each element i in active group n due to focal law, used with position of focus $F_{i,r}(Y, Z)$ for active focusing antenna array. The electronically set delay time is found with negative sign, resulting in transmitted waves arriving at the focal point $F_{i,r}(Y, Z)$ in the same time without delay $\Delta t_{i,r} = 0$. Focal law with $F_{i,r}(Y, Z) \rightarrow \infty$ is the case when antenna array is unfocused and all elements transmit simultaneously with electronic delay time $\Delta t_{i,r}^{AF}(Y, Z) \rightarrow 0$. In the case, when the DDF technology is not employed one takes into account that the electronically set delay time has only one focusing position $F_r(Y, Z)$.

According to conventional approach for back wall reflection [2–4], the received reflected signal from pipe wall edge in linear phased antenna array is formulated as follows

$$IB(Z) = I_{PA}^{Na}(Z) \cdot R \cdot \sum_{i=1}^{Na} \sum_r \left[\frac{|\Phi_{i,r}(Y, Z)|}{\sqrt{H_{i,r}(Y, Z)}} \right], \quad (9)$$

where

$$R = \frac{s}{2S - s} \quad (10)$$

$$|\Phi_{i,r}(Y, Z)| = \left| \frac{2 \sin \left[\frac{d}{2} k \frac{p \left(i - n - \frac{1}{2} \right) + rla - S_r(Y)}{H_{i,r}(Y, Z)} \right]}{\left(\frac{d}{2} k \frac{p \left(i - n - \frac{1}{2} \right) + rla - S_r(Y)}{H_{i,r}(Y, Z)} \right)} \right|, \quad (11)$$

R is a reflection coefficient from cross-section area (CSA) s , S is the pipe CSA, $|\Phi_{i,r}(Y, Z)|$ is the point function of spreading the reflector with circumference d . The rest of symbols are given above. When d aspires to 0, the point function of spreading is found for point reflector spreading in the spatial domain. The reflection coefficient, R , from pipe wall edge with orientation normal to antenna array is equal to 1.

All the calculations are made for investigated area of pipe perpendicular to its Z -axis from 5 mm to 16 m with increments of 5 mm. The investigated area perpendicular to Y -axis is equal to the circumference of the pipe: $la = \pi D$, and results are shown with increments of 1.93 mm. Time step of propagating waves is 6 ns. The amplitude of signal transmitted by antenna array is normalized to amplitude of a signal, transmitted on a distance of 5 mm from unfocused phase antenna array. The received reflected signal from pipe edge wall in phased antenna array is normalized to the reflected signal from pipe edge wall with normal orientation in respect to unfocused antenna array, transmitted on a distance of 5 mm from it. The dynamical focusing of phased antenna array at each point along Z -axis in figures, showing results, is denoted by DDF.

4 Results and Discussion

Figure 3a shows distance amplitude curves on Z -axis of pipe for $Na = 64$ elements of nominal frequency $f = 10$ kHz. All antenna array elements operate as one active group, when CSM is used. Calculations are carried out for one virtual aperture by using Eq. (2) and focal law for unfocused ($F = 100$ m) and focused ($F = 2, 4, 6$ and 10 m) phased antenna array.

Figure 3b presents the results for amplitude of the reflected signal from pipe wall edge, received in phased antenna array and calculated by using Eq. (9) at the same properties of phase antenna array, nominal frequency and focal laws. The distance from antenna array to pipe wall edge H is calculated on abscissa with increments of 5 mm from 5 mm to 16 m.

Results in Fig. 3a show that with increasing the focal distance, the amplitude decreases at focal point and focal distance of FWHM to Z -axis increases. This leads to the conclusion that by increasing focal distance F the effect of focusing decreases.

Results in Fig. 3b show significant decrease of amplitude of the reflected signal from pipe wall edge, compared to transmitted signal (see Fig. 3a) at the same

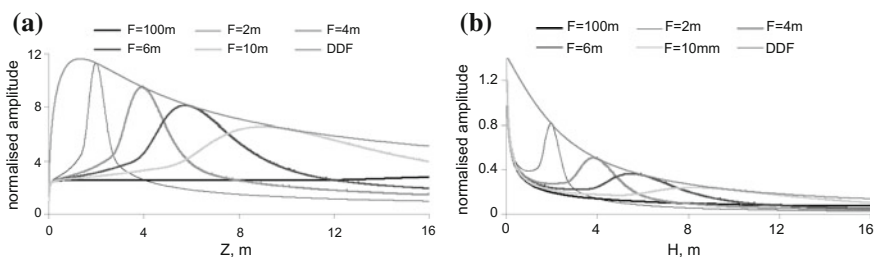


Fig. 3 Distance amplitude curves, constructed by using CSM, for one virtual (synthetic) aperture spreading from active group to Z -axis (a) and received by such active group after reflection from pipe wall edge (b)

distance H . Figure 3b demonstrates that the focusing effect reduces with smaller focal distance F compared to results given in Fig. 3a.

Figures 4a, b present results for unfocused ($F = 100$ m) and focused ($F = 4$ m) antenna array, respectively. The distance amplitude curves are present for $N_a = 64$ antenna array elements and nominal frequencies $f = 10, 30, 60$ and 100 kHz.

The results in Fig. 4a show decrease of amplitude for the same distance H with increasing nominal frequency f . The same nature of decreasing amplitude with increasing nominal frequency is seen in Fig. 4b, except for focal distance $F = 4$ m. For focused active group, decrease of FWHM along the acoustic axis with increasing the nominal frequency is found in Fig. 4b. Based on findings of Fig. 4, we can conclude that maximum focused amplitude (in focal point) of antenna array is not frequency dependent in reflection from pipe wall edge. When using SAFT the maximum amplitude in the focal point is frequency dependent.

CSM is used to build distance amplitude curves in Fig. 5a, b for unfocused with $F = 100$ m and focused with $F = 4$ m antenna array, respectively. Amplitude is shown for pipe end wall reflected signal in active group with $N_a = 24, 32$ and 64 elements and nominal frequency $f = 30$ kHz.

Findings in Fig. 5 show that increasing of amplitude with increasing number of elements N_a in an active group is true for equal values of distance H . Thus the amplitude of the received signal increases with increasing the number of elements in the active group.

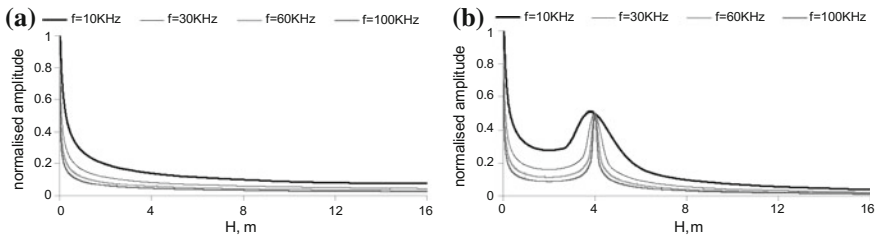


Fig. 4 Distance amplitude curves built by CSM for one virtual (synthetic) aperture received in unfocused (a) and in focused (b) active group, after pipe end wall reflection

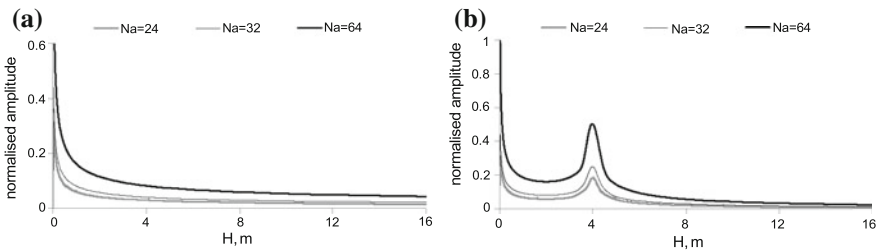


Fig. 5 Distance amplitude curves plotted by CSM for signal received after pipe end wall reflection for one virtual (synthetic) aperture in unfocused (a) and in focused (b) active group

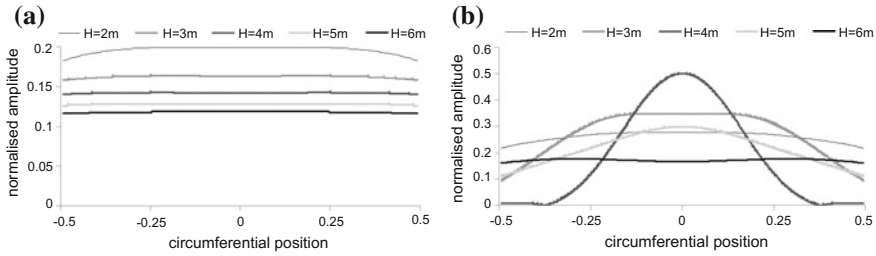


Fig. 6 Circumference amplitude curves for signal received after reflection from pipe wall edge for each virtual (synthetic) aperture in unfocused (a) and in focused (b) active group

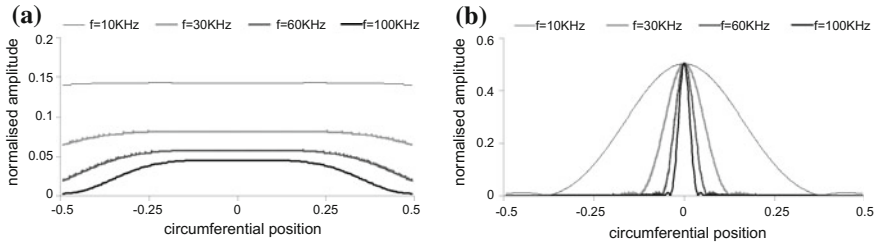


Fig. 7 Circumference amplitude curves for signal received after pipe wall edge reflection for each virtual (synthetic) aperture in unfocused (a) and focused (b) active group

The variations of amplitude on Y-axis of signal reflected from pipe end wall at distance $H = 2, 3, 4, 5,$ and 6 m from antenna array with $Na = 64$ elements and nominal frequency $f = 10$ kHz are presented in Fig. 6. SAFT is used to plot the findings for unfocused with $F = 100$ m and focused with $F = 4$ m antenna array normally oriented to the pipe end in Fig. 6a, b, respectively.

Circumference amplitude curves in Fig. 6a show that the signal amplitude is the same at any circumference position, but monotonically decreases with increasing distance H . Maximum amplitude of the field in Fig. 6b increases when distance H disposes closer to the focal point F . FWHM is 360 cm on circumference for $H = F = 4$ m.

This directional feature of ultrasonic field of a focused antenna array allows one to determine location and relative dimensions of reflector in the pipe circumference using conventional methods. Definition of the sizes of reflectors in pipe circumference direction is also carried out by using equipment to divide the antenna array into separate channels of active groups focusing to the area of interest in the test volume.

The determination of amplitude effect on the directional properties of unfocused ($F = 100$ m) and focused ($F = 4$ m) antenna arrays are plotted in Fig. 7a, b, respectively. The amplitude of signal reflected from pipe wall edge is studied at distance $H = 4$ m from antenna array for nominal frequencies $f = 10, 30, 60$ and 100 kHz. Circumference amplitude curves are plotted by using SAFT.

Figure 7 shows three times greater maximum amplitude in the focus spot for focused antenna array compared to unfocused one. Figure 7b demonstrates decreasing FWHM with increasing nominal frequency and constant maximum amplitude in focus. The summary amplitude of a focused system is the highest for nominal frequency $f = 10$ kHz and decreases with increasing the nominal frequency.

The conclusion from Fig. 7b is that actually the reflected signal amplitude from pipe wall edge at focusing distance, received in focused antenna array, decreases with increasing the nominal frequency. However, the signal amplitude, received from reflector with dimensions less than the size of FWHM = 30 mm (see Fig. 7b for $f = 100$ kHz), increases in high-frequency domain.

In Fig. 8, SAFT and DDF technique is used to plot circumference amplitude curves, received in focused antenna array after signal reflection from pipe wall edge at distance $H = 2, 3, 4, 5,$ and 6 m, received in antenna array of $N_a = 64$ elements. The results are shown for antenna array with nominal frequency $f = 10$ and 100 kHz, respectively.

The results in Fig. 8 show decreasing the FWHM size while increasing the frequency and the maximum amplitude on circumferential position 0 is constant for similar distance H . From the results of Fig. 8, we can conclude that for reflectors with circumferential size lower than the FWHM size, it is preferable to apply higher nominal frequencies considering the wave attenuation in material.

SAFT is used to plot circumference amplitude curves. The results are illustrated in Fig. 9a, b for reflected signal amplitude from pipe wall edge, received in unfocused ($F = 100$ m) and focused ($F = 4$ m) antenna array, respectively. The pipe wall edge disposes at distance $H = 4$ m from antenna array of $N_a = 24, 32,$ and 64 elements.

Figure 9 shows increasing the maximum amplitude while the number of elements in antenna array increases. The changes in amplitude allow us to conclude that the use of more elements in antenna array increases amplitude sensitivity to reflectors.

The ratio between maximum amplitudes for focused and unfocused antenna arrays at the same distance H is given by gain coefficient K . The gain coefficient

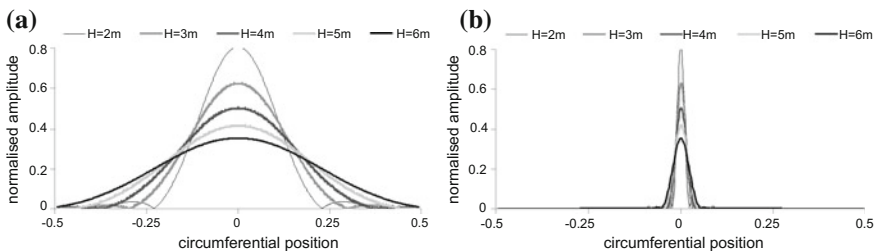


Fig. 8 Circumference amplitude curves of signal received after reflection from pipe wall edge for DDF active group and nominal frequency $f = 10$ kHz (a) and $f = 100$ kHz (b)

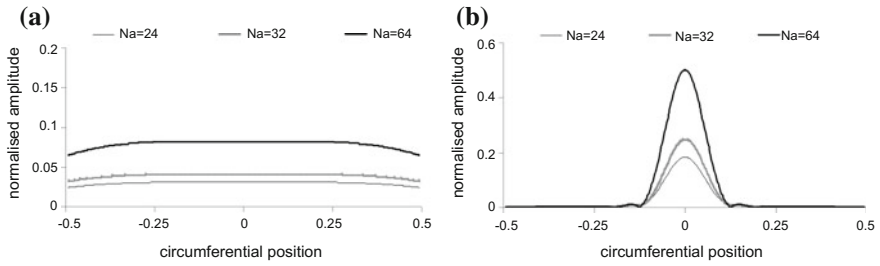
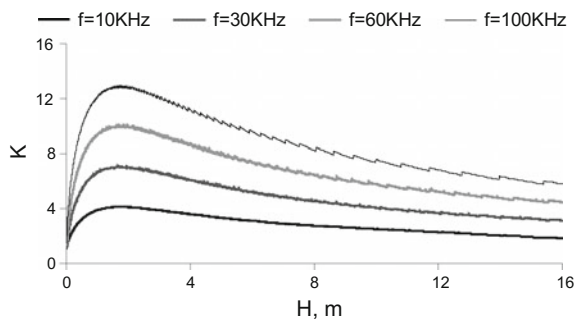


Fig. 9 Circumference amplitude curves for reflected signal from pipe wall edge in each virtual (synthetic) aperture, received by unfocused (a) and focused (b) active groups

Fig. 10 Gain coefficient K of focused antenna array built by CSM



K is studied for antenna array of $Na = 64$ elements and nominal frequency $f = 10, 30, 60,$ and 100 kHz. The results for transmitted signal are shown in Fig. 10 by using CSM.

The results in Fig. 10 show improvement in effect of focusing for signal amplitude, transmitted by focused antenna array compared to unfocused one with increasing frequency. For example, at distance $H = 2$ m and nominal frequency $f = 100$ kHz, gain coefficient is $K = 13$. Gain coefficient K decreases with increasing distance H . The FWHM value of gain coefficient is approximately $H = 18$ m. In correspondence with the results of Fig. 10 during operation of focused phased antenna array, it is recommended to apply as high as possible frequencies for a range no greater than the size of FWHM, taking into account attenuation of waves in the tested object.

5 Conclusion

Numerical model has been developed to demonstrate directional properties of ultrasonic field transmitted by phased antenna array in pipe. The information on the directional properties of torsion mode $T(0, 1)$ of phased antenna array in pipe of

diameter $D = 323.9$ mm and wall thickness $t = 9.5$ mm, is given by quantitative values of one-dimensional images of distance, circumferential amplitude curves and gain coefficient K .

The amplitude of unfocused phased antenna array monotonically decreases while distance of spreading waves H and nominal frequency f increase, and number of elements Na decreases. The maximum amplitude, displayed by CSM in the focusing area, does not change with variation of wave frequency f , while actually the summary amplitude presented by SAFT increases with decrease of nominal frequency. The size of FWHM of the signal amplitude increases with decreasing the nominal frequency. The results of distance and circumference amplitude curves of an active group show extended test range and improved amplitude sensitivity to reflectors using antenna array with more elements.

The study of the gain coefficient in frequency domain shows improvements in focusing technique effect at higher nominal frequencies. For distance $H = 2$ m gain coefficient is $K = 13$ and $K = 4$ for nominal frequencies of $f = 100$ kHz and $f = 10$ kHz, respectively.

References

1. G. Kino, *Acoustic Waves: Devices, Imaging and Analogue Signal Processing* (Prentice-Hall, New Jersey, 1987)
2. J. Davies, *Inspection of Pipes Using Low Frequency Focused Guided Waves*, Ph.D. thesis. Imperial College, University of London (2008)
3. I. Ermolov, *Theory and Practice of Ultrasonic Control* (Mashinostroenie, Moscow, 1981). (In Russian)
4. I. Ermolov, A. Vopilkin, V. Badalyan, *Calculations in Ultrasonic Testing* (Echo+, Moscow, 2000). (In Russian)
5. J. Davies, F. Simonetti, M. Lowe, P. Cawley, Review of synthetically focused guided wave imaging techniques with application to defect sizing, in *Review of Progress in Quantitative NDE*, vol. 25, ed. by D.O. Thompson, D.E. Chimenti (American Institute of Physics, Melville, New York, 2006), p. 142
6. C. Holmes, B. Drinkwater, P. Wilcox, Post-processing of the full matrix of ultrasonic transmit-receive array data for non-destructive evaluation. *NDT E Int.* **38**(8), 701 (2005)
7. A. Velichko, P. Wilcox, Excitation and scattering of guided waves: relationships between solutions for plates and pipes. *J. Acoust. Soc. Am.* **125**(6), 3623 (2009)

Interaction of Low-Frequency Guided Waves with Discontinuities

A.A. Nasedkina, A.R. Alexiev and J. Malachowski

Abstract Modern methods of ultrasonic nondestructive testing allow one to detect defects in pipes with the help of guided ultrasonic waves. This chapter studies the propagation of longitudinal and torsional ultrasonic low-frequency guided waves in a pipe with discontinuities and defects. The defects considered for investigations include notches, holes, and their combination. Solid and finite element numerical models are developed for a sample pipe without defect, and for sample pipes with various types of defects. In order to simulate the propagation of ultrasonic guided waves in an isotropic medium, an excitation load is applied to one end of the pipe. For longitudinal guided waves simulation, the load vector is directed along the length of the pipe, and for torsional guided waves simulation, the load vector is directed tangentially to the circumference of the pipe. The results of the simulations allow us to estimate the amplitude and transit time of the impulse reflected from the defect and to analyze how various defects influence the stress–strain state of the pipeline.

Keywords Ultrasonic guided wave · Low-frequency guided wave · Nondestructive testing · Defect detection · Torsional wave · Longitudinal wave · Finite element method · Stress–strain state

A.A. Nasedkina (✉)

I.I. Vorovich Institute of Mathematics Mechanics and Computer Science,
Southern Federal University, Rostov-on-Don, Russia
e-mail: anna.nasedkina@gmail.com

A.R. Alexiev

Institute of Mechanics of Bulgarian Academy of Sciences, Sofia, Bulgaria

J. Malachowski

Military University of Technology, Warsaw, Poland

© Springer International Publishing AG 2018

E.N. Barkanov et al. (eds.), *Non-destructive Testing and Repair of Pipelines*,
Engineering Materials, DOI 10.1007/978-3-319-56579-8_4

1 Introduction

Ultrasonic guided wave method is an effective method of defect detection in long-distance pipeline that lies deeply underground. In such cases, inner surface and even outer surface corrosion is very difficult to detect. Conventional ultrasonic methods of defect detection consist in point-by-point testing from the outer surface of a pipe. The major shortcomings of this technique are high costs and long inspection time. Additionally, an access to the outside surface often includes removal of the pipe coating to perform the test, and further re-installation of the coating when the testing is completed. Therefore, for long-distance pipelines this method becomes time-consuming and inefficient.

The method of damage detection by low-frequency ultrasonic guided waves provides an attractive alternative to conventional ultrasonic methods, when dealing with a long-range inspection of pipelines. Methods of ultrasonic nondestructive testing by guided waves have attracted considerable attention in the recent years. Ultrasonic guided waves are guided by the geometry of the object in which they propagate. Because of decreased attenuation loss, these waves transmit along total circumferential section of the pipe while propagating in the longitudinal direction. Guided ultrasonic waves can propagate at the distances of more than 100 m. Due to that, inspection time can be dramatically reduced, because long-distance pipelines can be inspected from a single position. Special equipment installed in one location of a pipe registers the waves reflected from defects, which indicates the presence of corrosion or other discontinuities [1].

Typically, three main acoustic modes of guided waves can propagate in a pipeline: longitudinal (axisymmetric), torsional, and flexural (antisymmetric). Interaction of guided waves with geometrical discontinuities in structures has been studied extensively in the recent years [2–7]. It has been shown that longitudinal guided waves have better sensitivity to shallow defects, whilst torsional waves have no velocity dispersion, because they propagate through the pipe with constant speed that does not depend on frequency and wall thickness.

An important step in the process of development and optimization of nondestructive-testing techniques is numerical simulation of the guided waves propagation. This chapter considers numerical model of the propagation of longitudinal and torsional ultrasonic low-frequency guided waves in a pipe with various types of defects, such as notches and holes. Mathematical problem statement of the wave propagation in a pipe gives transient initial boundary-value problem of the elasticity theory which is solved using finite element method implemented in commercial software ANSYS. In order to simulate the emission of the desired guided wave into the pipe, a special excitation function is applied at one of the pipe ends. For longitudinal guided waves simulation, the load vector is directed along the length of the pipe, and for torsional guided waves simulation, the load vector is directed tangentially to the circumference of the pipe. The results of the simulation can give information on the amplitude and the transit time of the impulse reflected from the defects and the pipe edges and help to analyze how various defects influence the stress–strain state of the pipeline.

2 Mathematical Modeling and Finite Element Approximations

We assume that the pipe is made of homogeneous isotropic material. Then the problem of the wave propagation in a pipe in the frames of the elasticity theory can be formulated as a transient dynamic problem. Let us consider an isotropic body that occupies a region Ω in three-dimensional space. Then in vector matrix notation, the resulting problem can be described by the set of equations.

$$\mathbf{L}^T(\nabla) \cdot \mathbf{T} = \rho \ddot{\mathbf{u}}, \quad \mathbf{T} = \tilde{\mathbf{N}} \cdot \mathbf{S}, \quad \mathbf{S} = \mathbf{L}(\nabla) \cdot \mathbf{u}, \quad (1)$$

where

$$\mathbf{L}^T(\nabla) = \begin{bmatrix} \partial/\partial x & 0 & 0 & \partial/\partial y & 0 & \partial/\partial z \\ 0 & \partial/\partial y & 0 & \partial/\partial x & \partial/\partial z & 0 \\ 0 & 0 & \partial/\partial z & 0 & \partial/\partial y & \partial/\partial x \end{bmatrix}, \quad \nabla = \begin{bmatrix} \partial/\partial x \\ \partial/\partial y \\ \partial/\partial z \end{bmatrix}, \quad (2)$$

ρ is the density, $\mathbf{u} = \mathbf{u}(\mathbf{x}, t)$ is the displacement vector, $\mathbf{x} = \{x, y, z\} \in \Omega$, t is the time, $\mathbf{T} = [\sigma_{xx}, \sigma_{yy}, \sigma_{zz}, \sigma_{xy}, \sigma_{yz}, \sigma_{xz}]$ is an array of the stress components σ_{kl} , \mathbf{C} is the 6×6 matrix of elastic stiffness, $\mathbf{S} = [\varepsilon_{xx}, \varepsilon_{yy}, \varepsilon_{zz}, 2\varepsilon_{xy}, 2\varepsilon_{yz}, 2\varepsilon_{xz}]$ is an array of the strain components ε_{kl} ($k, l = x, y, z$).

For an isotropic medium the matrix \mathbf{C} is given in the form

$$\tilde{\mathbf{N}} = \frac{E}{(1+\nu)(1-2\nu)} \begin{bmatrix} 1-\nu & \nu & \nu & 0 & 0 & 0 \\ & 1-\nu & \nu & 0 & 0 & 0 \\ & & 1-\nu & 0 & 0 & 0 \\ & & & \frac{1-2\nu}{2} & 0 & 0 \\ \text{sym} & & & & \frac{1-2\nu}{2} & 0 \\ & & & & & \frac{1-2\nu}{2} \end{bmatrix},$$

where E is the Young's modulus, ν is the Poisson's ratio.

To formulate a transient dynamic boundary-value problem, we complete Eq. (1) with boundary and initial conditions. Let $\Gamma = \partial\Omega$ be the boundary of the volume Ω . We consider one end Γ_1 of the pipe to be rigidly fixed

$$\mathbf{u} = \mathbf{0}, \quad \mathbf{x} \in \Gamma_1. \quad (3)$$

The excitation load is applied to the other end of the pipe Γ_2 :

$$\mathbf{L}^T(\mathbf{n}) \cdot \mathbf{T} = \mathbf{p}, \quad \mathbf{x} \in \Gamma_2, \quad (4)$$

where \mathbf{n} is the external unit normal vector, $\mathbf{p} = \mathbf{p}(\mathbf{x}, t)$ is the pressure vector.

The rest of the boundary $\Gamma_s = \Gamma \setminus (\Gamma_1 \cup \Gamma_2)$ is assumed to be free from stresses:

$$L^T(\mathbf{n}) \cdot \mathbf{T} = \mathbf{0}, \quad \mathbf{x} \in \Gamma_s. \quad (5)$$

For initial conditions, we assume that at the initial time moment $t = 0$ the displacement vector and velocity vector are equal to zero:

$$\mathbf{u}(\mathbf{x}, 0) = \mathbf{0}, \quad \dot{\mathbf{u}}(\mathbf{x}, 0) = \mathbf{0}, \quad \mathbf{x} \in \Omega \quad (6)$$

The formulated boundary-value problem (1)–(6) can be solved numerically by the finite element method. In order to derive the system of finite element equations, we apply a well-known technique of finite element approximations.

Let $\Omega_h \subset \Omega$ be the region occupied by the finite element mesh, $\Omega_h = \cup_m \Omega^{em}$, where Ω^{em} is a finite element with the number m . The approximate solution $\mathbf{u}_h \approx \mathbf{u}$ of Problem (1)–(6) can be expressed in the form of semi-discrete approximations:

$$\mathbf{u}_h = \mathbf{N}^T(\mathbf{x}) \cdot \mathbf{U}(t), \quad (7)$$

where \mathbf{N}^T is the matrix of basis functions, \mathbf{U} is the vector of the nodal degrees of freedom (nodal displacements).

We approximate the weak problem statement in a finite-dimensional space related to the basis functions $\mathbf{N}^T(\mathbf{x})$. Use of (7) and similar representations for the projection functions for the weak problem statement in Ω_h leads to the system of finite element equations with respect to the nodal displacements \mathbf{U} :

$$\mathbf{M} \cdot \ddot{\mathbf{U}} + \mathbf{K} \cdot \mathbf{U} = \mathbf{F}, \quad (8)$$

where $\mathbf{M} = \sum_m^a \mathbf{M}^{em}$, $\mathbf{K} = \sum_m^a \mathbf{K}^{em}$ are the global matrices composed of the corresponding element matrices, \mathbf{M}^{em} and \mathbf{K}^{em} are the mass matrix and the stiffness matrix, respectively, for finite element with number m , $\mathbf{F} = \sum_m^a \mathbf{F}^{em}$ is the global vector of external influences composed of the element vectors \mathbf{F}^{em} , which can be expressed by formulae:

$$\begin{aligned} \mathbf{M}^{em} &= \int_{\Omega^{em}} \rho \mathbf{N}^{em} \cdot (\mathbf{N}^{em})^T d\Omega, & \mathbf{K}^{em} &= \int_{\Omega^{em}} (\mathbf{B}^{em})^T \cdot \mathbf{C} \cdot \mathbf{B}^{em} d\Omega, \\ \mathbf{B}^{em} &= \mathbf{L}(\nabla) \cdot (\mathbf{N}^{em})^T, & \mathbf{F}^{em} &= \int_{\Gamma_1^{em}} \mathbf{N}^{em} \cdot \mathbf{p} d\Gamma. \end{aligned} \quad (9)$$

In (9) \mathbf{N}^{em} are the element matrices of approximate basis functions, Γ_1^{em} is the boundary, which approximates Γ_1 .

Due to (6), system (8) must be supplemented by initial conditions:

$$\mathbf{U}(0) = \mathbf{0}, \quad \dot{\mathbf{U}}(0) = \mathbf{0}, \quad \mathbf{x} \in \Omega. \quad (10)$$

3 Numerical Models of Defects and Initial Data for Simulations

The test pipe is made of steel and has the diameter of 114 mm and wall thickness of 6 mm. The test pipe is several meters long, but for numerical simulation only a part of the pipe around the defect is considered. The overall scheme of numerical model is shown in Fig. 1, where l is examined distance of the pipe and l_{def} is the distance from emitter to the defect. The guided wave propagation through the pipe is monitored at the monitoring plane in order to investigate the reflection from the defect.

We consider three cases of induced defects: (i) transverse notch with an initial length of 180 mm, a depth of 2 mm and a width of 2 mm (Fig. 2a); at computer simulation the length and the depth were varied; (ii) combination of a transverse notch with a length of 200 mm, a depth of 2 mm and a width of 2 mm and a round hole of \varnothing 10 mm (Fig. 2b); (iii) 360° circumferential notch of varied depth and width. Photos of real defects and their 3D solid models are shown in Fig. 2.

We study torsional and longitudinal guided wave propagation in pipes with the described above defects. Simulation of torsional guided waves, due to their antisymmetric mode, requires full 3D models of pipes with defects. Here torsional guided wave propagation will be considered for the first two types of defects with transverse notches.

Simulation of longitudinal guided wave propagation allows using simplified finite element models. In our case, due to an axisymmetric mode of longitudinal waves and symmetry of the considered types of defects with respect to longitudinal axis, it is enough to build only a half of the pipe model. Moreover, for the pipe with a circumferential notch the simulation of longitudinal wave propagation can be reduced to 2D (axisymmetric) case. Therefore, for simulation of longitudinal waves, we construct half 3D models of pipes with transverse notches and 2D model of axisymmetric pipe with circumferential notch.

Solid and finite element simulation was done in ANSYS finite element package. 3D full and half models were developed for the pipe without defect, the pipe with the transverse notch, and the pipe with the transverse notch and hole. 2D model of meridional section of the pipe was constructed for the pipe with the circumferential notch.

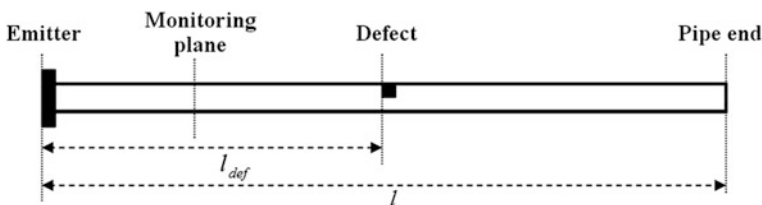


Fig. 1 Scheme of numerical model

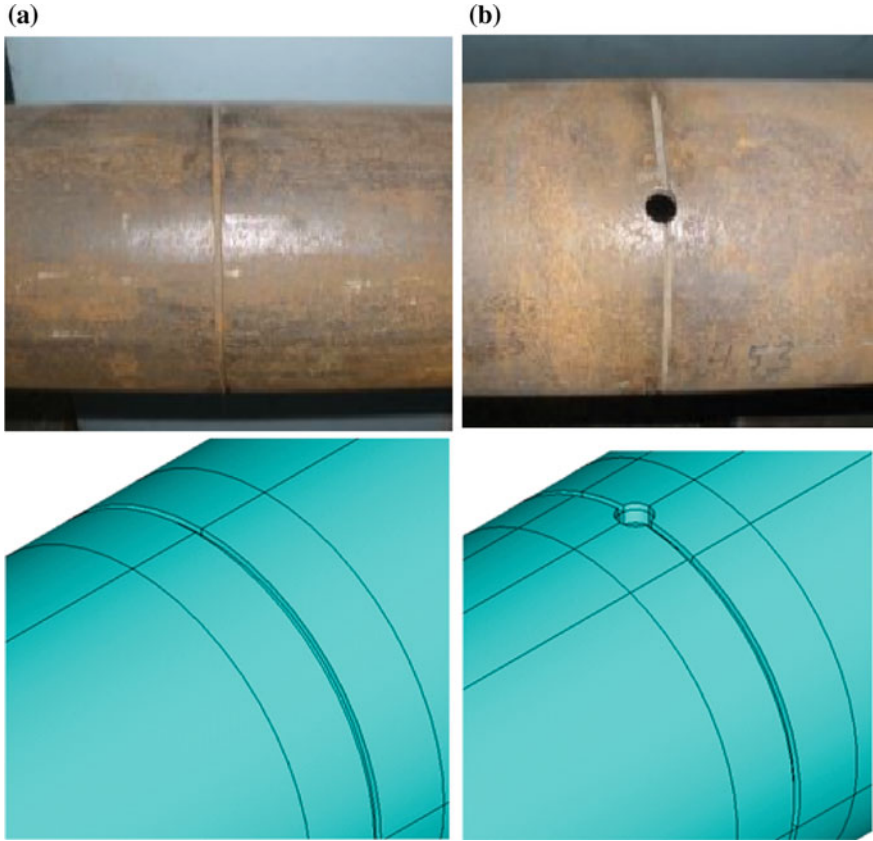


Fig. 2 Types of defects and their solid models: transverse notch (a) and transverse notch with a hole (b)

3D solid models were meshed with 3D eight-node brick elements Solid185 (Fig. 3a), which have three degrees of freedom in each node: displacements in nodal x , y and z directions. For 2D solid models, similar 2D Plane182 elements with linear approximation (Fig. 3b) were used. Plane182 elements have four nodes and two degrees of freedom in each node: displacements in nodal x and y directions.

ANSYS documentation [8] suggests using 20 elements in wave propagation direction per one wavelength and aspect ratio 5/1 to guarantee high-precision calculations. Therefore, for 6 mm wall thickness and 2 mm depth of defects, 6 finite elements per pipe thickness were used. The aspect ratio 5/1 was kept for 3D meshes, whereas squared elements with 1 mm edge length were used for 2D mesh of the axisymmetric pipe with the circumferential notch. Figure 4 shows 3D finite element meshes around the transverse notch (Fig. 4a) and the transverse notch with the hole (Fig. 4b).

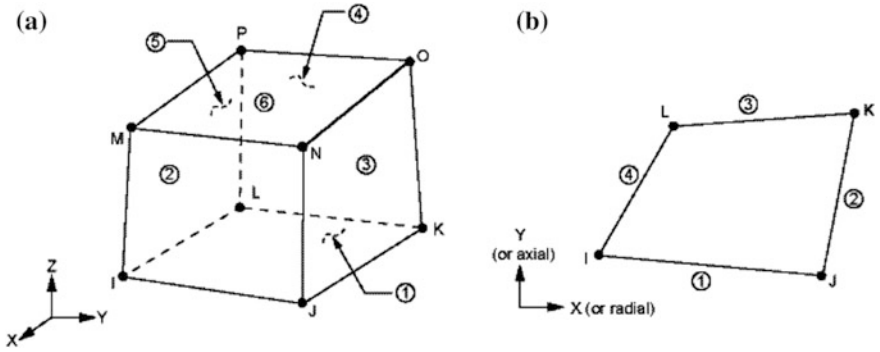


Fig. 3 Finite elements used for simulation in ANSYS: Solid185 (a) and Plane182 (b)

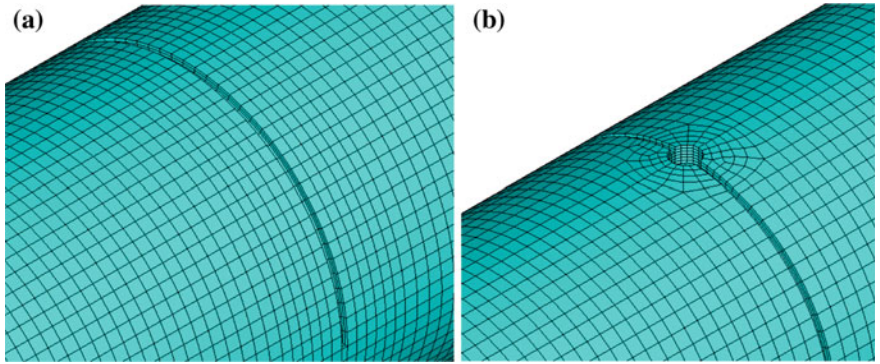


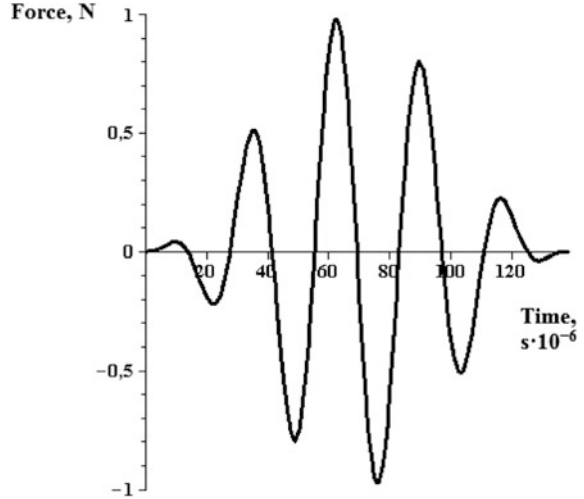
Fig. 4 3D finite element meshes around defects: transverse notch (a) and transverse notch with a hole (b)

The excitation impulse can be described by a known sinusoid function characterized by the number of cycles n and the working frequency f , which determine the calculated signal impulse time $\tau = n/f$. The form of the excitation function used in numerical simulation was taken from [9] and can be expressed as

$$F(t) = \begin{cases} 0.5(1 - \cos\frac{2\pi ft}{n}) \sin(2\pi ft), & 0 < t \leq \tau; \\ 0, & t > \tau; \end{cases} \quad (11)$$

where n is the number of pulse cycles, f is the central frequency, $\tau = n/f$ is the signal impulse time. The plot of the pulse-time signal of the excitation function (11) for the central frequency $f = 36,000$ Hz and $n = 5$ cycles is shown in Fig. 5. Here the calculated signal impulse time is $\tau = 138 \mu s$.

Fig. 5 Plot of pulse-time signal for 5 cycles at 36 kHz



For simulation in ANSYS, we apply surface load to the left of the pipe, which can be described a pressure function equivalent to force function (11)

$$P(t) = F_0 F(t) / S, \quad (12)$$

where n is the area of the outer surface with applied load, f is the value of the force, $F(t)$ is the excitation function (11).

Pressure function (12) can be used to model both torsional and longitudinal modes. The difference in the simulation of these two modes of guided waves is in the orientation of the load vector. Longitudinal guided waves propagate through compressional motion along the longitudinal axis of the pipe. Hence, in the case of longitudinal mode, the surface pressure load is directed along the normal to the pipe edge (Fig. 6a), which is a default surface load orientation in ANSYS. Torsional guided waves propagate via shearing motion parallel to the circumferential direction of the pipe. Therefore, in the case of torsional mode, the surface load vector should be directed along the tangent to the circumference of the pipe. Simulation in ANSYS required using special surface finite elements Surf154 to apply tangential pressure around the circumferential area. In particular, tangential surface pressure was applied to the outer surface of the first row of elements at the left end of the pipe (Fig. 6b).

Finite element simulation of ultrasonic guided wave propagation was implemented in full transient analysis. The material of the steel pipe was considered as linear isotropic material with elastic modulus $E = 205$ GPa, Poisson's ratio $\nu = 0.28$ and density $\rho = 7800$ kg/m³. In the experiment, the working frequency of the ultrasonic waves in the pipeline was 36 kHz. For numerical simulation, number of pulse cycles in the excitation load was taken to be $n = 5$ with signal impulse time $\tau = 138$ μ s, the force value was $F_0 = 100$ N, and the wave speed was $c = 3200$ m/sec for both torsional and longitudinal modes of guided waves. The examined

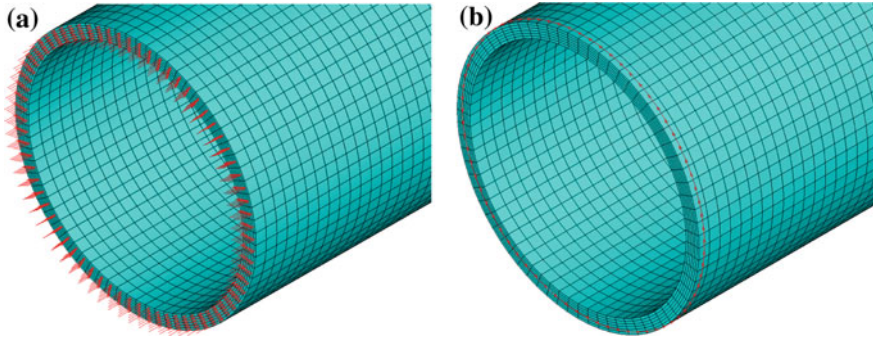


Fig. 6 Boundary conditions at the left end of the pipe: longitudinal mode (a) and torsional mode (b)

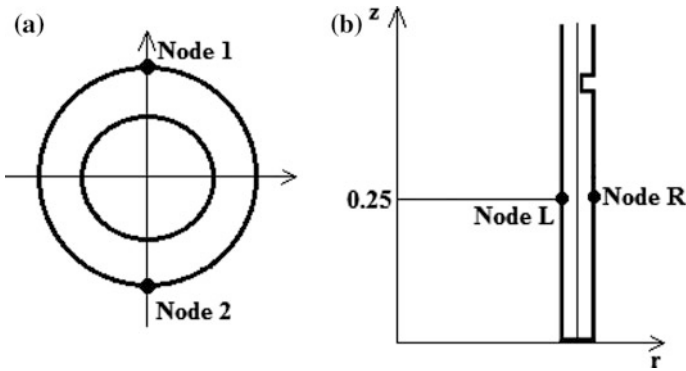


Fig. 7 Location of nodes at the monitoring plane: for 3D models with transverse notches (a) and for 2D model with circumferential notch (b)

distance l of the pipe was 1 m, with the defect located halfway $l_{\text{def}} = 0.5$ m from the left end of the pipe, where the impulse was excited. For the given length l of the pipe and the given wave speed c , in the absence of defects the excited impulse propagating in longitudinal direction should reach the opposite end of the pipe in $l/c = 312.5 \mu\text{s}$. In numerical simulation, the overall time period for the computations was taken to be three times larger: $t_{\text{end}} = 3l/c = 937 \mu\text{s}$. All computations were performed without taking into account damping.

In order to monitor the wave propagation along the pipe, we verify the reflected signal at the distance 0.25 m from the end of the pipe, where an emitter is located. We will consider representative nodes in the monitoring plane, where we will extract and analyze the computational results. For 3D models, as the simulated transverse notches are not axisymmetric, we consider two nodes, one in upper and one in lower part of the meridional section of the pipe at the monitoring plane (Fig. 7a). For the axisymmetric case of the pipe with the circumferential notch, we also consider two nodes at the monitoring plane (Fig. 7b), one at the outer surface (right) and one at the inner surface (left) of the pipe.

4 Results of Finite Element Simulation

In order to illustrate the propagation of ultrasonic guided waves through the pipes, we will consider the pictures of the equivalent stress distribution. The distribution of the equivalent stress is a good qualitative characteristic of the computation results, because the excitation signal is simulated as surface pressure load both for torsional and longitudinal waves. Figure 8 shows the comparison of torsional and longitudinal mode propagation in a full 3D model of the pipe without defects. It can be seen that at time moment $t = 262 \mu\text{s}$ the longitudinal wave (Fig. 8a) has reached the opposite end of the pipe, whereas the torsional wave (Fig. 8b) has only passed the middle part of the pipe. Also from Fig. 8, it can be observed that the longitudinal mode propagates faster than torsional mode.

The presence of defect causes the incident wave to reflect from it. Let us now consider the pictures of the equivalent stresses distribution in pipes with defects for the same time moment $t = 262 \mu\text{s}$. Figure 9 shows the comparison of torsional and longitudinal wave propagation in a full 3D model of the pipe with transverse notch. Longitudinal wave causes different forms of reflection from the transverse notch and deformation of the pipe than torsional wave. Moreover, it is observed that the longitudinal wave can generate new transmission modes.

Similar pictures of torsional and longitudinal mode propagation can be seen in Fig. 10, which illustrates propagation of guided waves through a transverse notch and a hole in 3D pipe. Here, even more dramatic interaction occurs between the guided waves and the defect, which causes greater deformation of the steel pipe (Fig. 10).

Let us take closer look at the values of equivalent stress in the monitoring plane. We extract results from several nodes in the monitoring plane (Fig. 7a) and plot graphs of the equivalent stresses versus time. It is clear that for a non-axisymmetric defect the curves of these dependences will have similar shapes

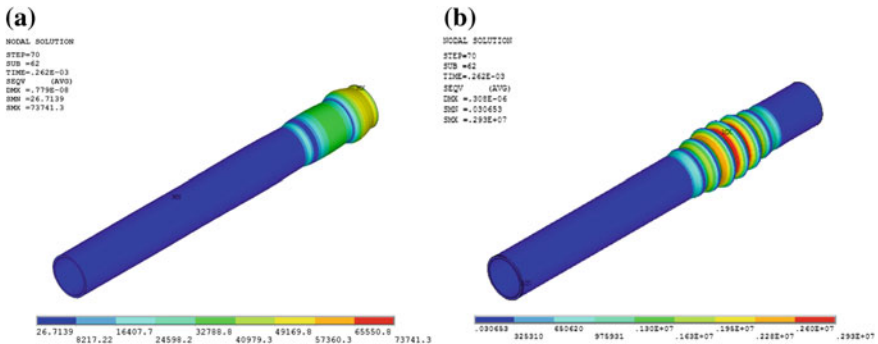


Fig. 8 Equivalent stress distribution at $t = 262 \mu\text{s}$ for the pipe without defect: longitudinal mode (a) and torsional mode (b)

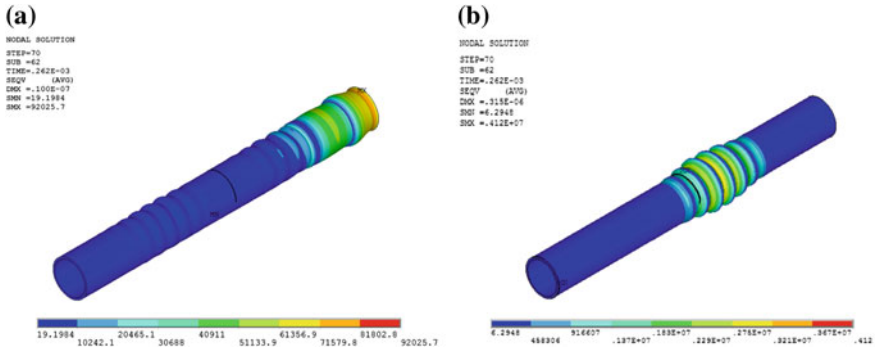


Fig. 9 Equivalent stress distribution at $t = 262 \mu\text{s}$ for the pipe with the transverse notch: longitudinal mode (a) and torsional mode (b)

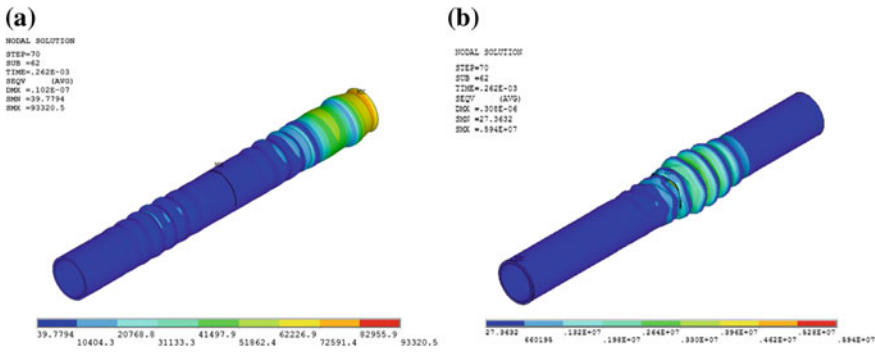


Fig. 10 Equivalent stress distribution at $t = 262 \mu\text{s}$ for the pipe with the transverse notch and a hole: longitudinal mode (a) and torsional mode (b)

for all nodes at the monitoring plane with some difference for upper and lower nodes. We first consider Node 1 located on the outer surface in the upper part of the pipe, where the transverse notch locates.

Figure 11 shows time records of equivalent stresses for torsional mode of guided wave in Node 1 of the monitoring plane. We can see that the incident torsional wave has passed the monitoring plane three times. Here we compare two types of defects, a transverse notch (Fig. 11a, green curve) and a transverse notch with a hole (Fig. 11b, blue curve). The plot for the pipe without defect is shown in black. The guided wave of torsional mode propagates through the pipe without dispersion and without reflection from the pipe walls. Therefore, in the absence of defect, the values of equivalent stress at the monitoring plane during the time period between the incident signal arrivals are equal to zero (see black curves in Fig. 11). The presence of defect generates reflected waves, which can be seen between the arrivals of incident wave (see green and blue curves in Fig. 11). The comparison of the graph for a pipe with transverse notch (green curve) with the graph for a pipe with

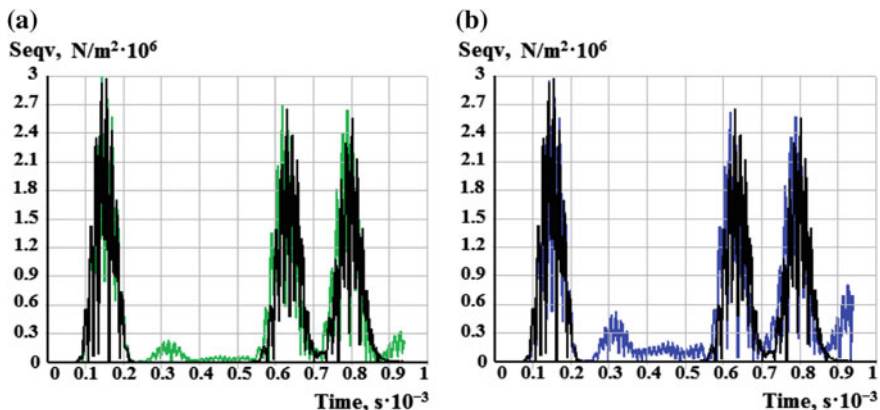


Fig. 11 Plots of equivalent stress histories for torsional wave propagation: pipe with transverse notch (**a**, *green curve*) and pipe with transverse notch with a hole (**b**, *blue curve*), compared to a pipe without defect (*black curve*)

transverse notch and a hole (blue curve) shows that the second type of defect generates larger amplitudes of reflected wave. In both cases, the first part of the reflected mode is larger than the second half. Moreover, from Fig. 11 we can see that the incident torsional signal arrives at the monitoring node at $t \approx 80 \mu\text{s}$, whereas the incident signal reflected from the pipe end returns to this node at $t \approx 550 \mu\text{s}$.

Now we consider the propagation of longitudinal waves. Figure 12 shows time records of equivalent stress for longitudinal mode of guided wave at Node 1 of the monitoring plane. We can notice that the incident longitudinal wave has passed the monitoring plane four and half times, which indicates that it propagates faster than torsional wave. Again we consider the same two types of defects, the transverse notch (Fig. 12a, green curve) and the transverse notch with the hole (Fig. 12b, blue curve). Here from the black curve in Fig. 12 we can observe that even in the absence of defect, the equivalent stress at the monitoring plane during the time period between the incident signal arrivals has tiny peaks. This result can be due to the reflection of the longitudinal wave from the pipe walls. As in the case of torsional wave, the reflected waves caused by the presence of defect can be noticed between the arrivals of incident signal (see green and blue curves in Fig. 12). Again, we can observe based on Fig. 12 that the transverse notch with the hole (blue curve) generates larger amplitudes of reflected waves than the transverse notch alone (green curve). However, in contrast to the case of torsional wave, the first half of the reflected mode is much smaller than the second half. From Fig. 12 we can observe that the incident longitudinal signal arrives at the monitoring node at the same time as it was for torsional signal ($t \approx 80 \mu\text{s}$). Meanwhile, the incident signal reflected from the pipe end returns to this node at $t \approx 340 \mu\text{s}$. Hence, the longitudinal signal travels faster than torsional signal.

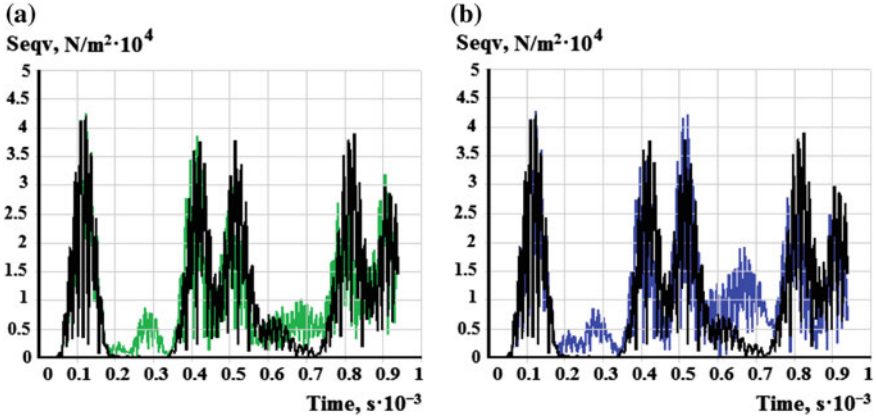


Fig. 12 Plots of equivalent stress histories for longitudinal wave propagation: pipe with transverse notch (**a**, *green curve*) and pipe with transverse notch with a hole (**b**, *blue curve*), compared to a pipe without defect (*black curve*)

The displacement values can be used to verify the excitation signal. For the torsional wave, which propagates via shearing motion in longitudinal direction of the pipe, the displacements $u_\theta = u_x$ for the nodes with $y > 0$ and $u_\theta = -u_x$ for the nodes with $y < 0$ when $x = 0$. These displacements have the order of 10^{-7} m compared to the displacements u_y and u_z , which have much smaller values: 10^{-20} m for the pipe without defect, 10^{-12} – 10^{-13} m in the presence of defects. Greater orders of the displacements u_θ indicate the torsional mode of the excited signal. Simulation of the longitudinal guided wave propagation has shown that all displacements have the same orders of 10^{-8} .

The influence of the defect size on the stress–strain state of the pipe has been studied for the defect in the form of a notch. Torsional guided wave propagation has been studied for the transverse notch of varied length and depth. Longitudinal guided wave propagation has been investigated for the full circumferential notch of varied width and depth, using axisymmetric model.

To analyze the influence of the transverse notch size on the torsional guided wave propagation, we consider two cases. In the first case, the depth of the transverse notch was varied from 2 to 6 mm (equal to the thickness of the pipe) with the step of 1 mm, and the length of the notch was constant and equal to 180 mm. Figure 13 shows plots of equivalent stress in two nodes of the monitoring plane in the 3D model (Fig. 7a) for different depth values during time period from 0 to 381 μ s. Based on Fig. 13, we can conclude that the amplitude of the reflected wave increases with increasing the defect depth. The difference between the results for Node 1, located in upper part of the pipe, and Node 2, located in the lower part of the pipe can be seen clearly. The amplitude of the reflected wave is considerably larger for Node 1 (see Fig. 13a), i.e., in the upper part of the pipe where the notch locates. Moreover, when the depth of the notch equals the thickness of the pipe (6 mm), the amplitude of the reflected wave equals the amplitude of the incident wave.

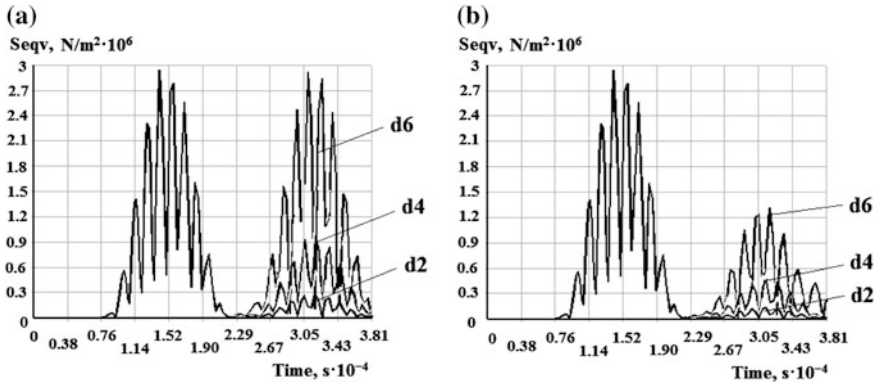


Fig. 13 Equivalent stresses of torsional guided waves: comparison of Node 1 (a) and Node 2 (b) for a pipe with varied depth of transverse notch ($d = 2, 4, 6$ mm)

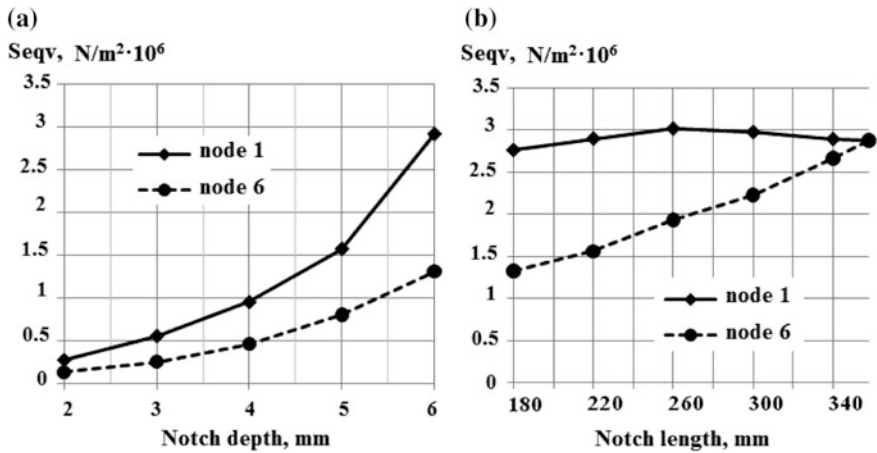


Fig. 14 Influence of the transverse notch on the maximal equivalent stress at the monitoring plane for the reflected torsional wave: notch depth (a) and notch length (b)

The dependence of maximal values of the equivalent stress of the reflected wave on the notch depth is summarized in Fig. 14a. Here we can observe significant increase of stress at Node 1 compared to those at Node 2. Moreover, when the depth of the notch is equal to the pipe thickness (6 mm), the maximal amplitude of the stress at Node 1 becomes twice larger than at Node 2.

In the second case of torsional wave propagation, the depth of the transverse notch was set constant and equal to 2 mm, and the length of the notch was varied from initial value of 180 to 358 mm (equal to the pipe circumference length) with the step of 40 mm. In this case, the plots of the equivalent stresses versus time, similar to those shown in Fig. 13, are not very informative. Therefore, we analyze

the maximal values of the equivalent stress and plot their dependences as functions of the notch length (Fig. 14b). Here we can observe that for Node 2, located in the lower part of the pipe, the stresses increase when increasing the notch length. The stresses at Node 1, located in the upper part of the pipe, remain almost constant. First, they slightly increase and then they slightly decrease with increasing the notch length. When the length of the transverse notch reaches its maximal value of 358 mm, i.e., the transverse notch becomes circumferential; the values of equivalent stresses at both nodes become almost equal.

Thus, from Fig. 14 we can conclude that the depth of the transverse notch has greater influence on the stress-strain state of the pipe than the length of the notch.

The influence of defect size on the longitudinal guided wave propagation was studied on example of full circumferential notch, where we used axisymmetric model of the pipe (Fig. 7b). Here we also analyzed two cases. In the first case, the depth of the notch was set constant and equal to 2 mm and the notch width was varied from 1 to 5 mm. In the second case, the width of the notch was set constant and equal to 2 mm and the notch depth was varied in the same manner from 1 to 5 mm.

The computations showed that the change of the notch depth had similar influence on the reflected wave as in the case of torsional guided wave interaction with transverse notch. Figure 15 shows plots of equivalent stress in two nodes of the monitoring plane in 2D model (Fig. 7b) for different depth values during time period from 0 to 320 μs . For longitudinal wave the amplitude of the reflected wave also increases considerably when increasing the defect depth. From Fig. 15 we can observe different results for Node L, located on the inner (left) surface of the pipe, and for Node R, located on the outer (right) surface of the pipe. The amplitude of the reflected wave for Node R is considerably larger. Moreover, when the depth of

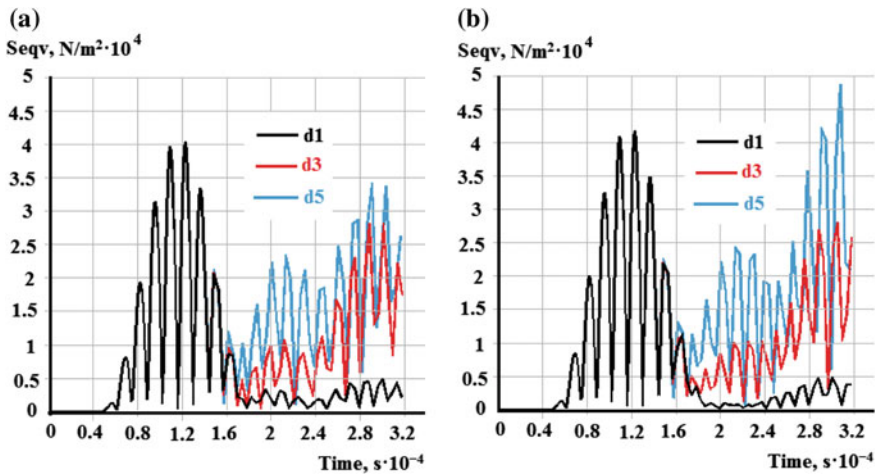


Fig. 15 Equivalent stresses of longitudinal guided waves: comparison of Node L (a) and Node R (b) for a pipe with varied depth of circumferential notch ($d = 1, 3, 5$ mm)

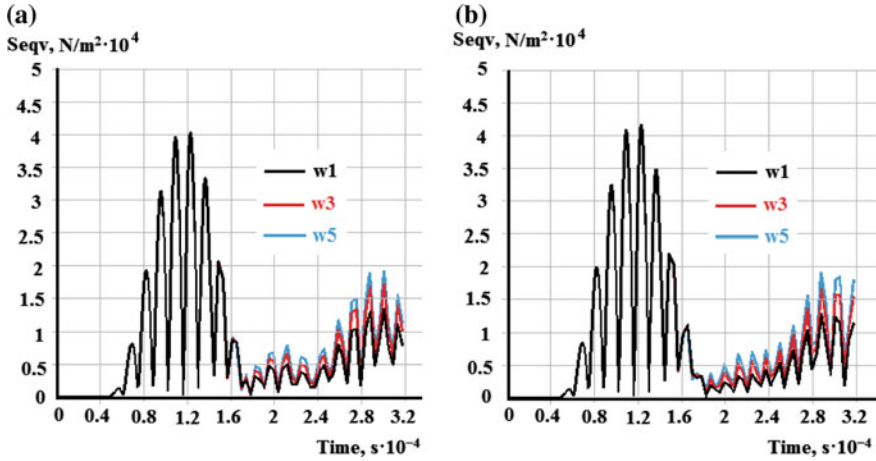


Fig. 16 Equivalent stresses of longitudinal guided waves: comparison of Node L (a) and Node R (b) for a pipe with varied width of circumferential notch ($d = 1, 3, 5$ mm)

the notch is close to the thickness of the pipe, the amplitude of the reflected wave equals the amplitude of the incident wave. This observation is similar to the case of torsional wave.

If we vary the notch width and plot the same graphs of equivalent stress at two nodes of the monitoring plane (Fig. 16), then we can see that there is almost no difference between Node L and Node R. The reflected wave increases with increasing the defect width, however, this increase is very small.

5 Conclusion

Results of numerical simulation of ultrasonic torsional and longitudinal guided wave propagation in a pipe with defects have been presented in this chapter. The defects considered included notches, holes and their combination. In order to investigate interaction of guided waves with discontinuities, finite element models of the pipes with defects were built in ANSYS finite element package. Full transient analysis was performed to simulate the guided wave propagation through the pipe. An incident signal was simulated as a surface pressure load applied to one end of the pipe. The mode of the guided wave was defined by the direction of the load vector. For longitudinal mode, the load vector was directed along longitudinal direction of the pipe, whereas for torsional mode the load vector was directed tangentially to the circumference of the pipe.

The simulation results gave information on the amplitude and the transit time of the impulse reflected from the defect. The pictures of equivalent stress distribution allowed us to analyze the stress–strain state of the pipe. The graphs of the

equivalent stresses *versus* time were plot for several nodes of the monitoring plane. The results were compared for two main types of defects, a transverse notch and a transverse notch with a hole. The comparison of results showed that the amplitude of the reflected wave was significantly larger for a transverse notch with a hole. The influence of the defect size on the stress-strain state of the pipe was analyzed for torsional wave propagating through a pipe with transverse notch of varied depth and length, and longitudinal wave propagating through a pipe with full circumferential notch of varied depth and width. The comparison of results for various values of the depth and length of the transverse notch allowed us to conclude that the notch depth had more significant impact than the notch length. The results for full circumferential notch showed that the notch width did not have significant influence compared to the notch depth.

References

1. M.N. Karmanov, V.M. Gorbik, Possibilities of practical application of low-frequency ultrasonic methods for defect detection in long-size objects by guided waves, in *7th National Scientific-Technical Conference and Exhibition*. Kiev, 112 (2013) (In Russian)
2. M.J.S. Lowe, D.N. Alleyne, P. Cawley, Defect detection in pipes using guided waves. *Ultrasonics* **36**(1–5), 147 (1998)
3. J. Li, On circumferential disposition of pipe defects by Long-range ultrasonic guided waves. *J. Pressure Vessel Technol.* **127**(4), 530 (2005)
4. W. Zhu, An FEM simulation for guided elastic wave generation and reflection in hollow cylinders with corrosion defects. *J. Pressure Vessel Technol.* **124**(1), 108 (2002)
5. A. Demma, The reflection of guided waves from notches in pipes: a guide for interpreting corrosion measurements. *NDT E Int.* **37**(3), 167 (2004)
6. M. Kharrat, W. Zhou, O. Bareille, M. Ichchou, Defect detection in pipes by torsional guided-waves: a tool of recognition and decision-making for the inspection of pipelines, in *Proceedings of the 8th International Conference on Structural Dynamics*, ed. by G. De Roeck, G. Degrande, G. Lombaert, G. Müller, EUROODYN 2011. Leuven, Belgium, 4–6 July 2011
7. A. Nasedkina, A. Alexiev, J. Malachowski, Numerical simulation of ultrasonic torsional guided wave propagation for pipes with defects. in *Advanced Materials. Manufacturing, Physics, Mechanics and Applications*, ed. by I.A. Parinov, C. Shun-Hsyung, V.Y. Topolov, Series Springer Proceedings in Physics, vol. 175, 475 (2016)
8. *ANSYS Mechanical APDL Theory Reference*. ANSYS Rel. 14.5. ANSYS Inc., Canonsburg (2012)
9. M.-F. Zheng, C. Lua, G.-z. Chenb, P. Men, Modeling three-dimensional ultrasonic guided wave propagation and scattering in circular cylindrical structures using finite element approach. *Phys. Procedia* **22**, 112 (2011)

Vibration-Based Damage Detection of Steel Pipeline Systems

A.A. Lyapin, Y.Y. Shatilov and A.A. Lyapin Jr.

Abstract This chapter is devoted to a numerical study of the vibration-based damage detection (VBDD) techniques of steel pipeline systems. VBDD techniques are thought to be worldwide non-destructive evaluation (NDE) techniques. VBDD techniques are based on detecting damage by using changes in the dynamic features of a structure that were a result of the defect. VBDD techniques have specific advantages over local NDE techniques. For example, VBDD techniques shortly estimate the state of the whole structure. Moreover, they have not restrictions to accessible components. Well-controlled numerical experiments of finite element model of steel pipeline system demonstrated that it is possible to reliably detect damage at different locations, as well as to locate VBDD techniques, applying relatively few sensors (strain gauges or accelerometers) and taking into account changes that happen to the essential vibration mode. Determination of eigenfrequencies and mode shapes for mechanical systems is one of the most important tasks, which allow receiving integrated information about the structure state. The aim of this chapter is to analyze the results of the vibration method for determining the degree of damage in pipeline system, and development of a software module for the damage localization in structures. In the result of this work, it was found, if mode shapes were well defined with a large number of measurement points, then the damage location could be determined with great accuracy, using any of the four VBDD techniques investigated. During this research, it was established that the probability of successful damage localization depends on the damage severity, the trials number. The latter is applied for getting the average mode shape, the distance between the support and the damage, the disposition of damage in respect to the nearest sensor, and the mea-

The original version of the book was revised: Incorrect author names have been corrected. The erratum to the book is available at https://doi.org/10.1007/978-3-319-56579-8_28

A.A. Lyapin · Y.Y. Shatilov (✉)
Don State Technical University, Rostov-on-Don, Russia
e-mail: art-web@mail.ru

A.A. Lyapin Jr.
I.I. Vorovich Institute of Mathematics Mechanics and Computer Sciences,
Southern Federal University, Rostov-on-Don, Russia

surement errors magnitude. The method is offered for calculating the probability of successful detection and localization of the damage. It is based on the measured mode shapes repeatability. As a conclusion, this research results demonstrate that VBDD techniques are a perspective tool to monitor structural health of pipeline systems. However, while these methods are capable to detect effectively small-size defect under well-controlled conditions, a significant amount of challenging work should be performed before the methods can be applied to real structures.

Keywords Pipeline systems · Defect · Damage detection · Structural vibration · Structural engineering · Structural health monitoring · Mode shapes

1 Introduction

This work is aimed to investigating the capability of vibration-based damage detection (VBDD) techniques to detect and define the location of small-scale damage of steel pipeline systems using a relatively small number of sensors. VBDD attracts attention of researchers for long time. Many VBDD methods have been worked out. However, they have not yet to be successfully used to operating engineering constructions.

This part reviews the state of the art in the VBDD methods, classifies these methods by the dynamic features and the procedures aimed at detecting damage, identifies principles and implementing procedures for each method, and discusses the advantages, requirements, and limitations relating to these methods.

The main and important step is signal processing. It is aimed to implementing the VBDD methods. Any successful implementing is based frequently on the signal processing quality.

Damage reconstruction for composite beams is demonstrated in [1] on the base of application of finite element method and experimental results comparison.

It is also well known that vibration-based damage detection could be successfully combined with other mathematical tools. As an example, the using of artificial neural networks for pattern recognition is demonstrated in [2] with the demonstration of accurate results and effective identification for damage value.

Another example of using one-dimensional convolutional neural networks for structural health monitoring and damage detection is present in [3], where authors developed novel and accurate methodic for real-time detection and localization of the damage.

For civil engineering, it is vital problem to detect damage in components of important objects like bridges. In [4], authors demonstrate technique of vibration-damage detection for steel truss bridge using four artificial damage scenarios. There were demonstrated highly sensitive features to present and divide the artificial damage. In addition, in [5], it is developed reconstruction technique for suspension bridge with pre-stressed cables.

Let us mention that overwhelming majority of articles concern damage detection in the structures without connections. However, it is also possible to implement this technique for analysis of bolted-connection [6].

The VBDD technique can be also successfully applied for technical objects. In [7], it was analyzed a damage detection procedure for composite helicopter main rotor blade. Moreover, the experimental results on damage reconstruction with corresponding sensitivity and robustness analysis were presented.

2 Numerical Research

Some researchers have pointed at the fact that it is possible to use the changes that take place in mode shape for detecting the damage presence and location. Changes of single-number measures for mode shape have been offered for detecting damage. The Modal Assurance Criterion (MAC) is a common single-number measure [8]. Its value of two modes φ and φ^* (e.g., a mode shape in the undamaged and damaged conditions, respectively) is determined as

$$\text{MAC} = \frac{\left| \sum_{j=1}^n \phi_j \phi_j^* \right|^2}{\sum_j \phi_j^2 \sum_j \phi_j^{*2}} \quad (1)$$

where n is the number of the degrees of freedom that defines the mode shape. Therefore, the MAC value points a degree of correlation between two corresponding modes. It varies from 0 to 1. The case, corresponding to 0 represents the absence of the correlation, and 1 presents the case of the total correlation. It is possible to interpret the deviation from 1 for a MAC value, derived as a result of comparing the measurements of two mode shapes for a considered structure as an indication of damage existing in the structure [9].

The Coordinate Modal Assurance Criterion (COMAC) differs from the MAC criteria because it gives local information, as well as combined information of number of modes. The COMAC for corresponding modal coordinate j and using m modes could be represented as

$$\text{COMAC}_j = \frac{\left| \sum_{i=1}^m \phi_{j,i} \phi_{j,i}^* \right|^2}{\sum_{i=1}^m \phi_{j,i}^2 \sum_{i=1}^m \phi_{j,i}^{*2}} \quad (2)$$

If the modal displacements at coordinate j from two measurements sets are the same, the COMAC value for this coordinate is equal to 1. The smallest COMAC value shows the most probable location of damage.

The MAC values could be used to indicate, which mode is the most benefiting at structural repairs. Moreover, the COMAC values give good indications of the presence and location of the repairs. In these tests, two of three repaired points were correctly identified [10, 11]; at the same time, two spurious locations were also identified. The success of damage localization using MAC and COMAC values depends on whether or not the modes and measurements of locations, used in the

analysis, adequately reflect the damage. Consequently, the conclusion was made that all the damaged areas could not be identified, as shown by the fact that one affected point was not correctly determined [10, 11].

The simplest way to use mode shapes is the consideration of the difference between the damaged and undamaged unit-norm normalized mode shapes. Since it is expected that damage causes a localized stiffness decrease, it is expected that the mode shape displacement will be greatly changed at the location of damage.

The primary purpose of the numerical study was to evaluate the capabilities of the damage detection methods in the absence of experimental uncertainties. This permitted an assessment of the feasibility in the following experimental study, and helped in its design. Moreover, one of the main goals of the numerical research was to define if few measurement points could accurately characterize the mode shapes to allow reliable detecting and localizing of small-scale damage. This issue is extremely valuable because a structure can arguably be instrumented only at few locations. Thus, methods seriously considered for implementing in the area should show that they can operate well when they are limited by few measurement locations, and under the restrictions related to a priori selection of these locations [12, 13].

The commercial finite element (FE) analysis package ANSYS was applied to make eigenvalue analyses with the purpose to generate the system natural periodicity and mode shapes. In spite of the fact that the undamaged system was symmetrical both transversely and longitudinally, the research of non-symmetrical damage states was prevented applying the symmetry boundary conditions to decrease the model size. The steel pipeline was set apart into eight-node three-dimensional brick pyramid elements [14].

Constraints in boundary conditions were imposed at the two support nodes of pipeline, located along the bottom line of the pipeline, preventing displacements in the vertical and horizontal directions, thus avoiding rigid body movement of the system (see Fig. 1). Moreover, the side faces were restrained in both the longitudinal and transverse directions. Elastic properties of physical components were applied as model parameters.

The model was calibrated to the first three natural frequencies and mode shapes of the undamaged physical system. Figure 2 demonstrates the mode shapes related to the first three modes that were obtained by using the FE model Fig. 3.

As soon as the model had been tested, damage that happened in the pipeline was modeled by eliminating a single element, with dimensions of 133×103 and $203.2 \times 152.4 \text{ mm}^2$ in plan with 2.4 and 7.125 mm thickness, respectively, from

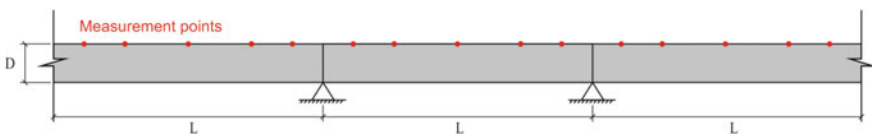


Fig. 1 Information model of steel pipeline

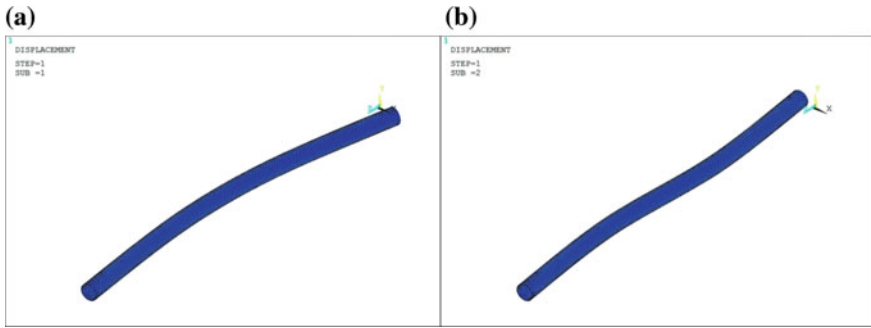


Fig. 2 Mode shape of the steel pipeline, generated by FE model: **a** 1st mode (58.99 Hz), **b** 2nd mode (75.52 Hz)

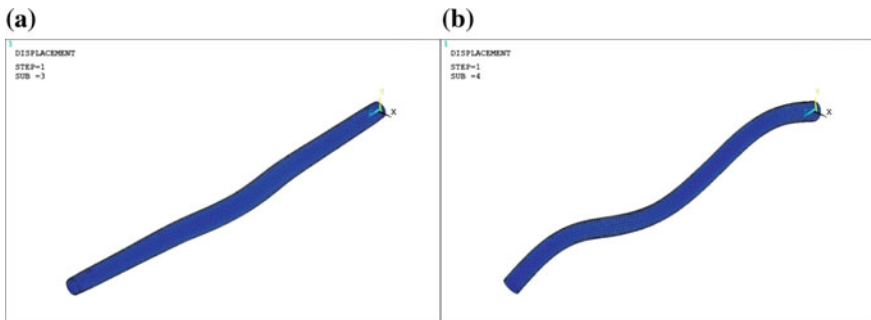


Fig. 3 Mode shape of the steel pipeline, generated by FE model: **c** 3rd mode (273.88 Hz), **d** 4th mode (317.22 Hz)

the top surface of the pipe. Such damage may be representative for deterioration of the material surface. The discrete nature of this simulated damage also allows one to investigate the potential precision of VBDD techniques in the localization of small-scale damage. We modeled 80 damage cases, each of which represented a specific damage location.

The intention of the FE analysis was to model acquiring the measured information from sensors that were attached to a physical system at few locations. Thus, the information on vertical displacement was taken from the FE-generated mode shapes of the system at few measurement points spaced uniformly along the pipe bottom side. Three cases were studied: (i) the case of seven measurement points, (ii) the case of 10 measurement points, and (iii) a well-defined reference case of 15 measurement points. In addition to these measurement points, we assumed that mode shape deflections were absent at the supports.

The performance of the damage detection methods when only the essential mode shape was applied had a great interest because in practice accurate measuring of higher mode shapes is much more complicated. Additionally, we also investigated

the first three flexural mode shapes to determine whether significant improvements could be realized by considering higher modes in the VBDD calculations. As described above, mode shapes were defined by measurements at 7, 10 and 15 points, in addition to zero displacements at supports. However, in order to obtain a better estimate of mode shapes, 5 and 11 measurement points were used. The intermediate mode shapes between measured locations were formed by applying a cubic spline interpolation method. According to the latter, cubic polynomials were applied to determine the mode shapes between data points. Continuity of both the second derivative at data points and the third derivative at the first interior data points were enhanced by the employed cubic spline definition routine. These mode shape vectors were unit-norm normalized to bring them to similar magnitudes prior to applying the five damage detection techniques. It is possible to define the unit-norm normalized mode shape by using the following formula:

$$\phi_i = \frac{\phi_{i0}}{\sqrt{\phi_{i0}^T \phi_{i0}}} \quad (3)$$

Once the mode shapes have been suitably normalized, the change in mode shape can be expressed as

$$\Delta\phi_i = |\phi_i^*| - |\phi_i|, \quad (4)$$

where ϕ_i and ϕ_i^* represent the i -th unit-norm normalized mode shapes before and after damage, respectively [15, 16].

Table 1 demonstrates the numerical results of the research capabilities of different vibration-damage detection methods to localize the damage of steel pipelines. Localization results were obtained by comparing first mode shape of undamaged and damaged construction on the base of Formula (4).

Then we studied the case of damage localization in steel pipe with a total length of 18 m, which had an outer diameter of 323.9 mm and a wall thickness of 9.5 mm. Figure 4 shows the performance of the four methods for location of damage at distance of 4.0 m from the left edge of the tube along the top line of a pipe. These plots were generated by applying only the essential mode shape before and after damaging the pipe that was nearer to the damage case with 5, 7, and 15 measurement points along the pipe. In each case, the highest positive peak corresponded to the predicted location of damage.

Figure 5 shows the distributions of the five parameters of damage detection, calculated using the fundamental mode shapes, defined by 7, 10, and 15 FE simulated measurement points, when damage was found into range of 4.0 m from the support point.

Figure 5a shows the mode shape change. The predicted locations of the damage were 4.08, 4.08, and 4.23 m, when 15, 10, and 7 FE simulated measurement points were used, respectively. The corresponding errors were 0.08, 0.08 and 0.23 m, respectively. The change in flexibility is shown in Fig. 5c. In this case, the predicted

Table 1 Results for defect localization in pipeline according to various defect dimensions, pipeline parameters and methods

Pipeline parameters (X42)			Defect dimensions				Defect localization (10 measurement points), distance from left support			
Out diameter (mm)	Wall thickness (mm)	L, Length of segment (mm)	Length (mm)	Width (mm)	Distance from left support (mm)	Depth (mm)	1st method (mm)	2nd ^a method (mm)	3rd ^a method (mm)	4th ^a method (mm)
219	6	5500	133	103	1200	2.4	1012	957	954	1051
						3.6	1114	1032	983	1109
						4.5	1263	1095	1058	1291
			Undamaged				-			
323.9	9.5	6000	203.2	152.4	2000	3.8	1687	1595	1590	1752
						5.7	1857	1720	1638	1848
						7.125	2105	1825	1763	2122
			Undamaged				-			

^a1st method (change in mode shape), 2nd method (change in mode shape curvature), 3rd method (change in flexibility), 4th method (damage index)

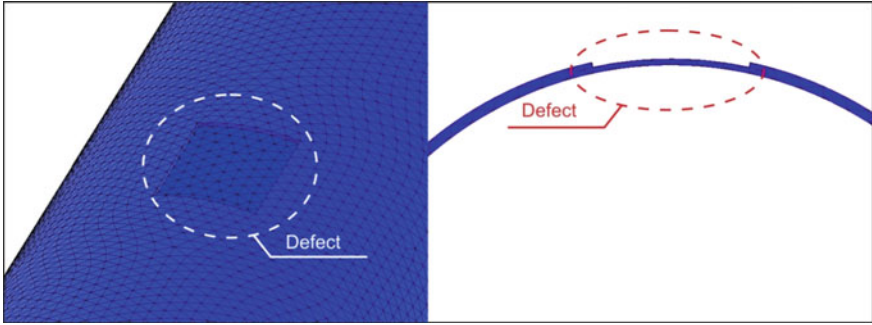


Fig. 4 Model of damaged steel pipe

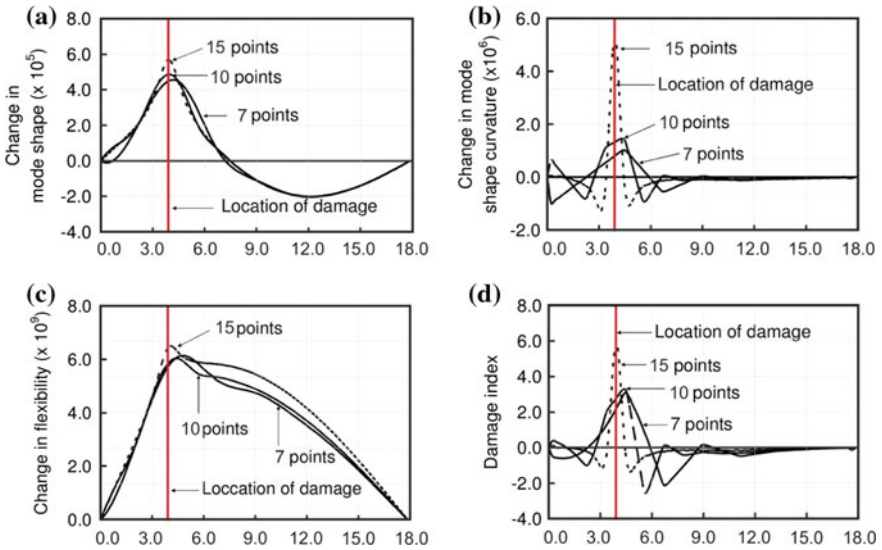


Fig. 5 Five VBDD methods to locate damage at a distance of 4 m from the pipe *left* edge (7, 10 and 15 measurement points) were used: **a** mode shape change, **b** mode shape curvature change, **c** flexibility change, **d** damage index

locations of the damage were 4.08, 4.38, and 4.60 m, when 15, 10, and 7 FE modeled measurement points were applied, accordingly with the relevant errors of 0.08, 0.38 and 0.60 m, respectively. Figure 5b, d, e show the change that take place in the mode shape curvature, change in the uniform flexibility curvature parameters, and damage index, respectively. Identical results were produced by these three methods. The damages were located at 4.08, 4.38, and 4.43 m, when 15, 10, and 7 FE simulated measurement points were used, respectively. The errors were therefore 0.08, 0.38, and 0.43 m, respectively.

The predicted damage location accuracy evidently improved when the number of measurement points grew for all five VBDD methods. Moreover, it was better to compare the change in mode shape method with other methods, when few measurement points were applied. All upward peak curves became sharper (i.e., the peak clarity improved) when the number of measurement points grew.

As a whole, for the VBDD methods under research, applying of three modes failed to improve the accuracy of damage localization over applying only one mode. Actually, as for the damage index method, the accuracy considerably grew when the damage was not located within a near-support area and few measurement points were applied.

3 Conclusions and Recommendations

VBDD methods can evaluate the condition of the entire structural component at a time and not limited to a survey of accessible regions [16]. The reliable values of the localization of the damaged area were obtained. It showed that the method, used to determine the damage index, predicted the location of the structural damage with a sufficient degree of accuracy, provided the first accurate determination of mode shape of the structure.

The numerical results found herein have shown the efficiency of the considered damage localization methods. Their application in practice will reduce the construction time of inspection to the preliminary determination of places for the accelerometer sensor.

The damage localization accuracy was directly proportional to the distance between measurement points. The growth of the number of measurement points will naturally cause proportional increase in accuracy of localization definition. Methods for determination of the damage index of the investigated structure showed their high efficiency at pinpointing the damage location, when mode shapes were very well determined with a lot of measurement points. In spite of the challenges related to practical achieving the level of mode shape definition, this result proves the reasonability of the VBDD theory and its benefit for localizing the damage [17, 18].

Acknowledgements The work is performed under the support of the Russian Foundation for Basic Research (RFBR) No. 15-01-04995.

References

1. E. Manoach, J. Warminski, L. Kloda, A. Teter, Numerical and experimental studies on vibration based methods for detection of damage in composite beams. *Compos. Struct.* **170**, 26 (2017)
2. K. Padil, N. Bakhary, H. Hao, The use of a non-probabilistic artificial neural network to consider uncertainties in vibration-based-damage detection. *Mech. Syst. Signal Process.* **83**, 194 (2017)

3. O. Abdeljaber, O. Avci, S. Kiranyaz, M. Gabbouj, D. Inman, Real-time vibration-based structural damage detection using one-dimensional convolutional neural networks. *J. Sound Vib.* **388**, 154 (2017)
4. K. Chang, C. Kim, Modal-parameter identification and vibration-based damage detection of a damaged steel truss bridge. *Eng. Struct.* **122**, 156 (2016)
5. W.R. Wickramasinghe, D.P. Thambiratnam, T. Chan, T. Nguyen, Vibration characteristics and damage detection in a suspension bridge. *J. Sound Vib.* **375**, 254 (2016)
6. T. Yin, Q. Jiang, K. Yuen, Vibration-based damage detection for structural connections using incomplete modal data by Bayesian approach and model reduction technique. *Eng. Struct.* **132**, 260 (2017)
7. F.L.M. dos Santos, B. Peeters, H. Van der Auweraer, L.C.S. Góes, W. Desmet, Vibration-based damage detection for a composite helicopter main rotor blade. *Case Stud. Mech. Syst. Signal Process.* **3**, 22 (2016)
8. Z. Zhou, *Vibration-Based Damage Detection of Bridge Superstructures*. (VDM Verlag, Germany, 2008), p. 55
9. O.S. Salawu, Bridge assessment using forced-vibration testing. *Am. Soc. Civ. Eng.* **32** (1995)
10. O.S. Salawu, C. Williams, Damage location using vibration mode shapes. in *Proceedings of the 12th International Modal Analysis Conference*, vol. 933 (Society of Experimental Mechanics, Bethel, 1994)
11. O.S. Salawu, Detection of structural damage through changes in frequency: a review. *Eng. Struct.* **19**(9), 718 (1997)
12. S.W. Doebling, C.R. Farrar, M.B. Prime, A summary review of vibration-based damage identification methods. *Shock and Vibration Digest* **30**(2), 91 (1998)
13. P. Cawley, R.D. Adams, The location of defects in structures from measurements of natural frequencies. *J. Strain Anal. Eng. Des.* **14**(2), 49 (1979)
14. B. Peeters, *System Identification and Damage Detection in Civil Engineering*, Ph.D. Thesis, Department of Civil Engineering, Katholieke Universiteit Leuven, Leuven, Belgium, 2000
15. Z. Zhou, L.D. Wegner, B.F. Sparling, Vibration-based detection of small-scale damage on a bridge deck. *J. Struct. Eng.* **133**(9), 1257 (2007)
16. P. Hajela, F.J. Soeiro, Recent developments in damage detection based on system identification methods. *Structural Optimization* **2**(1), 1 (1990)
17. J.R. Casas, A.C. Aparicio, Structural damage identification from dynamic-test data. *J. Struct. Eng.* **120**(8), 2437 (1994)
18. B. Peeters, J. Maeck, G. De Roeck, Vibration-based damage detection in civil engineering: excitation sources and temperature effects. *Smart Mater. Struct.* **10**(3), 518 (2001)

Localization of Impact Damage in Thin-Walled Composite Structure Using Variance-Based Continuous Wavelet Transform

R. Janeliukstis, S. Rucevskis, M.A. Sumbatyan and A. Chate

Abstract This work is focused on damage localization in thin-walled two-dimensional composite structures. A two-stage low-velocity impact damage with severities of 5 and 9 J is applied to CFRP plate in different positions and a dynamic vibration test is conducted in order to extract the resonance frequencies and corresponding deflection shapes of the structure before and after each stage of damage. Deflection shapes serve as an input for spatial continuous wavelet transform in two dimensions to calculate the damage index and standardize it for every wavelet function. Overall, 16 wavelet functions are used with scale parameters ranging from 1 till 16. The nontrivial problem of scale selection is avoided by computing the variance of normalized scalogram (VNS) over all the scales of consideration for every wavelet. Cross-correlation of VNS values between all the wavelets is performed to reveal the wavelet pairs of similar performance. These wavelet pairs are selected to compute the average VNS (AVNS). Later, a universal threshold is applied to filter the peaks of AVNS to yield the location of damage for each case of severity. Results suggest that a damage can be localized without the consideration of a specific wavelet and scale parameter.

Keywords Damage · Wavelet · Variance · Scale · Correlation · Impact · Composite · Deflection shape · Universal threshold · Plate · Scalogram

1 Introduction

Although composite materials are promising substitutes for metals, ceramics and polymers in many applications due to such qualities as high specific strength, stiffness, corrosion resistance and tailorable properties, they are vulnerable to

R. Janeliukstis (✉) · S. Rucevskis · A. Chate
Riga Technical University, Riga, Latvia
e-mail: Rims.Janeliukstis_1@rtu.lv

M.A. Sumbatyan
I.I. Vorovich Institute of Mathematics Mechanics and Computer Sciences,
Southern Federal University, Rostov-on-Don, Russia

various failure modes, such as matrix cracking, debonding, and delamination. The studies of low-velocity impact are important in case of composite materials because impact is one of the main failure modes of composites in through-thickness direction [1].

Numerous studies have been conducted on the effect of impact on composite materials [2–5]. Stellinginger et al. [2] found that existence of rubber layers between plies in carbon/epoxy laminate decreases the impact damage, while Topac et al. [3] used high-speed camera to record the evolution of impact fracture in CFRP laminate beam. Toivola et al. [4] observed that a combination of epoxy with a curing agent tetreglycidyl-4'-4 diaminodiphenylmethane with diethylenetriamine produces fluorescence phenomena when an epoxy resin system is subjected to impact, thus revealing even barely visible damage. Li et al. [5] detected presence of impact in CFRP structure using infrared thermography.

It is of crucial importance not only to detect presence of damage, but also to determine its location. Touching these issues is a vital part of Structural Health Monitoring (SHM) area that has only relatively recently established as a stand-alone branch of engineering. Among many damage identification methods of SHM, those that are the most widely used, are based on dynamic response of the structure. The underlying idea behind these methods is that the stiffness of the structure decreases locally in the region of damage. The dynamic parameters, mostly resonance frequencies and deflection shapes of the structure are extracted and subjected to some transformation in order to either detect damage or, taking a one step further, localize it. These methods for example are: Modal Curvature (MC) [6–10], Modal Flexibility (MF) [6, 11] and Modal Strain Energy (MSE) [11, 12] methods. In MC-based approach, one calculates the second derivative of mode shape and calculates its distribution over length of a beam or surface of a plate. Highest peaks indicate the location of damage. MF and MSE methods are based on the fact that presence of damage alters the structural parameters of flexibility (decreases) and strain energy, when structure deforms in its deflection shapes, respectively. The drawback of MC, MF, and MSE methods is that there is a necessity in reference data of undamaged structure to which the data obtained from a damaged structure is compared and their difference or ratio is expressed as a damage index.

Apart from the damage localization methods stated above, lately the most attention is directed to the Wavelet Transform (WT) method and its different modifications, which mainly include Continuous WT, Discrete WT, and also Wavelet Packet Transform (WPT) methods. This attention is justified by the fact that the WT methods do not require a reference information on a healthy structure and one can localize damage using data exclusively from a damaged structure. Large number of studies are devoted to damage localization in beam and plate structures using WT. Particular interest lies in damage localization in composite plates as those are widely used in advanced structures and vehicles. Vast studies on this subject have been conducted by Katunin et al. [13–17]. In [13], a crack damage was identified in a CFRP laminate rotor blade with complex nonlinear geometry. The conclusion was that the Discrete WT using B-spline wavelet function provided the best damage identification results. In [14] and [15], laminated polymer

composite plates with an artificial damage were considered and their mode shapes were used in damage localization using two-dimensional WT applying fractional B-spline wavelets with continuous parametric optimization. Study [16] was devoted to low-velocity impact damage localization in composite plates. Mode shapes were measured and used as an input data in the Discrete WT. Results suggested that quincunx nonseparable wavelets were able to detect even damage of low energy (different diameter impactors were used). These results were also supported with ultrasonic C-scans. In [17] honeycomb sandwich composite plates were subjected to typical composite damage, such as delaminations, cracks of a core and sheets and impact damages. Two-dimensional Discrete WT was performed on mode shapes of the plates and damage was successfully localized. Damage localization in composite plates was also conducted in [18], where two-dimensional Continuous WT was compared with two-dimensional Strain Energy and two-dimensional Gapped Smoothing methods and proved to be superior in terms of immunity to noise and reduced sensor data. Huang et al. [19] performed two-dimensional Continuous WT of a strain data of a loaded simply supported plate with integrated sensor network. Conclusion was that the method was not only able to locate damage but also to assess its severity. Yan et al. [20] investigated the possibility to detect damage in epoxy/glass fiber composite laminate plate with embedded piezoelectric actuator and sensors. Structural response was decomposed using WPT and damage was successfully detected.

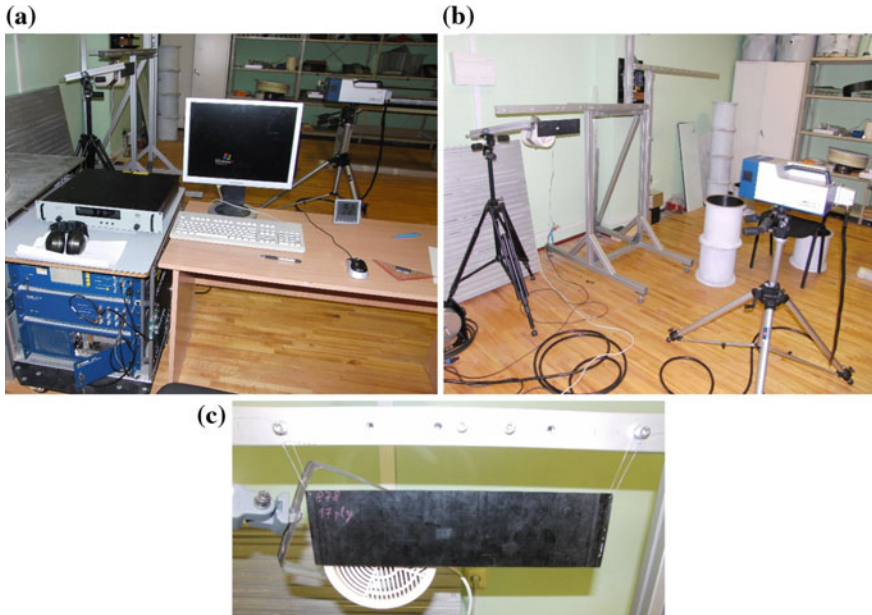
In present study, a CFRP plate with two successive impact damages (5 and 9 J) is considered. Dynamic vibration test is applied to estimate resonance frequencies and deflection shapes of the plate at free boundary conditions before and after each stage of damage. The measured mode shapes are used in damage localization algorithm involving the two-dimensional Continuous Wavelet Transform. Normalized wavelet scalogram is computed and its variance is calculated with respect to scale parameter, thus excluding scales from further computations. Reference data of healthy structure are not required, but also no need to select a particular wavelet for the analysis. It is due to a cross-correlation between variances of normalized wavelet scalograms of all the wavelets is performed in order to track down the wavelet pairs of similar performance. These pairs are selected and used in calculation of a damage index distribution over the surface of the plate. Then, the universal threshold is applied to extract insignificant values do not connected with damage. The final results suggest that the proposed damage identification procedure allows for approximate damage localization of relatively small severities.

2 Experimental Vibration Testing

A specimen considered in this study is a CFRC plate laminate with the lay-up [90/0/0/45/-45/-45/45/0/90/90/0/45/-45/-45/45/0/90] containing 17 plies with the following physical parameters (Table 1):

Table 1 Physical properties of CFRP laminate plate

Length (m)	Width (m)	Thickness (m)	Mass (kg)	Density (kg/m ³)
0.359	0.1	0.0021	0.11595	1538

**Fig. 1** Experimental set-up of vibration test: **a** overall view, **b** scanning head in the process of scanning the specimen, **c** close-up view of the plate specimen and loudspeaker

The dynamic testing of the plate involves measurement of its dynamic properties, namely, the resonance frequencies and corresponding deflection shapes. This procedure is carried out using a POLYTEC PSV-400-B non-contact scanning laser vibrometer. POLYTEC system consists of a PSV-I-400 LR optical scanning head equipped with a sensitive vibrometer sensor (OFV-505), OFV-5000 controller, PSV-E-400 junction box, a Bruel and Kjaer type 2732 amplifier, and a computer with a data acquisition board and PSV software (Fig. 1).

For the PSV acquisition system, it is required to define the location of outer edges of the specimen and then, a scanning grid, consisting of scanning points, uniformly distributed over the surface of specimen. Different geometries of scanning grid can be chosen along with a density of scanning points in either direction. Vibrations of a structure are measured in these points, in perpendicular direction to the surface of the structure. In this study, a rectangular grid has been chosen due to the rectangular shape of the specimen. The scanning grid of a composite plate consists of seven points on width and 21 points on length of the sample, yielding 147 scanning points in a whole.

Table 2 Specifications of dynamic testing

Signal	Periodic chirp with 9 V amplitude
Bandwidth	100 Hz–3.2 kHz
FFT lines	3101
Sample frequency	8.192 kHz
Resolution	1 Hz
Channel vibrometer voltage	10 V

The plate was suspended by thin threads, thus tested in the both edges free boundary conditions. A periodic chirp signal, generated by internal function generator, was passed to a loudspeaker to excite the plate. The scanning head measured a velocity of vibration in a scanning point and automatically moved the laser beam to a successive point of the scan grid. This measurement procedure involved validating the measurement with the signal-to-noise ratio. During the measurement, the photo-detector (highly sensitive digital decoder VD-07), measured the time-dependent vibration velocity. Then the measurements were performed; the time response of the plate, averaged 3 times at each point, was transformed to the frequency domain using Fast Fourier Transform yielding Frequency Response Function (FRF). The identification of resonance frequencies was conducted by using the peak picking method, studying FRF. The corresponding displacement deflection shapes were obtained by further post-processing of the data. Set-up parameters, used for the FRF measurements, are shown in Table 2.

At first, FRF was measured for a healthy plate that contained no damage. Two impacts of different severities and in different locations were carried out by using a low-velocity impact procedure. After each of impacts, FRF and deflection shapes were measured. The resonance frequencies and deflection shapes were not only used for comparison purposes, e.g., how damage affected the dynamic parameters of the structure, but deflection shapes also served as input data for our proposed damage localization algorithm.

3 Low-Velocity Impact Tests

Low-velocity impact tests were conducted using INSTRON Dynatup 9250 HV drop tower. Different impact energies were calculated by using the variation of impactor mass and drop height. The potential energy of the impactor at maximum height is transferred to a sample in the process of an impact. The impactor with hemispherical nose, a diameter of 20 cm and a mass of 2.25 kg was used in the test. In total, two impact tests with different energies were performed in order to assess the locations of damage with different severities.

The location of first impact with an energy of 5 J corresponds to orange circle in Fig. 2. After this impact, deflection shapes of the plate were measured. Then, the



Fig. 2 Photo of a composite plate with *orange* and *red* rings showing the location of 5 and 9 J impact damage, respectively (color figure online)

Table 3 Specifications of impact test

Impact no.	Impact energy (J)	Maximum load (kN)	Deflection at max load (mm)	Test height (m)	Impact velocity (m/s)
1	8.8383	5.6162	3.75	0.4532	2.8029
2	4.8986	3.7568	3.0091	0.2266	2.0867

second impact with an energy of 9 J was performed and its location is marked with a red circle in Fig. 2. After both impacts were made, the deflection shapes were measured one more time.

Details of impact testing set-up parameters are found in Table 3.

4 Damage Localization Methodology

In this chapter, location of damage in a CFRP plate is assessed by using two-dimensional CWT technique, which implies the use of so-called wavelets. Wavelets $\psi(t)$ are special functions with small oscillations, so that they have zero mean. Wavelets possess several distinctive properties, such as

- support width;
- may be orthogonal/biorthogonal;
- may be symmetric/asymmetric;
- the majority of wavelets are grouped in families, for example, Mexican Hat (mexh, esmexh, gabmexh), Derivative of Gaussian (dog, dog2, dog3), Morlet (morl, isomorl, esmorl, rmorl), etc.;
- may be isotropic or orthotropic in dependence on that how their properties depend on rotational angle in a plane.

Wavelet analysis is usually performed in time domain, meaning that they have a period and a frequency. This wavelet frequency is called central frequency of wavelet and it can be imagined as a frequency that wavelet would have if it has sinusoidal nature. Wavelet pseudo frequencies are obtained by dividing the central frequency with a scale factor s . The scale factor, also known as dilation parameter, is a real positive number, that depicts a compression ($0 < s < 1$), when window function is very narrow, therefore it is appropriate for high-frequency components. On the other hand, a tension ($s > 1$) of wavelet function along abscissa axis gives rise to the very wide windows that are suitable for the low-frequency components of the signal [21, 22]. This concept is based on *Heisenberg uncertainty principle*, which states that it is not possible to obtain high resolution in frequency and time simultaneously [23]. WT can adopt a flexible time-frequency window, thus this method exceeds different Fourier transform sub-techniques [24]. Spatial wavelet analysis is performed, as the name implies, in spatial domain, simply replacing time with coordinate, giving rise to wavelet function $\psi(x, y)$ [25, 26].

In its nature, WT is a convolution of analyzed signal $f(x, y)$ with a wavelet function $\psi(x, y)$ [27] and measures actually a correlation between $f(x, y)$ and $\psi(x, y)$ [16]. For a given value of s , $\psi(x, y)$ translates along x and y axes and convolves with every segment of signal $f(x, y)$. Large magnitude transform coefficients indicate places with high degree of correlation and vice versa.

In the damage identification procedure, large Wavelet Transform coefficients appear as spikes in WT plots of y versus x . The coordinates that correspond to these spikes contain the location of damage because damage can be imagined as a discontinuity of a signal.

The 2D CWT for a two-dimensional signal is given by Alamdari et al. [28]

$$W_{s,a,b} = \frac{1}{\sqrt{s^2}} \iint f(x, y) \cdot \psi^* \left(\frac{x-a}{s}, \frac{y-b}{s} \right) dx dy = \iint f(x, y) \cdot \psi_{s,a,b}^*(x, y) dx dy, \tag{1}$$

where asterisk denotes complex conjugation and $\psi_{s,a,b}(x, y)$ is a set of wavelet family functions, derived from a mother wavelet function $\psi(x, y)$ by using translation (parameters a and b) and expansion (parameter s) of the $\psi(x, y)$.

Damage index for each of mode shapes is depicted as follows:

$$DI_{i,j,s}^n = W_{i,j,s}^n = \iint_S w_{ij}^n \cdot \psi_{s,a,b}^*(x, y) dx dy, \tag{2}$$

where S is the area of the plate, w^n is the transverse displacement of the structure, n is the mode number, i and j are the numbers of grid points in x and y directions, respectively. However, mode shapes, measured in experimental conditions, are always damaged by measurement noise, which may lead to false peaks in damage index profiles, thus misleading data interpretation. In order to overcome this problem, it is proposed to summarize the results for all modes. The summarized

damage index is then defined as the average summation of damage indices for all modes and normalized with respect to the largest value of each mode

$$DI_{i,j,s} = \frac{1}{N} \sum_{n=1}^N \frac{DI_{i,j,s}^n}{\max(DI_{i,j,s}^n)}. \quad (3)$$

According to [12, 24], the damage indices, determined for each of elements, are then standardized as

$$SDI_{i,j,s} = \frac{DI_{i,j,s} - \mu_s}{\sigma_s}, \quad (4)$$

where μ_s and σ_s are scale-dependent mean value and standard deviation of damage indices in Eq. (3), respectively.

The detection of the most energetic features in the signal at different scale and space is of particular interest in damage identification. Such three-dimensional plots consisting of coefficients of CWT with respect to waveletscale and dimension of the structure are known as *wavelet scalograms* [21, 29]. More beneficial, however is a *normalized wavelet scalogram* (NWS), where WT coefficients are first normalized.

$$NSDI_{i,j,s} = \frac{SDI_{i,j,s}}{s^2} \quad (5)$$

$$NWS_{i,j,s} = NSDI_{i,j,s} * NSDI_{i,j,s} = |NSDI_{i,j,s}|^2 \quad (6)$$

Regions of maxima in NWS are called wavelet transform ridges, which in the case of spatial CWT correspond to a coordinate with the most energetic features of the signal. The ridges in NWS denote the location of damage for spatial CWT. In [30], it is stated that wavelet ridges might be used for monitoring of damage development in the structure.

Since there is no wavelet scalogram for a two-dimensional case, it is proposed in our damage identification methodology to compute a sum of NWS along x and y directions, giving rise to *summed normalized wavelet scalogram* θ that is only scale-dependent

$$\theta_s = \sum_j \sum_i NWS_{i,j,s} \quad (7)$$

The next step is to calculate a percentage of energy that normalizes wavelet scalogram and contains at each scale with respect to summed normalized wavelet scalogram at each scale. It yields a new introduced variable, called *fractional normalized wavelet scalogram* $\mathbb{C}_{i,j,s}$ as follows

$$\mathbb{C}_{i,j,s} = 100\% * \frac{NWS_{i,j,s}}{\mu(\theta_s)} = 100\% * \frac{NWS_{i,j,s}}{\mu\left(\sum_j \sum_i NWS_{i,j,s}\right)}, \quad (8)$$

where $\mu(\theta_s)$ denotes the mean value of θ .

The next step of calculations involves the computation of a damage index that is obtained by taking into account a variance of fractional normalized wavelet scalogram with respect to scale parameter, thus eliminating the scale variable from the damage localization procedure

$$\Gamma_{i,j} = \sigma^2(\mathbb{C}_{i,j,s}) = \sigma^2\left(100\% * \frac{NWS_{i,j,s}}{\mu\left(\sum_j \sum_i NWS_{i,j,s}\right)}\right) \quad (9)$$

The variable $\Gamma_{i,j}$ depends only on coordinates of the plate.

It is unknown a priori, which wavelet functions will be used better in different cases, therefore, it is proposed to define the localization of damage on pairs of highly correlated wavelets. This procedure is organized as follows:

- We calculate $\Gamma_{i,j}$ for all of the wavelet functions and analyze a *cross-correlation* of these values between all wavelets.
- Wavelet pairs with high correlation coefficient are extracted from the list of all wavelets. For all of these pairs, the average value of $\Gamma_{i,j}$ is calculated from individual $\Gamma_{i,j}$ of each wavelet in pair. For example, for the first and second highly correlated wavelet pairs, the average value of $\Gamma_{i,j}$ is computed as follows

$$\Gamma_{i,j}^1 = 0.5 \cdot \left(\Gamma_{i,j}^{1,1} + \Gamma_{i,j}^{1,2}\right), \Gamma_{i,j}^2 = 0.5 \cdot \left(\Gamma_{i,j}^{2,1} + \Gamma_{i,j}^{2,2}\right) \quad (10)$$

- If k is number of highly correlated wavelet pairs, then the *average correlated variance of normalized wavelet scalogram (ACVNWS)* is computed as

$$\overline{\Gamma}_{i,j} = \frac{1}{k} \sum_k \Gamma_{i,j}^k \quad (11)$$

- By considering the problem of damage localization, it is proposed to extract the values of $\overline{\Gamma}_{i,j}$ by applying an *universal wavelet threshold*

$$T = \sigma \sqrt{2 \ln(N)}, \quad (12)$$

where N in our case is the total number of data points and σ is the standard deviation of $\overline{\Gamma}_{i,j}$ distribution over plate. Originally, this threshold was adapted in image noise reduction routine by using wavelets [31–33].

- In the following calculations, the values of $\overline{\Gamma}_{ij}$ that do not pass the threshold value of T , are assigned a value of zero, otherwise these values are assigned a value of 1, forming a distribution of *thresholded average correlated variance of normalized wavelet scalogram* (TACVNWS):

$$\begin{aligned} \text{if } (\overline{\Gamma}_{ij} \ll T) &\rightarrow T\overline{\Gamma}_{ij} = 1 \\ \text{else} &\rightarrow T\overline{\Gamma}_{ij} = 0 \end{aligned} \quad (13)$$

5 Results and Discussion

The frequency response functions (FRFs) for damage cases of 5 J impact and additional 9 J impact, measured in a vibration test are shown in Fig. 3. For a reference, FRF of a healthy plate is also plotted.

Deflection shapes are extracted from FRFs and their amplitude is normalized to unity. In a whole, 12 deflection shapes are extracted from a healthy plate in the case with impact of 5 J and 16 shapes—in the case of combined 5 and 9 J impact damage. However, only the corresponding shapes are used in further calculations. The pairs of corresponding deflection shapes of the both damage cases are determined by using a correlation coefficient. A value close to 1 or -1 indicates a correlation between these shapes. As a result, nine pairs of corresponding deflection shapes are identified and three of these pairs are shown in Fig. 4.

Resonance frequencies, corresponding to identified pairs of deflection shapes are depicted in Table 4. As expected, the presence of damage lowers the values of resonance frequencies and this effect is more pronounced at higher resonances.

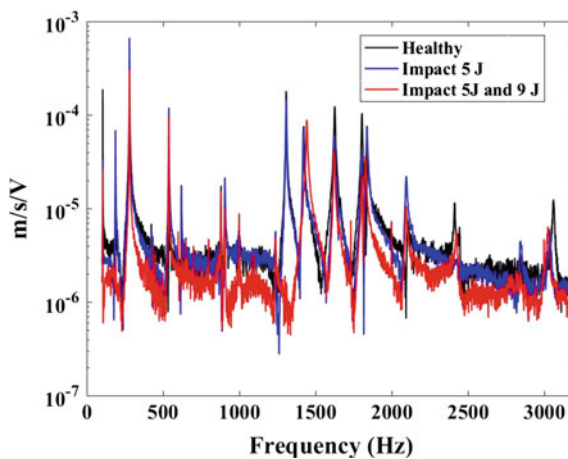


Fig. 3 Frequency response functions for two damage cases

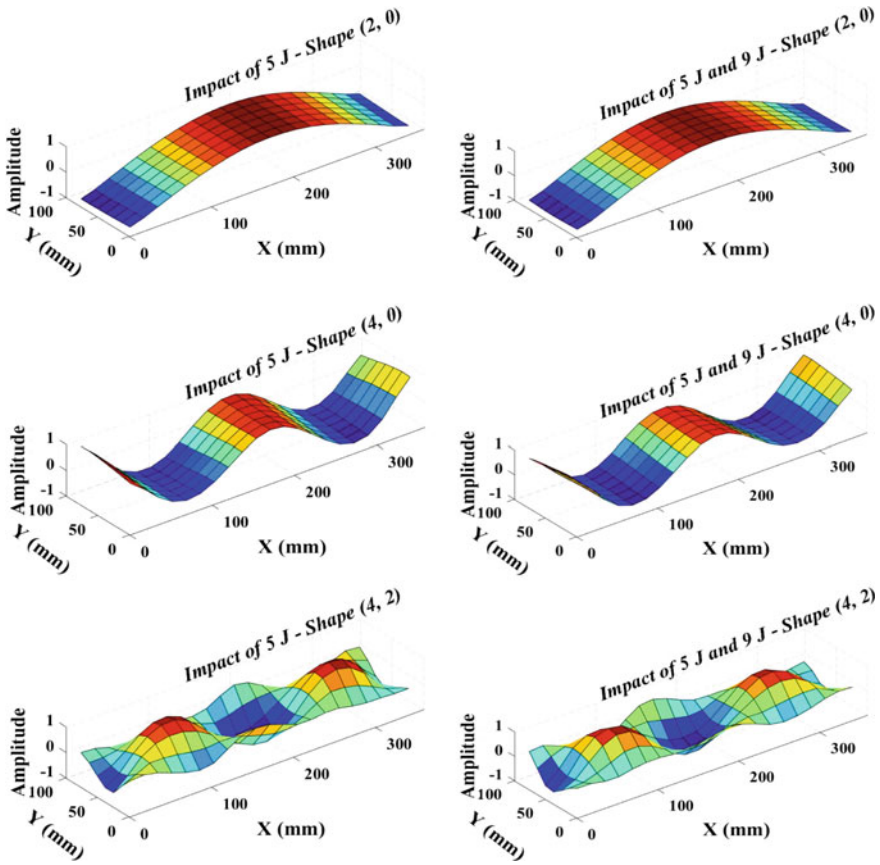


Fig. 4 Deflection shapes measured in dynamic tests for a composite plate containing 5 J and 5 J + 9 J impact damage

Table 4 Resonance frequencies of composite plate

Shape	Healthy	Impact 5 J	Impact 5 J + 9 J	Correlation coefficient
(2, 0)	105	105	105	0.994641
(1, 1)	188	188	189	0.987661
(3, 0)	280	280	280	0.979836
(4, 0)	539	539	539	0.962761
(3, 1)	622	621	620	-0.92806
(4, 1)	906	906	880	-0.80034
(2, 2)	1627	1626	1624	0.95612
(4, 2)	2101	2096	2094	0.84852
(9, 0)	3062	3036	3027	-0.88688

Also, the correlation coefficient is given and negative values with a magnitude close to 1 depict a phase shift of corresponding shapes in the moment of extraction.

The cross-correlation results of Γ_{ij} values between all 16 wavelets are shown in Fig. 5. The dark regions in cross-correlation maps represents low or no correlation, while white regions represent high correlation as indicated by the colorbar.

The selection of wavelet pairs then used in $\overline{\Gamma_{ij}}$ calculation is based on a threshold of correlation results. Basically, wavelet pairs, which performance exceeds a correlation threshold of 0.895 are selected for further analysis. The pairs exceeding this threshold are assigned by value of 1, otherwise 0, forming a matrix of zeros and ones, named *correlated average variance of normalized wavelet scalogram pairs* $C\overline{\Gamma_{ij}}$

$$\begin{aligned} \text{if } (\rho_{xy}(\overline{\Gamma_{ij}}) \ll 0.895) &\rightarrow C\overline{\Gamma_{ij}} = 0 \\ \text{else} &\rightarrow C\overline{\Gamma_{ij}} = 1, \end{aligned} \quad (14)$$

where $\rho_{x,y}$ is a correlation coefficient between pairs of $\overline{\Gamma_{ij}}$ values for wavelets.

Each wavelet function with a short-hand name from MATLAB R2016B is assigned a number from 1 to 16, as shown in Table 5. The results of cross-correlation between wavelets in Table 5 are shown in Tables 6 and 7. These $C\overline{\Gamma_{ij}}$ matrices are built for both cases of damage (5 and 9 J). It is worth noting that

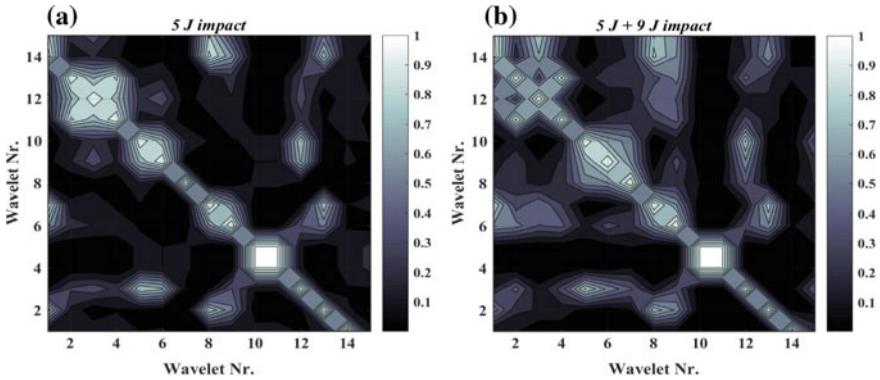


Fig. 5 Correlation maps of variances of SDI between all wavelets: **a** impact of 5 J, **b** impacts of 5 J + 10 J

Table 5 Numerical notation of wavelet functions used in algorithm

1	2	3	4	5	6	7	8
pethat	isomorl	rmorl	esmorl	morl	dog	Dog2	isodog
9	10	11	12	13	14	15	16
fan	wheel	gaus3	gaus2	mexh	esmexh	gabmexh	sinc

Table 6 $C\overline{\Gamma}_{ij}$ matrix for the case of 5 J impact

0	0	0	0	0	0	0	0	0	0	0	0	0	0	0
1	0	0	0	0	0	0	0	1	0	0	0	0	0	0
0	1	0	1	0	0	0	0	0	0	0	0	0	0	0
0	0	1	0	0	0	0	0	0	0	0	0	0	0	0
0	1	0	1	0	0	0	0	0	0	0	0	0	0	0
0	0	0	0	1	0	0	0	0	0	0	0	0	0	0
0	0	0	0	0	1	0	0	0	0	0	0	0	0	0
0	0	0	0	0	0	1	0	0	0	0	0	0	0	0
0	0	0	0	0	0	0	1	0	0	0	0	0	0	0
1	0	0	0	0	0	0	0	1	0	0	0	0	0	0
0	0	0	0	0	0	0	0	0	1	0	0	0	0	0
0	0	0	0	0	0	0	0	0	0	1	1	0	0	0
0	0	0	0	0	0	0	0	0	0	1	1	0	0	0
0	0	0	0	0	0	0	0	0	0	0	0	1	0	0
1	0	0	0	0	0	0	0	1	0	0	0	0	1	0
0	0	0	0	0	0	0	0	0	0	0	0	0	0	1

Table 7 $C\overline{\Gamma}_{ij}$ matrix for the case of 5 J + 9 J impact

1	0	0	0	0	0	0	0	0	0	0	0	0	0	0
1	0	0	0	0	0	0	0	0	0	0	0	0	0	0
0	1	0	1	0	0	0	0	0	0	0	0	0	0	0
0	0	1	0	0	0	0	0	0	0	0	0	0	0	0
0	1	0	1	0	0	0	0	0	0	0	0	0	0	0
0	0	0	0	1	0	0	0	0	0	0	0	0	0	0
0	0	0	0	0	1	0	0	0	0	0	0	0	0	0
0	0	0	0	0	0	1	0	0	0	0	0	0	0	0
0	0	0	0	0	0	0	1	0	0	0	0	0	0	0
1	0	0	0	0	0	0	0	1	0	0	0	0	0	0
0	0	0	0	0	0	0	0	0	1	0	0	0	0	0
0	0	0	0	0	0	0	0	0	0	1	1	0	0	0
0	0	0	0	0	0	0	0	0	0	1	1	0	0	0
0	0	0	0	0	0	0	0	0	0	0	0	1	0	0
1	0	0	0	0	0	0	0	1	0	0	0	0	1	0
0	0	0	0	0	0	0	0	0	0	0	0	0	0	1

these matrices are symmetric, thus bottom part of the matrices is shaded gray. The main diagonal is shaded red because the cross-correlation is performed between a particular wavelet and itself, so those values of one do not contribute to the selection of wavelet pairs. The cases, where the cross-correlation has passed the threshold, are shaded green.

As one can see, a total of three pairs of wavelets have passed the cross-correlation threshold for each of two damage cases. These wavelet pairs are given in Table 8.

Table 8 Wavelet pairs used in the calculation of $\overline{\Gamma}_{ij}$ for both cases of damage

isomorl-fan	5 J impact	pethat-isomorl	5 J + 9 J impact
rmorl-morl		rmorl-morl	
gaus2-gaus3		gaus2-gaus3	

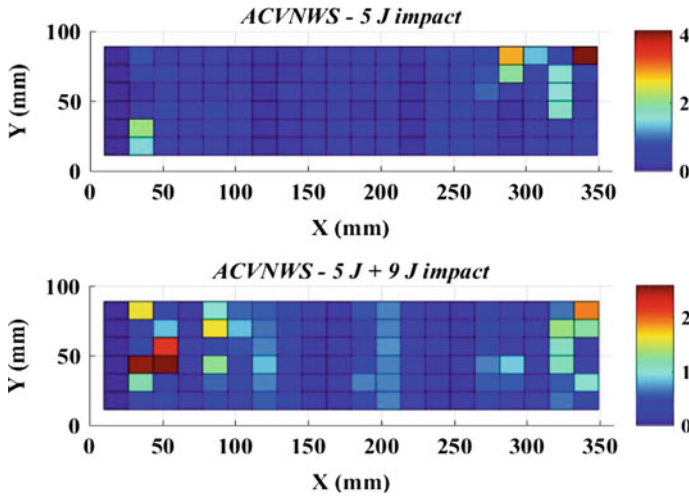


Fig. 6 Average correlated variance of normalized wavelet scalogram distributions for both damage cases

The $\overline{\Gamma}_{ij}$ distributions over the surface of a composite plate by using the selected wavelet pairs are computed with help of Eq. (11) and shown in Fig. 6.

For the case of 5 J impact, elevated values are located at the upper right corner of the plate and at the left, where the actual impact was made. However, moderate values are also found in the bottom left region no contributing to damage. In the 5 J + 9 J impact case, the highest values are found on the far left side of the plate in the vicinity of damage.

Universal threshold, according to Eq. (12) is applied to the distributions in Fig. 7. The calculated values for the universal threshold are shown in Table 9.

The values of T in Table 8 mean that if the values from Fig. 6 are larger than calculated values of T , they are assigned by value of 1. If values from Fig. 6 are smaller than T , they are set to zero. These distributions of threshold values of $\overline{\Gamma}_{ij}(T\overline{\Gamma}_{ij})$ are shown in Fig. 7.

Although smaller values of $\overline{\Gamma}_{ij}$ distributions are extracted, there are still some higher values in the profile that no contribute to the damage. In the case of 5 J impact, such values locate in the left part and at the top right corner of the plate, while in the case of 5 J + 9 J impact, these values at the top right and left corners of the plate.

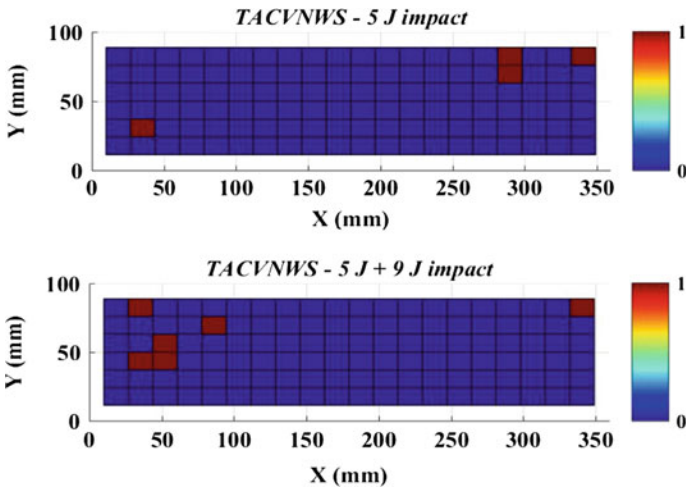


Fig. 7 Threshold average correlated variance of normalized wavelet scalogram distributions for both damage cases

Table 9 Values of universal threshold for both damage cases

<i>T</i>	5 J impact	5 J + 9 J impact
	1.7398	1.4749

Two values for the case of 5 J impact locate close one to other in the location of impact damage in the top right part of the plate and three neighboring values locate in the left part of the plate for 5 J + 9 J impact case in the approximate location of damage, suggesting that, in general, the proposed methodology is capable to localize impact damage even at small severity (5 J). However, in the case of 5 J + 9 J impact, only largest severity damage (9 J) is localized properly.

6 Conclusions

This study is devoted to localization of impact damage in thin (~2 mm) composite plate. Two successive impacts with severities of 5 and 9 J are applied by using low-velocity impactor and resonance frequencies along with corresponding deflection shapes of the plate are measured in a dynamic vibration test. These shapes are used as input data in a damage localization algorithm by using 2-D Continuous Wavelet Transform. Variance of normalized wavelet scalogram is calculated over the scale parameters for each of 16 wavelets considered in the study, thus excluding the scale out of the variables in damage localization problem. The problem of selection of the most appropriate wavelet function is solved by the

cross-correlation between performances of all wavelets, and the most highly correlated wavelet pairs are selected. These pairs are used in the calculation of damage index distributions over the plate. Universal threshold is applied in order to extract the lowest magnitude values that no contribute to damage.

According to final damage localization results, the proposed methodology is successful, although some discrepancy is present, especially in the case with damage of both severities because in this case the algorithm detects only the highest severity damage.

Acknowledgements This research has been performed under the funding from the Latvia State Research Programme, the grant agreement “Innovative Materials and Smart Technologies for Environmental Safety, IMATEH”.

References

1. D. Ginzburg, F. Pinto, O. Iervolino, M. Meo, *Compos. Struct.* **161**, 187 (2017)
2. E. Stellinginger, A. Kühhorn, M. Kober, *Compos. Struct.* **139**, 30 (2016)
3. T.O. Topac, B. Gozluklu, E. Gurses, D. Coker, *Compos. A* **92**, 167 (2017)
4. R. Toivola, P.-N. Lai, J. Yang, S.-H. Jang, A.K.-Y. Jen, B.D. Flinn, *Compos. Sci. Technol.* **139**, 74 (2017)
5. Y. Li, W. Zhang, Z.-W. Yang, J.-J. Zhang, S.-J. Tao, *Infrared Phys. Technol.* **76**, 91 (2016)
6. V.B. Dawari, G.R. Vesmawala, *Proc. Eng.* **51**, 119 (2013)
7. P. Qiao, K. Lu, W. Lestari, Wang, *J Compos. Struct.* **80**, 409 (2007)
8. P. Qiao, W. Lestari, *Compos. Struct.* **67**, 365 (2005)
9. M. Dilena, A. Morassi, *Mech. Syst. Signal Process.* **25**, 1485 (2011)
10. M. Cao, L. Ye, L. Zhou, Z. Su, R. Bai, *Mech. Syst. Signal Process.* **25**, 630 (2011)
11. J.-M. Ndambi, J. Vantomme, K. Harri, *Eng. Struct.* **24**, 501 (2002)
12. J.-T. Kim, Y.-S. Ryu, H.-M. Cho, N. Stubbs, *Eng. Struct.* **25**, 57 (2003)
13. A. Katunin, F. Holewik, *Arch. Civil Mech. Eng.* **13**, 287 (2013)
14. A. Katunin, P. Przystalka, *Eng. Appl. Artif. Intell.* **30**, 73 (2014)
15. A. Katunin, *Mech. Syst. Signal Process.* **25**, 3153 (2011)
16. A. Katunin, *Arch. Civil Mech. Eng.* **15**, 251 (2015)
17. A. Katunin, *Compos. Struct.* **118**, 385 (2014)
18. P. Qiao, W. Fan, *Int. J. Solids Struct.* **46**, 4379 (2009)
19. Y. Huang, D. Meyer, S. Nemat-Nasser, *Mech. Mater.* **41**, 1096 (2009)
20. Y.J. Yan, L.H. Yam, *Compos. Struct.* **58**, 29 (2002)
21. P.S. Addison, *The Illustrated Wavelet Transform Handbook, Introductory Theory and Applications in Science, Engineering, Medicine and Finance* (Taylor & Francis, New York-London, 2002)
22. H. Adeli, H. Kim, *Wavelet-Based Vibration Control of Smart Buildings and Bridges* (CRC Press, Taylor and Francis Group, Boca Raton, London, New York, 2009)
23. H. Kim, H. Melhem, *Eng. Struct.* **26**, 347 (2004)
24. W.L. Bayissa, N. Haritos, S. Thelandersson, *Mech. Syst. Signal Process.* **22**, 1194 (2008)
25. C.-C. Chang, L.-W. Chen, *Mech. Syst. Signal Process.* **19**, 139 (2005)
26. N. Wu, Q. Wang, *Int. J. Eng. Sci.* **49**, 253 (2011)
27. Y.F. Xu, W.D. Zhu, J. Liu, Y.M. Shao, *J. Sound Vib.* **333**, 6273 (2014)

28. M.M. Alamdari, J. Li, B. Samali, Arch. Civil Mech. Eng. **15**, 698 (2015)
29. S. Goswami, P. Bhattacharya, Int. Res. J. Eng. Technol. **2**(3), 2060 (2015)
30. M.M.R. Taha, A. Noureldin, J.L. Lucero, T.J. Baca, Struct. Health Monit. **5**(3), 267 (2006)
31. V. Sowjanya, G. SasibhushanaRao, A. Sarvani, Proc. Comput. Sci. **85**, 669 (2016)
32. A. Azzalini, M. Farge, K. Schenider, Appl. Comput. Harmon Anal **18**, 177 (2005)
33. X. Zhang, N. Feng, Y. Wang, Y. Shen, J. Sound Vib. **339**, 419 (2015)

Identification of Defects in Pipelines Through a Combination of FEM and ANN

A.N. Soloviev, Giang D.T. Nguen, P.V. Vasiliev and A.R. Alexiev

Abstract Defects identification method in the pipeline system is proposed. The method is based on a combination of finite element method (FEM) and artificial neural networks (ANNs). A finite element modeling of the monitoring system of the damaged state of the pipeline, which is a fragment of a pipe with a defect and piezoelectric actuators and sensors is carried out. The direct problem is reduced to initial boundary value problem of the theory of elasticity and electrodynamics. The inverse problem of identification of defects is reduced to the inverse geometrical problem. As additional information for the solution of inverse problems is the amplitude–time response (ATR) of electric potential on the free electrode sensors, the sensors were located before and after a defect, for measuring the reflected and transmitted acoustic waves excited by the actuators. Using this model, a set of direct problems is solved and a training set for the ANN is constructed. As the ANN architecture, we select a multilayer perceptron and back propagation learning algorithm is considered. The algorithm for the identification of defects contains several steps: (i) the location of a defect (determining the distance between the actuators and sensors and defect); (ii) determining the type of the defect (crack, volumetric defect); and (iii) the determination of the defect parameters (depth, slope of the crack, geometric parameters of the volume defect). A series of numerical experiments, in which the optimal ANN architecture, defined for each identification step, is performed.

A.N. Soloviev (✉) · P.V. Vasiliev
Don State Technical University, Rostov-on-Don, Russia
e-mail: solovievarc@gmail.com

A.N. Soloviev
I.I. Vorovich Institute of Mathematics, Mechanics and Computer Science,
Southern Federal University, Rostov-on-Don, Russia

G.D.T. Nguen
Viet Nam Maritime University, Hai Phong, Vietnam

A.R. Alexiev
Institute of Mechanics of Bulgarian Academy of Sciences, Sofia, Bulgaria

Keywords Identification · Crack · Defect · Finite element method (FEM) · Acoustic waves · Artificial neural network (ANN) · Inverse problems · Piezoactuator · Piezosensor · Amplitude–time response

1 Introduction

Reconstruction of defects in the pipeline caused by corrosion or by mechanical action is an important technical problem, the successful solution of which can prevent breakage of the pipes. Such identification may be carried out with instruments, which move along a pipeline and perform their monitoring. A more attractive way of detection is the use of acoustic sensors and receivers (piezoelectric transducer). They are mounted on a pipe and detect damage based on the reflected signals. Such a system should be equipped with software that allows us to identify the damage and its extent based on the analysis of the reflected or transmitted signal. Such software can be developed through the use of ANN [1]. Application of ANN in the problems of reconstruction of the damaged state of structural elements was described in works [2–8]. The use of different ANN architectures and algorithms was described in works [2–7]. Identification of defects in anisotropic plates by using ANN was present in work [8]. In work [4], the authors pointed out the advantages of identification methods that do not require the prior constructing of a mathematical model of the studied object.

In this paper, we developed a method of reconstruction of surface defects in pipes. Mathematically, the problem is reduced to the inverse geometrical problem of elasticity theory [9]. It is assumed that the defects locate on the outer or inner surfaces of the pipe and have axisymmetric configuration. Nonstationary acoustic signal is processed by actuator, located at some distance from the defect. The receiver locates there as well. The problem is solved in axisymmetric case using FEM. Finite element model of the pipeline track is built in the ANSYS. The signal (in the form of amplitude time response (ATR) of the radial and axial displacements) reflected from the defect is measured over time. The waves, reflected from the ends of the pipe segment, do not have time to come back to the receiver. In this way, the real conditions of an extended pipeline are modeled.

Analysis of the measured ATRs shows the possibility of their use in the inverse problems of identification of defects. The identification of defects may be carried out in two stages. At the first stage, the registration of a defect and the determination of the distance from the sensor to the defect are carried out. The problem of the first stage is solved on the base of the difference between the measured values of ATR for construction without defect and with the defect. Calculations show that the distance to the defect can be found using the signal arrival time, which is reflected by the defect. Thus, task of the first stage may be achieved by using hardware. The second stage provides the identification of the defect parameters (type, size, shape, volume, etc.). This task is much more difficult than the previous. Depending on the input information, it may have more than one solution. Artificial neural networks

are used as a tool for solving the inverse problem of the reconstruction of defects parameters. Artificial neural networks were originally designed for solving the problem of finding nonlinear dependencies. Unlike other algorithmic structures, there are not programmable, but trained on the data set, based on the different defect parameters. Training sets are constructed by solving direct problems in ANSYS. The trained network is able to correctly identify defect parameters. Input data for training ANN can be transformed by the FFT [10], which improves the identification process. The ANN architecture, ways of representing information, and the influence of defects sizes on the accuracy of the identification were studied in this chapter.

2 Formulation of Direct and Inverse Problems

2.1 Direct Problem

Formulation of direct problems is reduced to the initial boundary value problem of elasticity theory taking into account the energy dissipation adopted in finite element packages such as ANSYS, ACELAN, etc. The formulation consists of the following equations [11]:

$$\sigma_{ij,j} = \rho \ddot{u}_i + \rho \alpha \dot{u}_i, \quad i = 1, 2, 3 \quad (2.1)$$

$$\sigma_{ij} = c_{ijkl}(\varepsilon_{kl} + \beta \dot{\varepsilon}_{kl}). \quad (2.2)$$

$$\varepsilon_{kl} = \frac{1}{2} (u_{k,l} + u_{l,k}) \quad (2.3)$$

boundary conditions:

$$u_i|_{S_1} = u_i^0 \quad (2.4)$$

$$t_i = \sigma_{ij}n_j|_{S_k} = p_i \quad (2.5)$$

and initial conditions:

$$u_i|_{t=0} = g_i(x) \quad \dot{u}_i|_{t=0} = v_i(x) \quad x \in V_s. \quad (2.6)$$

Here ρ is the material density; u_i are the unknown components of the displacement vector; u_i^0, p_i are the known components of the displacement vector and surface loads; σ_{ij}, c_{ijkl} are the components of the stress tensor and elastic constants; s_k is the internal surface of the crack and the hole; and ε_{kl} are the components of the strain tensor. The factors α, β describe dissipative properties of the solid and are used in modern finite element analysis packages such as ANSYS, ABAQUS,

ACELAN, and so on. These factors are coupled with property of Q -linear oscillator through the following relationships [12]:

$$\alpha = \frac{2\pi f_{r1} f_{r2}}{Q(f_{r1} + f_{r2})}, \quad \beta = \zeta_d = \frac{1}{2\pi Q(f_{r1} + f_{r2})}, \quad (2.7)$$

where f_{r1} and f_{r2} are the first and second resonance frequencies, and Q is the quality factor.

The wave excitation and reception of the signal by using actuators and sensors, based on piezoelectric elements, are carried out. In this case, the linear theory of electrodynamics, taking into account the energy dissipation, is used. It is also taken into account in the ANSYS and ACELAN packages that

$$\rho \ddot{u}_i + \alpha \rho \dot{u}_i - \sigma_{ij,j} = f_i; \quad D_{i,i} = 0 \quad (2.8)$$

$$\sigma_{ij} = c_{ijkl}(\varepsilon_{kl} + \beta \dot{\varepsilon}_{kl}) - e_{ijk} E_k; \quad D_i + \zeta_d \dot{D}_i = e_{ikl}(\varepsilon_{kl} + \zeta_d \dot{\varepsilon}_{kl}) + \vartheta_{ik} E_k, \quad (2.9)$$

$$\varepsilon_{kl} = (u_{k,l} + u_{l,k})/2; \quad E_k = -\phi_{,k}, \quad (2.10)$$

where f_i are the components of the vector of the density of mass forces; D_i are the components of the electric induction vector; e_{ijk} are the third-rank tensor components of piezomoduli; E_i are the components of the electric field vector; ϕ is the electric potential function; ϑ_{ij} are the second-rank components of the tensor of dielectric permittivity; and α, β, ζ_d are negative damping coefficients [12].

Among the electrical boundary conditions, we note the conditions on the electrodes of actuator S_a and on the sensor electrode S_e , which is connected to an external electric circuit, or free:

$$\varphi|_{S_a} = \varphi_0 f(t) \quad (2.11)$$

$$\int_{S_e} \dot{D}_n ds = I, \quad (2.12)$$

where I is the current in the circuit (in the considered cases of free electrode it is equal to zero); φ_0 is the maximum value of the electric potential; and $f(t)$ is the function, describing the shape of the pulse (single step, used in the numerical results).

2.2 Inverse Problems

The inverse geometric problem of identification of cracks on the external or internal surface of the pipe is considered. The excitation of waves is carried out by the

piezoelectric actuator. As additional information, it used the ATR of electrical potential, measured by the piezoelectric sensors, disposed on the external surface of the pipe.

The solution of direct nonstationary problems for pipe fragment (Fig. 1, right) with a circular crack of depth dr (Fig. 1, left) on the outer or inner surface of the pipe is searched. Let h is the pipe length, r is the inner radius, tr is the thickness, s_1 is the distance between the first piezosensor and the defect, l_1 is the distance between the defect and edge of the pipe, s_2 is the distance from the piezoactuator to the second piezosensor, and l_2 is the distance from the second piezosensor to the edge of the pipe.

A fragment of pipe is considered, which in cylindrical coordinate system (r_*, θ, z_*) occupies an area $\Omega : r - \frac{tr}{2} \leq r_* \leq r + \frac{tr}{2}, 0 \leq \theta \leq 2\pi, 0 \leq z_* \leq l$.

A system of differential equations, describing wave processes in the pipe Eqs. (2.1)–(2.3), is used. The lower edge plane $z_* = 0$ is fixed; the upper edge plane and the inner cylindrical surface are free of stresses; the outer surface of the pipe also is free of stresses, too. Crack faces do not interact with each other; so they are free from mechanical stresses, too. The initial conditions correspond to the non-deformed tube at rest. Dynamic processes in the electroelastic environment (piezoactuators and piezosensors) are described by Eqs. (2.8)–(2.10). On the electrodes of piezoactuator, a potential difference (2.11) is given. One electrode of the piezosensor, which gives information on ATR of electric potential (2.10), is

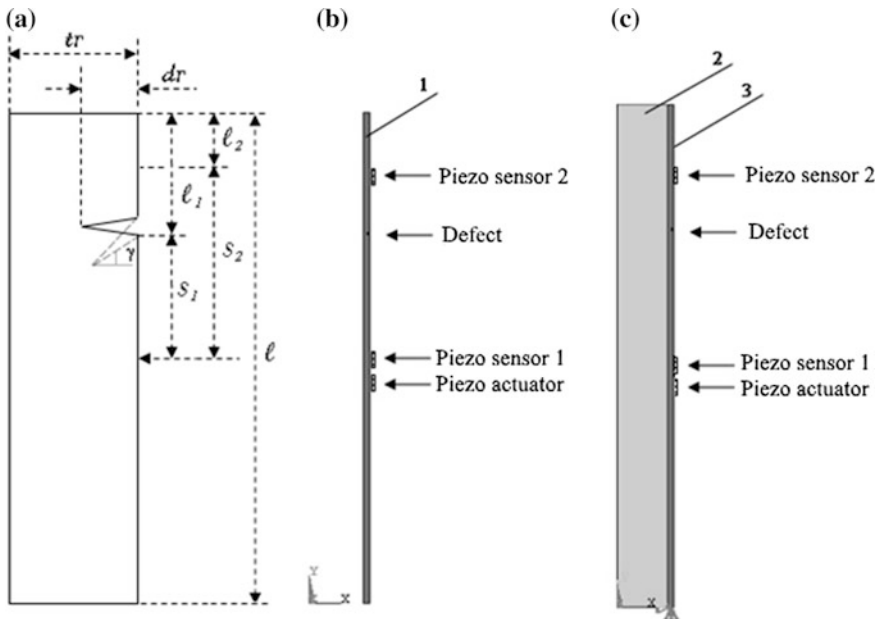


Fig. 1 a Pipe model with crack-like defect and shown dimensions; b pipe model without liquid; c pipe model with liquid (1, 3 metal, 2 liquid)

free. Wave processes that occur in the fluid filling the pipe are considered as acoustic ones. The impedance boundary conditions at the edges of the pipe simulate infinite acoustic environment.

Additional information for the solution of the inverse problem of identification of the crack is ATRs of electric potentials at the free electrode sensors (Fig. 1b, c):

$$\begin{aligned} \varphi|_{s_1} &= g_1(t) \\ \varphi|_{s_2} &= g_2(t) \end{aligned} \quad t \in [0, t_2] \quad (2.39)$$

where s_1, s_2 are the free electrodes of sensors 1 and 2, respectively (Fig. 1).

The values of s_1, dr, γ are required to identify; they characterize the crack (Fig. 1a). The distance from the first sensor to crack s_1 is determined at the first step; the crack penetration depth dr perpendicular to the surface is determined at the second step. Identification of defects is carried out by using ANN. The direct nonstationary problem for the pipe segment is solved for ANN training (Fig. 1, right). Let dr is the penetration depth and γ is the angle of the semicircular crack on the external or internal surface of the pipe (Fig. 1, left). The geometric parameters of the pipe are length $h = 2$ m, inner radius $r = 0.19$ m, thickness $tr = 0.02$ m, the distance from the first piezosensor to the defect $s_1 = 0.5$ m, the distance from the defect to the edge of the pipe $l_1 = 0.5$ m, the distance from the piezoactuator to the second piezosensor $s_2 = 0.7$ m, and the distance from the second piezosensor to the edge of the pipe $l_2 = 0.3$ m. Axisymmetric finite element model is built in ANSYS for Young's modulus $E = 2.0 \times 10^{11}$ Pa, density $\rho = 7800$ kg/m³, and Poisson's ratio $\nu = 0.3$.

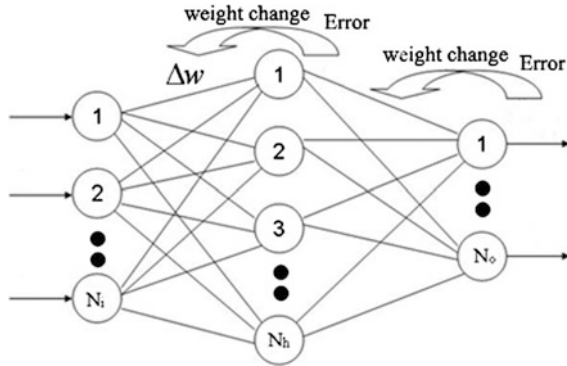
Excitation of the waves is performed by setting potential difference on the electrodes of the piezoactuator with step-like time dependence (the duration of action is 1×10^{-6} s). The measured data are the ATRs of the electric potential at the free piezosensor electrode, located on the external surface of the pipe. There are two cases of its location: (i) near to the piezoactuator, and (ii) at a distance from it. We assume that a defect locates between actuator and sensor (Fig. 1). Measurement of the signal, reflected from defect, is produced in the time interval $[t_1, t_2]$. We assumed, that t_1 is the time, when a reflected signal reaches sensor, t_2 is the time, when the signal, reflected from the pipe edges, reaches sensor: $t_1 = 2s_1/\nu$, $t_2 = 2(s_1 + l_1)/\nu$, $\Delta t = t_2 - t_1$ (where ν is the speed of the signal). For the second piezoelectric sensor, this interval is $t_1 = s_2/\nu$, $t_2 = (s_2 + 2l_2)/\nu$, $\Delta t = t_2 - t_1$.

3 Identification of Defects with the Use of Artificial Neural Networks

3.1 ANN Architecture

Multilayer network with back propagation is applied (Fig. 2). This architecture is perfectly suited for the task and combines the ease of implementation and performance.

Fig. 2 Explanation of the back propagation



Two hundred data vectors were formed, 90% of which were used for training and 10% for testing. Then the computer experiments were performed using ANN.

The square error, er , for a particular network configuration is determined by providing a network of all existing observations (n) and comparing the actual output values with the desired (target) values:

$$er = \frac{1}{2} \sum_{i=1}^n (d_i - y_i)^2, \tag{3.1}$$

where d is the desired network output; y is the real network output.

After training, the network can be used to predict output values. The accuracy of prediction is calculated according to the formula:

$$ex = \frac{100}{N * M} \sum_{i=1}^n \sum_{j=1}^m \left(1 - \left| \frac{dt_{i,j} - yt_{i,j}}{dt_{i,j}} \right| \right), \tag{3.2}$$

where n is the number of samples for testing; m is the number of output data; dt is the desired network output at testing; and yt is the actual network output at testing.

3.2 The Processing of Input Data for ANN

Figure 3a presents ATR of electric potential φ , measured by piezoelectric sensor (curve 1 represents the data that correspond to the case of the pipe without defect; curve 2 represents the data that correspond to the case of the pipe with defect $dr = 5$ mm; curve 3 is the difference between 1 and 2). Moreover, the time interval used for ANN training is specified.

Case 1. The input data for the neural network is the ATR of φ per the period of time $[t_1, t_2]$, marked by a dotted line in Fig. 3a.

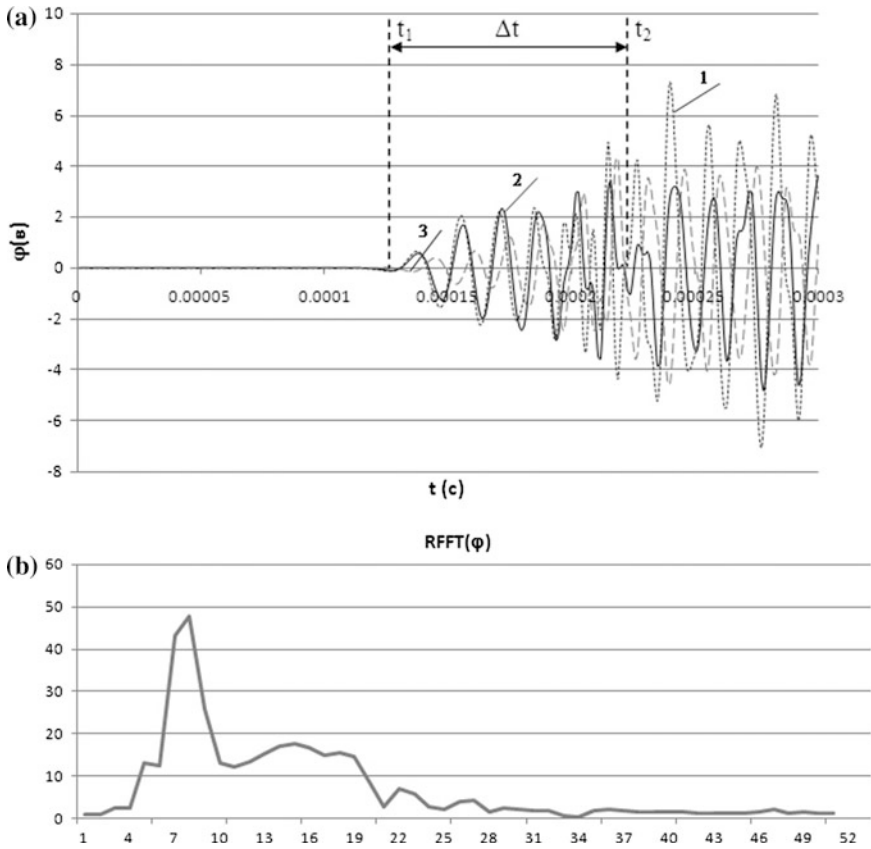


Fig. 3 **a** ATRs of electric potential φ for the pipe without the defect, with defect and their differences (input data for ANN correspond to case 1); **b** example of the ANN input data in case 2

Case 2. FFT algorithm is applied. Inputs to the neural network are values of the real parts of FFT (RFFT) (shown in Fig. 3b). In this case, the size of the input data decreases, so the training time will be less than in the first case.

4 Numerical Experiments

4.1 Determination of Distance to the Defect by Using Hardware

Figure 4 shows the difference between ATR of electric potential φ measured by the second piezosensor. Curve 1 represents the difference between φ for the empty pipe without defect and with it. Curve 2 represents the difference between φ of the pipe

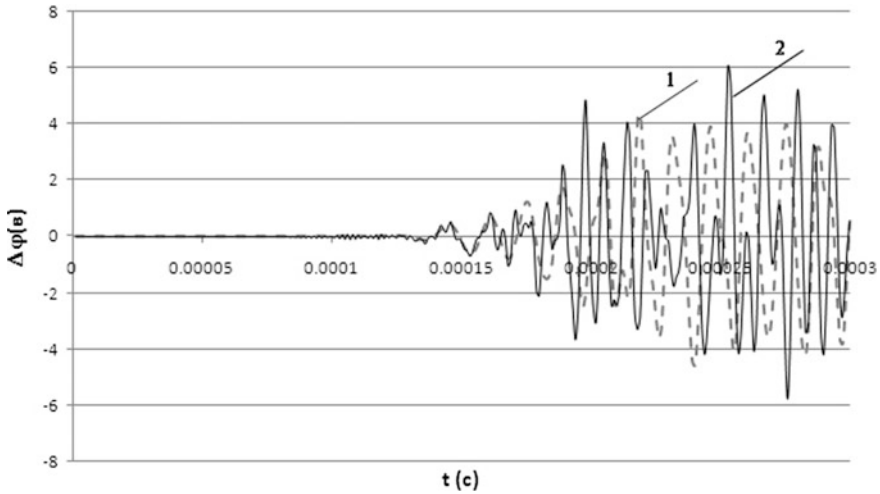


Fig. 4 Comparison of the difference between ATRs of the electric potential φ for the empty tube and the tube with the fluid

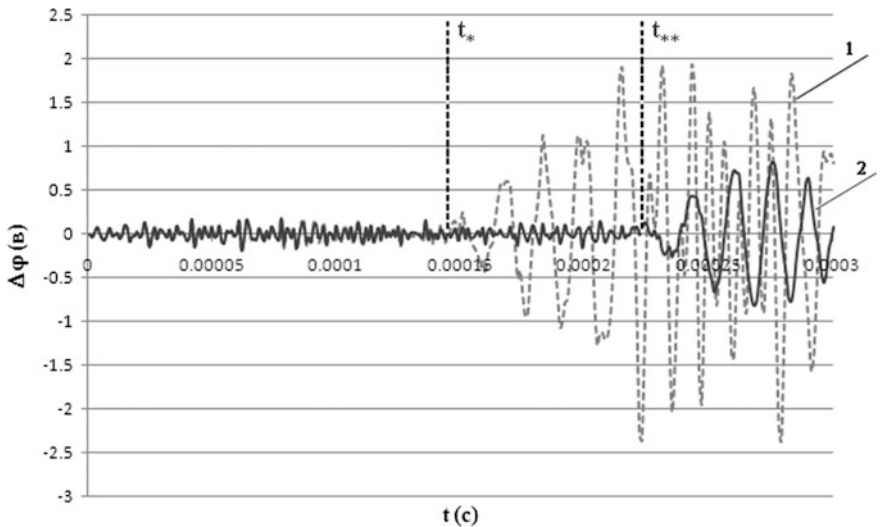


Fig. 5 Comparison of φ for the different defect positions

without defect filled with fluid and with the defect. The amplitudes and informative signal for empty pipe and filled with fluid are comparable, so further the ANN technology in the problem of identification of the defect is applied to an empty tube.

Figure 5 shows the difference between ATRs of electric potential φ measured by the first piezosensor. This case corresponds to an empty pipe with the different

distances s between the sensor and the defect. Curve 1 represents the difference between φ for the pipe without defect and with it on the external surface of the pipe. In the case of curve 1, $s_1 = 400$ mm. In the case of curve 2, $s_2 = 600$ mm. Using the time of arrival of the reflected signal t_* or t_{**} , we can estimate the distance to the defect. It is the first step in the identification of its parameters.

4.2 Determination of Distance to the Defect Using ANN

It was noted that the distance to the defect can be determined by using hardware according to the arrival time of the reflected signal. There is a possibility of the determination by using a trained neural network. It does not analyze the defect parameters, but identifies its location.

Table 1 shows the results of the identification of distance s to the defect by using ANN. The ANN structure is “200-20-1”. It uses 2000 training iterations and 200 input vectors (180—training, 20—testing); we assume that $s \in [1300, 1700]$ mm. The defects locate on the outer surface of the pipe. The line number indicates the type of the defect in Table 2.

The data, presented in Table 1, show that the error of determining the distance value equals 5% for “small” defects and reduces to 1.5% for “large” defects.

4.3 Determination of Defect Parameters Using ANN

The second step is to determine the crack depth, which is defined from range $dr \in [0, 9]$ mm in a numerical experiment. The discussed defects are roughly divided into three classes (see Table 2). This separation can be associated with

Table 1 Results of the identification of the distance to defect

№	Depth of the defect (dr) (mm)	Accuracy of identification (%)
1	2	94.92
2	5	97.11
3	8	98.67

Table 2 Defect classes

№	The depth of the defect (dr) (mm)
1	0–3
2	3–6
3	6–9

classification of defects according to the degree of damage and the danger of the destruction of the pipe. For each class within the training and testing, we analyzed 200 defects.

The reconstruction of defect parameters was performed for two cases: (i) defects, located on the outer surface of the pipe; and (ii) defects, located on the inner surface of the pipe.

4.3.1 Reconstruction of Perpendicular Cracks

Let us first consider the crack perpendicular to the pipe surface. In this case, the depth of the defect, dr , shall be identified. Two hundred data vectors were formed, 90% of which were used for training and 10% for testing. Thereafter, the computer experiments are performed using the ANN. Error, er (Fig. 6), and prediction accuracy were defined by the formulae (3.1) and (3.2).

The results of the training and testing in the case of the second sensor are shown in Tables 3, 4, 5 and 6.

Table 3 shows the ANN structures, which give the best identification results, namely 51 input neurons, 10 hidden neurons, and one output neuron.

Table 4 shows that the best result is obtained with 2000 training iterations.

The results of training and testing in the Case 2, using the first sensor, are shown in Tables 7 and 8.

The results of Tables 5, 6, 7 and 8 listed in rows 1–3 correspond to Table 2.

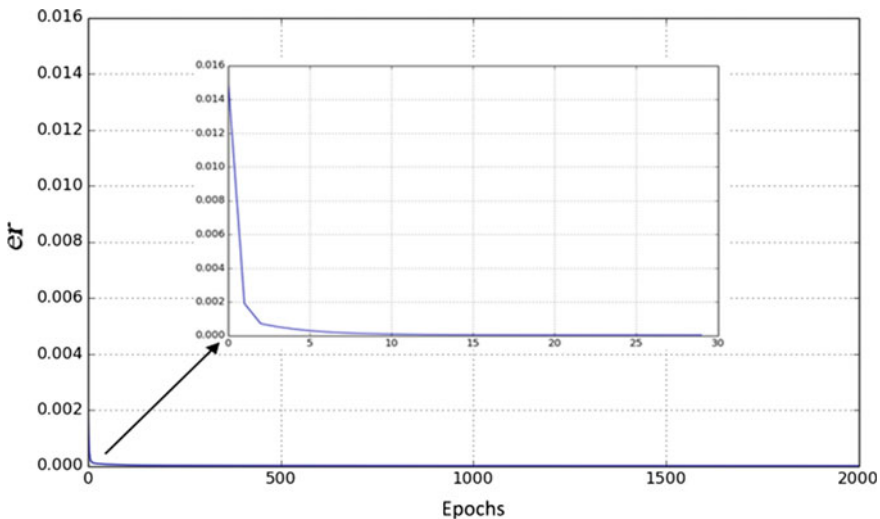


Fig. 6 Training error

Table 3 Results of training and testing ANN, using 2000 epochs and 200 input vectors (RFFT); different hidden layers are used and defects locate on the outer surface of the pipe

No.	ANN structure	Error (er)	Accuracy (ex) (%)
1	51-5-1	1.2×10^{-6}	99.58
2	51-10-1	8.6×10^{-7}	99.67
3	51-20-1	2.5×10^{-6}	99.22
4	51-30-1	1.9×10^{-5}	98.80
5	51-5-5-1	1.3×10^{-4}	96.97
6	51-10-10-1	1.2×10^{-6}	99.43
7	51-15-15-1	3.2×10^{-6}	99.17
8	51-20-20-1	3.5×10^{-6}	99.13

Table 4 Results of training and testing of ANN, using 200 input vectors (RFFT); different numbers of epochs are used and defects locate on the outer surface of the pipe

No.	ANN structure	Error (er)	Accuracy (ex) (%)
1	51-10-1	1000	99.37
2	51-10-1	2000	99.67
3	51-10-1	3000	99.46
4	51-10-1	4000	99.21

Table 5 Results of training and testing ANN using 2000 epochs; different values of the defect depth are used and defects locate on the outer surface of the pipe

No.	Amount of data	ANN structure	Error (er)	Accuracy (ex) (%)
1	200–all	100-20-1	2.1×10^{-6}	99.35
	200–RFFT	51-10-1	8.6×10^{-7}	99.67
2	200–all	100-20-1	3.8×10^{-6}	98.90
	200–RFFT	51-10-1	5.1×10^{-7}	99.64
3	200–all	100-20-1	3.5×10^{-6}	99.29
	200–RFFT	51-10-1	1.3×10^{-7}	99.87

Table 6 Results of training and testing ANN using 2000 epochs; different values of the defect depth are used and defects locate on the inner surface of the pipe

No.	Amount of data	ANN structure	Error (er)	Accuracy (ex) (%)
1	200–all	100-20-1	4.2×10^{-6}	99.24
	200–RFFT	51-10-1	6.1×10^{-6}	99.48
2	200–all	100-20-1	1.5×10^{-6}	99.71
	200–RFFT	51-10-1	7.0×10^{-7}	99.75
3	200–all	100-20-1	9.5×10^{-7}	99.70
	200–RFFT	51-10-1	9.8×10^{-7}	99.39

Table 7 Results of training and testing ANN using 2000 epochs; different values of the defect depth are used and defects locate on the outer surface of the pipe

No.	Amount of data	ANN structure	Error (er)	Accuracy (ex) (%)
1	200-all	100-20-1	8.4×10^{-6}	98.52
	200-RFFT	51-10-1	6.3×10^{-6}	98.62
2	200-all	100-20-1	2.7×10^{-6}	99.34
	200-RFFT	51-10-1	6.4×10^{-6}	99.07
3	200-all	100-20-1	7.7×10^{-7}	99.41
	200-RFFT	51-10-1	1.3×10^{-6}	99.27

Table 8 Results of training and testing ANN using 2000 epochs; different values of the defect depth are used and defects locate on the inner surface of the pipe

No.	Amount of data	ANN structure	Error (er)	Accuracy (ex) (%)
1	200-all	100-20-1	3.8×10^{-6}	98.95
	200-RFFT	51-10-1	6.5×10^{-6}	98.74
2	200-all	100-20-1	3.4×10^{-6}	99.26
	200-RFFT	51-10-1	4.1×10^{-6}	99.44
3	200-all	100-20-1	3.1×10^{-7}	99.68
	200-RFFT	51-10-1	2.5×10^{-7}	99.71

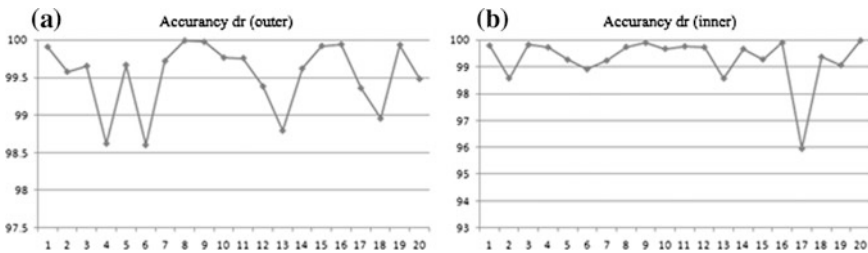


Fig. 7 Test results of identification of the defect depth

Figure 7 shows the test results of ANN (depth identification), displaying 20 examples with “10-01-51” architecture. The plots, shown in Fig. 7a, b, are built on the data, obtained by using the second row of Tables 5 and 6, respectively.

Figure 8 shows the results of identification in the case of using “noisy data” from formula (4.1). It is modeled the measurement error as

$$\tilde{X}(t) = X(t) + \delta P(t) \text{MAX}(|X(t)|), \tag{4.1}$$

where δ ranges from 1 to 10%, and $P(t)$ is the random variable uniformly distributed in the range $[-1, 1]$.

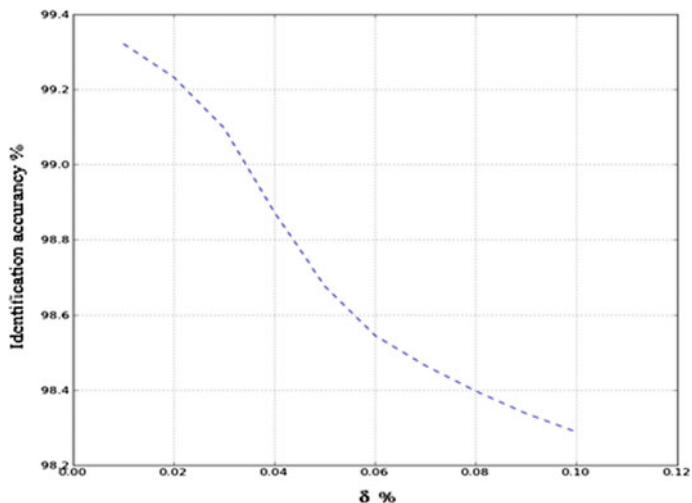


Fig. 8 Results of identification by using “noisy data”

Table 9 Results of training and testing ANN using 2000 epochs; different values of the defect depth and angle are used

No.	ANN structure	Error	Accuracy (%)	Sensor
1	100-10-2	0.0032	92.27	1
2	100-10-2	7.89×10^{-5}	95.95	1
3	100-10-2	0.3253	89.28	1
4	100-10-2	0.0119	97.39	2
5	100-10-2	3.91×10^{-5}	98.11	2
6	100-10-2	0.7315	84.47	2

4.3.2 Reconstruction of Inclined Cracks

In this section, we consider the identification of inclined cracks. Also as previously, defects are roughly divided into three classes (Table 2). We consider inclined cracks on the outer surface of the pipe. The inclination angle of the crack varies in the range $[-45^\circ; 45^\circ]$. Two hundred defects are used for each of the considered classes. The results of identification are shown in Tables 9, 10 and 11.

The numerical results showed that the identification error of inclined cracks does not exceed 10%. The architecture of trained ANN is 200-20-2 and 101-10-2. Thus, using the data, based on RFFT, accelerates more than two times speed of the learning process. For a more accurate reconstruction of defect parameters, the piezoelectric actuators and sensors, if it is possible in practice, should be located in the vicinity of the defect.

Table 10 Results of training and testing ANN using 2000 epochs; different values of the defect depth and angle are used

No.	ANN structure	Error	Accuracy (%)	Sensor
1	200-20-2	0.0024	95.32	1,2
2	200-20-2	1.48×10^{-5}	99.48	1,2
3	200-20-2	0.0146	92.52	1,2

Table 11 Results of training and testing ANN using 2000 epochs and 200 input vectors (RFFT); different values of the defect depth and angle are used

No.	ANN structure	Error	Accuracy (%)	Sensor
1	101-10-2	0.00059	96.75	1,2
2	101-10-2	8.71×10^{-6}	99.59	1,2
3	101-10-2	0.07695	92.19	1,2

5 Conclusion

In the result of this study, the method of the parameter identification of cracks on the outer or inner surface of the pipe, based on a combination of the finite element method and ANN, is developed. Additional information for the solution of the inverse problem of identification of the crack is ATRs of a radial and axial displacements and electric potential of piezosensor. This allows one to use the developed method in practice without complicated measurements. The study found that the preparation of the input data is the cornerstone in solving the problem. The most successful is the identification of the defect, based on the ATR, obtained by FFT. It is shown that the problem of identifying defects may be performed in two stages: (i) by determining the distance to the defect, and (ii) by determining its parameters.

Accuracy of determining the defect depth for the outer surface defect became 99.41 and 99.71% for the inner surface defect. Note that as additional information for the solution of inverse problems was used ATR of electrical potential of piezosensors, these sensors were located before the defect (for reflected signal) and after the defect (for passed signal). The results of numerical experiments showed that accuracy of the identification of defect parameters with trained ANN exceeded 95% at both locations of piezosensors. In the result of numerical experiments, we revealed ANN architectures that gave the best identification results, namely, 51 input neurons, 10 hidden neurons, and 1 output neuron.

In this architecture, we used the data, processed by the FFT. The size of input data was reduced, so the learning process became faster than in the case of using ATR data. Analysis of the input data showed that the ATR data could be used for identification defects in pipes, filled with fluid. The proposed identification algorithm was resistant to the error of input information.

Based on the foregoing, we conclude that the artificial neural network approach can be successfully used to identify defects on the surface of pipes by using the acoustic sensing of far field.

Acknowledgements This study for the first and third authors was supported by the Russian Science Foundation (Grant No. 17-08-00, 621).

References

1. S. Haykin, *Neural Networks: A Comprehensive Foundation* (John Wiley & Sons, NY, 1999), p. 823
2. A.A. Krasnoshchekov, B.V. Sobol', A.N. Soloviev, A.V. Cherpakov, Identification of defects crack-like defects in elastic structural elements on the basis of evolutionary algorithms. *Russ. J. Non-destr. Testing* **6**, 67 (2011)
3. P.S. Kurbatova, N.I. Saprunov, A.N. Soloviev, Use of neural networks in the task of determining defects in elastic bodies. in *Proceedings of X International Conference "Modern Problems of Continuum Mechanics"* (Southern Federal University Press, Rostov-on-Don, 2006), p. 75 (in Russian)
4. X. Fang, H. Luo, J. Tang, Structural damage detection using neural network with learning rate improvement. *Comput. Struct.* **83**(25), 2150 (2005)
5. V. Khandetsky, I. Antonyuk, Signal processing in defect detection using back-propagation neural networks. *NDT and E Int.* **35**(7), 483 (2002)
6. S.-W. Liu, J.-H. Huang, J.-C. Sung, C. Lee, Detection of cracks using neural networks and computational mechanics. *Comput. Methods Appl. Mech. Eng.* **191**(25), 2831 (2002)
7. Z. Waszczyszyn, L. Ziemiański, Neural networks in mechanics of structures and materials—new results and prospects of applications. *Comput. Struct.* **79**(22), 2261 (2001)
8. Y.G. Xu, G. Liu, Z. Wu, X. Huang, Adaptive multilayer perceptron networks for detection of cracks in anisotropic laminated plates. *Int. J. Solids Struct.* **38**(32), 5625 (2001)
9. A.O. Vatulyan, *Inverse Problems in Solid Mechanics* (Mir, Moscow, 2007), p. 224 (in Russian)
10. D.W. Kammler, *A First Course in Fourier Analysis* (Cambridge University Press, Cambridge, 2007)
11. V. Novatski, *Theory of Elasticity* (Mir, Moscow, 1975), p. 864
12. A.V. Belokon, A.V. Nasedkin, A.N. Soloviev, New scheme of the finite element dynamic analysis of piezoelectric devices. *J. Appl. Math. and Mech.* **66**(3), 491 (2002)

Dynamic Properties of Thin-Walled Structures Under Changing Pressure Conditions in the Contact Fluid

M.A. Sumbatyan, Evgeny N. Barkanov and A.E. Tarasov

Abstract We propose an analytical algorithm to study harmonic oscillation of a rectangular elastic plate in an incompressible fluid, with varying pressure conditions. Application of the two-dimensional Fourier transform leads to a two-dimensional integral equation with a two-dimensional integral as a kernel. The solution of the basic integral equation is represented as a series by the Chebyshev orthogonal polynomials. The problem is reduced to an infinite system of one-dimensional integral equations. The asymptotic approach allows us to solve each equation of the system independently. The solution of the integral equation leads to an ordinary differential equation of the fourth order for the function of the plate vibrations. The obtained solution determines the form of the oscillation. The results are given on example of the aluminum plate oscillations for a number of frequencies by varying air pressure density. The results are compared with experimental data.

Keywords Harmonic oscillation · Air damping · Incompressible fluid · Elastic plate · Integral equation

1 Introduction

A set of experiments has been made to study damping properties of the viscoelastic plates in terms of aerodynamics under the conditions of normal atmospheric pressure and rarefied air [1]. There have been studied experimentally the dependence of the aerodynamic characteristics of the plate versus physical characteristics and changes in the environment. The necessary pressure levels have been obtained

M.A. Sumbatyan · A.E. Tarasov (✉)
I.I. Vorovich Institute of Mathematics, Mechanics and Computer Science,
Southern Federal University, Rostov-on-Don, Russia
e-mail: aetarasov@sfedu.ru

E.N. Barkanov
Riga Technical University, Riga, Latvia

by using SMC T203-1-02 vacuum regulator and vacuum pump DOA-V510-BN. The experiments permitted to provide 80% pressure reduction.

In the present paper, we propose a mathematical background for such experiments, in order to evaluate the contribution of the air pressure parameter to the shape of plate vibrations. It turns out that the aerodynamic characteristics depend upon the variation of the pressure, as well as on some other physical parameters.

2 Mathematical Formulation of the Problem

Let a thin plane plate rectangular in plan, of the size $S = (-b, b) \times (-\ell, \ell)$, be placed into a homogeneous nonviscous incompressible fluid (see Fig. 1). The plate is forced to oscillate harmonically by an external input signal; then these vibrations propagate over the entire plate.

The perturbations introduced by the plate are assumed to be small, so that the problem is studied in linear approximation. Then all physical quantities are harmonic in time: $\tilde{A}(x, y, z, t) = \text{Re}\{A(x, y, z)e^{-i\omega t}\}$. The plate has the constant bending stiffness EJ and the linear mass density m .

The plate is assumed to be narrow: $b/\ell \ll 1$. Then the dynamic elastic behavior of the plate itself is defined by the following differential equation of beam oscillations along variable y :

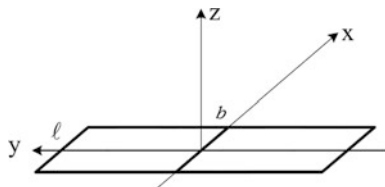
$$EJ \frac{d^4 W(y)}{dy^4} - m\omega^2 W(y) = Z(y) + p_0 b^2 (y - y_0), \quad Z(y) = \int_{-b}^b (p_- - p_+) dx, \quad (1)$$

where p_- and p_+ are the hydrodynamic pressures distributed under and above the plate. Function $p_0(y - y_0)$ indicates the amplitude of the external force harmonic in time and applied to the beam at $y = y_0$, wherein the multiplier b^2 is included in order to all the terms in Eq. (1) to have the same dimension.

The side edges of the plate are free of load:

$$\frac{d^2 W}{dy^2} = \frac{d^3 W}{dy^3} = 0, \quad (y = \pm\ell). \quad (2)$$

Fig. 1 Thin rectangular in plane plate $(-b, b) \times (-\ell, \ell)$



The hydrodynamic field is assumed to be potential. The perturbed velocity vector satisfies the Laplace equation, which follows from the following continuity equation:

$$\Delta\varphi = 0. \quad (3)$$

The perturbed pressure p is related to φ by the linearized Cauchy integral

$$\frac{\partial\tilde{\varphi}}{\partial t} + \frac{\tilde{p}}{\rho} = 0, \Rightarrow -i\omega\varphi + \frac{p}{\rho} = 0, \quad (4)$$

where ρ is the density of the fluid.

The hydrodynamic boundary conditions take the following form. The perturbations vanish at infinity: $\varphi \rightarrow 0, (x, y, z \rightarrow \infty)$. The pressure and the normal components of the velocity are continuous in our plate:

$$p_- = p_+, \frac{\partial\varphi_-}{\partial z} = \frac{\partial\varphi_+}{\partial z}, \quad z = 0, (x, y) \notin S \quad (5)$$

The impermeability of the plate implies

$$\frac{\partial\tilde{W}}{\partial t} = \frac{\partial\tilde{\varphi}}{\partial z}, \Rightarrow -i\omega W = \frac{\partial\varphi_-}{\partial z} = \frac{\partial\varphi_+}{\partial z}, \quad z = 0, (x, y) \in S. \quad (6)$$

Here we solve the hydrodynamic problem. From (5) and (6) it follows that $\partial\varphi/\partial z$ is even with respect to z , for all (x, y) . Therefore, potential φ is odd with respect to z for all (x, y) . Then, aerodynamic pressure p in (4) is also odd with respect to z , for all (x, y) . Thus, it is sufficient to find these basic functions only for $z \geq 0$.

Let us introduce the new unknown function $g(x, y)$:

$$\frac{1}{2}(p_+ - p_-)_{z=0} = p_+(x, y, +0) = \begin{cases} 0, & (x, y) \notin S \\ g(x, y) & (x, y) \in S \end{cases} \quad (7)$$

$$Z(y) = -2 \int_{-b}^b p_+ dx.$$

By applying two-dimensional Fourier transform along x and y variables, the formulated boundary value problem can be reduced to a dual integral equation:

$$\frac{1}{4\pi^2\omega^2\rho} \int_{-b}^b \int_{-l}^l K(\xi - x, \eta - y)g(\xi, \eta)d\xi d\eta = -W(y), \quad (|x| \leq b, |y| \leq \ell), \quad (8)$$

$$K(\xi, \eta) = \int_{-\infty}^{\infty} \int_{-\infty}^{\infty} \sqrt{\alpha^2 + \beta^2} e^{i(\alpha\xi + \beta\eta)} d\alpha d\beta. \tag{9}$$

3 Asymptotical Analysis of the Basic Integral Equation

The kernel in (9) can be written in the explicit form

$$K(\xi, \eta) = -\frac{2\pi}{(\xi^2 + \eta^2)^{3/2}}. \tag{10}$$

It is obvious that the kernel is hypersingular, as $\sqrt{\xi^2 + \eta^2} \rightarrow 0$. It is known [2] that the solution to integral equation with such a kernel vanishes near the edge S as square root of the distance. That is why we seek the solution to Eqs. (8) and (9) in the form of the following series:

$$g(x, y) = \sqrt{b^2 - x^2} \sum_{k=0}^{\infty} \frac{g_k(y)}{k+1} U_k\left(\frac{x}{b}\right). \tag{11}$$

Here the square root in front of series is the weight in the orthogonality property of the Chebyshev polynomials $U_k(x)$.

Let us substitute representation (11) into (8) and apply the scalar product of both the left- and right-hand sides of (8) with the set of function $\sqrt{b^2 - x^2} U_k(x/b), n = 0, 1, \dots$. Then, after integration over variables ξ and x (J_n is Bessel function of the order n) [3], we obtain the following infinite system of one-dimensional integral equations:

$$\begin{aligned} \frac{b^2}{4\rho\omega^2} \sum_{k=0}^{\infty} N_{nk}(\eta - y) g_k(\eta) d\eta &= F_k(y), \quad |y| \leq \ell, \quad n = 0, 1, \dots \\ F_n(y) &= - \int_{-b}^b \sqrt{b^2 - x^2} W(y) U_n\left(\frac{x}{b}\right) dx, \quad N_{nk}(\eta) = \int_{-b}^b L_{nk}(\beta) e^{i\beta\eta} d\beta, \tag{12} \\ L_{nk}(\beta) &= i^{k-n} (n+1) \int_{-b}^b \frac{J_{n+1}(b\alpha) J_{k+1}(b\alpha)}{\alpha^2} \sqrt{\alpha^2 + \beta^2} d\alpha, \quad n, k = 0, 1, \dots \end{aligned}$$

Since the half-width b of the plate is asymptotically small (compared with the semi-span ℓ), we take the kernel N_{nk} in the degenerated form ($b\beta \rightarrow 0$) [4]:

$$N_{nk}(\eta) \approx \int_{-\infty}^{\infty} L_{nk}(0) e^{i\beta\eta} d\beta = L_{nk}(0) 2\pi\delta(\eta). \quad (13)$$

Thus

$$L_{nk}(0) = 0, (k \neq n); \quad L_{nk}(0) = 2(n+1) \int_0^{\infty} \frac{J_{n+1}^2(\alpha)}{\alpha} d\alpha = 1. \quad (14)$$

Consequently, for $\lambda = \ell/b \rightarrow \infty$ the off-diagonal elements ($k \neq n$) of the system (12) vanish, and, in a first approximation the system is reduced to a set of independent relations:

$$\frac{\pi(-1)^n}{2(n+1)\rho\omega^2} g_n(y) = F_n(y), \quad |y| \leq \ell, \quad n = 0, 1, \dots \quad (15)$$

From the middle row of Eq. (12), due to orthogonality of the Chebyshev polynomials, it is clear that $F_n(y) \equiv 0, n \geq 1$, and therefore $g_n(y) \equiv 0, n \geq 1$. Consequently, among all the functions $g_n(y)$, the only nontrivial function is $g_0(y)$, which is easily obtained from (15) and (12):

$$\frac{\pi}{2\rho\omega^2} g_0(y) = F_0(y) = -\frac{\pi}{2} W(y), \Rightarrow \quad (16)$$

$$g(x, y) = \sqrt{b^2 - x^2} g_0(y) = -\rho\omega^2 \sqrt{b^2 - x^2} W(y). \quad (17)$$

4 Dynamic Deformation of the Plate

The differential equation which determines the amplitude of the oscillations of the plate, function $W(y)$, is obtained if one substitutes expression (17) to Eq. (1):

$$Z(y) = \int_{-b}^b [p_-(x, y) - p_+(x, y)] dx = -2 \int_{-b}^b g(x, y) dx = \pi\rho b^2 \omega^2 W(y). \quad (18)$$

Then (1) takes the following form:

$$\frac{d^4 W(y)}{dy^4} - \zeta^4 W(y) = \frac{p_0 b^2}{EJ} \delta(y - y_0), \quad (\zeta\ell)^4 = \frac{\ell^4 \omega^2}{EJ} (m + \pi\rho b^2). \quad (19)$$

The solution to the differential equation of the fourth order (19) with the boundary conditions (2) can be represented as the sum of the general solution of the homogeneous equation and a particular solution to the full equation:

$$W(y) = W_0(y) + W_p(y), \quad (20)$$

where

$$W_0(y) = A_1 \sin[\zeta(y + \ell)] + A_2 \sin h[\zeta(y + \ell)] + A_3 \sin[\zeta(y - \ell)] + A_4 \sinh[\zeta(y - \ell)], \quad |y| \leq \ell, \quad (21)$$

$$W_p(y) = \frac{p_0 b^2}{4EJ\zeta^3} \left\{ \frac{\cos[\zeta(\ell - y - y_0)] - \cos[\zeta(\ell - |y - y_0|)]}{\sin(\zeta\ell)} + \frac{\cosh[\zeta(\ell - y - y_0)] - \cosh[\zeta(\ell - |y - y_0|)]}{\sinh(\zeta\ell)} \right\}. \quad (22)$$

The four unknown constants A_1, A_2, A_3, A_4 can be easily found from the four boundary conditions (2). This allows us to determine the shape of the plate oscillations, function $W(y)$.

5 Numerical Results

The variation of the outer pressure affects the aerodynamics not directly but through a density, which decreases proportionally to reduction of pressure. The dependence of the degree of air rarefaction is strongly nonlinear, being represented through parameter ζ in (19) containing air density.

To compare the obtained results with the experimental data, we took a thin aluminum plate of length 0.3 m, width 0.2 m, and 2 mm thickness. The shape of the plate oscillations is calculated for different density values ρ , at a certain vibration frequency (to be more specific, at 700 Hz). The external input signal force is applied to the plate at the point $y_0 = 0$. Figure 2 demonstrates the diagrams of the oscillation function $W(y)$ for different densities ρ .

From Fig. 2 it can be seen that $\max |W(y)|, y \in (-\ell, \ell)$ increases with decreasing density values ρ . In the considered case, the total increase in the oscillation amplitude is about of 16%. We compared our results with the data taken from the experiments [1] obtained in the Riga Technical University for the same plate for the ninth vibration mode, the frequency of which is close to 700 Hz. The comparison with experimental data for this case is shown in Fig. 3.

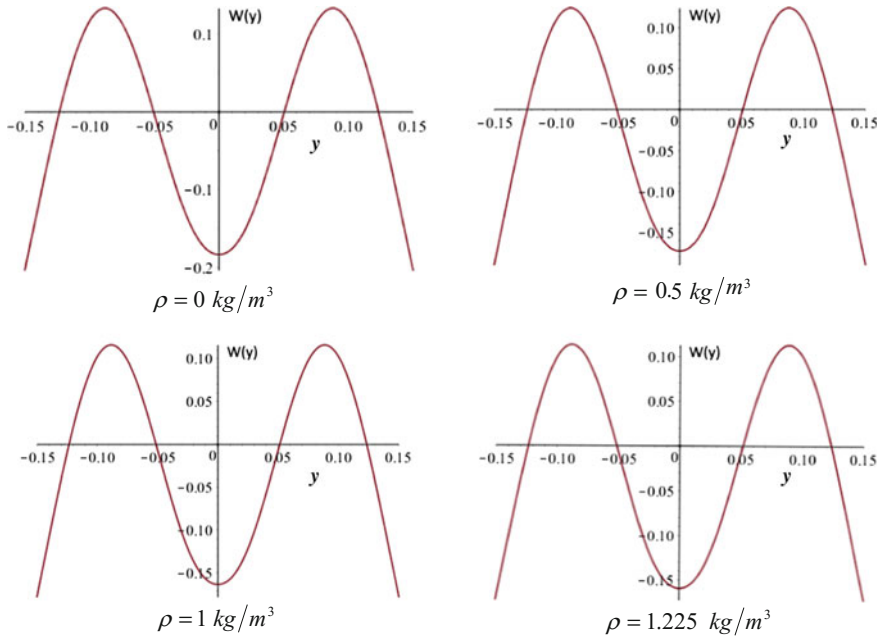


Fig. 2 Form of the aluminum plate oscillation $W(y)$; $\ell = 0.3 \text{ m}$, $b = 0.2 \text{ m}$, $h = 2 \text{ mm}$ at the frequency 700 Hz

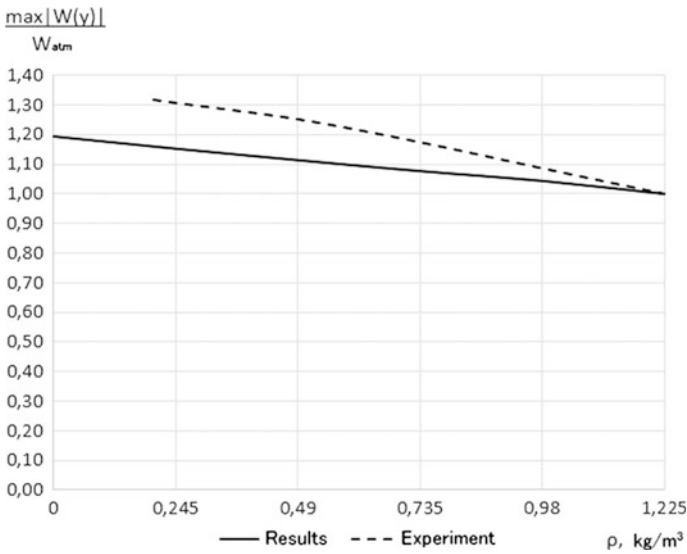


Fig. 3 Comparison of the max $|W(y)|$ versus ρ for the plate $\ell = 0.3 \text{ m}$, $b = 0.2 \text{ m}$, $h = 2 \text{ mm}$ at the frequency 700 Hz

References

1. M. Wesolowski, E. Barkanov, Air damping influence on dynamic parameters of laminated composite plates. *Measurement* **85**, 239 (2016)
2. M.A. Sumbatyan, A. Scalia, *Equations of Mathematical Diffraction Theory* (CRC Press, Boca Raton, 2004)
3. A.P. Prudnikov, Y.A. Brychkov, O.I. Marichev, *Integrals and Series* (Gordon and Breach Science Publishers, Amsterdam, 1986), pp. 1–3
4. A. Pompei, A. Rigano, M.A. Sumbatyan, Contact problem for a rectangular punch on the porous elastic half-space. *J. Elasticity* **76**, 1 (2004)

Part II
Volumetric Surface Defects
in Transmission Pipelines

Characterisation of Volumetric Surface Defects

Andrei Dumitrescu, Gh. Zecheru and A. Diniță

Abstract Large-diameter, high-pressure steel transmission pipelines are commonly used for the transportation of hydrocarbons and other fluids. An important issue regarding their exploitation and maintenance is the detection and assessment of defects that may develop in the steel pipe wall. Among the most frequent defects are the local metal loss defects (also named volumetric surface defects—VSDs) that are generated by corrosion and/or erosion processes. In the present chapter, after the characterisation of such defects, the main issue addressed consists of the comparative presentation of the methods and criteria used for the VSDs assessment, i.e., for the evaluation of the detected metal loss flaws in order to qualify them as either imperfections or defects and to define, if the case, the required pipeline maintenance works. A case study is also presented in order to illustrate such assessment for a given VSD with a complex geometry.

Keywords Transmission pipeline · Flaw/defect · Volumetric surface (local metal loss) defect (VSD) · Fitness-For-Service (FFS) · Remaining Strength Factor (RSF)

1 Introduction

Transmission pipeline systems, most of them buried, are commonly used for the onshore and offshore transportation of petroleum, liquid petroleum products, natural gas, liquefied petroleum/natural gas, water, etc. The great majority of such pipelines are made of large-diameter steel pipes and components, with the outside diameter range $D_e = 500\text{--}2000$ mm, operating at high pressures (the range of the maximum allowable working pressure is: MAWP = 6–100 bar). The transmission pipelines are providing services of great importance and therefore their maintenance and repair activities need special attention.

A. Dumitrescu (✉) · Gh. Zecheru · A. Diniță
Petroleum-Gas University of Ploiesti, Ploiești, Romania
e-mail: andrei.upg@gmail.com

During the operation of pipelines, various types of flaws can appear and develop in the steel pipe walls, being able to affect the proper functioning of the pipeline and also to cause critical unwanted events. The flaws (anomalies) that can be detected in the pipes of a transmission line can be classified in the following three categories:

- (i) geometric flaws, caused by the local deformation of the pipeline, which include all deviations of dimension and shape that modify significantly the configuration of the cross section of the steel pipe. The main types of such flaws are grooves and local deformations (also named dents). A picture of a dent detected on a gas pipeline is included in Fig. 1a;
- (ii) flaws of the metal loss type that consist of a general or local wall thinning of the steel pipes, by means of losing metallic material, due to corrosion and/or erosion processes. The local flaws of such a type, detected on the external or internal surface of a pipe, are also named volumetric surface flaws and one example is shown in Fig. 1b;
- (iii) crack-like flaws, that can be generated during the pipeline exploitation, due to the phenomena of fatigue, stress corrosion cracking, hydrogen-related cracking etc., or can be present in the steel pipes even since the transmission line has been put into service, being generated during pipes rolling or occurring in the weld joints of the pipes (see Fig. 1c).

When, at a periodic inspection of the technical condition of a given pipeline, flaws of any type are detected on its steel pipes, it is needed to assess if they have a significant negative influence upon the proper operation and loading capacity of the pipeline and therefore require maintenance measures to be taken and repair activities to be executed. Such an assessment will indicate which one from the following decisions is pertinent:

- (i) to qualify the flaws as *imperfections* and to maintain the pipeline in service, without performing maintenance works and without decreasing the operating pressure; in this case, no intervention is required on the pipeline;
- (ii) to qualify the flaws as *defects* and to decrease the pipeline operating pressure, until corrective maintenance works are applied, with or without removing the pipeline from service.

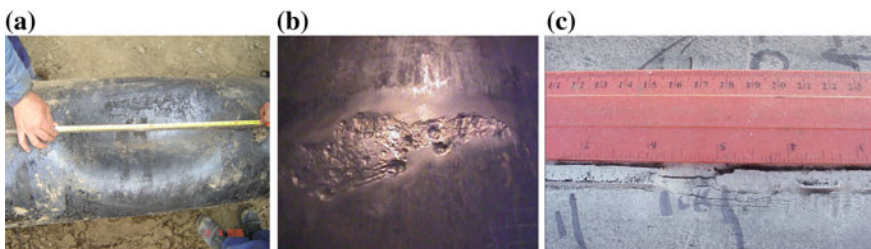


Fig. 1 Photographs of flaws/defects detected on natural gas transmission pipelines: **a** dent, **b** local metal loss, **c** cracks

Local metal loss defects, which are often named also volumetric surface defects (VSDs), of the transmission pipelines are the most important cause of pipelines failure during exploitation [1]. For instance, approximately 85% of the failures recorded in the last 10 years on the pipelines of the Romanian national natural gas transmission system have been caused by this type of defects. VSDs are the subject of the present Part 3, of this book.

According to API 579 standard [2], local metal loss defects, which may occur both on the outside and on the inside of the pipe, are classified in the following two categories:

- (i) *Local Thin Area (LTA)* is the local metal loss on the pipe surface; the length of a region of LTA is the same order of magnitude as the width;
- (ii) *Groove-Like Flaw (GRO)* is the local elongated thin spot caused by directional erosion or corrosion; the length of such flaw is significantly greater than its width, and it has to be mentioned that a sharp radius may be present at the base of a groove.

Typical flaws/defects of the type GRO (with different orientations) and LTA are shown in Fig. 2 together with their characteristic dimensions: s_p is the length (the extent in longitudinal/axial direction of the pipe), c_p is the width (the circumferential/transversal extent), g_f is the groove length, g_w is the groove width, and g_r is the radius at the base of a groove.

In order to detect any type of flaw existing in a steel pipe, the periodic inspection of the pipeline is needed. The methods used for such inspection can be classified in two categories: (i) methods verifying the condition of the corrosion protection coating of the pipeline and leading only to informative results; (ii) direct detection methods by means of “in-line” inspection, used after removing the corrosion protection and cleaning the external surface of the pipe. For flaws developed on the external surface of the steel pipe, visual examination and measuring with simple instruments can be sufficient. For flaws placed at the interior of the pipe,

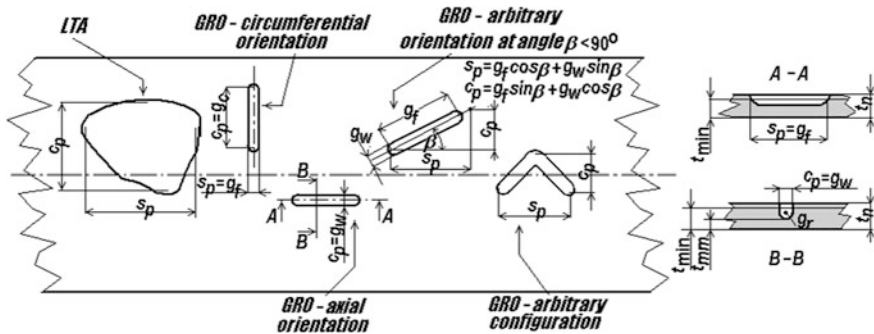


Fig. 2 Typical configurations of flaws of the type local thin area (LTA) and of groove-like flaws (GRO): t_n is the nominal pipe wall thickness, t_{min} is the minimum remaining pipe thickness

the definition with sufficient accuracy of their configuration and dimensions requires adequate nondestructive control methods.

The content and complexity of the activities preliminary to any of the repair procedures intended for transmission pipelines with any type of defect can considerably influence the decision regarding the procedure selection and the repair works program for a given pipeline.

The main activities preceding the execution of repairs (in which the nondestructive control methods detailed in Chapter “[Long-Range Ultrasonic and Phased Array Technologies](#)” of this book are also involved) are the following:

- (i) Detection and localization of the flaws existing in the steel pipe of the transmission line. To that purpose, it is possible to use either methods based on predictive models (describing the phenomena of degradation of the steel pipes in time and of the flaws generation on them) or methods based on the periodic pipelines inspection;
- (ii) Evaluation of the severity of the detected flaws, followed by their qualification as imperfections or defects, and definition of the pipeline areas that must be reinforced by performing maintenance works;
- (iii) Examination, by using nondestructive methods, of the areas, where defects (unacceptable anomalies) have been detected. Bell holes are dug in the areas with defects of the pipeline that require intervention with maintenance works; the corrosion protection coating is removed from the steel pipe; the external surface of the pipe is cleaned and blasted; and each area is examined by means of an adequate method, in view of precisely assessing the configuration, position, and size of the defects.

Once detected, the areas with VSDs placed at the exterior of the steel pipe are machined by grinding in order to round the micro-geometry of the flaws and consequently to diminish as much as possible the mechanical stress concentration effects in these areas. The areas with defects machined in such manner are again subjected to nondestructive examination in view of building their three-dimensional maps (an example is shown in Fig. 3) and defining the river bottom route and the critical profile of the thickness in axial direction (as indicated in Fig. 4 for a given damaged area of a pipeline) and, sometimes, in circumferential direction (using the methodology described in Sect. 2 below).

In the followings, the methods included in the requirements of specific widely used international standards and recommended to be used for VSDs assessment, i.e., for the evaluation of the detected flaws in order to define the required maintenance works, are addressed. Then, a case study is also presented to illustrate the defect evaluation methods.

In the following chapters, the assessment methods frequently used for damaged pipelines with VSDs are detailed and applied for some typical transmission pipelines. Chapter “[Assessment of the Remaining Strength Factor and Residual Life of Damaged Pipelines](#)” refers to the methods based on the evaluation of the

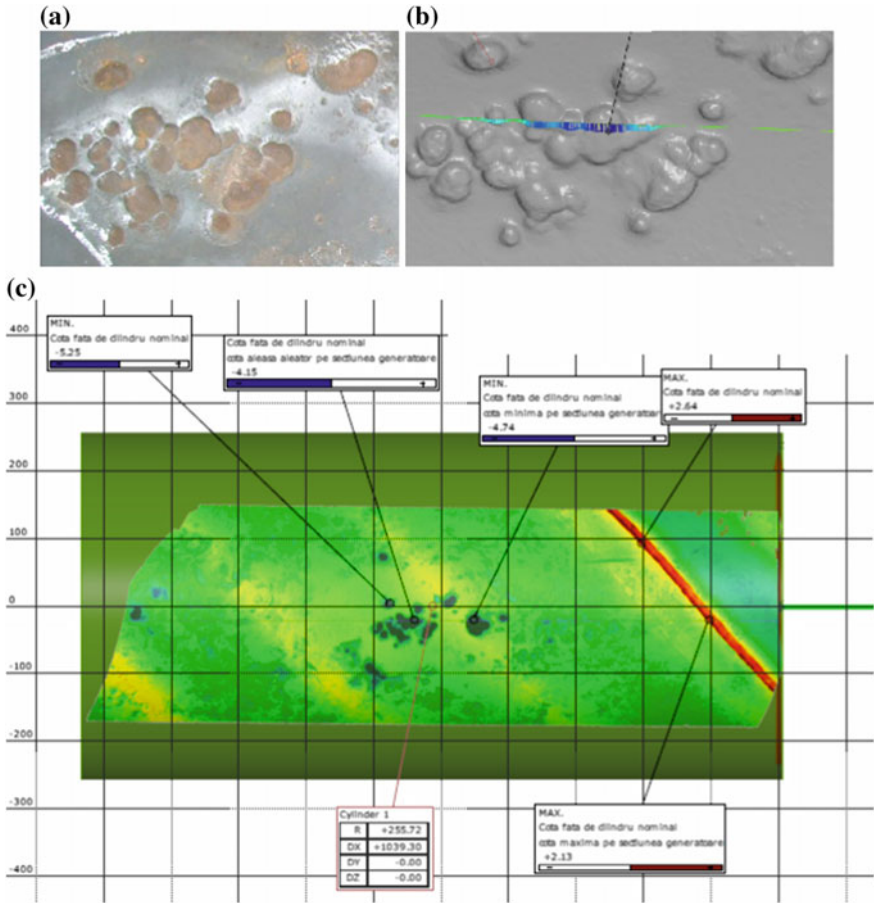


Fig. 3 Example of a three-dimensional map of the area with external VSDs of a pipeline: **a** photograph of the pipeline area with external VSDs; **b** scanned image of the damaged area; **c** three-dimensional map of the area with indications about the detected VSDs

remaining mechanical strength factor of the pipelines with VSDs, while Chapters “Assessment of Interacting Volumetric Surface Defects” and “Assessment of the Reinforcement Capacity of Composite Repair Systems for Pipelines with Interacting Defects” address the numerical assessment methods using finite elements for the case of pipelines with multiple, interacting VSDs.

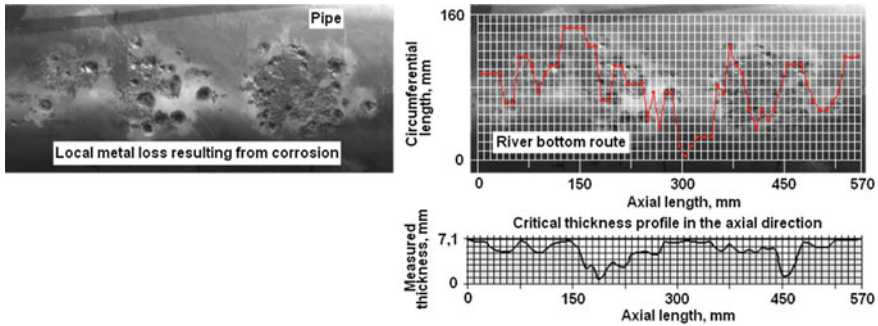


Fig. 4 Definition of the river bottom route and critical thickness profile for a pipeline area with VSDs (real case example)

2 Methods for the Assessment of Volumetric Surface Defects

The assessment of volumetric surface defects/ flaws consist, as already mentioned, of the evaluation of the severity of the flaws detected on a given transmission pipeline, their qualification as defects or imperfection and the definition of the damaged pipeline areas, the ones requiring reinforcement by means of maintenance works. In order to perform such assessment, the following data, grouped in categories, are required to be known [2]:

- (i) geometrical/dimensional characteristics of the investigated pipeline area/element: nominal outside diameter, D_e ; nominal/design thickness of the pipe wall, t_n , and the effective thickness, t , of the pipe wall, measured outside the VSD area at the time of assessment; pipe inside diameter, which can be calculated as $D_i = D_e - 2t_n$;
- (ii) operational conditions of the pipeline: design pressure p , maximum allowable working (operating) pressure $MAWP = p_0 \leq p$ and operating temperatures;
- (iii) values of the factors used for the pipeline design: design factor, F ($F < 1$); temperature derating factor, T ; longitudinal joint factor (for welded joints), J ;
- (iv) mechanical properties of the steel from which the pipes of the transmission line are manufactured: Young modulus, E ; minimum specified yield strength (normally expressed by the 0.5% total extension), $R_{t0.5}$; allowable stress considered for the pipeline design, $\sigma_a = FR_{t0.5}$ ($p = 2FR_{t0.5}t/D_e$); ultimate tensile strength, R_m ; percentage elongation at break (in 2 in./50.8 mm), A_{2in} ; Charpy V-notch impact energy, KV , etc.
- (v) geometrical characteristics of each individual defect and/or of each group of VSDs that interact, including VSD dimensions (length s_p , width c_p , and maximum depth d_{max}) and also other data, obtained as detailed below;
- (vi) estimated corrosion rate during the future operation of the pipeline.

The first stage of a VSD assessment consists of the geometrical characterisation of a given volumetric surface flaw, taking shape in a data sheet recording the flaw dimensions. In order to obtain this data sheet, we recommended the following steps:

Step 1. Specification of the characteristic dimensions of the pipeline with flaws, D_e and t_n , and definition of the dimensions s_p and c_p (shown in Fig. 2) describing the extent of the flaw on the surface (external or internal) of the pipe defective area. In case of multiple flaws that might interact, an additional **Step 2** is required (to assess if two or more adjacent defects can interact, according to one of the methods described in Chapter “Assessment of Interacting Volumetric Surface Defects”).

Step 3. Preparation of a plan for the measurement of the pipe wall thickness profile in the area of each individual flaw of the local metal loss type (shown in Fig. 5). This plan specifies the number, positions, and length of some inspection planes in the flaw area, defining the positions of the nodes, where the thickness measurements are taken. These planes are oriented both axially (the ones numbered $A_k, k = 1 \dots n_{pa}$) and circumferentially (those numbered $C_j, j = 1 \dots n_{pc}$) and they must be long enough to obtain a full characterization of the flaw. The number of the inspection planes is selected so that the following condition is fulfilled: $N = n_{pc} \times n_{pa} \geq 15$, while the distance between them is chosen in order to allow for a complete definition of the wall thickness profile in the flaw area.

Step 4. Measurement of the wall thickness $t_i, i = 1 \dots N$, in all N nodes of the inspection planes grid. The values resulting after measuring can be reported in a table (included in the flaw data sheet, as presented in Sect. 3 for a case study) and can also be used to draw the flaw configuration (as shown in Fig. 5). The obtained t_i values are also processed to define the minimum measured wall thickness, $t_{min} =$

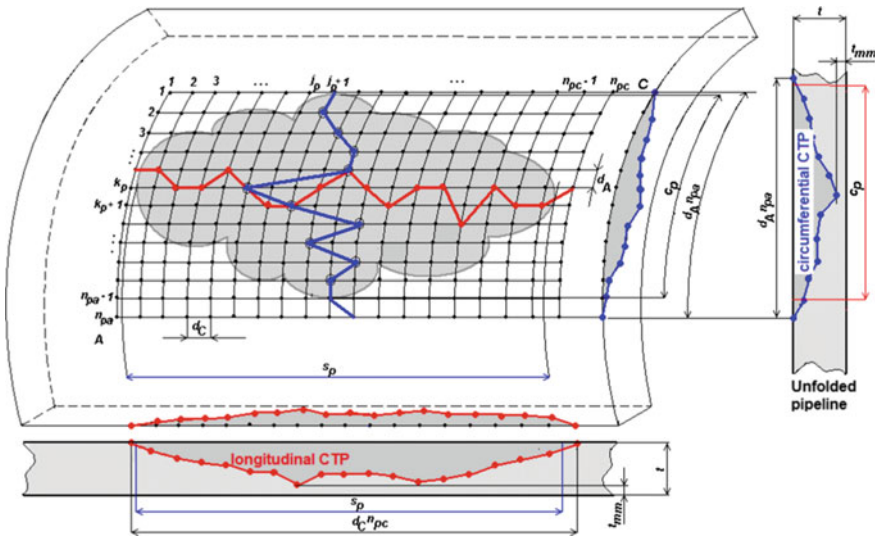


Fig. 5 Measurement plan and construction of the critical thickness profiles, CTPs, in a pipeline area with a VSD

$\min [t_i, i = 1 \dots N]$, and the effective (real, measured) thickness t of the pipe wall outside the flaw area. The maximum depth of the flaw can also be calculated as $d_{\max} = t - t_{\min}$.

Step 5. Statistical processing of the results of the wall thickness measurements in the flaw area $t_i, i = 1 \dots N$, to determine their mean value, t_{am} , their standard deviation, t_{sd} , and the coefficient of variation, COV, using the following equations:

$$t_{\text{am}} = \frac{\sum_{i=1}^N t_i}{N}; \quad t_{\text{sd}} = \sqrt{\frac{\sum_{i=1}^N (t_i - t_{\text{am}})^2}{N - 1}}; \quad \text{COV} = \frac{t_{\text{sd}}}{t_{\text{am}}}. \quad (1)$$

If $\text{COV} \leq 0.1$, the flaw is considered as a local thin area with a constant wall thickness having the value t_{am} (or, if a conservative assessment is needed, the value $t_{\min} \approx t_{\text{am}}$ is used). If $\text{COV} > 0.1$, the following step is required and the assessment will consider the real configuration of the thickness profile.

Step 6. Determination of the critical thickness profiles (CTPs) in the longitudinal direction (by projecting the minimum values of t_i , established in each circumferential plane C_j , on one of the A_k planes) and also in the circumferential direction (by projecting the minimum values of t_i , established in each longitudinal plane A_k , on one of the C_j planes), as it can be seen in Fig. 5.

A model for a VSD data sheet, obtained for a given pipeline, by using dedicated software developed by the authors in EXCEL, will be described in Sect. 3.

In order to assess, for each of the pipeline areas, where flaws have been detected, if the respective area is a damaged one (i.e., flaws are qualified as defects) and to take the decision if the area needs reinforcement (repair works), an evaluation procedure should be applied for each individual flaw or group of interacting flaws (for which an equivalent flaw is defined applying the methodology presented in Chapter “[Assessment of Interacting Volumetric Surface Defects](#)”). There are several such procedures, recommended by the existing international Norms (standards, codes, recommended practices, specifications, etc.) among which the most used are the followings: API 579 [2], ASME B31.G [3], DNV RP-F 101 [4], and BS7910 [5].

The VSDs evaluation procedures usually assess the residual mechanical strength of the pipeline with defects that can be expressed in terms of the Remaining Strength Factor (RSF), calculated as the ratio between the value of a characteristic defining the mechanical strength (or the maximum allowable mechanical load, that is the pipe internal pressure) of the pipeline with VSDs and the value of the same characteristic for the pipeline without VSDs (for more details about RSF, see Chapter “[Assessment of the Remaining Strength Factor and Residual Life of Damaged Pipelines](#)”). The obtained value of the RSF is then compared with a (minimum) allowable value, noted RSF_a . Usually, for transmission pipelines, the recommended RSF_a values are in the range 0.8–0.9 [2] and it can be defined in relation to the minimum acceptable level of the pipeline strength assessed during its design process.

If $RSF < RSF_a$, the evaluation procedure defines, based on the RSF value, the reinforcement level that must be guaranteed by performing the maintenance works in order to reestablish the pipeline initial loading capacity. As an alternative in this case, the operational pressure of the pipeline can be reduced so that no such works are needed. If $RSF \geq RSF_a$, maintenance works are not necessary, but it is recommended to assess the remaining operating life of the pipeline in order to schedule the future inspections and maintenance activities needed. The remaining life of a pipe area with VSD can be estimated based upon the minimum required wall thickness for the intended service conditions, the actual thickness and the area size measurements from an inspection, and an estimate of the anticipated corrosion/erosion rate and rate of change of the size of the VSD [2].

The latest version of American Standard ASME B31.G [3] provides four analysis procedures (ranging from Level 0 to Level 3), selected by the user depending on the quantity and quality of data available for the defect evaluation, and on the desired degree of refinement of the analysis. The Level 0 evaluation relies on the allowable values of the defect length and depth (values provided in [3] as a set of tables) and is intended to be conducted in the field without the need for detailed calculations. The rules and criteria used to determine the allowable values (as detailed in previous editions of ASME B31.G and valid for a minimum factor of safety of 1.39 and for pipelines operating with a hoop stress of 72% of the specified yield strength) and the two steps of a Level 0 assessment are as follows:

- (i) the maximum allowable depth of a VSD is equal to 80% of the effective pipe wall thickness, t . Therefore, a flaw having the maximum depth $d_{max} > 0.8t$ shall be qualified as defect and maintenance work must be defined, but a flaw for which $d_{max} < 0.1t$ is qualified as an imperfection and no maintenance activities are needed. In both cases, the evaluation ends, while, if $0.1t \geq d_{max} \geq 0.8t$, the evaluation continues with step (ii) below;
- (ii) the maximum allowable length of a VSD, s_{pa} , can be calculated with the formula:

$$s_{pa} = 1.12B_d\sqrt{D_e t}, \tag{2}$$

where

$$B_d = \min \left[\sqrt{\left(\frac{d_{pr}}{1.1d_{pr} - 0.15} \right)^2 - 1}; 4 \right] \text{ and } d_{pr} = \frac{d_{max}}{t}.$$

Therefore, a flaw having the length $s_p > s_{pa}$ is qualified as a defect and an evaluation of a superior level could be performed, while if $s_p \leq s_{pa}$, the flaw is an imperfection.

The Level 1 evaluation is a simple calculation that relies on single measurement of the maximum depth, d_{max} , and length, s_p , of a VSD. It can be conducted in the field by an individual with appropriate training and it is based on the criterion (3)

below, which, if fulfilled, the flaw is considered acceptable (and qualified as imperfection):

$$\sigma_F \geq k_s \sigma_H, \quad (3)$$

where σ_H is the hoop stress at the operating pressure, calculated as $\sigma_H = p_0 D_e / 2t$, k_s is a safety factor (according to [3] its minimum recommended/acceptable value should be equal to the ratio of the minimum hydrostatic test pressure required for the given pipeline and MAWP, but usually not less than 1.25) and σ_F is the estimated failure stress value (characterizing the remaining strength of the pipeline in the flaw area) that can be calculated using one of the following three methods:

(i) The original B31G method, based on the following equations:

$$\sigma_F = \begin{cases} \sigma_Y \frac{1 - \frac{2d_{\max}}{3t}}{1 - \frac{2d_{\max}}{3t} \frac{1}{M}} & \text{for } \frac{s_p^2}{D_e t} \geq 20 \\ \sigma_Y \left(1 - \frac{d_{\max}}{t}\right) & \text{for } \frac{s_p^2}{D_e t} < 20 \end{cases}, \quad (4)$$

in which σ_Y is the flow stress, defined in this case as $\sigma_Y = 1.1 R_{t0.5}$, and M is the bulging stress magnification factor, also named Folias factor, calculated according to this method as follows:

$$M = \sqrt{1 + 0.8 \frac{s_p^2}{D_e t}}. \quad (5)$$

(ii) The modified B31G method, using the following relationships:

$$M = \begin{cases} \left(1 + 0.6275 \frac{s_p^2}{D_e t} - 0.003375 \frac{s_p^4}{D_e^2 t^2}\right)^{1/2} & \text{for } \frac{s_p^2}{D_e t} \leq 50 \\ 0.032 \frac{s_p^2}{D_e t} + 3.3 & \text{for } \frac{s_p^2}{D_e t} > 50 \end{cases} \quad (6)$$

$$\sigma_F = \sigma_Y \frac{1 - 0.85 \frac{d_{\max}}{t}}{1 - 0.85 \frac{d_{\max}}{t} \frac{1}{M}}. \quad (7)$$

(iii) The API 579 Level 1 assessment [2] will be discussed later below.

Alternative to Eq. (3), the following criterion can also be used:

$$p_F \geq k_s p_0, \quad (8)$$

in which p_F is the estimated failure pressure, equal to $p_F = \sigma_F 2t / D_e$.

If the flaw is unacceptable (qualified as defect), the operating pressure in the pipeline can be reduced such that it is less than p_F / k_s .

The Level 2 assessment incorporates a greater level of detail than a Level 1 evaluation in order to produce a more accurate estimate of the failure pressure. It relies on detailed measurements of the corroded surface profile (using the CTPs) and involves repetitive computations, facilitated by the use of computer software or spreadsheets. The evaluation is performed using the Effective Area Method, also known as RSTRENG method, and it is based on the same criterion (3) or (8), but the failure stress is calculated by the equation:

$$\sigma_F = \sigma_Y \frac{1 - \frac{A}{A_0}}{1 - \frac{A}{A_0 M}}, \quad (9)$$

where A is the local VSD area in the longitudinal plane and A_0 is the local original metal (steel) area, calculated with the simple formula: $A_0 = s_p t$.

Finally, the Level 3 evaluation is a detailed analysis, such as a finite element analysis, of a specific flaw or group of interacting flaws, in accordance with a user-defined methodology, conducted by a specialist with appropriate expertise in the subject of Fitness-For-Service (FFS) assessment. As stated in [3], this analysis should accurately consider or account for all factors, which could affect the accuracy of the results, including loadings, boundary conditions, constraints, etc., and it should develop a failure criterion.

The DNV RP-F 101 recommended practice [4] has been developed based on the results of a joint industry project that generated a database of more than 80 burst tests on pipes containing machined VSDs (including complex-shaped and interacting defects). It provides both a calibrated partial safety factors approach and an allowable stress approach and is similar to the Level 2 assessment from [3], the acceptability of a flaw being defined by a criterion similar to (8). The estimated failure pressure is assessed based on a failure stress obtained using an equation similar to (7), in which the coefficient 0.85 is replaced by 1 (for the allowable stress approach) or by a partial safety factor (depending on the accuracy level of inspection determining the flaw depth), while the Folias factor, M , is calculated as follows:

$$M = \sqrt{1 + 0.31 \left(\frac{s_p}{\sqrt{D_e t}} \right)^2}. \quad (10)$$

Appendix G of the British Standard BS7910 [5] indicates a similar procedure to the Level 1 evaluation from [3] aiming at assessing if the failure pressure p_F is acceptable. Such pressure is calculated using Eqs. (7), in which the coefficient 0.85 is replaced by 1, for σ_F , Eq. (10) for the M factor, and considering the flow stress equal to the minimum specified tensile strength. Appendix G from [5] also provides, for a more refined analysis, recommendations for conducting nonlinear finite element analysis of corrosion flaws.

API Standard 579 [2] is dedicated to the Fitness-For-Service evaluation to be applied to the areas with different types of defects (including VSDs that are the subject of Part 5 of the standard) of a transmission pipeline. To that purpose,

three analysis procedures are defined (being equivalent to the Level 1, 2, and 3 methods from [3]) and a Level 1 evaluation procedure can be used alternatively with a Level 2 or 3 procedure.

Level 1 assessment considers the pipe internal pressure as the only load and the VSD to be evaluated is characterized by a single thickness and by one or two surface area dimensions (length and width). If there are significant thickness variations over the length of the flaw, this procedure may lead to conservative results and Level 2 assessment is recommended. Level 1 procedure comprises nine steps (the last one, which will not be discussed in this work, considering also the circumferential extent of the VSD), detailed in Part 5 from [2], and defines several criteria that shall be checked successively. In the first place, the following limiting flaw size criteria have to be fulfilled if the flaw is to be qualified as imperfection and considered acceptable (not requiring maintenance work):

$$R_t = \frac{t_{mm} - FCA}{t_c} \geq 0.20; \quad t_{mm} - FCA \geq 2.5 \text{ mm}; \quad L_{msd} \geq 1.8\sqrt{D_e t_c}, \quad (11)$$

where R_t is the remaining thickness ratio, t_c is the corroded pipe wall thickness outside the flaw area, usually calculated as $t_c = t - FCA$, FCA is the future corrosion allowance applied to the VSD area, and L_{msd} is the distance to the nearest major structural discontinuity.

Then, a screening criterion is applied, taking into account the values of the parameters R_t and λ (the longitudinal flaw parameter, defined as $\lambda = 1.285s_p/\sqrt{D_e t_c}$). It is considered that the longitudinal extent of the flaw is acceptable if the point defined by the intersection of the values of R_t and λ is, on a graph with the coordinates R_t and λ , above or on the curve defined by the equations below (with $RSF_a = 0.9$):

$$\begin{aligned} R_t &= 0.2 && \text{if } \lambda \leq 0.354 \\ R_t &= \left(RSF_a - \frac{RSF_a}{M_t} \right) \left(1.0 - \frac{RSF_a}{M_t} \right) && \text{if } 0.354 < \lambda < 20 \\ R_t &= 0.9 && \text{if } \lambda \geq 20 \end{aligned} \quad (12)$$

where M_t is the Folias factor based on the VSD longitudinal extent, defined as a function of λ by means of a complex polynomial function, detailed in Eq. (5) from Chapter “Assessment of the Remaining Strength Factor and Residual Life of Damaged Pipelines”.

If the above screening criteria are not fulfilled, then the remaining strength factor, RSF, shall be calculated as follows (with the M_t factor defined as mentioned above):

$$RSF = \frac{R_t}{1 - \frac{1-R_t}{M_t}}. \quad (13)$$

Finally, if $RSF \geq RSF_a$, the local metal loss flaw is acceptable for operation at the MAWP, which is defined in [2], Annex A, for the case in which the pipe is

subjected only to internal pressure load (there are no axial loads), by the following equation:

$$\text{MAWP} = \frac{\sigma_a z_L t_c}{R_c + 0.6 t_c}, \quad (14)$$

where z_L is the weld joint efficiency or quality factor from the original construction code (usually equal to 0.7) and $R_c = D_i/2 + \text{FCA}$.

If $\text{RSF} < \text{RSF}_a$, the flaw is not acceptable and it requires either the execution of repair works or the reduction of MAWP at the allowable value for the damaged pipeline, MAWP_r , defined as follows (see also Chapter “[Assessment of the Remaining Strength Factor and Residual Life of Damaged Pipelines](#)”): $\text{MAWP}_r = \text{MAWP} (\text{RSF}/\text{RSF}_a)$.

Level 2 assessment provides a better evaluation than Level 1, if the analyzed VSD has significant variations in the thickness profile, because it accounts for the local reinforcement effects of the varying wall thickness in the flaw area (using the CTPs). Level 2 procedure can be used to evaluate closely spaced regions of (interacting) VSDs and it can also evaluate damaged pipe areas with supplemental loads (external pressure, axial force, bending moment, torsion and shear, in addition to the internal pressure).

When used to assess pipeline with a complex VSD subjected to internal pressure only, Level 2 procedure is similar to Level 1, comprising ten steps from which the last one is used to assess its circumferential extent. First, the same limiting flaw size criteria have been checked, using conditions (11). Then, the longitudinal CTP shall be subdivided in a series of subsections, each one with a constant thickness t_i (starting from $t_1 = t_{\text{mm}}$; $t_i > t_{\text{mm}}$ for $i > 1$) and with the length s_i , approximating the actual VSD. The number and extent of such subsections should be selected based on the desired accuracy. For each subsection, the remaining strength factor, RSF_i , shall be calculated as follows:

$$\text{RSF}_i = \frac{1 - \frac{A^i}{A_0^i}}{1 - \frac{1}{M_i^i} \frac{A^i}{A_0^i}}, \quad (15)$$

in which $A_0^i = s_i t_c$ is the original metal area for subsection i , A^i is the real area of subsection i in the longitudinal plane and M_i^i is determined using the same table as for M_i factor in Level 1, but only for subsection i . The RSF, used in the assessment (for the entire flaw), will be the minimum value determined among all RSF_i values. Finally, RSF will be compared with RSF_a to evaluate the flaw exactly in the same manner as per Level 1 procedure. Details about RSF evaluation according to Level 2 procedure can be found in Chapter “[Assessment of the Remaining Strength Factor and Residual Life of Damaged Pipelines](#)”.

Level 3 procedure uses geometrical models of the defects close to the ones described by the obtained three-dimensional maps and accurate analysis techniques to determine the state of mechanical stress and strain that is generated in the areas

with VSDs, during pipeline operation. The finite element method is typically used for that purpose (guidelines being provided in [2], Appendix B), but other numerical methods such as the boundary element or finite difference method may also be used. The evaluation may be based on a linear stress analysis with acceptability determined using stress categorization, or a nonlinear stress analysis (recommended) with acceptability determined using a plastic collapse load.

Typically, a Level 1 evaluation procedure (as defined by [2] or [3]) is applied for the assessment of VSDs by means of using Flaw Acceptance Charts (FACs). Figure 6 shows an example of such chart [6]. Applying an evaluation procedure based on a FAC is simple: to each detected flaw, a characteristic point, with the coordinates $d_{pr} = d_{max}/t$ and $L_{pr} = s_p/(tD_e)^{0.5}$, is associated on the evaluation diagram, and the position of such point on the diagram determines the flaw qualification as *acceptable* (the pipeline operation can be continued without performing maintenance works) or *unacceptable*, i.e., as a defect (the pipeline must be reinforced in the area, where the defect locates).

Finally, it has also been stated that assessments regarding the VSDs growth rates (in depth, in length, and in width) can also be made for a transmission pipeline. To that purpose, information obtained at several successive inspections of the pipeline has to be available (an example is shown in Fig. 7). Such assessments are

Fig. 6 Example of flaw (VSD) evaluation using a flaw acceptance chart

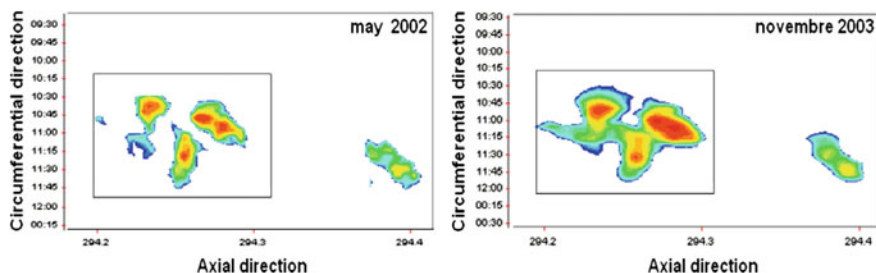
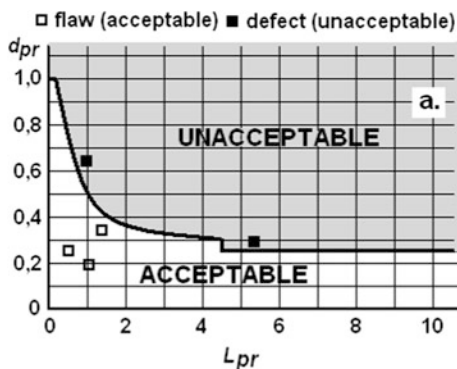


Fig. 7 VSDs evolution in time observed by means of successive inspections of a given pipeline

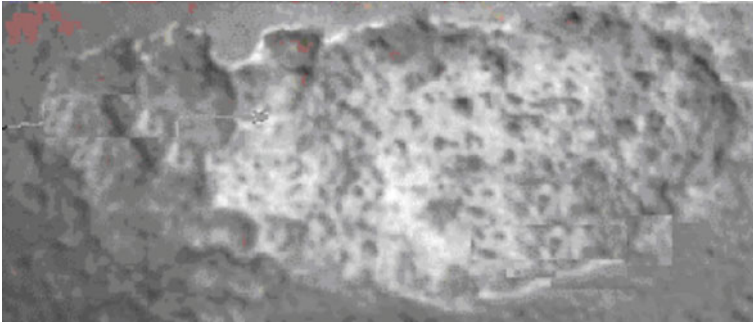


Fig. 8 Photo of the VSD detected in the damaged pipeline area investigated as case study

extremely useful to assess the remaining operating life of the pipeline, to define the time span between inspections and to schedule the maintenance works needed.

3 Case Study

In this section, a case study regarding the assessment of a complex geometry VSD, detected on a gas transmission pipeline, is present to illustrate the use of the procedures described in Sect. 2. The pipes were manufactured from L360/X52 steel (having the yield strength $R_{10.5} = 360$ MPa) and its operating pressure is equal to 7.5 MPa. The analyzed VSD is the one shown in the photo in Fig. 8, while the recording data sheet for this flaw, which summarizes the results of the geometrical characterisation performed according to Steps 1 to 6 from Sect. 2, is present in Table 1, where the CTP in the longitudinal direction is marked with red and the CTP in the circumferential direction is marked with blue.

The results of thickness measurement in the considered flaw area are plotted in Fig. 9, while the CTPs in both longitudinal and circumferential direction are shown in Fig. 10.

Let us apply the Level 0 assessment procedure from [3] for the flaw, characterized in Table 1 and Figs. 9, 10, which has the depth $d_{\max} = 7.5$ mm = $0.68 t$, and the length $s_p = 265$ mm. As a result, we obtained the maximum depth within the range of $0.1t \geq d_{\max} \geq 0.8t$, and the VSD length has been evaluated by comparing it with the allowable length given in Tables 3–5 M from [3], $s_{pa} = 39.9$ mm. As $s_p > s_{pa}$, the flaw has been qualified (according to Level 0) as a defect and an evaluation of a superior level should be performed.

The considered flaw has been also assessed according to the Level 1 procedure from ASME B31G, using a dedicated software developed by the authors and assuming a design factor $F = 0.72$, and the results obtained are summarized in Table 2. It can be seen that, for the moment, the flaw can be qualified as an imperfection and no maintenance works are required, but it should be monitored as, due to its possible growth, in time, it could become a defect.

Table 1 Recording data sheet for a flaw/defect of the type local metal loss (filled in for the damaged pipeline area considered as case study)

Data sheet number: _____ Date: _____
 Company: _____ Operational district: _____

Pipeline upon which the flaw has been detected	
Designation and position of the pipe line component	Pipe, KP 27
Nominal outside diameter of the pipe element, D_e , mm	508.0
Nominal wall thickness of the pipe element, t_n , mm	11.0
Inside diameter of the pipe element, $D = D_e - 2t_n$, mm	486.0
Flaw length (extent in the longitudinal direction), s_p , mm	265
Flaw width(extent in the circumferential direction), c_p , mm	118
Characteristics of the measurement plan	
Number of inspection planes oriented circumferentially, n_{pc}	19
Distance between the inspection planes oriented circumferentially, d_A , mm	15
Number of inspection planes oriented axially, n_{pa}	13
Distance between the inspection planes oriented axially, d_C , mm	10
Instrument used to measure the flaw depth	

Table with the wall thicknesses measured in the nodes of the inspection planes grid, t_i , mm

	C_1	C_2	C_3	C_4	C_5	C_6	C_7	C_8	C_9	C_{10}	C_{11}	C_{12}	C_{13}	C_{14}	C_{15}	C_{16}	C_{17}	C_{18}	C_{19}	CTP_c	
A_{11}	11.0	11.0	11.0	11.0	11.0	11.0	11.0	11.0	11.0	11.0	11.0	11.0	11.0	11.0	11.0	11.0	11.0	11.0	11.0	11.0	11.0
A_2	11.0	11.0	11.0	11.0	10.0	10.6	9.5	10.7	9.5	10.0	10.5	11.0	11.0	10.6	10.7	11.0	10.8	11.0	11.0	9.5	
A_3	11.0	11.0	10.5	9.5	9.0	9.3	8.5	8.0	7.5	8.0	8.2	8.5	9.0	10.0	10.6	11.0	11.0	11.0	11.0	7.5	
A_4	11.0	10.8	10.0	9.5	9.0	8.7	7.3	7.5	7.2	7.5	8.0	8.0	8.5	8.6	9.5	9.5	11.0	11.0	11.0	7.2	
A_5	11.0	9.4	9.5	9.0	6.8	6.3	6.5	7.0	6.4	6.0	7.6	7.0	8.0	8.0	9.0	9.0	10.0	11.0	11.0	6.0	
A_6	11.0	10.0	7.8	7.2	8.0	4.0	6.0	5.5	5.4	6.2	6.0	6.5	5.7	5.5	6.5	7.6	8.0	10.0	11.0	4.0	
A_7	11.0	10.0	9.5	9.0	8.7	6.1	5.0	3.5	6.1	6.5	7.0	6.2	6.5	5.7	4.8	7.5	7.8	9.6	11.0	3.5	
A_8	11.0	10.5	9.5	9.2	9.0	7.4	6.4	6.2	6.3	7.1	6.4	7.0	7.0	7.0	6.0	8.0	9.5	9.7	11.0	6.0	
A_9	11.0	11.0	11.0	10.0	9.5	8.5	6.8	7.2	6.4	7.3	8.0	8.5	7.4	9.0	7.5	9.0	10.2	9.8	11.0	6.4	
A_{10}	11.0	11.0	11.0	10.3	11.0	10.0	8.2	9.3	8.4	8.0	7.5	8.0	8.5	9.5	9.0	9.6	11.0	10.5	11.0	7.5	
A_{11}	11.0	11.0	11.0	10.7	10.6	11.0	9.4	10.1	9.2	9.0	9.5	9.5	9.3	10.3	10.6	10.4	10.8	10.7	11.0	9.0	
A_{12}	11.0	11.0	11.0	11.0	11.0	10.6	10.4	10.3	10.4	10.5	10.6	10.5	10.6	11.0	10.5	11.0	10.9	11.0	11.0	10.3	
A_{13}	11.0	11.0	11.0	11.0	11.0	11.0	11.0	11.0	11.0	11.0	11.0	11.0	11.0	11.0	11.0	11.0	11.0	11.0	11.0	11.0	
CTP_a	11.0	9.4	7.8	7.2	6.8	4.0	5.0	3.5	5.4	6.0	6.0	6.2	5.7	5.5	4.8	7.5	7.8	9.6	11.0		

Results of the statistical analysis of the thickness values measured in the flaw area

Calculated characteristic	Formula	Result
t – effective/measured wall thickness of the pipe element, mm	-	11.0
t_{mm} – minimum measured wall thickness of the pipe element, mm	-	3.5
t_{am} – mean value of the measured wall thickness values, mm	$t_{am} = \frac{\sum_{i=1}^N t_i}{N}$	8.87
t_{sd} – standard deviation of the values t_i , mm	$t_{sd} = \sqrt{\frac{\sum_{i=1}^N (t_i - t_{am})^2}{N - 1}}$	1.794
COV – coefficient of variation of the values t_i	$COV = \frac{t_{sd}}{t_{am}}$	0.228

Prepared by

Name, surname and position	
Signature	

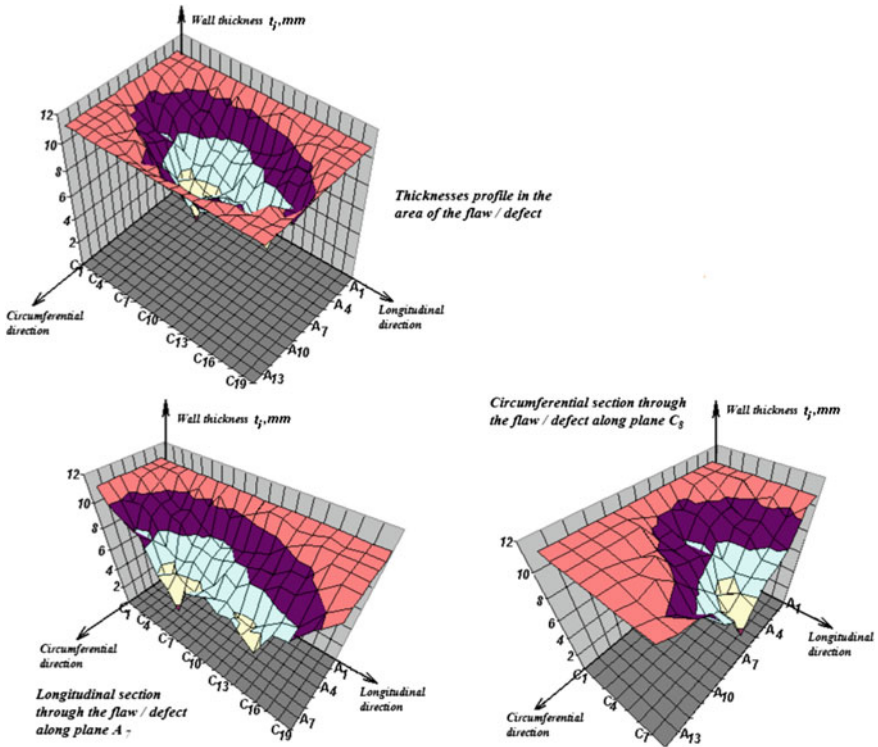


Fig. 9 Graphical presentation of the wall thickness measurement results, in the area of the investigated flaw/defect

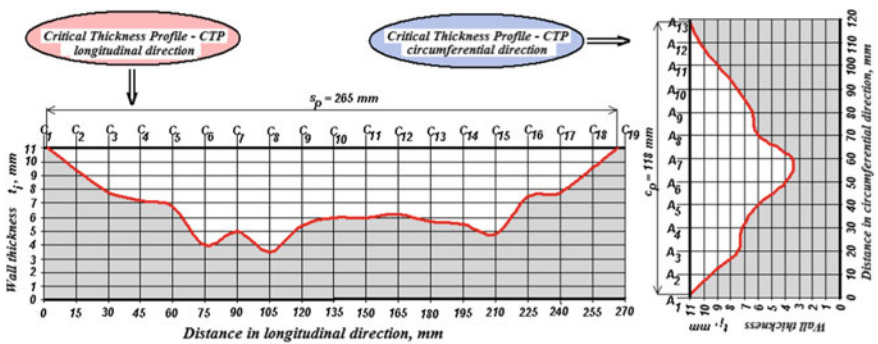


Fig. 10 Critical thickness profiles in longitudinal and circumferential directions, in the area of the investigated flaw/defect

Table 2 Summary of the VSD assessment according to ASME B31G, Level 1

Flaw qualification	Imperfection
Maximum allowable length of the flaw for its given depth ($d_{\max} = 7.5$ mm)	334.8 mm
Maximum allowable depth of the flaw for its given length ($s_p = 265$ mm)	7.9 mm
Maximum allowable working pressure, MAWP	11.23 MPa
Safe working pressure (of the pipeline with flaws)	7.78 MPa

Chapter “[Assessment of the Remaining Strength Factor and Residual Life of Damaged Pipelines](#)” includes, in Sect. 2, another case study for a complex geometry VSD, evaluated by means of the assessment of the remaining strength factor, according to the procedures from API 579 [2], Level 1 and 2 (considering only the internal pressure loading).

4 Conclusions

This chapter aimed at characterizing the local metal loss defects, also named Volumetric Surface Defects (VSDs). The main issue consisted of the discussion of the methods and criteria used for a local metal loss flaw assessment, in order to qualify it as either imperfection or defect and to define, if the case, the required pipeline maintenance works. The most used flaw evaluation methods defined by the international Norms presently in force (standards, codes, recommended practices, specifications) have been briefly described and then applied to a real case study, a complex VSD detected on a gas transmission pipeline.

Comparing the VSD assessment procedures and criteria, taking also into account the results obtained for the case study, the following conclusions can be drawn:

- presently there is no set of criteria and no procedure that are unanimously accepted to assess if a given local metal loss flaw can be qualified as an imperfection or as a defect;
- the used evaluation procedure are classified in some Norms [2, 3] in different levels (ranging from 0 or 1 to 3) with an increasing level of accuracy. The higher level procedures are recommended for VSDs with complex geometry, if supplemental loads should be considered (in addition to the main loading of a transmission pipeline—the internal pressure) or when a lower level procedure finally qualifies a flaw as a defect.

The most relevant VSD assessment methods will be further investigated in the following two Chapters (“[Assessment of the Remaining Strength Factor and Residual Life of Damaged Pipelines](#)” and “[Assessment of Interacting Volumetric Surface Defects](#)”).

References

1. G. Zecheru, E.I. Lata, G. Draghici, A. Dinita, in *Proceedings of the 2nd South East European IIW International Congress*, Sofia, p. 204 (2010)
2. API 579/ASME FFS-1, *Fitness-For-Service* (2007)
3. ASME B31.G, *Manual for Determining the Remaining Strength of Corroded Pipelines* (2009)
4. DNV RP-F 101, *Corroded Pipelines, Recommended Practice* (2015)
5. BS 7910, *Guide to Methods for Assessing the Acceptability of Flaws in Metallic Structures* (2005)
6. G. Zecheru, E.I. Lata, G. Draghici, *Mecanica ruperii – Buletinul ARMR*, **17**, 11 (2005)

Assessment of the Remaining Strength Factor and Residual Life of Damaged Pipelines

Gh. Zecheru, Andrei Dumitrescu, P. Yukhymets, A. Gopkalo
and M. Mihovski

Abstract The transmission pipelines intended for the transportation of hydrocarbons (petroleum, liquid petroleum products, natural gas, liquefied petroleum or natural gas) or other fluids are subjected, during their operation, to corrosion processes that may generate on the steel pipe surface local metal loss flaws/defects (also named volumetric surface defects, VSDs). The evaluation of these defects represents an important issue regarding the pipelines exploitation and maintenance. Typically, such assessment aims at the evaluation of the remaining mechanical strength (that can be expressed most conveniently by the remaining strength factor, RSF) of the damaged steel pipes. Sometimes, for pipelines susceptible to low cycle fatigue failure in the stress concentration areas such as VSDs, their residual life should also be assessed. Both these issues are covered by the present chapter. First, the pertinent modalities for the definition and determination of RSF for the transmission pipelines on whose steel pipes volumetric surface defects/flaws have been detected are presented and discussed. In the case of hydrocarbon transmission pipelines containing flaws of the local metal loss type, we consider that it is important to assess their remaining strength not only in relation with the attainment of the serviceability limit state (as defined in international Norms presently used for such assessment), but also in relation with the achievement of an ultimate limit state (pipe failure/bursting). Therefore, the modalities proposed by the authors for the evaluation of a RSF related to the attainment of an ultimate limit state of the pipeline (bursting) are also briefly presented. Second, the results of some cyclic

Gh. Zecheru · A. Dumitrescu (✉)
Petroleum-Gas University of Ploiesti, Ploiești, Romania
e-mail: andrei.upg@gmail.com

P. Yukhymets
E.O. Paton Electric Welding Institute,
Ukrainian National Academy of Sciences, Kiev, Ukraine

A. Gopkalo
G.S. Pisarenko Institute for Problem of Strength,
Ukrainian National Academy of Sciences, Kiev, Ukraine

M. Mihovski
Institute of Mechanics of Bulgarian Academy of Sciences, Sofia, Bulgaria

hydraulic tests performed on a full-scale pipe sample with VSDs are described. Their main goal was to define a modality to evaluate the residual life of a pipeline by taking into account the features of the relative position of the defect with respect to the weld seam of the steel pipe.

Keywords Flaw/defect · Volumetric surface defect (VSD) · Remaining strength factor (RSF) · Residual life · Serviceability/ultimate limit state · Bursting · Low cycle fatigue

1 Introduction

The corrosion processes affecting transmission pipelines intended for various fluids (petroleum, liquid petroleum products, natural gas, liquefied petroleum or natural gas, water, etc.) can generate on both inner and outer surfaces of the steel pipes the local metal loss flaws, also named volumetric surface flaws (characterized in Chapter “[Characterisation of Volumetric Surface Defects](#)”). The stress concentration effect of each flaw (determined by its configuration and characteristic dimensions), that can be expressed synthetically either by the maximum level of the stresses generated in the defective area during the pipeline operation or by the maximum value of the safe working/operating pressure of the pipeline, can be evaluated by applying the procedures presented in Chapter “[Characterisation of Volumetric Surface Defects](#)”. The aim of such assessment is to decide if a flaw detected on the steel pipes of a transmission line is qualified as a defect (if it affect its loading capacity and consequently the damaged area of the pipeline requires maintenance works) or as an imperfection (when repair activities are not needed, as it is acceptable to operate the pipeline containing the flaw).

A simple and efficient modality to perform an assessment for a transmission pipeline containing flaws is represented by the calculation of the Remaining Strength Factor (RSF) (defined in Chapter “[Characterisation of Volumetric Surface Defects](#)”) that is actually a measure of the maximum stress level that can be generated in the pipe wall without the danger of failure in the VSD area. In other words, when designing the pipeline, a minimum acceptable level for its mechanical strength has been imposed, and this level can be defined by an acceptable value, symbolized RSF_a , for which the usual value is 0.8–0.9 (see Chapter “[Characterisation of Volumetric Surface Defects](#)”).

The main mechanical loading of an onshore transmission pipelines is actually its internal pressure (due to the transported fluid) and RSF should, therefore, be correlated with the ratio between the inner pressures from the pipeline with and without VSDs for which the conditions of a serviceability limit state (the condition beyond which the pipeline does not meet its functional requirements) are attained in the steel pipe. As the stresses and strains generated in the steel tubes wall during pipeline operation are required to be of elastic nature only, RSF should be correlated with the pressures at which the limit state characterized by the occurrence of

plastic deformations in the most loaded areas is reached. Such limit state is defined by an intensity of the stresses (generated in these areas) reaching the level of the (effective) yield strength, R_p , of the steel from which the pipes are manufactured.

Nonetheless, a serviceability limit state is (conservatively) considered for the pipelines design. This condition, reached before the one defined above, corresponds to the state for which the stresses in the pipe attain the level of the allowable stress, $\sigma_a = FR_{pm}$ (where $F < 1$ is the design factor, defined as a function of the pipeline location class, the quality of the welded joints, etc., and $R_{pm} \leq R_p$ is the specified minimum yield strength of the pipe steel). As a result, the pipelines adequately designed have a loading capacity reserve which allows for the small flaws which might develop in the pipe wall to be able to be tolerated (qualified as imperfections), if their presence does not affect the pipeline operational safety, and therefore a (minimum) allowable level, RSF_a , can be defined for RSF.

By evaluating a damaged pipeline area (with VSDs), if this area is characterized by a value $RSF \geq RSF_a$, the pipeline can continue to work at the operating pressure level (repair is not needed). At the same time, if $RSF < RSF_a$, there are two options:

- (i) to execute maintenance work and repair the damaged area in order to reestablish the pipe loading capacity;
- (ii) to keep the pipeline with the detected VSDs operational, but to decrease the working pressure at the level of the maximum allowable (safe) working/operating pressure for the damaged pipeline (with VSDs), p_{od} .

This pressure level can be defined by using the RSF value from the equation:

$$p_{od} = \min \left[1; \frac{RSF}{RSF_a} \right] \cdot p_{ao}, \quad (1)$$

where p_{ao} is the maximum allowable working pressure for the pipeline (without any VSD).

However, for the pipelines transporting combustible fluids (crude oil, liquid petroleum products or natural gas), it is important to assess the remaining strength not only in relation with the limit state previously defined, but also in relation with the attainment of an ultimate limit state (pipe failure/bursting), accompanied by explosive failure, by leakage and, eventually, by the ignition of a quantity of fluid from the pipeline. Such maximum gravity events are taken into account when assessing the technical risk attached to the operation of transmission pipelines. Consequently, when assessing the residual mechanical strength of the transmission pipelines containing VSDs, it is necessary to consider not only the RSF value calculated with Eq. (1), but also the value of a remaining strength factor related to the attainment of the ultimate limit state (pipeline bursting), noted RSF_u , and defined by the ratio of the bursting pressure of the pipeline with VSDs, p_{bd} , to the bursting pressure of the pipeline without any flaw, p_b .

By considering the above, the formula recommended, instead Eq. (1), for the assessment of the p_{od} level for the pipelines containing VSDs is the following [1]:

$$p_{od} = \min \left[\min \left[1; \frac{RSF}{RSF_a} \right]; \min \left[1; \frac{RSF_u}{RSF_{ua}} \right] \right] \cdot p_{ao}, \quad (2)$$

where RSF_{ua} is the minimum allowable level of RSF_u , for which we propose: $RSF_{ua} = 0.7 - 0.9$.

In the following section, the most used modalities for the calculation of the values of the remaining strength factors (both RSF and RSF_u) of a damaged pipeline section (containing VSDs) are presented and compared.

2 Assessment of the Remaining Strength Factor for Pipelines with VSDs

For the calculation of the RSF , by considering the serviceability limit state, the international Norms presently used [2–5] propose several formulae, some of them being presented in Chapter “[Characterisation of Volumetric Surface Defects](#)”. It has to be mentioned that a RSF value can be deducted also from equations like (4), (7) and (9) of Chapter “[Characterisation of Volumetric Surface Defects](#)”. We take into account that it could be calculated as the ratio of the estimated failure stress value, σ_F , defined by the mentioned equations as a function of the flow stress $\sigma_Y = 1.1 R_{t0.5}$, to the specified yield strength, $R_{t0.5}$.

The procedures recommended by [2, 3] require that the assessment of a pipeline with a VSD should evaluate, in the first step, the longitudinal extent of the critical thickness profile (CTP, see Chapter “[Characterisation of Volumetric Surface Defects](#)”, Sect. 2) of the defect and should determine the remaining strength factor for the pipeline with the detected VSD.

The most frequent form of the equation used for the definition of the RSF for the case in which the detected VSD has a simple profile and can be characterized as a local thin area, having a value of the coefficient of variation, $COV \leq 0.1$ (calculated as defined in Chapter “[Characterisation of Volumetric Surface Defects](#)”, Sect. 2, step 5), is the following one:

$$RSF = \frac{1 - k_d \frac{d_{max}}{t}}{1 - k_d \frac{1}{M_t} \frac{d_{max}}{t}} \quad (3)$$

in which k_d is a coefficient taking into account the configuration of the longitudinal profile of the flaw (usually, $k_d = 0.67 - 1$), d_{max} is the maximum depth of the defect, t is the effective thickness of the steel pipe wall, M_t is a Folias factor, defined in Chapter “[Characterisation of Volumetric Surface Defects](#)”, where also some of Eqs. (5, 6, 10), proposed for its calculation, are included. Equation, similar to (3) for the RSF assessment, is Eq. (13) of Chapter “[13Characterisation of Volumetric Surface Defects](#)”, proposed in [2].

If the detected VSD is characterized by a value of the coefficient of variation, $COV > 0.1$, the RSF is determined, considering the real configuration of the CTP. For this purpose, the standard [2] indicates the following equation:

$$RSF = \min \left[\frac{1 - \frac{A_{d,i}}{A_{0,i}}}{1 - \frac{1}{M_{t,i}} \frac{A_{d,i}}{A_{0,i}}}; \quad i = 1 \dots n_d \right], \quad (4)$$

where the areas $A_{d,i}$ and $A_{0,i}$ are defined for a sequence of divisions of the CTP ($i = 1 \dots n_d$), selected by considering the indications from Fig. 1; $M_{t,i}$ is a Folias factor, which considers the pipeline weakening due to the presence of a flaw with the length, corresponding to the subdivision $i = 1 \dots n_d$ of the CTP; $M_{t,i}$ can be evaluated with the following equation [2]:

$$M_{t,i} = \sum_{j=0}^{10} C_j \lambda_i^j = \sum_{j=0}^{10} F_j s_{p,i}^j, \quad i = 1 \dots n_d \quad (5)$$

where $s_{p,i}$ is the length of subdivision $i = 1 \dots n_d$, $C_j, j = 1 \dots 10$ are constants, having the values mentioned in Table 1, and λ_i and F_j are defined by the following equations:

$$\lambda_i = \frac{1.285 s_{p,i}}{\sqrt{D_e t}} = \beta_p s_{p,i}, \quad i = 1 \dots n_d; F_j = C_j \beta_p^j, \quad j = 1 \dots 10. \quad (6)$$

In order to calculate the RSF by using Eq. (4), we propose the following procedure in six steps, easy to implement using dedicated computer software:

- (i) draw on the CTP the axes of the coordinate system, as indicated in Fig. 1, with the origin O in the transversal plane, in which the thickness t_{mm} (and the maximum flaw depth $d_{max} = t - t_{am}$; for a conservative assessment, $d_{max} = t - t_{mm}$) are recorded and divide the length of the defect, s_p , into 2 segments with the lengths s_{p1} and s_{p2} , respectively ($s_p = s_{p1} + s_{p2}$);

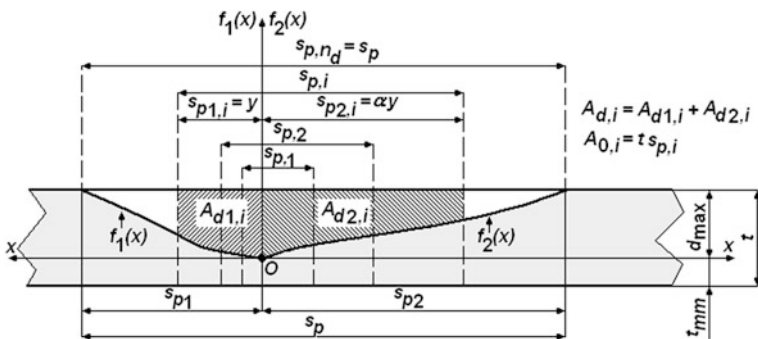


Fig. 1 CTP division for determining the RSF for a given pipeline with a flaw

Table 1 The values of the constants from the analytical expression of the Folias Factor [2]

C_0	1.0010
C_1	-1.4195×10^{-2}
C_2	2.9090×10^{-1}
C_3	-9.6420×10^{-2}
C_4	2.0890×10^{-2}
C_5	-3.0540×10^{-3}
C_6	2.9570×10^{-4}
C_7	-1.8460×10^{-5}
C_8	7.1553×10^{-7}
C_9	-1.5631×10^{-8}
C_{10}	1.4656×10^{-10}

(ii) determine the expression for two statistical regression polynomials, that describe analytically the CTP portions, found on both sides of the origin O :

$$f_1(x) = \sum_{i=1}^m A_i x^i \quad \text{and} \quad f_2(x) = \sum_{i=1}^m B_i x^i; \tag{7}$$

obviously, these functions simultaneously satisfy the following conditions: $f_1(0) = f_2(0) = 0$ and $f_1(s_{p1}) = f_2(s_{p2}) = d_{\max}$;

- (iii) determine the sequence of subdivisions of CTP ($i = 1 \dots n_d$); each of the subdivisions (with the length $s_{p,i}$) is made from two portions $s_{p1, i} = y$ and $s_{p2, i} = \frac{s_{p2}}{s_{p1}} y = \alpha y$; clearly, this manner of selecting the divisions corresponds to the conditions $n_d \rightarrow \infty$; $s_{p,i} = (1 + \alpha)y$, with $y \in (0; s_{p1}]$;
- (iv) compute the areas $A_{0,i} = t(1 + \alpha)y$ and $A_{d,i} = A_{d1,i} + A_{d2,i}$, as follows:

$$\begin{aligned} A_{d1,i} &= d_{\max} y - \int_0^y f_1(x) dx = \sum_{i=1}^m \frac{A_i}{i+1} y^{i+1}; A_{d2,i} \\ &= d_{\max} \alpha y - \int_0^{\alpha y} f_2(x) dx = \sum_{i=1}^m \frac{B_i \alpha^{i+1}}{i+1} y^{i+1}; \end{aligned} \tag{8}$$

(v) calculate RSF using the formulae:

$$\text{RSF} = \min \left[\text{RSF}(y) = \frac{1 - Q(y)}{1 - \frac{Q(y)}{M_r(y)}}; \quad y \in (1; s_{p1}] \right], \tag{9}$$

$$Q(y) = d_{\max} - \sum_{i=1}^m D_i y^i; M_t(y) = \sum_{j=0}^{10} F_j y^j, \tag{10}$$

where $D_0 = \frac{d_{\max}}{t}$; $D_i = \frac{A_i + B_i z^{i+1}}{(i+1)(1+z)^i}$, $i = 1 \dots m$; and $F_j = C_j \beta_p^j$, with $\beta_p = \frac{1.285(1+z)}{\sqrt{D_e t}}$;

(vi) search for the local extrema of the function $\text{RSF}(y)$, in the range $y \in (0; s_{p1}]$, between the roots of the equation $\text{RSF}(y) = 0$, which is equivalent to:

$$M'_t(y)Q(y)[Q(y) - 1] - M_t(y)Q'(y)[M_t(y) - 1] = 0, \tag{11}$$

where $M'_t(y)$ and $Q'(y)$ are the derivatives with respect to the variable y of the functions $M_t(y)$ and $Q(y)$. Considering the root y_m of Eq. (11), which corresponds to a minimum of $\text{RSF}(y)$ and locates in the range $(0; s_{p1})$, the value of the remaining strength factor $\text{RSF} = \text{RSF}(y_m)$ is then obtained.

The procedure described above is illustrated by the following case study. On a pipeline with the outside diameter $D_e = 508$ mm and the effective wall thickness $t = 8.8$ mm, a VSD has been detected with the length $s_p = 105$ mm, the width $c_p = 50$ mm and the maximum depth $d_{\max} = 5.5$ mm ($t_{\text{mm}} = t - d_{\max} = 3.3$ mm; $s_{p1} = 35$ mm and $s_{p2} = 70$ mm; $\alpha = 2$; $\beta_p = 0.0577$). The CTP of the analysed defect is drawn in Fig. 2a and it is described analytically in Table 2, which contains the coefficients for the functions $f_1(x)$ and $f_2(x)$ from Eq. (7); $f_2(x)$ has two analytical expressions, $f_{21}(x)$ and $f_{22}(x)$, in the domains mentioned in Fig. 2a. The results obtained by applying the procedure for the RSF calculation for the case study are present in Fig. 2b and in Table 3 (where RSF_{LTA} represents the RSF value calculated with Eq. (13) from Chapter “Characterisation of Volumetric Surface Defects”, considering the VSD a local thin area defect).

The results of the case study have highlighted the following issues regarding the calculation of the RSF for pipelines with VSDs:

- The characterization of the RSF for pipelines with VSDs using the RSF_{LTA} value, computed considering $d_{\max} = t - t_{\text{mm}}$, is very conservative and is not recommended for the cases in which the CTP of the flaw area gives values of $\text{COV} > 0.1$.

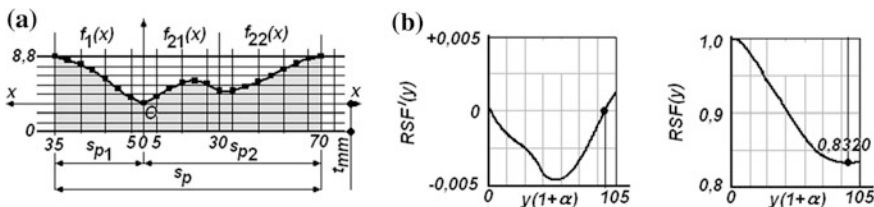


Fig. 2 The CTP configuration for the flaw considered for the case study (a) and the graphical synthesis of the results obtained (b)

Table 2 Coefficients of the polynomial functions describing the CTP for the case study

$f_1(x)$ coefficients		$f_2(x)$ coefficients		
A_1	3.63567×10^{-2}	B_0	–	14.48446
A_2	2.08766×10^{-2}	B_1	8.25999×10^{-2}	-9.5483×10^{-1}
A_3	-8.42340×10^{-4}	B_2	1.74695×10^{-2}	2.16010×10^{-2}
A_4	9.83982×10^{-6}	B_3	-9.97680×10^{-4}	-1.4000×10^{-4}
–	–	B_4	1.26350×10^{-5}	–

Table 3 Summary of the results obtained for the considered case study

VSD characteristics			Remaining strength factor			
t_{am} (mm)	t_{sd} (mm)	COV	RSF (s_{p1})	RSF _{LTA} ^a	RSF _{LTA} ^b	RSF
6.2590	1.4205	0.2269	0.8332	0.6091	0.8440	0.8320

^acalculated considering $d_{max} = t - t_{mm} = 5.5$ mm; ^bcalculated considering $d_{max} = t - t_{am}$

- The calculation of RSF_{LTA}, for pipelines with VSDs having COV > 0.1, considering $d_{max} = t - t_{am}$, does not always give the possible minimum value, by means of which the real reduction of the pipe loading capacity due to the existence of VSDs can be appreciated.
- The RSF values determined with Eq. (4), applying the subdivision procedure proposed above, describe with a high level of confidence the remaining strength of pipelines with VSDs. However, the application of this laborious procedure is not always justified, because obtained RSF values are very close to the values of RSF(s_{p1}), that can be obtained more easily.

Based on the previous remarks, we propose the following two-step approach for the problem of obtaining the RSF for pipelines with VSDs characterized by COV > 0.1:

- (i) calculate RSF(s_{p1}) and RSF_{LTA} (considering $d_{max} = t - t_{am}$) and then the value:

$$RSF_m = \min[RSF(s_{p1}); RSF_{LTA}]; \quad (11)$$

- (ii) compare RSF_m with RSF_a; if both values are close, determine RSF with Eq. (4), using the procedure proposed above; otherwise make a pertinent decision regarding the pipeline with VSDs (if maintenance works are required or not) by comparing the values RSF_m and RSF_a.

The methods for the calculation of RSF detailed above refer to the case of the serviceability limit state. If the ultimate limit state of pipeline bursting is considered, for the evaluation of RSF_u defined by the ratio between p_{bd} and p_b , as previously explained, the results presented by the authors in [1] could be used. Based on the analysis and interpretation of the bursting test results for pipelines with/without VSDs from an experimental database (including our own experimental programs),

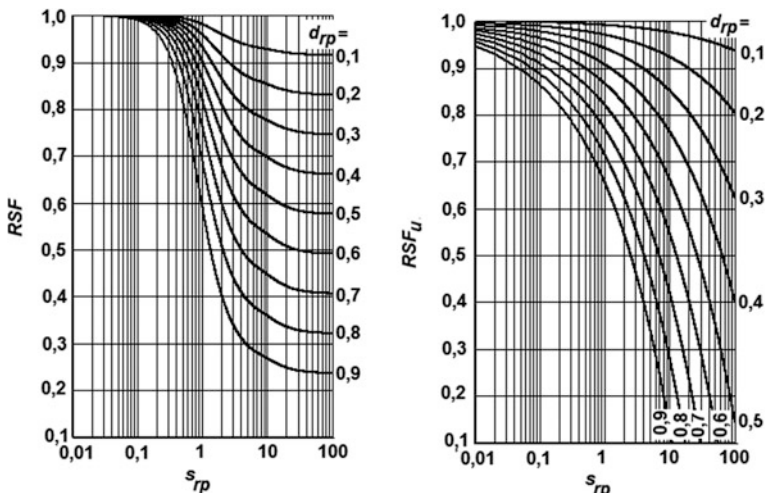


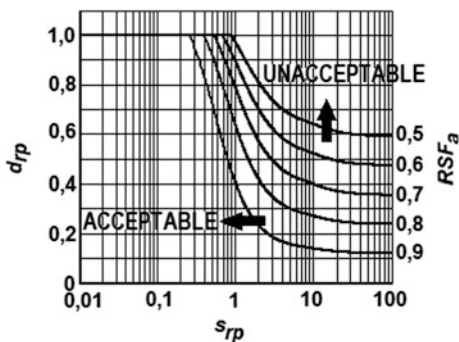
Fig. 3 Example of diagrams for the evaluation of RSF and RSF_u for the pipelines with VSDs

the various relationships proposed in literature for the calculation of the bursting pressure (for both p_{bd} and p_b) have been ascertained and a consistent multitude of equations has been defined to compute RSF_u .

The calculation results for both RSF and RSF_u can be synthesized under the form of evaluation diagrams for VSDs, extremely useful for a fast assessment of the remaining mechanical strength of the damaged pipelines areas and for an operative decision-making process regarding the need for maintenance works. Example of such diagrams, defining the RSF as a function of the relative length of the defect, $s_{rp} = \frac{s_p}{\sqrt{D_i t}}$, for different values of the relative depth of the VSD, $d_{rp} = d_{max}/t$, are shown in Fig. 3 [1].

After defining the allowable levels, RSF_a and RSF_{ua} , for RSF and RSF_u , Flow Acceptance Diagrams, of the type presented as an example in Fig. 4 for the case of RSF, describing analytically the condition $RSF \geq RSF_a$ (based on Eq. (3) for RSF

Fig. 4 Example of a flaw acceptance diagram [1]



assessment and several possible values for RSF_a), can be built. The use of such chart for the evaluation of a given volumetric surface flaw is simple and was explained in Chapter “[Characterisation of Volumetric Surface Defects](#)”.

3 Assessment of the Residual Life of Pipeline with VSDs in the Weld Area

High loading level and the non-stationary stress–strain state of transmission pipelines create the prerequisites for their low cycle fatigue failure in the areas with stress concentration effects, among which volumetric surface defects (VSDs) are most frequent.

This section presents the results of a cyclic hydraulic testing of a full-scale pipe sample with model defects and the manner of taking into account the features of the relative position of the defect and the weld seam as well as the features of the weld joint material when the residual life of a pipeline is evaluated.

For the preparation of the full-scale sample, a pipe with longitudinal weld, $\text{Ø}530 \times 8 \times 2435 \text{ mm}^3$, made of 17G1S steel, has been used. Pressurizing of the specimen was provided by welding of semi-elliptical bottoms to the ends of the pipe.

On the outer surface of the pipe, six volumetric surface defects (VSDs) were electrochemically etched. A length of defects was equal to 50 mm, a width was 15 mm and a depth varied from 0.38 to 0.88 of the pipe wall thickness. They were arranged as follows: on the weld (defects D2 and D3); half of width on the weld and the other half on the base metal (D5); at a distance of 5 mm from the weld (D4); at a distance of 16 mm from the weld (D6); at distance of 400 mm from the weld (D1). Figure 5 shows a fragment of the full-scale specimen with defects on it.

Fig. 5 Fragment of the full-scale specimen with VSDs





Fig. 6 Hourglass samples for mechanical testing

In the first stage of the cyclic hydraulic testing, the sample was subjected to loading under a pulsed inner pressure of 0.2–7.5 MPa with the frequency from four to five cycles per minute. After 10,090 cycles, the maximum cycle pressure was increased up to the second level of 9 MPa. After the first failure, as in the subsequent similar cases, the defect was repaired, and the test was continued.

To determine the mechanical properties (tensile strength characteristics and low cycle strength) of the weld metal (WM), of the metal of the heat affected zone (HAZ) and of the base metal (BM), specimens with the working part length of 3 mm and the diameter of 6 mm were manufactured (see Figs. 6 and 7).

Tensile and low cycle fatigue tests were carried out by using an electrohydraulic machine 3201UE20 at the air temperature from 18 to 20 °C in accordance with the requirements of GOST 1497 [6], ISO 12106 [7], and ASTM E606 [8]. The cyclic loading of the laboratory samples by axial tension-compression was performed under a controlled strain amplitude applied with a constant rate of 0.1%/s and an asymmetry of the cycle $R_z = -1$.

In the case of the hourglass sample (Fig. 6), strain measurement in the test portion of the sample was performed by using a strain gauge glued on the extensometer. The strain value, which was determined by the extensometer in order to control the hourglass sample cycling, was selected in accordance with the required strain in the test portion of the sample.

At a cyclic loading with the same strain amplitude, the diagrams of the cyclic deformation of the metal in various zones differ mainly in the magnitude of the plastic strain per cycle (see Fig. 8). The plastic strain of the HAZ samples is 28.5% higher than that of the BM samples. At the same time, the WM samples have ductility values, according to tensile test, 23% lower than those of the BM samples. The stress kinetics of the samples from various zones indicate the cyclic stability of the material in all the welded joint zones. A sharp decrease in the stress amplitude in

Fig. 7 Location of test portion (I) of hourglass sample in the HAZ

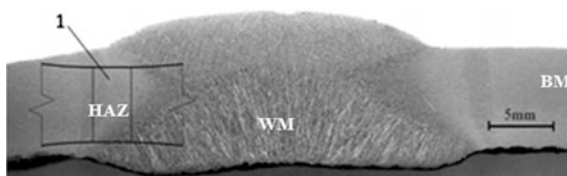


Fig. 8 Deformation diagrams of samples from various zones of the welded joint, at strain amplitude $\epsilon_a = 0.623\% = \text{const}$

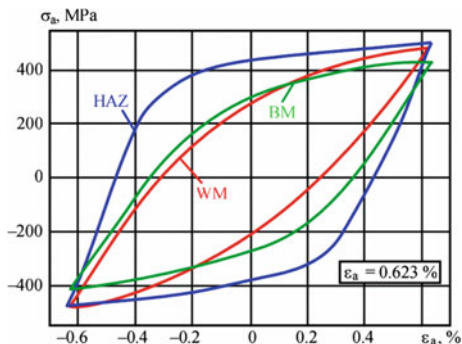
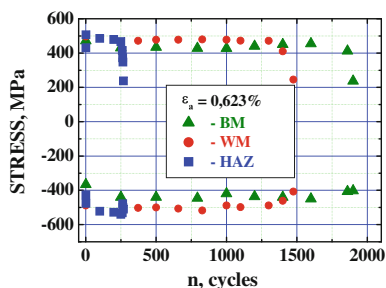


Fig. 9 Kinetics of stresses in samples from zones of the welded joint



the final stage of the loading is explained by the significant development of a fatigue crack (see Fig. 9).

Figure 10 shows the plots of the cyclic fatigue life N_f of the samples from different welded joint zones of the pipe. According to the experimental data, the HAZ metal has the shortest fatigue life. A rather small difference in the plastic strain per cycle for the BM and WM (see Fig. 8) results in minor differences in their cyclic durability.

In addition, the assessment of the material damage by homogeneity parameter m , which reflects its structural state, has been made. The parameter m was determined

Fig. 10 Fatigue life of samples from the welded joint zones

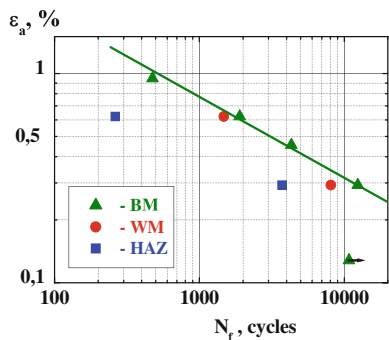
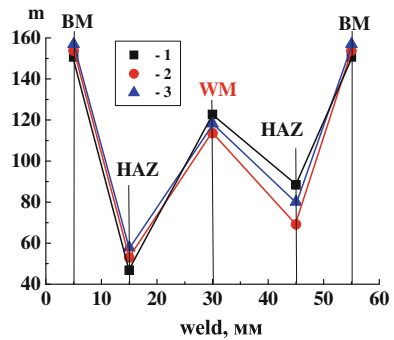


Fig. 11 Distribution of homogeneity parameter m in the cross-section of the welded joint (see Fig. 7): 1 inner surface of the pipe; 2 neutral zone; 3 outer surface of the pipe



by calculation of the dispersion of 35 HRB measurements carried out with hardness tester Computest in each zone of welded joint [9]. Higher values of the parameter correspond to a lower level of HRB dispersion and, accordingly, to the better structure and lower degree of damage. Smaller values of m , on the contrary, correspond to higher degree of damage.

The distribution of parameter m in a cross-section of the welded joint (see Fig. 11) shows that damage of the HAZ is by 65.3% higher than the one in the BM. This fact indicates a high probability of failure in this area.

Experimental evaluation of the impact of the distance between VSD and weld on the cycle life of the welded joint was carried out during the test specimens with model defect (see Fig. 12).

Tests were carried out under control of the longitudinal strain using an extensometer with the base of 25 mm and with the measurement of strain on the defect surface with an extensometer having the base of 6 mm. Figure 13 shows dependence of cyclic durability of laboratory samples with VSD on the strain amplitude.

As follows from the obtained data, the presence of VSD decreases the cycle life 2–6 times. The greatest decreasing in cycle life has been demonstrated by the specimens with VSD at the weld.

Figure 14 shows the test results of the full-scale sample reduced to the first-level cycles ($P_{min} = 0.2 \text{ MPa}$; $P_{max} = 7.5 \text{ MPa}$). The conducted calculations and the

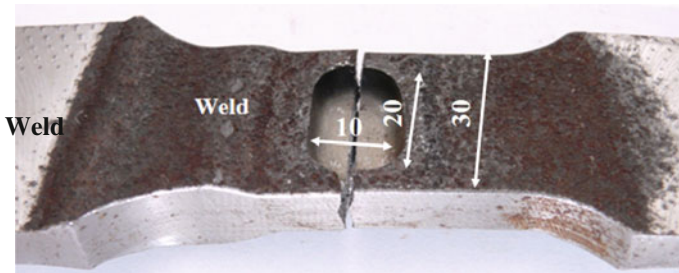


Fig. 12 Broken laboratory sample with VSD after low cycle fatigue test

Fig. 13 Cyclic durability of laboratory samples in the initial state (without VSD) and with VSD

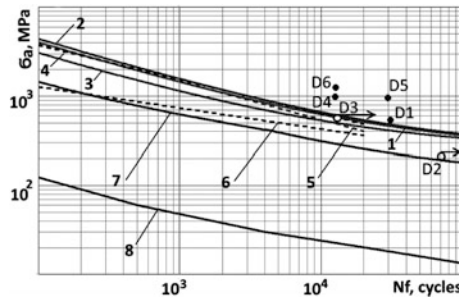
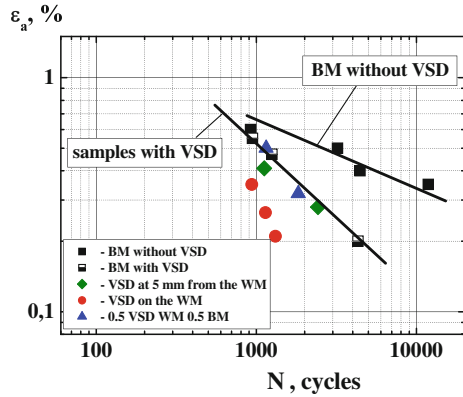


Fig. 14 Test results of full-scale sample: D1 to D6—defect numbers; *filled circle* destruction of D1, D4, D5 and D6; *open circle* predicted destruction of D2, damage at the moment of D3 repair; 1–3 fatigue curves of BM, WM and HAZ according to Eq. (1); 4–6 experimental fatigue curves of BM, WM and HAZ, respectively; 7 fatigue curve ($n_N = 10, n_e = 2$) of BM according to Eq. (1); 8 design fatigue curve for low-alloyed steel [11]

full-scale experimental investigation indicated the presence of interaction between the stress fields of the weld and the VSD. The degree of such interaction was determined by the geometrical parameters of these stress raisers and by the distance between them.

The results of the tensile testing of the samples from the BM, WM and HAZ zones were used to plot the fatigue curves (curves 1–3 in Fig. 14) according to Langer’s equation [10]:

$$\sigma_a = \left[\frac{\ln[1/(1 - \psi) \cdot E]}{4 \cdot N_f^m} \right] \mp \sigma_{-1} \tag{12}$$

where σ_a is the amplitude of the conditionally elastic stress, MPa; σ_{-1} is the endurance limit, $\sigma_{-1} = 0.4\sigma_t$; E is the material modulus of elasticity ($E = 2 \times 10^5$ MPa); and m is the material constant ($m = 0.5$).

On the base of the obtained data, it is recommended to perform the calculation of the pipeline residual life by using the equation of the fatigue curve, considering the defect location and the mechanical and fatigue properties of the respective zone of the welded joint. If the required fatigue characteristics are not available, the design fatigue curve, based on the mechanical properties of the base metal, may be used with the safety factors for durability and strain assumed to be $n_N = 10$ and $n_e = 2$, respectively.

4 Conclusions

The main issue of the present chapter was to present the methods based on the evaluation of the remaining strength factor, RSF, used for the assessment of volumetric surface flaws, in order to define the required pipeline maintenance works, if needed (in the case the flaw is qualified as a defect).

The chapter proposes and describes a procedure for the evaluation of VSDs with complex geometry, based on the method from the API standard [2]. This procedure can, in many cases, be simplified, without any consequences regarding the precision of the assessment of the remaining strength of pipelines with VSDs.

The authors consider that, when assessing the residual mechanical strength of transmission pipelines containing VSDs, it is necessary to consider not only the RSF value related to the serviceability limit state, as defined by the Norms presently used, but also the value of a RSF related to the attainment of the ultimate limit state of pipeline bursting, RSF_u , defined by the ratio between the bursting pressure of the pipeline with VSDs and the bursting pressure of the pipeline without any flaw.

The assessment of the residual life of a pipeline with defects susceptible to low cycle fatigue in the VSD stress concentration area has also been investigated based on cyclic hydraulic tests performed on a full-scale pipe sample, leading to the conclusion that the pipeline residual life should be calculated using the equation of the fatigue curve and considering the VSD location and the mechanical and fatigue properties of the welded joint area.

References

1. Gh Zecheru, P. Yuhymets, Gh Draghici, A. Dumitrescu, *Rev. Chim.* **66**(5), 710 (2015)
2. API 579/ASME FFS-1, *Fitness-For-Service* (2007)
3. ASME B31.G, *Manual for Determining the Remaining Strength of Corroded Pipelines* (2009)
4. DNV RP-F 101, *Corroded Pipelines, Recommended Practice* (2015)

5. BS 7910, *Guide to Methods for Assessing the Acceptability of Flaws in Metallic Structures* (2005)
6. GOST 1497, *Metals. Methods of Tensile Testing*. Ministry of Ferrous Metallurgy of the USSR (1984) (In Russian)
7. ISO 12106, *Metallic Materials—Fatigue Testing—Axial Strain Controlled Method*. International Organization for Standardization (2003)
8. ASTM E606, *Standard Recommended Practice for Constant Amplitude Low-Cycle Fatigue Testing*. American Society for Testing and Materials (2004)
9. A. Lebedev, N. Musika, N. Volchek, *Probl. Strength* **4**, 5 (2002)
10. S.V. Serensen, *Material Resistance to Fatigue and Brittle Fracture*. Atomizdat (1975) (In Russian)
11. PNAE G-7-002-86, *Rules of Strength Calculation for Equipment and Pipelines of Nuclear Power Plants*. Metallurgiya (1973) (In Russian)

Assessment of Interacting Volumetric Surface Defects

M.I. Chebakov, Gh. Zecheru and V.A. Chebanenko

Abstract On the inside and/or outside surfaces of the steel pipes of the transmission lines intended for the transportation of hydrocarbons (petroleum, liquid petroleum products, natural gas, liquefied petroleum or natural gas) or other fluids (water, ammonia, etc.) clusters or colonies of volumetric surface defects (VSDs) can be generated. Each defect from such a colony can interact with the neighbouring defects, such that the stress concentration effects determined by a group/cluster of defects can be superior to the ones generated by the presence of individual defects. Therefore, the present chapter has the following goals: (i) definition of the factors that determine VSDs interaction: the characteristic dimensions of the pipeline (diameter and wall thickness); mechanical properties of the steel from which the pipeline containing the defects is manufactured (Young modulus, Poisson's ratio, specified minimum yield strength, minimum tensile strength, minimum specified value of the percentage elongation, etc.); type, shape and characteristic dimensions of VSDs (length/axial extent, width/circumferential extent, maximum depth, etc.); distances between adjacent flaws/defects (in both axial and circumferential directions); complexity and intensity of the mechanical loads of the pipeline on which defects are placed (operating pressure and maximum intensities of other loads/forces and moments); (ii) comparative analysis of the criteria (from Norms presently in force: standards, codes, recommended practices, specifications, etc.) with which it can be assessed if adjacent defects from a VSD group or colony interact; (iii) description of the methods for the assessment of the shape and characteristic dimensions of the defect equivalent to a cluster of interacting VSDs; (iv) definition of the modalities for the evaluation of the effects of interacting VSDs groups upon the remaining mechanical strength of pipelines with

M.I. Chebakov (✉) · V.A. Chebanenko

I.I. Vorovich Institute of Mathematics, Mechanics and Computer Science,
Southern Federal University, Rostov-on-Don, Russia
e-mail: chebakov@math.sfedu.ru

Gh. Zecheru
Petroleum–Gas University of Ploiesti, Ploiești, Romania

V.A. Chebanenko
Southern Scientific Center of Russian Academy of Science, Rostov-on-Don, Russia

such defects; (v) investigation of the influence of the interaction between two adjacent defects on the stress and strain states in the defects area by means of finite element analyses.

Keywords Volumetric surface defect (VSD) · Colony of flaws/defects · Interacting flaws/defects · Safe working pressure · Finite elements

1 Introduction

The corrosion and/or erosion processes, at which the transmission pipelines intended for various fluids (petroleum, liquid petroleum products, natural gas, liquefied petroleum or natural gas, water, etc.) are subjected, can generate on the inner or outer surfaces of their steel pipes clusters or colonies of volumetric surface defects (VSDs). The stress concentration effect of each VSD, expressed synthetically by the maximum level of the stresses generated in the defect area during the operation of the pipeline and respectively by the maximum value of the safe working pressure of the pipeline (without reaching an ultimate limit state, of the type global yielding or failure/bursting of the pipeline), can be evaluated by applying the procedures recommended in [1–3] and discussed in Chapters “[Characterisation of Volumetric Surface Defects](#)” and “[Assessment of the Remaining Strength Factor and Residual Life of Damaged Pipelines](#)”. However, if the components of group or colony of defects interacts, the stress concentration effects can be enhanced and amplified, thus leading to a sensible decrease of the safe working pressure of the pipeline containing the defects.

The factors determining/influencing the occurrence and extent of the interaction of the components of a colony or cluster of VSDs can be grouped in the following categories:

- Factors concerning the characteristic dimensions (nominal wall thickness, t_n , and outside diameter, D_e or interior diameter, $D_i = D_e - 2t_n$) of the pipeline components (pipes, elbows, bends, tees, fittings) with defects and the properties of mechanical strength, plasticity and toughness (yield strength $R_{0.5}$, ultimate tensile strength R_m , percentage elongation at break A , Charpy V-notch impact energy KV , etc.) of the steel from which these components are manufactured.
- Factors regarding the type, shape and characteristic dimensions of VSDs (length/axial extent, s_p , width/circumferential extent, c_p , maximum depth, d_{max} etc.) and distances between adjacent flaws/defects (in the axial direction, s_d , and in the circumferential direction, c_d); for a colony with a number of n defects, each defect is assigned one number $i = 1, \dots, n$ and the characteristic dimensions of the defects ($s_{p,i}$; $c_{p,i}$; $d_{max,i}$, $i = 1, \dots, n$) and the distances between the defects ($s_{d,i-j}$; $c_{d,i-j}$, $i, j = 1, \dots, n$, $i \neq j$) are noted.
- Factors concerning the type and level of loading for the pipeline containing the defects (maximum working pressure, p_o , the allowable stress value considered

for the pipeline design, expressed under the form $\sigma_a = k_p R_{t0.5}$, $k_p < 1$, the level and frequency of pressure fluctuations during pipeline operation, the intensity and the static or dynamic character of the action of the forces and/or moments that may accidentally load the damaged components of the pipeline).

2 Criteria and Procedures for the Assessment of Interacting Defects

The international Norms presently applicable (standards, codes, recommended practices, specifications etc.) recommend a series of criteria and procedures with the help of which it can be assessed if the components of a colony of defects interacts and the geometrical configuration and the characteristic dimensions of the defect equivalent to a cluster of interacting VSDs can be defined [1–5]. The synthetic presentation, made below, of the main such criteria and procedures allows for their comparative analysis and evaluation in view of selecting the ones recommended for application.

The Standard [1] recommends the following analysis procedure for the colonies of VSDs detected on pipelines in view of defining the interacting defects:

- For each component $i = 1, \dots, n$ of the group of VSDs that is analysed, a circumscribed box DC_i , with the sides (oriented in the axial and circumferential directions) $s_{p,i}$; $c_{p,i}$ is drawn (on the unfolded pipeline);
- Around each DC_i , another box, DDC_i , is drawn, having the following characteristics: (i) it has parallel sides with the ones of DC_i and it surrounds symmetrically DC_i ; (ii) its sides have the lengths $2s_{p,i}$; $2c_{p,i}$, $i = 1, \dots, n$;
- The groups of defects $(i; j)$, $i, j = 1, \dots, n$, whose DDC_i intersect are considered to interact and, for them, the boxes DC_{i-j} , with the sides $s_{p,i-j}$; $c_{p,i-j}$ are drawn; they represent the extents (axial and circumferential) of the individual defect equivalent to the group of defects $(i; j)$, $i \neq j$, that interact; the maximum depth of the equivalent defect is considered equal to $d_{\max,i-j} = \max[d_{\max,i}; d_{\max,j}]$.

The procedure is repeated considering, at the next step, both the individual defects and the individual defects, with the extents $s_{p,i-j}$; $c_{p,i-j}$ equivalent to the interacting groups of defects. The manner of applying this procedure is suggestively described, for a cluster of VSDs with $n = 4$ defects, in Fig. 1.

The Standard [4] specifies the rules/criteria presented in the followings to assess if a component i of a group of VSDs (generated by corrosion processes in the base metal of the pipelines components and/or in the areas adjacent to their welded joints) can be considered/treated as an individual/isolated/independent defect.

- The maximum depth of the defect satisfies the condition:

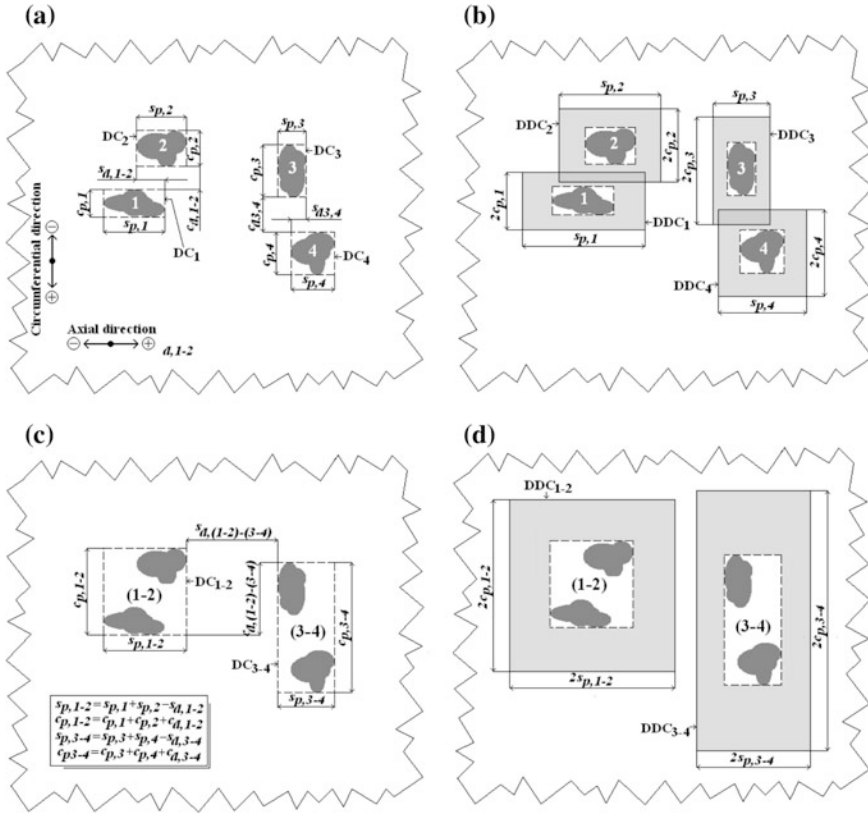


Fig. 1 Example of the application of the procedure recommended in [1]

$$d_{\max,i} < 0.2t_n. \tag{1}$$

- The distances to any adjacent defect j satisfy simultaneously the criteria:

$$s_{d,i-j} > 2\sqrt{D_e t_n}; \quad c_{d,i-j} > 3\sqrt{D_e t_n}; \tag{2}$$

The Standard [4] also specifies that a component i of a cluster of VSDs interacts with a neighbouring component j (from the same cluster) if the following criterion is fulfilled:

$$[\text{RSF}_{sd,i} \text{ or } \text{RSF}_{sd,j}] > \text{RSF}_{sd,i-j}, \tag{3}$$

The Remaining Strength Factors—RSFs, $\text{RSF}_{sd,i}$, $\text{RSF}_{sd,j}$ and $\text{RSF}_{sd,i-j}$ are defined by the formulae:

$$RSF_{sd,i} = \frac{1 - K_{d,i}}{1 - Q_{d,i}K_{d,i}}; \quad RSF_{sd,j} = \frac{1 - K_{d,j}}{1 - Q_{d,j}K_{d,j}}; \quad RSF_{sd,i-j} = \frac{1 - K_{d,i-j}}{1 - Q_{d,i-j}K_{d,i-j}}, \quad (4)$$

in which $K_{d,i} = A_{d,i}/A_{0d,i}$; $K_{d,j} = A_{d,j}/A_{0d,j}$; $K_{d,i-j} = A_{d,i-j}/A_{0d,i-j}$, with $A_{0d,i} = s_{p,i}t_n$; $A_{0d,j} = s_{p,j}t_n$; $A_{0d,i-j} = s_{p,i-j}t_n$; $A_{d,i} = s_{p,i}d_{max,i}$; $A_{d,j} = s_{p,j}d_{max,j}$; $A_{d,i-j} = A_{d,i} + A_{d,j}$, and $Q_{d,i}$, $Q_{d,j}$ and $Q_{d,i-j}$ are defined by the equations:

$$Q_i = \sqrt{1 + 0.31 \frac{s_{p,i}^2}{D_i t_n}}; \quad Q_j = \sqrt{1 + 0.31 \frac{s_{p,j}^2}{D_j t_n}}; \quad Q_{i-j} = \sqrt{1 + 0.31 \frac{s_{p,i-j}^2}{D_{i-j} t_n}}, \quad (5)$$

the axial extent of the individual defect equivalent to the group of defects (i ; j), $i \neq j$, $s_{p,i-j}$ is defined based on the indications from Fig. 2.

The Standard [5] recommends to consider one at a time, for the analysis of a colony of interacting defects, each defect of the cluster, then the defects equivalent to each pair of adjacent defects (i ; j), $i \neq j$, then the defects equivalent to the pairs of defects (i ; j), $i \neq j$, combined with the adjacent individual defects and so on, up to the individual defect equivalent to the entire colony (with n components) of interacting defects. If the multitude of defects defined in this manner has a number n_e of components and the values $RSF_{sd,k}$ corresponding to each defect $k = 1, \dots, n_e$

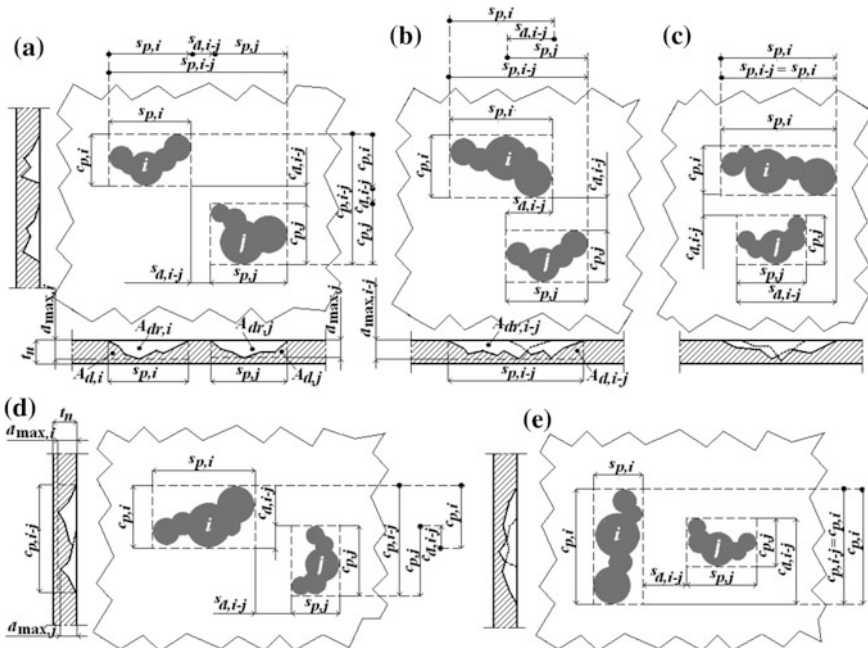


Fig. 2 Assessment of the extent of the defect equivalent to a group of two adjacent defects

of this multitude are calculated, with the adequate formula from the group (4), the stress concentration effect induced by the presence of the analysed colony of defects will correspond to $\min RSF_{sd,k}$, $k = 1, \dots, n_e$, and to the lowest level of the bursting/failure pressure, p_{fd} , of the pipeline containing the defects, $p_{fd} = p_f \min RSF_{sd,k}$, p_f being the bursting/failure pressure of the pipeline without defects [6, 7].

The evaluation of the colonies of VSDs based on the recommendations of [4] is conservative, because the weakening considered for the longitudinal section of a pipeline due to the presence of some individual VSDs or defects equivalent to colonies of VSDs (expressed with the help of the areas, $A_{d,i}$, $A_{d,j}$ or $A_{d,i-j}$, calculated as a product between the axial extent of the defects and their maximum depth) are superior to the real ones, $A_{dr,i}$, $A_{dr,j}$ or $A_{dr,i-j}$, as it can be observed examining Fig. 2. For a better evaluation of the stress concentration effects due to the presence of colonies of interacting defects, one should use the areas $A_{dr,i}$, $A_{dr,j}$ or $A_{dr,i-j}$, calculated by applying the principles formulated in [6].

The Code [3] recommends the evaluation of the clusters of VSDs (detected on the transmission and distribution pipelines for liquid hydrocarbons) by taking into account, for the pairs of defects ($i; j$) belonging to such a cluster, the two types of interactions described in Fig. 3. The pairs of defects ($i; j$) corresponding to type I are considered as interacting, if $c_{d,i-j} < 6t_n$, the equivalent defect having the extents $s_{p,i-j} = s_{p,i} + s_{p,j} - s_{d,i-j}$ and $c_{p,i-j} = c_{p,i} + c_{p,j} + c_{d,i-j}$ and the maximum depth $d_{\max,i-j} = \max [d_{\max,i}; d_{\max,j}]$. The pairs of defects ($i; j$) corresponding to type II are considered as interacting, if $s_{d,i-j} < 1$ in. (25.4 mm), the equivalent defect has the extents $s_{p,i-j} = s_{p,i} + s_{p,j} + s_{d,i-j}$ and $c_{p,i-j} = c_{p,i} + c_{p,j} - c_{d,i-j}$ and the maximum depth $d_{\max,i-j} = \max [d_{\max,i}; d_{\max,j}]$. It has been mentioned that Code [3] recommended to use, when determining RSF for pipelines with defects, the real areas of the defects $A_{d,i} = A_{dr,i}$; $A_{d,j} = A_{dr,j}$ and $A_{d,i-j} = A_{dr,i-j}$.

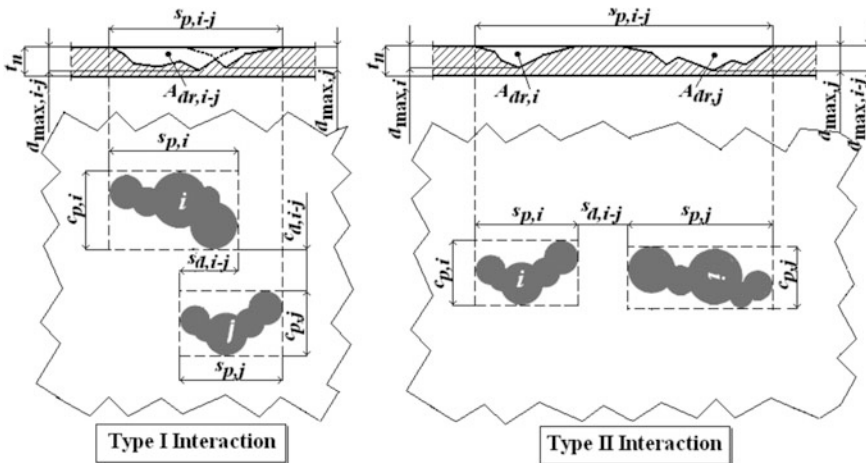


Fig. 3 Types of interacting defects considered by the standard [3]

The Code [2] and its Supplement [4] consider that two adjacent defects (i ; j) interact if $s_{d,i-j} < 3t_n$ and/or $c_{d,i-j} < 3t_n$; for each group of interacting defects (i ; j), the axial and circumferential extent of the equivalent defect is defined as shown in Fig. 2.

The Standard [6] states that the defects of a pair (i ; j) interact if the following conditions are fulfilled: $s_{d,i-j} < \min[s_{p,i}; s_{p,j}]$ and/or $c_{d,i-j} < \min[c_{p,i}; c_{p,j}]$. It is also mentioned that [2, 4, 6] recommended to use, when determining *RSF* for the pipelines with defects, the areas $A_{d,i} = 0.67s_{p,i}d_{\max,i}$; $A_{d,j} = 0.67s_{p,j}d_{\max,j}$; $A_{d,i-j} = 0.67(A_{d,i} + A_{d,j})$.

In order to assess the stress and strain that are generated in the areas of some colonies of VSDs (with different shapes and reciprocal positioning of the defects composing them), while the pipelines which contain them are subjected to internal pressure loading, finite elements analyses can successfully be performed. In practice, all detected VSDs are machined by grinding in order to round their micro-geometry and to diminish as much as possible the mechanical stress concentration effects. Results of such kind of analyses, performed for the case of two machined VSDs, grouped in a cluster, are included in the following section of this chapter.

3 Finite Element Modelling

In this section, several problems for a damaged pipeline with volumetric surface defects, subjected to internal pressure loading, were considered. In all cases, it is considered that the defects were caused by surface corrosion and that they were subsequently machined by grinding in order to eliminate the stress concentration effects. All the corrosion defects have been machined to the shape of a rectangular “pocket” with rounded corners (see Fig. 4). It is interesting as a first step to obtain data for a single VSD and then to compare it with the case of two defects.

In order to study the mentioned problems, the finite element modeling in Siemens NX package was performed. The models used to investigate the pipes with defects were developed depending parametrically on the initial data on the parameters describing the problem (see Fig. 5). This approach allows automation of the calculation process. In the examined models, L360/API X52 steel has been assumed as pipe material.

Due to the symmetry of the problem, a whole body can be reduced to a quarter for the ease of calculations (see Fig. 6a) by using symmetry constraints in NX. In addition, the problem has been assumed linear, due to the assumption that the occurrence of plastic deformations indicates that pipeline segment is no longer repairable with in-service repair techniques and should be replaced.

In order to model this body, 10-node 3D tetrahedral mesh element CTETRA (10) was chosen. It is a standard NX Nastran element for modeling complicated meshes. At the edges and surface of the defect, with the help of mesh control tools,

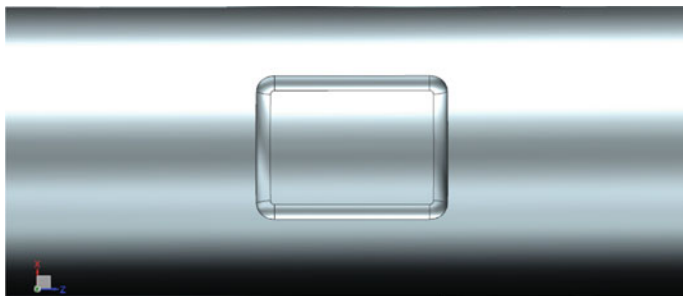
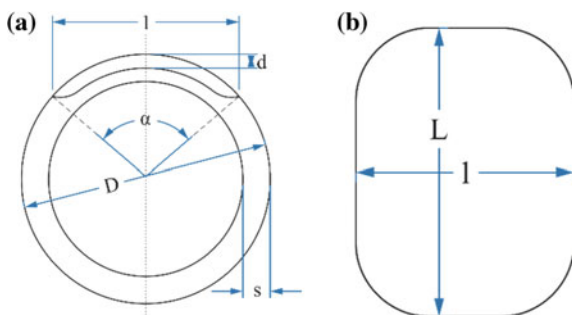


Fig. 4 Geometry of pipe segment with one VSD

Fig. 5 Parametrization of pipe model: **a** cross-section of tube, **b** defect



it was chosen to make a higher density of elements by setting their size smaller than the thickness of the wall in the defect area (see Fig. 6b).

In the first stage, several computational experiments were performed with the created model with the purpose of obtaining basic ideas about stress and strain distributions in the pipe segment, subjected to internal static pressure loading. The results for the case when inner pressure was 1.6 MPa and the geometrical parameters of the tube were equal to those in Table 1 are present in Fig. 7.

As it can be seen from Fig. 7a, the stress concentration localizes in the place, where the rounded corner of the defect links with the main surface of the VSD. The maximum displacements locate in the same area. For better estimation of this effect, it is useful to obtain information about stresses on the edges of the defect, both in lateral and in longitudinal directions.

The results shown in Figs. 8 and 9 indicate that the maximum stress jump of about 140 MPa occurs near the longitudinal edge of the pocket and a smaller one of about 40 MPa occurs near the lateral edge.

In the second stage, the problem with two defects placed symmetrically with the geometrical parameters from Table 1 was considered. We have considered two

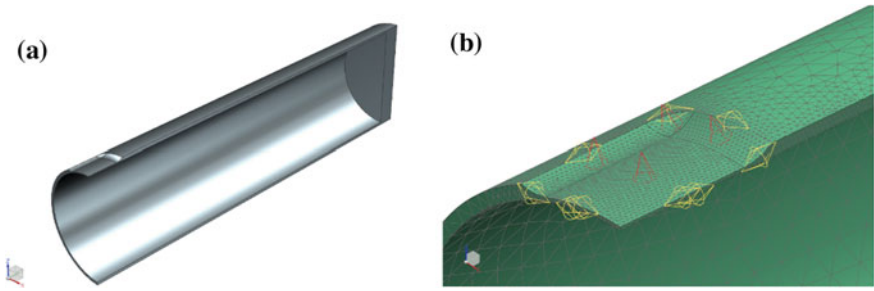


Fig. 6 Quarter model of the body, simplified due to symmetry considerations: **a** model, **b** finite element mesh in the defect zone

Table 1 Geometrical parameters for quarter model of the pipe

Parameter	Value
Tube length	2440 mm
Tube diameter (D)	323.9 mm
Wall thickness (s)	8.8 mm
Half length of the defect ($L/2$)	106.56 mm
Defect thickness (d)	6.60 mm
Half opening angle ($\alpha/2$)	28.27°

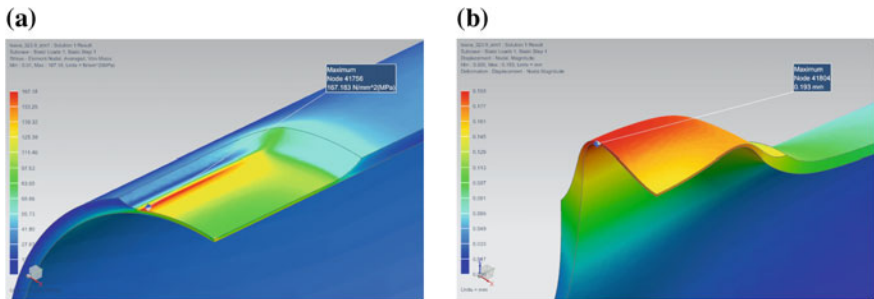


Fig. 7 Finite element solution for the quarter of the body: **a** von Mises stresses, **b** deformed shape with displacements

types of the relative defect location: symmetrical longitudinal and symmetrical circumferential.

For the case of the longitudinal defect location, two identical defects were placed symmetrically with the distance F between them (see Fig. 10a). To assess if it is necessary to machine two separated defects or a single defect but with the length equal to $2L + F$, a “double defect” (see Fig. 10b) with such length was also examined.

Figure 11 shows that for small distance between the defects (from 1 to 30% of the defect length), maximum stress values are less than in the case of a single

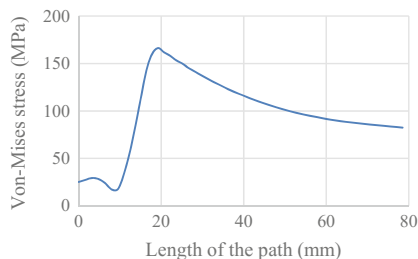
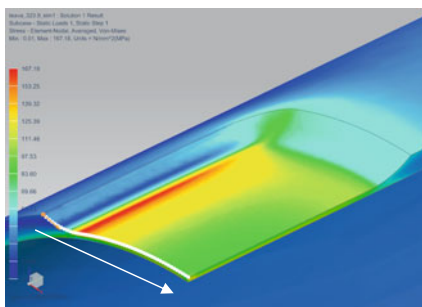


Fig. 8 von Mises stresses along the width of the defect

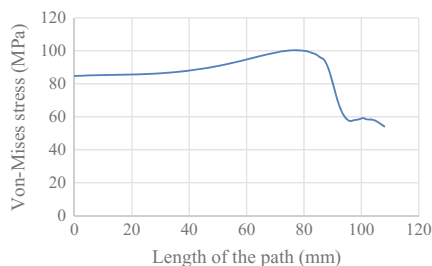
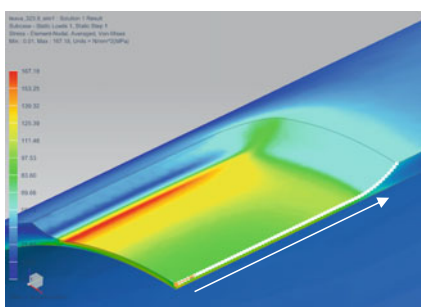


Fig. 9 von Mises stresses along the length of the defect

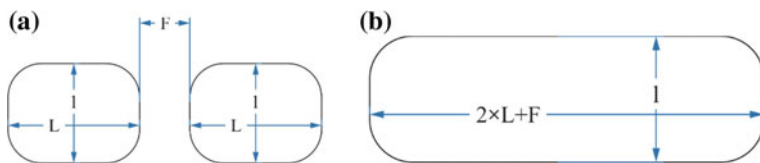


Fig. 10 Parametrization of pipe model: **a** for two defects, **b** for doubled defect

defect. For the double defect, the reverse trend appears. Nevertheless, since the distance equals about 150% of the defect length, maximum stress values become constant and it can be stated that in such a case the defects do not interact. Consequently, we can assess that, in order to eliminate additional stresses, it is better to machine two defects with moderate space between them rather than to machine a large one in case of the longitudinal defect location.

In the last case, two defects placed symmetrically in the circumferential direction with the angle A between their borders were considered. Taking into account the

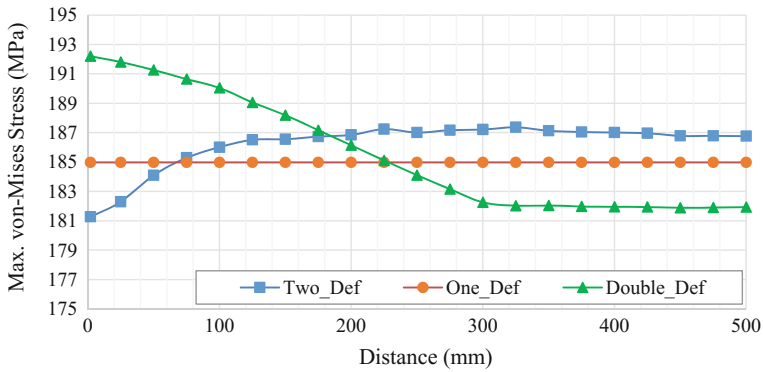


Fig. 11 Relation between maximum von Mises stress in defect zone and longitudinal distance between two VSDs

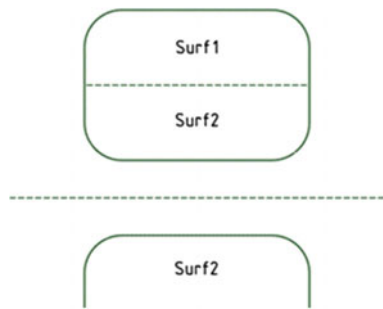


Fig. 12 Defect sub-surfaces

non-symmetrical stress distribution in the defects area for such a location, the defect surface was separated into two sub-surfaces (see Fig. 12). A “double angle defect” with the angular width equal to $2\alpha + A$ was also examined.

The results from Fig. 13 show that, for an angle between defects less than 70° , the maximum stress values concentrate on the distant edges and appear higher than in the single defect case. However, on the nearer edges, stress values are much lower than in the single defect case. For the double defect, the stress values are the same as in the case of a single defect for all the angle values. Therefore, we can state that there is no practical use in the mechanical processing two smaller defects rather than a large one in the case of the circumferential location of the defects.

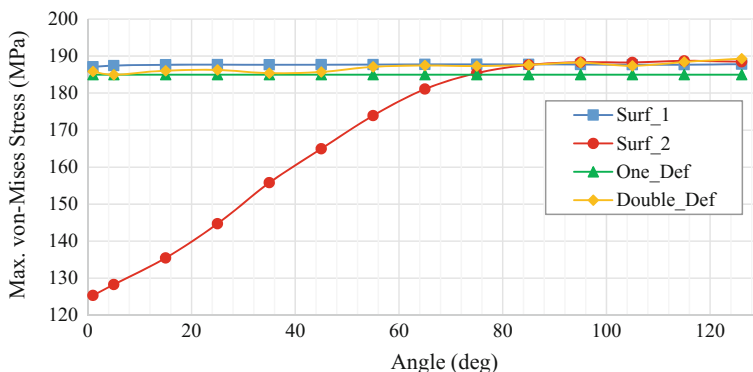


Fig. 13 Relation between maximum von Mises stress in the defect zone and the angle between borders of two VSDs

4 Conclusions

The analysis of the main criteria and procedures that can be applied to assess if the components of a colony of defects interacts, along with the finite element modeling of the interaction between two VSDs, have been performed. They have highlighted the following main issues:

- presently there is not any set of criteria and any procedure unanimously accepted used to assess if the components of a colony of defects interact;
- the criteria presently used comprise, as reference/influence parameters for the incidence of interaction between the components of a colony of defects, either their extent (axial and circumferential) and the distances (in the axial and circumferential directions) between them or the wall thickness of the pipeline on which the defects are placed;
- the concentration of stress and strain localizes in the area, where the rounded corner of the defect links with the main surface of the defect;
- in order to eliminate additional stresses, it is better to machine two defects with moderate space between them rather than to machine a larger one in the case of the longitudinal defect location;
- there is no practical use in machining two smaller defects rather than a larger one in the case of the circumferential defects location.

Acknowledgements This research was supported by the Russian Ministry of Education and Science, project No. 0110-11/2017-48 (9.4726.2017) and the Russian Foundation for Basic Research, project No. 16-08-00852.

References

1. API Standard 579:2007/ASME FFS-1:2007, *Fitness for Service* (2007)
2. ASME B31.8-2010, *Gas Transmission and Distribution Piping Systems* (2010)
3. ASME B31.4-2009, *Pipeline Transportation Systems for Liquid Hydrocarbons and Other Liquids* (2009)
4. ASME B31G-1991 & 2009, *Manual for Determining the Remaining Strength of Corroded Pipelines, A Supplement to ASME B31 Code for Pressure Piping* (2009)
5. BS 7910:2005, *Guide to Methods for Assessing the Acceptability of Flaws in Metallic Structures* (2005)
6. CSA Z662-03, *Oil and Gas Pipeline Systems* (2003)
7. Gh. Zecheru, I. Lata, Gh. Draghici, *Mecanica ruperii—Buletinul ARMR* **17**(11) (2005)

Part III
Materials Used for the Composite Repair
Systems of Transmission Pipelines

Review on Materials for Composite Repair Systems

V.P. Sergienko, S.N. Bukharov, E. Kudina, C.M. Dulescu
and I. Ramadan

Abstract The given chapter presents a review of the materials, presently employed within the composite repair systems (based on reinforcing wraps/sleeves made of polymeric materials), and intended for the areas with volumetric surface defects (also named local metal loss defects) of the transmission pipelines for the transportation of hydrocarbons (petroleum, liquid petroleum products, natural gas, liquefied petroleum or natural gas) or other fluids (water, ammonia, etc.). The categories of materials investigated are polymeric fillers (used to fill the volumetric surface defects and to reconstruct the external configuration of the pipe before repairing it), fibre reinforced composites (the main component of the repair system ensuring its mechanical strength), adhesive materials (used to bind the successive layers of the reinforced composite wrap).

Keywords Transmission pipelines · Composite repair system · (Polymeric) composite material · Filler · (Reinforcing) fibres · Adhesive

1 Introduction

Composite materials systems are presently one of the most promising repair systems intended for transmission pipelines. They offer a combination of numerous advantages, including strength, lightweight, corrosion resistance, etc. (a detailed presentation of such advantages and of the technologies used can be found in Chapter “[Comparative Analysis of Existing Technologies for Composite Repair Systems](#)”).

V.P. Sergienko (✉) · S.N. Bukharov · E. Kudina
V.A. Belyi Metal Polymer Research Institute of National Academy
of Sciences of Belarus, Gomel, Belarus
e-mail: sergienko_vp@mail.ru

C.M. Dulescu · I. Ramadan
Petroleum-Gas University of Ploiesti, Ploiești, Romania

The polymeric composite materials (PCMs) have been employed for the critical structural and repair purposes in the petroleum and oil-refining industry beginning from the early 1960s. Today there are several types of repair systems using PCMs. The differences between them are mainly the materials and technology used (see also Chapter “[Comparative Analysis of Existing Technologies for Composite Repair Systems](#)”). Among the most known brands in the European countries, we mention RES-Q (TD Williamson), Fiba Roll, Clock Spring, Diamond wrap (Citadel Technologies). The most used systems in CIS countries are Intra (KRM), GARS couplings, UKMT couplings, RCM couplings, Tekhnoplast.

The main principle of repairing the defective areas of the transmission pipelines using composite materials consists of the redistribution of the circumferential loads from the steel pipe wall by partially transferring them onto the fibres of the composite material.

As also specified in Chapter “[Comparative Analysis of Existing Technologies for Composite Repair Systems](#)”, any repair system, using composite materials, intended for transmission pipeline systems, is defined as a combination of the following elements: substrate (steel pipe repaired); surface preparation (of the substrate in the repaired area); polymeric filler (used to fill the defects and to reconstruct the external configuration of the pipe before repair); composite material wrap and its components (polymeric resin matrix and reinforcing material with fibres or a tape/band made from composite material and polymeric adhesive); repair procedure (filler and composite wrap application procedures, and verification procedures for the repair quality).

One of the standard and efficient methods of repair, using composite materials, involves the application of a three-component system that includes a reinforcing fibrous fabric, a binder in order to form a bonding between the composite and the pipe, as well as between every next wrap of the fabric and a formulation (primer) applied directly on the defective area and possessing a high compressive strength to transfer the load.

As reinforcing materials for the composite systems used for pipeline repair by wrapping may commonly serve continuous fibres, roving, tapes, cloth, as well as textile materials both woven and nonwoven, knitted and braided. Different sequence of stages can be employed at repair by the composite technology, namely: impregnation, laying, consolidation and forming.

Thermosetting resins are the most often used as adhesives/binders, among them being polyester, vinylester, epoxide, phenol formaldehyde resins and others. They are selected based on the following criteria: (i) requirements of the operating conditions of the pipeline system, (ii) type of repair, (iii) technological recommendations.

Keen interest has been paid lately to thermoplastic polymers as matrix materials intended for the composites used for pipeline repair. Their use in this field requires their refinement in what concerns their viscosity reduction and time of curing during wrapping.

2 Filler Materials

A critical element of the composite repair systems is the *material used to fill* the defect and other voids under the composite sleeve/wrap. This material transfers the load from the thin ligament of the defect and distributes it quickly and uniformly to the reinforcing wrap. The important properties of this material are modulus and compressive strength. Since the material is fully constrained under the reinforcing sleeve, compressive strength becomes the key factor to consider. The most used filler is a highly thixotropic, two components epoxy system, formulated to provide adjustability of “working time” for both warm and cold temperature applications [1].

Note that the conditions for the transmission pipelines exploitation are quite varied. There is also a large variety of composite materials with different properties, as well as different methods of their application. Hence, in addition to the recovery of the carrying and transport capacities, pipelines corrosion protection is also possible using those materials. They should meet several requirements, from which the following are the most important ones [2]:

- (1) water impermeability, preventing material pores from soil moisture saturation and thus avoiding contact between the electrolyte and the surface of the protected metal;
- (2) high adhesion to metal, preventing unsticking of the coating under local fracture and electrolyte penetration under the coating;
- (3) continuity, guaranteeing coating reliability, since coating slightest porosity would result in the formation of electrolytic cells and would trigger corrosion;
- (4) chemical stability, guaranteeing durable operation in aggressive environment;
- (5) electrochemical neutrality: separate coatings should not participate in a cathode process; otherwise, this could cause coating fracture during the performance of electrochemical protection of the metal construction;
- (6) mechanical strength needed to stand the exploitation loads applied;
- (7) thermal resistance needed to stand thermal softening during coating of “hot” objects and low-temperature embrittlement during transmission pipeline coating in winter;
- (8) dielectric properties determining the electric resistance; they are needed to avoid the formation of corrosion products; they also determine the economic effect of performing electro-chemical protection;
- (9) object protection from corrosion and chemical impacts;
- (10) properties facilitating mechanization of in situ coating deposition;
- (11) non-deficiency (wide application of sufficiently available materials);
- (12) economy (the cost of repair materials should be much lower than that of the protected object).

Neither natural nor artificial materials meet all those requirements. Hence, material selection depends on the current conditions of pipeline exploitation, availability of raw materials, technology of repair coating deposition, etc. Those factors specify the range of materials suitable for steel pipes repair and coatings [3].

The paper [4] studies the needs of transmission pipelines capital repair and specifies the basic requirements to coatings materials for deposition in field conditions. The advantages of monolayer polyurethane coatings are confirmed comparing the technical-exploitation parameters and technologies of deposition of several types of modern coatings. The basic properties of the initial materials and the “Protegol” coating are specified.

Reference [5] describes the technology of using meltable powder synthetic resins for corrosion-resistant coatings of pipelines, as well as respective deposition systems. That technology emerged in the 1950s, when the EPOK resin was used for the first time as coating. The paper also presents the use of modern synthetic resins for this purpose.

Two types of polymeric composite materials (PCMs) are used for the repair of pipeline defects: fillers and sleeve composites. PCM fillers are used to fill defects owing to metal loss along the pipe thickness (pores, voids, etc.). Sleeve PCM guarantee the recovery of the carrying and transport capacities of pipes with defects.

Various PCM are used as fillers of the in-between space of hermetical sleeves. Epoxy resins are the most popular as binders of those composites. The fillers based on polyurethane and special concrete, as well as liquid fillers as by-products of oil processing, are also known.

Usage of epoxy-based composites. In the recent decade, epoxy-based composites are mostly used to repair pipelines with different diameters. An epoxy compound is popular in oil industry as filler used for transmission pipeline repair applying the composite-sleeve technology (defects may be due to corrosion or may be of technological origin—cracks with depth amounting to 70% of the wall thickness, voids with depth amounting to 90% of the nominal wall thickness, welded joint defects, etc.). The compound is also used for the repair of concrete and metal components, undergoing significant mechanical loads during exploitation and being in contact with aggressive environment.

The most popular methods of repair using epoxy-based composites are described in Refs. [6–8]. Study [9] discusses filling and sleeve polymeric composite materials used for the repair of defects with small surface area (scratches, scores, caverns, pitting corrosion defects). Those PCM-adhesive “Monolit” (VNIIGAZ) molecule-metals of the company “Diamant-Metallplastic” GmbH (Germany), displayed high adhesion and strength during tests and exploitation. Some sleeve PCM are the following ones: flexible anisotropic rolled glass plastic (FARGP), composite spiral sleeve (CSS), carbon unidirectional band (UOL-300-1).

Patent [10] specifies a method and material for in-service pipeline repair. A compound cylindrical sleeve is mounted on the damaged section. It is supplied with upper and lower branch pipes. Circular clearance between the sleeve and the pipeline is also provided. Sleeve faces are to be sealed hermetically, and the epoxy-based composite material is fed to the circular clearance through the lower branch pipe. This is done until the PCM sticks out of the exits of the upper branch pipes. Hermetical sealing of the sleeve faces is performed using elastic gasket, and the composite is prepared from epoxy resin based on epoxy oligomer, hardener containing amide and amide-sol groups, and powder filler. The proportion is the

next: epoxy resin—100 mass units, hardener—10 to 60 mass units and powder filler—20 to 800 mass units.

Requirement to the physical–chemical and mechanical properties of modern compounds for transmission pipelines repair, using the composite-sleeve technology, as well as subsequent norms, are specified in Tables 1 and 2 [11]. The characteristics of a typical commercial filler material, used at composite systems for the repair the pipelines, are presented in Table 3 [1].

The company Shaw Ind. Ltd. (U.S.A.) patented a structure of external anti-corrosion coating of pipelines. The coating consists of epoxy primer and external shell fabricated from polyolefin. The ring space between the primer and the olefin shell is filled with a mix of epoxy resin and polyolefin, whereas the relation between the compounds varies along the thickness of the intermediate layer. Close to the primer, the material of the intermediate layer is mainly epoxy resin, while close to the external shell it is polyolefin [12].

Reference [5] describes an application of aluminium and iron powder as fillers, as well as a hardener being a mixture of polyamide resin, diethylene triamino methyl phenol, tris-(dimethyl amino methyl)-phenol and aluminium, for the preparation of epoxy-based composites. A specific combination between the components guarantees increase of fracture strength and elasticity limit [13]. To increase adhesion of the epoxy coating to the pipe metal surface, the company “Pirin Chemical Services” (U.K.) designed a reactive to protect the pipeline from corrosion. Prior to the deposition of the epoxy coating, a layer of silicon oxide of chrome or iron is deposited on the pipe external surface [14].

As study [15] proved, the account for factors significantly affecting the efficiency of stress relaxation helps to the formulation of the following requirements to fillers injected into the in-between space of hermetical sleeves:

- minimal volumetric shrinkage during hardening (polymerization) up to negative values;
- maximal elastic characteristics: Young’s modulus and Poisson’s ratio;
- high fluidity of the liquid phase for efficient filling of the in-between space;
- minimal deterioration of the elastic properties in time and under different temperature;
- resistance to aggressive environment;
- chemical and corrosion inertness with respect to pipe steels.

Table 1 Properties of the non-hardened compound (just after mix preparation) [11]

No.	Characteristic, dimensions	Norm	Test method
1	Living capacity (time of gelatin formation) under °C, min, not less than	60	Method of adhesion association
2	Dynamic viscosity after 10 min. Subsequent mixing of the components (25 °C) Pa s, not more	7.0	GOST25276-82
3	Fluidity (25 °C), mm, not less	105	PrEN 12706

Table 2 Properties of the hardened compound (hardening for 24 h within a recommended temperature range) [11]

No.	Designation of the characteristic, measurement units	Norm ^a	Test method
1	Tension strength, MPa, not less	10.0	GOST 11262-80
2	Relative extension at fracture, %, not less	0.7	GOST 11262-80
3	Elasticity modulus at tension, GPa, not less	1.7	GOST 950-81
4	Maximal compression stress, after 24 h, MPa, not less, after 7 days, MPa, not less	70.0 90.0	GOST 4651-82
5	Relative strain at maximal compression stress, %, not less	5.0	GOST 4651-82
6	Elasticity modulus at tension, GPa, not less	1.9	GOST 950-81
7	Limit strength at fracture, MPa, not less	15.0	GOST 14760-69
8	Limit strength at shear, MPa, not less	3.0	GOST 14759-69

^aAll values are obtained at test temperature of 23 ± 2 °C

Table 3 Characteristics of filler produced by WrapMaster, Inc. [1]

Filler	Compressive strength (MPa)	Elongation (%)	Shore D hardness	Open time 2:1 mix ratio
PermaPutty#FKC	95 at 25 °C 70 at 60 °C	Under 1%	Above 80	40–50 min at 40 °C 220–240 min at 0 °C

Composites based on polyurethane and combined epoxy-urethane binders. The company “T.I.B. Chemie” (Germany) developed a new two-component polyurethane, type Protogol 32–55, for underground pipelines. The new coating does not contain solvents and its polymerization time is short. High adhesion to the metal surface is observed after the end of the polymerization, while the surface has been previously cleaned by means of sand and pellet jets. The new coating does not require the use of a primer, and it can be deposited on pipelines whose operational temperature is up to 70 °C [16]. The “Denso North America” company (USA) has developed a new epoxy-urethane composite for pipeline coating, which does not contain isocyanates and cancerous resins [17].

Bitumen-polymer composites. Patent [18] describes a composite applicable in the preparation of materials for coatings of butts, welded joints, contiguities and bonds between rolled roof sheets, as well as materials for hydro-insulating coatings of foundations and pipelines. A serious technical task consists in how to increase adhesion of the composite coating to metal or concrete. The following solution to the problem posed is found: (i) the binder consists of bitumen, polymer, industrial waste oil as plasticizer and chalk as mineral filler; (ii) yet, its new feature is the contents of synthetic rubber SKD or rubber waste as polymer admixture; (iii) the component proportions are the following: bitumen 73.8–88.8 mass%; synthetic rubber SKD or rubber waste 5.5–23.5 mass%; waste of industrial oil 0.2–1.5 mass%; mineral filler

(chalk) 0.5–1.2 mass%. The composites can be used also as semi-products for the preparation of bitumen-polymer materials by dissolving the composite into bitumen melt. Bitumen-polymer binder is low cost thanks to the use of waste of industrial oils in its preparation, and the waste is not bound to regeneration.

The “Servicised Ltd.” company (U.K.) is specialized in in situ coating of pipes and fittings. The designed corrosion-resistant coatings consist of a thick layer of adhesion compound and a tough elastic band. Such insulation has high adhesive properties and resistance to cathode peeling. Cold deposition of the insulation is performed, and it is compatible totally with coal-resin-based coatings, bitumen coatings and epoxy coatings, which are deposited on in-service pipes [19].

Thus, a wide variety of filler materials, majority of which epoxy-based composites, have been developed nowadays. They are used in the efficient repair of main pipelines with corrosion-mechanical damage. However, the low resistance to cathode peeling and low impact strength are some of the basic shortcomings of epoxy materials. In this respect, specific studies of how to increase their properties and impact strength run recently. Yet, there is no evidence on the effect of thermal stresses owing to the different coefficients of thermal expansion of materials of the system “metal–epoxy composite–metal”. Note also that cyclic loads operate during transmission pipelines exploitation, and they are essential factor of epoxy composite peeling. Nevertheless, the problems of decrease of pipeline vibration at the expense of increase of the elastic-damper characteristics of epoxy-based hardening composites, have not been tackled in literature.

3 Fibre-Reinforced Materials

Application of continuous fibre fillers and matrix polymers in formation of the load-bearing layer from the unidirectional composite materials is restricted by a number of factors, including the propensity to cracking at tension in transversal direction under the pulsed inner pressure loading. To lower the probability of cracking, the reinforcing elements are used in the form of different structural types of textile materials. The structure of the reinforcing textile carcass defines the density of the fibre packing and the efficiency of achieving mechanical properties of the fibres in the composite as a whole. The structural reinforcing systems are subdivided into four types: discrete, continuous, plane weaving (2D), and spatial (3D). The structures with the continuous fibres are characterized by the highest efficiency of utilizing their properties. These structures are most typical for the wrap fibrous systems. Their shortcoming consists in the low interlayer strength. The spatial reinforcing systems are devoid of the expressed planes of the weak shear resistance, tear and cracking. Named type of the carcass is the most appropriate for the critical repair cases.

A woven fabric composite is normally a laminate comprised of a number of lamina, each one consisting of one layer of fabric embedded in the selected matrix

material. Individual fabric lamina are directionally oriented and combined into specific multiaxial laminates for the application to specific envelopes of strength and stiffness requirements. Figure 1 shows the mains type of fabrics used to obtain the composite wraps intended for pipeline repair.

The fibres most frequently used to reinforce composite materials intended for pipeline repair are glass fibres, present in over 90% of such materials. There are two types of glass fibres: E-glass (most cost-efficient and therefore commonly used) and S-glass (having a somewhat higher corrosion resistance and mechanical strength). Other reinforcing fibres used for pipes repair systems are carbon and aramid fibres, with a higher stiffness and strength than glass fibres, but also more expensive. For this reason, they are normally used for special applications. Table 4 compares the main characteristics of the different type of fibres presently in use for pipeline repair.

The composite materials used to repair pipelines are based on a polymeric resin matrix that is most commonly made of: unsaturated polyester/vinyl ester, epoxy, phenolic polymers, and polyurethane. Epoxy resin is characterised by a very good adhesion, low shrinkage, high mechanical strength, easy processing, and good chemical resistance. Nonetheless, its properties are negatively influenced by moisture and its curing is slower compared to polyester resins, which are fast processing resins with a very low cost. Phenolic matrix presents a good hardness, together with chemical and thermal resistance.

The polyurethane-based resin is compatible with different types of commercial glass and carbon fibres. The excellent intrinsic toughness of this resin leads to highly impact and fatigue-durable composites. Particularly, the combination polyurethane resin—glass fibre offers unique opportunities from the point of view of the cost-efficiency ratio. In Table 5, the properties of the most often used polymeric matrixes are presented.

The best mechanical properties in a composite depend mainly on fibre orientation, but the adhesion between the fibre and the matrix is also important. The fibres are loaded through the matrix and, to obtain a good performance, the load must be transferred effectively to the fibre, and a strong fibres/matrix bond is also required. The translation of fibre properties to composite properties depends on many factors in addition to the rule of mixtures.

Table 6 presents the typical mechanical properties of a composite material consisting of glass biaxial fibre fabric in epoxy matrix [20]. It is noted that the

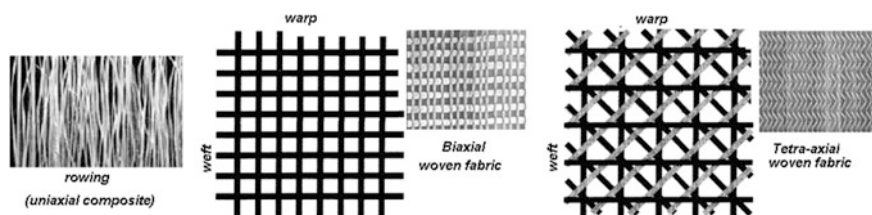


Fig. 1 Types of fibres and woven fabrics

Table 4 Comparison of fibres properties [59]

Fibre type	Tensile modulus (GPa)	Ultimate tensile strength (MPa)	Density (kg/m ³)	Strain at break (%)
E-glass	27	770–1435	2600	2.5
S-glass	33	1750	2600	2.8
Carbon	140	2350	1700	1.4–1.8
Aramide (Kevlar)	45–48	2140–2250	1400	3.3–3.7

Table 5 Properties of polymeric matrixes

Properties	Units	Epoxy	Polyester	Phenolics	Polyurethane
Density	kg/m ³	1150	1120	1.40 × 10 ³	950–1100
Modulus of elasticity	GPa	2.5	3.4	8.3	2.8
Tensile strength	MPa	60	60	50	80
Elongation	%	4	2	1	5–10
Flexural yield strength	MPa	120	113	69	470
Compressive strength	MPa	140	NA	NA	NA
Thermal expansion (20 °C)	°C ⁻¹	50 × 10 ⁻⁶	31 × 10 ⁻⁶	40 × 10 ⁻⁶	49 × 10 ⁻⁶

NA not available

Table 6 Typical mechanical properties for E-glass woven/epoxy composite [20]

Properties	The purpose for which it is used	
	Standard structural	Dual purpose (structural/adhesive)
Cured resin content (%)	33	48
Density (kg/m ³)	1800	1600
Tensile strength (MPa)	430	330
Tensile modulus (GPa)	36	19
Compressive strength (MPa)	410	340
Compressive modulus (GPa)	25	22
Flexural strength (MPa)	550	450
Flexural modulus (GPa)	26	23
Interlaminar shear (MPa)	18	26

properties of such composite can be tuned by varying the fibre volume fraction. The influence of the fibres volume is exemplified for a composite fibre glass/polyester in Table 7, where it is shown that the longitudinal modulus and the longitudinal strength increase with the rise of the volume fraction in fibres.

The values of the properties, obtained for most composite materials, greatly depend on the testing performed. Determination of elasticity modulus can be especially controversial. The stress/strain response can be nonlinear, so where and

Table 7 Effect of the volume fraction of the fibres on the composite mechanical properties [59]

Fibre's volume fraction v_f (%)	Tensile modulus (GPa)	Ultimate tensile strength (MPa)	Strain at break (%)
0 (polyester matrix)	4.1	64	2.7
12	6.63	75	2.3
21	8.2	96	2.3
32	10.2	118	2.6
44	12.3	149	3.1

Table 8 Comparative physical-mechanical characteristics of the organic, glass, carbon and basalt fibres

Property	^a Glass		^a Carbon	^a Aramid	Basalt
	E-Glass	S-2 Glass [©]	T700SC	K49	BF-3
Density (gm/cc)	2.58	2.46	1.80	1.45	2.75
Tensile strength (MPa)	3445	4890	4900	3000	4100
Tensile modulus (GPa)	72.3	86.9	230	112.4	225
Compression strength (MPa)	1080	1600	1570	200	1280
Strain to failure (%)	4.8	5.7	1.5	2.4	3.5
CTE ($10^{-7}/^{\circ}\text{C}$)	54	29	-38	-48.6	55
Softening point	846	1056	>350	>150	>980

^aThe data for Glass, Carbon and Aramid were adopted from [60]

how measurements are performed can greatly influence the results. As a result, composite materials, which may be substantially different in references, may have little or no difference in modulus. Reported differences may be entirely the result of test and calculation differences.

An original investigation in the framework of the INNOPIPES project involved studies of the vistas in using textile structures from basalt fibres in the reinforcing carcass. In contrast to the organic, glass and carbon fibres used traditionally in the repair composite wraps, the basalt ones possess from 5 to 8 times lower water absorption, higher resistance to vibration and strength against sound fluctuations, higher chemical resistance, e.g. to acidic media. Besides, basalt fibres show 15 times less weight loss as compared to the glass fibres. The comparative physico-mechanical characteristics of the fibres are listed in Table 8.

The properties of basalt fibres BF-3 produced in Russian Federation shown in Table 8 were determined by using special equipment for mechanical testing in WAT (Poland) and in MPRI (Belarus). The knitted textile structures prepared from the basalt fibres were 40 cm wide. They were saturated with an epoxy-phenolic binder that combines the epoxide resin modified by phenol formaldehyde and an aminophenolic hardener AF-22. The polymeric matrix used for preparing the repair composite on the base of basalt fibres is resistant to the action of the multiple sign-varying temperatures (from -100 to $+125$ $^{\circ}\text{C}$), impact and vibration loads, influence of different atmospheric factors, e.g. high humidity.

The composite material produced as described above for wrapping steel pipes displays the most optimal combination of mechanical, chemical and technological characteristics as compared to other known commercial composites.

4 Adhesive Materials

One of the serious problems in reconstruction of the external geometry of the pipe in the zone of volumetric surface defects is the formation of micro-cracks in the bearing layers of the pipes and interfacial delamination at temperature fluctuations in the environment due to the difference in the coefficients of the volume thermal expansion of steel and the repair composite. To solve this problem the internal sealing layer is applied. Moreover, special adhesives (primer layer) are used to increase adhesion of the composite to the pipe.

For the adhesives, the following criteria were used as guidelines [21]:

- be easy to mix and use under field conditions;
- remain workable for a minimum of 45 min at field application temperatures;
- cure within from 2 to 4 h over the range of 35–10 °C;
- have a lap shear strength of at least 4.1 MPa for both composite and steel bonds;
- be compatible with cathodic protection systems;
- be resistant to wet soils for extended periods;
- have a shelf life of at least 12 months;
- operate over a wide range of temperatures;
- be capable of 20 years durability under worst-case conditions.

Different adhesive formulations, including thin films, liquid epoxies, urethanes, and methacrylate formulations were screened to determine which material was best suited for bonding the multiple layers under worst-case operating conditions.

Among the advantages of adhesives making them more and more attractive for the customers are the following:

- the possibility to join different materials, e.g. metals, plastics, rubbers, fibrous materials, etc.;
- efficient joining of thin sheet metallic and non-metallic materials;
- improved stress distribution in the joint making it more resistant to the dynamic loading;
- simplicity and profitability of joining by adhesives;
- broadening of the range of available materials;
- growth of design possibilities;
- ameliorated corrosion resistance of the products;
- refined appearance of the product or structure.

Nevertheless, like in any other technology there are some shortcomings in using adhesives, including

- it may be necessary to employ a special surface treatment for the substrates joined in provision of durable adhesive joints operating in hostile media;
- the adhesive joints are able to withstand not very high threshold temperatures in contrast to the welded or riveted joints;
- strength and fracture energy of adhesives at tension or shear is lower than the metals have. This is why adhesives show promise in bonding thin metal plates. Adhesives may be efficient for bonding thick metal parts only when the parts glued possess rather large contact area or the adhesive used is compression sensitive.

Therefore, to attain the highest efficiency of the adhesive in the process of obtaining an adhesive joint, one should keep to a number of requirements:

- during the first stage of forming the adhesive joint, it is necessary to ensure the interphase contact between the adhesive and the substrate;
- to maintain high-performance characteristics and life of the adhesive joint the substrate should be subjected to surface pretreatment;
- to reach a robust interfacial contact, the adhesive should be used in a liquid state at the initial stage of the adhesive joint formation;
- to ensure resistance of the final item or structure to applied stresses or deformations the adhesive after application on the substrate should be evenly cured.

A broad variety of adhesives of different purposes and fields of application are carefully studied today. The materials used for making a glue layer when repairing transmission pipelines from the oil and gas industry in field conditions are based mainly on bitumen, resin, acrylate, as well as chlorinated polymers [22], epoxy-acrylate resins, epoxide and phenolic resins, and other [23]. As basis for composite materials, rubber is used more often because it can ensure elasticity and plasticity of the final composite.

Thanks to above-mentioned properties and their correlation with resistance to hostile and corrosive agents, there is a growing tendency to using rubbers as a main binder in the glue compounds. Specific properties of synthetic rubbers are the most efficiently realized in the protective elastic coatings withstanding not only chemical agents but also erosion damage, along with sign-varying deformations and temperature fluctuations [24–26].

Natural rubber. In early 1980s, Aubrey and Sherriff have proposed a material based on natural rubber, with different proportion of cross-linking agents. As cross-linking agents were used a poly- β -pinene and a modified pentaerythritol rosin ester. The prepared materials proved a good adhesion to a plane glass substrate and confirmed that the time-temperature equivalent principle could be applied to the adhesion [27].

In the field of pipeline coatings, natural rubber is usually employed for pressure-sensitive adhesives formulation. The literature presents a large number of components used in adhesive coating formulation as tackifying agents, fillers, catalysts or antioxidants [28]. Regarding the adhesion expressed as tack—the

debonding force per area of contact and expressed as N/m^2 , several conclusions can be drawn:

- tack increases with the amount of tackifier and filler up to an optimum value;
- when coumarone-indene resin is used as tackifier, the tack passes through a maximum at 60% rubber in composition;
- loop tack of silica-filled epoxidized natural rubber (25 and 50 wt%) composite materials with coumarone—indene as the tackifying resin were investigated using, highest values of tack being reported for the samples with 20 and 40 phr silica;
- it is important to keep the molecular weight of rubber at optimal values, near $6.89 \times 10^4 \text{ kg kmol}^{-1}$; high value of molecular weight leads to high viscosity, with a negative impact over adhesion performances [28, 29].

Generally, the adhesion of natural uncured rubber to metal is weak. To increase the direct adhesion between metallic substrate and natural rubber is necessary to use silane coupling agent with functional group as amino, thiol, glycidoxo, and isocyanate groups or other coupling agents which can modify the polarity at the interface [30]. The investigation of Sangaet et al. revealed that high adhesion strength was obtained in the presence of the amino functional groups. Moreover, the adhesion strength was optimized and cohesive failure occurred when 3-(trimethoxysilyl) propylamine was used to modify the CS surface properties [30].

Silicone rubbers. The adhesion between silicone rubbers and metal was studied by Picard et al. [31]. The silicone rubbers show good resistance against UV, high temperature, solvents and ozone exposure and are typically used as coating with silica filler. A strong adhesion of the silicone rubber coating to metallic substrate can be assured by covalent bonding. In order to obtain this type of bonding, it is necessary to use a primer. Generally, as primer can be used blends of vinyl-based organosilane and organotitanate in organic solvent [31, 32]. Higher adhesion performances were obtained in the case of a primer composed of a vinyl-functionalized silicone resin, vinyltrimethoxysilane and organotitanate compounds as catalysts of hydrolysis/condensation reactions. The explanation of this behaviour resides in the chemical compatibility between the primer component and the silicone rubber. It becomes clear that the adhesive strength in the interface can be ameliorated by improving the mutual diffusion of the chains between the primer film and elastomer surface (see Fig. 2). It is necessary that both components must be polymer type, chemical compatible, and mutual miscible [31].

At the same time, it was observed that the ratio of alkoxy/hydroxyl functions in silicone resins does not influence the coating adhesion to metal [31]. Depending on the composition of the used primer, the adhesive strength was in range of $1.2\text{--}9.8 \text{ N mm}^{-1}$ [9]. Moreover, literature shows a wide range of compounds, which can be used in primer formulation to increase the adhesion of silicone elastomers [33].

Nitrile Rubber. Nitrile rubber, another type of rubber, used in coating composite materials formulation, has a superior resistance to grease, oil, plasticizers, organic solvents, both aliphatic and aromatic, relative to other polymer and a

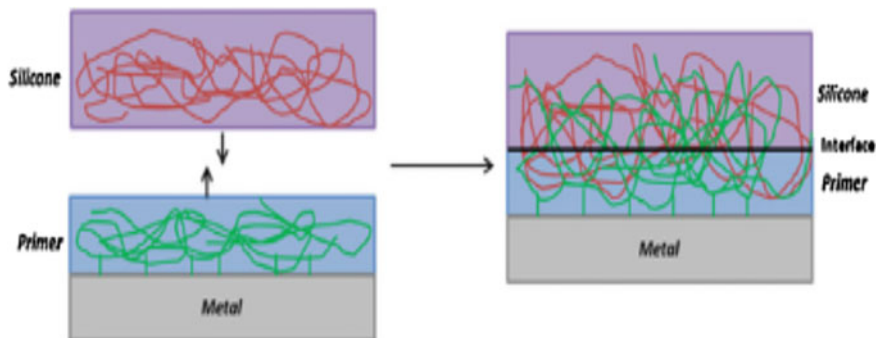


Fig. 2 Mutual diffusion of the primer and elastomer chains [32]

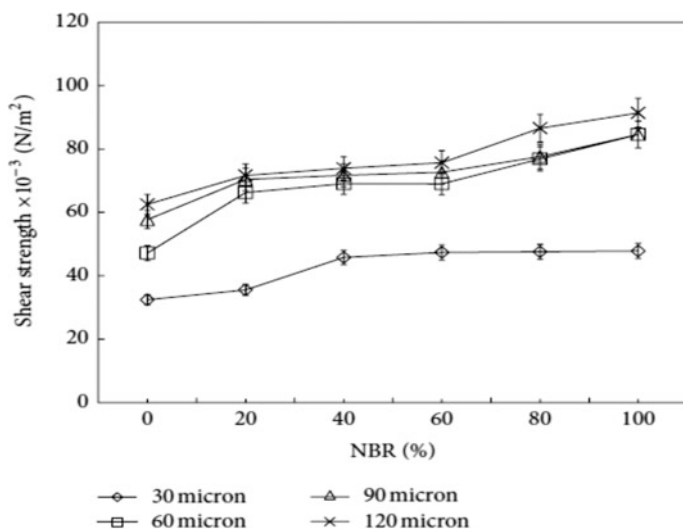


Fig. 3 Shear strength variation with nitrile rubber content in nitrile/standard rubber mixture at various coating thicknesses [34]

high-temperature resistance. In combination with phenolic or epoxy resins, nitrile rubber shows good adhesion performances, especially to polar surfaces. To keep the adhesion of the nitrile rubber coating to metallic substrate a high content of nitrile rubber in the composition of the prepared composite coating is recommended [34]. Shear strength variation with nitrile rubber content in nitrile/standard rubber mixture, at various coating thicknesses is present in Fig. 3.

On the other hand, it was observed that the adhesion property increases with the coating thickness. This behaviour can be associated with the presence of higher amount of adhesive, which enhances the viscoelastic response of the blend adhesive, simultaneously with the mechanical interlocking and anchorage of the adhesive in the pore and irregularities in the adherent [34].

To improve physical–mechanical properties of the glue joints based on thermoplastic rubbers (nitrile rubber), it is useful to introduce, e.g., a resin able to impart stickiness (the most often, colophony) and a thermosetting resin (heat-activated alkyl-phenolic in 10–30% amount), metal oxides and other traditional additives [35].

Styrene-Butadiene (SB) Rubber. This type of rubber has low building tack. However, because it has also excellent substrate compatibility, SB rubber is used in coating composite formulation in presence of tackifying resins, low molecular weight polymers, or plasticizers, or master batch processing. Analysing composite materials starting from styrene butadiene rubber, divinylbenzene as cross linker, bisphenol-A as resin and montmorillonite modified with a quaternary ammonium salt, it was observed that various content in montmorillonite leads to a better dispersion inside the epoxy matrix and, therefore, improves the interfacial adhesion [36].

Investigations on mechanical properties of an epoxy coating prepared, starting to modified *epoxy resins* with different ratios of synthesized epoxy terminated *polybutadiene* (ETPB), were carried out [37]. Polybutadiene rubber has a low chemical compatibility with epoxy resins. The adhesion performances of epoxy resin to the metallic substrate were improved by addition of the ETPB concentration, due to carbonyl groups formed during the chemical modification of epoxy resin. These modifications in the epoxy resin structure lead to polarity increase, enabling the interaction between substrate and the composite material [37].

Of specific practical interest are the pressure-sensitive adhesives. Their important feature is the ability to experience the state of a high viscous-flow just as during formation of the adhesive joint, so in operation [25]. The pressure-sensitive adhesives (PSAs) constitute the materials forming adhesive bonds with the surface of the element being glued under temperatures of about 20–30 °C, immediately after a slight pressure application. All PSAs are based on a polymer. The rubbers like isoprene or natural polybutadiene or other, as well as chlorinated polymers (PCVC, CCPE, PCP, etc.) are intensively applicable today as the base for the PSAs [22]. In addition to the polymer binder, the PSAs include different agents to improve tackiness, since rubber is insufficiently sticky by itself [38]; also, the components are added to refine the cohesive tack as well as fillers and antipyridines [25].

Other polymers. A study on a composite material synthesized starting from *polychloroprene rubber* as polymer matrix, phenolic resin and silicon dioxide shows the increase of tackifier resin. Silicon dioxide in the adhesive formulation reduces the shear strength of metal-to-metal adhesive joints down to 74.16% [39].

The *polyurethanes* have the advantages of low viscosity, excellent bonding with the matrix material without special sizing of the fibres, relatively low price and fast reaction time [40–43]. Polyurethanes themselves offer good adhesion to a number of substrates due to their elasticity and structural properties [44]. There are several inferior properties of waterborne polyurethanes (low mechanical strength, high reactivity of isocyanate groups toward water and chemical resistance) limiting polyurethane applications [44–46]. To increase the qualities of polyurethane coatings is necessary to compatibilize the organic and inorganic phases [47].

That means to use compounds able to facilitate covalent bonding of the polyurethane coating to metallic substrate. The incorporation of alkoxy silane end groups or hydrotalcites in the polyurethane chains will modify bonds polarity, improving the adhesion of polyurethane coating to pipeline substrate [44, 47]. Sardon considers that 5–15 wt% alkoxy silane is the optimal range to increase the adhesion, without making the coating too rigid, unable to adhere to the substrate phases [47].

Epoxy adhesives. Numerous epoxy adhesive compositions having a wide range of curing time and conditions (hot or cold cured) have been developed lately. They are designed to glue metallic and composite materials, as well as glass and carbon plastics in the on-line and field conditions. Epoxy adhesives are characterized by the minimal water absorption as compared to other thermosetting materials, universal adhesive and technological properties. Adhesives fill the clearances from 0.3 to 0.5 mm, while keeping shear strength of the adhesive joint not less than 14.0 MPa at 20 °C and 1.8 MPa under 150 °C. Adhesives are durable within the temperatures from –60 to +125 °C. The adhesive joints formed by the glue filling are waterproof, resistant to the tropical and fungi environments, and lasting temperature effects until 125 °C [48].

Epoxy adhesives of grades UP-5-177 and UP-5-177-1 [48] may be used to glue surfaces of metal and glass fibre structures in underwater conditions at 0–35 °C. They are also good at impregnation of the glass cloth patches glued onto damaged areas of metal and glass fibre structures on the moist surface or in aqueous medium. They ensure a glass fibre bending strength of 300–400 MPa, when cured in air for 7 days, and of 200–300 MPa, if cured in water at 20 °C for 7 days.

Adhesive “Aqua”, based on modified epoxide oligomers, is recommended to glue both metal and non-metallic surfaces of structural materials (glass fibre, plastics, ceramics) and to heal damaged areas (cracks, dimples, voids) in repairing metallic structures with humid or underwater surfaces under the temperatures from –5 to +35 °C [23, 49–51]. To conduct repair works on humid surfaces, acrylate glues of “Sprut” series are highly efficient [23].

The materials based on epoxy resins of the types “REM-steel”, “REM-aluminium” and “PGR-4” (Russia) are recommended for repair works on the transmission pipelines from the oil and gas industry. They are durable for more than 30, 60 and 120 min under 10–35 °C and their resistance to static bending is 40, 30 and 81 MPa, respectively, in these conditions. Their compositions are based on epoxy oligomers and also contain 65 ± 5 mass% of fine-dispersed ingredients: REM-steel containing stainless steel powder; REM-aluminium with aluminium powder [23]. Potting compounds are also successfully used for repair of the grades “Abaterm” and “Unigerm” (Russia).

The compound adhesives of the “Anatarm” type are the cold-cured filled compositions characterized by their consistency from the flowing till the paste-like state, having cure rate from 24 to 48 h at 20 °C, whereupon reaching their maximal strength. As the base for the compound, adhesives usually serve as modified epoxy resins, cured by amine compounds having various reactivities. Vitality of adhesives is from 10 to 60 min, resistance to a uniform tear under 20–25 °C is 25–35 MPa. The compound adhesives show high adhesion to various substrates (metals and

alloys, ceramics, plastics and other), have required hardness in a solid state and may be subjected to machining [52]. A series of compounds displaying elevated elasticity has been developed for repairing trunk oil and gas pipelines operating without stoppage (“Abaterm-218”) on the base of epoxy-acrylate products with addition of reinforcing mineral and metal fillers.

Intensive R&D works are performed in the field of the paste and fluid cold-cure epoxy compounds for bonding and repair of different surfaces by such well-known companies as Weicon (F.R.G.), 3M Innovative Properties (U.S.A.) and Hexcel Corporation (U.S.A.). Weicon, e.g., has developed two-component epoxy adhesives of cold curing that do not contain solvents, while possessing high strength of metal splices, as well as polymer composites, the materials reinforced by glass and carbon fibres, different plastics, ceramics, glass and so on. Novel adhesives, to name but a few: WEICON Easy-Mix S 50, WEICON Easy-Mix N 50/5000, WEICON Easy-Mix Metal, WEICON Epoxy Minute Adhesive, are saving and easy to use (due to special packaging with a dozer). They are characterized by a wide range of advantageous properties, including different vitality times from 3–4 to 45 min, cure rate from 1 to 2 days, viscosity (from fluid to pastes) able to serve for different purposes, including vertical surfaces. Named adhesives are operable within the temperature range from -50 to $+80-145$ °C [48].

Specialists of Hexcel Co. have developed a two-component epoxy adhesive of Redux 870 A/B-type intended for bonding fibrous composites and metals. This adhesive is cured at 23 °C for 5 days, displays perfect shear strength of the splice at room temperature and elevated ones.

Various epoxide adhesive compounds have been elaborated in the 3M Innovative Properties. Proposed by them, two-component adhesive compositions have the first component in the form of epoxy oligomers, while the other is a mixture of two hardeners in combination with the agents improving impact strength (usually particles of the nucleus-shell structure), and a filler with the particle size 0.5–500 μm . Named adhesive compounds are characterized by a perfect shear strength within a wide temperature range, from -55 to 135 °C [48].

Widely applicable in the repair technologies are today the high-filled composite-based adhesives with a high metal and ceramic content. As for the halogen paste compositions, they need fine refinement of titanium, special steels and aluminium. The share of high-dispersed fillers in the composition may reach 85%. The origin of interactions between the polymers and highly reduced metal particles consists in enveloping particles by the polymers and creation of the complex polymer chains to provide for a strong adhesion of the composites [53]. Application of the paste-like composites on the metal, plastic or ceramic surfaces makes possible to seal damaged areas, built-up worn-out patches, heal corrosion or erosion defects. Upon blending and application of the paste compositions, they solidify within 2–3 min in natural conditions (“Rapid”, Russia) or 2–3 h (Standard, Russia). After hardening, the high-filled composites acquire such metal properties as colour, structure, possibility of machining, including grinding, milling drilling, polishing, and coating application. These compositions demonstrate new qualities, among which the main one is corrosion resistance [53].

The above-mentioned diversity of properties of adhesives provides the advantage of choosing an adhesive from the whole assortment that will comply with all technical requirements imposed on adhesive joints of a respective pipeline repair system.

5 Conclusions

The research literature offers a broad description of the materials used for repairing pipelines, including fillers, fibre-reinforced materials, binders/adhesives, sealing materials, etc. Composite materials on the polymer binders are the most promising in this sphere. Their analysis has proved that the composites based on epoxy resins or their combinations with other resins or silicates are preferable in providing the most efficient repair of the transmission pipelines subjected to mechanical/corrosion damage.

A wide variety of filler materials being the most of all epoxy-based composites, have been developed nowadays. They are used in the efficient repair of main pipelines with corrosion/mechanical damage. However, the low resistance to cathode peeling and low impact strength are some of the basic shortcomings of epoxy materials. Note also that cyclic loads operate during pipeline exploitation, and they are essential factor of epoxy composite detachment. Nevertheless, the problems of decreasing the pipeline vibration at the expense of increase of the elastic-damper characteristics of epoxy-based hardening composites have not been tackled in literature.

The most widely used adhesives in repair technology are polymeric composites, based on epoxy resins and rubbers. The increase of operational properties of adhesives is achieved by modifying the main binder, as well as the introduction of a number of fillers and corrosion inhibitors.

Finally, it has to be stated that fibre-reinforced composite materials are typically *anisotropic* materials, and their mechanical properties have directive dependence. Such materials are often *orthotropic* (with three orthogonal planes of micro-structural symmetry) or *transversely isotropic* (having a single material direction and an isotropic response in the plane orthogonal to this direction); an *isotropic* material response is independent of orientation [55–57].

Accordingly, while an isotropic material is characterised only by *two* independent elastic constants (Young's modulus, E , and Poisson's ratio, ν), an orthotropic material has *nine* such constants: E_i —Young's modulus in direction i ($i = 1, 2, 3$); ν_{ij} —Poisson's ratio, representing the ratio of a transverse strain to the applied strain in uniaxial tension; G_{ij} —shear moduli, representing the shear stiffness in the corresponding i - j plane. A transversely isotropic material needs only *five* independent elastic constants for its characterisation, while a fully anisotropic material would require, in the most general case, 21 independent elastic constants [55].

Consequently, any supplier or manufacturer of a composite repair system must provide the following information: type of the composite material (anisotropic,

orthotropic, transversely isotropic, isotropic); the independent elastic constants for the composite material and the necessary tests to obtain the values of these constants.

The standards presently in use (ASME PCC-2 [58] or ISO 24817 [61]) impose the definition of the following properties for the composite material (see also Chapter “Development of an Experimental Programme for Industrial Approbation”): tensile modulus, strain to failure and strength in the axial direction; Poisson’s ratio in the circumferential direction (i.e., load direction circumferential, contraction axial); shear modulus.

It is also possible to estimate the properties of a composite material based on the known properties of its components (reinforcing fibres and polymeric matrix). A methodology for such assessment can be found in [57].

References

1. Wrap Master Inc., *Perma Wrap Instalation Manual*. <http://www.wrapmaster.us/>
2. M.V. Kuznetsov, V.F. Novoselov, P.I. Tugunov, V.F. Kotov, *Anti-Corrosion Protection of Pipelines and Reservoirs* (University Textbook, Moscow, Nedra, 1992). (in Russian)
3. L.P. Skugorova, *Materials for the Construction of Gas-Oil Pipelines and Depositories*, 3d revised edition (University Textbook, Moscow, Neft i Gas, 1996), p. 350 (in Russian)
4. Ya.A. Serednitski, O.F. Itkin, Materials for en-route and basic insulation and oil-gas pipelines. *Neft i Gaz Prom.* **5**, 48 (1999) (in Russian)
5. J.G. Dickerson, Usage of melted epoxy resins for pipeline protection. FBE evolves to meet industry need for pipe line protection. *Pipe Line and Gas Ind.* **3**, 67 (2001)
6. Patent No. 2008118394, Russia (2008) (in Russian)
7. Patent No. 2007125125, Russia (2007) (in Russian)
8. Patent No. 2258725, Russia (2003) (in Russian)
9. Instruction for the repair of damaged pipes of main pipelines using polymer composite BCH 39-1.10-001-99, OAO “Gasprom”, vved. (2000) (in Russian)
10. Patent No. 2251047, Russia (2004) (in Russian)
11. New and traditional epoxy materials. *Epoxy Compounds “Smel”*. Moscow, EPITAL (2013). <http://www.epital.ru/tube/smel.html> (in Russian)
12. Patent No. 5300336, USA (1994)
13. Patent No. 2184132, Russia (2002) (in Russian)
14. *Industrial* **4**(1), (1986)
15. V.I. Mahnenko, E.A. Velikoivanenko, A.S. Milenin et al., Admissible pressure of fillers for hermetical sleeves used for the repair of main pipelines. *Avtom. Svarka* **8**, 25 (2011). (in Russian)
16. Polyurethane coating developed for corrosion protection. *Pipeline and Gas J.* **3**, 12 (1995)
17. Epoxy-urethane insulation for pipelines. New products and literature. *Pipeline and Gas J.* **5**, 14 (1992)
18. Patent No. 2184751, Russia (2002) (in Russian)
19. Serviuap’s pipeline protection system. *Water and Waste Treat (Or. Brit.)* **5**, 46 (2000)
20. *Composite Materials Handbook. Polymer Matrix Composites Materials Usage, Design, and Analysis*, vol. 3 (Department of Defense Handbook, U.S.A. 2002)
21. D.S. Lesmana, *Long Term Durability of Composite Sleeve Repair and its Application as a Permanent Pipeline Repair in Indonesia, Petromin-Pipelinier*, January–March (2013). <http://www.pm-pipelinier.safan.com>

22. S.G. Niziev, Protecting pipes from corrosion using modern insulation coatings factory and field application. *Territory Neftegaz* **6**, 24 (2004). (in Russian)
23. A.P. Petrova, V.V. Kulikov, Properties of adhesive materials used in the repair and reconstruction works. *Adhesives. Sealants. Technol.* **8**, 2 (2008). (In Russian)
24. A.L. Labutin, *Anti-corrosion and Sealing Materials Based on Synthetic Rubbers*, vol 257 (Leningrad, Chemistry, 1982) (in Russian)
25. A.E. Zaikin, S.Yu. Sofina, O.V. Stoyanov, Polymer adhesive tape for anticorrosive isolation of pipelines. *Bull Kazan Univ Technol.* **6**, 98 (2010) (in Russian)
26. A. Pizzi, K.L. Mittal, *Handbook of Adhesive Technology*, 2nd edn. (Marcel Dekker Inc. 2003)
27. D.W. Aubrey, M. Sherriff, *J. Appl. Polym. Sci.* **18**, 2597 (1980)
28. I. Khan, B.T. Poh, *J. Polym. Environ.* **19**, 793 (2011)
29. I. Khan, B.T. Poh, *Mater. Des.* **32**, 2513 (2011)
30. J. Sang, S. Aisawa, K. Miura, H. Hirahara, O. Jan, P. Jozef, M. Pavol, *Int. J. Adhes. Adhes.* **72**, 70 (2017)
31. L. Picard, P. Phalip, E. Fleury, F. Ganachaud, *Prog. Org. Coat.* **87**, 250 (2015)
32. L. Picard, P. Phalip, E. Fleury, F. Ganachaud, *Prog. Org. Coat.* **80**, 120 (2015)
33. L. Picard, P. Phalip, E. Fleury, F. Ganachaud, *Prog. Org. Coat.* **87**, 258 (2015)
34. B.T. Poh, J. Lamaming, G.S. Tay, *J. Coatings*, Article ID 369352 (2014)
35. A. Beiersdorf, Adhesive tape and its use. Germany Patent Proposal No. 19840361, 09 Mar 2000
36. M.A. Ahmed, U.F. Kandil, N.O. Shaker, A.I. Hashem, *J. Radiat. Res. Appl. Sci.* **8**, 549 (2015)
37. H. Yahyaie, M. Ebrahimi, H.V. Tahami, E.R. Maf, *Prog. Org. Coat.* **76**, 286 (2013)
38. K. Shibata, Y. Tanaka, Pressure-sensitive rubber adhesive and pressure-sensitive adhesive sheet made using the same. USA Patent No. 6518355, 11 Feb 2003
39. J. Lasprilla-Botero, M. Álvarez-Láinez, D.A. Acosta, *Int. J. Adhes. Adhes.* **3**, 58 (2017)
40. L.M. Paim, J.M.L. dos Reis, H.S. da Costa Mattos, Analysis of a glass fibre reinforced polyurethane composite repair system for corroded pipelines at elevated temperatures. in *IV International Symposium on Solid Mechanics*. MecSol, Porto Alegre, Brazil (2013)
41. B.S. Chiou, P.E. Shoen, *J. Appl. Polym. Sci.* **83**, 212 (2002)
42. J. John, M. Bhattacharya, R.B. Turner, *J. Appl. Polym. Sci.* **86**, 3097 (2002)
43. S. Desai, I.M. Thakore, B.D. Sarawade, S. Devi, *Eur. Polym. J.* **36**, 711 (2000)
44. Y.H. Han, A. Taylor, M.D. Mantle, K.M. Knowles, *J. Non-Cryst. Solids* **353**, 313 (2007)
45. B.K. Kim, J.S. Yang, S.M. Yoo, J.S. Lee, *Colloid Polym. Sci.* **281**, 461 (2003)
46. H. Sardon, L. Irusta, M.J. Fernández-Berridi, J. Luna, M. Lansalot, E. BourgeatLami, *J. Appl. Polym. Sci.* **120**, 2054 (2011)
47. H. Sardon, L. Irusta, A. González, M.J. Fernández-Berridi, *Prog. Org. Coat.* **76**, 1230 (2013)
48. I.A. Sharova, Domestic and foreign experience in the development of epoxy adhesives of cold-setting. *Electron. Scientific J. Proc. VIAM* **7** (2014)
49. http://viam-works.ru/ru/articles?art_id=684 (in Russian)
50. S.N. Gladkikh, *Adhesives. Sealants. Technol.* **8**, 6 (2007). (in Russian)
51. S.N. Gladkikh, L.N. Kuznetsova, *Adhesives. Sealants. Technol.* **1**, 17 (2004). (in Russian)
52. S.N. Gladkikh, V.M. Kolobkova, E.N. Basharina, *Adhesives. Sealants. Technol.* **7**, 813 (2006). (in Russian)
53. V.S. Smirnov, N.N. Parakhina, A.F. Murokh, Z.S. Khamidulova, V.I. Milov, D.A. Aronovich, I.P. Rogacheva, A.P. Sineokov, E.F. Knyazev, The use of adhesives in the repair of operating gas pipelines. *Adhesives. Sealants. Technol.* **9**, 22 (2009). (in Russian)
54. O.M. Ivantsov, B.I. Miroshnichenko, L.A. Paley, *Pipeline Repair Technology*. <http://www.eprussia.ru> (in Russian)
55. P. Kelly, *Solid Mechanics, Part I, Section 6.2. Anisotropic Elasticity*. <http://homepages.engineering.auckland.ac.nz/pkelo15/SolidMechanicsBooks/>
56. C.A. Felippa, E. Onate, Stress, strain and energy splitting for anisotropic elastic solids under volumetric constraints. Report CU-CAS-02-09, Centre for Aerospace Structures (2002)
57. Ch. Decolon, *Analysis of Composite Structures* (Elsevier, 2002)

58. ASME PCC-2, *Repair of Pressure Equipment and Piping. Part 4, Non-metallic and Bonded Repairs* (2015)
59. H. Andersson, D. Vysochinskiy, *Reinforcement of Existing Steel Pipes Using Composite Materials—High Temperature Applications*, Master's Thesis, CHALMERS University of Technology, Göteborg, Sweden (2008)
60. R.L.I. Hausrath, A.V. Longobardo, High strength glass fibres and markets, in *Fibreglass and Glass Technology: Energy-Friendly Compositions and Applications*, ed. by F.T. Wallenberg, P.A. Bingham (Springer, New York, 2011)
61. DD ISO/TS 24817, *Petroleum, Petrochemical and Natural Gas Industries—Composite Repairs for Pipework—Qualification and Design, Installation, Testing and Inspection* (2006)

Techniques for Non-destructive Material Properties Characterisation

Evgeny N. Barkanov, M. Wesolowski, P. Akishin and M. Mihovski

Abstract Universal non-destructive techniques, adapted or developed for an effective and accurate characterisation of mechanical properties of composite materials, used in the advanced repair systems of pipelines with volumetric surface defects, are presented. There is static approach using three-points-bending tests and two dynamic methods: impulse excitation and inverse technique based on low-frequency vibrations. An experimental evaluation of the elastic material properties of laminated composites has allowed to validate the examined non-destructive techniques, to demonstrate their simplicity and reliability as well as to define their advantages and limitations.

Keywords Non-destructive characterisation · Three-points-bending test · Impulse excitation method · Inverse technique · Vibration test · Laminated composites · Elastic material properties

1 Introduction

Modern composite materials have promising perspectives for an application in the advanced composite repair systems of pipelines with volumetric surface defects. The technical data of composites could be estimated by using conventional fracture methods [1, 2], ultrasonics [3–5] or mixed numerical-experimental techniques using low-frequency vibrations [6–8].

The static measurements to determine the stiffness parameters of compositematerials are based on the direct measurements of strain fields. Boundary effects,

E.N. Barkanov (✉) · M. Wesolowski · P. Akishin
Riga Technical University, Riga, Latvia
e-mail: barkanov@latnet.lv

M. Mihovski
Institute of Mechanics of Bulgarian Academy of Sciences, Sofia, Bulgaria

sample size dependencies and difficulties in obtaining homogeneous fields of stresses and strains are some of the most serious problems. However, the main shortcoming is their destructive evaluation. Traditionally, at least three separate static tests should be performed in order to measure four elastic constants of unidirectional laminate. For the properties such as shear moduli, the quasi-static tests very often yield poor results.

Two main difficulties characterise an application of ultrasonic methods. First, many relevant materials have high damping properties, so that it is hard to obtain strong ultrasonic transmission. This is why the stiffness constants of thin unidirectional plates are more investigated by ultrasonic methods for graphite/epoxy, ceramic matrix and glass fibre composites. In the cases of non-unidirectional materials and when the plate thickness becomes important (20 mm), the ultrasonic immersion technique loses its accuracy because of attenuation due to damping and diffraction. Second, many of the materials under study are composites of one kind or another with some type of structure in millimetre range. This can cause significant dispersion of sound waves with wavelengths below a few millimetres, which often turn out to be the order of magnitude of the wavelengths used in conventional ultrasonic testing.

The general idea of the mixed numerical–experimental technique by using low-frequency vibrations is minimisation of the error functional, which describes a difference between the experimental and numerical parameters of structural responses. This approach has considerable advantages for characterisation of the mechanical properties of composite materials mostly due to its non-destructive character that enables many repeated tests on the same specimen. Moreover, for some types of materials, like composites, it is important to avoid introducing damage in the test specimen. The mixed numerical–experimental technique provides more flexibility and less restriction in a choice of the test specimen geometry. By using this approach, the in-plane mechanical properties are always evaluated without major discrepancies for laminated single-material plates. However, for thick laminated plates requiring characterisation of the out-of-plate material properties and laminated plates made of different materials, considerable difficulties appear.

The present study is devoted to universal non-destructive techniques, adapted or developed for characterisation of the mechanical properties of composite materials, used widely in the advanced repair systems to bring an efficiency of the damaged section of pipeline up to the level of undamaged. Static approach using three-points-bending tests and two dynamic methods: impulse excitation and inverse technique based on low-frequency vibrations have been successfully applied for the non-destructive material properties characterisation of carbon/epoxy prepreg (SEAL® Texipreg HS 160 RM) panels to demonstrate their simplicity, reliability and accuracy as well as to define their advantages and limitations.

2 Non-destructive Techniques

Three methods, namely the static approach using three-points-bending tests, the impulse excitation method and the inverse technique based on vibration tests could be used for an accurate and reliable non-destructive characterisation of the mechanical material properties. It is necessary to note that two first approaches are applied only for characterisation of the elastic material properties but the last approach could be successfully used for identification of the elastic, hysteretic and viscoelastic material properties in wide frequency and temperature ranges [9].

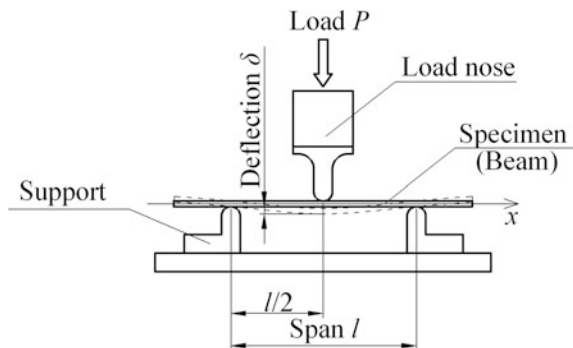
2.1 Three-Points-Bending Test

Non-destructive static approach based on the three-points-bending tests [10] and beam-like specimens (Fig. 1) is applied for determination of their elastic material properties. The maximum deflection of the simply supported beam with a rectangular cross-section is at $x = l/2$ and is given by Timoshenko and Gere [11]

$$w_{\max} = \frac{Pl^3}{4bh^3E} \equiv \delta \quad (1)$$

where P is the applied load, l is the span length, b and h are the width and thickness of the beam, E is the Young modulus of the beam and δ is the measured centre deflection of the beam. This expression can be used for determination of the Young modulus of material in terms of the measured centre deflection, applied load and geometry of the beam. In order to keep this approach non-destructive, it is important to ensure the deflection δ fully recovered at the end of each bending test. For this reason, the static approach is only applicable for the elastic behaviour of materials, which can be obtained usually for the strains less than 0.5%.

Fig. 1 Three-points-bending test



For the need of the present study, Eq. (1) can be rearranged to the following form:

$$\frac{\delta}{Pl} = \frac{1}{4bh^3E} l^2 \quad (2)$$

Set of three-points-bending tests carried out at different values of span l will generate series of values δ_i/Pl_i , where i denotes the subsequent span lengths. The plot demonstrating the dependence of δ_i/Pl_i on l_i^2 gives a straight line which slope is equal to

$$g = \frac{1}{4bh^3E} \quad (3)$$

from which Young modulus is calculated as

$$E = \frac{1}{4bh^3g} \quad (4)$$

By another way, Eq. (1) permits one to derive the Young modulus without subsequent Eqs. (2)–(4), i.e.

$$E = \frac{Pl^3}{4bh^3\delta} \quad (5)$$

According to the standard rules, this result can be averaged in the form

$$E = \frac{\Delta Pl^3}{4bh^3\Delta\delta} \quad (6)$$

where ΔP , $\Delta\delta$ denote the respective increases in the linear range [12]. As a result, specification of different span lengths for the beam-bending test is unnecessary.

It is necessary to note that systematic errors arise in this approach especially during the span length measurements. To decrease these errors, tests should be performed for a possible high number of spans. In contrary, the high number of spans will increase the number of experiments and the time needed for an estimation of Young modulus. Therefore, a compromise must be found between the desired accuracy and time spent to perform all the experiments.

2.2 Impulse Excitation Method

Vibration test, based on the impulse excitation [13], is adopted for determination of the elastic properties of beam-like specimens (Fig. 2). This method, originally developed for the testing of heavy concrete specimens, can be applied for a

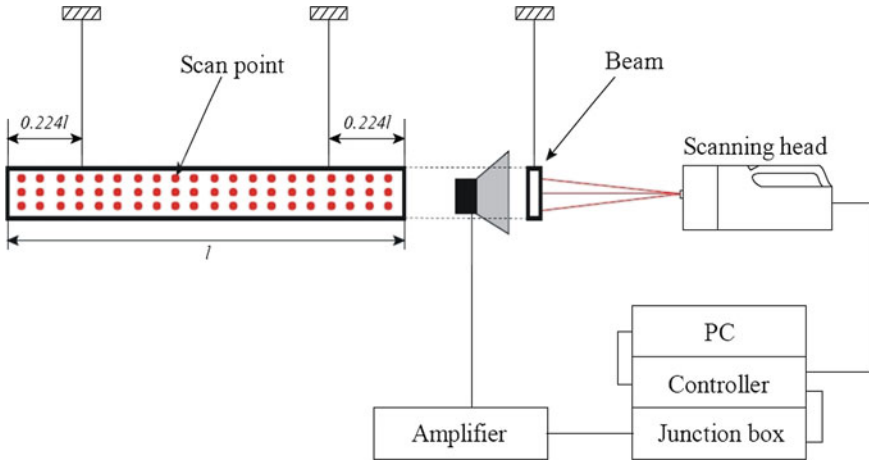


Fig. 2 Experimental setup, used in the impulse excitation method

lightweight structure providing the non-contact vibration excitation and sensing, so that no additional mass will corrupt the resonance frequencies. Beam-like specimens, used in this method, have specific resonances that are determined by the frequency equation [14]. In order to compute elastic properties, it is necessary to establish dimensions, density and experimental fundamental frequencies in bending and twisting of the beam with free-free boundary conditions.

Using the fundamental frequency in bending, the Young modulus in the longitudinal direction of the beam can be calculated as follows:

$$E = 0.9465 \frac{\rho f_b^2 l^4}{h^2} T \tag{7}$$

where ρ is the density, f_b is the fundamental frequency in bending, h and l are the thickness and length of the beam, and T is the correction factor, which for $l/h \geq 20$ is

$$T = 1 + 6.585 \left(\frac{h}{l}\right)^2 \tag{8}$$

The beam fundamental frequency in twisting can be used to calculate the in-plane shear modulus as

$$G = 4\rho f_t^2 l^2 R \tag{9}$$

Fig. 3 Antinodes location in the beam twisting mode shape

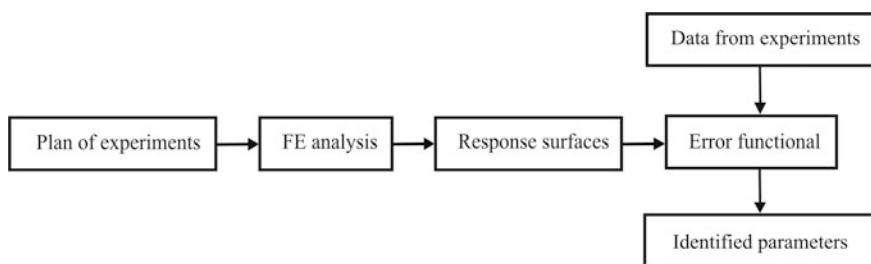
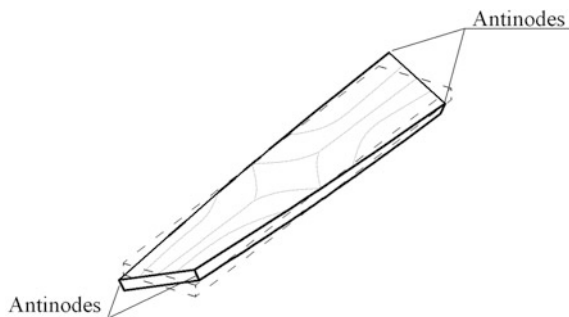


Fig. 4 Inverse procedure

where f_t is the fundamental frequency in twisting and R is the correction factor determined as follows:

$$R = \frac{1 + \left(\frac{b}{h}\right)^2}{4 - 2.521 \frac{h}{b} \left(1 - \frac{1.991}{e^{\pi(b/h)} + 1}\right)} \left(1 + \frac{0.00851 n^2 b^2}{l^2}\right) - 0.06 \left(\frac{nb}{l}\right)^{\frac{3}{2}} \left(\frac{h}{b} - 1\right)^2 \quad (10)$$

where n is the number of antinodes—locations that have a local maximum displacement in the unconstrained beam at the resonant frequency (Fig. 3).

2.3 Inverse Technique

The inverse technique, applied in the present study, is shown in Fig. 4. It uses vibration tests and consists of the experimental setup, the numerical model and the material parameters identification procedure, developed by applying a non-direct optimisation method, based on the planning of the experiments and a response

surface method in order to considerably decrease the computational efforts [15]. The first step involves the planning of the investigation depending on the number of measured parameters and experiments. Next, a finite element analysis is applied at the reference points of the experimental design and the dynamic parameters of the structure are calculated. At the third step of this technique, these numerical data are used to determine simple functions using a response surface method. Simultaneously, vibration experiments are carried out to measure the natural resonance frequencies of the structures. The identification of the material properties is performed at the final step of the method by minimising the error functional, which describes the difference between the experimental and numerical parameters of the structural responses.

2.3.1 Experimental Setup

Usually two experimental setups are used in the identification procedures based on vibration tests to determine the dynamic characteristics of structures. The first is based on the impulse technique and uses contact measurements by accelerometers; the second is based on the non-contact laser measurements. In the both cases, the PCB impulse hammer or shaker, or loudspeaker, or piezoelectric actuators, glued to the investigated object, are applied to produce excitations.

In the present study, the eigenfrequencies of laminated composite plates have been determined by using POLYTEC laser scanning vibrometer PSV-400-B operating on the Doppler principle and measuring back-scattered laser light from a vibrating structure to determine its vibration velocity and displacement. These plates have been suspended by using two thin threads in the upper corners to realise free-free boundary conditions. They are excited by the loudspeaker SP-106WP with the periodic chirp signal provided by the internal generator. An experimental setup is identical to the setup presented in Fig. 2 changing the suspended beam by the investigated plate. The input and output signals are converted to the frequency domain by fast Fourier transformation in a signal analyser and the frequency response functions are created. After that, these frequency response functions are exported to the modal analysis program, where natural frequencies are calculated.

2.3.2 Numerical Model

Since an analytical closed-form solution is impossible for the natural frequencies of plates with completely free boundary conditions, the finite element method is used in the present inverse technique. Commercial finite element code ANSYS is applied for the vibration analysis of laminated composite plates, which are modelled with the linear layered structural shell elements SHELL 99. An eigenvalue problem for the undamped free vibrations is solved with the block Lanczos mode extraction method to determine structural eigenfrequencies and corresponding eigenmodes.

2.3.3 Material Identification Procedure

The main idea of the material identification procedure based on vibration tests and non-direct optimisation methodology is that simple mathematical models (response surfaces) are determined only using the finite element solutions for the reference points of the plan of experiments. The identification parameters are obtained by minimising the error functional, which describes the difference between the measured and numerically calculated parameters of the structural responses. The calculation of the identification functional is significantly simplified in this case compared to conventional optimisation methods.

Planning of experiments. Let us consider a criterion for the planning of the experiments that is independent on the mathematical model chosen for the designed object or process. The initial information for the development of the plan is the number of factors n and the number of experiments k . The points of experiments in the domain of factors are distributed as regularly as possible. For this reason the following criterion is used

$$\Phi = \sum_{i=1}^k \sum_{j=i+1}^k \frac{1}{l_{ij}^2} \Rightarrow \min \quad (11)$$

where l_{ij} is the distance between the points numbered i and j ($i \neq j$). Physically, it is equal to the minimum of the potential energy of the repulsive forces for the points with unit mass, if the magnitude of these repulsive forces is inversely proportional to the distance between the points.

For each number of factors n and for each number of experiments k , it is possible to determine a plan of experiments, but it requires a considerable computing time. Therefore, each plan of experiment is only determined once and can be used for various design situations. Each plan of experiments is characterised by the matrix of plan B_{ij} . The domain of factors is determined as $x_j \in [x_j^{\min}, x_j^{\max}]$ and the points of experiments are calculated using the following expression

$$x_j^{(i)} = x_j^{\min} + \frac{1}{k-1} (x_j^{\max} - x_j^{\min}) (B_{ij} - 1), \quad i = 1, 2, \dots, k, \quad j = 1, 2, \dots, n \quad (12)$$

Response surface method. In the present study, the form of the regression equation is a priori unknown. There are two requirements for the regression equation: accuracy and reliability. Accuracy is characterised by the minimum of the standard deviation of the table data from the values given by the regression equation. By increasing the number of terms in this equation, it is possible to obtain a complete agreement between the table data and the values obtained from the regression equation. However, it is necessary to note that the predictions in the intervals between the points of the table could be not so good. To improve the accuracy of the predictions, it is necessary to decrease the distance between the points of

experiments by either increasing the number of experiments or decreasing the domain of factors. The reliability of the regression equation can be characterised by assuming that the standard deviations for the points of the table and for any other points are approximately the same. Obviously, the reliability is higher for a smaller number of terms in the regression equation.

The regression equation can be written in the following form:

$$y = \sum_{i=1}^p A_i f_i(x_j) \quad (13)$$

where A_i are the coefficients of the regression equation, and $f_i(x_j)$ are the functions from the pool of simple functions $\theta_1, \theta_2, \dots, \theta_m$ which are assumed to satisfy to expressions

$$\theta_m(x_j) = \prod_{i=1}^s x_j^{\xi_{mi}} \quad (14)$$

where ξ_{mi} are positive or negative integers, including zero. The derivation of the equation from the pool of simple functions is carried out in two steps: (i) the selection of the perspective functions from the pool and (ii) a step-by-step elimination of the selected functions.

At the first step, all variants are tested using a least square method and the function, which leads to a minimum of the sum of the deviations, is chosen for each variant. At the second step, the elimination is carried out by using the standard deviation defined as

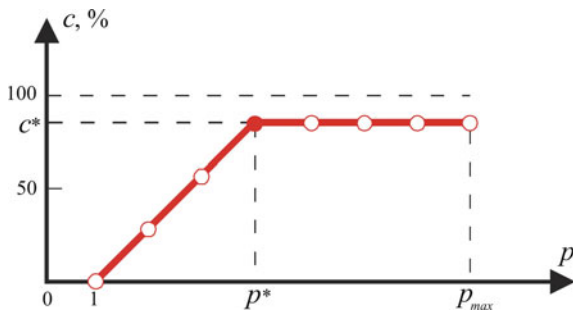
$$\sigma_0 = \sqrt{\frac{S}{k-p+1}}, \quad \sigma = \sqrt{\frac{1}{k-1} \sum_{i=1}^k \left(y_i - \frac{1}{k} \sum_{j=1}^k y_j \right)^2} \quad (15)$$

or the correlation coefficient given by:

$$c = \left(1 - \frac{\sigma}{\sigma_0} \right) * 100\% \quad (16)$$

where k is the number of experimental points, p is the number of selected perspective functions and S is the minimum of the sum of the deviations. It is more convenient to characterise the accuracy of the regression equation using the correlation coefficient (Fig. 5), since it is particularly sensitive to the choice of selected functions. If insignificant functions are eliminated from the regression equation, the reduction of the correlation coefficient is negligible. If only significant functions are presented in the regression equation, eliminating one function leads to an important decrease of the correlation coefficient.

Fig. 5 Diagram of elimination for the correlation coefficient



Error functional minimisation. In the case of identification of the elastic material properties, the error functional, which describes the difference between the experimental and numerical parameters of the structural responses, can be written as a least squares error estimator:

$$\Phi(x) = \sum_{n=1}^N \left[\frac{(f_n^{\text{EXP}})^2 - (f_n^{\text{FEM}})^2}{(f_n^{\text{EXP}})^2} \right]^2 \Rightarrow \min \quad (17)$$

where f_n^{EXP} are the experimentally determined resonant frequencies, f_n^{FEM} are the numerically calculated eigenfrequencies (obtained from the response surfaces), $\mathbf{x} = \{x_1, x_2, x_3, x_4\} = \{E_1, E_2, G_{12}, \nu_{12}\}$ is the vector of unknown parameters and N is the total number of eigenfrequencies considered in the analysis.

To minimise the error functional, the following constrained nonlinear optimisation problem must be solved

$$\min \Phi(x), H_i(x) \geq 0, G_j(x) = 0 \quad i = 1, 2, \dots, I, j = 1, 2, \dots, J \quad (18)$$

where I and J are the numbers of the inequality and equality constraints. This problem is replaced by an unconstrained minimisation problem, in which the constraints are taken into account with the penalty functions. The random search method [16] is used to solve the formulated optimisation problem.

3 Characterisation of Elastic Material Properties

An experimental evaluation of the elastic material properties of laminated composites is carried out to validate the non-destructive techniques described above and to demonstrate their accuracy, reliability and efficiency. For this purpose, two unidirectional composite panels with 16 layers made of carbon/epoxy prepregs (SEAL[®] Texipreg HS 160 RM) have been produced. Ten specimens have been

Table 1 Specimens for characterisation

Specimen	Stacking sequence	a (mm)	b (mm)	h (mm)	ρ (kg/m ³)
Plate 1 ^a	[0] ₁₆	290.0	200.0	2.60	1546.6
Plate 2 ^b	[90] ₁₆	290.0	200.0	2.61	1546.6
Beam 1 ^a	[0] ₁₆	292.0	19.5	2.60	1546.6
Beam 2 ^a	[0] ₁₆	291.0	20.0	2.60	1546.6
Beam 3 ^a	[0] ₁₆	290.0	19.5	2.60	1546.6
Beam 4 ^a	[0] ₁₆	290.0	19.5	2.60	1546.6
Beam 5 ^b	[90] ₁₆	290.0	20.0	2.61	1546.6
Beam 6 ^b	[90] ₁₆	290.0	19.5	2.61	1546.6
Beam 7 ^b	[90] ₁₆	289.0	20.0	2.61	1546.6
Beam 8 ^b	[90] ₁₆	289.0	19.5	2.61	1546.6

^aCut out from the Panel 1 along principal direction x

^bCut out from the Panel 2 along principal direction y

prepared from these panels. There are two plates and eight beams cut out from the panels along their principal directions (Table 1).

3.1 Application of Three-Points-Bending Test

Three-points-bending tests (Fig. 1) are executed by using the ZWICK Z-100 system with the load cell of 10 kN. It allows an application of quasi-static loading with speed of 0.01 mm/s in the middle of span for determination of the elastic properties of beam-like specimens, located on two supports. The deflection of the beam is determined by the measurement of the loading nose motion.

All beam specimens have been used in three-points-bending tests to define the material Young modulus in principal directions. Six static tests have been performed for each beam with the following span lengths: 140, 120, 100, 80, 60, 40 mm. The first test of each beam with the span length of 140 mm has been terminated and corresponding load P has been stored, when the deflection in the middle of span is equal to the beam thickness ($\delta_1 = h$). This deflection provides the strain level less than 0.5% that means an elastic behaviour of the beam. All subsequent tests of the beam have been stopped when the applied load has reached the value P determined for δ_1 . For each span length, the load-deflection curves (Fig. 6a) have been preserved for an estimation of the deflection δ_i used for the calculation of δ_i/Pl_i and subsequent their plot on l_i^2 (Fig. 6b). Then the linear approximation has been used to determine the slopes g for all tested beams. Using Eq. (4), the Young modulus of each tested beam has been calculated and presented in Table 2.

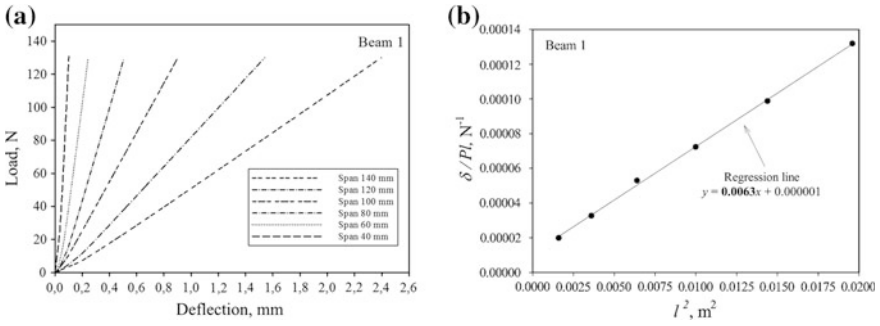


Fig. 6 Three-points-bending tests for *Beam 1*: **a** load-deflection curves for different span length, **b** regression line after six experiments

Table 2 Young moduli obtained from three-points-bending tests

Specimen	g	E_1 (GPa)	E_2 (GPa)
Beam 1	0.00630	115.78	—
Beam 2	0.00601	118.33	—
Beam 3	0.00621	117.48	—
Beam 4	0.00624	116.90	—
Beam 5	0.0770	—	9.13
Beam 6	0.0795	—	9.18
Beam 7	0.0816	—	8.62
Beam 8	0.0810	—	8.90
Average	—	117.12	8.95

3.2 Application of Impulse Excitation Method

An experimental setup (Fig. 2) based on the POLYTEC laser scanning vibrometer PSV-400-B and loudspeaker SP-106WP is used in the impulse excitation method for measurement of the frequency response functions for all tested beams in the frequency range of 0–1.6 kHz. The free-free boundary conditions are realised by suspending the beams on two thin threads at the locations of nodal lines of the beam-bending mode. Such boundaries are used to obtain both—the fundamental bending and twisting frequencies and corresponding mode shapes of all beam specimens (Fig. 7). Using Eqs. (7) and (9), the Young and shear moduli have been calculated and presented in Table 3.

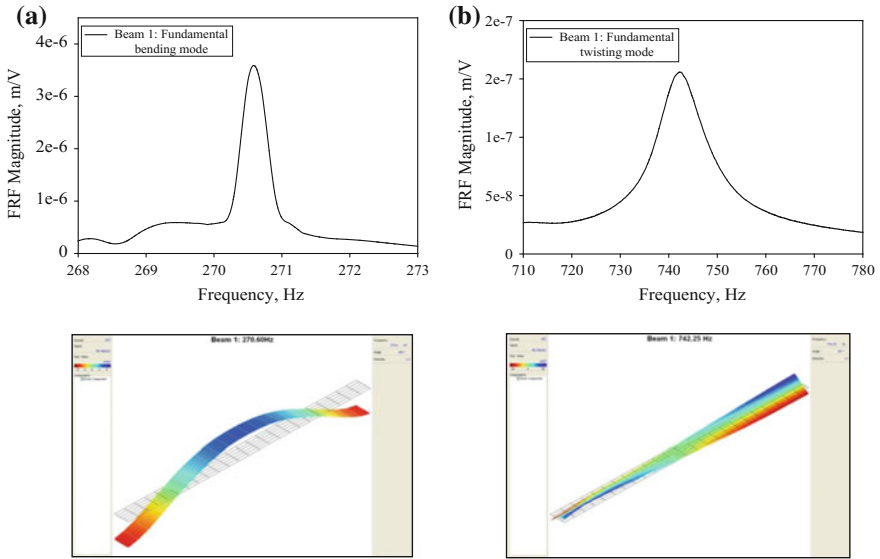


Fig. 7 Frequency response functions and corresponding mode shapes for *Beam 1*: **a** fundamental bending mode, **b** fundamental twisting mode

Table 3 Young and shear moduli obtained by impulse excitation method

Specimen	f_b (Hz)	f_t (Hz)	E_1 (GPa)	E_2 (GPa)	G_{12} (GPa)	T	R
Beam 1	270.60	742.25	115.28	–	4.53	1.000522	15.68
Beam 2	272.75	741.25	115.52	–	4.74	1.000526	16.45
Beam 3	273.85	742.75	114.86	–	4.50	1.000529	15.69
Beam 4	274.40	741.50	114.99	–	4.49	1.000529	15.69
Beam 5	75.60	741.5	–	8.69	4.67	1.000533	16.34
Beam 6	76.30	742.75	–	8.85	4.47	1.000533	15.57
Beam 7	75.20	740.50	–	8.48	4.63	1.000537	16.34
Beam 8	75.10	744.50	–	8.45	4.46	1.000537	15.57
Average	–	–	115.16	8.62	4.56	–	–

3.3 Application of Inverse Technique

The plan of experiments has been developed for 4 design parameters and 101 experiments with the following borders for the identified parameters:

Table 4 Identified material properties of single layer

Specimen	Plate 1		Plate 2
N	10 frequencies	7 frequencies ^a	10 frequencies
E_1 (GPa)	117.90	117.00	116.6
E_2 (GPa)	8.98	8.77	8.94
G_{12} (GPa)	4.12	3.89	4.30
ν_{12}	0.47	0.38	0.34

^aWithout modes (2,3), (1,3), (2,2)

$$100 \leq E_1 \leq 120 \text{ GPa}$$

$$7 \leq E_2 \leq 10 \text{ GPa}$$

$$3 \leq G_{12} \leq 5 \text{ GPa}$$

$$0.25 \leq \nu \leq 0.50$$

Then, the free vibration analysis of laminated composite plate modelled with the linear layered structural shell elements and having the finite element mesh of 30×30 has been performed for 101 experimental points, and ten first dynamic characteristics have been determined. Using these numerical values, the approximating functions (response surfaces) for all eigenfrequencies have been obtained with the correlation coefficients higher than 90%. Independently, an experimental modal analysis has been performed for the plates with completely free boundary conditions, while the plate has been suspended vertically by using two thin threads, attached to its corners. Excitation is produced by using a loudspeaker to avoid any influence on the object from exciting devices. Minimising the error functional (Eq. 17), the material properties have been found for both investigated plates (Table 4). These values have been used subsequently in the finite element analysis in order to verify the identified material properties by comparing the actual experimental results to those obtained numerically. The relative errors between experimental and numerical results, which are quantifying an accuracy of the identification procedure, are given in Table 5.

It is assumed in the present inverse technique, if the average value of residues is lower than 1%, the identification procedure has been performed successfully. The average relative error of 1.39% indicates that some error sources had an influence on the results. Since the plates have been tested experimentally in the same conditions, the source of the higher error for Plate 1 should be sought for among the numerical model errors. This can be the deviation of fibre placement from the assumed lamination angle, because the thickness of the plates has been measured carefully and no curvature has been found on the plate's edges. In this case, the modes (2,3), (1,3) and (2,2) should be eliminated from the inverse procedure [17]. The identification has been repeated for Plate 1 with a reduced number of resonant frequencies $N = 7$ and new set of engineering constants has been obtained (Table 4) and verified (Table 5). It is seen from the obtained results that proper

Table 5 Verification of eigenfrequencies for laminated plates

Specimen	Plate 1					Plate 2		
N	10 frequencies			7 frequencies		10 frequencies		
Mode n	f_n^{EXP} (Hz)	f_n^{FEM} (Hz)	Δ (%)	f_n^{FEM} (Hz)	Δ (%)	f_n^{EXP} (Hz)	f_n^{FEM} (Hz)	Δ (%)
1 (1,1)	76.0	78.2	2.81	76.0	0.00	76.3	76.4	0.13
2 (0,2)	158.0	161.4	2.11	159.6	1.00	78.0	77.6	0.52
3 (1,2)	220.0	226.5	2.87	221.9	0.86	178.5	176.5	1.13
4 (2,0)	278.1	280.3	0.78	278.4	0.11	212.2	210.6	0.76
5 (2,1)	316.0	319.5	1.10	316.3	0.09	321.0	318.7	0.72
6 (0,3)	444.0	448.4	0.98	442.0	0.45	415.0	412.7	0.56
7 (2,2)	460.0	457.2	0.61	448.3	2.61	524.0	519.5	0.87
8 (1,3)	500.0	504.1	0.81	495.9	0.83	578.0	580.9	0.50
9 (2,3)	712.0	717.6	0.78	702.2	1.40	598.5	600.0	0.25
10 (3,0)	760.0	767.7	1.00	763.4	0.45	667.5	666.8	0.10
Average			1.39		0.78			0.55

frequency selection gave the possibility to reduce the average relative error by 44% and to decrease it to an acceptable level of 0.78%. The value of Poisson's ratio has been reduced very significantly in this case.

It is necessary to note that the present inverse technique gives the possibility also to identify the transverse shear moduli G_{13} and G_{23} of laminated composites. However, due to the lack of a noticeable transverse shear effect, which expected for such a low thickness to length ratios of the test plates, these parameters have not been used as the design variables in the identification problem.

3.4 Comparison of Identified Parameters

The elastic properties of the constituent layers of laminated composite panels have been determined by using three non-destructive techniques (Table 6) giving different numbers of estimated engineering constants. One vibration test has been required for an identification of four engineering constants using plate specimens and the inverse technique procedure. Only two vibration tests have been carried out to estimate three engineering constants using beam specimens and the method, based on impulse excitation. Two engineering constants have been estimated from six static tests for one beam specimen. Table 6 shows a good correlation between the identified material properties, obtained by different methods.

Table 6 Verification of the identified material properties, obtained by different methods

Method	Three-points-bending test	Impulse technique	Inverse technique ^a
E_1 (GPa)	117.12	115.16	116.80
E_2 (GPa)	8.95	8.62	8.85
G_{12} (GPa)	–	4.56	4.10
ν_{12}	–	–	0.36

^aAverage values from specimens Plate 1 and Plate 2

4 Conclusion

An experimental evaluation of the elastic material properties of laminated composites has allowed to validate the developed non-destructive techniques and to demonstrate their accuracy and reliability. The advantages and limitations of the applied methods can be summarised as follows:

- (1) An application of three-points-bending tests allows only determination of the Young moduli in the principal directions of orthotropic plates. To obtain results with higher accuracy, few experiments are necessary in dependence of the required span lengths. Despite of this, the advantage of the method is its non-destructive nature and simple experimental setup.
- (2) Simple and effective method for the engineering constants identification appears, when the vibration method, based on impulse excitation, is utilised. The Young moduli in the material principal directions as well as the in-plane shear modulus are estimated applying this method that in the case of isotropic materials characterisation presents the full set of material properties and requires only one beam specimen. Two vibration tests and two beam specimens are necessary in the case of orthotropic materials characterisation. If the beam specimens can be provided with a sufficient length-to-width ratio, the method can be recommended for a fast estimation of the material mechanical properties. It is also important to provide a non-contact excitation and vibration sensing for characterisation of lightweight specimens in order to avoid any influence of additional mass on the resonant frequencies. The advantage of the method over the proposed static approach is little preparation of experimental setup and short measurement time.
- (3) Among all proposed methods for the elastic properties characterisation, an approach based on the inverse technique is most suited for the convenient, fast and accurate identification of a full set of the elastic properties of orthotropic materials. In this case only one vibration test is needed to acquire the resonant frequencies of each plate, which then are used in the inverse procedure. However, in the case of isotropic materials, the approach based on impulse excitation is looked as more effective since all engineering constants could be determined in a shorter time by this method.

Although the static and impulse excitation methods do not provide information about all engineering constants in the case of orthotropic material characterisation, they can be used as preliminary tests in order to assess the initial bounds of engineering constants for the identification procedure with application of the inverse technique. They can be also used as known characteristics reducing the number of design parameters and therefore improving the identification results.

References

1. R.F.S. Hearmon, *Introduction to Applied Anisotropic Elasticity* (Oxford University Press, Oxford, 1961)
2. B. Gommers, I. Verpoest, P. Van Houtte, *J. Compos. Mater.* **32**(4), 310 (1998)
3. L. Filipczynski, Z. Pawlowski, J. Wehr, *Ultrasonic Methods of Testing Materials* (Butterworths, London, 1966)
4. Y. Okabe, N. Takeda, M. Sekiguchi, *J. Compos. Mater.* **33**(18), 1743 (1999)
5. S. Mistou, M. Karama, *J. Compos. Mater.* **34**(20), 1696 (2000)
6. P.S. Frederiksen, *J. Compos. Mater.* **31**, 360 (1997)
7. A.L. Araujo, C.M. Mota Soares, M.J. Moreira de Freitas, P. Pedersen, J. Herskovits, *Compos. Struct.* **50**, 363 (2000)
8. J. Auzins, A. Chate, R. Rikards, E. Skukis, *ZAMM Zeitschrift fur Angewandte Mathematik und Mechanik* **95**(10), 1012 (2015)
9. E. Barkanov, E. Skukis, B. Petitjean, *J. Sound Vib.* **327**, 402 (2009)
10. ASTM Standard D790—07e1, Test Methods for Flexural Properties of Unreinforced and Reinforced Plastics and Electrical Insulating Materials
11. S.P. Timoshenko, J.M. Gere, *Mechanics of Materials* (Van Nostrand Reinhold Company, New York, 1972)
12. EN ISO 14125:2001, Fibre-Reinforced Plastic Composites—Determination of Flexural Properties
13. ASTM Standard E 1876—07, Standard Test Method for Dynamic Young's Modulus, Shear Modulus and Poisson's Ratio by Impulse Excitation of Vibration
14. G. Pickett, *Proc. ASTM* **45**, 846 (1945)
15. R. Rikards, H. Abramovich, T. Green, J. Auzins, A. Chate, *Mech. Adv. Mater. Struct.* **10**(4), 335 (2003)
16. A. Janushevskis, T. Akinfiev, J. Auzins, A. Boyko, *Proc. Estonian Acad. Sci. Eng.* **10**(4), 236 (2004)
17. E. Barkanov, M. Wesolowski, W. Hufenbach, M. Dannemann, *Comput. Struct.* **146**, 152 (2015)

Characterization of Elastic Properties of Metals and Composites by Laser-Induced Ultrasound

V.V. Kozhushko, V.P. Sergienko, Y.N. Mirchev and A.R. Alexiev

Abstract The development of new materials and composites with desired mechanical properties requires methods for evaluation of their elastic moduli. The direct measurements of the shear and longitudinal ultrasonic pulse are the simplest approach for solution of these tasks. Among the drawback of the traditional ultrasonic methods are narrow bandwidth and necessity of the relatively large volume of the material for testing. Laser excitation of ultrasound is based on optoacoustic conversion that induces bulk pulses of about tens nanosecond duration and can be applied for time-resolved measurements of velocities. The paper considers several experimental arrangements, which combine laser excitation of probe ultrasonic pulses and their detection for measuring the velocities of longitudinal and shear pulses. The features of detection in single crystal and polycrystalline nickel as well as steel specimens are discussed.

Keywords Laser-induced · Ultrasound · Scattering · Elastic moduli · Non-destructive testing · Optoacoustics

1 Introduction

The ultrasonic waves imply spreading of mechanical motion of particles with frequencies above megahertz that is evidently connected with the elastic properties of media. Considering simple case of isotropic media, there are two modes of longitudinal or compression and shear or transverse wave propagation. The velocities

V.V. Kozhushko (✉) · V.P. Sergienko
V.A. Belyi Metal Polymer Research Institute of National Academy
of Sciences of Belarus, Gomel, Belarus
e-mail: kozhushko@laser-ultrasound.com

Y.N. Mirchev · A.R. Alexiev
Institute of Mechanics of Bulgarian Academy of Sciences, Sofia, Bulgaria

of these modes depend on the stiffness tensor and density of material according to the expression:

$$C_L = \sqrt{\frac{\lambda + \mu}{\rho}}, \quad C_S = \sqrt{\frac{\mu}{\rho}}, \quad (1)$$

where C_L and C_S are the longitudinal and shear velocities of material, λ , μ are Lamé constants connected with a stiffness tensor in Voigt notation as $C_{11} = \lambda + 2\mu$, $C_{44} = \mu$ for isotropic material, and ρ is the density of material [1].

Thus, the measurements of the velocities of ultrasonic waves or more generally pulses, which comprise of wave packet, yield the moduli of material. Two tasks have been solved, namely: the excitation of media and detection of these disturbances in time. The time-resolved methods employ short pulses with broadband spectra in contrast to the resonant methods, which measure disturbance during the long-time period and consider narrower frequency range, but in the both approaches, the dimensions of the specimens bind the experimentally obtained data with stiffness tensor. The advantage of the pulse-resolved method is a simple calculation of the moduli on the base of experimental data, while the resonant methods can be employed for materials, which have anisotropy of elastic properties owing to the texture or residual stresses induced by rolling or local overheating. The numerical methods for solution of the direct problem of modal analysis can be employed for evaluation of the specimen with anisotropy of elastic properties. These approaches allow the measurements of the propagation velocities of shear and longitudinal pulses and determination of the stiffness tensor that is keynote task of material science.

Nowadays ultrasound solves numerous tasks of non-destructive testing, properties evaluation and noninvasive medical diagnostics that evidently means appropriate excitation of probe pulse and the following successful detection. There are established well-known approaches of ultrasound excitation and detection as, for instance, by piezoelectric or electromagnetic acoustic transducers.

The materials of the sensitive elements of piezoelectric transducers are lead zirconate titanate (PZT) ceramics or polymeric films of polyvinylidene fluoride (PVDF), which have been polarized. Transducers employ inverse and direct piezoelectric effects to switch between operation in transmitter–receiver modes for excitation of the probe pulses and detection of its returned part. The thickness and the area of the sensitive element determine the operational bandwidth, capacity, sensitivity and other characteristics of single transducer. Applied high voltage pulse induces deformation and launches probe ultrasonic pulses; afterwards the transducer is switched into the receiving mode. In order to deliver the probe pulses the acoustical contact is provided between transducer and specimen by couplant, such as liquid or gel. There are transducers, which induce longitudinal pulses with spectra covering different bands up to hundreds megahertz. It should be mentioned that this is cost-effective method, which needs a couple of integrated circuit chips and high voltage power supply. The most often highlighted drawback of

piezoelectric transducers is mechanical contact that reduces the operational bandwidth. There is alternative solution called dry contact, which employs a thin rubber layer attached to the transducer's front surface. It can pass sufficient amount of the pulse energy into specimen, when the couplant is harmful for the specimen or surface treatment is difficult. Obviously, dry contact approach also suffers from the reduction of the operational bandwidth. The excitation of shear pulse employs internal reflection of initially longitudinal pulses from the prism surface. The evaluation of moduli can be carried out by immersion of the specimen in water bath with a remark that liquids convert shear waves to longitudinal waves. It is noteworthy that piezoelectric transducers can be applied for task of moduli evaluation to the largest set of materials as porous media, plastics, fiber-reinforced composites, dielectrics, alloys, metals, etc.

The electromagnetic acoustic transducers (EMATs) can be applied for non-contact excitation and detection of ultrasonic pulses owing to Lorenz forces in conductive materials and/or forces on the magnetization vector and magnetostrictive effect in ferromagnetic metals. The operational bandwidth of EMATs depends on the properties of the materials and for both cases of excitation and detection can exceed 50 MHz [2]. The generation of transient electromagnetic field requires powerful current source to feed coil in biasing permanent magnetic field. The sensitive elements of these transducers are simple varnished copper wire coils, which are set in the biasing permanent magnetic field. The arrangements of the permanent biasing magnets allow excitation of longitudinal and shear waves propagating perpendicular to the surface of specimen. The main shortcoming of the technique is low efficiency of conversion for pulse excitation since the skin depth decreases penetration of transient electromagnetic field that limits the high-frequency excitation. The amplitude of the coil signals, induced in detection, decreases with distance from the metal surface or gap between coil and specimen that requires as close as possible location for better performance.

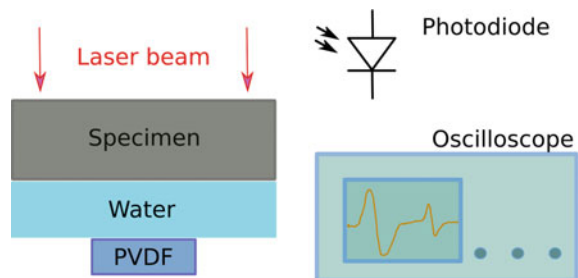
The laser-induced ultrasound or optoacoustics is a technique, which overcomes some shortcomings of conventional methods [3, 4]. The main advantage of optoacoustic pulses relates to the noncontact excitation of ultrasound with essentially broadband spectrum. There are several all-optical arrangements, which comprise of laser excitation and detection units and are very attractive for industry due to the capability of operation without surface treatment at elevated temperature. Unfortunately, all-optical laser-induced ultrasound is a very expensive tool while numerous tasks of properties evaluation can be solved in laboratory conditions by combination of laser excitation and one of the conventional transducers as, for instance, piezoelectric transducers or EMATs, which are used only for detection and can be called, respectively, as sensors or detectors of broadband ultrasonic pulses. The aim of the paper is to show advantages of laser-induced ultrasound in comparison with traditional approaches for solving the task of bulk velocity measurements. The paper considers several experimental arrangements and deals with measurements in single crystal Ni(100), polycrystalline nickel and steel 40× (Russian notation) or 5140 (American notation) that reveals features of excitation, elastic mode conversion, ultrasonic scattering and detection methods.

2 Excitation and Detection of Optoacoustic Pulses

As it was mentioned before, optoacoustics implies generation of the ultrasound due to the conversion of the laser pulse energy. An example of experimental arrangement is present in Fig. 1. The Q-switched solid state Nd:YAG laser operating on a wavelength of $1.064 \mu\text{m}$ or 532 nm with pulse duration of $<10 \text{ ns}$ is a typical source used for the excitation of broadband ultrasonic pulses. The needed energy is about 10 mJ per pulse and the maximum power density at the specimen's surface is below 20 MW/cm^2 , which is a limit for thermoelastic excitation. The fast photodiode as, for instance, Hamamatsu S5971, triggers the digital oscilloscope with the analogue bandwidth of at least 100 MHz . The coaxial cable connects the input of oscilloscope with the output of broadband preamplifier, which increases the signal induced in the sensitive element of detector or transducer. The oscilloscope usually averages the signals for reduction of a noise of electronics.

The measurements of longitudinal pulses velocity employ the specimens in the form of plate or disk with parallel faces for time-resolved detection of the series of echoes or reverberations. The efficiency of laser radiation conversion to elastic pulses depends on both properties of absorbing and transparent media and parameters of laser radiation, such as spot geometry and envelope of the pulse intensity. The absorption coefficient defines penetration depth and the volume of the material, where the heat sources are deposited. The absorption of optical or near infrared radiation is above 10^4 cm^{-1} in metals, but it is noteworthy that significant a part of radiation can be reflected by the surface. The in-depth penetration of optical radiation is not more than several tens of nanometers from the interface with transparent medium hence the heat sources localize at the surface of the metal. The heat capacity, density and heat conductivity define the process of heat spreading from the initially deposited sources. The heat penetration depth can be obtained from expression $\sqrt{\chi\tau}$, where χ is the heat diffusivity of material and τ is the laser pulse duration. This expression defines the heat diffusion length $\sim 0.5 \mu\text{m}$ into nickel and around $1 \mu\text{m}$ for aluminum and copper, which are relatively good heat conductors. These distances are significantly smaller than traveling path of acoustical pulse during the same time, therefore the interaction of heat and elastic waves can be omitted and the solution of heat distribution and acoustical waves obtained consistently. The local nonstationary increase of the temperature involves

Fig. 1 Arrangement for measurement of laser-induced longitudinal pulse velocity



fast expansion and excitation of the elastic pulses, which duration is comparable with laser pulse envelope. The method of transfer functions can be applied for separation parameters of laser radiation such as envelope of the laser pulse intensity and the form of the laser spot from the properties of transparent and absorbing media, where the ultrasonic pulses can be induced [3].

The simple one-dimensional approach implies dominant excitation of longitudinal pulses that can be managed by wide laser spot in comparison with traveling distance of sample thickness. This is the most often used approach for solution of numerous tasks of non-destructive testing and properties evaluation. The Fourier transformation allows the calculation of the spectra of induced pulses that is well described in the literature. The spectrum of the excited longitudinal pulse can be expressed as follows:

$$P(f) = K(f)I_0L(f), \quad (2)$$

where $K(f)$ is a transfer function describing the efficiency of optoacoustic transformation, which depends on the properties of absorbing and transparent media, I_0 is the intensity of the laser pulse and $L(f)$ is the spectrum of the envelope of the laser pulse. Thus, the spectrum of optoacoustic pulse is proportional to the spectrum of the laser pulse that relates to thermoelastic regime of excitation with fluence $<20 \text{ MW/cm}^2$ on the metal surface. The efficiency of conversion can be around $1 \text{ Pa/(W/cm}^2)$ and it is frequency dependent but some arrangements diminish this dependencies due to insignificant variation in the bandwidth of the laser intensity envelope spectrum [5]. The pressure pulses with peak amplitude of 20 MPa and strain up to 10^{-4} can be launched in metal. The increasing of the laser fluence leads to the ablation mode, where the sublimation of the overheated layer of material exerts normal to the surface of the specimen and induces dominantly longitudinal elastic pulse.

An example of signal detected in single crystal nickel disk by piezoelectric transducer is present in Fig. 2. The transducer's sensitive element is 25 μm -thick PVDF film of 2 mm diameter. The operation of the amplifier in 'short-circuit current' mode allows detection of the frequency in the range from 3 MHz up to 90 MHz at the level -20 dB [6]. The part of the primary pulse passes the metal-water interface while the rest part of the pulse reflects back to the volume of the specimen. The transition (T) and reflection (R) coefficients for amplitude of pulse, which propagates from medium with impedance z_1 to medium with impedance z_2 :

$$T = \frac{2z_2}{z_1 + z_2}, \quad R = \frac{z_2 - z_1}{z_1 + z_2}, \quad (3)$$

where z_1 and z_2 are the acoustical impedances of media. The reflection coefficient for nickel-water interface is $R = -0.94$, where the negative sign means the changes of pulse phase to opposite one's as, for instance, from compression to dilatation. The phase of presented pulses are conserved due to additional reflection at nickel-air interface with $R = -1$ due to the fact $z_2/z_1 \ll 1$. It is noteworthy that the

attenuation of ultrasound in coupling water layer increases with the square of the frequency that should be taken into account.

The efficiency of excitation of longitudinal pulses is higher in ablative mode but leads to insignificant damage of the surface that is acceptable for the solution of the task of moduli evaluation. However, the immersion of the specimen in optically transparent liquid also increases the efficiency of optoacoustic conversion that worth to be discussed. The boundary conditions of equality of the temperatures and heat fluxes take place at the interface water–metal, but the temperature raising in liquid induce stronger thermoelastic strain because of at least one order of magnitude higher thermal expansion coefficient. Because the acoustical impedances of liquids are lesser but comparable with those of metals, hence the next point relates to the acoustic loading of the interface, since it is some intermediate case between acoustically free and rigid boundary conditions [5]. The experiments show increase of the efficiency of longitudinal pulse excitation by modification to the initially dry interface to liquid covered. This is simple way to increase peak-to-peak amplitude and magnifies the low frequencies part of the spectrum. The estimations show that the temporal form of laser-induced pressure pulse is close to the envelope of laser pulse intensity and has pronounced compression phase for one-dimensional approach. The launched probe pulses undergo changes of spectrum and wave front during the propagation in the specimen that decreases the peak-to-peak amplitude.

The primary longitudinal pulse arrives at about $1.8 \mu\text{s}$ after triggering of photodiode that includes traveling time through the coupling water layer and time for passing the specimen. The echoes or reverberations arrive for the same time, afterwards. The interval between zero-crossing points of neighboring pulses corresponds to the time required for traveling over double thickness of the specimen that can obviously be used for evaluation of the velocity. The obtained value of longitudinal velocity is $5.32 \pm 0.02 \text{ km/s}$. The peak-to-peak amplitudes of the

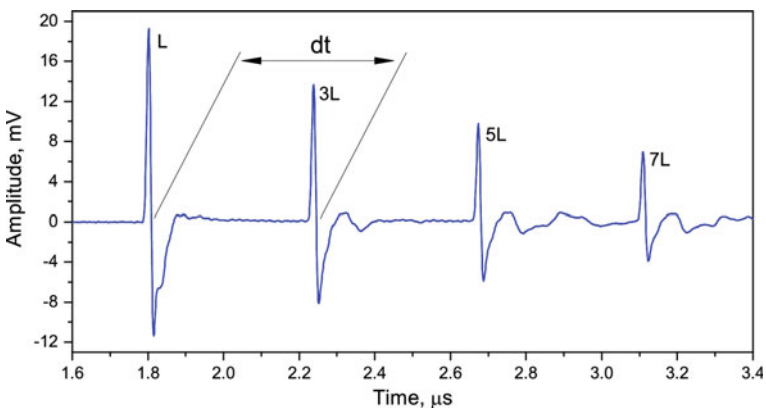


Fig. 2 Optoacoustic signal in $1.16 \pm 0.02 \text{ mm}$ -thick Ni(100) single crystal disk measured by PVDF transducer. The *symbols* near pulses show the pass distance in number of thicknesses, for instance, *L* means one and $3L$ —three thicknesses for longitudinal pulse

pulses state decay due to the losses, which comprise of attenuation and diffraction. The possible reasons of attenuation are considered below, while diffraction is the more general phenomenon. The initially induced pressure pulse has plane wave front with Gaussian distribution of pressure amplitude over its cross-section, which relates to the area irradiated by laser beam. The present signal was induced by laser beam of 6 mm diameter and it detected by PVDF sensor with 2 mm diameter of the sensitive element. Ultrasonic beam should possess axial symmetry and spreads into the bulk of the specimen. The axial location of the sensor yields the best capability for longitudinal pulse detection. The influence of diffraction can be expressed as

$$D = \frac{\lambda x}{a^2} \quad (4)$$

where D is the diffraction factor, λ is the wavelength of ultrasound, x is the traveling distance, a is the diameter of the laser spot on the metal surface. The diffraction is negligible for selected frequency or wavelength when $D < 1$ and the wave front can be considered as plane at the axis of the beam. The wave front changes with propagation distance and in the far diffraction zone, it can be considered as spherical that corresponds to the case $D > 1$ defining conditions for one-dimensional arrangement. The situation is complex for broadband pulse spectrum, which experience deviation of wave vectors from the axial propagation. These deviations involve waves during propagation starting from low-frequency part to the highest part of pulse spectrum. It is assumed that dispersion is negligible, while declined waves induce both reflected and refracted shear and longitudinal pulses [1]. This explains the distortions between echoes of longitudinal pulse in Fig. 2.

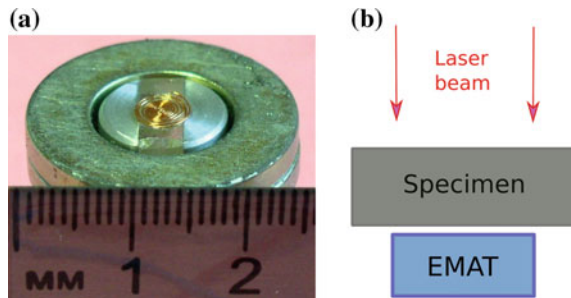
The piezoelectric transducers can be applied to any kind of materials from polymers to metals and their main advantage is good sensitivity with possibility to operate in the bandwidth compared with noncontact laser methods. The electrical signal of sensitive element should be delivered to input of oscilloscope that requires the using of amplifier with broadband operation. The present signals were obtained by PVDF film sensor with preamplifier which operates in ‘short-circuits current’ mode, which provides broader and mainly high-frequency detection and insensitive to the slow pressure variations. The time constant $T = 2\pi RC$ is product of sensitive element capacity and resistor in electrical circuit. The detection of the frequencies about 100 MHz is possible when time constant < 5 ns that is fulfilled in our circuit with the sensitive element capacity of 12 pF and 50 Ω input of resistor. The charge induced on the electrodes of the sensitive element flows through the resistor. This voltage drop is connected with the positive input of operational amplifier. The output signal of operational amplifier is time derivative of the pressure pulse in contrast to the ‘voltage’ detection mode, which allows increasing the sensitivity in low-frequency range for detection of the narrower frequency bandwidth by increasing the time constant. The thickness resonance of 25 μm -thick PVDF film yields the high frequencies border of about 90 MHz at -20 dB level (construction details are present in [5]). It is possible speculate about widening the frequency

range by using of the commercially available thinner films of 9 μm , but due to the frequency increasing attenuation of ultrasound in water, the thickness of coupling layer reduced with decreasing of interval between echoes in water.

Contactless detection of laser-induced ultrasound by EMAT transducer is well-promising approach for solution of numerous tasks of material science. The sensitive element of designed EMAT transducer is simple pancake coil of $\text{Ø}5$ mm with 10 windings of lacquered copper wire of $\text{Ø}0.15$ mm (see Fig. 3). The estimated inductance of the coil is 0.2 μH . The coil is placed at the center of cylindrical NdFeB permanent magnet with the inner diameter of 13 mm and the outer diameter of 25 mm. The measured field of 0.25 T partly magnetizes the specimen but it is far from the saturation of magnetization. The operational amplifier is close integrated with coil and it is placed in aluminum housing. The previous experiments demonstrated time-resolved detection of laser-induced longitudinal optoacoustic pulses in 0.4 mm-thick steel, where the spectrum of the primary pulse was in the range from 5 MHz up to 200 MHz [7].

The measurements were carried out with the same power density as in the case of PVDF sensor and, therefore laser-induced pressure pulses should have the amplitude, but peak-to-peak amplitude of signals is lower. The main contribution to the detected signals is due to the magnetostriction of nickel. The absence of the coupling water layer yields the faster arriving of the laser-induced longitudinal pulse afterwards the shear pulse appears. It is noteworthy that the area of the coil is comparable with the cross-section of the beam of about 6 mm that allowed detection of laser-induced longitudinal and shear pulses. The beams of these pulses have different directivity and continuously change the wave front. The top water layer increased the amplitude of initially induced longitudinal pulse and other pulses, which were induced due to at least one conversion of longitudinal beam. The fact of increasing of longitudinal pulse intensity is well-known [6]. However, water layer did not significantly change the amplitude of pure shear pulses since their efficiency of excitation depends mainly on the spatial distribution of the laser intensity at the surface. The reflection of deviated pulses induces two modes every time. Figure 4 clearly shows the complexity of ultrasonic field even in single crystal specimen. The obtained values of longitudinal and shear waves were 5.23 ± 0.02 km/s and 3.69 ± 0.02 km/s, respectively. It proves the fact that direction $\langle 100 \rangle$ of cubic crystals is soft with the lowest values of the velocities.

Fig. 3 Image of the detection coil in the *middle* of EMAT permanent magnet (a), experimental arrangement (b)



By considering in Fig. 2 the signal, obtained by PVDF sensor, one can conclude that the distortions between the reverberations are caused by refracted and converted pulses at nickel–water interface to longitudinal pulses propagating towards detector. Obviously, the shear pulses are deviated from the normal to the surface and pass longer distance than the specimen’s thickness that is difficultly to estimate but can be used as the first approximation [7]. The considered experimental arrangement allows using the arriving time of the primary longitudinal pulses for velocities measurements that is very attractive in the case of strong damping of ultrasound, when the peak-to-peak amplitude of echoes signal is very low.

3 Attenuation and Scattering of Ultrasonic Pulses

The attenuation of ultrasound relates to the irreversible conversion of the elastic energy to heat. The damping is attributed to several phenomena such as hysteresis, thermoelastic damping and internal friction associated with defects such as the

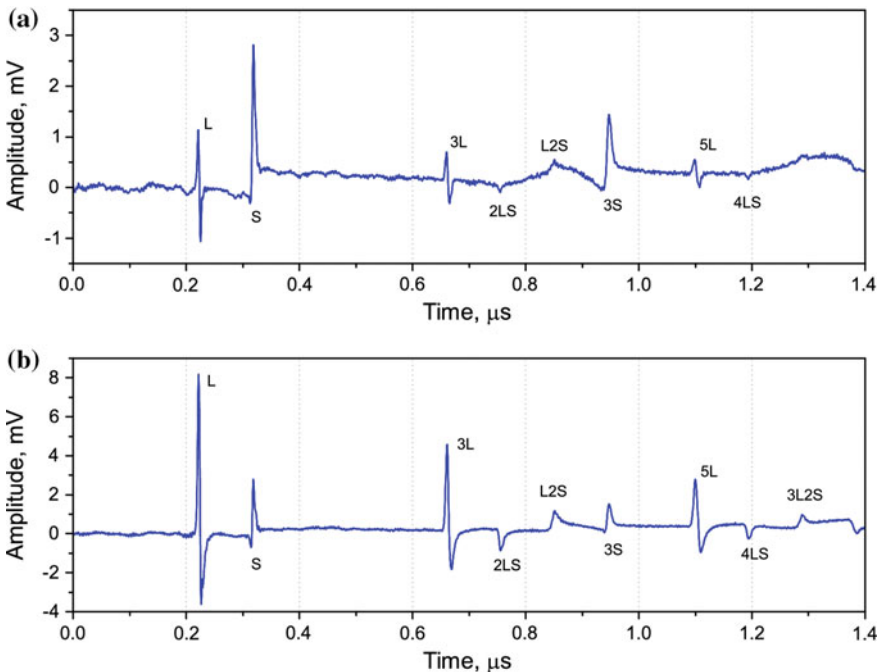


Fig. 4 Optoacoustic pulses, detected in 1.16 ± 0.02 mm-thick Ni (100) disk, by EMAT in accordance with experimental arrangement without water layer (a). The irradiated surface of the disk was immersed in water, while the laser energy and position of the specimen were fixed. The peaks are assigned by mode of traveling pulses as longitudinal (*L*) and shear (*S*), where the *number* before letter means quantity of the pass thicknesses for this mode

atoms of impurities and dislocations. Generally, the attenuation increases with frequency while some terms demonstrate different frequency dependences and therefore dominate in different frequency ranges. It is rather difficult task to separate the contribution of different factors into experimentally measured attenuation of ultrasound. The damping of ultrasound reduces mainly the high-frequency part of the spectrum and, therefore, the peak-to-peak amplitude.

The single crystal materials possess anisotropy of physical properties in contrast to glasses and polymers, which are examples of isotropic materials. The most metals and composite materials can be considered only as statistically isotropic media that means their properties are equal for different directions at the distances, which are significantly larger than the sizes of local inhomogeneities. As polycrystalline materials comprises of randomly oriented grains their size strongly influence on the scattering, which implies conversion of initially propagating ultrasonic waves at the grain boundaries to refracted and reflected waves of both modes. Thus, the scattering also decreases the amplitude of the probe pulse with distance. The unified theory of scattering has defined dependences of attenuation α for three possible regimes according to the relation of propagating wavelength and mean value of grain size [8]:

- (i) Rayleigh scattering, $d < \lambda$ for $\alpha \propto d^3 f^4$;
- (ii) Stochastic scattering, $d \approx \lambda$ for $\alpha \propto d f^2$;
- (iii) Geometric scattering, $d > \lambda$ for $\alpha \propto 1/d$.

These expressions were used in numerous attempts to reveal the mean value of microstructure of polycrystalline materials by measured attenuation. In order to estimate the regime of scattering for operational bandwidth of laser-induced ultrasound, the value of longitudinal velocity in metals is around 5 km/s that means the bandwidth from 1 MHz up to 100 MHz comprises of the wavelengths from 5 mm down to 50 μm , respectively. The mean value of grain size is around 50 μm and, therefore, the scattering should be described in the terms of Rayleigh and stochastic scattering. This transition regime has some specialties. Unfortunately, experiments show discrepancy with theoretical estimations and the task of microstructure evaluation by measured attenuation of ultrasound is not solved up to now. Clearly, elastic moduli of single crystal cell should be averaged over all possible grain orientations to characterize the macroscopic value of elastic moduli. The averaging procedure uses invariant of anisotropy, which shows how strong is difference of moduli for statistically isotropic medium, $\varepsilon = C_{11} - C_{12} - 2C_{44}$.

The invariants show the degree of anisotropy and can be used for estimation of the velocities in statistically isotropic media without texture. The elastic moduli of metals with cubic cell and the invariants of anisotropy are present in Table 1. Voigt averaging procedure gives the upper value for velocities operating with stiffness tensor in contrast to Reuss procedure, which employs compliance tensor and Hill procedure, which gives a mean value of the mentioned above Voigt and Reuss averaging procedures [2, 8].

Table 1 Moduli of single crystal cells and calculated anisotropy invariants

Material	C_{11} (GPa)	C_{12} (GPa)	C_{44} (GPa)	ε (GPa)
Fe	229.3	134.1	116.7	-138.2
Ni	248.1	154.9	124.2	-155.2
Cu	168.4	121.4	75.4	-103.8
Al	109.3	57.5	30.1	-8.4

According to the unified scattering theory, the averaged values of longitudinal and shear velocities are defined as

$$C_L = C_{11} - 2\varepsilon/5, \quad C_S = C_{44} + \varepsilon/5 \quad (5)$$

that means that the value of longitudinal wave velocity is higher in polycrystals in contrast to shear velocity, which is lower for considered metals with cubic cell. According to the calculated values of anisotropy invariant, the aluminum demonstrates the lowest scattering of elastic waves. The strong anisotropy implies multiple scattering with conversion of elastic waves that produces disturbance over the whole specimen, but in contrast to the optical scattering elastic waves can be coherent in time with the ballistic waves [9].

Besides the grain microstructure, ferromagnetic materials possess domain structure, which contributes additional noise, since specimen is not completely magnetized. The mean value of domain size is comparable with the grain size in the case of polycrystalline materials. The signals obtained by PVDF and EMAT in 2.4 mm-thick polycrystalline nickel disk are present in Fig. 5. Piezoelectric transducer demonstrates higher peak-to-peak amplitude of longitudinal pulses, while EMAT detects primary longitudinal pulse and the following ‘microstructure’s noise’, which masks the shear pulse and the first reverberation $3L$, which can be identified only due to the signal of PVDF. The measured velocity of longitudinal pulses by PVDF sensor is 5.73 ± 0.02 km/s and it is equal to 5.71 ± 0.02 km/s by EMAT. The obtained signals reveal the complexity of shear pulse’s detection in the case of polycrystalline specimens.

Among the results of the unified theory is conclusion about stronger scattering of shear waves in comparison with longitudinal waves in the transition regime from Rayleigh to stochastic scattering, where the scattering satisfies weaker the second power law frequency dependence for longitudinal waves in such strongly anisotropic material as iron. The favorite conditions for longitudinal pulse excitation yielded the range from 5 up to 200 MHz in 0.4 mm-thick steel that was possible due to the short traveling distance and conserved coherent ballistic waves [10]. However, the scattering of the laser-induced longitudinal probe pulse disturbs the whole volume of the specimen and proper detection of coming later shear pulse is very difficult due to the microstructure’s noise, which conceals the weak shear pulse as it is shown in Fig. 5b. The possible solution relates to suppression of the longitudinal pulse excitation and magnification of the shear pulses. Such arrangement can be carried out by cylindrical lens, which focuses the laser radiation into elongated spot with lateral size about $50 \mu\text{m}$ as it is present in Fig. 6. The form of

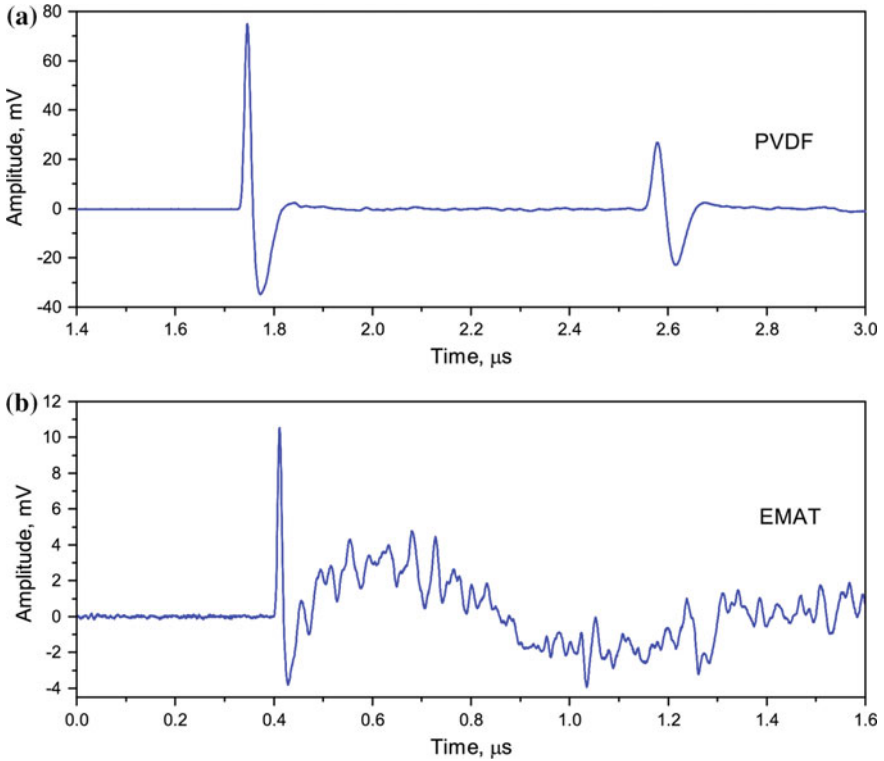


Fig. 5 Optoacoustic pulses detected in 2.4 ± 0.05 mm-thick polycrystalline nickel disk by PVDF (a) and EMAT (b) transducers, while the power density was equal for both cases

induced wave front can be complex for longitudinal and shear ultrasonic beams, but its mean position is around moving cylindrical surface in the far diffraction zone. The focusing induces the ablation of material and launches initial longitudinal waves normally to the surface while shear waves spread within the narrower angle in bulk [11]. The application of half-cylindrical specimen's form and noncontact detection by EMATs is obvious.

The evaluation of the properties of construction materials such as steel is important task of material science. Because steel is the complex composite of iron, carbon and other elements, the microstructure has significant local inhomogeneities and the propagation of high frequencies is challenge. The half-disk specimen of steel 40× (Russian notation) was prepared on turn/mill machine with nominal radius of 10 mm and thickness of 5 mm, see the Fig. 6b. The steel 40× contains about 0.40% of carbon and more than 0.8%, but less than 1.5% of chromium. American notation of the similar steel sort is 5140 that can be used for references. The series of signals measured in steel specimen according to the sketch in Fig. 6a are present in Fig. 7. The signals were averaged 64 times for reduction of electronics noise. This arrangement allowed to decrease sensitivity of EMAT to the

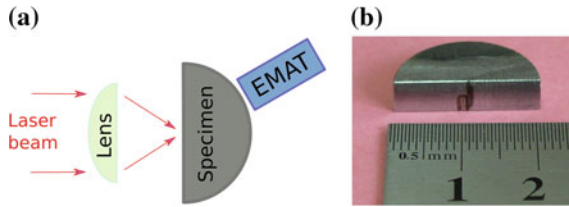
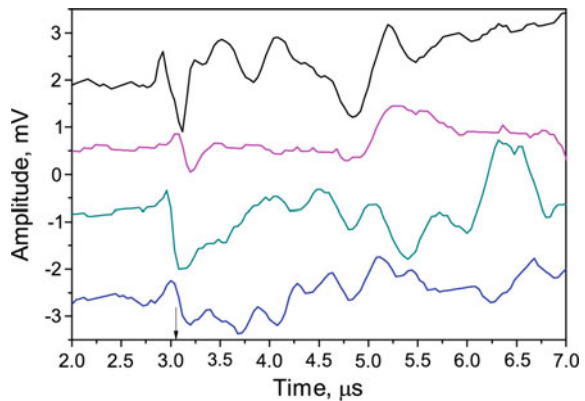


Fig. 6 Experimental arrangement of efficient excitation of shear optoacoustic pulses (a), 5 mm-thick specimen of steel 40× (Russian notation) with the radius of 10 mm (b), where the black vertical sign is the imprint of the laser spot

Fig. 7 Optoacoustic signals measured at four different loci of cylindrical surface of the steel 40× specimen. Signals are vertically shifted. The arrow points out the mean value of arriving time of shear pulses at 3.06 μs



disturbance induced by primary longitudinal pulse and to recognize the shear pulses arriving at about 3.05 μs afterwards the scattered ultrasonic waves or ‘microstructure’s noises’ come.

The mean experimental value of the shear pulse velocity in series of measurements was calculated from the ratio of radius and mean time of zero-crossing point. The accuracy of velocity estimation relates to the errors of traveling distance and measuring time interval from the exciting laser pulse to the arriving of the ultrasonic pulse. The slide gauge yields the actual radius of the half-disk 10 mm that is used for calculation. The thickness can be measured with the accuracy of 0.05 mm, that yield the instrumental mistake of about 0.5% for the distance 10 mm, while the relative error decreases with traveling distance. The oscilloscope with analogue bandwidth of 200 MHz and discretization rate of 1 GS/s was used that provided the temporal resolution about 5 ns. The relative error of velocity measurements is the sum of the relative errors for distance and time. Since the velocity of shear waves is less than the velocity of compression waves the contribution of relative value of time error for shear pulse is less and yields 0.2% for presented steel 40× specimen with the radius of 10 mm. The total relative mistake of shear velocity measurements is 1.2%. The measured shear pulse velocity is 3.27 ± 0.04 km/s. The measured by

hydrostatic weighting method density of specimen is $7810 \pm 10 \text{ kg/m}^3$ and calculated shear modulus is $83 \pm 2 \text{ GPa}$, which is reasonable in comparison with table values.

4 Discussions

The irradiation of the metal specimen surface by nanosecond laser pulses induces shear and longitudinal ultrasonic pulses while their directivity and efficiency depend on the transparent media properties and the intensity distribution over the laser spot cross-section. In order to achieve better temporal resolution in measurements, the highest frequencies should be launched into material and detected by transducers, but the scattering and attenuation significantly reduce mainly in this part of the spectrum. The wide spot of laser beam launches the longitudinal pulse due to the thermoelastic sources at air–metal interface that implies bipolar temporal form of signal with dominated high-frequency part of the spectrum. The covering of the metal surface by transparent liquid allows one to increase the low-frequency part of the spectrum and launches the longitudinal pulse with pronounced compression phase. The fluence above 20 MW/cm^2 overheats and evaporates surface's particles, which exert normal to the surface and increase the amplitude of longitudinal pulses.

The shear pulses generation requires strong gradient of heat deposited sources at the surface of the specimen that can be done by focusing the laser radiation. The round laser beam spot launches shear waves into the bulk of the material, unfortunately, their directivity is not normal to the surface [9]. The small linear size of the source can be consider in the far zone as a point source but the amplitude of the pressure quickly decreases with distance. The appropriate solution uses cylindrical lens and half-cylindrical specimen. The laser spot is located along the geometrical axis of half-cylinder or half-disk. Among the advantages is the quasi-cylindrical divergence, which allows decrease the influence of diffraction and partly conserve the low frequencies of the pulse spectrum in comparison with point-like source, since diffraction influences on the form of the ultrasonic beam and the spectrum of the pressure pulse. The bandwidth of the transducers for detection of laser-induced ultrasound should consider the range from 5 MHz up to 50 MHz with some deviations due to the anisotropy of the material and the microstructure.

The broadband detection should measure the useful part of ultrasound spectrum. Obviously, there are no conditions for equality of loss during propagation as well flat sensitivity over the bandwidth, which is induced initially. Despite the essentially broadband spectrum of laser-induced ultrasonic pulses the detection is possible only for narrow range, which should contain mean and high frequencies corresponding to the range from 20 up to 50 MHz in the case of polycrystalline metals or steels. The capacity of 2 mm diameter sensitive element of PVDF transducer provided the operation in the 'short-circuit current' mode in contrast to 'voltage' detection mode [10]. This frequency range is comparable with the

bandwidth of optical detection systems, which operation region is significantly narrower to their capabilities band in the case of polycrystalline specimen [11].

Actually optical methods employ different type of interferometers, which are sensitive to vertical displacement or velocity of the surface particles. It was stressed before that the presence of the short transient ultrasonic pulse induces the noise of microstructure over the whole volume of the specimen. These elastic waves are coherent and arrive after the primary longitudinal pulse to the area of the detection laser spot with a diameter about tens of micrometers. The contribution of scattered field depends on the laser spot locus and in the case of coarse microstructure its amplitude can be comparable with displacement induced by primary pulse or echoes therefore the measurements of the shear pulses is more difficult task for optical methods. EMAT and PVDF transducers show some advantages at measuring bulk ultrasonic pulses in metal due to intrinsic averaging of the useful signal over the larger area in comparison with optical methods. As the area of piezoelectric sensor is more than 100 times larger, these transducers demonstrate higher peak-to-peak amplitude in comparison to the 'microstructure's noise' and better sensitivity to the useful probe pulse and its echoes. EMATs also average the signal at the surface of the specimen over the area of coil. Despite unique capabilities regarding operation at elevated temperatures, noncontact excitation and detection of ultrasound via all-optical technique suffers due to impossibility to highlight useful signals or reverberations of the pulses from the scattered ultrasonic field or 'microstructure's noise'. The averaging of the signals over several detection points does not widens the spectrum and does not improve the accuracy of time-resolved measurements since the coherent ballistic and scattered waves propagate along the specimen distance [9].

The task of estimation of mean grain size of polycrystalline materials is very attractive for material sciences and industry since microstructure strongly influences on strength and hardness. There were carried out numerous experiments, which stated the decrease of the attenuation with smaller size of the grains. This task seems to be very similar to determination of the scatterer size in turbid media by measuring the intensity diagram of scattered optical waves. The lengths of diffusion and attenuation are defined in penetration depth distance, where the radiation is coherent and the amplitude decays. The laser-induced acoustical pulses are essentially broadband and experience multiple scattering at the grain boundaries that changes the spectrum and wave front of ultrasonic beam with distance. The immersion methods with piezoelectric sensors measure averaged ballistic waves, which experience moderate deviation from the initial direction of ultrasonic beam propagation. The optical methods are very sensitive to the scattered ultrasonic field, which is coherent in the case of low attenuation but arrives later to the locus of the detection laser spot. The signals of EMAT show both features due to the integrating the ballistic waves over the area of the detection coil while the scattered coherent field over the same area yields 'microstructure's noise'. The presence of coherent and incoherent ultrasonic radiation for a wide range of ratio between the diffusion length and sample thickness is feature of acoustic scattering and measurements.

The induced disturbance decays slowly in the thicker specimen while the thinner specimens require shorter probe pulses and broader bandwidth.

The direct measurement of longitudinal and shear pulse velocities is not single approach for moduli evaluation. Ultrasonic and electromagnetic acoustic resonances are competitive techniques. Laser-induced resonant ultrasonic spectroscopy (LRUS) is an alternative method, which uses lasers for excitation and for measuring the elastic properties of the specimen with defined geometry [12]. The detection of the vertical particle displacement by laser interferometer at the surface of the specimen yields the vibrations' modes distribution, which depends on density and averaged stiffness tensor of the material. The correct identification of the modes uses convergence of the experimental results and modeling by varying moduli.

5 Conclusions

The laser-induced ultrasound is rapidly developing technique, which allows efficient excitation of bulk and surface ultrasonic pulses with essentially broad spectrum. The diffraction, attenuation and scattering lead to distortion of the wave front and to narrowing spectra of pulses propagating in the polycrystalline materials that decrease the peak-to-peak amplitudes with traveling distance, while the accuracy of the task of velocities measurement requires high frequencies detection. The measurements of longitudinal pulse velocity can be carried out by variety of the experimental arrangements but due to the noise of microstructure, the intrinsic instrumental averaging of PVDF transducers yields better performance. The initial localization of shear pulse sources along the cylinder axis and efficient excitation owing to focusing demonstrated successful combination of laser-induced pulses with EMATs, which are well-promising noncontact detection tools in the case of ferromagnetic materials, that can be employed for solutions of tasks both as material science as non-destructive testing.

References

1. H. Kolsky, *Stress Waves in Solids* (Dover Publications, 2003)
2. M. Hirao, H. Ogi. *EMATs for Science and Industry: Noncontacting Ultrasonic Measurements* (Springer, 2003)
3. V.É. Gusev, A.A. Karabutov, *Laser Optoacoustics* (American Institute of Physics, New York, 1993)
4. C.B. Scruby, L.E. Drain, *Laser Ultrasonics: Techniques and Applications* (Taylor & Francis, 1990)
5. V.V. Kozhushko, G. Paltauf, H. Krenn, S. Scheriau, R. Pippan, *J. Appl. Phys.* **107**, 94905 (2010)
6. I.M. Pelivanov, D.S. Kopylova, N.B. Podymova, A.A. Karabutov, *J. Appl. Phys.* **106**, 1 (2009)

7. A.A. Karabutov, N.B. Podymova, E.B. Cherepetskaya, *J. Appl. Mech. Tech. Phys.* **54**, 500 (2013)
8. F.E. Stanke, G.S. Kino, *J. Acoust. Soc. Am.* **75**, 665 (1984)
9. Tourin A., Derode A., Fink M., in *1999 IEEE Ultrason. Symp.Proceedings. International Symposium (Cat. No. 99CH37027)* **1**, 711 (2000)
10. V.V. Kozhushko, G. Paltauf, H. Krenn, *Acoust. Phys.* **59**, 250 (2013)
11. J. Kim, K.-Y. Jhang, *Int. J. Precis. Eng. Manuf.* **16**, 905 (2015)
12. D.H. Hurley, S.J. Reese, F. Farzbod, *J. Appl. Phys.* **111**(5), 053527 (2012)

Experimental Characterization of Composite Material Properties

P. Yukhymets, R.I. Dmytriienko, I. Ramadan and S.N. Bukharov

Abstract For determination of actual mechanical properties of composite material used in the manufacture of natural samples the original technique was proposed. Experimental characterization of composite material, intended for the repair of damaged pipelines during optimization of its service characteristics, revealed that introduction of disperse fillers in epoxy resin had a positive effect on the mechanical properties. Intensive experimental study showed that concentration of montmorillonite nanofiller had a significant impact on dynamic modulus of elasticity of composite materials based on epoxide resin while application of perforated metal tape in polymer resin composites demonstrated increasing of composite mechanical strength.

Keywords Composite material · Tensile test · Disperse filler · Dynamic modulus · Perforated metal tape

1 Introduction

Investigations in composite materials properties in the course of project implementation were carried out mainly for:

- (i) determination of actual mechanical properties of the materials used in the manufacture of natural samples with bandage for using them in calculation of the bandage geometric parameters;

P. Yukhymets (✉) · R.I. Dmytriienko
E.O. Paton Welding Institute, Kiev, Ukraine
e-mail: yupeter@ukr.net

I. Ramadan
Petroleum-Gas University of Ploiesti, Ploiești, Romania

S.N. Bukharov
V.A. Belyi Metal Polymer Research Institute of National
Academy Science of Belarus, Gomel, Belarus

- (ii) optimization of service characteristics of composite materials used for the repair of damaged pipelines in view of features of subsequent operation.

2 Actual Mechanical Properties

2.1 Materials of Reinforcing Element and Resin

As a reinforcing element during preparation of full-scale specimens I3 and I4 was used straight roving (Fig. 1) from fiberglass EC10 1680N-U10(168) [1], where in designation E—general purpose glass; C—continuous thread; 10—nominal diameter of elementary filament, μm ; 1680—nominal linear density, teks; N —for winding; U10—lubricant; 168—linear density of complex threads, teks. Single strand of roving consisted of ~ 1200 filaments. The roving was used in combination with epoxy resin KDA-HI [2].

Strength characteristics of the polymer matrix according to manufacturer's information after standard mode curing (100–180 °C during 2 h):

- flexural strength—90–110 MPa;
- tensile strength—75–80 MPa;
- impact strength—5–10 kJ/mm^2 ;
- elongation—5.5–8%.

2.2 Test Samples of Composite Material

To determine the mechanical properties of the composite material, the samples in the form of loop were manufactured. Specimen consisted of two branches, a and b (Fig. 2a). The loop formed by winding of the roving, soaked with epoxy, on special rig (Fig. 2c). During the winding the roving was stretched by force, which value was varied (Table 1).

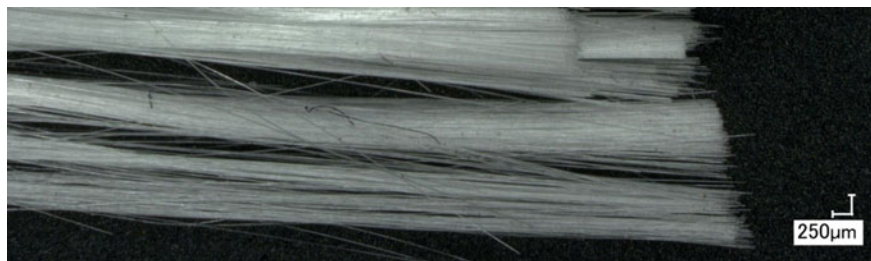


Fig. 1 Roving used as reinforcing element

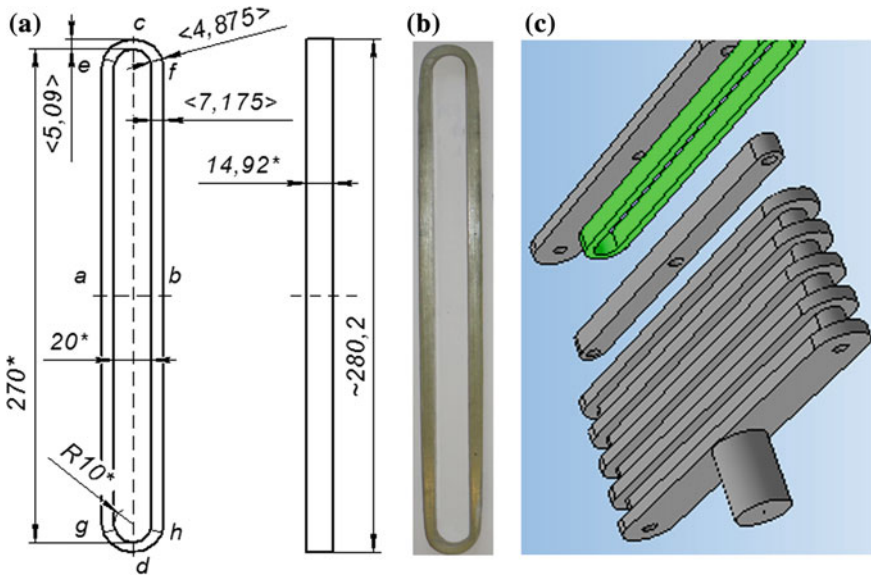


Fig. 2 Tensile sample: **a** geometrical dimensions: *asterisk* the same dimensions for all samples; $\langle \rangle$ average size; *a, b, c, d, e, f, g, h* sections of sample; **b** sample before test; **c** rig for samples preparation

Table 1 Characteristics of tensile samples

Parameter		Section	Sample				
			P1	P2	P3	P4	P5
Preliminary tension of roving N_1 , kg ^a			2	4	3	3.5	0.1
Number of roving turns			80	80	80	80	75
Width, mm	Branch	a	7.3	6.8	6.7	7.0	8.0
		b	7.1	6.8	6.5	7.0	8.6
	Rounding	c	4.9	5.1	5.3	4.9	5.2
		d	4.9	5.0	4.9	5.2	5.5
		e	4.8	4.6	4.8	5.0	5.0
		g	4.9	4.7	4.7	4.9	5.0
		f	4.9	4.7	5	4.8	5.0
		h	4.9	4.6	4.7	5.0	5.5
Location of fracture in section			g	f	e	e	g

^aAmplitude variation during winding ± 1.5 kg

2.3 Test Results of the Composite Material

The test was carried out on machine Instron 8802 using biaxial extensometer 2620-614 with longitudinal and transverse base of measurement (25 and 15 mm, respectively, Fig. 3). The speed of deformation was 10 mm/min.

Figure 4 gives details of the sample P2 tension. Linear dependence between tensile load and force is true in all range of deformation up to the sample break.

Summary of the test results of specimens P1–P5, brought to single roving, are present in Table 2. It should be noted that dependence of the destructive force and ultimate deformation on preliminary tension of roving was not detected.

2.4 Tensile Test of the Roving

The test was carried out on machine Instron 8802 equipped with snail grips (Fig. 5a) and extensometer 2620-601. The sections of the roving, spooled from reel,

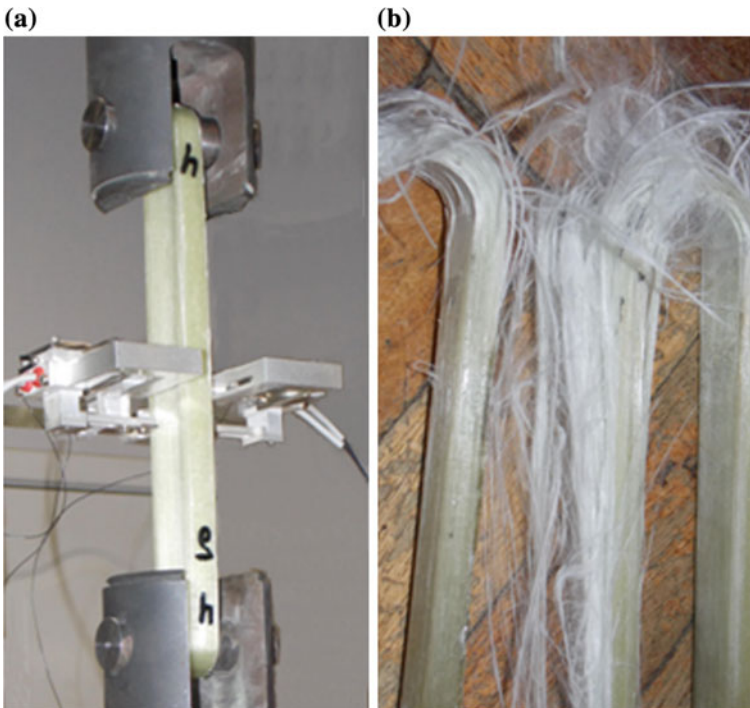


Fig. 3 Tensile test: **a** sample in grips; **b** features of samples fracture

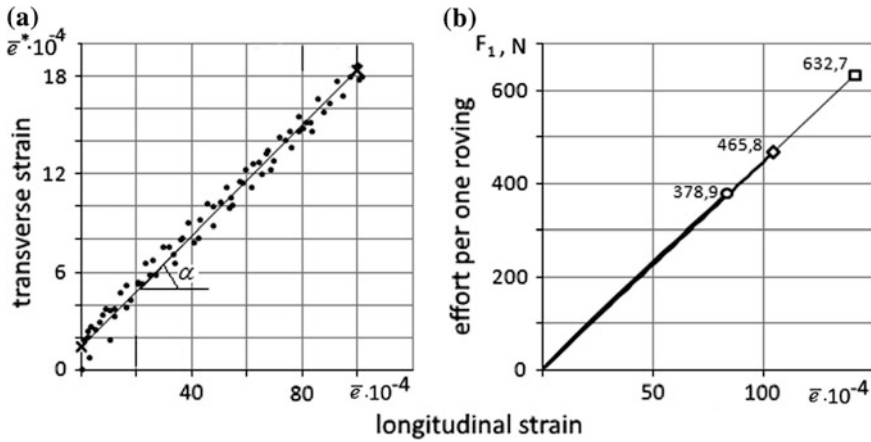


Fig. 4 Tension of sample P2

Table 2 Results of tensile tests

Sample→	P1	P2	P3	P4	P5	Average
Preliminary tension of roving (N)	19.6	39.2	29.4	34.3	1	24.7
Fracture force (kN)	95.28	101.23	99.19	96.04	99.87	98.32
Maximal strain (%)	1.36	1.44	1.59	1.39	1.58	1.47
Poisson's ratio (μ)	0.179	0.196	0.164	–	0.147	0.172
Young's modulus ^a E (MPa)	32,721	34,645	31,673	33,079	25,518	31,527
Tensile strength ^a (MPa)	445.0	498.9	503.6	459.8	403.2	462.1

^aThickness in the middle part of the loop was used in the calculation of the mechanical properties of composite

were used as samples with next parameters: measuring base is 52.5 mm, length of working section is 140 mm, speed of displacement during test is 30 mm/min.

Test diagrams of samples are present in Fig. 5b. Comparison of test results of the roving and composite material is given in Table 3.

2.5 Additional Research of the Material

2.5.1 Linear Density of the Roving

A sample of roving with length of 100 ± 1 mm was weighed on Denver Instrument APX-60 (maximum permissible weight is 60 g, measuring accuracy is 0.1 mg) (Table 4).

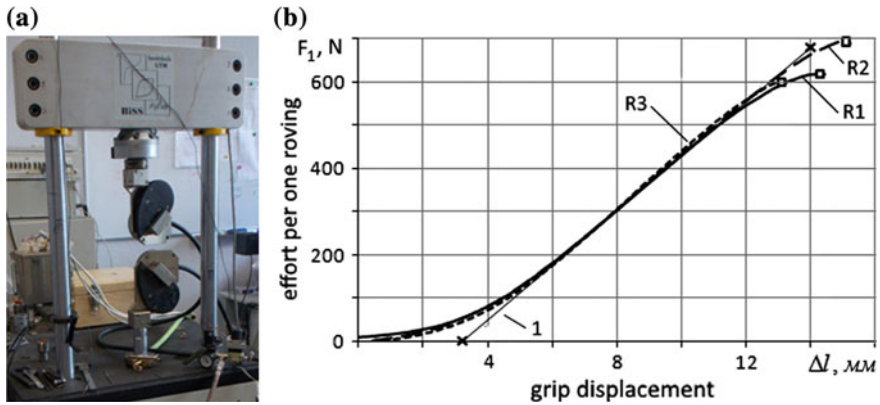


Fig. 5 Tensile test of roving: **a** general view of the roving test; **b** tensile diagram: *R1*, *R2*, *R3* Samples marking; *1* Approximation of diagrams with linear dependence

Table 3 Test results of the roving and composite material

Roving			Composite material		
Sample	\bar{e}	F_1, H	Sample	\bar{e}	F_1, H
R1	0.0164	620	P1	0.0133	595.5
R2	0.0131	690	P2	0.0142	632.7
R3	0.0170	600	P3	0.0144	620.0
			P4	0.0124	600.3
			P5	0.0159	665.8
Average	0.0155	636.7	Average	0.0140	622.9
min	0.0131	600	min	0.0124	595.5
max	0.0170	690	max	0.0159	665.8

The difference in linear density of roving, according to measurements is 1721.4 teks and certificate is 1760 teks was $\sim 2.2\%$.

2.5.2 Photomicrography of the Roving

Based on pictures (Fig. 6), average filament diameter was $\sim 10 \mu\text{m}$.

2.5.3 Measurement of the Cross-Section Area of Roving

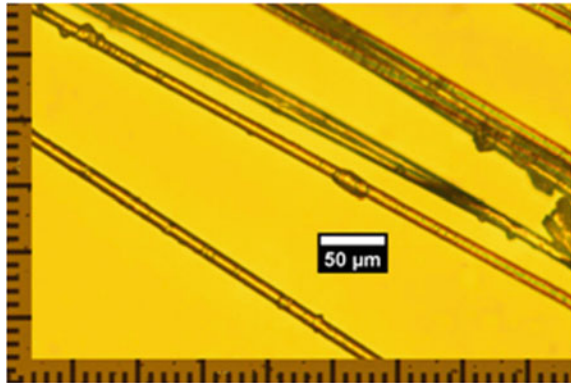
After dense packing of 57 roving strands in a groove under tension force of $\sim 50 \text{ N}$, the calculated cross-section area of 1 roving amounted to 1.044 mm^2 .

Note that average area per 1 roving of samples P1–P5 was: for sections (a, b) 1.36 mm^2 ; (c, d) 0.96 mm^2 ; (e, f, g, h) 0.92 mm^2 , respectively (Fig. 6).

Table 4 Weight of roving with 1 m length

No. weighing	1	2	3	4	5	6	7	8	9	Average
Weight (g)	1.7214	1.7215	1.7212	1.7214	1.7215	1.7214	1.7214	1.7214	1.7215	1.7214

Fig. 6 Filaments of roving



3 Optimization of Service Characteristics

3.1 Effect of Disperse Fillers

The effect of disperse fillers including nanoparticles on the mechanical properties of epoxy based composites for the repair of pipelines using composite-muff technology has been studied [3]. Epoxy resins of different grades (ED-20 and E-181) have been used as binders for composite materials. As the disperse fillers the following materials have been used: metal powder, carbonyl iron, graphite, calcium stearate, and various epoxy-silicates of metals. The composites have been prepared by mixing all components at low shear. The results demonstrated that an introduction of disperse fillers in epoxy resin had a positive effect on the mechanical properties of examined composites.

The plot, shown in Fig. 7a, proves that the elasticity modulus of the composite materials increases by 5–15%. The plot in Fig. 7b proves that material yield strength increases by 16–35% in dependence on the filler type. Analysis of mechanical fracture pattern shows that the introduction of fillers leads to embrittlement of the composite material as compared to the initial resins. This causes the need for the introduction of additional plasticizers of the matrix phase.

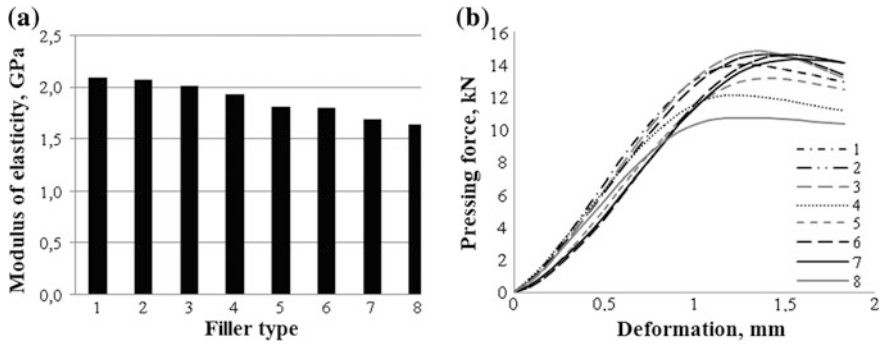


Fig. 7 Effect of the disperse fillers on the elasticity modulus of the composite (a) and yield strength (b) of epoxy-based composites (1-graphite (GKZ) + calcium stearate, 2-metal powder (Fe), 3-carbonyl iron (VKZ), 4-graphite (GKZ) + epoxy silicate Cu + cal

3.2 Dynamic Mechanical Characteristics

An experimental study of the dynamic mechanical characteristics of composite materials based on epoxide resins and intended for a composite-sleeve pipeline technology has been performed. The aim of the investigation was to estimate an efficiency of their application in raising resistance of the pipelines to hydraulic shock and vibration. Series of physic-chemical methods, namely: the compounding (mechanical mixing) method, plasticization, and impregnation of organic and inorganic fillers have been considered in the present study. The tests were conducted using a dynamic mechanical analyzer Q-800 in order to determine the dynamic characteristics of the materials as a function of time, temperature, and frequency following double cantilever geometry. Modifiers that provide the best mechanical properties, including epoxy silicate iron, graphite, and calcium stearate, have been defined by the results of static and dynamic mechanical tests. As follows from the plots presented in Fig. 8 dependence of the dynamic modulus of elasticity on the concentration of montmorillonite (MMRT) nanofiller (with varying from 1 to 10%) has an extreme kind. The maximum value of E_d is reached at 5 mass% of montmorillonite concentration.

The dependence of the dynamic modulus of elasticity on the mass concentration of montmorillonite correlates with the results of acoustic tests of sandwich structures with a damping layer of the composites based on epoxy resin, as presented in Fig. 9. It is very important to note that introduction the montmorillonite nanofiller of optimum concentration in epoxy matrix provides increase in the sound-transmission in the low and medium frequency ranges up to 40 dB, and has no significant effect on the density of the composite material for damping layer. As a result, it does not increase the total weight of the layered composite structure.

New formulations of epoxy composites containing nano-sized silicate filler—montmorillonite, providing an increase in the coefficient of mechanical losses of up

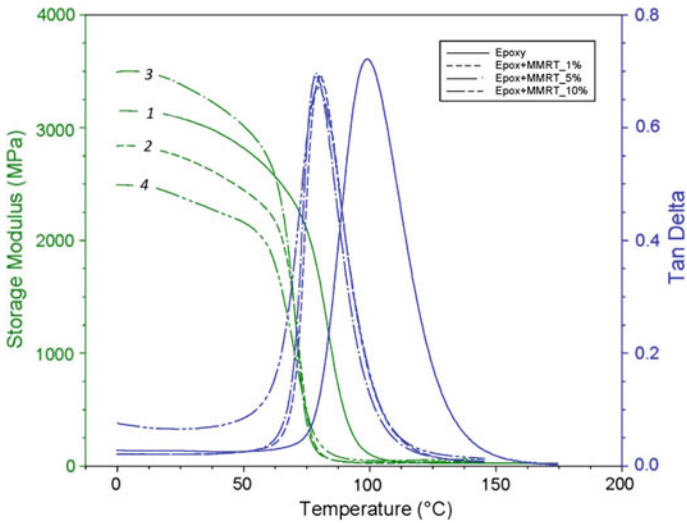


Fig. 8 Temperature dependences of the storage modulus and mechanical loss tangent of epoxy composites of different compositions: 1 Initial composition (epoxy resin without fillers); 2 Composition with 1 wt% MMRT; 3 Composition with 5 wt% MMRT; 4 Composition with 10 wt % MMRT

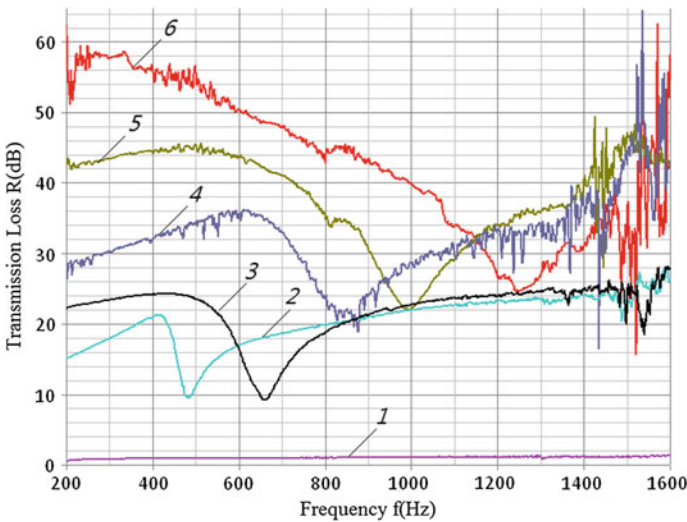
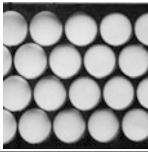
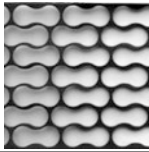
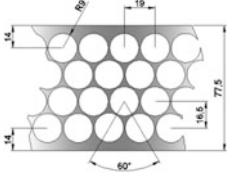
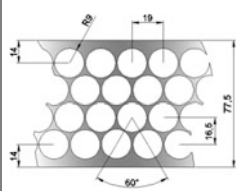


Fig. 9 Transmission loss of the materials and layered structures: 1 Foamed polyurethane (thickness of 25 mm); 2 Steel plate (thickness of 1 mm); 3 Absorbing and damping layers without a steel plate (thickness of 8 mm); 4, 5, and 6 Structures with a damping layer based on nano-modified epoxy resin containing 10, 1, and 5 wt% MMRT, respectively

Table 5 Metal punch tapes used samples main characteristics

Tape common view		
Technical drawings		
Type	A	C
Steel	08ps-OM-T-2-T	50-T-S-N
Standard	GOST 503-81	GOST 2284-79
$F_{t,max}$ (N)	5539.86	10052.61
σ_v (N/mm ²)	220.65	406.81
$\Delta l_{t,pl.}$ (mm)	6.54	2.25
Relative strain $\varepsilon_{F,max}$	0.039320	0.012107

to 30%, offset $tg\delta_{max}$ at lower temperatures on 25–30 °C and rising to 20% of $tg\delta_{max}$ were proposed in result of studies. Wherein the incorporation basalt fibers into the composite as reinforcing fillers compensates undesirable reduction of dynamic modulus associated with the introduction of the montmorillonite and increases it by 8.3% compared to the initial composition.

3.3 Using of Perforated Metal Tapes

Utilization of two types of perforated metal tapes in polymer resins has been investigated for an application in pipelines repair. Main characteristics of metal punch tapes are present in Table 5. The mechanical properties of obtained composites (Fig. 10a) have been evaluated by three-point bending tests (Fig. 10b). Results are present in Fig. 10c. Application of perforated metal tape in polymer resin composites demonstrates increasing of mechanical strength, which is very important for material used for repairing of pipelines.

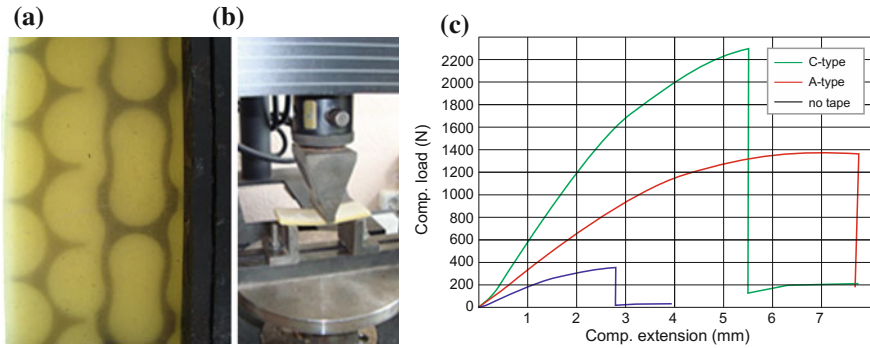


Fig. 10 Polymer–metal punch tape composite sample in translucent lighting (a), three-point deformation test (b), and their test results (c)

4 Conclusions

- (i) We proposed original technique for determining the mechanical properties of a composite material based on glass fibers and epoxy resin.
- (ii) Introduction of disperse fillers in epoxy resin had a positive effect on the mechanical properties of examined composites.
- (iii) Concentration of montmorillonite nanofiller had a significant impact on dynamic modulus of elasticity of composite materials based on epoxide resin.
- (iv) Application of perforated metal tape in polymer resin composites demonstrated increasing of composite mechanical strength.

References

1. G. 17139, *Fiberglass. Roving. Specifications*, Minsk, 2000 (In Russian)
2. T. U. 24.6-0030314547-002, *Epoxy Resin* KDA-HI, 2004 (In Russian)
3. E.F. Kudina, E. Barkanov, N.S. Vinidictova, Use of nano-structured modifiers to improve the operational characteristics of pipelines’s protective coatings, class. Phys. Chem. **42**(5), 512 (2016)

Part IV
Technologies Used for the Composite
Repair Systems of Transmission Pipelines

Comparative Analysis of Existing Technologies for Composite Repair Systems

E. Kudina, S.N. Bukharov, V.P. Sergienko and Andrei Dumitrescu

Abstract The given chapter presents a comparative analysis of the technologies presently employed for the repair, using reinforcing wraps/sleeves made of polymeric composite materials, of the areas with volumetric surface defects (also named local metal loss defects) of the transmission pipelines intended for hydrocarbons (petroleum, liquid petroleum products, natural gas, etc.) or other fluids. The above-mentioned technologies are also compared with other pipeline repair technologies (using metallic components and eventually requiring welding operations to be performed) in order to underline their advantages especially in the conditions in which it is preferable, due to the economic benefits, to perform the repair works on the in-service pipeline (without stopping the fluid supply). In addition, the technologies used to apply coating systems (containing polymeric composite materials) intended for the corrosion protection of the transmission pipelines or for the repair of such protection system are also compared and analysed.

Keywords Composite material · Wraps/sleeves · Repair system/technology · Transmission pipeline

1 Introduction

The activities of transporting various fluids present essential services that must be provided continuously. They typically use transmission pipelines systems (the great majority of which are made from steel pipes and components) intended for hydrocarbons (petroleum, liquid petroleum products, natural gas, liquefied petroleum or natural gas) or other fluids (water, ammonia, etc.). Therefore, the techno-

E. Kudina (✉) · S.N. Bukharov · V.P. Sergienko
V.A. Belyi Metal Polymer Research Institute of National Academy
of Sciences of Belarus, Gomel, Belarus
e-mail: kudina_mpri@tut.by

A. Dumitrescu
Petroleum-Gas University of Ploiesti, Ploiești, Romania

logical procedures, selected and normally used for the repair of these pipelines, need to be applied without removing the pipelines out of service. Thus, they should be executed onto the pipeline under pressure (subjected to the internal pressure loading due to the transported fluid).

The conventional methods for transmission pipelines repair supposed total drainage of the transported fluid from the damaged section, and this is a costly operation. In conditions of serious fund deficiency, in-service pipelines repair becomes quite actual and is presently preferred. Such an approach decreases shortage of petroleum or gas supply, pipe replacement expenses, the amount of fluid released in the environment, as well as gas losses during gas pipelines blow-through. As experience of leading companies in the branch of fuel-energy technologies proves, the cost of in-service repair can be 20–25 times lower than at traditional repair methods. Hence, in-service repair is justified from both economic and environmental points of view. Furthermore, long-term planning of local repairs is also possible, allowing one to maintain continuously safe operation of transmission pipelines.

The present day situation can be characterised by the fact that modern diagnostic methods are able to detect various critical defects, while the terms and cost of construction of new transmission lines make difficult the timely substitution of the outdated pipe portions. In this connection, a request arises for the development of inexpensive and not laborious, but at the same time effective and reliable, methods of repairing pipelines [1].

The common technological procedures, used to repair damaged pipelines (on which defects of any type have been detected), consist of the consolidation (by applying patches, sleeves, composite materials wraps, etc.) or replacement of the pipeline segments with defects and they can be classified and codified as shown in Fig. 1 [2]. The choice of a specific repair technology depends on the degree of the pipe damage, and the task is to restore the pipeline transport and carrying capacities.

The advantages of the pipeline repair methods using sleeves/wraps made of composite materials (code *0000-10*, highlighted in Fig. 1) are the following:

- the possibilities to perform repair on in-service pipelines;
- low time expenditure;
- increased lifespan of the entire transmission pipeline system;
- the wrap structure is lighter and stronger than a steel structure;
- the composite wrap has corrosion resistance and wear resistance;
- the possibility of usage on bent areas of the pipeline or on pipeline components.

Due to the advantages mentioned above and visible also in the comparison summarised in Table 1 [3], in the last years the repair procedures without welding have imposed themselves. Such procedures normally use composite materials wraps and they represent the repair method that is studied in the present book. Furthermore, if welding operations are performed on in-service (under pressure) pipelines, special requirements shall be imposed to the welding technologies, as detailed in [4, 5].

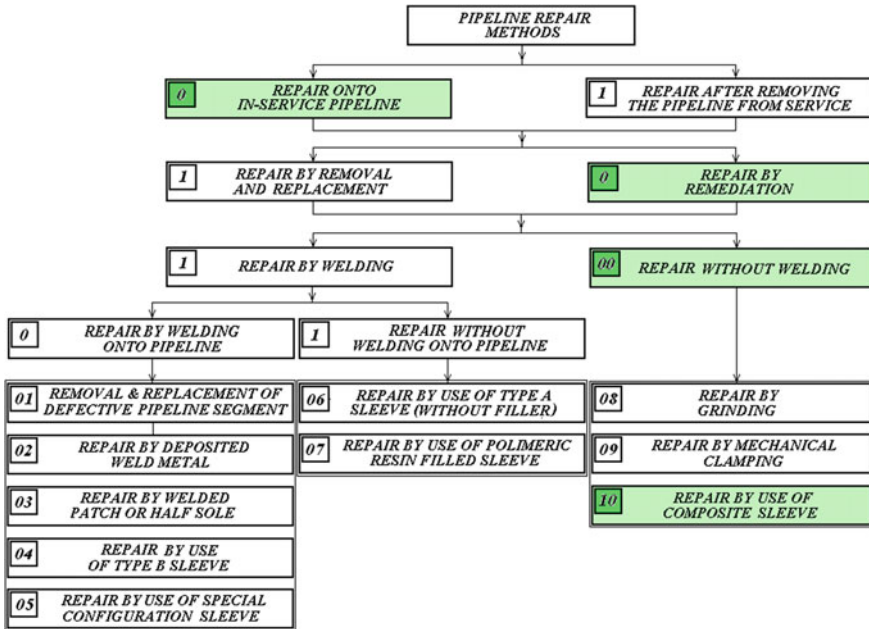


Fig. 1 Classification and codification of the repair procedures used for transmission pipelines

Table 1 Comparison between different repair technologies used for transmission pipelines

Criterion	Repair technology		
	Cut out and replace	Welded steel sleeve	Composite wrap/sleeve
Production loss ^a	Major	Minor	None
Labour force required	Large	Large	Small
Labour skill level	High	High	Moderate
Welding	Substantial	Substantial	None
Radiography required	Yes	Yes	None
Heavy equipment required	Major	Major	None
Time scale	Major	Major	Minor
Price	High	High	Reasonable

^aBecause the pipeline is taken out of service or due to some modifications in the manner of operation of the pipeline while performing maintenance works

The repair of the areas with volumetric surface defects (VSDs), also named local metal loss defects (whose assessment is detailed in Chapters “Characterisation of Volumetric Surface Defects”, “Assessment of the Remaining Strength Factor and Residual Life of Damaged Pipelines” and “Assessment of Interacting Volumetric Surface Defects”), of the transmission pipelines by means of applying composite

materials sleeves/wraps has been used from some time. However, the problems afferent to the application of this repair procedure did not found yet technical solutions fully underlain and unanimously accepted. For this reason, we will compare in the present chapter the technologies using composite materials presently employed for pipeline repair, while Chapter “[Design of Composite Repair Systems](#)” will detail the design methods for the wraps made of such materials applied to reinforce a damaged pipeline section.

The activities to be carried out in order to repair the transmission pipelines with composite materials systems and the sequence in which they should be performed are summarised in the diagram from Fig. 2, drawn by processing the information from [6].

The extended use of composite repair systems has been reflected also in the international Norms regarding transmission pipelines maintenance and repair activities. Currently, there are two standards involving such issues: ASME PCC-2, Part 4 [7] and ISO/TS 24817 [8], entirely dedicated to composite repair.

The standard [7], in Article 4.1, provides the requirements for pipeline repair using a qualified non-metallic repair system, and defines the repair systems as those fabricated from a thermoset resin used in conjunction with fibres reinforcement (fibres shall be continuous). It also specifies the type of composite materials that can be used to repair the pipelines: the allowed such materials for the composite repair system include, but are not limited to glass, aramid or carbon fibre reinforcement, in a thermoset polymer (e.g., polyester, polyurethane, phenolic, vinyl ester or epoxy) matrix.

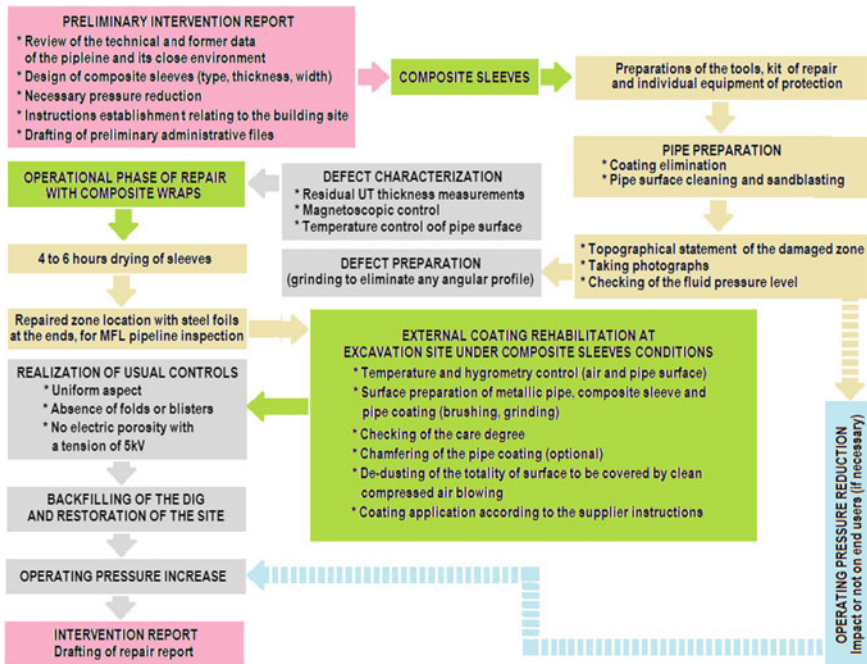


Fig. 2 Activities of pipeline repair using composite materials sleeves or wraps

The standard [8] defines composite repair laminates as those with carbon (CFRP), glass (GRP), aramid (AFRP), polyester, or any other similar sort of reinforcement material in a polyester, vinyl ester, epoxy or polyurethane matrix (other fibre and matrix types are also allowed). It covers the requirements and recommendations for the design, installation, testing and inspection for the external application of composite repairs to pipe work suffering from corrosion or other source of damage. ISO 24817 [8] also contains the following definitions: *Composite* is the thermoset resin system, reinforced by fibres; *Reinforcement* is the fibre, embedded in the resin system, with the remark that reinforcement results in mechanical properties superior to those of the base resin.

At the moment, the composite materials repair systems that are recommended and mostly widely used are based on a polymeric matrix (e.g., polyester, polyurethane, phenolic, vinyl ester or epoxy resin), reinforced by including fibres or fabrics made of continuous fibres (e.g., aramid, carbon, glass or polyester fibres or fabrics).

2 Transmission Pipeline Repair Technologies Using Composite Materials

The attempt of avoiding heavy machinery in the pipeline repair process led to the tendency to use more often the composite materials systems. The glass plastics density is four times lower than the one of steel, although the strength limit of the former is twice higher than of the latter. The first company that suggested a repair system with a rolled glass plastics was Argus, Ltd. (USA) [1]. Such system consisted of a band of rolled glass plastics (made of a unidirectional high-modular glass roving approaching by its elasticity modulus the one of the steel), installed on the damaged portion by winding, using a binding composition.

The construction and the technologies, employed to obtain the composite wraps/sleeves used to repair the defects, detected on transmission pipelines, represents an important item to be analysed for proper application of the repair procedure by using composite materials. Currently, several technical solutions are used for the complex repair wraps, made of composite materials. The main types of repair systems can be grouped into three categories:

1. Repair systems with composite wrap, obtained by wrapping a composite band/tape, known under the name *Layered Systems* (e.g., Clock Spring, Perma Wrap, Fiba Roll), that are the first widely used types of composite repair systems, applied on straight pipes or pipeline components. However, they have a limited usage for the repair of transmission pipelines because they are only applicable for rectilinear areas of pipes.
2. Repair systems with composite wrap of the monolithic type, which uses as components a polymeric matrix/resin and an arming material (reinforcing fibres). The wrap is obtained by applying on the steel pipe, in successive layers,

two components. They are known under the name *Wet lay-up system* (e.g., Armour Plate Pipe Wrap, Black Diamond, Aquawrap, Plug-n Wrap “PLUS”; ICECHIM Bucharest Wrap Repair/IWR, presented in Chapter “[Development of an Experimental Programme for Industrial Approbation](#)”). They can be used for the repair of both the rectilinear (straight) areas of transmission pipelines and the non-rectilinear components (elbows, bends, tees, valves, etc.); they have versatility and can be used on subsea pipelines or hot pipelines.

3. *Hybrid* repair systems (for example Rhinowrap, Furma Wrap, Power Sleeve, EAwrap, Viper-Skin, Ridge Back) use complex composite wraps, obtained by combining the repair components of the Layered Systems and Wet lay-up systems.

The layered systems can also be grouped in the following two sub-categories:

- (1) *CS-like wraps* (with various commercial trademarks: Clock Spring, Perma Wrap, Weld Wrap, Snap Wrap, etc.) use a tape/band made of composite material and a polymeric adhesive. At the same time, the wrap is obtained by whipping the tape on the steel pipe of the transmission line, the adherence of the band upon the steel pipe and the one between the successive tape layers of the wrap are guaranteed by applying the adhesive on them. The tape from which the wrap layers are obtained is a composite material, armed with fibres (woven or not-woven, long or short, oriented or non-oriented), and the repair wrap, obtained on the steel pipe, is a stratified composite, made up from this tape (which in its turn is a composite) and the polymeric adhesive applied between the band layers;
- (2) *FR-like wraps* (Fiba Roll, Syntho-Glass, etc.) use a self-adhesive tape of composite material with a complex structure. At the same time, the wrap is made by whipping the tape on the steel pipe, the adherence of the tape upon the pipe and the adherence between the successive tape layers of the wrap are guaranteed by the adhesive substances, incorporated in the tape, impregnated on the arming component of the tape and/or applied before whipping.

Figure 3 shows some of the most used trademarks of composite repair systems: Clock Spring (Fig. 3a) [9] and Fiba Roll (Fig. 3b) [10]. They are both layered systems, belonging to each of the two sub-categories defined above, while Black Diamond (Fig. 3c) [11] is a wet lay-up system.

Any repair system (using composite materials, intended for transmission pipeline systems) is defined by the international standards in use [7, 8] as a combination of the following elements (for which the qualification tests have to be performed):

- (i) the substrate (the steel pipe or pipeline component which is repaired);
- (ii) surface preparation (the preparation of the substrate surface in the area that is to be repaired);
- (iii) the polymeric filler (used to fill the defects and to reconstruct the external configuration of the substrate, before applying the composite material sleeve/wrap);

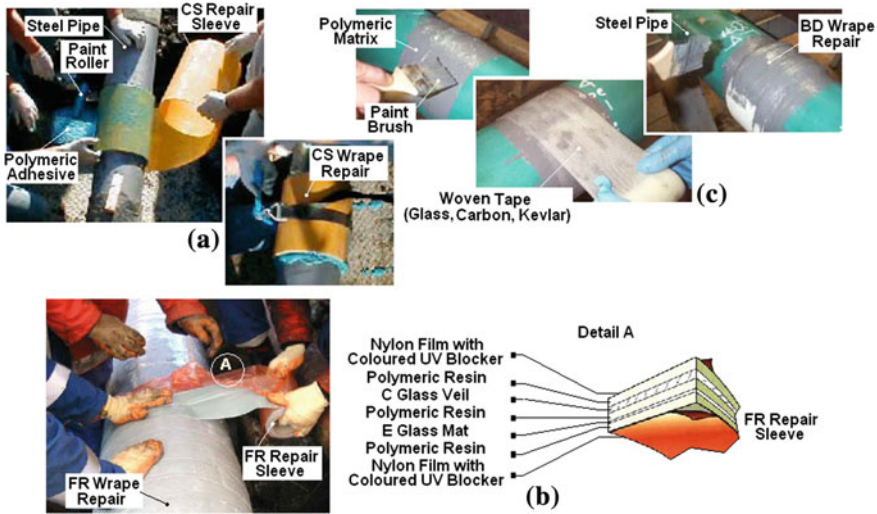


Fig. 3 Modalities of executing the composite materials wraps for pipelines repair: **a** Clock Spring (CS) wrap; **b** Fiba Roll (FR) sleeve; **c** Black Diamond (BD) wrap

- (iv) the repairing wrap/sleeve from composite material and its components: the polymeric resin matrix and the reinforcing material with fibres or the band from composite material and the polymeric adhesive (binder);
- (v) the repair procedure (the polymeric filler and composite wrap application procedures, and the verification procedures for the assessment of the repair quality).

It should be underlined that a polymeric resin itself cannot provide the needed strength of the repair system, especially for the case of medium and high-pressure transmission pipelines. Therefore, to achieve a high-quality repair when using polymers, some strengthening elements should be employed. It is expedient to use composite materials containing, e.g., a matrix component fabric with epoxide (or other) resins able to form a monolithic structure around the damaged pipe.

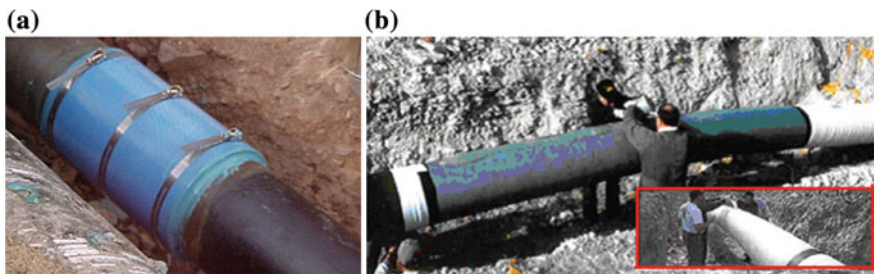
The most known trademarks of commercial repair system using composite materials and their manufacturing companies are listed in Table 2 [9–12]. Figure 4 shows two of the most used repair systems, the layered system Snap Wrap (Fig. 4a), developed by the Clock Spring Company [9], and the wet lay-up system Strong Back (Fig. 4b).

Analysing the information available in respect to the composite repair technologies, it can be seen that not all manufactures provide all data needed for installing and/or depositing the composite materials as many repair systems lack installation guidance, risk assessment and qualification data. Some manufacturers require that the repairs must be performed by qualified personnel, only certified by

Table 2 Commercial trademarks of composites repair systems for transmission pipelines

Type of system	Repair system registered trademarks	Manufacturing company
L	ClockSpring [®] ; Snap Wrap	Clock Spring Company LP
L	Perma Wrap; Weld Wrap [™]	Wrap Master, Inc.
L	Fiba Roll; FibaClad	FTI Group
W	Black Diamond [®] ; Diamond wrap [®] Subsea [™] Diamacor [™] ; Rhinowrap [®]	Citadel Technologies
W	Technowrap2 K [™] /Splashzone [™] / Potable [™] Techno wrap PRS [™] /H.P.PRS [™] /Core [™]	Walker Technical
W	Furma Wrap	Furmanite
W	CRSCarbon-Ply	ITW Wind Group
W	RES-Q [®] WrapS; RES-Q [®] WrapS/HT	T.D. Williamson
W	Power Sleeve [®] ; Aquawrap [®]	Power Wrap
W	EAWrap [™] /EAWrap-WG [™]	EA Services, Inc.
W	ArmorPlate [®] 360MP/UW/ZED/HT	Armour Plate, Inc.
W	Pipe Assure [™]	CSIRO (Australia)
W	REINFORCEKIT [®] 4D	3X Engineering
W	Strong Back	Strong Back Corp.
W	Syntho-Glass [®] XT/24; Syntho-Sleeve [®] Syntho-Shield [™] ; Trans-Wrap [™] ; Viper-Skin [™]	NRI—Neptune Research International
W	A+ Wrap [™] ; Forma Shield [™] ; Atlas [™] Splash Gard [™] ; Pipe Wrap [®] ; Gen Wrap [™]	Milliken Infrastructure
L	Ridge Back [™]	

L Layered system; W Wet lay-up system

**Fig. 4** Composite repair systems: **a** Snap Wrap (layered); **b** Strong Back (wet lay-up)

them. So in case of using certain products the manufacturers should be contacted, i.e. pipe dimensions, defect size, operating pressure and temperature should be mentioned for a future intervention/repair.

2.1 Reinforced Composite Materials Bands Used for Pipeline Repair

The layered repairing wrap involves a band/tape of the reinforcing material impregnated by a polymeric composite compound. The reinforcing material is usually a fabric, network or tape (maybe a thread, or cord, cloth, fibre, etc.). Glass, basalt, carbon and organic fibres, such as Kevlar, high-strength, high-modular or polyethylene fibres, and ceramics can also be used. The use of glass fabrics helps to improve strength of the wrap. Glass materials are resistant to corrosion, moisture and hostile media. Carbon fibres are the most promising in raising rigidity and strength, but they could trigger corrosion processes in case of direct contact with the steel pipe. Out of a variety of carbon fibres, the most efficient seem to be the carbon tapes. The woven carbon tapes, in which the base consists of unidirectional carbon fibres, while in direction of the weft some other types of fibres are used (glass or ester), are also very promising. These tapes can be manufactured in various structural modifications, e.g., unidirectional or without a certain direction, woven or braided, in the form of a linen or other.

Regarding the components for composite materials used for impregnation, the modified epoxide resins are most often used [13–16]. In addition, polyether, phenolic or polyacrylic resins, polyurethanes, epoxidized vinyl ether resin modified by urethane fragments, coal tar resin, the combinations thereof, etc. can be employed. Modification of epoxidized by urethane fragments vinyl ether resin enables to combine high chemical stability at elevated temperatures with perfect wettability of the fibres (e.g., carbon ones), which ensures high tightness of the wrap. The use of the epoxy polyurethane compound with filler, known for its strength, durability and low shrinkage as compared to the epoxide formulation, is considered highly promising. The prepregs (a reinforced impregnated material) can be manufactured by direct pressing, (wet) winding, blowing, rolling or vacuum moulding [17].

Technologies as Clock Spring (USA), GARS and REPMOS (Russia) are used for composite repair kits. Figure 5 presents a repair scheme for a transmission pipeline using a layered repair system with a tape of reinforced polymeric composite material [18]. The layered repair system that seems to be presently the best known one is based on the “Clock Spring” collar [9] (presented in Fig. 6). Such repair system uses composite materials made of fibreglass and a resin matrix and it is applicable for the structural reinforcement of pipelines with the outside diameter ranging between 102 and 1422 mm, having corrosion defects with a remaining pipe wall thickness up to 20% from the nominal one. It can also be used to repair other mechanical defects, including dents, and it provides ductile fracture arrest properties.

The advantages of the reinforced polymeric materials wraps include service life of the material up to 42 years (materials AP-1, RU), operation temperature from 80 to 1200 °C (material ATP-1, RU). The disadvantages are the following: labour and time intensiveness (wetting or impregnation of fibres or fabric), use of solvents, chemical agents, ageing of the polymer tapes, loss of adhesion, incompatibility of

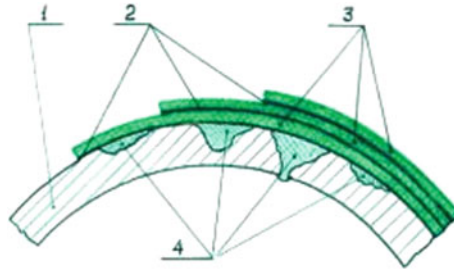


Fig. 5 A pipeline repair system using polymeric composite material with the installation of a three-layer closed reinforcing glass-polymer tape: 1 steel pipe wall; 2 polymeric adhesive material PGR-4 (RU); 3 glass-polymer tape; 4 polymeric filler material REM-steel (RU)

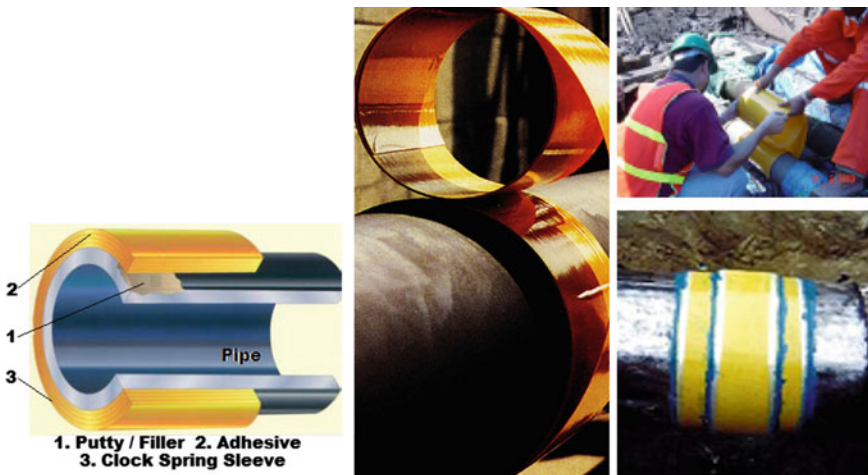


Fig. 6 Design and installation of Clock Spring composite wrap for pipeline repair [9]

the tape materials and the impregnated reinforcing one (low interfacial activity), limited viability of the binder. The composition used for treating reinforcing elements (binding resin, hardener) should possess an optimal complex of properties: a low-viscosity solution must have perfect wettability and high reactivity at solidification to provide the formation of a hard and strong composite.

The systems of protective coatings that involve several layers of the polymeric tape (glass tape or other) coiled spirally round the pipe and having an adhesive layer between the layers and the pipe surface belong to the composite collars. Among their drawbacks is a low level of tube necking and just slight perfection of the

bearing capacity of the defective tube. Moreover, such method needs participation of machinery since winding of the tape requires a free (proportional to the pipe diameter) space around the pipeline in the repair zone.

A protective composite material system proposed by the company INTRA (RU) to repair mechanical and corrosion damages (with a wall thinning up to 90%) includes an epoxide primer, a glass fibre or carbon fibre-based reinforcing fabric impregnated by a polyurethane composition and a fixing tape [19]. The technological process includes application of the epoxide primer, activation of a reel of the composite material in solution, wrapping of the pipe by the composite material (wrapping over the composite material) application of the fixing tape. Among the advantages of this material are fast application and curing, possibility to apply onto the surfaces of any configuration, operation under high environmental temperatures (up to 250 °C), and resistance to chemical and hostile media.

2.2 Pipeline Repair Using Composite Sleeves and Combined Protective Coupling Systems

A composite sleeve is a modern technological tool for repairing pipelines and the components connecting the pipes of any geometry, as well as branches, passages, T-joints, crossbars, etc. Table 3 summarises the types of repair systems using composite sleeves, while Table 4 lists the methods of repairing pipelines by fibre-reinforced composites presently used in the European countries and USA.

The effect of strengthening the defective portions in the transmission pipelines using sleeves consists in the redistribution of circular stresses between the pipe wall and the repair structure due to the pressure difference of the inner pressure during repair and maintenance. To restore the bearing capacity of a pipeline with mechanical and corrosion damages (including a through-wall damage) or in order to transfer some pipeline sections into a higher loading category, it is possible to instal a sleeve fitting able to increase reliability of the pipeline. Such a sealing sleeve could be also made of steel, as an alternative to composite materials, and it is a repair system that is mounted by means of circular welds directly to the pipe wall (with special caution when welding onto an in-service pipeline) or to the bypass rings. The main types of steel sealing sleeves are the ones with technological rings (Fig. 7a) and the volume sleeves with polymeric resin filling (Fig. 7b) [21, 22].

The method of increasing pipe strength using steel couplings with polymeric filling is widely spread for the transmission pipelines (Fig. 7b) [23–28]. Such a technology is also called composite-coupling method. A split steel coupling with the inner diameter greater than the outer diameter of the pipeline is centred and welded by longitudinal welds onto the damaged section. The coupling faces are

Table 3 Types of pipeline repair systems using sleeves [20]

Application temperature	Temperature of working environment	Complete solidification time	Repair materials
0–100 °C	≤ 260 °C	From 1 to 8 h	Glass or carbon fibre, epoxy resin, polyurethane composition
	≤ 100 °C	2 h	Reinforcing glass-polymer composite tape of glass plastics; polyester resin
	≤ 150 °C		Carbon fibre and epoxide
From –15 to 40 °C	150 °C (220 °C short term effect) 255 °C—material deformation	1 h	Nylon film; enriched resin layer; glass fibre veil of C-type; E-type glass fibre matrix; Vinyl ether epoxy resin
From –60 °C	≤ 80 °C		Glass-reinforced plastics from anisotropic glass fibres impregnated with binder composition
From –60 °C	≤ 80 °C	≤ 2 h	Anisotropic roll glass plastics
From 5 °C	–150 to 110 °C	1.5 h (24 h—gaining strength)	Glass-reinforced plastics
From 5 to 50 °C		2–8 h	Glass grid, materials Rem-steel, REM-aluminium (levelling material) adhesive PGR4
From –60 °C	≤ +140 °C		Metallized film, izolon, mastic, carbon fibre

filled with a quickly cured sealant, while the space formed between the tubes is filled through the technological holes by a polymeric harden able compound. This is a universal repair technology for all types of flaw making possible the in-service repair of pipelines [1, 21, 22]. However, great resources are needed to apply this technology. The repair quality depends considerably on keeping to the technological requirements. For instance, during filling the space between the pipes by the composite material, there is a probability for the air bubbles formation.

The couplings using both steel and composite materials are subdivided into the holdfast ones and loose couplings. The repair using the loose steel coupling is related to a temporary repair, while the one using a holdfast coupling is a permanent repair. The main difference of the holdfast coupling is in their ability to compensate the inner pressure on the defective portion by way of creating a contact outside pressure.

The technologies of sealing leakages using composite couplings has been used and still remains a requisite procedure in emergency repair at such companies as

Table 4 Research, development and practices in fibre-reinforced composite repair of pipes

Description	Type of application
Glass fibre reinforced repair with vinylester resin on steel pipe	Through-wall defect and repair mechanism
Glass fibre reinforced joint with vinylester resin on composite pipe under UV curing	Pipe joint and curing effects
Water-activated glass and carbon wrap on metal pipe	External corrosion and mechanical gauge/dent
Glass fibre reinforced precured and flexible repairs	External and internal repair with localised flaws with 70% wall thickness
Carbon fibre reinforced flexible system with epoxy resin on steel pipe	Improvement of flexural capacity
Glass and carbon fibre hybrid repair on steel pipe	External localised metal loss
Carbon fibre/epoxy composite wrap with epoxy putty on steel pipe	External axisymmetric and localised flaws with 50% wall thickness
Glass-reinforced flexible wrap with epoxy adhesive on steel pipe	Through-wall localised corrosion
Glass fibre reinforced wrap and bolted steel clamp repair on steel pipe	Through-wall repair
Carbon and glass fibre wet lay-up and cured spiral sleeves on metal and concrete pipes	External and internal repair
Carbon fibre reinforced repair on metal loss and weld defects on steel pipes	External and internal repair
Glass epoxy composite repair wrap with epoxy putty on steel pipe	External localised flaws with 80% metal loss
Glass fibre reinforced overwrap with epoxy resin on steel pipe	External flaws with 80% wall thinning
Epoxy cured glass fabric, which is then cured to form a fibre-reinforced composite	External repair of onshore and offshore steel pipe
Fibreglass composite sleeve, an adhesive and a filler material on metal pipe	Corrosion or mechanical damage of low-pressure pipe
Carbon fibre reinforced flexible system with epoxy resin on metal pipe	Corrosion or mechanical damage
Glass fibre reinforced precured spiral sleeve	External blunt and localised metal loss

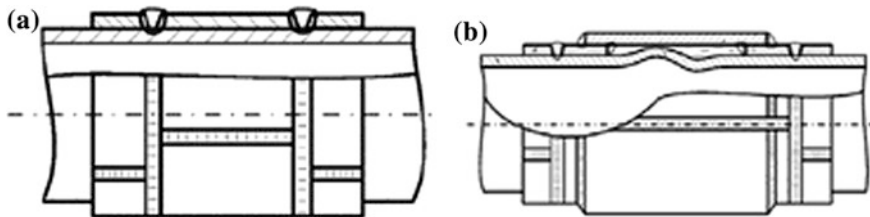


Fig. 7 Structure of hermetical steel sleeves: **a** sleeve with technological rings; **b** bulk sleeve with fillers

Royal Dutch Schell (Holland), BP (GB), LUKOIL Overseas (Europe), AGIP (Italy) and other. The advantages of the named technology are the gradual reduction of the amount of downtime leading to dramatic expenses, which improves the industrial and ecological safety.

Thermocontractable wrapping bands and couplings as well as the equipment for application are manufactured by Raychem (USA, Japan, Belgium), Tuboscope Vetco, Ameron (USA), Canusa (Canada), VNIIST (Russia), etc.

Steel couplings are used more often than other types. One of the shortcomings of steel repair systems is their large weight demanding hoisting machinery and creation of anticorrosion protection of the repair component itself. Furthermore, the use of fasteners and threaded parts complicates an in-field conducted assembly.

New Technologies Co. (Russia) has suggested a design of the holdfast glass–plastic coupling RSM (Fig. 8). This design has certain negative features, such as limited size of the repaired pipes (720–1420 mm), inability to fully cover the perimeter due to the tightening joint design, probable violation of tightness in conditions of prolonged vibratory loads.

The operating principle of the UKMT couplings is the compensation of the inner pressure in the pipeline through the creation of a contact pressure outside when the tightening torque of the bolts reaches a considerable value. This creates conditions for the assembly under the guaranteed-quality working pressures in contrast to the couplings mounted without a preliminary stress (Fig. 8b, c). The coupling consists of two half-shells connected with each other by a hinge from one side and by four bolt joints from the other side [1]. This coupling is made in factory conditions; therefore, the quality of the repair involving the coupling is independent of the outer conditions and the human factor. The metallic parts of the UKMT structure are made of stainless steel, so they are not subjected to corrosion [1].

The repair system consisting of elastic-flexible tape spirals made of composite materials has gained popularity in the protection of the crack-like and corrosion defects on the pipeline walls. It is made in the form of belts or bands fastened by a cured adhesive composition. The elastic-flexible tape helix consists of 2–10 layers, each involving two systems of interwoven threads in the form of a cloth. The tape spirals are reinforced by a system of fibres (e.g., alumoborosilicate glass threads) running along the tape spiral to provide the memory effect. The composition epoxy

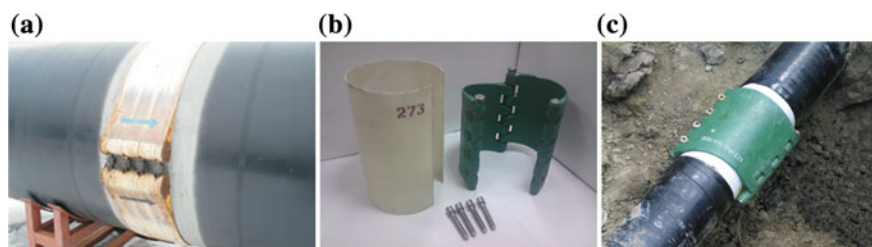


Fig. 8 Designs of composite couplings: **a** Coupling RSM (RU); **b** Coupling UKMT (RU); **c** pipeline section repaired using coupling UKMT (RU)

resin/phenol-formaldehyde lacquer can be used as a polymeric adhesive. This repair system is highly strong; however, its production process is complex and laborious, especially in the forming stage [29–32].

The main advantage of the coupling protective systems is the increased durability of the pipeline sections repaired. Their shortcomings are laboriousness of the process and certain difficulties in the assembly of the rigid metal coupling around a curved pipe section.

The presently adopted methods of mounting the reinforcing couplings (both with and without welding) are rather expensive, they require high-qualified workers, they increase pipe wall stresses and are performed in out of service pipeline conditions.

It follows from above-said that the coupling technologies predetermine the need in the refined methods and approaches to pipe repair. The new technologies are including application of coatings and the use of highly strong plastics, reinforced ones and composite materials [33–37]. The repair works using polymers tend to reduce expenses; they limit embrittlement and residual stresses in contrast to the traditional methods performed by welding or mechanical couplings. Moreover, polymer composites do not oxidise and may prevent corrosion propagation in the damaged pipe section.

The couplings with filling belong to the repair joints for a long-life operation. In a general case, they look like a rigid metal shell installed tightly on the external side of the reinforced pipeline section. This shell most often consists of two couplings welded together and eventually also mechanically fixed on the pipe. The space between the pipeline and the shell (half-shell space) is filled under pressure by a composite material—mainly a self-curing adhesive compound on an epoxide or polyurethane base [21, 22, 34–37]. Very promising in this respect are polyester resins, especially the isophthalic ones. The two-component filling compositions are also known; they consist of methacrylate and a peroxide activator filled by inert filler (glass spheres). Moreover, the variants of using concrete or some incompressible fluid are possible. Pressurised filling of the under-coupling space by the incompressible fluid (e.g., oil) helps to unload the repaired section thus transferring a part of the load on the shell. Nevertheless, the fluid may be squeezed from depressurised coupling during operation. In this connection, it is preferable to fill the under-coupling space by composite materials like self-curing after press-fitting, not shrinking or expanding at curing and having forecasted material characteristics.

The repair compound REPMOS (RU) is a two-component epoxy-urethane system having a resin part and a curing part fed into the inter-pipe space by mechanised means. This repair composition is intended for the repair and recovery works on the damaged transmission pipeline sections with application of the metallic divided couplings.

The advantages of these materials are the following: total rehabilitation of the capacity of the pipeline, possibility of in-service repair, high quality of repair

materials ensured in factory production, mechanisation of the process and environmental safety.

Known in the art technology, Bellhole (pitting) is related to a promising and effective technology of pipeline repair, including recovery of the external insulation coatings. This technology presupposes the next stages of repair works: application of the new insulation, e.g., repair of damaged sections by the collars Wrap Master (Perma Wrap and Weld Wrap), and application of the insulation coating, e.g., cold-pack tapes Polyken, or two-component polyurethane coating like Acothane (Metrot Co.).

Finally, it should be noted that the use of the systems of composite materials, reinforced by glass fibres, reduces the cost of the repair works involving rather expensive mechanical couplings, helps to avoid welding operations and reduces idle time.

3 Technologies Using Composite Materials for Corrosion Protection Systems

One of the most important factors that guarantee durability for a transmission pipeline is the anticorrosion protection and high service characteristics. Pipeline durability and fail-free operation depend much on the efficiency of its corrosion protection.

The use of composite materials in the pipe insulation repair techniques is considered in the most countries as showing vistas [20]. Each decade is noted by the appearance of novel insulation materials in this field, new coating systems, technologies for their application and equipment thereof for factory and in-field mounting, while the quality of these insulating coatings is gradually upgraded. Furthermore, the conditions of construction and maintenance of the transmission pipelines are becoming toughened. This includes construction under low temperatures, development of marine oil and gas fields, deep-sea pipe-laying, construction of pipeline sections by directional drilling, by micro-tunnelling, operation of pipelines up to 100 °C, etc. Although there exists a system of standards adopted in practice and the level reached globally in this field gives opportunities to obtain economic and reliable formulae of the materials, technologies and equipment for laying underground pipelines, a number of unsolved problems still remain.

To make a protective coating function reliably, it should meet a series of requirements, from which the most important are: mechanical characteristics, adhesion to steel, resistance to cathodic delamination, perfect dielectric parameters, low moisture and oxygen penetrability, resistance to UV and heat ageing [38]. Insulator coatings are intended to function within a wide temperature range during construction and usage and to maintain protection of the pipeline against corrosion within a minimum possible service life.

A broad spectrum of protective coatings available today differs in the manner of application and their properties make possible to successfully protect pipeline surfaces. According to [39], anticorrosion coatings are subdivided into the following categories:

- (i) insulating coatings, applied in factory conditions, from which the most applicable are the epoxide ones (fine-film and two-layered), three-layer coatings, hot-applied bands (including thermocontractable cold-pack bands), coal tar pitch and bitumen coatings;
- (ii) insulating coatings, applied in semi-movable conditions, from which the most applicable are: hot-pack bands, liquid coatings, cold-pack bands, coal tar pitch, bitumen coats;
- (iii) insulating coatings, applied in-field conditions (cold-pack and hot-pack bands);
- (iv) insulating coatings, used to protect crosswise welded joints: cold-pack bands (polyvinyl chloride and polyethylene), liquid coatings based on the raw and modified coal tar pitch as well as on polyurethane or epoxide binders, thermocontractable cuffs;
- (v) insulating coatings, used for repairing and reconditioning pipelines, the most widely used are the cold-pack bands and liquid coats.

Considering the features of the technological formation of the protective coatings, the insulation materials used to repair pipelines by the method of wrapping can be classified as follows: (i) band coatings; (ii) combined coatings (with polymeric adhesives); (iii) reinforced band materials (using fabrics, threads, fibres, etc.). We can also relate the following protective systems: (iv) obtained by means of a coupling or bandage/wrap; (v) combined coupling systems (using polymeric adhesives/binders).

3.1 Band Coatings

Due to its high manufacturability, the method of insulating pipes by cold-pack band wrapping is intensively used today in laying new and restoring old pipelines (insulation in-field conditions). The structure of the polymer band coating for the field conditions consists of a layer of adhesive primer, a layer of polymeric insulation band and a layer of polymeric wrap. The total thickness of the coating is not less than 1.2 mm.

The pipes insulated in factory conditions have more layers of the insulation wrap. The total thickness of such a coating is not less than 1.2 mm for the pipes up to 273 mm in diameter, and not less than 2.4 mm for the pipes up to 820 mm in diameter, inclusive.

According to the method of application onto the pipes, the coatings are subdivided into three types [20]: (i) polyethylene and polyvinyl chloride bands with an adhesive layer intended for both field and factory conditions; (ii) band coatings consisting of a plastic film and a sticky layer, applied separately on the pipe prior to wrapping; (iii) layered bands consisting of several PVC layers or a polyethylene (PE) film with a sticky layer from either butyl rubber or coal tar pitch.

There are also petrolatum bands used in a cold state that show good adhesive properties and low moisture penetrability. Their essential drawback is a low strength. This is why such bands are used only in combination with other coatings.

The use of adhesive polymeric bands in the in-field insulation of gas pipelines is limited by the pipe diameter less than 820 mm and operation temperature below 40 °C. For the oil pipelines, it is accepted to use the band coatings in-field conditions for pipe diameters up to 1420 mm, but the total thickness of the coating should be not less than 1.8 mm (two layers of the insulation band and one layer of the protective wrap are applied).

The functions of the insulation band and the protective wrap differ within the polymeric band coating system. The insulation band is to provide the coating adhesion to steel, resistance to the cathodic delamination, to form a protective barrier against water, soil electrolyte and oxygen (corrosion-active agents) penetration to the pipe surface. The protective wrap serves mainly to increase the mechanical and impact strength of the coating. It preserves the coating from damaging when laying the pipes in the trench and covering them by earth, during contraction of the soil and technological shifts of the pipeline.

The cold-pack bands show such properties as high anticorrosion protection, manufacturability and they are not so harmful for the workers and environment in contrast to other insulation coatings (see Fig. 9).

The main suppliers for the polymeric band coatings are: Polyken Pipeline Coating Systems (USA), Altene (Italy), Nitto Denko Corporation, Furukawa Electric (Japan). Among multilayer insulation systems used in field to repair insulation coatings, the most popular are considered the cold-pack coatings of the companies: Polyken (their service temperatures range between 65 and 121 °C) [40, 41], Vanguard (having high mechanical strength, it is used in the zones with



Fig. 9 Rehabilitation of the damaged pipe section using cold-pack band

elevated soil shifts). The Russian manufacturers produce the bands of the types NKPE-45, NKPE-63, Polilen. For insulation of the curved and short pipeline sections, thermocontractable bands of the brands Wrapid Tape, Canusa Clad [42] are used.

Along with the general-purpose bands with the working temperature up to 66 °C, the bands resistant to elevated shifts are produced for operation at temperatures up to 95 °C and on large-diameter pipes, also the high-temperature bands withstanding up to 121 °C temperature and the ones for the low-temperature wrapping [43].

Thermocontractable couplings used for insulating butts of the grades GTS-65, GTS-80, GTS-HT, GTS-HT PP, PMA, PLOX, KLOX, WLOX, CSK TBK [42] are in fact compatible with any type of insulating coatings on the main body of the pipe.

Since the factory insulation dominates today and surpasses any of the known field insulation by all parameters, the accent of application of the cold-pack bands has shifted to their use in pipeline rehabilitation, too.

The advantages of the band coatings are their high manufacturability at application on the pipes in both factory and in-field conditions, good electric characteristics, low moisture and oxygen permeability and a wide range of applications.

The main disadvantages of the polymeric band coatings are their low resistance to shear under the action of the earth sink, insufficiently high impact strength of the coatings, and low biological resistance of the adhesive layer of the coating [44]. In addition, service life of the polymer band coatings lasts from 7 to 15 years, being twice to four times less than the normative depreciation term for the trunk pipelines (not less than 33 years). It is known that in the result of ageing and drying of the adhesive layer under the film layer, corrosion appears under the film and it can propagate in time.

The coatings from the adhesive polymeric bands, based on the 1 + 1 scheme (1 layer of insulation band + 1 layer of the adhesive protective PE-based wrap), have turned to be ineffective in practice. It was proved that due to a high permeability (for water and oxygen) of the protective PE layer, corrosion was detected under the film almost in all cases after 3 or 4 years of pipeline operation, which led to the loss of the coating adhesion to metal. We should take into account the principle that permeability is inversely proportional to the number of the coating layers, and that in provision of the same thickness, permeability would be less. Therefore, the more layers the coating contains, and the most effective would be the coating structure from the polymeric adhesive bands, obtained according to scheme 2 + 1 (2 insulation band layers + 1 layer of protective adhesive wrap.). However, the data cited in [45, 46] proves that water permeability of the insulation coatings 1 + 1 and 2 + 1 becomes actually identical after one or two years of operation. The major cause is the water permeability of the insulation bands and wraps between the coils. The solution to this problem is the application of the bands and wraps having a two-sided adhesive layer. The named technological solution has increased stickiness of the coating from 6.5 to 10 times and reduced water permeability from 2 to 5 times.

The adhesive layer ensures cohesion of the materials, therefore it should have high technological characteristics and preserve adhesiveness within a wide temperature range. The adhesive layer should bear specific properties aimed at the simplification of dismantling the external protective insulation from the metallic surface or the primer (e.g., epoxide one). As an adhesive layer, it is possible to use the ethylene + butylene copolymer [44], or PE-acrylate copolymer [47], a polar ethylene copolymer (co-monomer is chosen from the group consisting of acrylate and the acrylic acid) [48].

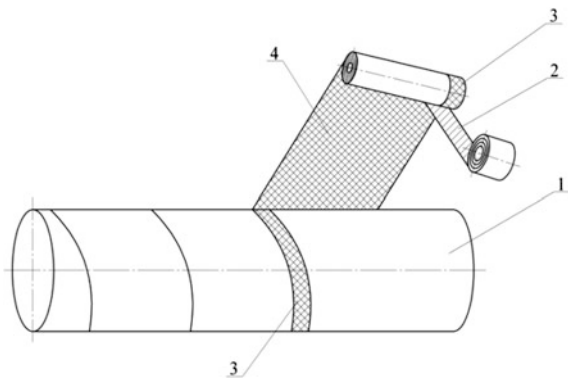
3.2 Combined Band Coatings

Structurally, such coatings consist of a layer of adhesive primer, an insulating layer from a composite material, a layer of the insulating polymeric band, and possibly a layer of the polymeric protective wrap. The combined band-polyethylene coatings are intensively employed at present to provide anticorrosion protection for the pipelines of small and medium diameters. The coating can be applied onto the pipes either at the manufacturing site or in-field conditions. Structurally, the coating consists of a layer of adhesive primer, a layer of a double PE tape (0.45–0.63 mm thickness) and an external layer from extruded PE (1.5–2.5 mm thickness). The total thickness of the combined band-PE coating is 2.2–3.0 mm [49].

The wrapping is wound on the pipes in coils with separation of the antiadhesive film (see Fig. 10). Such design of the insulation bands/wraps makes possible to connect the previous and the next coils of the bands/wraps with the external and internal layers (layers 3 and 4, Fig. 10). It hampers corrosion of the pipe steel by increasing the separation force and reducing the water permeation between the coils of the insulation bands/wraps in the overlaps.

The PE tape in the structure of the combined coating is applied over the adhesive primer and fulfils the main insulation functions, while the external PE layer protects the band coating against mechanical damage at transportation, loading–unloading,

Fig. 10 Application schematic of insulation bands and wraps with an antiadhesive band: 1 pipeline; 2 removable antiadhesive band; 3 adhesive layer on the external side of the polymeric base; 4 adhesive layer on the internal side of the polymeric base



as well as during construction and assembly works. Addition of the epoxide layer in the structure improves essentially the adhesive properties of the coating as it eliminates a dangerous problem of the two-layer coats, due to its consequences, i.e. the hazard of delamination during operation.

Furthermore, it is possible to use some adhesive activated by heating (melting). Such adhesive may be any sealant based on polyamides, polyolefins, polyurethanes, polysulphides, etc. [49–51]. The most effective among them are those based on ethylene etherpolymer.

Different adhesive primers and double polyethylene tapes can be used as isolation material in the combined coating, among the ones manufactured by the companies: Polyken Pipeline Coating Systems (USA), Altene (Italy), Nitto Denko Corporation (Japan) and insulation bands NKPEL 45, NKPEL 63, Polilen (Truboizolyatsiya Co, Russia).

The combined band-PE coatings cede in their properties to the factory-made two-layer and three-layer ones, but they are superior considerably as compared to the polymeric band coatings for the pipelines [38]. The combined band-PE coating is mainly used for the external insulation of the crude oil trunk pipelines and of the low-pressure gas pipelines.

For instance, Shaw Ind. Ltd. (USA) has proposed an anticorrosion insulation that includes an epoxide primer and an external sheath made of polyolefin [52]. The annular space between the primer and the sheath is filled by a mixture of epoxide resin and polyolefins. The correlation of the components varies at a gradient to the intermediate layer thickness, meaning that near the primer the intermediate layer consists mainly from the epoxide resin, while closer to the external sheath the concentration of polyolefins grows. The insulation developed by Kendall Co. (USA) consists of a primer layer and a band spirally applied over the primer layer [43]. Both the primer and the insulation band are prepared on the base of rubber. Since the primer is additionally doped with a special reagent hindering the formation of hydroxyl ions, the cathodic delamination in the insulation is thus prevented.

There are some combined coatings whose components are poorly correlated, namely the hot-pack bitumen-polymeric mastics for continuous re-insulation of pipelines. The bitumen mastics are characterised by inadequate service characteristics because some required operation regimes and parameters cannot be observed during mechanical application in the field conditions. Moreover, in the traditional designs of bitumen coatings, the reduction of the protective properties is partially compensated by the increased current of the cathodic protection, whereas in the combined coatings the compensation cannot be exercised due to the screening effect of the polymeric cover.

The coatings Densopol use tapes made of reinforced polymeric materials [46]. It includes a primer and two tape layers, where the primer is a petrolatum solution. The first layer of the wrapping is a petrolatum tape, reinforced by the glass fibres, while the external layer is made of a flexible and strong PVC tape. To protect pipe walls from cracking and corrosion and to improve reliability, an elasto-flexible tape spiral with continuous coils of the tape (10–20 layers) of the composite material

[53] is proposed. The layers consist of two interwoven threads; the ratio thread/polymer binder ranges between 1/0.37 and 1/0.57.

The company Armstrong World Ind. (USA) has patented a method of application of a phosphate-ceramic insulation coating with the use of a non-woven interlacing of the fibre [54]. Another pipeline coating known, used for insulation, comprises a high-strength composite wrap made of glass fibres that are interwoven and covered by rubber [55].

Wrapping materials for pipes produced by “Vivian Regina” (SAR) consist of the non-woven felt or cloth of glass fibres impregnated by a specific polymeric adhesive to show both chemical and biological resistance. The improved strength is ensured by the longitudinal orientation of the staple glass braid.

3.3 The Causes of Defects Appearing on Wrapped Insulation Coating

The quality of the coatings on the external surface of underground pipelines defines the efficiency of insulation materials and depends on the composition of the initial material, structure and properties of the formed coating, application technology on the pipe surface, coating structure, operation conditions of the pipeline, and so on.

The occurrence of defects in the insulation coatings is induced by the following main causes [46]:

- (i) low-quality application of the primer on the pipeline;
- (ii) use of poor quality insulation materials;
- (iii) low adhesion of the coating to metal;
- (iv) technological peculiarities of application of the insulating layer (e.g., interval between primer application on the pipe surface and the wrapping tape is insufficient for the total evaporation of the solvent, which leads to swelling under the little permeable film and reduction of adhesive strength between the layers of the coating);
- (v) the defects occurring at the application of polymeric insulation tapes (folding, wrinkles, embossing, that result from using tapes with different thicknesses, shear of the coils at tape application, insufficient tension of the tapes, insufficiently clean base surface, violation of temperature conditions for coating application, etc.);
- (vi) the defects occurring in the course of insulation-laying works during the pipeline covering with earth;
- (vii) soil influence: the mechanical effect leads to shear or tensile stresses in the coating that bring about scuffing, folding or embossing; physico-chemical effects when the surface-active components of the soil environment promote washing of plasticizers out of the insulation coatings; elevated humidity leads to augmented cracking of the coating and reduced service life;

- (viii) insufficient electrochemical protection of pipelines (potential difference at the pipe/earth interface);
- (ix) breach of operation conditions of the pipeline due to temperature drop at transportation of the products, exceeding of temperature norms during pumping, etc.;
- (x) residual defectiveness of the metal pipes, along with formation and accumulation of defects in the pipe walls;
- (xi) ageing of the insulation material.

Along with above-said, there exists a difficulty in the estimation of the technical state of both the insulation coating and the pipeline itself. This is connected with inhomogeneity of the ageing process in the composite materials used, as well as the processes of structural changes in the pipe walls along the pipeline length. This depends on the soil and climatic conditions in the pipe-laying area, quality of the construction and mounting works, raw materials, loading of the pipeline and other factors.

It has been mentioned that the construction of the insulating coating used and the residual defectiveness of the pipes are the major criteria that define the quality of the repair and further remaining life of the pipeline.

The main criteria that improve the reliability of a transmission pipeline and define its life span are the following from the viewpoint of the coating system:

- improved quality of the materials for the insulation system;
- quality of the technologies, used for the application of insulation materials during overhaul repair;
- quality of the insulation coating;
- service characteristics of the coating material;
- competitiveness of the coating material regarding its cost and technology.

4 Requirements for the Composite Materials Used for Pipeline Repair or Insulation Coating Systems

The analysis of the composition, structure and the main causes of defects in the materials used, together with the technologies for repairing transmission pipelines with the help of composite materials wraps/sleeves and forming the wrapping insulation coatings on the external surfaces of pipelines, has led to the formulation of a series of criteria for the choice of materials for repair and insulation coatings systems for the transmission pipelines.

The selected composite materials should possess the following properties:

- availability, i.e. to be commercially manufactured in acceptable amounts as ready-made or as ingredients;

- simplicity of execution in-field conditions by using the initial components commercially available;
- environmental safety;
- durability in climatic conditions of a given pipeline operation;
- possibility to perform repair works all-year round;
- simplicity of application or possibility of mechanisation of the application process;
- acceptable technical properties of the composite materials, including viscosity, viability, fluidity, time of curing, perfect wettability of the reinforcing composite solution, high impregnation capacity of the reinforcing material;
- good adhesion of the formed composite wrap to the pipe metal;
- flexibility in winding/wrapping works under varying temperature;
- elimination of corrosive or chemical effect on the pipe component being protected;
- resistance to water hampering and electrolyte contact with the pipe surface;
- chemical resistance ensuring the wrap stability under the effect of hostile media;
- mechanical strength enduring service loads and external effects during insulation and pipe-laying operations;
- thermal resistance conditioned by the temperatures of brittleness and softening that should be controlled in winter time or when applied on hot components;
- dielectric properties and electrochemical neutrality that define the resistance to current and prevent corrosion occurrence between the pipe steel and electrolyte, as well as the wrap itself, thus making electrochemical protection more efficient;
- the efficiency of the wrapping system able to provide a tight layer after layer wrapping, avoiding air bubbles;
- economic efficiency, including cost of the repair system that must be several times lower than the cost of the pipe repaired, and the repair technology must be more beneficial than the scheduled repair;
- the possibility to execute repair works on the in-service pipeline.

In spite of a wide spectrum of composite materials available today for both insulation and repair systems, the materials that meet all the above-mentioned requirements cannot be found. Therefore, when searching for an optimal protective or repair system, one should take into account certain operating conditions of the pipeline, technological processes of application of the composite materials and their efficiency in the given conditions, economic benefits from the repair works by the selected materials on a pipeline in question.

5 Conclusions

The composite materials have been proven as promising for the execution of repair works on transmission pipelines. The main advantages of the repair systems, using such materials are the following:

- better physical and mechanical properties (resistance to corrosion, wear resistance, strength, elasticity, light weight), when compared to metallic materials;
- technological advantages (available technologies for performing in factory and in-field conditions; a wide range of formulations, aggregate states, application technologies; environmental safety; possibility of application without high-temperature effects like fire or welding; does not need high-qualified staff; may be performed without usage of special or heavy equipment; can be made on an in-service pipeline; probability to use on curved portions, T-joints, bends or sections with difficult access);
- economic benefits (efficient cost to quality ratio, reduction of repair expenses due to the possibility of execution on in-service pipelines, low time intensiveness, increase of the pipeline service life, more efficient than the scheduled repair).

The most efficient materials able to ensure high service characteristics of the repair systems and insulation coatings are the combined and reinforced systems, achieved by wrapping composites. The analysis of the conducted works and performance of rehabilitated pipelines has shown high manufacturability of the protective coatings and repair wraps that involve either epoxide polyurethane adhesives or their combinations with other polymers or modifications in various ratios.

The practical achievement of the named advantages of the composite materials may result in high service characteristics of the repaired pipeline (rehabilitation of the bearing capacity, resistance to corrosion, gains in the lifespan of the pipe components).

References

1. *An Advanced Method of Pipeline Repair*. <http://www.to-inform.ru/index.php/articles/64>
2. G. Zecheru, G. Draghici, E.I. Lata, A. Dinita, in *Petroleum—Gas University of Ploiești Bulletin, Technical Series*, **LXII**(2), 9 (2010)
3. G. Zecheru, E.I. Lata, G. Draghici, A. Dinita, in *Proceedings of the 2nd South East European IIW International Congress*, Sofia (2010), p. 204
4. G. Zecheru, F.M. Birsan, A. Dumitrescu, G. Draghici, *Sudura Rom. Weld. Soc. J.* **XXV**(4), 20 (2015)
5. G. Zecheru, F.M. Birsan, A. Dumitrescu, G. Draghici, *Sudura Rom. Weld. Soc. J.* **XXVI**(1), 14 (2016)
6. L. Lenarde, *Preparing for the Hydrogen Economy by Using the Existing Natural Gas System as a Catalyst*, Naturally Project WP4, *Operational Management of Integrity—Principles of Resource Allocation Relating to Pipeline Integrity Management* (2008)
7. ASME PCC-2, *Repair of Pressure Equipment and Piping*, Part 4, *Non-metallic and bonded repairs* (2015)
8. DD ISO/TS 24817, *Petroleum, Petrochemical and Natural Gas Industries—Composite Repairs for Pipework—Qualification and Design, Installation, Testing and Inspection* (2006)
9. *The Clock Spring Company*. <http://www.clockspring.com>
10. *Rehabilitation of Corroded Pipelines and Pipes with Fiba Roll* (Catalogue Fiba Roll, FTI Ltd., 2006)

11. *Black Diamond by Citadel Technologies*. <http://cittech.com/portfolio/blackdiamond>
12. *RES-Q Wrap Design & Installation of RES-QTM Composite Wrap on Pipelines*. T.D. Williamson. <http://www.tdwilliamson.com>
13. EP Patent No. 30181233
14. USA Patent No. 4213486
15. USA Patent No. 4510007
16. USA Patent No. 3502492
17. *NPO Fiberglass*, http://www.advtech.ru/npostekloplastik/prod7_pokritie_ap-1.php
18. *Repair of Defective Pipes of Gas Transmission Pipelines Using Polymer Composite Materials*. <http://www.remneftegaz.ru/info/708>
19. *Composite Repair*. <http://www.belzona.com/ru/applications/valves.aspx>
20. I.N. Vorobyev, The advantage of using the composite materials for repairing pipelines. *J. Oil Gas* **32(7)** (2013) (in Russian)
21. A.S. Milenin, Repair of trunk pipelines without decommissioning: practical recommendations of the Institute of Electric Welding E.O. Paton NAS Ukraine, in *Non-destructive Testing and Technical Diagnostics: Materials 7 National Scientific and Engineering Conf. Exhibition*, Kiev, p. 351 (2012) (in Russian)
22. R.R. Shafikov, Repair of trunk pipelines using welding and related technologies without stopping pumping gas. *Territory Oil Gas* **6**, 80 (2009) (In Russian)
23. RU Patent No. 2314453 (in Russian)
24. RU Patent No. 2104439 (in Russian)
25. RU Patent No. 2134373 (in Russian)
26. RU Patent No. 2191317 (in Russian)
27. RU Patent No. 2213289 (in Russian)
28. V.A. Bobylev, V.I. Korolkov, Epoxide materials for trench-free repair of pipelines. *Paint Varnish Industry*, No. 5 (2010) http://www.chimexltd.com/content/data/store/images/f_603_48899_1.pdf (in Russian)
29. USA Patent No. 4700752
30. RU Patent No. 2097646 (in Russian)
31. RU Patent No. 2162562 (in Russian)
32. RU Patent No. 2156398 (in Russian)
33. A.R. Bunsell, J. Renard, *Fundamentals of Fibre Reinforced Composite Materials* (Institute of Physics Publishing, Bristol, 2005)
34. Z. Roslaniec, G. Broza, K. Schulte, Nanocomposites based on multiblock polyester elastomers (PEE) and carbon nanotubes (CNT). *Compos. Interfaces* **10**, 95 (2003)
35. S.A. Kumar, M. Alagar, V. Mohan, Studies on corrosion-resistant behavior of siliconized epoxy interpenetrating coatings over mild steel surface by electrochemical methods. *J. Mater. Eng. Perform.* **11**, 123 (2002)
36. A. Aglan, A. Allie, A. Ludwick, L. Koons, Formulation and evaluation of nano-structured polymeric coatings for corrosion protection. *Surf. Coat. Technol.* **202**, 370 (2007)
37. S.A. Kumar, T. Balakrishnan, M. Alagar, Z. Denchev, Development and characterization of silicone/phosphorus modified epoxy materials and their application as anticorrosion and antifouling coatings. *Prog. Org. Coat.* **55**, 207 (2006)
38. *Protection of Pipelines Against Corrosion Using Modern Insulation Coatings*. <http://www.ankort.ru/story2.php>
39. *Pipeline Corrosion Protection*. http://www.arguslimited.com/ru/pipeline_corrosion_protection
40. *Insulation Systems for Pipelines "Polyken"*. <http://arguslimited.com/public/upload/files/brochures/polyken.pdf> (in Russian)
41. *Insulation Tape Material System "Polyken"*. <http://www.ngscomplex.ru/poliken/poliken.html> (in Russian)
42. *Heat-shrinkable Cuff and Kits*. http://ehms.ru/corros_isol_fore_canusa.php
43. *New Insulation Technologies*. http://www.ntiz.ru/pokritija_truboprovodov (in Russian)
44. EP Patent No. 247877A

45. R.A. Kharisov, A.R. Habirova, F.M. Mustafin, R.A. Habirov, Current status of protecting pipelines from corrosion polymer coatings. Oil Gas Bus (2005) (in Russian)
46. F.M. Mustafin, Review of methods of protection of pipelines against corrosion insulation coatings. Oil Gas Bus (2003) (in Russian)
47. EP Patent No. 1049751A
48. RU Patent No. 2477299 (in Russian)
49. USA Patent No. 4455204
50. USA Patent No. 4287034
51. RU Patent No. 2132993 (in Russian)
52. USA Patent No. 5300336
53. RU Patent No. 2162562 (in Russian)
54. USA Patent No. 5415824
55. USA Patent No. 551868

Design of Composite Repair Systems

Gh. Zecheru, Andrei Dumitrescu, A. Diniță and P. Yukhymets

Abstract This chapter presents a critical analysis of the existing procedures, described and commented in [1], proposed for the design of the reinforcing wraps/leeves, made of composite materials. These wraps are applied in the areas with volumetric surface defects (VSDs, also named local metal loss defects) of the transmission pipelines, intended for hydrocarbons (petroleum, liquid petroleum products, natural gas, liquefied petroleum or natural gas) or other fluids (water, ammonia etc.). The procedure developed by the authors is selected and the results of its application for the design of the composite materials reinforcing wraps, applied in the areas with VSDs of transmission pipelines, are analysed. The present chapter also highlights the technical requirements regarding the definition and qualification of the pipelines repair systems using composite materials and the information, which must be made available as input data for the design of the reinforcing wraps, intended for various practical applications (repair of pipelines with different locations, shapes and dimensions of VSDs). The issues discussed and the solutions formulated in the following can be useful both to the providers or manufacturers of the components of the composite materials repair systems and to the ones dealing with the design and execution of the maintenance works for the pipelines, belonging to the transmission systems of hydrocarbons or other fluids.

Keywords Transmission pipeline · Composite repair system · Composite wrap design · Finite element

Gh. Zecheru · A. Dumitrescu (✉) · A. Diniță
Petroleum-Gas University of Ploiesti, Ploiești, Romania
e-mail: andrei.upg@gmail.com

P. Yukhymets
E.O. Paton Electric Welding Institute, Ukrainian National Academy of Sciences,
Kiev, Ukraine

1 Introduction

As specified in Chapter “Comparative Analysis of Existing Technologies”, any repair system (with composite materials, intended for pipelines and transmission lines systems, made of steel pipes and components) is defined in the Norms presently in force [2, 3] as a combination of the following elements (for which qualification tests have been performed): (i) substrate (pipe or pipeline component repaired); (ii) surface preparation (of the substrate in the repaired area); (iii) polymeric filler (used to fill the defects and to reconstruct the external configuration of the substrate, before applying the composite); (iv) composite material wrap and its components (polymeric matrix and reinforcing material with fibres or tape, made of composite material and polymeric adhesive); (v) repair procedure (filler and composite wrap application procedures and verification procedures for the repair quality).

The types of repair systems presently in use are [2–14] (see also Chapter “Comparative Analysis of Existing Technologies”):

- (i) repair systems with composite wraps, obtained by wrapping a composite tape/band, named *layered systems* (Clock Spring, Perma Wrap, Weld Wrap, etc.); they are the first used types of composite repair systems;
- (ii) composite repair systems of monolithic type, obtained by applying successive layers of polymeric resin and reinforcing fibres, named *wet lay-up systems* (Armor Plate Pipe Wrap, Black Diamond, Aqua wrap, etc.); they can be used to repair both the straight areas of the pipelines and the elbows, bends, tees, etc.;
- (iii) *hybrid* repair systems, using complex composite wraps, obtained by combining the repair components of both layered and wet lay-up systems (see, for instance, the repair systems proposed in [6]).

At the moment, the composite repair systems that are recommended and most widely used are the ones based on composite materials with polymeric matrix, reinforced by incorporating either fibres or fabrics, obtained from continuous fibres.

2 Analysis of the Design Procedures for the Composite Materials Repair Systems

The procedures currently applied for the design of the repair systems with composite wraps comprise the following sequence of steps (presented schematically in Fig. 1) [1]:

- (i) evaluation of the mechanical strength of the pipeline without VSDs;
- (ii) evaluation of the mechanical strength of the pipeline with VSDs and assessment of the opportunity of the repair by applying a composite wrap/sleeve;

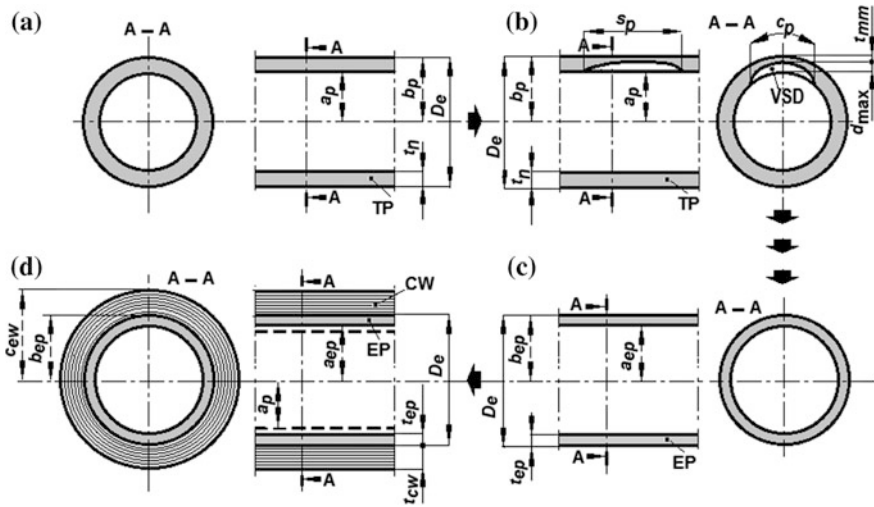


Fig. 1 Sequence of steps for the design of the repair systems with composite wraps for the transmission pipelines (TP) with VSDs (EP equivalent pipeline)

- (iii) definition of the characteristic dimensions of the pipeline without VSDs equivalent (in terms of its mechanical strength) to the pipeline with VSDs;
- (iv) design of the composite wrap/sleeve, consisting of the selection and definition of the material properties for the composite wrap and of the calculation of the composite wrap dimensions.

The first stage of such a procedure consists of the specification and the analysis of the design and operational parameters of the pipeline (without VSDs):

- (i) the design/operating technical conditions of the pipeline: design pressure, p_c ; maximum working/operating pressure, $p_o = MWP \leq p_c$; additional/supplementary loads (axial load, F_a , bending moment, M_b , torsional moment, M_t , shear load, F_s); maximum and minimum operating temperatures, t_{max} and t_{min} ;
- (ii) outside diameter, D_e , and nominal wall thickness, t_n (of the steel pipes used to construct the transmission pipeline);
- (iii) the effective mechanical properties of the steel pipes: Young modulus, E_p ; yield strength, R_{yp} (expressed by the upper yield strength, R_{eHp} , the proof strength, plastic extension, $R_{p0.2p}$, or the proof strength, total extension, $R_{t0.5p}$); tensile strength, R_{mp} ; percentage elongation after fracture, A_{fp} ; Poisson's ratio, μ_p ; full-size Charpy V-notch absorbed energy KV_p (or other toughness properties, at t_{min}); allowable stress, $\sigma_{ap} = f_d R_{yp} = p_{ao}(D_e - t_n)/(2t_n)$, where f_d is the design factor for the pipeline, and p_{ao} is the maximum allowable working/operating pressure of the pipeline, $p_{ao} = MAWP \geq p_c$.

Obviously, to these parameters we should add the data, regarding the characteristic dimensions of the VSD, detected on the pipeline: maximum depth, d_{\max} ; minimum remaining thickness, $t_{\min} = t_n - d_{\max}$; circumferential extent or width, c_p , longitudinal/axial extent or length, s_p .

The second stage of this procedure consists of the assessment of the severity of the VSD, detected on the transmission pipeline, and the evaluation of its residual mechanical strength, in order to decide if repair works are required. Such an assessment should be performed, using one of the methods, described in Part 2. The parameter with which the residual mechanical strength of a pipeline with VSD is usually appreciated is its maximum (safe) working/operating pressure $p_d = \text{RSF} \cdot p_{ao}$, where RSF is the Remaining Strength Factor, which can be determined, using one of the methods, recommended in [1] and described in Chapter “Assessment of the Remaining Strength Factor and Residual Life of Damaged Pipelines”.

By considering the operational requirements of the pipeline, the acceptability criteria (for the pipeline operation without repairing, by using a composite wrap, the area which contains the VSD) can be formulated for the defect, under the form $p_d \geq p_{da}$ or $\text{RSF} \geq \text{RSF}_a$. Here p_{da} (usually considered as equal to p_o) is the minimum allowed level for the pipeline working pressure p_d , and RSF_a is the minimum allowable level for the remaining strength factor, RSF (for details regarding RSF, see Chapters “Characterisation of Volumetric Surface Defects” and “Assessment of the Remaining Strength Factor and Residual Life of Damaged Pipelines”). If above acceptability criteria are not fulfilled, the decision to repair the transmission pipeline by applying a composite wrap in the VSD area should be taken into account. Until the execution of the maintenance works is programmed, it will be necessary to operate the pipeline at a pressure less or equal to p_d .

If the decision to reinforce the pipeline, applying a composite wrap, has been taken into account, the third stage of the design procedure is performed. It consists of the assessment of the characteristic dimensions of an equivalent pipeline (EP), defined as a pipeline without VSD, made of pipes from the same steel as the one with VSD. It has the same mechanical strength as the pipeline area containing the VSD. Because, as it can be seen in Fig. 2, the EP is considered to have the same outside diameter, D_e , as the pipeline with VSD, and its maximum (safe) working pressure is $p_d = \text{RSF} p_c$, its characteristic dimensions (wall thickness, t_{ep} , inside radius, a_{ep} and outside radius, b_{ep}) can be determined by using the following equations:

$$t_{ep} = \frac{p_d}{2\sigma_{ap} + p_d} D_e; \quad a_{ep} = \frac{D_e}{2} - t_{ep}; \quad b_{ep} = \frac{D_e}{2}. \quad (1)$$

The repair of a transmission pipeline by applying a composite material system presumes the definition of all the elements of the applied repair system: substrate, surface preparation, polymeric filler, composite wrap and repair procedure. For the design of the composite wrap, dimensions (thickness t_{cw} and length/axial extent l_{cw}), the physical and mechanical properties of the composite material (of the type

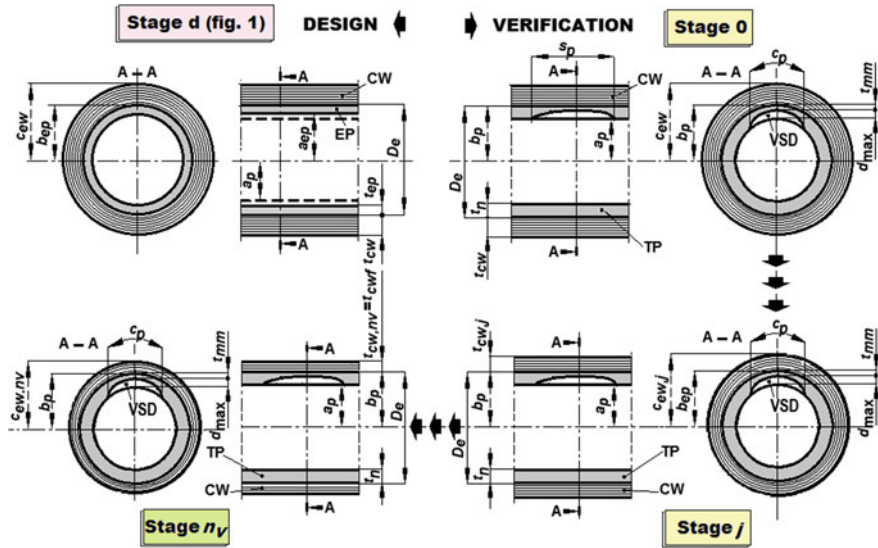


Fig. 2 Steps for the confirmation and finalization of the design solutions for composite wraps used to repair transmission pipelines

polymeric resin + reinforcing fibres or composite tape + polymeric adhesive) need to be known (in addition to the information, obtained during the stages previously performed):

- (i) elastic constants (taking into account that the overlapped layers from which the composite wrap is made have the behaviour of orthotropic plates): tensile modulus in circumferential direction, E_{cc} , and in axial direction, E_{ac} ; Poisson’s ratio in circumferential direction (load in circumferential direction, contraction in axial direction), μ_c , and shear modulus, G_c ;
- (ii) tensile strength: short-term, in circumferential direction, R_{mcc} , and in axial direction, R_{mac} , and long-term (defined as greater or equal to 1000 h), in circumferential direction, R_{mclc} , and in axial direction, R_{malc} ;
- (iii) elongation at break in circumferential direction, A_{cc} , and in axial direction, A_{ac} ;
- (iv) other properties: bending/flexural modulus, E_{bc} ; flexural strength, R_{mbc} ; impact resistance (Izod), KV_{ic} ; hardness (Barcol, Shore etc.); adhesion to steel, A_{dsc} ; thermal expansion coefficient in the circumferential direction, α_{cc} , and in axial direction, α_{ac} .

The mechanical properties of the composite materials for the most used composite repair systems can be found in [1, 4–16]. They have been also presented and discussed in Chapter “Comparative Analysis of Existing Technologies”. We took into account the following issues, pointed out in [1], regarding the availability of information regarding the characterization of the materials, used for composite repair systems:

- (i) information, regarding the physical and mechanical properties, guaranteed for (ensured by) these materials is not provided or it is insufficient;
- (ii) the manner in which the properties of the composite materials are modified in time is not specified (the long-term values of the mechanical properties are missing in almost all brochures and presentation documents of the composites); therefore, when designing a composite wrap, it is recommended to use a factor for the decrease in time of the mechanical strength (service factor), $f = 0.50\text{--}0.67$ [2];
- (iii) the information available is not always correlated with the material types delivered; as an example, it is stated that delivered composite tapes can be executed with different contents of chopped rovings from glass fibres E (225, 300, 450, or 600 g/m²), but only one set of properties is given for the composite band, even if, as known, the properties of the composite materials armed with fibres change depending on the volumetric fraction of fibres, which they contain [7];
- (iv) it is necessary to require to the provider of the composite repair kits, as accompanying documents, the design procedure for the composite wrap and the warranty certificates for the values of the mechanical properties considered for the assessment of the wrap dimensions (thickness t_{cw} and length/axial extent, l_{cw}).

After the selection of the composite material, from which the wraps are made, for the repair of a transmission pipeline, on which a VSD (not through-wall) has been detected, and knowing its physical and mechanical properties, the next stage is performed. At this stage, the wrap characteristic dimensions that, as previously mentioned, are the thickness t_{cw} and the length l_{cw} , are defined.

For the definition of the composite wrap thickness, t_{cw} , several methods have been proposed, presented and commented in [1]. Take into account that the pipeline containing the VSD is subjected, during its operation, only to the internal pressure loading due to the transported fluid, $p_o \leq p_c \leq p_{oa}$ (there are no additional/supplementary loads on the pipeline, that is axial load, $F_a = 0$, shear load, $F_s = 0$, bending moment, $M_b = 0$, torsional moment, $M_t = 0$). Moreover, during the application of the composite wrap over the VSD, $p_o = p_r \in [0; p_d]$, with $p_d = \text{RSF} \cdot p_c$. Then the equations for the assessment of the wrap thickness, t_{cw} , corresponding to the methods presented in [1], are the following:

- the equation, obtained applying the *Design Methodology for Underlying Substrate does not Yield* [2] and the *Design Based on Substrate—Allowable Stress* [3], which assume that, during pipeline operation, plastic deformations do not occur in the steel pipe, containing the VSD (with a reduced thickness due to the VSD presence):

$$t_{cw} \geq \frac{D_e p_c}{4 R_{yp}} \frac{E_p}{\min\left(\frac{E_{cs}}{2}; E_{ac}\right)} f_p (1 - \text{RSF}), \quad (2)$$

in which the (dimensionless) factors for pipeline loading is $f_p = p_o/p_{ao} \leq 1$;

- the equation, obtained applying the *Design Methodology for Underlying Substrate Yields* [2] and the *Design Based on Repair Laminate Allowable Strains* [3], which assume that, during pipeline operation, plastic deformations are generated in the steel pipe, containing the VSD (with a reduced thickness due to the VSD presence), and, while the composite wrap is applied, the pipeline is out of service (without internal pressure):

$$t_{cw} \geq \frac{R_{yp}}{E_{cc}\epsilon_{acc}} [f_d t_n - t_{mm}] = t_n \frac{R_{yp}}{E_{cc}\epsilon_{acc}} [f_d + d_{rd} - 1], \quad (3)$$

where d_{rd} is the relative VSD depth, defined as $d_{rd} = d_{max}/t_n \leq 1$, and the allowable (long-term) strain value of the composite in circumferential direction, ϵ_{acc} , is obtained, based on the indications from [1–3];

- the (conservative) equation, obtained by considering in (3), $t_{mm} = 0$ or $d_{rd} = 1$:

$$t_{cw} \geq \frac{D_e - t_n}{2} \frac{p_{ao}}{E_{cc}\epsilon_{acc}} = t_n \frac{R_{yp} f_d}{E_{cc}\epsilon_{acc}} = t_n \frac{\sigma_{ap}}{\sigma_{acc}}; \quad (4)$$

- the equation, resulting from the assessment and processing of the methodology, proposed in [9]:

$$t_{cw} \geq \frac{D_e - t_n}{2} \frac{p_{ao}}{R_{mcc}} \frac{1 - RSF}{ff_t} = t_n \frac{R_{yp}}{R_{mcc}} \frac{f_d(1 - RSF)}{ff_t}, \quad (5)$$

in which f_t , named temperature derating factor, is defined, based on the indications from [1] in order to multiply the service factor f ;

- the equation obtained by the authors, starting from the formulation, proposed in [10] for the assessment of the bursting pressure, p_{bdp} , of a pipeline, which has been repaired by applying a composite wrap with the thickness t_{cw} :

$$t_{cw} \geq t_n \frac{R_{mp}}{R_{mcc}} \frac{1}{ff_t} \left[\frac{2}{(\sqrt{3})^{n_{sp} + 1}} \frac{1}{1 - 2t_{tp}} + d_{rd} - 1 \right], \quad (6)$$

where $n_{sp} = 0.224 \left(\frac{R_{mp}}{R_{yp}} \right)^{0.604}$, and $t_{tp} = t_n/D_e$;

- the equation, defined by the authors, taking into account that the pipeline is a multi-layered tube (the inner layer being a steel pipe with the dimensions, corresponding to the EP, calculated with the equations from the group (1), and the outer layer being a composite wrap, applied to repair the pipeline area, where a VSD exists) and formulating the condition for this pipeline to withstand the pressure p_c :

$$t_{cw} \geq \frac{D_e}{2} \left[\sqrt{\frac{K_{EP} - \mu_c + 1}{K_{EP} - \mu_c - 1}} - 1 \right], \tag{7}$$

$$K_{EP} = \frac{E_{cc}}{E_p} \frac{1}{k_{ep}^2 - 1} \left[\frac{8t_{tp}k_{ep}^2}{t_{tp}(3k_{ep}^2 + 1) - k_{ep}^2 + 1} - K_{EP0} \right]; \tag{8}$$

$$K_{EP0} = (k_{ep}^2 - 1)(1 - \mu_p) + 2,$$

where $k_{ep} = b_{ep}/a_{ep} > 1$, a_{ep} and b_{ep} are the EP radii, calculated from (1).

In order to assess the composite wrap length, l_{cw} , the following equation is used [1–3]:

$$l_{cw} \geq s_p + 2(s_{tl} + s_{ol}), \tag{9}$$

where the overlap length, s_{ol} , corresponds to the distance, with which the wrap exceeds (in the pipeline axial direction, on its both sides) the VSD with the length s_p , and the tape length, s_{tl} , corresponds to the projection on the pipeline axial direction of the bevel from each extremity of the wrap; s_{tl} and s_{ol} are adopted so that the following conditions are observed [1–3]:

$$s_{ol} = \max[1.77\sqrt{D_e t_n}; s_{olr}]; \quad s_{tl} \geq k_L t_{cw}; \tag{10}$$

in which the reference length s_{olr} and the coefficient k_L have the values: (i) $s_{olr} = 38$ mm (1.5 in.) and $k_L = 1.1$, if the pipeline is not subjected to additional/supplementary axial loads; (ii) $s_{olr} = \max\left[\frac{E_{acc} s_{acc} t_{cw}}{A_{dsc}}; 38$ mm (1.5 in.)] and $k_L = 5.0$, if the pipeline is subjected to additional axial loads.

The design equations presented above have been compared by applying them in several case studies; the analysis of the obtained results has led to the following conclusions:

- the values of wrap thickness, t_{cw} , that are obtained, for a given application, using the Eqs. (1)–(8), are distributed in a very extended range of values, fact that raises suspicions regarding the credibility and/or pertinence of the hypotheses, made when developing some of these equations;
- some equations were defined based on calculation models, which ignore the fact that the mechanical loadings of a pipeline, repaired by applying a composite wrap can be partially transferred to the wrap only if complying with the deformations continuity conditions; therefore, these equations lead to optimistic evaluations (lesser values for the thickness t_{cw}) of the efficiency of the transmission pipeline repair by using composite wraps;
- some of the proposed equations were obtained using over-conservative calculation models, which exaggeratedly consider the effects of the reduction of the

pipeline loading capacity due to the VSD presence and, as a consequence, lead to values of the composite wrap thickness, t_{cw} , much greater than the ones effectively needed.

Taking into account the remarks above, the authors have proposed an improved alternative, with respect to the one described in [1], for the design of the composite wraps, used to repair transmission pipelines.

3 A New Design Procedure for the Composite Materials Repair Systems

The procedure proposed for the design of a composite wrap, which is applied in an area with VSDs of a transmission pipeline, comprises the following stages:

- Specification and confirmation of the input data of the application, distributed in the following categories:
 - the characteristic dimensions of the pipes from the transmission line: outside diameter, D_e , and wall thickness, t_n , to which correspond: $t_{tp} = t_n/D_e$, a_{ep} and b_{ep} calculated with Eq. (1);
 - the (effective) mechanical properties of the steel pipes of the transmission line: E_p ; R_{yp} , R_{mp} , A_{fp} , and μ_p ;
 - the design conditions and the normal working/operating conditions of the pipeline: p_c ; $p_o = MWP \leq p_c$, F_a and F_s ; M_b and M_t ; f_d ; to which correspond: $\sigma_{ap} = f_d R_{yp}$ and $p_{ao} = MAWP \geq p_c$;
 - the characteristic dimensions of the VSD, detected on the pipeline: maximum depth, $d_{max} = k_{de} t_n$, axial extent, s_p , and circumferential extent, c_p , to which correspond: the relative depth $d_{rd} = d_{max}/t_n = k_{de}$, relative axial extent $s_{rd} = s_p/(D_e t_n)^{0.5}$ and relative circumferential extent $c_{rd} = c_p/(D_e t_n)^{0.5}$ for VSD;
 - the properties of the composite wrap: E_{cc} , E_{ac} , μ_c , R_{mcc} , R_{mclc} , A_{cc} , ε_{c0} and ε_{a0} (with the meaning specified above and/or in [1–3]);
 - the conditions for the application of the composite wrap for the pipeline repair: $t_{mc} - t_{rs}$, Δt , p_r , f_t , σ_{acc} , ε_{acc} and ε_{aac} (with the meaning specified in [1–3]);
- Determination of the characteristic dimensions (thickness t_{cw} and length l_{cw}) of the composite wrap applied over the VSD, when repairing the pipeline, applying the equations from the groups (7)–(10); assessment of the values: a_{ep} , b_{ep} —see the equations from the group (1); outside radius of the wrap, $c_{ew} = b_{ep} + t_{cw}$, as well as the ratios: $k_{ep} = b_{ep}/a_{ep}$; $k_c = c_{ew}/b_{ep}$;
- Primary verification of the design solution obtained at the previous stage, using the calculation scheme proposed in [16] and performing the following steps:

- determination of the pressure, q_{pc} , at the contact between the steel pipe and the composite wrap, using the equation:

$$q_{pc} = \frac{2p_o}{K_{EP0} + R_{PC}K_{ECO}}, \quad (11)$$

where

$$\begin{aligned} K_{EP0} &= (k_{ep}^2 - 1)(1 - \mu_p) + 2; K_{ECO} = (k_c^2 - 1)(1 + \mu_c) + 2; R_{PC} \\ &= \frac{E_p k_{ep}^2 - 1}{E_{cc} k_c^2 - 1}; \end{aligned} \quad (12)$$

- evaluation of the of stress and strain states in the pipeline area, in which the composite wrap has been applied, using the equations:

$$\sigma_{rp}(r_p) = \frac{p_o - k_{ep}^2 q_{pc}}{k_{ep}^2 - 1} - \frac{p_o - q_{pc}}{k_{ep}^2 - 1} \frac{b_{ep}^2}{r_p^2}; \sigma_{\theta p}(r_p) = \frac{p_o - k_{ep}^2 q_{pc}}{k_{ep}^2 - 1} + \frac{p_o - q_{pc}}{k_{ep}^2 - 1} \frac{b_{ep}^2}{r_p^2}; \quad (13)$$

$$u_p(r_p) = \frac{1 - \mu_p}{k_{ep}^2 - 1} \frac{p_o - k_{ep}^2 q_{pc}}{E_p} r_p + \frac{1 + \mu_p}{k_{ep}^2 - 1} \frac{p_o - q_{pc}}{E_p} \frac{b_{ep}^2}{r_p}; \varepsilon_{\theta p}(r_p) = \frac{u_p(r_p)}{r_p}, \quad (14)$$

where $\sigma_{rp}(r_p)$ and $\sigma_{\theta p}(r_p)$ are the stresses in the radial and circumferential directions, $u_p(r_p)$ is the radial displacement, and $\varepsilon_{\theta p}(r_p)$ are the circumferential strains, in the points of the pipe section placed at the radius $r_p = (a_p) \dots a_{ep} \dots b_{ep}$;

- assessment of the state of stresses and strains in the composite wrap applied to repair the pipeline, with the help of the equations:

$$\sigma_{rc}(r_c) = \frac{q_{pc}}{k_c^2 - 1} \left[1 - \frac{c_{ew}^2}{r_c^2} \right]; \sigma_{\theta c}(r_c) = \frac{q_{pc}}{k_c^2 - 1} \left[1 + \frac{c_{ew}^2}{r_c^2} \right]; \quad (15)$$

$$u_c(r_c) = \frac{1}{k_c^2 - 1} \frac{q_{pc}}{E_{cc}} \left[(1 - \mu_c)r_c + (1 + \mu_c) \frac{c_{ew}^2}{r_c} \right]; \varepsilon_{\theta c}(r_c) = \frac{u_c(r_c)}{r_c}, \quad (16)$$

where $\sigma_{rc}(r_c)$ and $\sigma_{\theta c}(r_c)$ are the stresses in the radial and circumferential directions, $u_c(r_c)$ are the radial displacements, and $\varepsilon_{\theta c}(r_c)$ are the circumferential strains in the points of the composite wrap placed at the radius $r_c = b_{ep} \dots c_{ew}$;

- validation of the design solutions (t_{cw} and l_{cw}), for which are simultaneously fulfilled:

- (i) the strains continuity condition: $\varepsilon_{\theta p}(b_{ep}) = \varepsilon_{\theta c}(b_{ep})$;
 - (ii) the pipe strength condition: $\sigma_{\theta p}(a_p) \leq \sigma_{ap}$;
 - (iii) the wrap strength condition: $\sigma_{\theta c}(b_{ep}) \leq \sigma_{ac}$;
 - (iv) the wrap strains acceptability conditions: $\varepsilon_{\theta c}(b_{ep}) \leq \varepsilon_{acc}$;
- Final confirmation and adjustment/correction of the design solution (t_{cw} and l_{cw}), using a numerical analysis with the finite elements method for the pipeline, containing the VSD and having the composite wrap, applied on it; an iterative calculation with n_v cycles/steps is performed (see Fig. 2); at the first step, the design solution (t_{cw} and l_{cw}) is considered, and, at the following steps, $j = 1 \dots n_v$, the design solutions ($t_{cw,j} = t_{cw} - \delta_{t,j}$ and l_{cw}) are analysed sequentially; the final solution ($t_{cwf} = t_{cw,n_v}$ and l_{cw}), analysed at the step $j = n_v$, corresponds to the pipeline repairing wrap, having the thickness $t_{cwf} = \min\{t_{cw}; t_{cw,1}; t_{cw,2} \dots t_{cw,n_v}\}$ and integrally complying to the conditions, specified above (strains continuity, pipe strength, wrap strength, and wrap strains acceptability conditions).

In order to highlight the features and the advantages of the application of the design procedure for the composite materials for repair systems, intended for transmission pipelines with VSDs, in the followings a case study is present, aiming at the design of a composite wrap for the repair of a natural gas transmission pipeline. The initial data and the characteristics of the repair system considered for the case study are the followings:

- (i) the characteristic dimensions of the pipes from the transmission line: $D_e = 508$ mm and $t_n = 8$ mm, to which correspond: $t_{rp} = t_n/D_e = 0.01575$; $a_p = 246$ mm; $b_p = 254$ mm;
- (ii) the (effective) mechanical properties of the pipes made of L290N/X42N steel of the transmission line: $E_p = 200$ GPa; $R_{yp} = 320$ MPa > 290 MPa; $R_{mp} = 450$ MPa > 415 MPa; $A_{fp} = 18\%$; $\mu_p = 0.3$;
- (iii) the design conditions and the normal working conditions of the pipeline: $p_c = 6.5$ MPa, $p_o = \text{MWP} = 6.0$ MPa $\leq p_c$, $F_a = F_s = 0$, $M_b = M_t = 0$ and $f_d = 0.72$, to which correspond: $\sigma_{ap} = f_d R_{yp} = 230.4$ MPa and $p_{ao} = \text{MAWP} = 7.26$ MPa;
- (iv) the characteristic dimensions of the VSD (separated, without interaction) detected on the internal surface of the pipeline: $d_{max} = k_{de} t_n$, with $k_{de} = 0.6$, $c_p = 63.75 - 255.00$ mm and $s_p = 127.5$ mm, to which correspond: $d_{rd} = k_{de}$, $c_{rd} = 1-4$ and $s_{rd} = 2$;
- (v) the characteristics of the composite wrap (of the type polymeric resin + reinforcing fibres): $E_{cc} = 20$ GPa, $E_{ac} = 16$ GPa, $\mu_c = 0.35$, $R_{mcc} = 320$ MPa, $R_{mclc} = 155$ MPa ($f = 0.5$), $A_{cc} = 1.5\%$ ($E_{cc}/E_{ac} = 1.25 < 2$, $\varepsilon_{c0} = \varepsilon_{a0} = 0.0040$);
- (vi) the conditions for the application of the composite wrap for repairing the pipeline: $t_{mc} - t_{rs} = 60$ °C, $\Delta t = 0$ °C, $p_r = 0$ ($f_r = 0.977$, $\varepsilon_{acc} = \varepsilon_{aac} = 0.0039$; $\sigma_{acc} = 136.5$ MPa), the meaning of these parameters are specified in [1].

The initial data, required to perform the case study (specified above), are complete, in accordance with the requirements, formulated in Sect. 2, and therefore

the characteristic dimensions (thickness t_{cw} and length l_{cw}) of the composite wrap have been assessed. By considering the pipeline allowable working pressure, $p_{ao} = \text{MAWP} = 7.26$ MPa and applying Eqs. (7) and (8), we obtain: $K_{EP0} = 2.037$; $K_{EP} = 16.24$ and $t_{cw} = 16.5$ mm. By considering $s_p = 127.5$ mm, $s_{olr} = 38$ mm and $k_L = 5.0$, and applying Eqs. (9) and (10), we obtain: $s_{ol} = 112.8$ mm, $s_{tl} = 82.5$ mm and finally $l_{cw} = 400$ mm $> s_p + 2(s_{tl} + s_{ol}) = 325$ mm.

The design solution ($t_{cw} = 16.5$ mm; $l_{cw} = 325$ mm) corresponds to the following characteristics of the pipeline without VSD, equivalent (from the viewpoint of the loading capacity) to the pipeline with VSD: $p_d = 5.95$ MPa; $t_{ep} = 6.48$ mm; $a_{ep} = 247.5$ mm and $b_{ep} = b_p = 254$ mm; the composite wrap has the thickness $t_{cw} = 16.5$ mm, the outside radius $c_{ew} = b_{ep} + t_{cw} = 270.5$ mm, and the ratios $k_{ep} = b_{ep}/a_{ep}$; $k_c = c_{ew}/b_{ep}$ have the values $k_{ep} = 1.026$ and $k_c = 1.065$.

The design solution ($t_{cw} = 16.5$ mm; $l_{cw} = 325$ mm) has been considered and its primary verification has been performed, considering the pipeline working pressure, $p_{ao} = \text{MAWP} = 7.26$ MPa and applying Eqs. (11)–(16), we obtain: $q_{pc} = 1.33$ MPa; $K_{EP0} = 2.037$; $K_{EC0} = 2.175$; $R_{PC} = 4.082$. The distributions of the radial stresses $\sigma_{rp}(r_p)$ and $\sigma_{rc}(r_c)$, the circumferential stresses $\sigma_{\theta p}(r_p)$ and $\sigma_{\theta c}(r_c)$, the radial displacements $u_p(r_p)$ and $u_c(r_c)$ and the circumferential strains $\varepsilon_{\theta p}(r_p)$ and $\varepsilon_{\theta c}(r_c)$, for $r_p = (a_p) \dots a_{ep} \dots b_{ep}$ and $r_c = b_{ep} \dots c_{ew}$ are shown in Fig. 3. The design solution ($t_{cw} = 16.5$ mm; $l_{cw} = 325$ mm) was validated, because all the conditions were fulfilled: (i) the condition of strains continuity, as $u_p(b_{ep}) = u_c(b_{ep}) = 0.2811$ mm; $\varepsilon_{\theta p}(b_{ep}) = \varepsilon_{\theta c}(b_{ep}) = 0.0011$; (ii) the condition of pipe strength: $\sigma_{\theta p}(a_p) = 228.3$ MPa $\leq \sigma_{ap} = 230.4$ MPa; (iii) the condition of wrap strength: $\sigma_{\theta c}(b_{ep}) \leq \sigma_{acc} = 136.5$ MPa; (iv) the condition of wrap strains acceptability: $\varepsilon_{\theta c}(b_{ep}) = 0.0011 \leq \varepsilon_{acc} = 0.0039$.

Following the primary verification, presented above, the design solution ($t_{cw} = 16.5$ mm; $l_{cw} = 325$ mm) was validated, and considered applicable for the existence of VSD on the pipeline with $s_p = 127.5$ mm, at any circumferential extent c_p . By considering the design solution ($t_{cw} = 16.5$ mm; $l_{cw} = 325$ mm), its final confirmation and adjustment/correction was performed by using a numerical analysis with the finite elements method.

The application of the finite elements method for the pipeline, containing VSD and repaired with a composite wrap, involved the following particularities:

- (i) the finite elements of the type SOLID187 were used. SOLID187 (see Fig. 4) is a higher order 3-D element, with a quadratic displacement behaviour, well suited to model irregular meshes, defined by 10 nodes, each one having three degrees of freedom, and it has plasticity, hyperelasticity, creep, stress stiffening, large deflection, and large strain capabilities;
- (ii) the analysis was performed in the elastic region, because a design solution for the composite wrap is considered acceptable only, if the following conditions were fulfilled simultaneously: $\sigma_{\theta p}(r_p) \leq R_{yp} = 320$ MPa, $r_p = (a_p) \dots a_{ep} \dots b_{ep}$ and $\sigma_{\theta c}(r_c) \leq \sigma_{acc}$, $r_c = b_{ep} \dots c_{ew}$;
- (iii) the condition for the validation of the design solution $\sigma_{\theta p}(r_p) \leq R_{yp}$, $r_p = (a_p) \dots a_{ep} \dots b_{ep}$, was used (instead the condition $\sigma_{\theta p}(r_p) \leq \sigma_{ap}$, because the

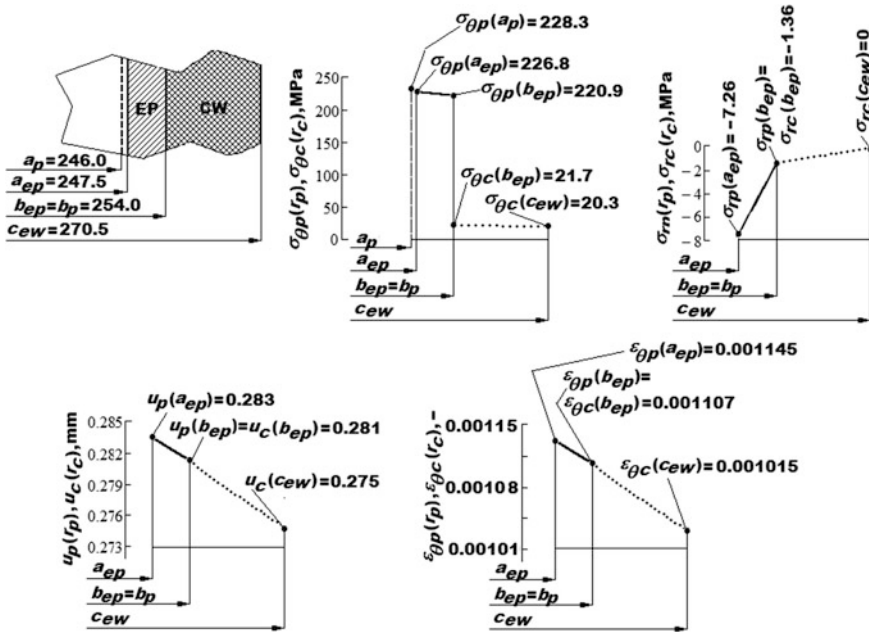


Fig. 3 Results of the primary verification of the design solution for the case study

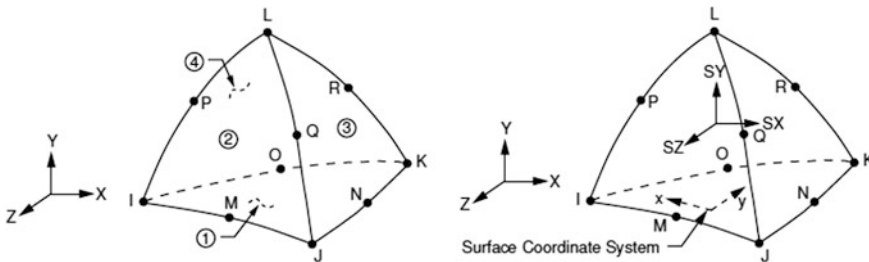


Fig. 4 SOLID187 element description

maximum stresses (in the pipe, repaired with composite wrap) were localized in the defect area;

- (iv) the design solutions for the composite wrap were analysed considering, one at a time, three scenarios, with different values ($c_p = 63.75; 127.5; 255.00$ mm and $c_{rd} = 1, 2, 4$) for the circumferential extent of the VSD. Three different values of the wrap thickness ($t_{cw} = 16.5; 12.5; 8.5$ mm) have been analysed, while its length remained the same ($l_{cw} = 325$ mm).

The geometry of the finite element model is shown in Fig. 5, including details of the VSD for each scenario, while the results of the verification and finalization (adjustment and/or correction) of the design solutions for the composite wrap

applicable for the pipeline with VSD considered in the case study are summarized in Table 1 and in Fig. 6.

It has to be mentioned that the stress values, obtained in the composite wrap were rather low and therefore they are not indicated in Fig. 6. According to the results of the finite elements analysis, the initial design solution ($t_{cw} = 16.5$ mm; $l_{cw} = 325$ mm) was validated, but also the second solution considered ($t_{cw} = 12.5$ mm; $l_{cw} = 325$ mm) was applicable for the VSD with $s_p = 127.5$ mm, for all possible scenarios, regarding its circumferential extent. Moreover, also the third design solution ($t_{cw} = 8.5$ mm; $l_{cw} = 325$ mm) was applicable, but only for the first two scenarios, regarding the VSD (only for a defect with a circumferential extent less or equal to 127.5 mm).

The case study presented above underlines that the new procedure, proposed for the design of the composite wraps, applied in a transmission pipeline area with VSDs is very good, ensuring that: (i) the mechanical strength of the repaired pipeline is at the level corresponding to the pipeline without defects; (ii) the minimum thickness (and, consequently, the minimum cost) is obtained for the composite wraps that are used for the repair of the pipeline areas, containing volumetric surface defects.

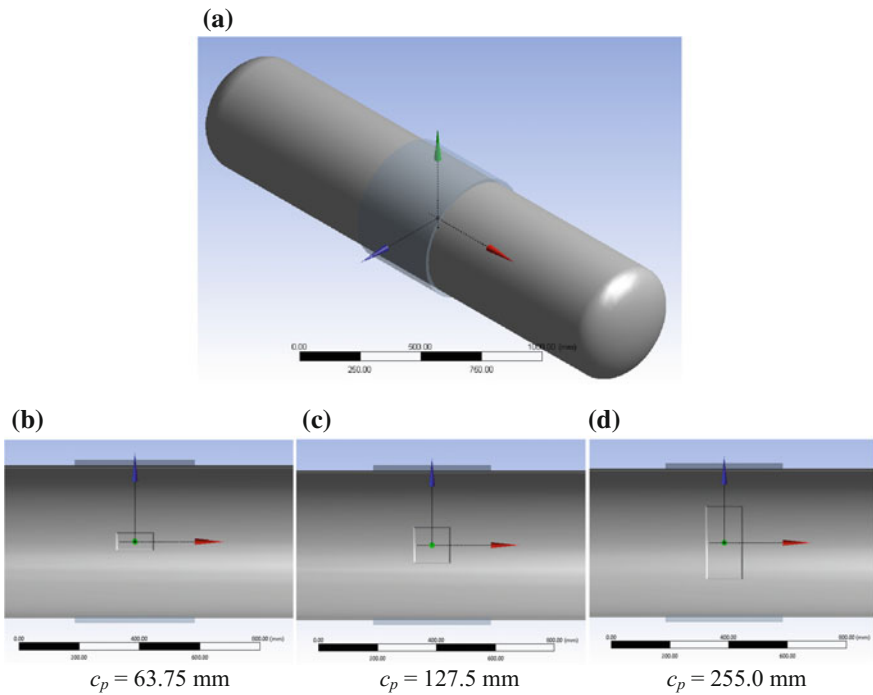


Fig. 5 Geometry of the finite elements model: **a** general view; **b** VSD detail for scenario 1; **c** VSD detail for scenario 2; **d** VSD detail for scenario 3

Table 1 Results of the application of finite elements numerical analysis for the finalization of the design solution for the composite wrap in the case study

Scenario No.	VSD characteristic dimensions			Maximum hoop stress n VSD area (MPa)
	d_p (mm)	s_p (mm)	c_p (mm)	
Design solution I—composite thickness 16.5 mm (Fig. 6a)				
1	4.8	127.5	63.75	169.4
2			127.5	189.8
3			255.0	289.5
Design solution II—composite thickness 12.5 mm (Fig. 6b)				
1	4.8	127.5	63.75	181.5
2			127.5	199.1
3			255.0	310.5
Design solution III—composite thickness 8.5 mm (Fig. 6c)				
1	4.8	127.5	63.75	207.0
2			127.5	218.6
3			255.0	339.4

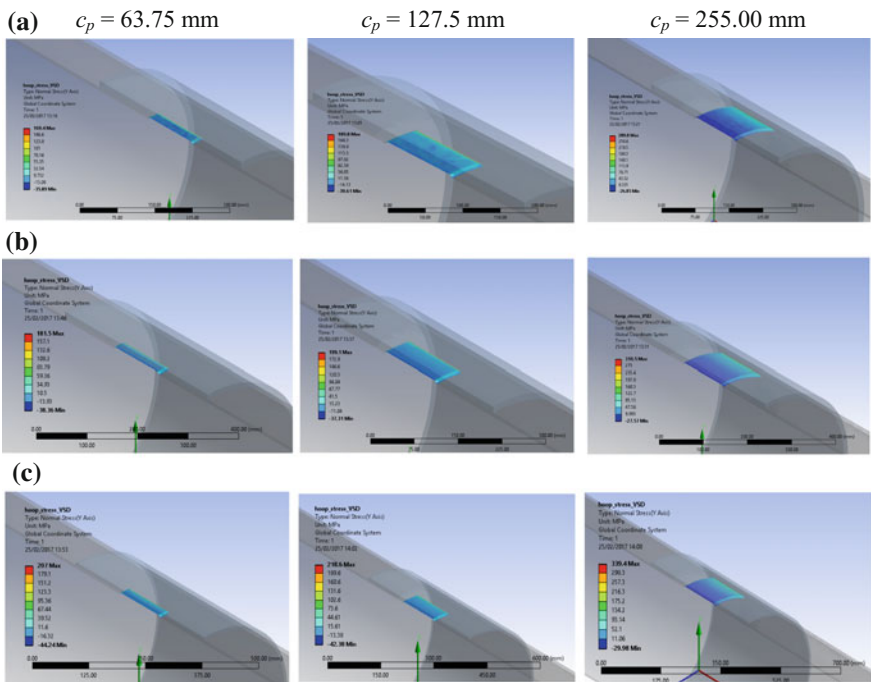


Fig. 6 Results of the application of finite elements numerical analysis for the completion of the composite wrap design solution for the three scenarios of the case study: **a** design solution I ($t_{cw} = 16.5$ mm); **b** design solution II ($t_{cw} = 12.5$ mm); **c** design solution III ($t_{cw} = 8.5$ mm)

4 Conclusions

The issues analysed and discussed in the present chapter have led to the following conclusions, regarding the design of the composite materials wraps/sleeves, intended for the transmission pipelines repair:

- The procedure, proposed by the authors for the design of the composite wraps, which are applied in a pipeline area with VSDs, is very advantageous, because: (i) it takes into account the real manner, in which the pipeline and the composite wrap work together (during the normal operation of the pipeline and not in the case of reaching an ultimate limit state of pipeline failure); (ii) it allows for the assessment of the thickness and length of the composite wrap, considering the influence of both the axial extent, s_p , and circumferential extent, c_p , of the VSDs existent on the pipeline.
- The authors consider that the design procedure, described in this chapter, could be applied and verified by all the specialists, dealing with the management and operation of the maintenance systems of the transmission pipelines, intended for hydrocarbons (petroleum, liquid petroleum products, natural gas, liquefied petroleum, or natural gas) or other fluids (water, ammonia, etc.). If the results obtained will confirm the advantages underlined in this chapter, the procedure could be included in the technical Norms, of the type [2, 3, 17–19].

References

1. G. Zecheru, G. Drăghici, A. Dumitrescu, P. Yukhymets, *Petroleum-Gas University of Ploiesti Bulletin, Technical Series*, **LXVI**(1), 105 (2014)
2. ASME PCC-2, *Repair of Pressure Equipment and Piping*, Part 4, *Nonmetallic and Bonded Repairs* (2015)
3. DD ISO/TS 24817, *Petroleum, Petrochemical and Natural Gas Industries—Composite Repairs for Pipework—Qualification and Design, Installation, Testing and Inspection* (2006)
4. C.E. Jaske, B.O. Hart, W.A. Bruce, *Pipeline Repair Manual*. Pipeline Research Council International, Inc., Contract No PR-186-0324, Arlington, Virginia, U.S.A. (2006)
5. J. Bedoya, C.R. Alexander, T. Precht, Repair of high-pressure pipe fittings using composite materials, in *Proceedings of IPC2010, 8th International Pipeline Conference*, Calgary, Alberta, Canada (2010)
6. C.R. Alexander, C. Brooks, Development and evaluation of a steel—composite hybrid composite repair system, in *Proceedings of IPC 2012, 9th International Pipeline Conference*, Calgary, Alberta, Canada (2012)
7. *Rehabilitation of Corroded Pipelines and Pipes with FibaRoll*, Catalogue FibaRoll/FTI Ltd (2006)
8. G. Zecheru, G. Draghici, G. Dumitru, A. Dinita, *Studies for the Identification of Repair Technologies for the Defects of the Type Metal Loss on Pipelines under Pressure, Using Complex Wraps*. Final report for the research contract No. 39/2007, Petroleum-Gas University of Ploiesti (2008) (In Romanian)
9. *RES-Q Wrap Design & Installation of RES-QTM Composite Wrap on Pipelines*, T.D. Williamson S.A., www.tdwilliamson.com

10. C.R. Alexander, Pipeline integrity. Remediation and Repair, *SGA Conference, Linking People, Ideas, Information*, Houston, Texas (2007)
11. O.H. Bjornoy, M.J. Marley, Assessment of Corroded Pipelines: Past, Present and Future, in *Proceedings of the 11th International Offshore and Polar Engineering Conference*, Stavanger, Norway (2001)
12. G. Zecheru, I.E. Lața, G. Drăghici, A. Diniță, Mechanical properties of a new composite sleeve for pipeline repair. *Materiale Plastice* **1** (2011)
13. T.A. Netto, U.S. Ferraz, S.F. Estefen, The effect of corrosion defects on the burst pressure of pipelines. *J. Constr. Steel Res.* **61**, 1185 (2005)
14. X.-K. Zhu, B.N. Leis, Theoretical and numerical predictions of burst pressure of pipelines. *Trans. ASME* **129** (2007)
15. *Composite Materials Handbook*, Vol. 3: *Polymer Matrix Composites Materials Usage, Design, and Analysis*, Department of Defense Handbook (2002)
16. G. Zecheru, I.E. Lața, G. Drăghici, A. Diniță, With and without welding maintenance technologies for the gas transmission pipelines, *Proceeding of the 2nd South East European IIW International Congress*, Sofia (2010)
17. ASME B31.4, *Liquid Transportation System for Hydrocarbons, Liquid Petroleum Gas, Anhydrous Ammonia and Alcohols* (2003)
18. ASME B31.8, *Gas Transmission and Distribution Piping Systems* (2003)
19. ASME B31G, *Manual for Determining the Remaining Strength of Corroded Pipelines, A Supplement to ASME B31 Code for Pressure Piping* (1991 & 2009)

Part V
Simulation of Advanced Composite
Repair Systems of Transmission
Pipelines

Finite Element Stress Analysis of Pipelines with Advanced Composite Repair

A. Diniță, I. Lambrescu, M.I. Chebakov and Gh. Dumitru

Abstract The efficiency of the composite material wraps, used to repair hydrocarbon transmission pipelines with local metal loss defects (also called volumetric surface defects—VSD), depends on the parameters (pipe material and geometry, VSD geometry, loading conditions, etc.) used within the numerical analyses and experimental tests. On coupled interactive system “piping → defect (VSD) → polymeric filler → polymeric adhesive → layer of different types of fibers → closing polymeric adhesive”, subjected to internal pressure, it is performed quantitative and qualitative evaluating the influence of these structural components and the availability of bearing capacity. As the most adequate pipe materials have been considered the ISO steel grades L290 and L360. The pipe and VSD geometries have been selected with aim to compare the results of our research work with a similar study, i.e., extensive experimental program, presented in different sections. The preliminary results of FEA simulations were obtained in the plastic behavior region. At the first phase of the analysis, the following optimal values for the mechanical properties of the filler, used in the composite repair system have been evaluated as follows: Young modulus $E_f = 25,000\text{--}35,000$ MPa and tensile strength $R_m = 60$ MPa. At the second phase, the mechanical properties of the composite material wrap, used for repair, have been considered and their optimal values have been defined as follows: Young modulus $E_c = 60,000$ MPa and tensile strength $R_{mC} = 600$ MPa, corresponding to the higher values assumed in the analyses.

A. Diniță (✉) · I. Lambrescu · Gh. Dumitru
Petroleum-Gas University of Ploiesti, Ploiești, Romania
e-mail: adinita@upg-ploiesti.ro

M.I. Chebakov
I.I. Vorovich Mathematics, Mechanics and Computer Sciences Institute,
Southern Federal University, Rostov-on-Don, Russia

Keywords Finite element analysis (FEA) • Composite wrap • Filler • Volumetric surface defect (VSD) • Mechanical properties • Stress

1 Introduction

The scientific research, regarding the effect of the composite wrap (used for repair pipelines with volumetric surface defect–VSD) on bearing capacity of these pipelines, was conducted in this chapter. The finite element analysis (FEA) was performed on three types of pipes and two different pipe steels (X42/L290 and X52/L360) were used. For each of the pipes, three different VSDs were considered; the geometrical dimensions of the pipe and VSDs are present in Table 1.

2 Material Properties of the Pipelines Used for the Numerical Analyses

Material nonlinearities are found by the nonlinear relationship between stresses and strains that is the stress is a nonlinear function of strain. The relationship is also path dependent (except for the case of nonlinear elasticity and hyperelasticity), so that the stress depends on the strain history as well as the strain itself. In order to perform such a plastic behavior analysis, the Ramberg–Osgood models were used for the two steels (see Table 2; X42–Fig. 1, X52–Fig. 2) [1, 2].

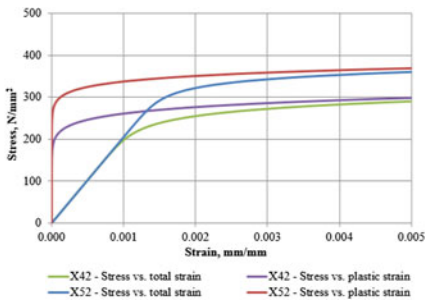
Table 1 Geometric dimension of pipes and VSD used in FEA

	SMYS, $R_{0.5}$ (N/mm ²)	Tensile strength, R_m (N/mm ²)	Outside diameter, D_e (mm)	Wall thickness, t_n (mm)	Depth of VSD, D (mm)			Length of VSD, s_p (mm)	Width of VSD, c_p (mm)
					40% t_n	60% t_n	75% t_n		
X42 steel	290	415	323.9	9.5	3.8	5.7	7.1	203.2	152.4
			508.0	16.0	6.4	9.6	12.0	330.0	238.0
			711.0	20.0	8.0	12.0	15.0	436.0	334.0
X52 steel	360	460	323.9	8.0	3.2	4.8	6.0	203.2	152.4
			508.0	12.5	5.0	7.5	9.4	318.0	238.0
			711.0	17.5	7.0	10.5	13.1	445.0	334.0

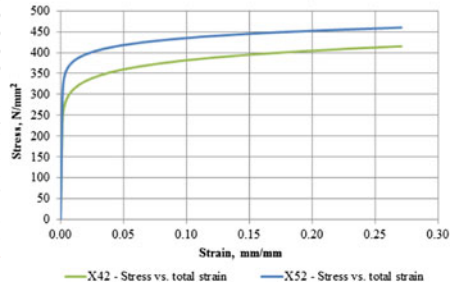
Table 2 Mechanical properties of steels, used in FEA simulations [3]

Ramberg-Osgood parameters for pipe material as specified in API 5L						Ramberg-Osgood	
API 5L grade	R _{t0.5} min. yield stress (N/mm ²)	ε _o yield strain (%)	R _m ultimate tensile stress (MPa)	ε _u ultimate tensile strain (%)	E Elastic modulus (GPa)	α coefficient	N exponent
X42	290	0.5	415	26.5	205	2.55	12.03
X52	360	0.5	460	24.5	205	1.86	17.99

x42				x52			
σ	ε total	ε elastic	ε plastic	σ	ε total	ε elastic	ε plastic
N/mm ²	mm/mm	mm/mm	mm/mm	N/mm ²	mm/mm	mm/mm	mm/mm
0	0.00000	0.00000	0.00000	0	0.00000	0.00000	0.00000
10	0.00005	0.00005	0.00000	10	0.00005	0.00005	0.00000
20	0.00010	0.00010	0.00000	20	0.00010	0.00010	0.00000
30	0.00015	0.00015	0.00000	30	0.00015	0.00015	0.00000
40	0.00020	0.00020	0.00000	40	0.00020	0.00020	0.00000
50	0.00024	0.00024	0.00000	50	0.00024	0.00024	0.00000
60	0.00029	0.00029	0.00000	60	0.00029	0.00029	0.00000
70	0.00034	0.00034	0.00000	70	0.00034	0.00034	0.00000
80	0.00039	0.00039	0.00000	80	0.00039	0.00039	0.00000
90	0.00044	0.00044	0.00000	90	0.00044	0.00044	0.00000
100	0.00049	0.00049	0.00000	100	0.00049	0.00049	0.00000
110	0.00054	0.00054	0.00000	110	0.00054	0.00054	0.00000
120	0.00059	0.00059	0.00000	120	0.00059	0.00059	0.00000
130	0.00063	0.00063	0.00000	130	0.00063	0.00063	0.00000
140	0.00068	0.00068	0.00000	140	0.00068	0.00068	0.00000
150	0.00073	0.00073	0.00000	150	0.00073	0.00073	0.00000
160	0.00078	0.00078	0.00000	160	0.00078	0.00078	0.00000
170	0.00084	0.00083	0.00001	170	0.00083	0.00083	0.00000
180	0.00089	0.00088	0.00001	180	0.00088	0.00088	0.00000
190	0.00095	0.00093	0.00002	190	0.00093	0.00093	0.00000
200	0.00102	0.00098	0.00004	200	0.00098	0.00098	0.00000
210	0.00110	0.00102	0.00007	210	0.00102	0.00102	0.00000
220	0.00120	0.00107	0.00013	220	0.00107	0.00107	0.00000
230	0.00134	0.00112	0.00022	230	0.00112	0.00112	0.00000
240	0.00154	0.00117	0.00037	240	0.00117	0.00117	0.00000
250	0.00182	0.00122	0.00060	250	0.00122	0.00122	0.00000
260	0.00224	0.00127	0.00097	260	0.00128	0.00127	0.00001
270	0.00284	0.00132	0.00153	270	0.00134	0.00132	0.00002
280	0.00373	0.00137	0.00237	280	0.00140	0.00137	0.00004
290	0.00502	0.00141	0.00361	290	0.00148	0.00141	0.00007
300	0.00689	0.00146	0.00542	300	0.00159	0.00146	0.00012
310	0.00956	0.00151	0.00805	310	0.00173	0.00151	0.00022
320	0.01335	0.00156	0.01179	320	0.00195	0.00156	0.00039
330	0.01868	0.00161	0.01707	330	0.00229	0.00161	0.00068
340	0.02611	0.00166	0.02445	340	0.00283	0.00166	0.00117
350	0.03636	0.00171	0.03465	350	0.00368	0.00171	0.00197
360	0.05038	0.00176	0.04862	360	0.00502	0.00176	0.00327
370	0.06941	0.00180	0.06761	370	0.00715	0.00180	0.00535
380	0.09504	0.00185	0.09318	380	0.01049	0.00185	0.00864
390	0.12927	0.00190	0.12736	390	0.01569	0.00190	0.01379
400	0.17466	0.00195	0.17271	400	0.02369	0.00195	0.02174
410	0.23445	0.00200	0.23245	410	0.03590	0.00200	0.03390
415	0.27096	0.00202	0.26894	420	0.05434	0.00205	0.05229
				430	0.08195	0.00210	0.07985
				440	0.12290	0.00215	0.12075
				450	0.18311	0.00220	0.18091
				460	0.27090	0.00224	0.26865



$$\epsilon = \frac{\sigma}{E} + \frac{\alpha \cdot R_{\epsilon 0.5}}{E} \left(\frac{\sigma}{R_{\epsilon 0.5}} \right)^N$$



Properties of Outline Row 6: X42			
	A	B	C
1	Property	Value	Unit
2	Density	7.85E-06	kg mm ⁻³
3	Isotropic Elasticity		
4	Derive from	Young's Modulus and Poisson's Ratio	
5	Young's Modulus	2.05E+05	MPa
6	Poisson's Ratio	0.3	
7	Bulk Modulus	1.7083E+05	MPa
8	Shear Modulus	78846	MPa
9	Multilinear Isotropic Hardening	Tabular	
10	Scale	1	
11	Offset	0	MPa
12	Tensile Ultimate Strength	415	MPa

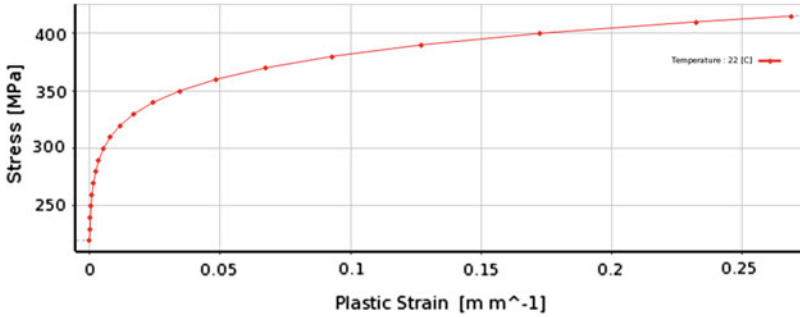


Fig. 1 Multilinear isotropic hardening used for X42

Properties of Outline Row 6: X52			
	A	B	C
1	Property	Value	Unit
2	Density	7.85E-06	kg mm ⁻³
3	Isotropic Elasticity		
4	Derive from	Young's Modulus and Poisson's Ratio	
5	Young's Modulus	2.05E+05	MPa
6	Poisson's Ratio	0.3	
7	Bulk Modulus	1.7083E+05	MPa
8	Shear Modulus	78846	MPa
9	Multilinear Isotropic Hardening	Tabular	
10	Scale	1	
11	Offset	0	MPa
12	Tensile Ultimate Strength	460	MPa

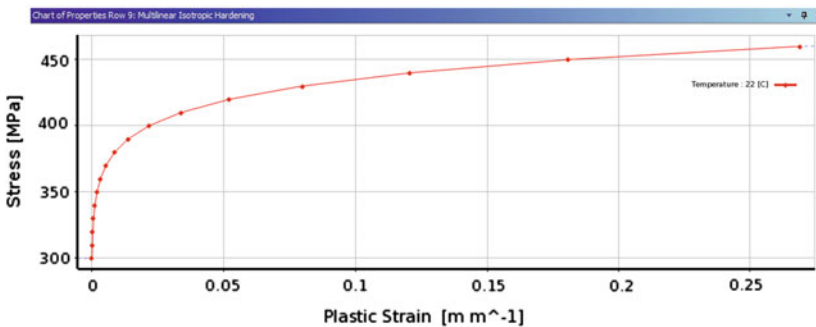


Fig. 2 Multilinear isotropic hardening used for X52

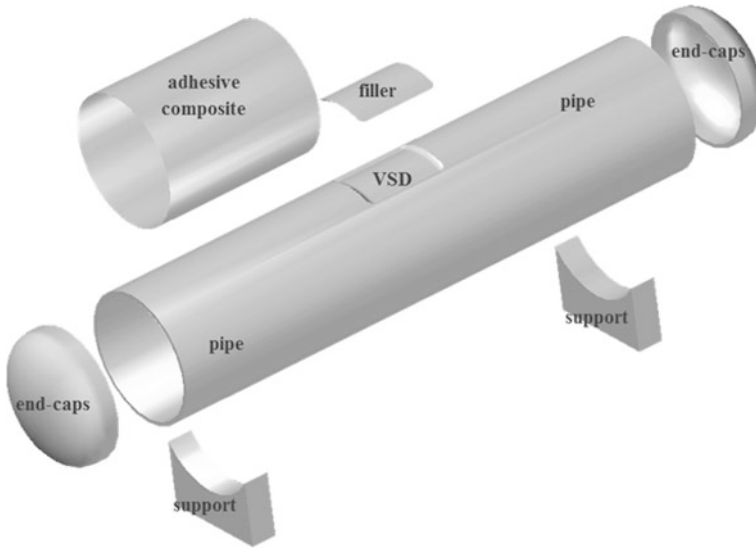


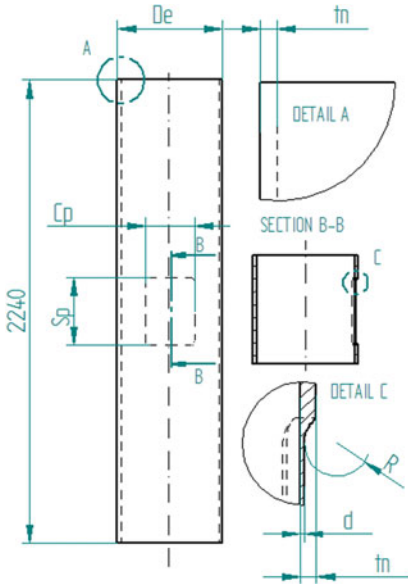
Fig. 3 Complete geometry of the model used in FEA

3 Geometric Models of the Pipelines Used for the Numerical Analyses

The first step to simulate a scenario using FEA [3] is to create the geometric model and in this case, the Geometric Module from ANSYS was used. Three different models were created for three pipe diameters used ($D_e = 323.9$ mm, 508 mm, 711 mm). For FEA simulations, assembly of geometric bodies was created. The complete model (see Fig. 3) has the following geometric features:

- Pipe with volumetric surface defect (VSD) (Fig. 4);
- Semi-elliptical end-caps (Fig. 5);
- Two fixed supports (Fig. 6);
- Filler (Fig. 7);
- Composite wrap (Fig. 8), realized from layer of adhesive and layer of composite, placed over one another.

The complete dimensional information, about the model's geometry used in FEA, is present in Table 3.



1:10

Fig. 4 Geometry of the pipe with VSD

Fig. 5 Geometry of pipe end-caps

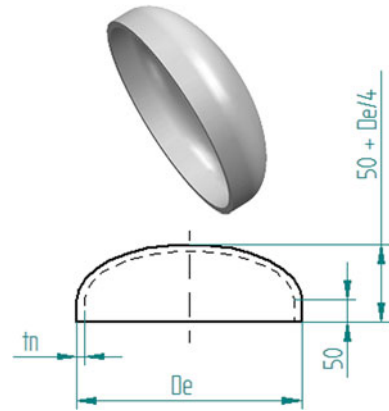


Fig. 6 Geometry of pipe supports

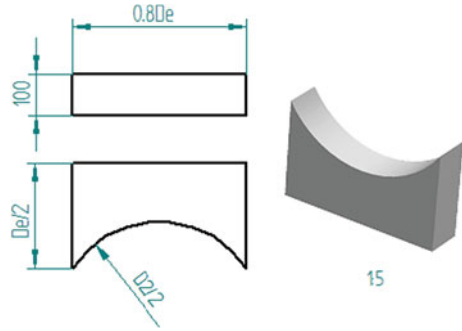


Fig. 7 Geometry of filler

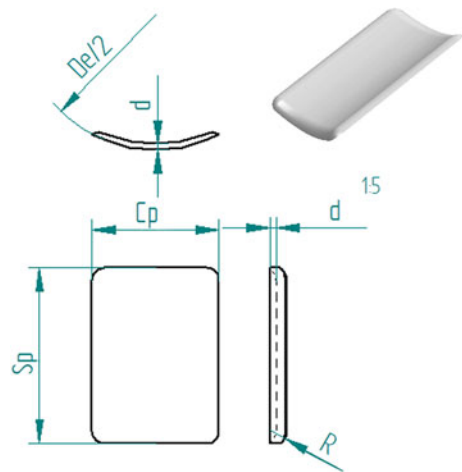


Fig. 8 Geometry of composite wrap

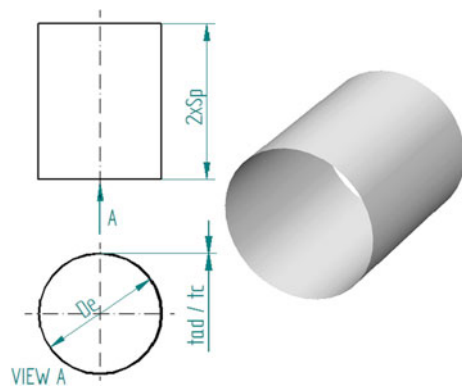


Table 3 Dimensional characteristic for the FEA model

Outside diameter, D_e (mm)	Wall thickness, t_n (mm)	Depth of the VSD, d (mm)			Length of the VSD, s_p (mm)	Width of the VSD, c_p (mm)	Fillet radius, R (mm)	Adhesive thickness, t_{ad} (mm)	Adhesive thickness, t_{tes} (mm)
		40%	60%	75%					
<i>Pipe dimensions for X42 steel</i>									
323.9	9.5	3.8	5.7	7.1	203.2	152.4	19	0.25	0.50
508	16	6.4	9.6	12.0	330	238	32		
711	20	8.0	12.0	15.0	436	334	40		
Outside Diameter, D_e (mm)	Wall thickness, t_n (mm)	Depth, d (mm)			Length, s_p (mm)	Width, c_p (mm)	Fillet radius, R (mm)	Adhesive thickness, t_{ad} (mm)	Adhesive thickness, t_c (mm)
		40%	60%	75%					
<i>Pipe dimensions for X52 steel</i>									
323.9	8	3.2	4.8	6.0	203.2	152.4	16	0.25	0.50
508	12.5	5.0	7.5	9.4	318	238	25		
711	17.5	7.0	10.5	13.1	445	334	35		

4 Stress Intensity Versus Pressure Level in Unrepaired Pipe with VSD and Filler

The main influence of a repair using composite wrap is given by the filler, which can also be called “load transfer” [1, 2]. The efficiency of the pipeline repair is directly caused by the way the composite wrap works, by sharing the hoop stress developed in pipeline wall. In order to quickly characterize the mechanical properties of the filler, the simulations were conducted on pipeline with VSD and corresponding filler, without the composite wrap. It was analyzed the stress intensity in unrepaired pipe with VSD, considering a variation of the pressure from 0 to 12 MPa. By using these diagrams, it can be established the state of the pipeline with VSD at different pressures. Figure 9 presents the variation between the stress intensity and the level of pressure in the unrepaired pipeline with VSD.

5 Stress Level Versus Mechanical Properties of the Filler

The optimal filler mechanical properties (*Young’s Modulus and Ultimate Tensile Stress*) for obtaining a better and significant reduction of the stress level in VSD area was determined considering three cases:

- A. **First case study—Ø323.9.** Figures 10 and 11 shows the influence of stress intensity level in VSD with the filler Young’s Modulus (for two ultimate tensile strength $R_m = 60$ and 90 N/mm^2) for the Ø323.9 pipe. Analyzing the information from these plots it was drawn the conclusion that the optimal

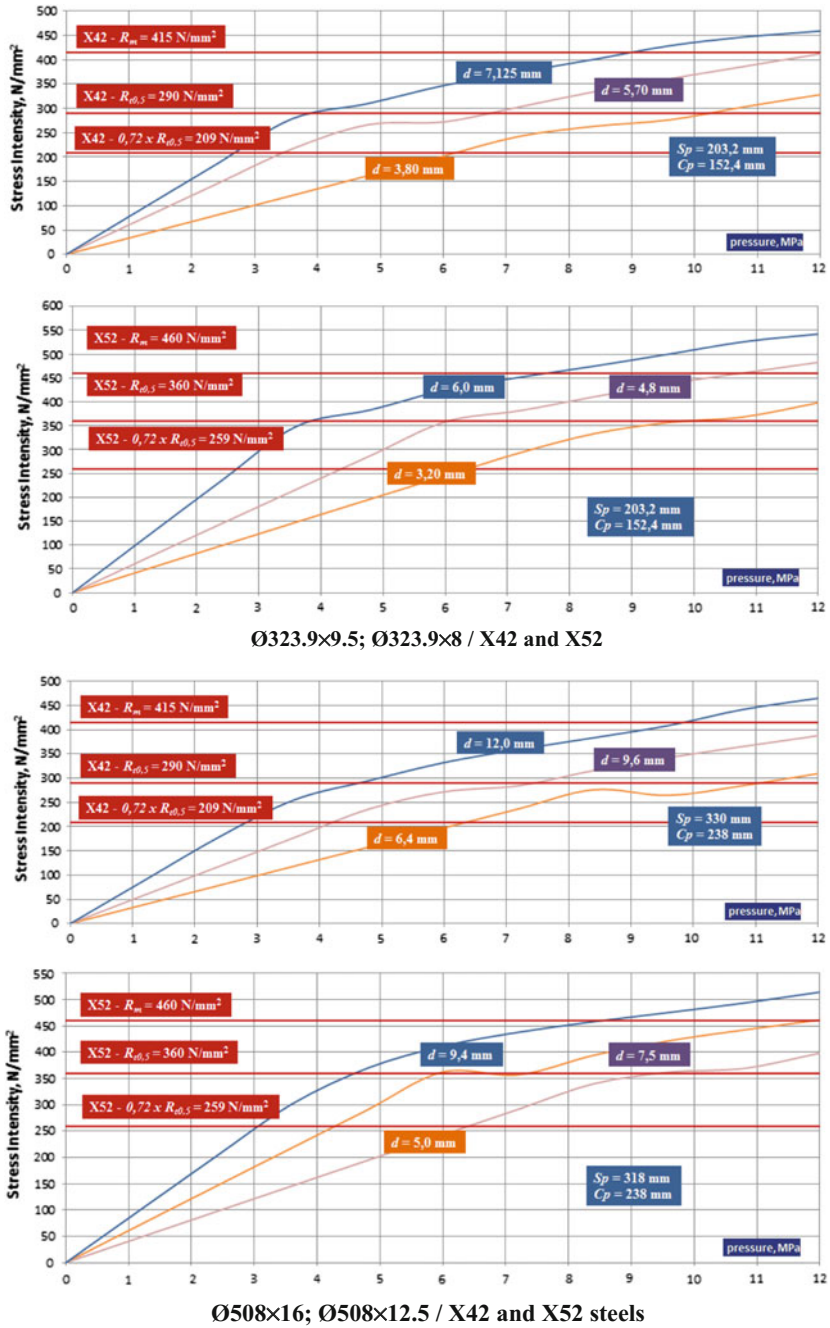


Fig. 9 Stress intensity versus pressure level in unrepaired pipe with VSD

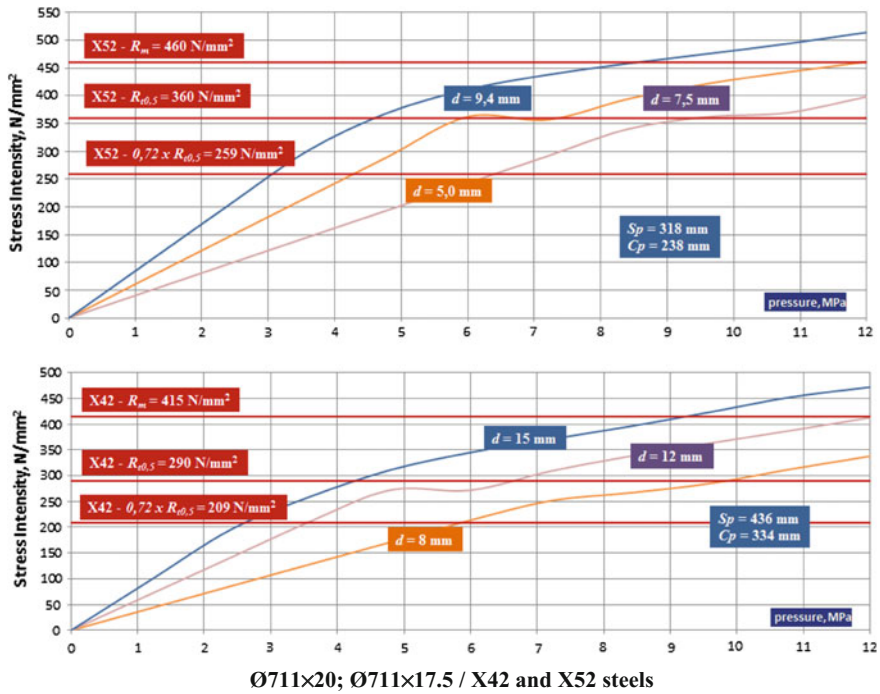


Fig. 9 (continued)

mechanical properties for filler, from stress point of view, are: $E = 25,000\text{--}35,000$ MPa and $R_m = 60$ N/mm².

- B. **Second case study—Ø508.** Analyzing the information obtained from FEA, it was drawn the conclusion that the optimal mechanical properties for filler, from stress point of view, are the same as in the first case: $E = 25,000\text{--}35,000$ MPa and $R_m = 60$ N/mm².
- C. **First case study—Ø711.** Analyzing the information obtained from FEA, it was drawn the conclusion that the optimal mechanical properties for filler, from stress point of view, are the same as in the first case: $E = 25,000\text{--}35,000$ MPa and $R_m = 60$ N/mm².

6 The Evaluation of Mechanical Properties of Composite Wrap Versus Stress Intensity in Pipe with VSD

The next step was to take into account the mechanical properties of the composite wrap, used for repairing the pipeline with VSD. The specific characteristics of the different used composite wraps (formed from one layer of adhesive and one layer of

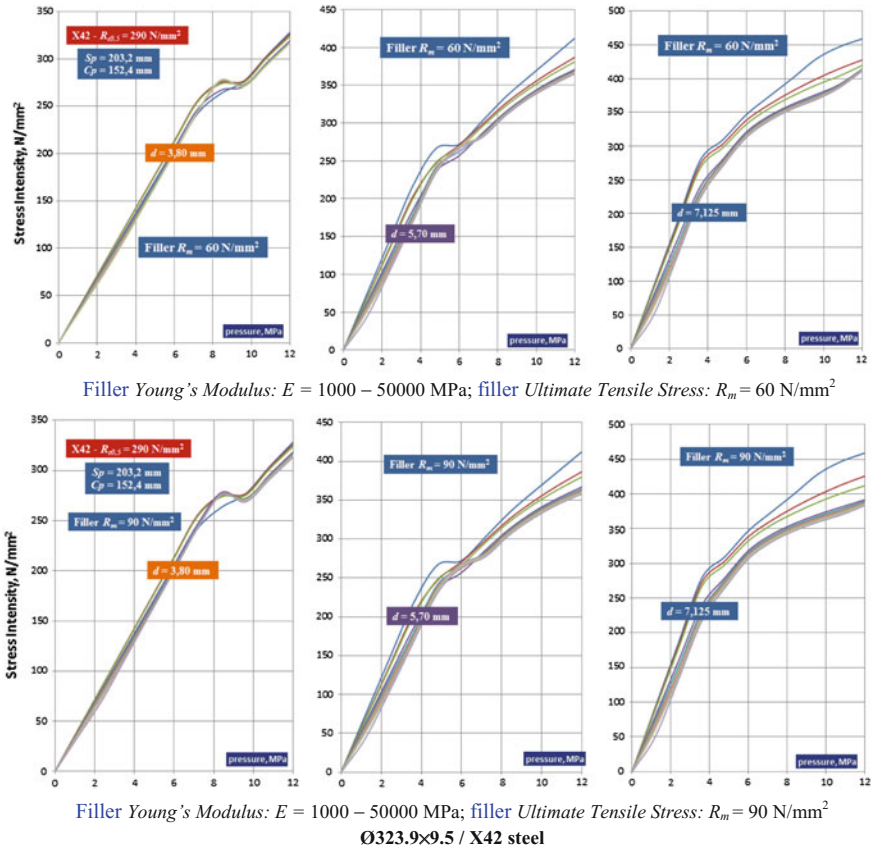


Fig. 10 Stress level versus pressure for pipe with VSD and with different types of filler

composite) were selected from goods of various companies, manufacturing these types of materials. Mechanical properties of the composite wrap were analyzed taking into account the Young's modulus, the Poisson's ratio, and the ultimate tensile strength. For each case studied was created a plot, which represents the variation of the stress intensity versus inner pressure in the pipe for different VSD geometric characteristics. At this stage of the research, the composite was considered as isotropic material with uniform characteristics in all directions. The orthotropic case will be taken into consideration during the next research. For determining the influence of the composite wrap characteristics on the stress intensity level in VSD area, the following values were chosen:

- (i) **Filler:** $E_f = 30,000$ MPa, $R_{m_f} = 60$ N/mm², $\mu_f = 0.3$, 1.0% allowable strain;
- (ii) **Adhesive:** $E_{ad} = 17,000$ MPa, $R_{m_{ad}} = 40$ N/mm², $\mu_{ad} = 0.3$, 30% allowable strain, thickness $t_{ad} = 0.25$ mm;

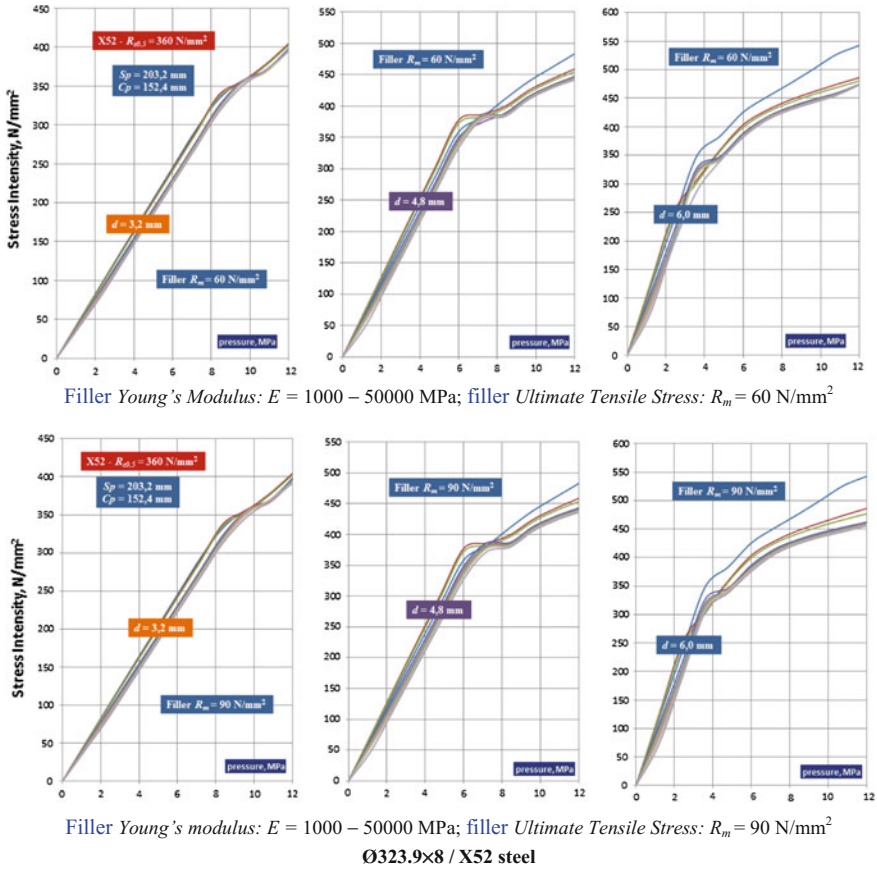
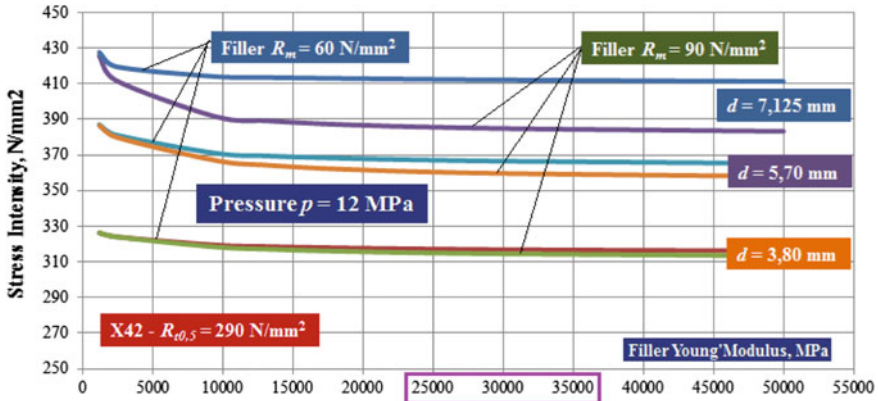


Fig. 10 (continued)

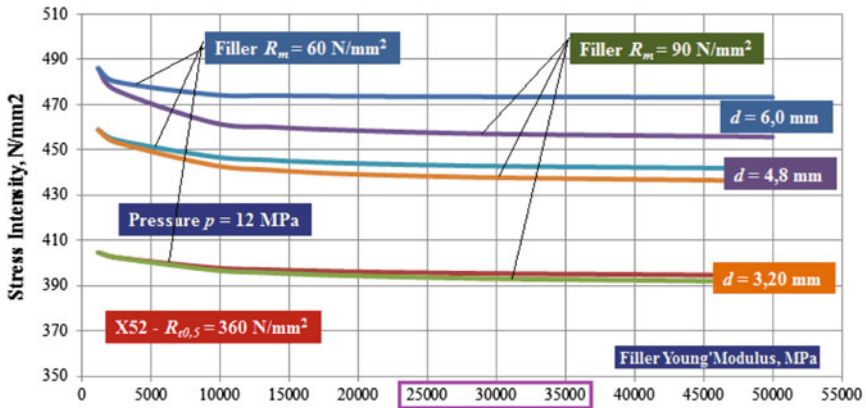
(iii) **Composite:**

- (a) lower: $E_c = 8000$ MPa, $R_{m,c} = 80$ N/mm², $\mu_c = 0.28$, 0.3% strain to failure, thickness $t_c = 0.50$ mm;
- (b) medium: $E_c = 30,000$ MPa, $R_{m,c} = 300$ N/mm², $\mu_c = 0.28$, 0.3% allowable strain, thickness $t_c = 0.50$ mm;
- (c) higher: $E_c = 60,000$ MPa, $R_{m,c} = 600$ N/mm², $\mu_c = 0.28$, 0.3% allowable strain, thickness $t_c = 0.50$ mm.

The simulation was conducted for all three cases ($\text{Ø}323.9$, $\text{Ø}508$, $\text{Ø}711$) using a composite wrap formed of 6 layers of adhesive and 6 layers of composite with the characteristics mentioned above. Evaluating the results obtained from these simulations the following conclusions can be drawn:



Ø323.9x9,5 / X42 steel – pressure of 12 MPa



Ø323.9x8 / X52 steel – pressure of 12 MPa

Fig. 11 Maximum stress intensity versus filler Young’s modulus

- (i) taking into account an isotropy of the material for the composite, the optimal values for mechanical properties of the composite, from viewpoint of the possibilities to obtain a lower value for the stress intensity, are the following: $E_c = 30,000$ MPa, $R_{m_c} = 300$ N/mm², $\mu_c = 0.28$ (we must also consider the higher cost of a composite wrap with very strong mechanical properties);
- (ii) the thickness of the composite wrap (6×0.25 mm of adhesive plus 6×0.50 mm of composite) assures a good load transfer between the filler and the pipe wall, but this thickness varies from one producer to another in large limits, from 0.5 mm for one layer of Black Diamond to 1.6 mm for one layer of Clock Spring composite;

- (iii) the decreasing values of the stress intensity in the VSD area were directly caused by the depth of the VSD:
- at small-depth defects ($\text{Ø}323.9$: $d = 3.8$ mm in a pipe wall of 9.5 mm) the stress decreased into limits of 20–30 N/mm² for a pressure value of 6 MPa and 30–40 N/mm² for a pressure value of 12 MPa;
 - at deeper defects ($\text{Ø}323.9$: $d = 7.125$ mm in a pipe wall of 9.5 mm) the stress decreased into limits of 60–100 N/mm² for a pressure value of 6 MPa and into 90–130 N/mm² for a pressure value of 12 MPa.

7 Analysis of Composite Wrap Thickness with Respect to ISO/TS 24817:2006

At the final stage of the research, some simulations were conducted in order to verify the maximum thickness of the composite (t_c) computed with Eq. 1 from ISO/TS 24817:2006 (Petroleum, petrochemical and natural gas industries—Composite repairs for pipework—Qualification and design, installation, testing, and inspection).

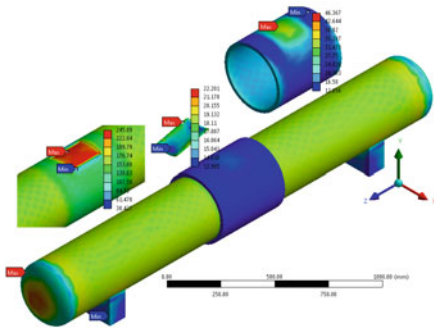
$$t_c = \frac{1}{\varepsilon_c \cdot E_c} \left(\frac{p_{eq} \cdot D_e}{2} - 0.72 \cdot R_{t0.5} \cdot t_s \right) \quad (1)$$

The composite wrap thickness was calculated taking into account the following observations: $p_{eq} = 12$ MPa (equivalent design pressure) is considered equal to p (design internal pressure); $d = 0.75t_n$ (worst-case scenario); $t_s = t_n - d$ is the minimum thickness of remaining substrate wall, mm. It was considered that in the moment of the pipe repair, the strain of the composite wrap was independent of the live pressure [4]. The mechanical properties for the materials, involved in the FEA (steel, filler and composite wrap), are the following:

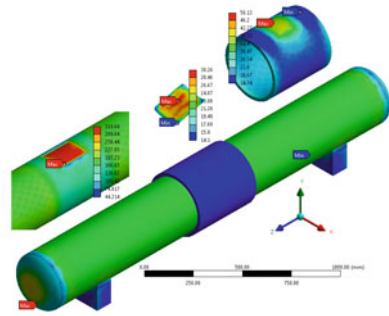
- (i) **Steel:** X42 and X52
- (ii) **Filler:** $E_f = 30,000$ MPa; $R_{m_f} = 60$ N/mm²; $\mu_f = 0.3$, 1.0% allowable strain;
- (iii) **Adhesive:** $E_{ad} = 17,000$ MPa; $R_{m_{ad}} = 40$ N/mm²; $\mu_{ad} = 0.3$; 30% allowable strain;
- (iv) **Composite:** $E_c = 30,000$ MPa; $R_{m_c} = 300$ N/mm²; $\mu_c = 0.28$; 0.25% allowable strain (ε_c).

The detailed FEA simulation results, regarding the analysis of the composite wrap thickness, obtained by using Eq. (1) from ISO/TS 24817:2006, are present in Fig. 12.

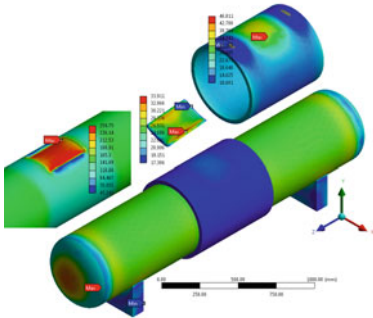
The results of the FEA, regarding the composite wrap thickness, are present in Table 4.



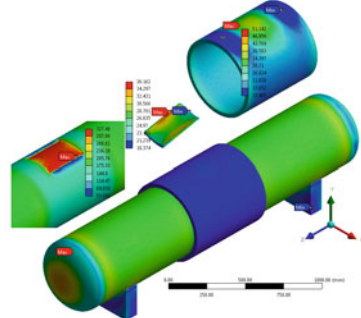
$\text{Ø}323.9 \times 9.5 / \text{X42}; d = 0.75t_n; t_c = 19.3 \text{ mm}$



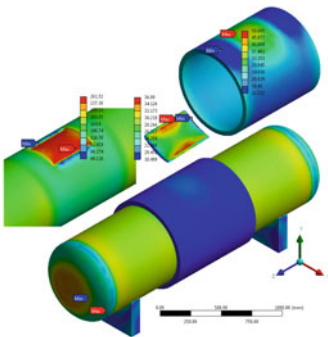
$\text{Ø}323.9 \times 8 / \text{X52}; d = 0.75t_n; t_c = 19 \text{ mm}$



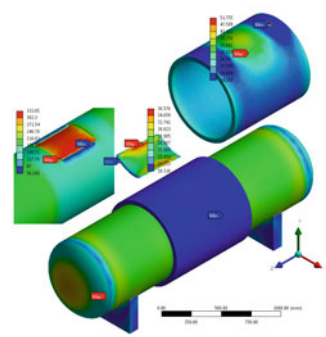
$\text{Ø}508 \times 16 - \text{X42}; d = 0.75t_n; t_c = 29.50 \text{ mm}$



$\text{Ø}508 \times 12.5 - \text{X52}; d = 0.75t_n; t_c = 29.84 \text{ mm}$



$\text{Ø}711 \times 20 - \text{X42}; d = 0.75t_n; t_c = 42.96 \text{ mm}$



$\text{Ø}711 \times 17.5 - \text{X52}; d = 0.75t_n; t_c = 41.76 \text{ mm}$

Fig. 12 Stress intensity for composite wrap repaired pipe with VSD

Table 4 Composite wrap thickness analysis with respect of ISO/TS 24817:2006

X42	CASE I Ø323.9×9.5	A. Pipe without VSD	$\max_{\sigma_{pipe}} = 211.54 \text{ N/mm}^2$
		B. Pipe with VSD	$\max_{\sigma_{VSD}} = 458.81 \text{ N/mm}^2$
		C. Pipe with composite wrap: $d = 0.75t_n$; $s_p = 203.2 \text{ mm}$; $c_p = 152.4 \text{ mm}$; $t_s = 2.375 \text{ mm}$; $t_c = 19.3 \text{ mm}$ (Eq. 1)	$\max_{\sigma_{pipe_VSD}} = 245.89 \text{ N/mm}^2$ $0.72R_{t0.5} < \sigma_{VSD} < R_{t0.5}$
	CASE II Ø508×16	A. Pipe without VSD	$\max_{\sigma_{pipe}} = 205.27 \text{ N/mm}^2$
		B. Pipe with VSD	$\max_{\sigma_{VSD}} = 465.00 \text{ N/mm}^2$
		C. Pipe with composite wrap: $d = 0.75t_n$; $s_p = 330 \text{ mm}$; $c_p = 238 \text{ mm}$; $t_s = 4 \text{ mm}$; $t_c = 29.50 \text{ mm}$ (Eq. 1)	$\max_{\sigma_{pipe_VSD}} = 259.75 \text{ N/mm}^2$ $0.72R_{t0.5} < \sigma_{VSD} < R_{t0.5}$
	CASE III Ø711×20	A. Pipe without VSD	$\max_{\sigma_{pipe}} = 229.72 \text{ N/mm}^2$
		B. Pipe with VSD	$\max_{\sigma_{VSD}} = 471.92 \text{ N/mm}^2$
		C. Pipe with composite wrap: $d = 0.75t_n$; $s_p = 436 \text{ mm}$; $c_p = 334 \text{ mm}$; $t_s = 5 \text{ mm}$; $t_c = 42.96 \text{ mm}$ (Eq. 1)	$\max_{\sigma_{pipe_VSD}} = 261.52 \text{ N/mm}^2$ $0.72R_{t0.5} < \sigma_{VSD} < R_{t0.5}$
X52	CASE IV Ø323.9×8	A. Pipe without VSD	$\max_{\sigma_{pipe}} = 211.54 \text{ N/mm}^2$
		B. Pipe with VSD	$\max_{\sigma_{VSD}} = 542.45 \text{ N/mm}^2$
		C. Pipe with composite wrap: $d = 0.75t_n$; $s_p = 203.2 \text{ mm}$; $c_p = 152.4 \text{ mm}$; $t_s = 2 \text{ mm}$; $t_c = 19 \text{ mm}$ (Eq. 1)	$\max_{\sigma_{pipe_VSD}} = 319.64 \text{ N/mm}^2$ $0.72R_{t0.5} < \sigma_{VSD} < R_{t0.5}$
	CASE V Ø508×12.5	A. Pipe without VSD	$\max_{\sigma_{pipe}} = 205.27 \text{ N/mm}^2$
		B. Pipe with VSD	$\max_{\sigma_{VSD}} = 514.23 \text{ N/mm}^2$
		C. Pipe with composite wrap: $d = 0.75t_n$; $s_p = 318 \text{ mm}$; $c_p = 238 \text{ mm}$; $t_s = 3.125 \text{ mm}$; $t_c = 29.84 \text{ mm}$ (eq. 1)	$\max_{\sigma_{pipe_VSD}} = 327.49 \text{ N/mm}^2$ $0.72R_{t0.5} < \sigma_{VSD} < R_{t0.5}$
	CASE VI Ø711×17.5	A. Pipe without VSD	$\max_{\sigma_{pipe}} = 229.72 \text{ N/mm}^2$
		B. Pipe with VSD	$\max_{\sigma_{VSD}} = 527.43 \text{ N/mm}^2$
		C. Pipe with composite wrap: $d = 0.75t_n$; $s_p = 445 \text{ mm}$; $c_p = 334 \text{ mm}$; $t_s = 4.375 \text{ mm}$; $t_c = 41.76 \text{ mm}$ (Eq. 1)	$\max_{\sigma_{pipe_VSD}} = 333.05 \text{ N/mm}^2$ $0.72R_{t0.5} < \sigma_{VSD} < R_{t0.5}$

8 Aspects Regarding the Structural Optimization of Composite Wrap Used for Re-establishing the Integrity of Pipeline Using FEA Method with COSMOS Program

On coupled interactive system “piping → defect (VSD) → polymeric filler PF → polymeric adhesive → layer of different type of fiber N_b → closing polymeric adhesive, subject to internal pressure”, it is performed quantitative and

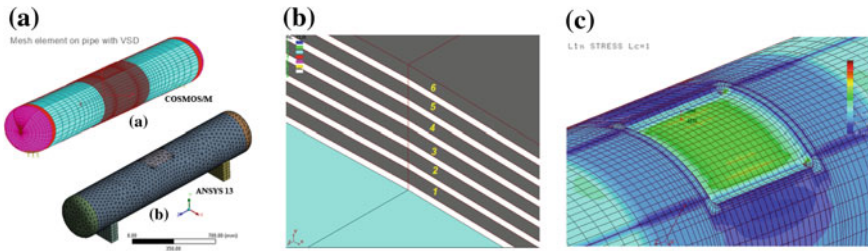


Fig. 13 Complex parameterized meshing interactions: **a** ensemble; **b** mesh detail, if composite system consists of six layers ($N_b = 6$); **c** stresses distribution in Coulomb–Tresca–Guest third resistance theory, σ_{III} , in pipe, in VSD area

qualitative evaluating the influence of these structural components and the availability of bearing capacity. To ensure credibility/validation of numerical simulations were used two programs COSMOS/M and ANSYS applied to the same parameterized models with mesh, processed in Fig. 13. Model variables are elasto-mechanical characteristics of the materials used for repair pipelines [5].

In these parameterized models, tubular metallic wall of the pipe is discretized by 4 finite volume elements (SOLID) on thickness with eight nodes, uniformly arranged in radial direction, thereby ensuring a good convergence of the nonlinear response characteristics. The adhesive polymer is modeled by finite volume element type SOLID with thickness $\Delta s = 0.25$ mm, composite fiber is modeled by finite volume element type SOLID with eight knots and thickness $\Delta s = 0.5$ mm, as it results from the processing imagines presented in Fig. 13b [6, 7].

Numerical results are present in post-processing plots of the distortions and response of mechanical stress (see Figs. 14, 15, 16, 17, 18 and 19), structured

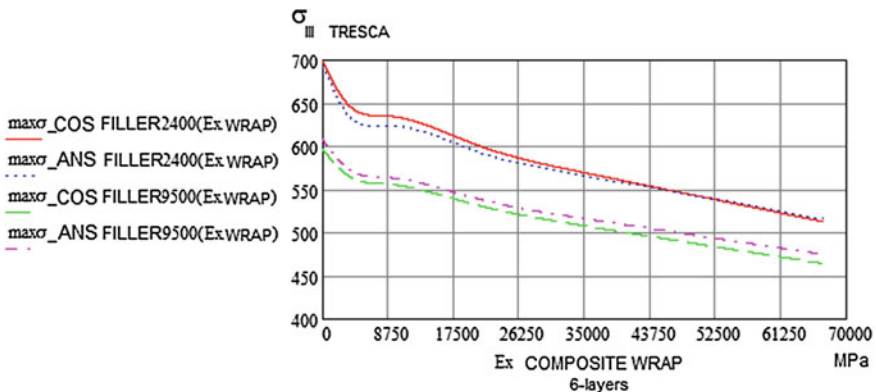


Fig. 14 Influence of the weak and very weak filler over the bearing capacity of the pipe on a wide range of elasticity modulus of the composite wrap (where max σ_{COS} are the stresses from Coulomb–Tresca–Guest third resistance theory, σ_{III} is obtained in COSMOS/M; max σ_{ANS} are the stresses from Coulomb–Tresca–Guest third resistance theory, σ_{III} is obtained in ANSYS 13)

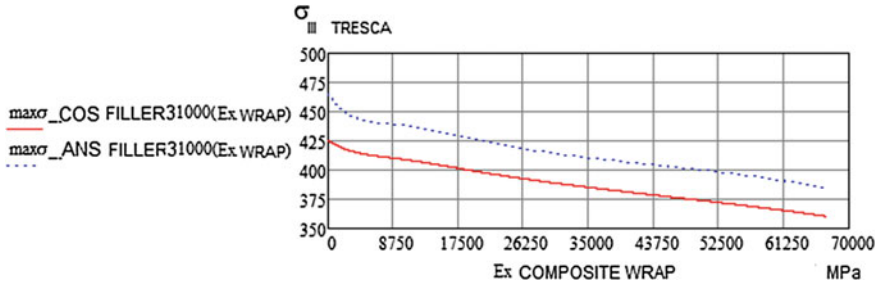


Fig. 15 Influence of the medium and hard filler over the bearing capacity of the pipe on a wide range of elasticity modulus of the composite wrap (where $\max \sigma_{COS}$ are the stresses from Coulomb–Tresca–Guest third resistance theory, σ_{III} obtained in COSMOS/M; $\max \sigma_{ANS}$ are the stresses from Coulomb–Tresca–Guest third resistance theory, σ_{III} is obtained in ANSYS 13)

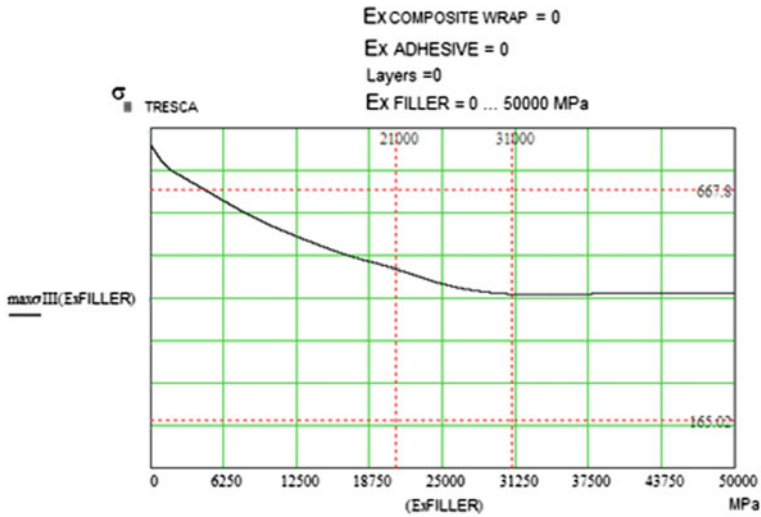


Fig. 16 Influence of the filler quality over the bearing capacity of the pipe on a wide range of elasticity modulus of the filler— $E_{XFILLER}$, in only filler version

according to the variables of the model analysis, varied over a wide range of Young’s modulus and Poisson’s ratio [7].

9 Conclusions

The total strains obtained are lower for X52 steel than X42 steel, this indicates that, in the X52 case, the pipe with VSD could work at a higher pressure than 12 MPa, in the same stress conditions. The stress intensity level (Fig. 20) in the repaired pipe

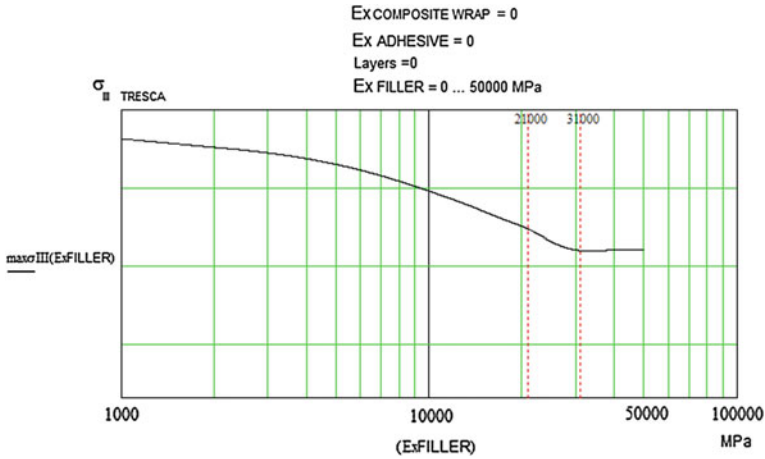


Fig. 17 Influence of the filler quality over the bearing capacity of the pipe on a wide range of modulus of elasticity of the filler— $E_{XFILLER}$, in only filler version (semi-logarithmic scale)

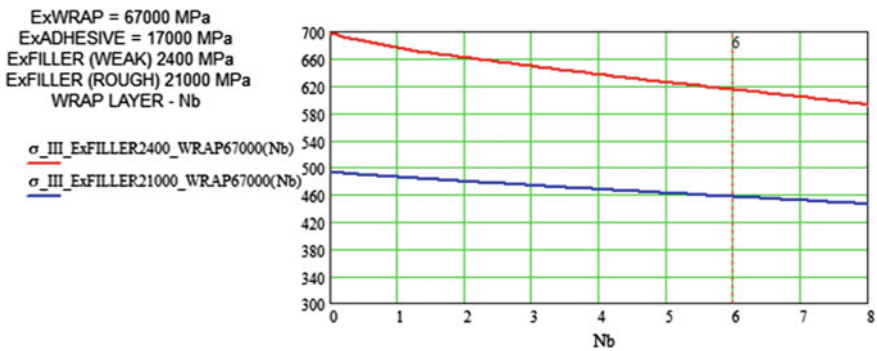


Fig. 18 Dependence between the number of higher quality composite layer N_b ($E_{XWRAP} = 67,000$ MPa) and two filler types (week $E_{XFILLER} = 2400$ MPa and very week $E_{XFILLER} = 21,000$ MPa)

with VSD (pressure of 12 MPa) is found between the limits of $0.72R_{t0.5}$ (209 N/mm^2 for X42 and 259 N/mm^2 for X52) and $R_{t0.5}$ (290 N/mm^2 for X42 and 360 N/mm^2 for X52) for all cases simulated with FEA despite the fact that Eq. (1) from ISO/TS 24817:2006 was used for the stress of $0.72R_{t0.5}$.

The main observation regarding this aspect is that the mentioned normative do not take into consideration the effect of the filler on the maximum level of the stress intensity. The load transfer between the filler and the pipe wall plays an important role in the stress level in VSD area.

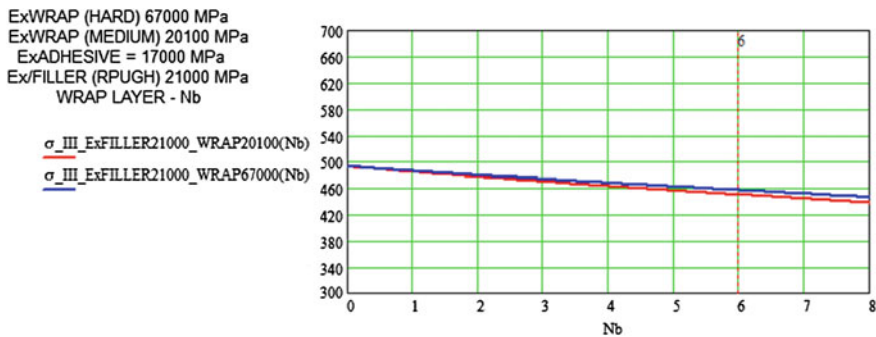


Fig. 19 The dependence between the number of composite layer N_b , with a higher quality of filler ($Ex_{FILLER} = 21,000$ MPa) and two composite versions ($Ex_{WRAP} = 20,100$ MPa, $Ex_{WRAP} = 67,000$ MPa)

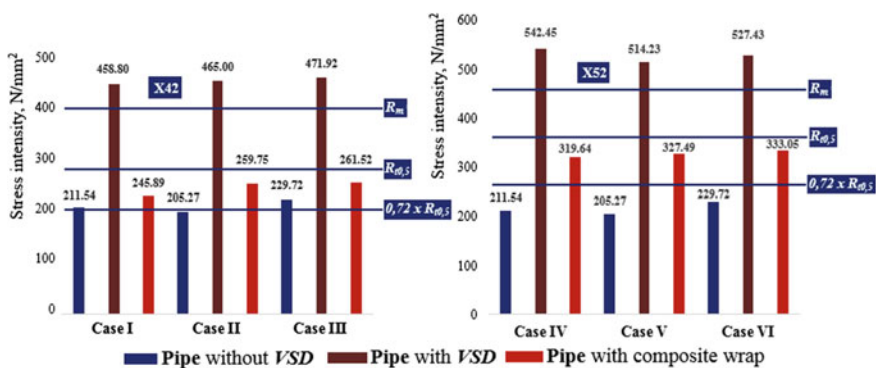


Fig. 20 Comparing of stress intensity level in cases simulated by FEA

From the analysis of the charts, presented in Figs. 14, 15, 16, 17, 18 and 19, we state the important role of quality of the filler on the availability of bearing capacity of the coupled interactive system. We stand out and determine quality requirements for filler for the moment when the filler changes the local tension in the metallic wall of the pipe—the filler interacts with the metal wall, as seen in the analyzed case, moving stress concentrator away from defect area. It is found that if the number of layers $N_b > 6$ then we cannot register a decrease of equivalent stresses sensitive to mechanical stresses in Coulomb–Tresca–Guest third resistance theory.

Acknowledgements This study was financially supported by the 7th EU Frame Program, Maria Curie Initiative, Project “INNOPIPES”, PIRSES-GA-2012-318874 (“Innovative methods of nondestructive control and composite repair of pipelines with defects of their surface with the use of composites”).

References

1. J.M. Duell, J.M. Wilson, M.R. Kessler, Analysis of a carbon composite overwrap pipeline repair system. *Int. J. Press. Vessels Pip.* **85**(11), 782 (2008)
2. N. Saeed, H. Ronagh, A. Virk, Composite repair of pipelines, considering the effect of live pressure-analytical and numerical models with respect to ISO/TS 24817 and ASME PCC-2. *Compos. B* **58**, 605 (2014)
3. Theory Reference for the Mechanical APDL and Mechanical Applications, ANSYS, April 2009
4. *ISO/TS 24817:2006*, in *Petroleum, petrochemical and natural gas industries—Composite repairs for pipework—Qualification and design, installation, testing and inspection* (2006)
5. W.-F. Chan, E.N. Lui, *Handbook of Structural Engineering*, 2nd edn. (CRC Press, New York, 2005)
6. E.M. Alawadhi, *Finite Element Simulations Using ANSYS* (CRC Press Taylor & Francis Group, New York, 2010)
7. B.J. Mac Donald, *Practical Stress Analysis With Finite Elements* (Glasnevin Publishing, Dublin, Ireland, 2007)

Finite-Element Modeling of a Repaired Pipeline Containing Two Volumetric Surface Defects

M.I. Chebakov, R.D. Nedin and A.A. Lyapin

Abstract In the modern petroleum industry it is vital to provide reliability and proper operation of transmitting pipelines, which are often subjected to various defects including volumetric surface defects (VSDs) arisen as a result of corrosion or erosion. In this, we consider a problem of computer simulation of pipeline fragment subjected to two VSDs and repaired by setting a composite wrap of a special structure. The algorithm of automatic finite-element model building based on the initial problem parameters is developed. The computational experiments on the influence of different parameters of the problem on a stress strain state of the pipe are conducted and discussed.

Keywords Pipe · Defect · Stress · Finite element

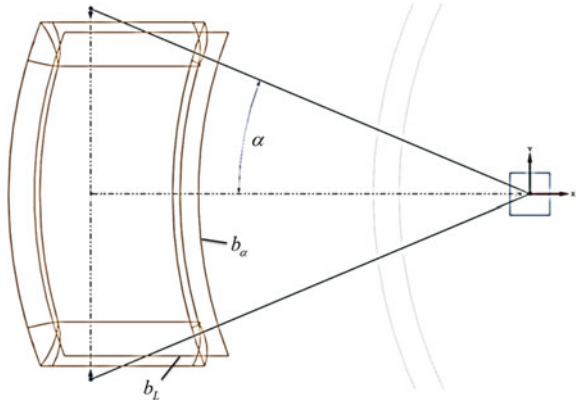
1 Finite-Element Model

Let us consider a static problem for a damaged steel pipe under inner pressure. It is assumed that the pipe has two volumetric surface defects being a result of corrosion or erosion; both defects arose at the outer pipe surface. In order to remove the corroded material, the defects are subjected to a special machining treatment: at the defects sites, two pockets are cut in the form presented in Fig. 1. Each pocket has a shape of curvilinear parallelepiped with blended edges. Such shape is chosen as the most efficient one reducing the stress concentrators at the pocket surface.

The procedure of cutting such pockets on the pipe obviously leads to the reduction of its strength properties. In order to strengthen the pipe, the empty pocket spaces are filled with a special polymer (further we shall refer it as ‘filler’), and then a special laminate wrap is put on the pipe so that both defects remain under the wrap. The laminate wrap consists of several composite layers (generally made of

M.I. Chebakov · R.D. Nedin (✉) · A.A. Lyapin
I.I. Vorovich Institute of Mathematics, Mechanics and Computer Science,
Southern Federal University, Rostov-on-Don, Russia
e-mail: rdn90@bk.ru

Fig. 1 Geometry of the pocket cut at the site of the defect



some orthotropic composite such as fiberglass) bonded with each other by thin adhesive interlaying. In practice, such wraps are set on damaged pipes by using the rolling technique.

Due to the complex geometry of the defected pipe and the structure of the composite wrap, it is necessary to use some numerical algorithm to treat the problem stated. One of the most widespread and efficient numerical method for such problems is the finite-element method [1–3]. In the present research, we have used the finite-element package Siemens NX in order to solve numerically the problem formulated. In this package, we have developed a complete finite-element (FE) model of the whole piece of the defected pipe, the composite wrap, and the fillers. The FE model is fully parametrical and multipurpose; by setting a list of parameters including the geometry and material of the pipe, the fillers and the wrap, and the solution accuracy, one may easily obtain the final FE solution. In particular, the FE model constructed allows us to set one or two machined defects of smoothed rectangular shape of any sizes and position at the pipe surface; these defects can have different sizes and locations. The parameters are set in the corresponding Excel file.

With the help of the FE model developed, one may perform the automatic execution of all the main stages of the finite-element simulation such as editing geometry and materials properties of the whole model, creating and refining FE mesh, and recalculating the FE solution.

In the framework of the simulation algorithm developed, the pipe body was initially segmented into several parts in order to provide specific refinement of FE mesh. Figure 2 depicts the particular example of the refined FE mesh. The numbers 1–3 in the figure correspond to different sizes of the finite elements used. Such meshing will be used for all the numerical examples listed below. It is worth noting that the inner surface of the pipe was meshed in the same way as the outer surface. To mesh the pipe, we used 3D tetrahedral FE mesh and mesh control at the defect faces to dense FE mesh in the defect area and, consequently, to refine the FE solution.

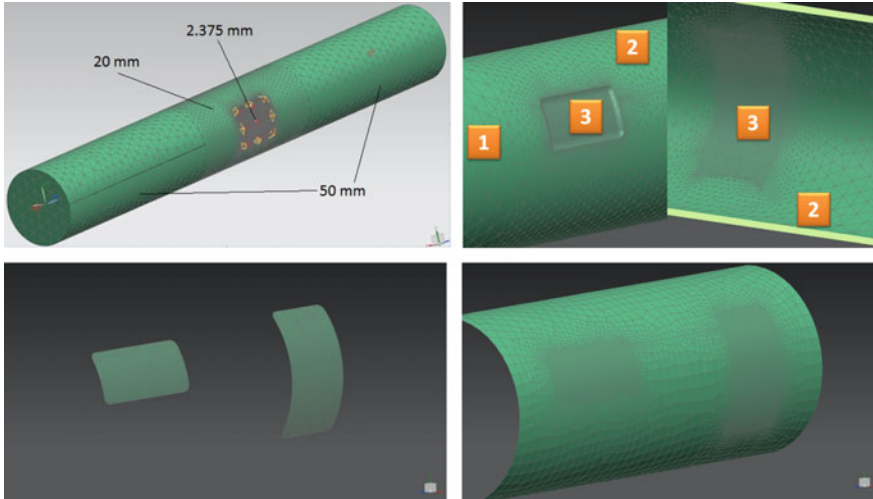


Fig. 2 Finite-element meshing of the pipe, fillers and wrap

2 Numerical Experiments

All the numerical experiments below are present for the steel pipe made of API X52 steel. The exterior diameter of the pipe is 323.9 mm, the total wall thickness is 8 mm. The pipe is subjected to the internal pressure of value 7 MPa. The polymer filled in pockets is isotropic material with the Young modulus $E = 30$ GPa, tensile strength $T = 60$ MPa and maximum possible elongation $A = 1\%$. The composite load-bearing material is assumed orthotropic with the following mechanical characteristics: $E_1 = 30$ GPa (the Young modulus in the circumferential direction), $E_2 = E_3 = 2$ GPa; the Poisson's ratios in all the directions are 0.3, the shear moduli are the same $G_{12} = G_{13} = 1$ GPa, and $G_{23} = 0.5$ GPa; $T = 300$ MPa; $A = 2\%$. These parameters correspond to the fiberglass material with the fibers directed circumferentially.

Now let us consider four cases of locations and sizes of the machined defects. Here we reduce the circumferential size of the defect to the right, see Fig. 3. Note that the wrap and fillers are not present in this figure. In this series of numerical experiments, we test a model case, when the cut pockets are rather deep in order to see the nature of stress distribution. The defects sizes and relative coordinate are listed in Table 1.

In Fig. 4 the fields of displacements for the original (unwrapped) pipe for all the four cases considered are compared. The largest values are depicted in red. The corresponding color scale is show on the left side of each solution. The values are present in mm.

Figure 5 shows the stress fields for the original pipe for the four considered cases. The values are shown in MPa.

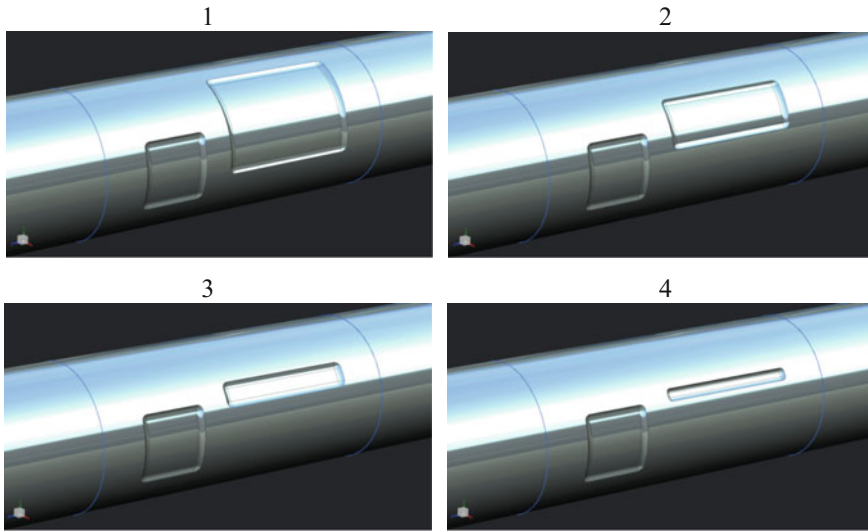


Fig. 3 Four cases considered for different locations and sizes of the machined defects

Table 1 Defects parameters

Name	# 1	# 2	# 3	# 4	Description
<i>Defect # 1</i>					
x_L	1400	1400	1400	1400	Longitudinal coordinate of the defect center (mm)
x_a	0	0	0	0	Circumferential coordinate of defect (°)
b_L	76.2	76.2	76.2	76.2	Half length of the defect (mm)
α	26.96	26.96	26.96	26.96	Half angular size (°)
s	6	6	6	6	Depth of the defect (mm)
r	19	19	19	19	Radius of the defect (mm)
<i>Defect # 2</i>					
x_L	1100	1100	1100	1100	Longitudinal coordinate of the defect center (mm)
x_a	30	30	30	30	Circumferential coordinate of defect (°)
b_L	160	160	160	160	Half length of the defect (mm)
α	40	20	10	5	Half angular size (°)
s	6	6	6	6	Depth of the defect (mm)
r	19	19	19	10	Radius of the defect (mm)

The same fields are shown in Figs. 6 and 7 for the repaired pipe with fillers and composite wrap. The borders of the wrap may be seen on the pipe surface. One may observe that the magnitudes of maximum displacements and stresses are much less than in the original pipe subjected to the same pressure. The nature of these fields will be discussed in detail below.

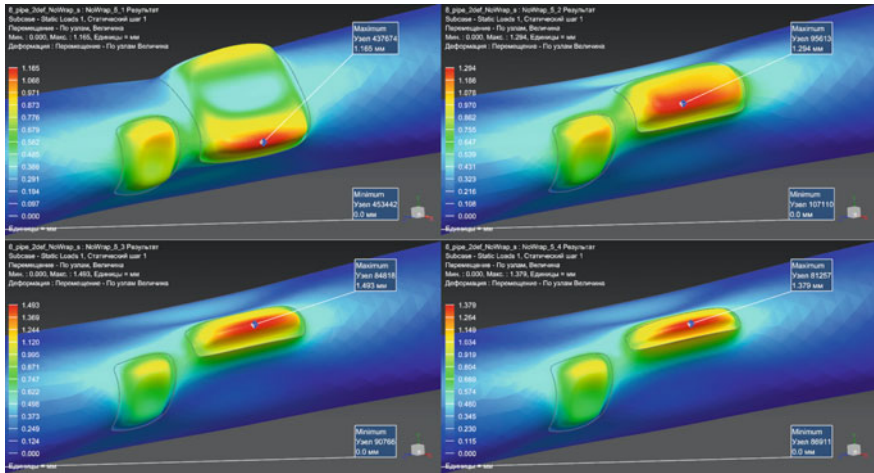


Fig. 4 Comparison of displacements for the unwrapped pipe

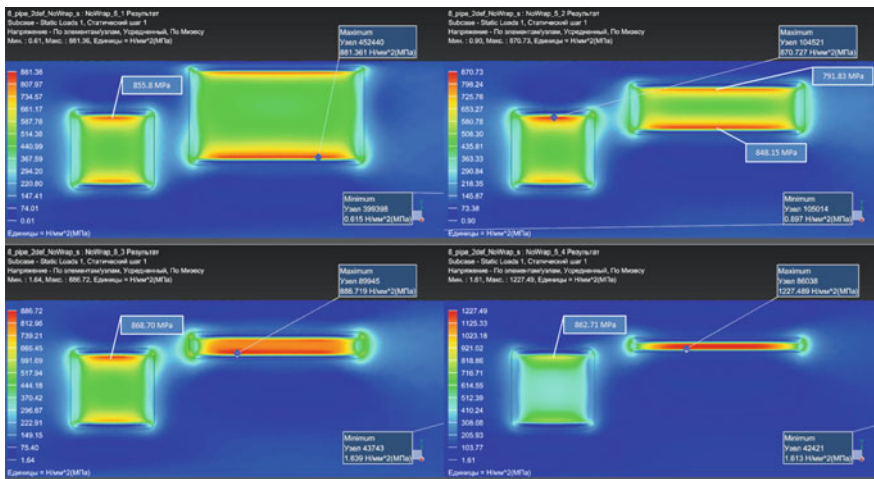


Fig. 5 Stress comparison for the unwrapped pipe

In Fig. 8, a stress distribution on the bottom layer of the composite wrap is given.

Figure 9 shows stress field at the fillers surfaces.

In other analysis, we compared stress fields arising in the areas of the defects of the same shapes and sizes, when we located them at one generatrix (i.e. the circumferential coordinates of both defects were the same, see Fig. 10) and at one circumference (the longitudinal coordinates of the defects were the same) and then changed the distance between them. Each defect had the following sizes:

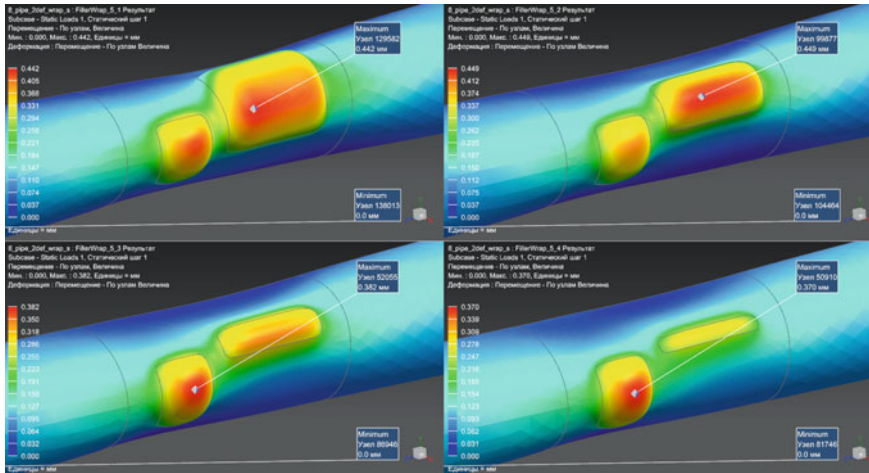


Fig. 6 Comparison of displacements for the wrapped pipe

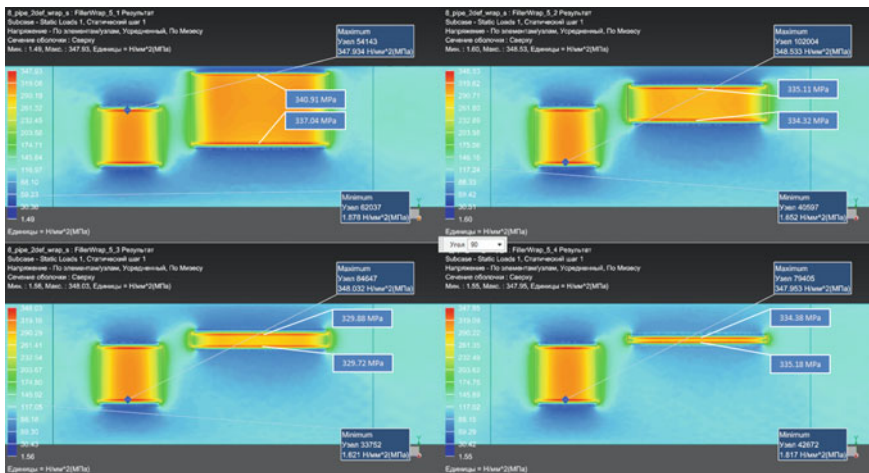


Fig. 7 Stress comparison for the wrapped pipe

$b_L = 76.2 \text{ mm}$, $\alpha = 26.96^\circ$, $s = 6 \text{ mm}$ (depth), $r = 19 \text{ mm}$ (curvature radius of the rounded edges).

In the first case, when we change a distance between the same defects—pockets, located at one generatrix, there is no difference between the corresponding stress fields. In other words, the distance between the pockets does not effect on the stress. On the other hand, in the frames of the second experiment, we revealed that the circumferential distance between the pockets affects the stress field. From Figs. 11 and 12 we may observe that if the distance between the pockets is small enough

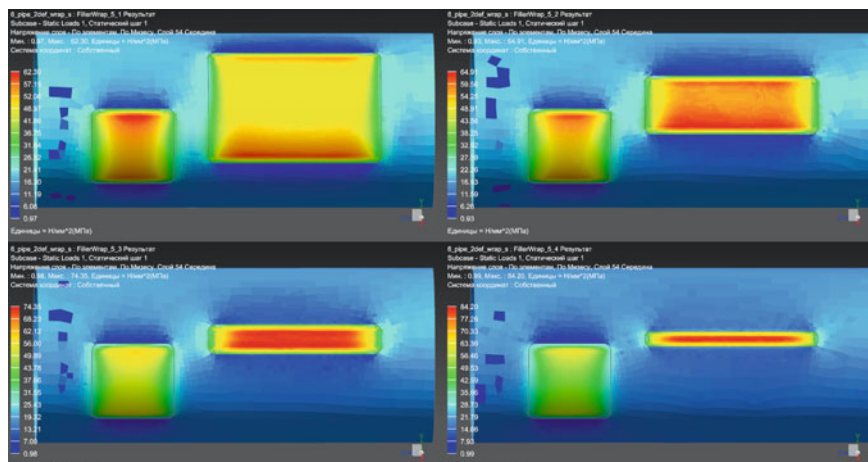


Fig. 8 Stress distribution on the wrap's bottom layer

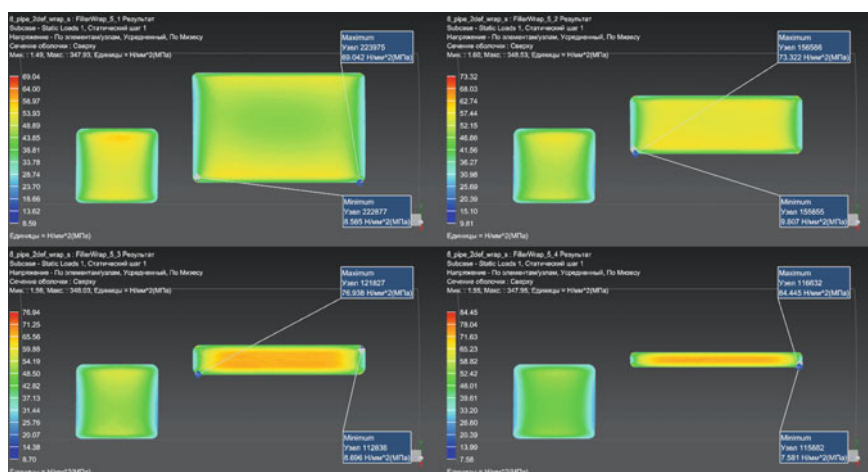


Fig. 9 Stress distribution on the fillers

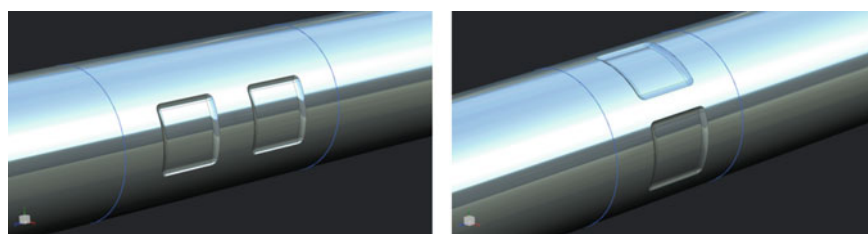


Fig. 10 The same pockets located at one generatrix (on the left) and at one circumference (on the right)

Fig. 11 Stress on the cross-sectional line in the middle of the defect area; a case of large distance between the pockets

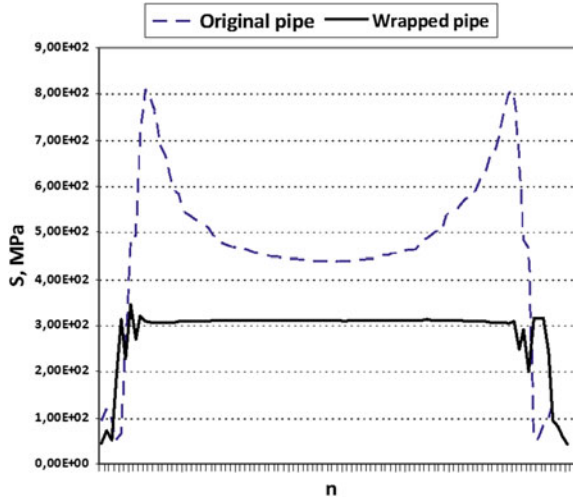
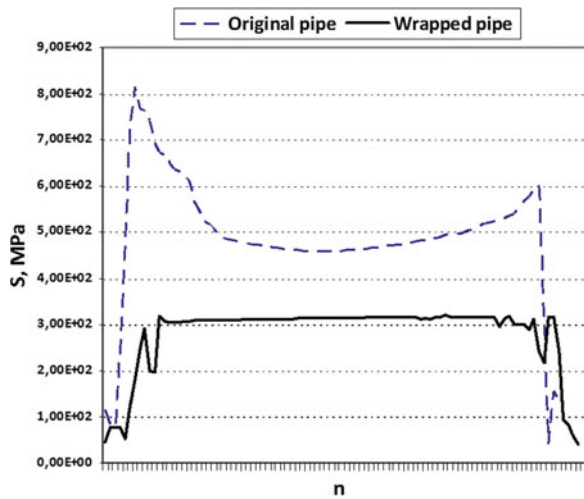


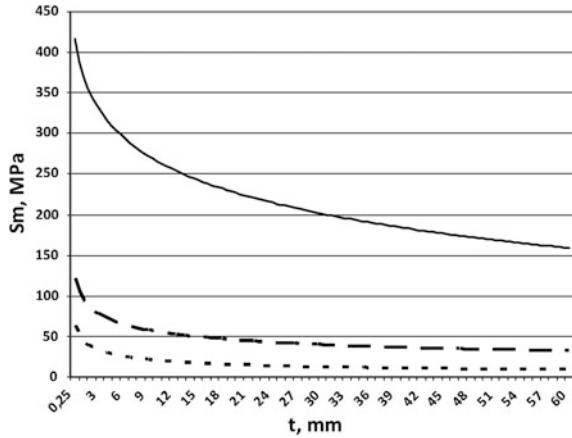
Fig. 12 Stress on the cross-sectional line in the middle of the defect area; a case of small distance between the pockets



(particularly, less than the circumferential size of each pocket), then the stress peaks at the neighbor edges of the pockets significantly reduce. For the wrapped pipe we may observe the flattening of the stress graph at the whole line and elimination of stress concentrators; the average value of the stress significantly reduces at that.

We also analyzed the influence of the total thickness (t) of the composite wrap on the maximum stresses (S_m) arising at the steel pipe, wrap and fillers, see Fig. 13. Here we tested a single homogeneous composite part with a thickness of 2.75 mm and the adhesive of 0.25 mm in thickness, so the total wrap thickness was 3 mm. We may see that the nature of all the plots is close to the logarithmic one. Hence,

Fig. 13 Maximum stress in the upper composite layer of the steel pipe (*solid line*), wrap (*dashed line*) and fillers (*dotted line*)



analyzing these plots, one may pick the most optimal thickness of the wrap in order to reduce significantly the stress concentrators.

In practice, the yield stresses are not allowable in transmission pipelines hence we conducted the linear analysis when solving the stated problem in NX. However, some values of stresses in the computational experiments above exceed the yield stress value for steel; this should be interpreted as the model problem. The solution of this model problem showed that machining of the defects at such a depth (i.e., cutting too deep pockets) leads to arising of too high stress concentrators that are not allowable in the pipe. So, in practice, it is necessary to simulate the FE solution within the model proposed every time by investigating the damaged pipe in order to estimate the possibility of its repair via composite wrapping.

3 Conclusion

In the chapter, we presented a finite-element model of a pipeline under inner pressure, subjected to two volumetric surface defects. It was assumed that, at first, the defects were machined and filled by a homogeneous polymer, and then the pipe was repaired by setting on it a special laminate-composite wrap consisting of several composite layers bonded together with an adhesive. The finite-element model of the considered pipeline was fully automatic and parametrically depended on all the initial problem parameters. The analysis of various parameters of the machined defects on stress-strain state of the pipe was performed. The influence of the wrap properties on its efficiency was estimated. A series of the corresponding computational experiments were provided and discussed.

Acknowledgements The research was conducted with the support of the Russian Foundation for Basic Research (Proj. # 16-01-00354 A), Southern Mathematical Institute (Vladikavkaz Scientific Center of RAS) and Grant of the President of the Russian Federation MK-5440.2016.1.

References

1. A.A. Lyapin, M.I. Chebakov, A. Dumitrescu, Gh Zecheru, *Mech. Compos. Mater.* **51**(3), 333 (2015)
2. Gh Zecheru, P. Yukhymets, Gh Draghici, A. Dumitrescu, *Rev. Chim.* **66**(5), 710 (2015)
3. Gh Zecheru, I.E. Lata, Gh Draghici, A. Dinita, *Materiale Plastice* **48**(1), 88 (2011)

Assessment of the Reinforcement Capacity of Composite Repair Systems for Pipelines with Interacting Defects

I. Lambrescu, V.A. Chebanenko, D.V. Gusakov and A.V. Morgunova

Abstract This chapter is devoted to the investigation of a damaged pipeline segment with two volumetric surface defects (VSDs) located on the outer or inner surfaces. The segment was subjected to static inner pressure in the linear elastic domain, since when stresses go beyond this limit the defect is no longer accepted. The main attention is focused on the interaction between these two defects and on how this interaction influences the stress–strain state in the pipeline segment. Moreover, the problem with two volumetric surface defects was divided into two cases. First, when defects are not repaired at all. Second, when composite wrap was applied in the damaged zone. In order to solve these problems, series of computational experiments were performed with the help of finite element modeling using ANSYS and Siemens NX packages.

Keywords Pipeline · Two defects · Corrosion · Finite element · In-service repair · ANSYS · NX

1 Introduction

During the operation of oil-and-gas pipelines, many engineering problems arise. One of them is the repair of various defects in the pipeline, for example, defects occurring in welds, damages caused by external mechanical impacts, cracks and surface corrosion [1–4]. The most common methods of repair presently used are the

V.A. Chebanenko · D.V. Gusakov · A.V. Morgunova
Vorovich Mathematics, Mechanics and Computer Sciences Institute,
Southern Federal University, Rostov-on-Don, Russia

V.A. Chebanenko
Southern Scientific Center of Russian Academy of Science,
Rostov-on-Don, Russia

I. Lambrescu (✉)
Petroleum-Gas University of Ploiești, Ploiești, Romania
e-mail: ilambrescu@upg-ploiesti.ro

complete replacement of the damaged segment of a pipeline, and the employment of techniques involving welding. Both these approaches require welding operations performed on in-service pipeline, because stoppage of the pipeline operation results in significant financial losses. In this context, nowadays the objective of the development of pipe repair techniques (like using composite wraps) without the need of welding directly on the pipeline [5–8] is highly relevant. Moreover, in order to assess a need to repair the damaged pipeline and to define the most suitable repair method, it is necessary to provide the assessment of the defects at the pipe wall and the evaluation of stresses and strains generated by their presence.

In our previous studies [9, 10] we have considered several problems for a damaged pipeline with one or two volumetric surface defects (VSDs). We have obtained a similarity criterion, which helped to estimate the maximum stress values in the pipeline with VSDs. Moreover, the results of investigation of the mutual influence between two defects showed, that in order to eliminate additional stresses it is better to create two defects with moderate space between them rather than to form a large one in the case of the longitudinal defect location. In the case of the circumferential location of defects we found out, that it is better to machine one bigger defect instead of two smaller ones.

All previously considered problems were restricted only to longitudinal and circumferential cases of VSDs location. With this viewpoint, it is interesting to consider an arbitrary location of two VSDs in order to study its influence on strain–stress state of pipeline segment. It is worth noting that composite wrap was not considered in our previous works, so it is tempting to study such a case, too. In addition, it would be interesting to study problems for two inner VSDs with arbitrary locations. To fill this gap, we undertook this study.

In this chapter, we consider several cases for a pipeline with two volumetric surface defects subjected to internal pressure. In the first part, the case of two VSDs on external surface is investigated. Influence of the composite wrap is also studied. The second part is devoted to the pipe segment with two VSDs on the internal surface. In all cases, we considered the defects, caused by surface corrosion, which then were subjected to a mechanical treatment (grinding) in order to eliminate the sources of stress concentration. In the corroded area, a rectangular “pocket” with rounded corners was machined. For the inner defects, obviously, it is not possible to apply any mechanical treatment, however, we considered as acceptable for theoretical reasons to admit machined-like defects.

In order to draw pertinent conclusions, we compare the results obtained by using finite element analysis with previously defined criteria for assessing interactions of defects (more details can be found in Sect. 3.3). For this moment, only three criteria were considered

- (i) the criterion [11, 12], stating that two defects will interact, if the distance between them is less than triple thickness of the pipe;
- (ii) the criterion [13], stating that two defects will interact, if an imaginary rectangle around the defect with dimensions two times greater than the

axial and circumferential dimensions of the defect, will intersect other defect (see Fig. 1).

- (iii) the criterion [14], stating that if a circumferential spacing, \varnothing , between adjacent defects, satisfies the inequality

$$\varnothing < 360^\circ \frac{3}{\pi} \sqrt{\frac{s}{D}} \tag{1}$$

then these two defects cannot be treated as isolated, if the axial spacing between the adjacent defects, F , satisfies inequality

$$F < 2.0\sqrt{Ds} \tag{2}$$

So, two defects will interact if

$$\frac{1 - \frac{d}{s}}{1 - \frac{d}{sQ}} > \frac{1 - \frac{1}{s} \frac{2dL}{2L+F}}{1 - \frac{1}{sQ_{12}} \frac{2dL}{2L+F}}, \tag{3}$$

with d is the maximum defect depth and where

$$Q = \sqrt{1 + 0.31 \left(\frac{L}{Ds}\right)^2} \tag{4}$$

and

$$Q_{12} = \sqrt{1 + 0.31 \left(\frac{2L+F}{\sqrt{Ds}}\right)^2} \tag{5}$$

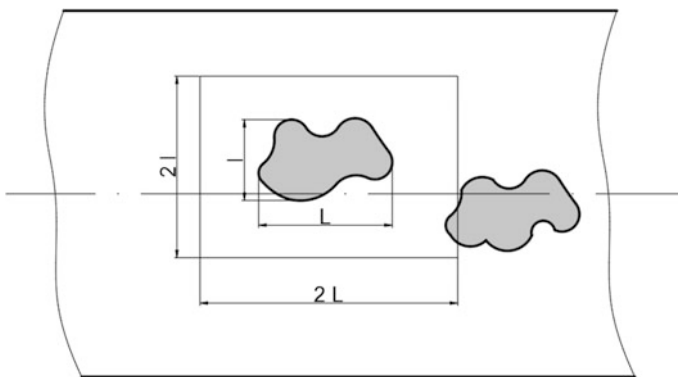


Fig. 1 Interaction of defects according to API 759, Part 4

Equations (1)–(5) were adapted to our particular case, when two defects had the same length and depth. Moreover, the notation of [14] was changed to accommodate our notations.

To perform the analysis of the above-mentioned problems, we have modified previously developed models in ANSYS and Siemens NX software [9, 10] in the sense of parameterization of the model in order to allow a large number of analyses. In the examined models, we used Steel X52 as the pipe material.

2 Analysis

2.1 General Considerations of Finite Element Analysis

The general approach for modeling the pipe is present in Fig. 2:

Analysis type: static structural;

Nonlinear effects: are not considered;

Element type: SOLID187.

The structure was divided, for meshing reasons, into three zones

- Zone 1—Element size = Pipe Thickness—Defect depth
- Zone 2—Element size = Pipe Thickness
- Zone 3—Element size = Automatic sizing

As already mentioned, the element used was a tetrahedral type, Element SOLID187, depicted in Fig. 3.

We considered the pipe fixed at both ends, see Fig. 4.

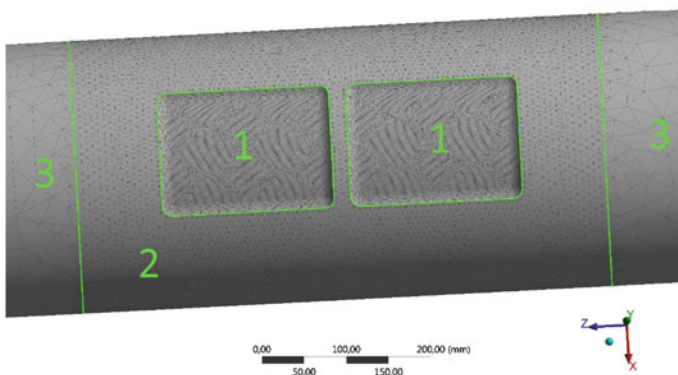


Fig. 2 Considered model of pipe

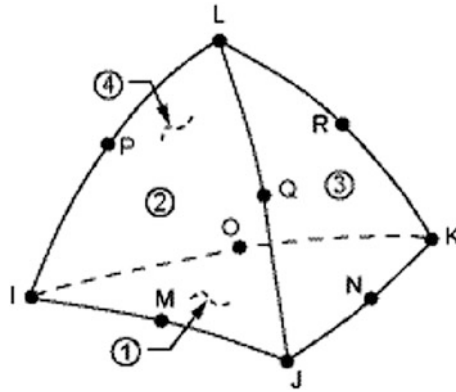


Fig. 3 Element SOLID187

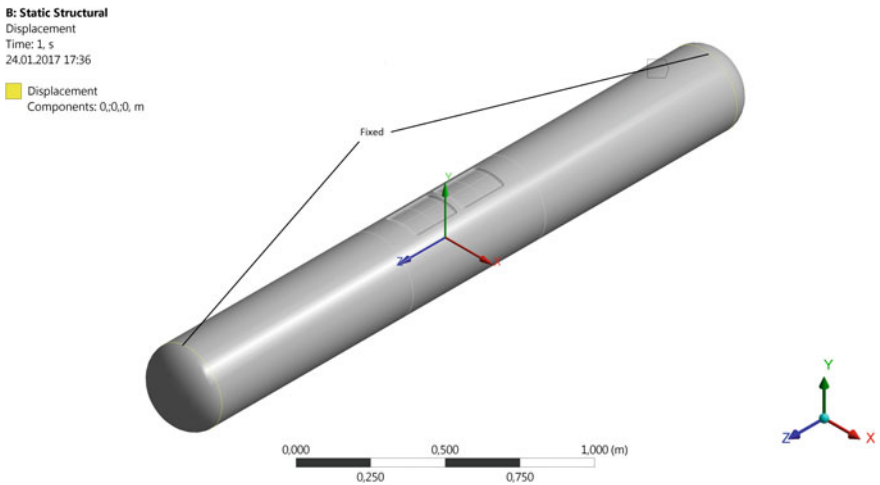


Fig. 4 Geometric conditions

2.2 Interaction Between Two VSDs Without Repair, on the External Surface

In the first part of our research, we investigated the mutual influence of two machined VSDs on the external surface of the pipeline segment. Our goal was to obtain relations between maximum Von Misses stresses and relative location of defects. In addition, it was interesting to investigate the application of composite wrap on these defects and to compare it with unwrapped cases. In order to do this, we have considered three pipes with different geometrical parameters and wrap's

Table 1 Geometrical parameters of the pipe

Parameter	Case 323 (mm)	Case 508 (mm)	Case 711 (mm)
Pipe diameter (D)	323.9	508	711
Wall thickness (s)	8	12.5	17.5
Defect length (L)	203.2	318	445
Defect depth (d)	6	9.4	13.1
	4.8	7.5	10.5
	3.2	5	7
Defect width (l)	152.4	238	334

thicknesses equal to those in Table 1. Throughout this chapter, pipe's length and internal pressure value were 2440 mm and 1.6 MPa, respectively.

As can be seen, for the 323.9 mm pipe, three depths of defects were considered. This approach will be used in the future for all other pipe diameters.

The 3D models used to investigate the pipes with defects were developed using a parametric approach, the parameters being the dimensions presented in Fig. 3 and listed in Table 1. In order to set the relative position of the two defects, one has introduced two variables: α corresponding to the circumferential distance between defects and F corresponding to the axial distance between defects (see Fig. 5). This approach allows automation of the calculation process.

The first step was to perform a series of computational experiments in order to assess how the defects interact. It has been performed by retaining the maximum Von Mises stress in the defect area for each case.

A case corresponds to one point in a 5×10 grid (see Fig. 6), defined varying both parameters α and F . These two parameters change into the following ranges: α changes from 0° to 90° with a 10° step, while F changes from $0.1 L$ to L with five intermediate values. Each point describes a combination of the two parameters α and F .

The second step was to define, for each pipe diameter, two matrices, both with dimensions 5×10 (the same with the grid points). We will call them "criteria

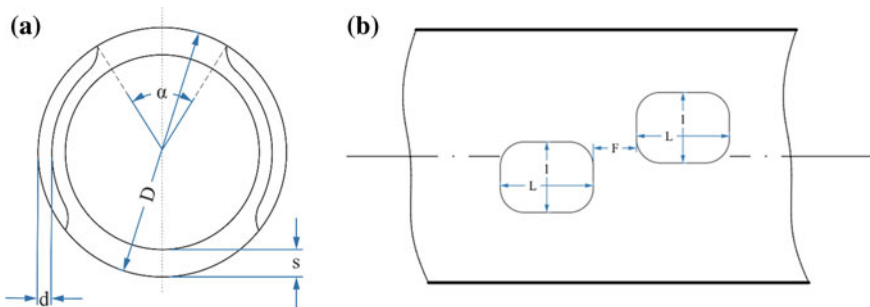


Fig. 5 Parametrization of pipe model: **a** cross-section of tube (circumferential location), **b** longitudinal location

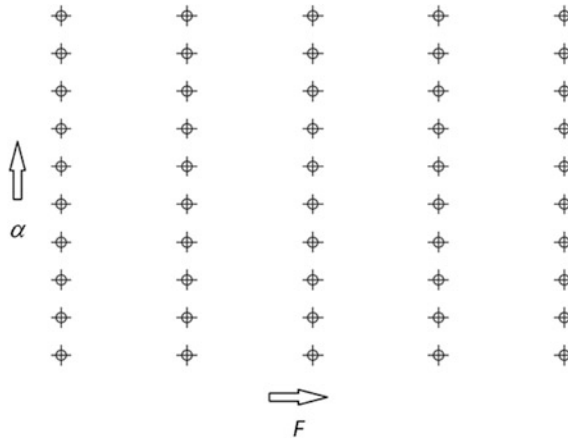


Fig. 6 Grid points

	323.9 mm	3 x s API 759		24 mm 101.6 mm						
Axial distance	0	10	20	30	40	50	60	70	80	90
20	20	20	20	20	20	20	20	20	20	20
50	50	50	50	50	50	50	50	50	50	50
100	100	100	100	100	100	100	100	100	100	100
150	150	150	150	150	150	150	150	150	150	150
200	200	200	200	200	200	200	200	200	200	200

	3 x s API 759	24 mm 76.1 mm								
Circumferential distance	0	10	20	30	40	50	60	70	80	90
20	-152.20	-123.94	-95.67	-67.41	-39.14	-10.88	17.39	45.65	73.92	102.18
50	-152.20	-123.94	-95.67	-67.41	-39.14	-10.88	17.39	45.65	73.92	102.18
100	-152.20	-123.94	-95.67	-67.41	-39.14	-10.88	17.39	45.65	73.92	102.18
150	-152.20	-123.94	-95.67	-67.41	-39.14	-10.88	17.39	45.65	73.92	102.18
200	-152.20	-123.94	-95.67	-67.41	-39.14	-10.88	17.39	45.65	73.92	102.18

Fig. 7 Criteria matrices

matrices”. Each point of the matrices represents a distance between defects. For one matrix, it will be the axial distance, for the other one—the circumferential distance (expressed also in mm). For the 323.9 mm pipe, these two matrices are present in Fig. 7.

In these matrices, italic fonts show distances smaller than the API 759 limit (101.6 mm for axial distance and 76.1 mm for circumferential distance).

The highlighted cells present distances which satisfy the first criterion for assessing interactions of defects (smaller than triple pipe thickness).

The area, enclosed by the rounded corner rectangle, corresponds to the third criterion considered for the 6 mm defect depth.

For each of the criteria, the final area with interfering defects should be an intersection of the areas of both matrices (the dark edge rectangle for the API 759 criterion and the lighter one, for the first criterion). These final regions are represented only for the circumferential distance matrix in Fig. 7.

The third step in our analysis was to perform for each case (a point on the grid) a finite element analysis and retain the maximum Von Mises stress. These values are associated to the corresponding grid points, and contour plots were produced.

On these contour plots three rectangles were superimposed, which corresponded to the three criteria for assessing interactions of defects. The bigger rectangle (red continuous lines) corresponded to the second criterion, the smaller rectangle (black continuous lines) corresponded to the first criterion, while the black rectangle, drawn with dashed line, described the third criterion.

For the defects without repair, the results are present in Figs. 8, 9 and 10.

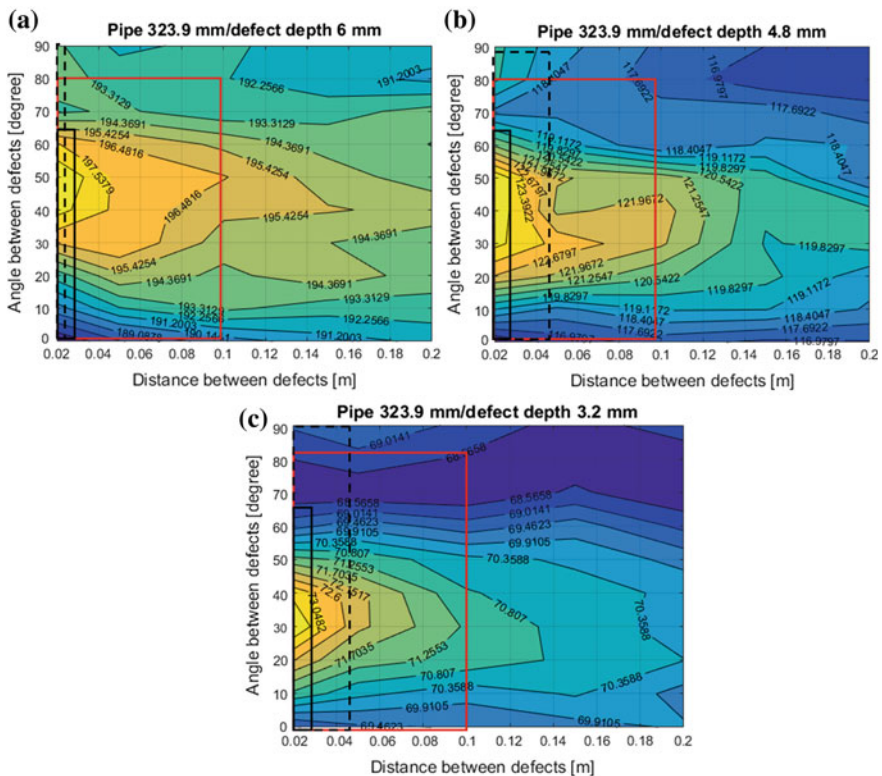


Fig. 8 Stress distribution for 323.9 mm pipe: **a** defect depth is 6 mm, **b** defect depth is 4.8 mm, **c** defect depth is 3.2 mm

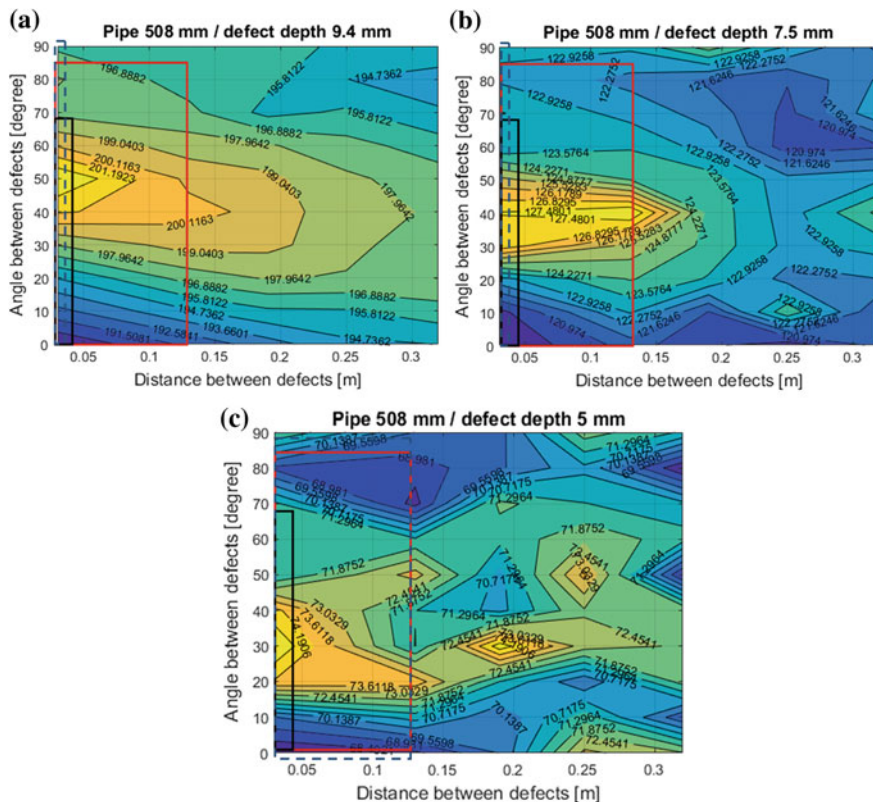


Fig. 9 Stress distribution for 508 mm pipe: a defect depth is 9.4 mm; b defect depth is 7.5 mm; c defect depth is 5 mm

2.3 Interaction Between Two VSDs for the Repaired Pipe

As already mentioned in the introductory paragraph 2.2, we also considered the case, when the pipe was subjected to a repair process, consisting in applying a composite wrap.

The model of the repaired pipe is present in Fig. 11, while the corresponding dimensions are present in Table 2.

The process of repairing the pipeline, damaged by surface corrosion, consists of several stages. At the first stage, damaged zones are subjected to a mechanical treatment in order to eliminate the sources of stress concentration. Then, the machined “pockets” are filled with some compound filler, so that to restore the lost volume. The properties of the compound filler are present in Table 3.

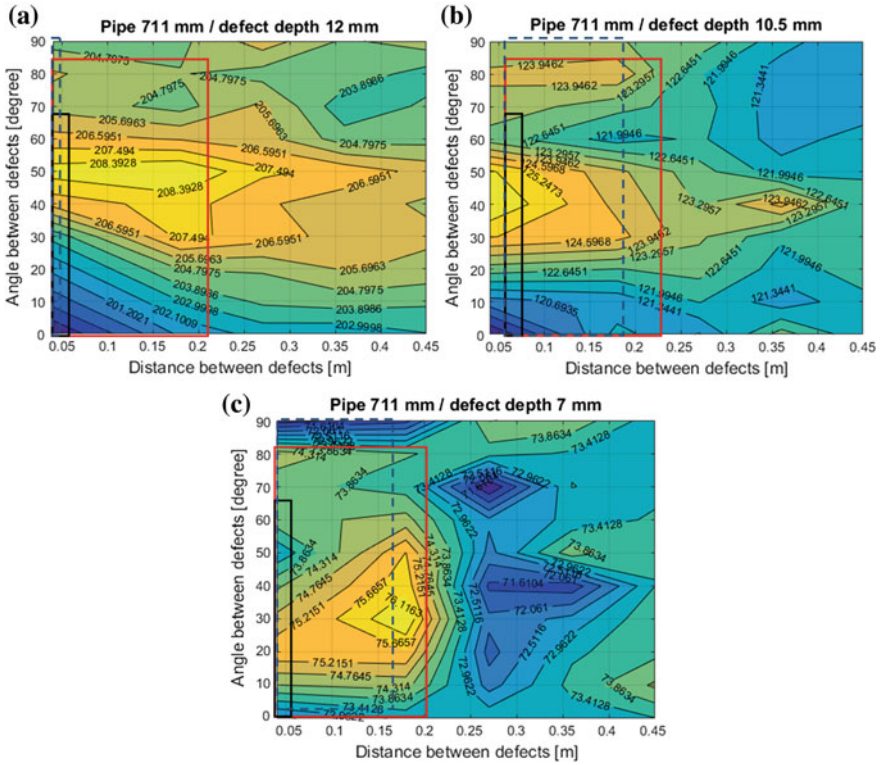


Fig. 10 Stress distribution for 711 mm pipe: **a** defect depth is 13.1 mm; **b** defect depth is 10.5 mm; **c** defect depth is 7 mm

As far as the wrap is concerned, the properties are present in Table 4. The fabric and adhesive types of the wraps were considered.

Using the same general settings for the finite element analysis, for the 5×10 grid of properties, we obtained results, presented in Figs. 12, 13 and 14, where above-mentioned three rectangles are not shown, since the considered criteria operate only on no-wrap defects.

Figure 15 presents the stress distribution for a 323.9 mm pipe, a defect depth of 6.0 mm, a distance between the two defects of 162.6 mm and an angular distance of 60° ; a wrap length of 384.5 mm and a wrap thickness of 5 mm; an internal pressure of 1.6 MPa.

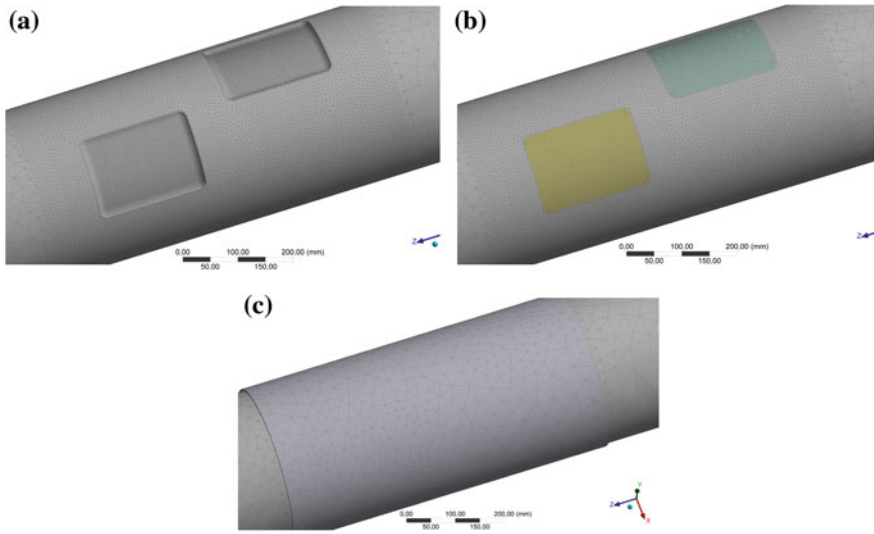


Fig. 11 Finite element model for pipe with wrap: **a** pipe with defects, **b** pipe with filler, **c** pipe with wrap

Table 2 Geometrical parameters of the pipe, including wrap

Parameter	Case 323 (mm)	Case 508 (mm)	Case 711 (mm)
Pipe diameter (D)	323.9	508	711
Wall thickness (s)	8	12.5	17.5
Defect length (L)	203.2	318	445
Defect depth (d)	6	9.4	13.1
	4.8	7.5	10.5
	3.2	5	7
Defect width (l)	152.4	238	334
Thickness of wrap (t)	5	8	12

Table 3 Filler properties

Young modulus	3000 MPa
Poisson's ration	0.316
Shear modulus	1139.8 MPa

Table 4 Wrap properties

Reinforcement fabric—epoxy carbon woven		Adhesive—resin polylite	
Young modulus XY	59160 MPa	Young modulus	3000 MPa
Young modulus YZ	59160 MPa	Poisson’s ration	0.316
Young modulus XZ	7500 MPa	Shear modulus	1139.8 MPa
Poisson’s ration XY	0.04		
Poisson’s ration YZ	0.3		
Poisson’s ration XZ	0.3		
Shear modulus XY	17500 MPa		
Shear modulus YZ	2700 MPa		
Shear modulus XZ	2700 MPa		

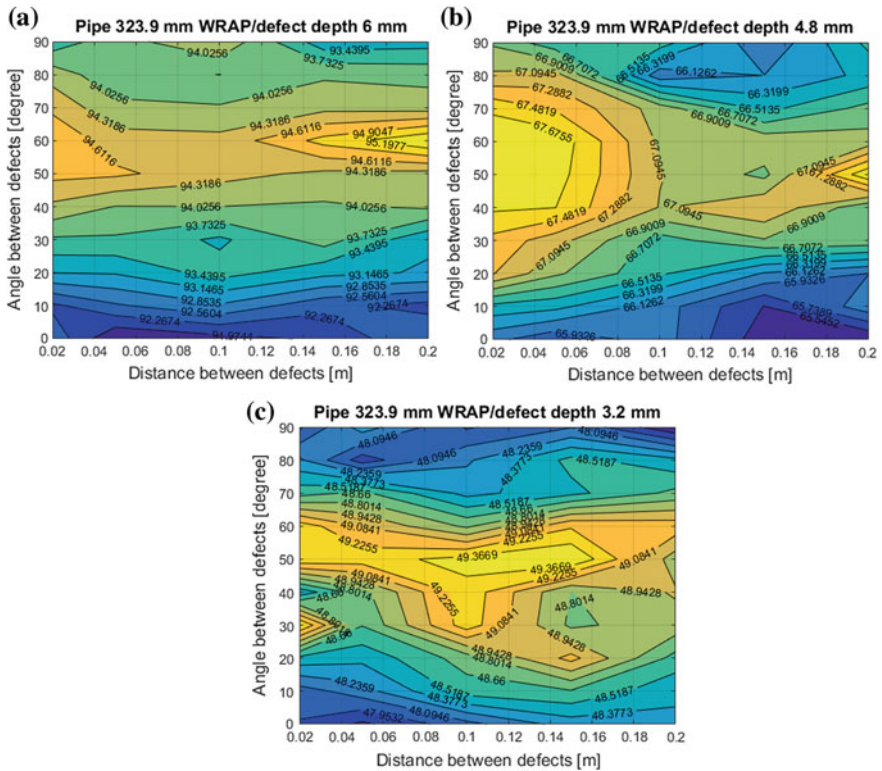


Fig. 12 Stress distribution for 323.9 mm pipe with wrap: **a** defect depth is 6 mm; **b** defect depth is 4.8 mm; **c** defect depth is 3.2 mm

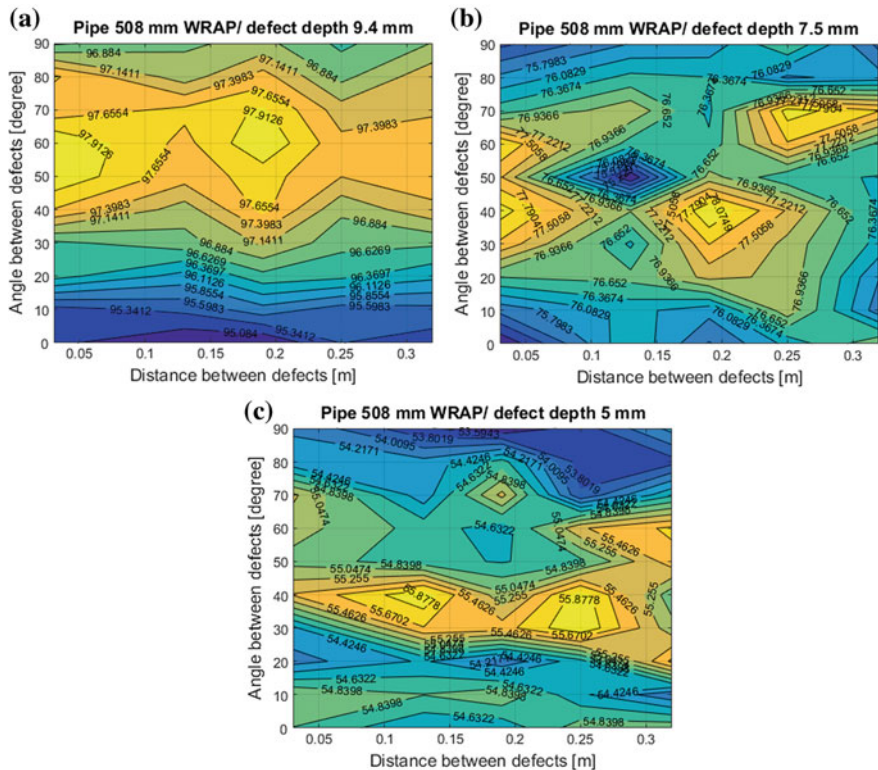


Fig. 13 Stress distribution for 508 mm pipe, with wrap: **a** defect depth is 9.4 mm; **b** defect depth is 7.5 mm; **c** defect depth is 5 mm

3 Conclusions

3.1 Unrepaired Pipeline Case (Without Composite Wrap)

The analysis of the data presented in Figs. 8, 9 and 10, can be summarized in Table 5.

The columns of *Angular position of maxima* and *Axial position of maxima* are obtained for a 2% decreasing in the stress value within the grid.

3.2 Repaired Pipeline Case (with Composite Wrap)

The analysis of the data presented in Figs. 10, 11 and 12, can be summarized in Table 6.

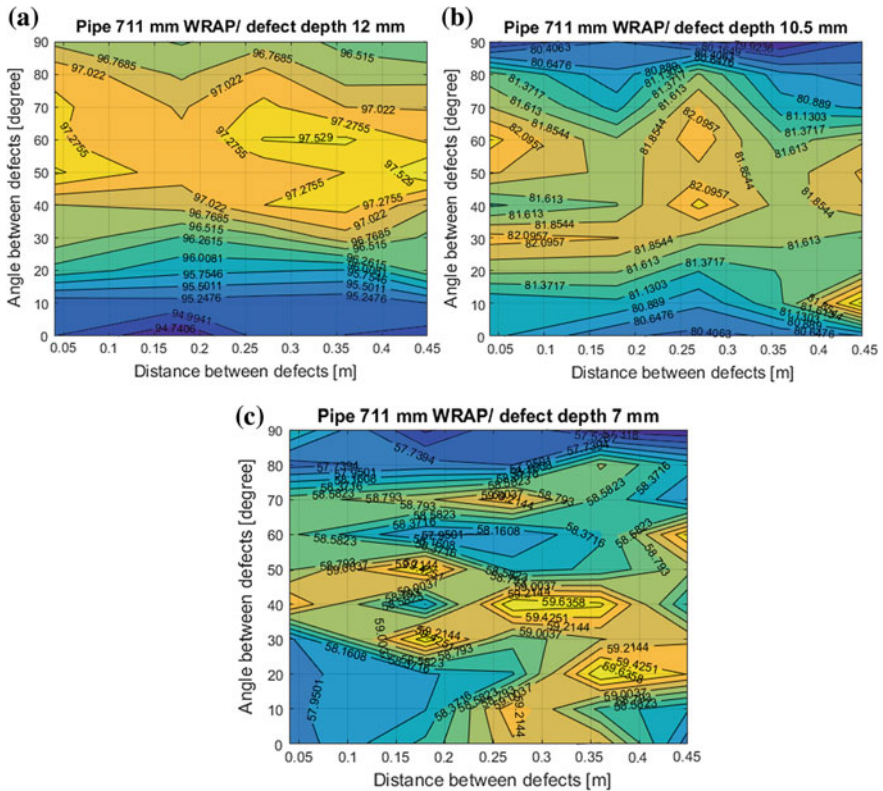


Fig. 14 Stress distribution for 711 mm pipe, with wrap: **a** defect depth is 13.1 mm; **b** defect depth is 10.5 mm; **c** defect depth is 7 mm

3.3 General Remarks

The analysis of Tables 5 and 6 allows one to make the following conclusions:

- (i) as the defect depth decreases, the mutual influence between considered two defects decreases;
- (ii) as the depth of the defect decreases, the band shape of the maxima area is replaced by an island-like distribution of maxima;
- (iii) we expect that the angular position of the maxima is dependent on the width of the defects, in the sense that when the angular distance (parameter α in Fig. 5) approaches a value that has a certain relation with the angular dimension of the defect, the influence between defects increases;
- (iv) the maximum values of stress and deformation correspond to the same position in the defect area. However, in the stress case the maximum values on the two boundaries can be different (5–7%);

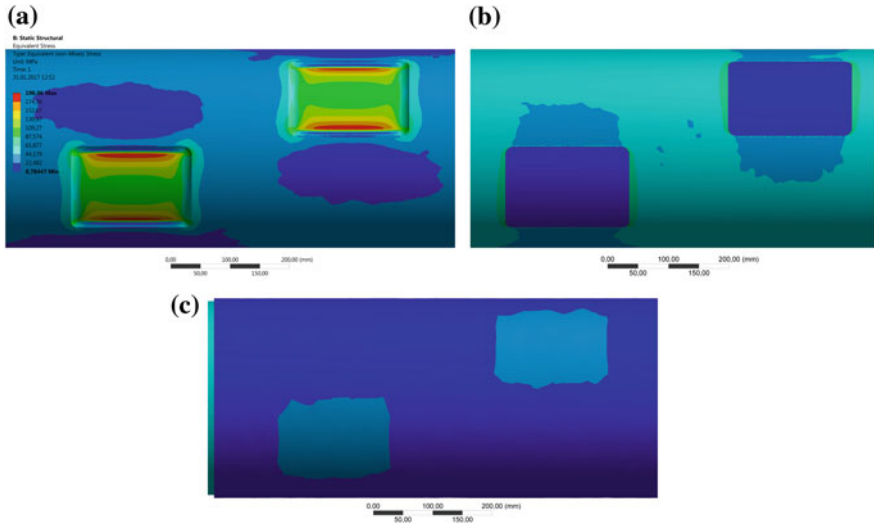


Fig. 15 Stress distribution for 323.9 mm pipe: **a** pipe without wrap, **b** pipe with wrap, and filler (wrap is not present), **c** pipe with wrap

Table 5 Unrepaired pipeline case

Pipe diameter (mm)	Defect depth (mm)	Angular position of maxima (°)	Axial position of maxima	Comments
323.9	6.0	30–60	100 mm (under)	The area with maxima has a banded shape, with a tendency of reducing its length as the depth of the defect decreases
	4.8	20–50	50 mm (under)	
	3.2	20–40	20 mm (under)	
508.0	9.4	40–60	190 mm (under)	As the defect depth decreases, the band shape of the maxima area disappears, being replaced by an island-like distribution
	7.5	30–50	130 mm (under)	
	5.0	20–40	130 mm (under)	
711.0	13.1	45–80	A whole length of the grid	The band-shape distribution is still present for 13.1 and 10.5 mm depths, but with maxima displaced to the right hand for the 7 mm depth of defect
	10.5	30–50	180 mm (under)	
	7.0	20–50	180 mm (under)	

Table 6 Repaired pipeline case

Pipe diameter (mm)	Defect depth (mm)	Angular position of maxima (°)	Axial position of maxima	Comments
323.9	6.0	30–80	–	A band-like distribution of maxima is still present, spreads across the length of the grid with reduced variation over the grid
	4.8	20–90	–	
	3.2	20–70	–	
508.0	9.4	20–90	A whole length of the grid	For the 9.4 mm depth, a band-like shape of maxima extends a whole length of the grid with two maxima.
	7.5	30–60	Island-like distribution	For the 7.5 and 5 mm depths, the island-like distribution is clear
	5.0	–		
711.0	13.1	20–80	A whole length of the grid	The tendency for the replacement of the band-shape maxima with an island-like distribution is also present
	10.5	20–80	–	
	7.0	–	–	

Table 7 Relative difference between maximum and minimum stress spreading over 5 × 10 points grid

<i>s</i>	6 mm	4.8 mm	3.2 mm
323.9 mm	Relative max–min difference [%]		
No wrap	6.88	7.42	7.88
Wrap	3.99	3.71	3.71
<i>s</i>	9.4 mm	7.5 mm	5 mm
508 mm	Relative max–min difference [%]		
No wrap	6.88	6.6	9.99
Wrap	3.41	4.72	4.81
<i>s</i>	13.1 mm	10.5 mm	7 mm
711 mm	Relative max–min difference [%]		
No wrap	5.58	6.68	7.65
Wrap	3.37	3.79	4.58

- (v) the presence of wrap tends to reduce the interaction between defects. Table 7 presents the relative difference between maximum and minimum stress spreading over the grid. The table supports our statement that presence of the wrap reduces the influence between defects;
- (vi) our analysis is consistent with the conclusions on two criteria considered, especially with API 759 criteria for defects without wrap;
- (vii) in the case of defects with wrap, our results conclude that the three criteria considered are not valid.

3.4 Further Developments

In order to better assess the interaction between defects, and also how the presence of filler and wrap can modify this mutual influence, we plan in the future to continue our research in the following directions:

- (i) to increase the number of analyzed cases by considering other defects dimensions;
- (ii) to improve preparation of the contour plots by increasing the number of contours and interpolation of the results;
- (iii) a more advanced processing of the contour plots by using image processing techniques, in order to obtain a more accurate interpretation of the tendencies appearing.

Acknowledgements This work was conducted with partial support of the Russian Foundation for Basic Research (No. 15-08-00849a, 16-08-00740, 16-58-52013 MNT_a) and Russian State Mission 007-01114-16 PR (project 0256-2015-0074).

References

1. A.P. Teixeira, C.G. Soares, T.A. Netto, S.F. Estefen, Reliability of pipelines with corrosion defects. *Int. J. Press. Vessels Pip.* **85**(4), 228 (2008)
2. M. Cerit, K. Genel, S. Eksi, Numerical investigation on stress concentration of corrosion pit. *Eng. Fail. Anal.* **16**(7), 2467 (2009)
3. J.E. Abdalla Filho, R.D. Machado, R.J. Bertin, On the failure pressure of pipelines containing wall reduction and isolated pit corrosion defects. *Comput. Struct.* **132**, 22 (2014)
4. M.K. Khalajestani, M.R. Bahaari, Investigation of pressurized elbows containing interacting corrosion defects. *Int. J. Press. Vessels Pip.* **123**, 77 (2014)
5. S.R. Hall, M.D. Raizenne, D.L. Simpson, A proposed composite repair methodology for primary structure. *Composites* **20**(5), 479 (1989)
6. W.F. Cole, Technical justification of repairs to composite laminates. *Int. J. Adhes. Adhes.* **19**(2), 107 (1999)
7. A. Chris, J. Bedoya, *An updated perspective on using composite materials to reinforce offshore pipelines and risers*. Proceedings of IOPF, vol. 1 (2011)
8. S. Nariman, H. Ronagh, A. Virk, Composite repair of pipelines, considering the effect of live pressure-analytical and numerical models with respect to ISO/TS 24817 and ASME PCC-2. *Compos. B Eng.* **58**, 605 (2014)
9. I. Lambrescu, M. Chebakov, V. Chebanenko, D. Gusakov, A. Morgunova, Investigation of the mutual influence of two machined volumetric surface defects of transmission pipeline, in *Innovative Solutions in Repair of Gas and Oil Pipelines*, ed. by E. Barkanov, M. Mihovski, V. Sergienko (Bulgarian Society for Non-destructive Testing Publishers, Sofia, 2016), p. 183
10. V.A. Chebanenko, D.V. Gusakov, I. Lambrescu, A.V. Morgunova, in *Sensitivity Analysis of the Static Problem for a Pipe with Two Volumetric Surface Defects*, ed. by I.A. Parinov, S.-H. Chang, M.A. Jani. Proceedings of the 2016 International Conference on Physics, Mechanics of New Materials and Their Applications (Nova Science Publishers, New York, 2017), p. 367 (in press)

11. ASME B31.8-2010, in *Gas Transmission and Distribution Piping Systems* (2010)
12. ASME B31G-1991 & 2009, in *Manual for Determining the Remaining Strength of Corroded Pipelines*, A supplement to ASME B31 Code for Pressure Piping (2009)
13. API Standard 759:2007/ASME FFS-1:2007, *Fitness for Service* (2007)
14. BS 7910:2005, in *Guide to Methods for Assessing the Acceptability of Flaws in Metallic Structures* (2005)

Modeling of the Contact Interaction Between Steel Pipe and Composite Bandage

I. Lvov and D.A. Beschtnikov

Abstract The possible contact interaction schemes for steel cylindrical shell and composite bandage fitted on it are considered. For each contact interaction scheme the mathematical model is developed. Possibility of implementation of different contact interaction scheme is numerically researched. It is shown that contact without separation is possible for definite thickness of the bandage. The results are present in form of plots.

Keywords Cylindrical shell · Composite bandage · Contact problem · Timoshenko-type shells theory

1 Introduction

An important step in designing of the repair connection is consideration of the interaction between the composite band and steel pipe. Analysis of the stress state of these structures requires formulation and solution of contact problems of the interaction of shells. Specificity of contact problems for thin-wall structural elements is significant results depending on the type of kinematic hypotheses underlying the theory of shells.

Applications of the classical Kirchhoff–Love theory of shells [1–4], the theory of Timoshenko-type shells [5, 6], and the Reissner–Vlasov theory of transverse compression [7] showed that the most significant differences between these theories arise in solving the contact problems. This is manifested in the fact that the distribution of the contact pressures between the interacting elements depends not only on the geometrical and physical parameters of these elements, but also on the type

The original version of the book was revised: Incorrect author names have been corrected. The erratum to the book is available at https://doi.org/10.1007/978-3-319-56579-8_28

I. Lvov (✉) · D.A. Beschtnikov
National Technical University, Kharkiv Polytechnical Institute, Kharkiv, Ukraine
e-mail: lvovgi@kpi.kharkov.ua

of theory used in their simulation [8]. A study of these problems is of great theoretical importance, and it has been widely discussed [8–17]. In these works, the features of thin-walled elements interaction with rigid and elastic bodies were considered by using various thin shells theories.

Due to the widespread of composite materials in the manufacture of structural parts, particular interest presents contact problem for anisotropic shells [18–21]. In [22–28], the interaction of anisotropic shells with each other and with metallic elements was considered. Among them, much attention is paid to the shells of revolution, and in particular—the cylindrical shells as the most common in various fields of modern technology.

The need for the study of contact problems for composite shells with the involvement of various hypotheses is caused by their relatively low transverse shear stiffness. In [28], the problem was solved for a cylindrical shell being in contact with the composite bandage for perfect conditions of continuous contact. In [24], the problem of the loose-fitting bandage for steel composite cylindrical shell was considered using the classical Kirchhoff–Love theory.

In this work, we carried out a study of contact interaction schemes for cylindrical steel shell and a composite bandage using Timoshenko-type theory of shells.

2 Statement of the Problem

Figure 1 shows the calculation scheme of the repair pipeline. Orthotropic composite bandage freely planted on isotropic cylindrical shell. The cylindrical shell is considered infinitely long and bandage has finite width $2L$. It is assumed that the shell thickness, h , the radius of curvature of its middle surface, R , as well as the thickness of the bandage, h_b , correspond to the condition of thin shells [2, pp. 5–6]. The steel shell is loaded by internal pressure, P .

In [13, 17], within the framework of the classical theory and the theory of Timoshenko-type shells, it is shown that for a shell with a rigid bandage, the following three schemes of contact interaction are possible: (i) a contact in the corner points of the bandage (Fig. 2a); (ii) a contact in the corners and the central points of the bandage (Fig. 2b); (iii) a contact in the corner points, and in the central part of the bandage (Fig. 2c).

The aim of this work is to study the feasibility of schemes of a contact interaction shown in Fig. 2 for a shell with orthotropic bandage, if the shells theory of

Fig. 1 Designed model

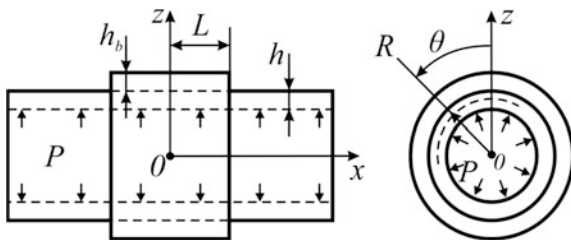
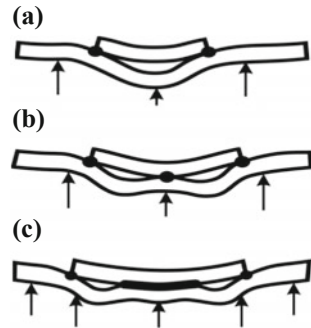


Fig. 2 Possible schemes of contact interaction



Timoshenko type is used for mathematical modeling. In order to achieve this goal the values of the bandage’s “critical lengths” are defined. These “critical lengths” correspond to the transition from one scheme to another contact.

3 Mathematical Modeling and Analysis of Results

For the considered contact problem, the Tymoshenko-type shell theory is used in which shear deformation is taken into account. In dependence on the width of the bandage L , different schemes of contact interaction are possible between the shell and the bandage. For each of the interaction schemes, the limit parameter L is formulated, for which the scheme is possible. The calculations are carried out at the following fixed parameters of structure: $R = 505$ mm; $h = 10$ mm; $h_b = 40$ mm; $P = 6$ MPa. The shell is made of steel and has the elastic constants: $E = 200$ GPa; $\nu = 0.3$. As bandage material, we considered glass-reinforced plastic with the following mechanical characteristics: $E_x = 18.6$ GPa; $E_\theta = 24.6$ GPa; $G_{xz} = 3$ GPa; $\nu_{x\theta} = 0.15$.

3.1 Scheme of Contact in the Corner Points of the Bandage

The first contact scheme (Fig. 2a) can be divided into two sections: I ($0 < x < L$) – section with a bandage; II ($x \geq L$) – section without a bandage.

By using for each section the governing equations for displacement and rotation angles, it is possible to obtain the following system of equations:

$$0 < x < L \quad \frac{d^2 W^I}{dx^2} + \frac{d\gamma^I}{dx} - 2g^2 W^I = \frac{-P}{kGh}; \quad \frac{d^2 \gamma^I}{dx^2} - b\gamma^I - b \frac{dW^I}{dx} = 0;$$

$$\begin{aligned} \frac{d^2W_{b^I}}{dx^2} + \frac{d\gamma_{b^I}}{dx} - 2g_b^2W_{b^I} = 0; \quad \frac{d^2\gamma_{b^I}}{dx^2} - b_b\gamma_{b^I} - b_b\frac{dW_{b^I}}{dx} = 0 \\ x \geq L \quad \frac{d^2W^{II}}{dx^2} + \frac{d\gamma^{II}}{dx} - 2g^2W^{II} = \frac{-P}{kGh}; \quad \frac{d^2\gamma^{II}}{dx^2} - b\gamma^{II} - b\frac{dW^{II}}{dx} = 0 \end{aligned} \tag{1}$$

where, W^I, W^{II} are the displacements of the shell on the first and second sections, respectively; γ^I, γ^{II} are the angles of a rotation of a shell normal element; W_b^I, γ_b^I are the displacement and rotation angle of the bandage; g^2, g_b^2, b, b_b are the parameters depending on the material characteristics of the bandage and shell sizes:

$$\begin{aligned} 2g^2 = \frac{E}{kGR^2}, \quad b = \frac{kGh}{D}, \quad D = \frac{Eh^3}{12(1 - \nu^2)}, \quad G = \frac{E}{2(1 + \nu)}, \quad k = 5/6, \\ 2g_b^2 = \frac{c_{11}c_{22} - c_{12}^2}{kc_{11}G_bR_b^2}, \quad b_b = \frac{kG_bh_b}{D_b}, \quad D_b = \frac{c_{11}h_b^3}{12}, \quad G_b = c_{66}, \\ c_{11} = \frac{E_x}{1 - \nu_{x\theta}\nu_{\theta x}}, \quad c_{12} = \frac{E_{\theta}\nu_{x\theta}}{1 - \nu_{x\theta}\nu_{\theta x}}, \quad c_{12} = \frac{E_{\theta}}{1 - \nu_{x\theta}\nu_{\theta x}}, \quad c_{66} = G_{xz} \end{aligned}$$

Let us consider the first four equations of the system (1), which describe the behavior of the structure in the first section $0 < x < L$. The equations do not include contact force, since interaction between the steel shell and the bandage will be reflected in the boundary conditions at point $x = L$. In this case, the solutions for the displacement and rotation angles of the shell on the first section bandage can be searched separately: the first and second equations of (1) for the shell; the third and fourth equations of (1) for the bandage. Systems of these equations are similar, however, in the following, we find solutions for the shell.

The solutions for the unknown functions W^I, γ^I are searched as the sums of the general solution of the homogeneous and the particular solution of the inhomogeneous system of differential equations (first and second equations (1)). A particular solution for the angle is zero, and for deflection, it is

$$\bar{W}^I = \frac{P}{2g^2kGh}$$

Searching for the general solution of the homogeneous system of differential equations leads to the necessity to solve an eigenvalue problem with the following fourth order characteristic equation:

$$s^4 - 2g^2s^2 + \lambda^4 = 0, \quad \lambda^4 = 2g^2b \tag{2}$$

The roots of the characteristic Eq. (2) can be written as follows:

$$s_{1,2} = -\beta_1 \pm i\alpha_1, \quad s_{3,4} = \beta_1 \pm i\alpha_1, \quad \beta_1 = \sqrt{\frac{\lambda^2 + g^2}{2}}, \quad \alpha_1 = \sqrt{\frac{\lambda^2 - g^2}{2}}$$

There are the following three cases, which may be for the values of radicals g^2 and λ^2 : (i) $g^2 > \lambda^2$ —all roots of the equation are real; (ii) $g^2 = \lambda^2$ —the equation has multiple roots; (iii) $g^2 < \lambda^2$ —the equation has complex roots. For widely varying design parameters, the complex roots are realized for the Eq. (2). In this case, the solution can be expressed in the form:

$$W^I = d_1 e^{-\beta_1 x} \cos(\alpha_1 x) + d_2 e^{-\beta_1 x} \sin(\alpha_1 x) + d_3 e^{\beta_1 x} \cos(\alpha_1 x) + d_4 e^{\beta_1 x} \sin(\alpha_1 x) + \bar{W}^I \tag{3}$$

Solution for γ^I has the same form like (3) but with the constant t_j instead of d_j . Constants d_j and t_j are mutually dependent and they complete the eigenvectors for each eigenvalue s_j . By substituting solutions for W^I and γ^I in the first two equations of system (1) and equating the coefficients of the respective functions, it is possible to obtain an algebraic system of equations from which the relation of the constants t_j and γ^I is extracted. Using this relation the solution for the angle γ^I can be written through constants d_j

$$\gamma^I = d_1 e^{-\beta_1 x} [-K_{11} \cos(\alpha_1 x) - K_{12} \sin(\alpha_1 x)] + d_2 e^{-\beta_1 x} [K_{12} \cos(\alpha_1 x) - K_{11} \sin(\alpha_1 x)] + d_3 e^{\beta_1 x} [K_{11} \cos(\alpha_1 x) - K_{12} \sin(\alpha_1 x)] + d_4 e^{\beta_1 x} [K_{12} \cos(\alpha_1 x) + K_{11} \sin(\alpha_1 x)] \tag{4}$$

where

$$K_{11} = b \frac{\beta_1 (\beta_{12} - \alpha_{12} - b) + 2\beta_1 \alpha_{12}}{(\beta_{12} - \alpha_{12} - b)^2 + 4\beta_{12} \alpha_{12}}, \quad K_{12} = b \frac{\alpha_1 (\beta_{12} - \alpha_{12} - b) - 2\beta_{12} \alpha_1}{(\beta_{12} - \alpha_{12} - b)^2 + 4\beta_{12} \alpha_{12}}$$

Similarly from the third and fourth equations of system (1), the solutions for bandage displacement W_b^I and rotation angle γ_b^I are obtained. For the eigenvalue problem, the roots of the characteristic equation take the forms

$$s_{1,2} = -\beta_2 \pm i\alpha_2, \quad s_{3,4} = \beta_2 \pm i\alpha_2, \quad \beta_2 = \sqrt{\frac{\sqrt{2g_b^2 b_b} + g_b^2}{2}},$$

$$\alpha_2 = \sqrt{\frac{\sqrt{2g_b^2 b_b} - g_b^2}{2}}$$

The displacement and rotation angle of the bandage, respectively, written as

$$W_b^I = d_5 e^{-\beta_2 x} \cos(\alpha_2 x) + d_6 e^{-\beta_2 x} \sin(\alpha_2 x) + d_7 e^{\beta_2 x} \cos(\alpha_2 x) + d_8 e^{\beta_2 x} \sin(\alpha_2 x) \tag{5}$$

$$\gamma_b^I = d_5 e^{-\beta_2 x} [-K_{21} \cos(\alpha_2 x) - K_{22} \sin(\alpha_2 x)] + d_6 e^{-\beta_2 x} [K_{22} \cos(\alpha_2 x) - K_{21} \sin(\alpha_2 x)] + d_7 e^{\beta_2 x} [K_{21} \cos(\alpha_2 x) - K_{22} \sin(\alpha_2 x)] + d_8 e^{\beta_2 x} [K_{22} \cos(\alpha_2 x) + K_{21} \sin(\alpha_2 x)] \tag{6}$$

where

$$K_{21} = b_b \frac{\beta_2(\beta_{22} - \alpha_{22} - b_b) + 2\beta_2\alpha_{22}}{(\beta_{22} - \alpha_{22} - b_b)^2 + 4\beta_2^2\alpha_{22}^2}, \quad K_{22} = b_b \frac{\alpha_2(\beta_{22} - \alpha_{22} - b_b) - 2\beta_2^2\alpha_2}{(\beta_{22} - \alpha_{22} - b_b)^2 + 4\beta_2^2\alpha_{22}^2},$$

Let us consider the last two equations of (1), which describe a behavior of the structure in the second section $x \geq L$. The solutions for displacement W^{II} and rotation angle γ^{II} of the shell for the second section have the same forms like solution for the first sections (3), (4), but they have other independent constants, two of which can be found from the infinite shell's length condition. The solutions for the second section have the following forms:

$$W^{\text{II}} = d_9 e^{-\beta_1 x} \cos(\alpha_1 x) + d_{10} e^{-\beta_1 x} \sin(\alpha_1 x) + \bar{W}^{\text{II}}, \quad \bar{W}^{\text{II}} = \frac{P}{2g^2 k G h} \quad (7)$$

$$\gamma^{\text{II}} = d_9 e^{-\beta_1 x} [-K_{11} \cos(\alpha_1 x) - K_{12} \sin(\alpha_1 x)] + d_{10} e^{-\beta_1 x} [K_{12} \cos(\alpha_1 x) - K_{11} \sin(\alpha_1 x)] \quad (8)$$

The unknown constants d_j are determined from the boundary conditions:

$$x = 0: \quad \gamma^{\text{I}} = \gamma_{b^{\text{I}}} = 0; \quad Q_{1^{\text{I}}} = Q_{1b^{\text{I}}} = 0;$$

$$x = L: \quad M_{1b^{\text{I}}} = 0; \quad W^{\text{I}} = W^{\text{II}} = W_{b^{\text{I}}}; \quad \gamma^{\text{I}} = \gamma^{\text{II}}; \quad M_{1^{\text{I}}} = M_{1^{\text{II}}}; \quad Q_{1^{\text{I}}} - Q_{1^{\text{II}}} = -Q_{1b^{\text{I}}}$$

With the gradual increment of the bandage width, the solution for the first contact scheme will be valid while the displacement of the bandage at the point $x = 0$ is greater than displacement of the shell. Let us call the first critical value L^* the bandage width, for which the bandage displacement and shell displacement at the point $x = 0$ are equal to each other. Calculations show that the first critical value is $L^* = 22.28$ mm for the specified parameters. Figure 3 shows a series of curves, which describe the dependence of L^* on the bandage and the shell thicknesses.

Figure 3 shows that for different thicknesses of the bandage and shell, the value of the first critical bandage width or extremely low or comparable to its thickness, making unreasonable to use of the theory of thin shells. This shows that for a steel cylindrical shell and an orthotropic composite bandage with the given parameters and within Timoshenko-type shell theory the scheme with the contact in the corner points cannot be realized.

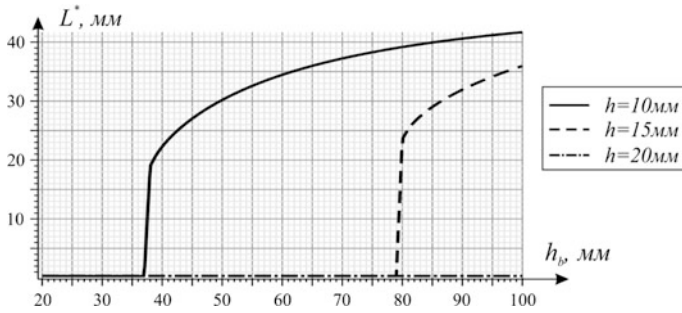


Fig. 3 L^* versus thicknesses of the bandage and shell

3.2 Contact at the Corner and the Central Points of the Bandage

Let us consider the contact scheme shown in Fig. 2b. This scheme is described by the same system of Eq. (1) as the first contact scheme. Accordingly, all solutions for the unknown functions $W^I, \gamma^I, W_b^I, \gamma_b^I, W^{II}, \gamma^{II}$ still are the same (3)–(8). Only the boundary conditions at point $x = 0$ are changed, due to appearance of contact interaction in this point

$$x = 0 : \quad \gamma^I = \gamma_{b^I} = 0; \quad W^I = W_{b^I}; \quad Q_{1^I} = -Q_{1b^I};$$

The solution for the second contact scheme will be valid until the curvature of the bandage and the shell at point $x = 0$ will be equal to each other. This condition determines the second critical value L^{**} , at which interaction of the bandage and shell passes to the third contact scheme.

Calculations show that for various design parameters, the second critical value does not differ from the first critical value, therefore plots in Fig. 3 are also valid for L^{**} . In this case, we can say that the second contact scheme does not arise as the first one in the framework of Timoshenko-type shell theory for the considered structure.

3.3 Contact in the Corner Points, and in the Central Part of the Bandage

Obviously, the third contact scheme (Fig. 2c) is realized for the given structure. In this case, the domain of the unknown functions can be divided into three sections: I ($0 < x < l$)—the contact section of the shell and the bandage l ; II ($l < x < L$)—section of the gap between the bandage and the shell; III ($x \geq L$)—section of the

shell without the bandage. The governing equation system for the displacement and rotation angles is written below

$$\begin{aligned}
 0 < x < l \quad & \frac{d^2 W^I}{dx^2} + \frac{d\gamma^I}{dx} - 2g^2 W^I = \frac{-(P - P_K)}{kGh}; \quad \frac{d^2 \gamma^I}{dx^2} - b\gamma^I - b \frac{dW^I}{dx} = 0; \\
 & \frac{d^2 W_{b^I}}{dx^2} + \frac{d\gamma_{b^I}}{dx} - 2g_b^2 W_{b^I} = \frac{-P_K}{kG_b h_b}; \quad \frac{d^2 \gamma_{b^I}}{dx^2} - b_b \gamma_{b^I} - b_b \frac{dW_{b^I}}{dx} = 0; \quad W_{b^I} = W^I; \\
 l < x < L \quad & \frac{d^2 W^{II}}{dx^2} + \frac{d\gamma^{II}}{dx} - 2g^2 W^{II} = \frac{-P}{kGh}; \quad \frac{d^2 \gamma^{II}}{dx^2} - b\gamma^{II} - b \frac{dW^{II}}{dx} = 0; \\
 & \frac{d^2 W_{b^{II}}}{dx^2} + \frac{d\gamma_{b^{II}}}{dx} - 2g_b^2 W_{b^{II}} = 0; \quad \frac{d^2 \gamma_{b^{II}}}{dx^2} - b_b \gamma_{b^{II}} - b_b \frac{dW_{b^{II}}}{dx} = 0 \\
 x \geq L \quad & \frac{d^2 W^{III}}{dx^2} + \frac{d\gamma^{III}}{dx} - 2g^2 W^{III} = \frac{-P}{kGh}; \quad \frac{d^2 \gamma^{III}}{dx^2} - b\gamma^{III} - b \frac{dW^{III}}{dx} = 0
 \end{aligned} \tag{9}$$

The form of solutions for the displacement and the rotation angle on the second shell section W^{II} , γ^{II} coincide with (3) and (4), and the displacement and rotation of the bandage $W_{b^{II}}$, $\gamma_{b^{II}}$ coincide with (5) and (6). The solutions for unknown functions W^{III} , γ^{III} have the form (7) and (8), respectively.

Let us consider the first five equations (9), which describe the behavior of the structure of the contact section $0 < x < l$. By excluding the contact pressure from the Eq. (9) and using condition $W_{b^I} = W^I$, the system of equations for the first section can be written as follows:

$$\begin{aligned}
 \frac{d^2 W^I}{dx^2} + m \frac{d\gamma^I}{dx} + m_b \frac{d\gamma_b^I}{dx} - 2\tilde{g}^2 W^I &= \frac{-P}{\tilde{\Lambda}}; \\
 \frac{d^2 \gamma_b^I}{dx^2} - b_b \gamma_b^I - b_b \frac{dW^I}{dx} &= 0; \quad \frac{d^2 \gamma^I}{dx^2} - b\gamma^I - b \frac{dW^I}{dx} = 0
 \end{aligned} \tag{10}$$

where

$$m = \frac{Gh}{G_b h_b + Gh}, \quad m_b = \frac{G_b h_b}{G_b h_b + Gh}, \quad 2\tilde{g}^2 = \frac{2g_b^2 G_b h_b + 2g^2 Gh}{G_b h_b + Gh}, \quad \tilde{\Lambda} = k(G_b h_b + Gh).$$

The general solution for each unknown functions W^I , γ^I , γ_b^I is the sum of general and partial solutions of the homogeneous and heterogeneous system of Eqs. (10), respectively. Among partial solutions is not zero only the solution for displacement

$$\tilde{W}^I = \frac{P}{2\tilde{g}^2 \tilde{\Lambda}}$$

Searching for the solution of the homogeneous system of differential Eqs. (10) leads to necessity to solve the eigenvalue problem with the following sixth-order characteristic equation:

$$s^6 + a_1s^4 + a_2s^2 + a_3 = 0 \tag{11}$$

where $a_1 = mb + m_b b_b - b - b_b - 2\tilde{g}^2$, $a_2 = -mbb_b - m_b b_b b + bb_b + 2\tilde{g}^2(b + b_b)$, $a_3 = -2\tilde{g}^2 b b_b$

Analysis of Eq. (11) indicates that it may have the following roots: real roots, which are different; multiple real roots; two real roots and two pairs of complex conjugate roots. For thin shells and real materials, the case of two pairs of complex conjugate roots and two real roots s_5, s_6 are realized

$$s_{1,2} = -\tilde{\beta} \pm i\tilde{\alpha}, \quad s_{3,4} = \tilde{\beta} \pm i\tilde{\alpha}$$

In this case, the solution has the form

$$\begin{aligned} W^I &= d_{11}e^{-\tilde{\beta}x} \cos(\tilde{\alpha}x) + d_{12}e^{-\tilde{\beta}x} \sin(\tilde{\alpha}x) + d_{13}e^{\tilde{\beta}x} \cos(\tilde{\alpha}x) \\ &\quad + d_{14}e^{\tilde{\beta}x} \sin(\tilde{\alpha}x) + d_{15}e^{s_5x} + d_{16}e^{s_6x} + \tilde{W}^I \\ \gamma^I &= t_{11}e^{-\tilde{\beta}x} \cos(\tilde{\alpha}x) + t_{12}e^{-\tilde{\beta}x} \sin(\tilde{\alpha}x) + t_{13}e^{\tilde{\beta}x} \cos(\tilde{\alpha}x) \\ &\quad + t_{14}e^{\tilde{\beta}x} \sin(\tilde{\alpha}x) + t_{15}e^{s_5x} + t_{16}e^{s_6x} \\ \gamma_{b'} &= k_{11}e^{-\tilde{\beta}x} \cos(\tilde{\alpha}x) + k_{12}e^{-\tilde{\beta}x} \sin(\tilde{\alpha}x) + k_{13}e^{\tilde{\beta}x} \cos(\tilde{\alpha}x) \\ &\quad + k_{14}e^{\tilde{\beta}x} \sin(\tilde{\alpha}x) + k_{15}e^{s_5x} + k_{16}e^{s_6x} \end{aligned}$$

Relationship between the constants d_j, t_j, k_j is possible to determine by substituting these solutions into the system (10). In viewpoint of these relationships, the solutions for γ^I and γ_b^I can be written in terms of the constants d_j in the form

$$\begin{aligned} \gamma^I &= d_{11}e^{-\tilde{\beta}x}[-K_{11}\cos(\tilde{\alpha}x) - K_{12}\sin(\tilde{\alpha}x)] + d_{12}e^{-\tilde{\beta}x}[K_{12}\cos(\tilde{\alpha}x) - K_{11}\sin(\tilde{\alpha}x)] \\ &\quad + d_{13}e^{\tilde{\beta}x}[K_{11}\cos(\tilde{\alpha}x) - K_{12}\sin(\tilde{\alpha}x)] + d_{14}e^{\tilde{\beta}x}[K_{12}\cos(\tilde{\alpha}x) + K_{11}\sin(\tilde{\alpha}x)] \\ &\quad + d_{15}K_{13}e^{s_5x} + d_{16}K_{14}e^{s_6x} \end{aligned}$$

where

$$\begin{aligned} K_{11} &= b \frac{\tilde{\beta}(\tilde{\beta}^2 - \tilde{\alpha}^2 - b) + 2\tilde{\beta}\tilde{\alpha}^2}{(\tilde{\beta}^2 - \tilde{\alpha}^2 - b)^2 + 4\tilde{\beta}^2\tilde{\alpha}^2}, & K_{12} &= b \frac{\tilde{\alpha}(\tilde{\beta}^2 - \tilde{\alpha}^2 - b) - 2\tilde{\beta}^2\tilde{\alpha}}{(\tilde{\beta}^2 - \tilde{\alpha}^2 - b)^2 + 4\tilde{\beta}^2\tilde{\alpha}^2} \\ K_{13} &= \frac{bs_5}{s_5^2 - b}, & K_{14} &= \frac{bs_6}{s_6^2 - b} \end{aligned}$$

$$\begin{aligned} \gamma_{b^I} = & d_{11}e^{-\tilde{\beta}x}[-K_{21} \cos(\tilde{\alpha}x) - K_{22} \sin(\tilde{\alpha}x)] \\ & + d_{12}e^{-\tilde{\beta}x}[K_{22} \cos(\tilde{\alpha}x) - K_{21} \sin(\tilde{\alpha}x)] \\ & + d_{13}e^{\tilde{\beta}x}[K_{21} \cos(\tilde{\alpha}x) - K_{22} \sin(\tilde{\alpha}x)] + d_{14}e^{\tilde{\beta}x}[K_{22} \cos(\tilde{\alpha}x) + K_{21} \sin(\tilde{\alpha}x)] \\ & + d_{15}K_{23}e^{s_5x} + d_{16}K_{24}e^{s_6x} \end{aligned}$$

$$K_{21} = b_b \frac{\tilde{\beta}(\tilde{\beta}^2 - \tilde{\alpha}^2 - b_b) + 2\tilde{\beta}\tilde{\alpha}^2}{(\tilde{\beta}^2 - \tilde{\alpha}^2 - b_b)^2 + 4\tilde{\beta}^2\tilde{\alpha}^2}, \quad K_{22} = b_b \frac{\tilde{\alpha}(\tilde{\beta}^2 - \tilde{\alpha}^2 - b_b) - 2\tilde{\beta}^2\tilde{\alpha}}{(\tilde{\beta}^2 - \tilde{\alpha}^2 - b_b)^2 + 4\tilde{\beta}^2\tilde{\alpha}^2},$$

$$K_{23} = \frac{b_b s_5}{s_5^2 - b_b}, \quad K_{24} = \frac{b_b s_6}{s_6^2 - b_b}$$

The general solution contains 16 arbitrary constants d_j . Another unknown is the length of the contact region l . To find all the unknown constants the following seventeen boundary conditions are used

$$\begin{aligned} x = 0: \quad & \gamma^I = \gamma_{b^I} = 0; \quad \frac{dW^I}{dx} = 0; \\ x = l: \quad & W^I = W^{II} = W_{b^{II}}; \quad \gamma^I = \gamma^{II}; \quad \gamma_{b^I} = \gamma_{b^{II}}; \\ & M_{1^I} = M_{1^{II}}; \quad M_{1b^I} = M_{1b^{II}}; \quad Q_{1^I} - Q_{1^{II}} = -(Q_{1b^I} - Q_{1b^{II}}) = 0 \\ x = L: \quad & M_{1b^{II}} = 0; \quad W^{II} = W^{III} = W_{b^{III}}; \quad \gamma^{II} = \gamma^{III}; \\ & M_{1^{II}} = M_{1^{III}}; \quad Q_{1^{II}} - Q_{1^{III}} = -Q_{1b^{III}} \end{aligned}$$

The equations system, resulting from the boundary conditions, is nonlinear with respect to the contact region length l . The solution of nonlinear system was found numerically by using the mathematical package Maple.

For the third contact scheme, an important question is to discuss the possibility of the disappearance of the gap area and the occurrence of the continuous contact between the shell and the bandage. In [8, 13, 17], it was shown that in the cases of the classical theory and the Timoshenko-type shell theory, the continuous contact between isotropic shell and rigid bandage is not realized. The same feature was demonstrated in [24] for cylindrical shell with a composite bandage in the framework of classical theory.

Figure 4 presents the numerical results for the gap area length $(L - l)$ at different values of thickness and width of the bandage. The plot for the bandage thickness of 40 mm shows that the unlimited increase in the width of the bandage, the gap area length asymptotically approaches a constant value. For a thinner bandage, the gap disappears and contact area covers the entire width of the bandage.

These equations can be used to solve the problem of the contact shells glued to the bandage. If the first five equations of the system (9) are considered in the interval $0 < x < L$, then this corresponds to a mathematical model of a contact shell, glued to the bandage. Contact pressure P_k at the point $x = L$ can take a negative or a positive value. Figure 5 shows plots of the contact pressure at the point $x = L$ by

Fig. 4 Length of the gap, when the bandage is not glued to the shell

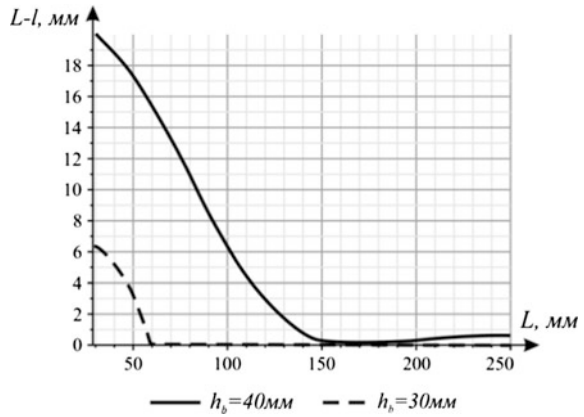
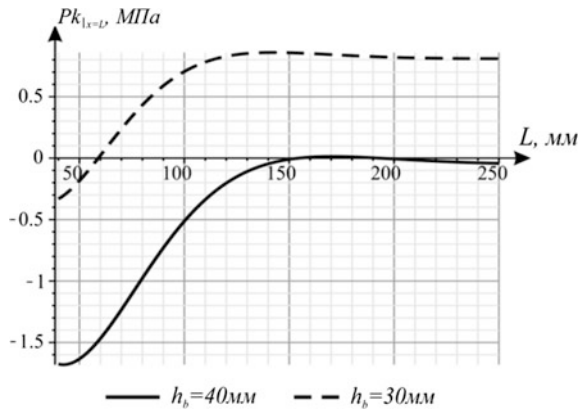


Fig. 5 Contact pressure at the point $x = L$, when the bandage is glued to the shell



increasing the width of the bandage for 30 and 40 mm bandage thickness. These plots confirm the assertion that continuous contact with the shell is realized for certain thickness of the bandage.

4 Conclusions

The paper discusses the possible schemes of contact interaction of a cylindrical steel shell and a composite bandage by using Timoshenko-type theory of shells. Numerical calculations show that the scheme with contact in corner points, as well as the contact scheme in the corner and the central points of the bandage cannot be realized for thin shells. Contact of shell with bandage occurs in the corner points and the gap exists in the central part. It was found that at a certain thickness of the bandage between it and the shell can be offensive non-separated contacts.

It is a qualitatively new result in the contact interaction study in metal–composite thin-walled structures.

References

1. V.I. Mossakovskiy, V.S. Gudramovich, E.M. Makeev, *Contact Problem for the Theory of Shells and Rods* (Mashinostroenie, Moscow, 1978), p. 248 (in Russian)
2. V.V. Novogilov, *The Linear Theory of Thin Shells* (Politehnika, Lvov, 1991), p. 656 (in Russian)
3. S.P. Timoshenko, S. Voynarovskiy-Kriger, in *Plates and shells* (Nauka, Moscow, 1966), p. 636 (in Russian)
4. E. Ventsel, T. Krauthammer, *Thin Plates and Shells: Theory, Analysis and Applications* (Marcel Dekker, New York, 2001), p. 651
5. K.Z. Galimov, U.P. Artyuhin, S.N. Karasev, *The Theory of Shells with a Glance of the Transverse Shear*. (Kazan University Press, Kazan, 1977), p. 211 (in Russian)
6. B.L. Peleh, *The Theory of Shells with Finite Shear Stiffness*. Kiev Naukova Dumka **246** (1973) (in Russian)
7. S.A. Kabriz, E.N. Michailovsky, P.E. Tovstic, K.F. Chernih, V.A. Shamina, *General Nonlinear Theory of Thin Shells* (St. Petersburg University Press, St. Petersburg, 2002), p. 388 (in Russian)
8. M.V. Bloh, About model selection in contact problem of thin-walled bodies. *Appl. Mech.* **XIII**(5), 34 (1977)
9. U.P. Artyuhin, S.M. Karimov, Contact problem for cylindrical punch with a cylindrical shell. *Invest. Theory Plates Shells* **23**, 21 (1972). (in Russian)
10. U.P. Artyuhin, S.N. Karasev, Action rigid stamp on the shallow spherical shell, and the plate. *Invest. Theory Plates Shells* **9**, 211 (1972). (in Russian)
11. U.P. Artyuhin, S.N. Karasev, Some contact problem in the theory of thin plates. *Invest. Theory Plates Shells* **10**, 159 (1973). (in Russian)
12. E.I. Grigolyuk, V.M. Tolkachev, Axisymmetric contact problem of cylindrical and spherical shells. *Invest. Theory Plates Shells* **22**, 3 (1990). (in Russian)
13. F.M. Detinko, V.M. Fastovsky, About bandage installation on cylindrical shell. *Appl. Mech.* **2**(2), 124 (1975)
14. S.N. Karasev, About one contact problem for the hollow cylinder under action of the plane strain. *Invest. Theory Plates Shells* **11**, 185 (1975). (in Russian)
15. S.N. Karasev, U.P. Artyuhin, Influence of transverse shear and crimping on contact pressure distribution. *Invest. Theory Plates Shells* **12**, 68 (1976). (in Russian)
16. S.N. Karasev, U.P. Artyuhin, Contact interaction between plates and rigid bodies. *Invest. Theory Plates Shells* **11**, 148 (1975). (in Russian)
17. G.I. Lvov, A.N. Tkachuk, About influence of kinematic hypotheses on nature of a contact interaction between cylindrical shell and bandage. *Vestnik NTU KhPI* **32**, 98 (2006). (in Russian)
18. S.A. Ambartsumyan, in *General Theory of Anisotropic Shells* (Nauka, Moscow, 1974), p. 446 (in Russian)
19. A.N. Guz, Mechanics of composite materials and structure elements. Kiev Naukova Dumka **1**, 267 (1982). (in Russian)
20. I.J. Amiro, V.A. Zaruckij, A.N. Guz, Methods of shells calculation: theory of ribbed shells. Kiev Naukova Dumka **2**, 267 (1980). (in Russian)
21. J.M. Grigorenko, A.T. Vasilenko, A.N. Guz, Methods of shells calculation: theory of shells with variable stiffness. Kiev Naukova Dumka **4**, 543 (1981). (in Russian)

22. S. Vereshaka, V. Daniltsev, D. Gigilyi, Strength calculation of fiber-glass plastic pipes in the area of flange connection. *Mech, Eng.* **12**, 9 (2013)
23. B.L. Peleh, N.A. Sukchorolsky, Contact problems of the theory of elastic anisotropic shells. *Kiev Naukova Dumka* **216** (1980) (in Russian)
24. H. Altenbach, D.A. Beschetsnikov, G.I. Lvov, K. Naumenko, V.G. Sukiasov, Kontaktwechselwirkung einer Rohrleitung mit der Reparaturbandage aus einem Kompositwerkstoff. *Forschungim Ingenieurwesen* **78**, 59 (2014)
25. E. Barkanov, D. Beschetsnikov, G. Lvov, Effect of technological tensioning on the efficiency of reinforcement of pipelines with composite bands. *Mech. Compos. Mater.* **50**(6), 725 (2015)
26. D.A. Beschetsnikov, G.I. Lvov, *Optimal design of preload under installing composite bandages on pipelines*. In: NDT Days 2014. Proceedings of the XXIX International Conference, Sozopol, Bulgaria, p. 545 (2014)
27. B.V. Kopey, A.V. Maksymuk, N.N. Shcherbyna, Analysis of contact stresses in structural joints of composite shell with steel banding. *Mech. Compos. Mater.* **36**(1), 67 (2000)
28. O.V. Maksymuk, N.M. Shcherbyna, Contact interaction of cylindrical shells of different lengths. *J. Math. Sci.* **178**(4), 455 (2011)

Experimental and Numerical Research of Renovated Pipeline Prototype with Surface Defect

Evgeny N. Barkanov, I. Lvov and D.A. Beschtnikov

Abstract For experimental and numerical investigation of the repaired pipeline prototype, the small-scale vessel model was produced. At the first stage of the experiment, the deformed state of the vessel with an artificially created surface defect was studied by the tensometry method. At the second stage, a fiberglass wrap was installed on the steel vessel together with the system of strain gages. The prototype of the pipeline was loaded with internal pressure. Finite-element modeling of both stages of the experiment was performed to compare the theoretical and experimental data.

Keywords Pipelines · Surface defect · Composite wrap

1 Introduction

Repair of main pipelines with surface defects using composite bandages is an effective means of restoring their capacity for work. The success of this repair is ensured by the rational design of the bandage connection. The basis of the design is the investigation of the stressed state of the repaired pipeline section under the influence of operational loads. Calculations of the stressed state of pipelines with bandages are given considerable attention. The problems of the contact interaction of cylindrical shells with composite bands have been discussed in [1–3], in which the features of the contact pressures distribution between a pipeline and a bandage are investigated. The possible contact interaction schemes for steel cylindrical shell

The original version of the book was revised: Incorrect author names have been corrected. The erratum to the book is available at https://doi.org/10.1007/978-3-319-56579-8_28

E.N. Barkanov
Riga Technical University, Riga, Latvia

I. Lvov (✉) · D.A. Beschtnikov
National Technical University, Kharkiv Polytechnical Institute, Kharkiv, Ukraine
e-mail: lvovgi@list.ru

and composite bandage fitted on it are considered [1]. For each contact interaction scheme the mathematical model is constructed. Possibility of implementation of different contact interaction scheme is numerically researched. It is shown that contact without separation is possible for definite thickness of the bandage. The results are presented in form of graphs. The mathematical model for a contact problem of cylindrical shell with a composite wrap was developed in [2]. To improve an effectiveness of composite repair the preload of a prepreg was proposed. The optimal magnitude of preloading was obtained for various repair situations. The stress state in the local defect zone was investigated in [4, 5]. The finite element method has been used to investigation of plastic deformations and stresses in the pipeline. The calculation was carried out using of the nonlinear plasticity model for the pipeline material. The level of stresses in various areas of the structure is analyzed.

To verify the reliability of theoretical results, it is important to conduct experimental studies of repair connections. The technical complexities and high cost of such experiments on full-scale models lead to the need for experimental studies on prototypes of smaller dimensions. The present work is devoted to an experimental study of the stress state of a cylindrical vessel with a surface defect. Geometric parameters of the vessel, defect and composite wrap are chosen so that the edge effects in the zone of the spherical bottoms do not spread to the bandage area. This ensured the adequacy of the model to the long pipeline. To assess the effectiveness of repair, the stress state was investigated before and after installing the repair wrap. A complete analog of the experimental repair compound was investigated numerically by the finite element method.

2 Experimental Setup

The special setup was created for the experimental study of stress–strain state in the surface defect area of the pipeline and the experimental confirmation of the efficiency of the repair by installation of composite wrap. The experimental setup consists of three main components (see Fig. 1): (i) the object of study (the steel cylindrical vessel with a surface defect); (ii) the loading system—plunger pump, connecting tubes, manometer; and (iii) the measuring system (a set of strain gages with a measuring device СИИТ-3).

Object for investigation. The low-size gas vessel of carbon steel is used as prototype of a pipeline. The main properties of the vessel are present in Table 1.

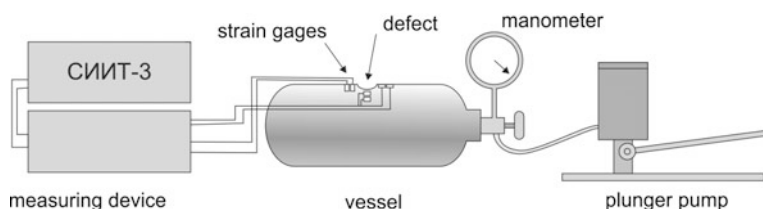


Fig. 1 Scheme of the experimental facility

Table 1 Main parameters of the vessel

Volume, l	Diameter, mm	Wall thickness, mm	Working pressure, MPa
5	140	5	10

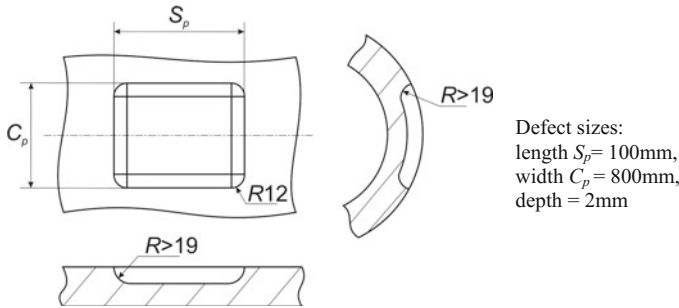


Fig. 2 Scheme of the defect and accepted defect sizes

The vessel complies with the requirements of a long shell. It means that boundary effects at the connections of spherical and cylindrical parts of the vessel disappear quickly and do not reach the central part of the vessel. Below, we present calculation of the size of spreading boundary effects L_{be} :

$$L_{be} = \frac{\pi}{\beta} \beta = \sqrt{4 \frac{3(1 - \nu^2)}{R^2 t_b^2}} = 44 \text{ mm}$$

where E , ν are the elastic modulus and Poisson’s ratio of the vessel’s material; t_b is the thickness of the vessel wall; R is the radius of the neutral surface.

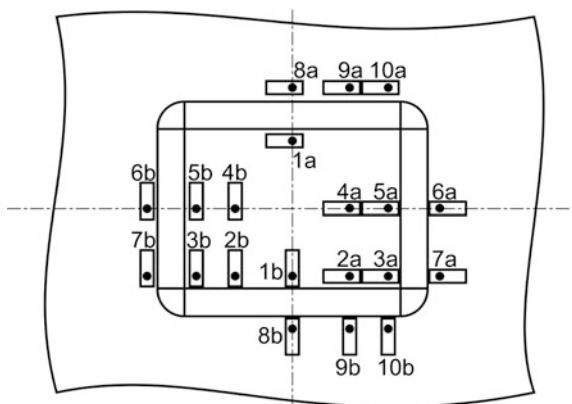
All technical operations of defect applying and measurements are executed at the middle part of the vessel, where the boundary effects are absent. In the middle of the vessel, the small area of the vessel wall has been removed by milling. This area of reduced wall thickness models the pipe surface defect. The modeled defect is a schematization of damage from action of surface corrosion or erosion. Scheme of the defect is shown in Fig. 2.

Loading device. For pressurizing the vessel, the oil is pumped into the vessel by the plunger pump. The plunger pump consists of tank with oil, valve for the oil discharge and arm for the pump. Level of pressure is measured by a manometer. The pump and manometer are connected to the vessel nipple through tubes and tee.

Measuring equipment. Strain measurement at the area of the defect is implemented through the tensometry method. This method is the most effective and economically reasonable for the following effort. The strain gages with base of 5 mm and conversion ratio of $K = 2.1$ are used in the measuring circuit.

Conversion ratio of a sensor K (or ratio of strain sensitivity) is the relation of the output signal in the form of relative change of his resistance ($\Delta R/R$) to input signal from strain (ϵ):

Fig. 3 Scheme of the strain gages gluing



$$K = \frac{\Delta R/R}{\varepsilon}$$

When we know conversion ratio and relative change of a strain gage's resistance, we can evaluate the strain. The sensors are placed at the area of the defect according to the scheme in Fig. 3. Strain gages are disposed into the area of the defect and at his boundary. They are concentrated at the places of hopping geometry in the form of filets that correspond to stress concentrators.

Whereas the defect is symmetrical, the stress-strain state around the defect is symmetrical, too. S-S state for the pair of points 1a-1b, 2a-2b, 3a-3b, 4a-4b, ..., 10a-10b is absolutely identical. Each of the pairs of points has, respectively, two strain gages, one of them is oriented along the axial direction (strain gages of group "a") and second is oriented along the circumferential direction (strain gages of group "b"). Thus, taking readings from the strain gages of each pair, we define the axial and circumferential strains for each pair of points. All strain gages are connected to the high-precision measuring device СИИТ-3.

3 Conduction of the Experiment

Conducting the experiment is planned in two stages: measurements for vessel, which is free from a wrap; measurements for vessel, which is strengthened by a composite wrap.

The first stage of the experiment is divided into the following steps:

- Calibration of strain gages;
- Preparation of the vessel surface and drawing the defect on it;
- Gluing of strain gages and soldering of the measuring circuit;
- Connection to the vessel plunger pump;

- Pressurize the vessel and performing of measurements. Optionally repeating the measurements;
- Statistical data processing.

Second stage:

- Filling the defect by a composite filler and installation of a on the vessel;
- Connection to the vessel plunger pump;
- Pressurize the vessel and fulfillment of measurements. Optionally repeating the measurements;
- Statistical data processing.

The first stage of the experiment. As mentioned previously, for the strain measurement, the strain gages with base of 5 mm and nominal conversion ratio of $K = 2.1$ are used. Calibration of the strain gages showed insignificant deviation of their K from nominal value. Figure 4 shows the photo of measuring circuit of strain gages.

After assembly of experimental facility, the sets of experiments were carried out:

- (i) internal pressure of 1.5 MPa—9 measurements;
- (ii) internal pressure of 4 MPa—7 measurements.

Description of experimental data and their analysis are present in Sect. 4.

The second stage of the experiment. Previous to installing of the wrap, the area of the defect was filled by a composite paste made from epoxy resin and powder of lead plumbate. Obtained filler after curing has density sufficient for load transmission from the area of the defect to the installed wrap. Glass fabric impregnated with an epoxy resin is used for wrapping. The installed composite wrap has the following sizes: a length of 160 mm and a thickness of 4.5 mm.

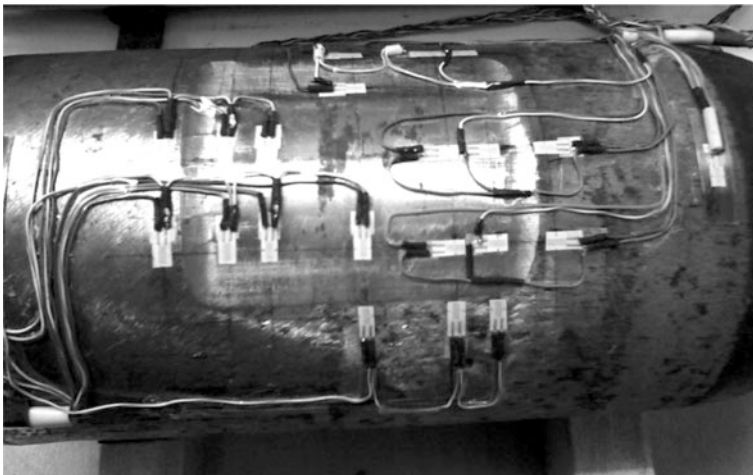


Fig. 4 Measuring circuit of strain gages

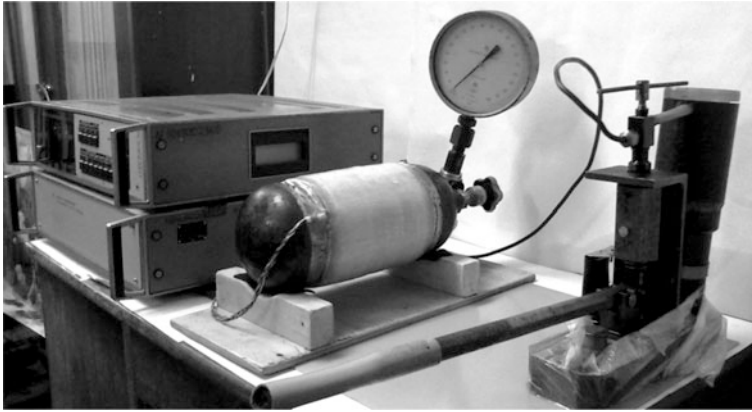


Fig. 5 Experimental facility and the wrapped vessel

Figure 5 shows the photo of the experimental facility and the wrapped vessel. After assembly of experimental facility, the sets of experiments were carried out:

- (i) internal pressure of 1.5 MPa—10 measurements;
- (ii) internal pressure of 4 MPa—10 measurements.

4 Analysis of Results

Results of the experiment after preliminary statistical treatment and also results of finite-element (FE) modeling for an additional verification of the obtained experimental data are present in this section.

For assessment of confidence interval of strain measurements the Student's t -distribution was used. This distribution is most adequate for describing the sample when sample size is small. The probability density function of the Student's t -distribution is specified by formula:

$$\varphi(t) = \frac{\Gamma\left(\frac{k+1}{2}\right)}{\sqrt{\pi k} \Gamma\left(\frac{k}{2}\right)} \left(1 + \frac{t^2}{k}\right)^{-\frac{k+1}{2}}$$

where Γ is the gamma function, k is the number of degrees of freedom specified like difference between sample size n , and number of parameters estimated through sample (in our case $k = n-1$).

The confidence interval for a measured value was evaluated by the inequalities:

Table 2 Results of strain measurements at pressure 1.5 MPa

Point	Direction of strain	Vessel without wrap			Vessel with wrap		
		Strain AVG	Confidence interval	Deviation from AVG, %	Strain AVG	Confidence interval	Deviation from AVG, %
1a	Axial	3.49E-05	2.91E-06	8.33	2.57E-05	1.71E-06	6.65
2a	Axial	4.28E-05	4.81E-06	11.24	2.76E-05	1.71E-06	6.19
3a	Axial	5.25E-05	4.91E-05	93.45	3.26E-05	1.76E-06	5.41
4a	Axial	4.38E-05	4.79E-06	10.94	2.82E-05	1.59E-06	5.63
5a	Axial	5.31E-05	4.18E-06	7.86	3.58E-05	2.28E-06	6.38
6a	Axial	3.17E-06	1.90E-06	59.97	7.24E-06	1.27E-06	17.58
7a	Axial	8.47E-06	4.41E-06	52.12	1.10E-05	2.08E-06	18.81
8a	Axial	2.60E-05	4.40E-06	16.89	1.89E-05	1.48E-06	7.87
9a	Axial	2.33E-05	4.37E-06	18.75	a	a	a
10a	Axial	2.39E-05	4.13E-06	17.27	1.73E-05	2.21E-06	12.78
1b	Circum.	1.77E-04	4.76E-06	2.70	1.34E-04	6.87E-06	5.15
2b	Circum.	1.58E-04	4.38E-06	2.78	1.39E-04	5.69E-06	4.09
3b	Circum.	1.53E-04	3.93E-06	2.57	1.35E-04	4.91E-06	3.64
4b	Circum.	1.64E-04	4.72E-06	2.89	1.28E-04	4.14E-06	3.24
5b	Circum.	1.60E-04	4.08E-06	2.54	1.29E-04	3.77E-06	2.92
6b	Circum.	1.01E-04	3.77E-06	3.75	9.24E-05	6.68E-05	4.51
7b	Circum.	1.14E-04	3.65E-06	3.21	9.77E-05	3.92E-06	4.01
8b	Circum.	a	a	a	a	a	a
9b	Circum.	5.50E-05	3.55E-06	6.46	6.59E-05	4.57E-06	6.93
10b	Circum.	5.88E-05	3.88E-06	6.59	6.93E-05	4.37E-06	6.30

^aThe strain gage was broken

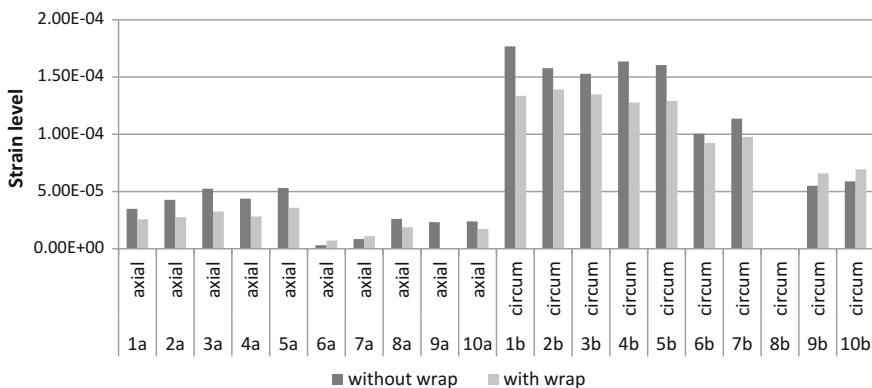


Fig. 6 Strain in measurement points at pressure 1.5 MPa

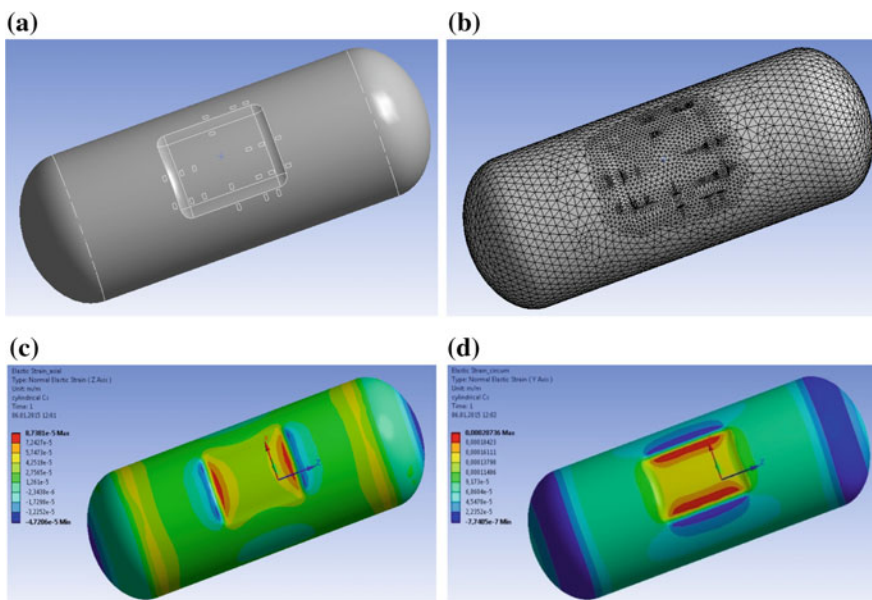


Fig. 7 FE analysis for vessel without wrap: **a** solid model, **b** FE model, **c** distribution of axial strain, **d** distribution of circumferential strain

$$m - \frac{s}{\sqrt{n}} t_{\alpha,k} < a < m + \frac{s}{\sqrt{n}} t_{\alpha,k}$$

where m is the sample mean (AVG), s is the mean-square deviation, $t_{\alpha,k}$ is the sample fractile depended on k , and α was specified through confidence probability. The confidence interval was estimated with the confidence probability equal 99%.

Table 3 Comparison of results of the experiment and finite-element analysis

Point	Direction of strain	Experiment	ANSYS	Difference, %	Point	Direction of strain	Experiment	ANSYS	Difference, %
1a	Axial	3.49E-05	3.48E-05	0.35	1b	Circum	1.77E-04	1.90E-04	6.97
2a	Axial	4.28E-05	4.13E-05	3.52	2b	Circum	1.58E-04	1.90E-04	17.00
3a	Axial	5.25E-05	6.00E-05	12.51	3b	Circum	1.53E-04	1.72E-04	11.15
4a	Axial	4.38E-05	4.86E-05	9.85	4b	Circum	1.64E-04	1.48E-04	10.56
5a	Axial	5.31E-05	7.32E-05	27.42	5b	Circum	1.60E-04	1.42E-04	12.99
6a	Axial	3.17E-06	1.86E-05	82.93	6b	Circum	1.01E-04	1.05E-04	4.25
7a	Axial	8.47E-06	2.02E-05	58.09	7b	Circum	1.14E-04	1.08E-04	5.24
8a	Axial	2.60E-05	2.31E-05	12.70	8b	Circum	^a	1.75E-05	100.00
9a	Axial	2.33E-05	2.70E-05	13.77	9b	Circum	5.50E-05	2.00E-05	175.15
10a	Axial	2.39E-05	3.03E-05	21.07	10b	Circum	5.88E-05	2.70E-05	117.92

^aThe strain gage was broken

The results of experiment at pressure of 1.5 MPa are present in Table 2 and Fig. 6.

The results of finite-element modeling of vessel without wrap are present in Fig. 7 and Table 3.

The results of simulation of vessel with wrap and comparative data of FE analysis are present in Tables 4, 5 and Figs. 8–10.

Measurements in points 1a, 2a, 4a, 5a, 8a, 10a, 1b, 2b, 3b, 4b, 5b, 6b, 7b have a deviation from AVG no more than 19% and they show reducing of values of axial and circumferential strains after installation of the wrap. For vessel without wrap, results of measurements in these points coincide with results of finite-element analysis in margin of error 20% (see Table 3).

For vessel without wrap, a large dispersion of measurements is observed (93.45%) in point 3a, but AVG coincides with results of FE analysis with error 12.51%. For vessel with wrap, the measurements in this point have a small dispersion 5.41%. The results show reducing of strain level in point 3a after installation of the wrap.

In points 6a, 7a, the dispersion of measurements from AVG reaches 60% and does not confirm results of FE analysis. Therefore, results in these points were excluded from consideration.

Table 4 Mechanical properties^a of wrap and filler

Wrap (glass–fiber plastic)						Filler	
E_{xz} , GPa	6	μ_{xy}	0.18	G_{xy} , GPa	3	E , GPa	8
E_y , GPa	20	μ_{yz}	0.15	G_{yz} , GPa	4	μ	0.36
E_z , GPa	18.6	μ_{xz}	0.42	G_{xz} , GPa	3	–	–

^aValues of the properties were selected approximately

Table 5 Comparison of results of finite-element modeling (pressure 1.5 MPa)

Point	Direction	Vessel without wrap	Vessel with wrap
		Strain value	Strain value
1a	Axial	3.48E–05	2.95E–05
2a	Axial	4.13E–05	3.30E–05
3a	Axial	6.00E–05	4.47E–05
4a	Axial	4.86E–05	3.86E–05
5a	Axial	7.32E–05	5.15E–05
6a	Axial	1.86E–05	8.06E–06
7a	Axial	2.02E–05	7.78E–06
8a	Axial	2.31E–05	2.23E–05
9a	Axial	2.70E–05	2.57E–05
10a	Axial	3.03E–05	2.75E–05
1b	Circumferential	1.90E–04	1.52E–04
2b	Circumferential	1.90E–04	1.52E–04

(continued)

Table 5 (continued)

Point	Direction	Vessel without wrap	Vessel with wrap
		Strain value	Strain value
3b	Circumferential	1.72E-04	1.39E-04
4b	Circumferential	1.48E-04	1.34E-04
5b	Circumferential	1.42E-04	1.25E-04
6b	Circumferential	1.05E-04	9.42E-05
7b	Circumferential	1.08E-04	9.47E-05
8b	Circumferential	1.75E-05	3.78E-05
9b	Circumferential	2.00E-05	3.91E-05
10b	Circumferential	2.70E-05	4.25E-05

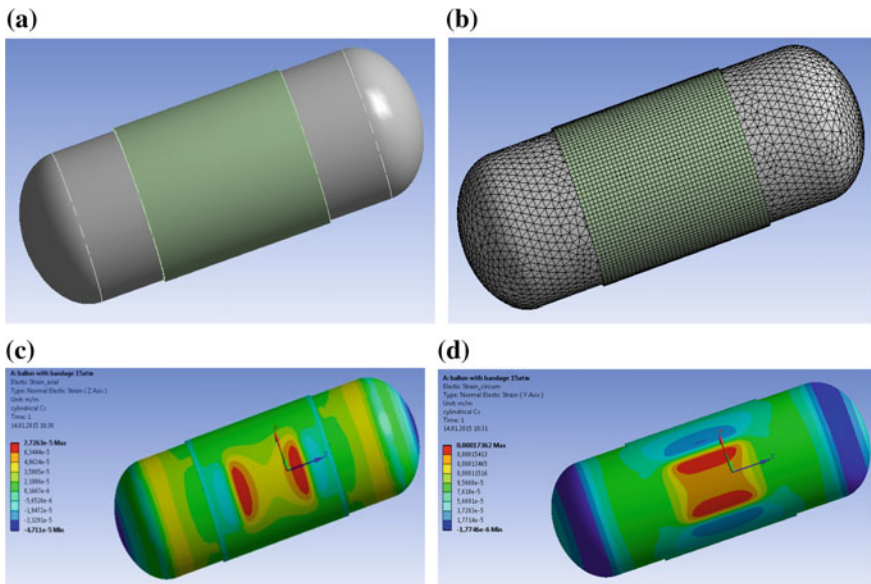


Fig. 8 FE analysis for vessel with wrap: **a** solid model, **b** FE model, **c** distribution of axial strain, **d** distribution of circumferential strain

In points 8b, 9a, data analysis is not possible because strain gages were broken at the first stage (before installation of wrap) or at the second stage of experiment (after wrapping).

Values of measured strains in points 9b, 10b do not coincide with results of FE analysis for vessel without wrap, but dispersion of measurements does not exceed 7% which indicates the efficiency of performed measurements. Experimental data, obtained in points 9b, 10b, shows increase of circumferential strains after

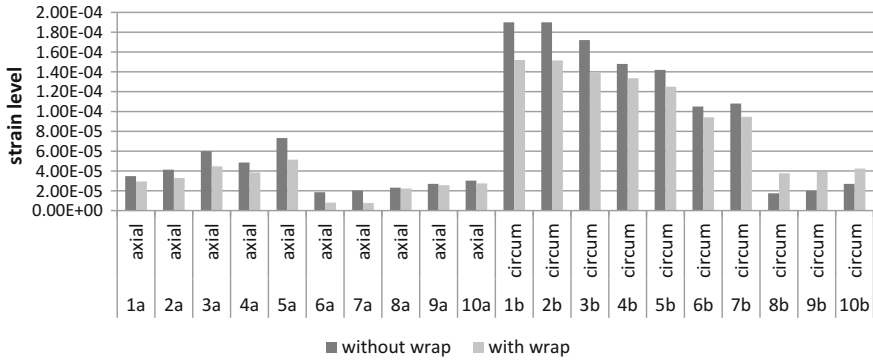


Fig. 9 Comparison of strain values

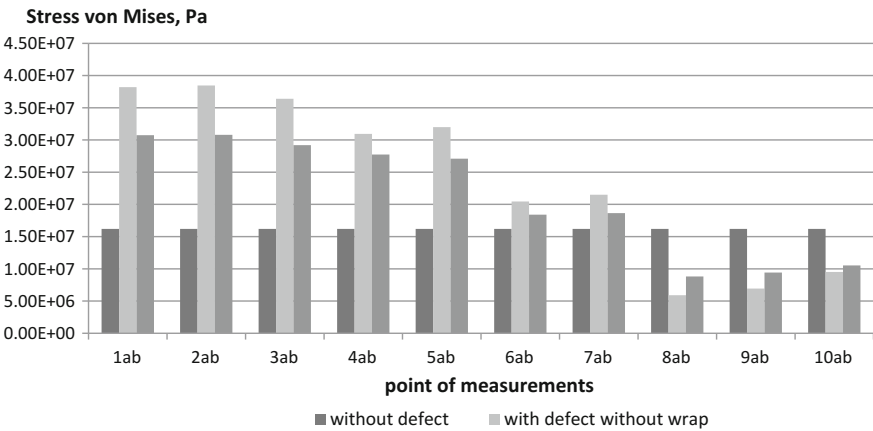


Fig. 10 Comparison of equivalent stresses

installation of the wrap and this is qualitatively confirmed by results of FE analysis (see Fig. 9).

The results of experiment at pressure 4 MPa are present in Table 6 and Fig. 11

The results of comparison of finite-element modeling with experiment for vessel without wrap are present in Table 7. The results of experiment and finite-element modeling in the case of internal pressure of 4 MPa have the same trend like for pressure of 1.5 MPa. Experiments and computations for pressure of 4 MPa were executed with aim of additional validation.

Table 6 Results of strain measurements at pressure 4 MPa

Point	Direction of strain	Vessel without wrap			Vessel with wrap		
		Strain AVG	Confidence interval	Point (%)	Direction of strain	Strain AVG	Confidence interval (%)
1a	Axial	8.11E-05	5.04E-06	6.22	6.82E-05	3.65E-06	5.35
2a	Axial	1.06E-04	4.07E-06	3.83	7.43E-05	2.12E-06	2.86
3a	Axial	1.29E-04	8.86E-05	68.84	8.76E-05	3.29E-06	3.75
4a	Axial	1.08E-04	5.98E-06	5.55	7.37E-05	2.13E-06	2.89%
5a	Axial	1.34E-04	5.73E-06	4.28	9.53E-05	3.68E-06	3.86
6a	Axial	1.95E-04	7.31E-04	374.95	1.92E-05	1.76E-06	9.16
7a	Axial	1.55E-05	5.88E-06	37.93	2.93E-05	2.72E-06	9.26
8a	Axial	6.18E-05	5.98E-06	9.68	5.09E-05	3.01E-06	5.91
9a	Axial	5.31E-05	6.51E-06	12.26	a	a	a
10a	Axial	5.55E-05	6.10E-06	10.99	4.59E-05	4.50E-06	9.79
1b	Circum.	4.55E-04	4.74E-06	1.04	3.51E-04	4.88E-06	1.39
2b	Circum.	4.02E-04	1.92E-06	0.48	3.64E-04	5.41E-06	1.49
3b	Circum.	3.93E-04	2.65E-06	0.67	3.48E-04	4.01E-06	1.15
4b	Circum.	4.20E-04	5.29E-06	1.26	3.36E-04	3.68E-06	1.10
5b	Circum.	4.14E-04	5.67E-06	1.37	3.40E-04	3.77E-06	1.11
6b	Circum.	2.54E-04	1.92E-06	0.76	2.43E-04	6.37E-06	2.63
7b	Circum.	2.88E-04	5.89E-06	2.04	2.54E-04	4.03E-06	1.59
8b	Circum.	a	a	a	a	a	a
9b	Circum.	1.36E-04	5.73E-06	4.22	1.70E-04	4.50E-06	2.65
10b	Circum.	1.43E-04	5.01E-06	3.49	1.79E-04	3.21E-06	1.80

^aThe strain gage was broken

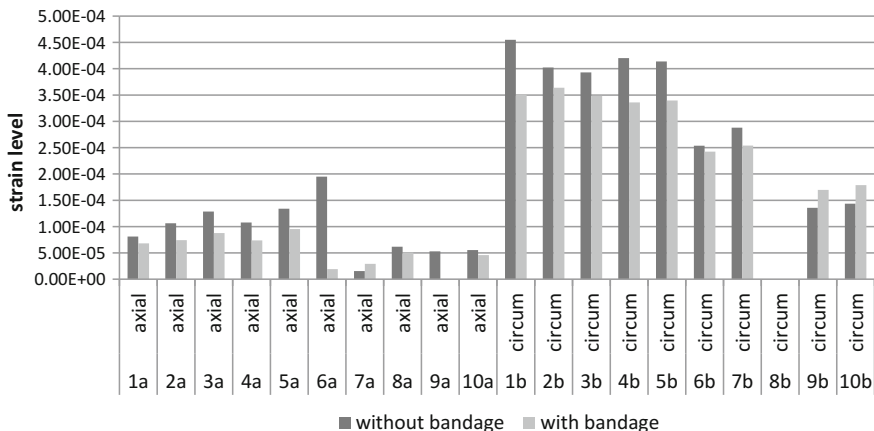


Fig. 11 Strain in measurement points at pressure 4 MPa

5 Conclusion

On the basis of obtained results from executed experimental research and finite-element modeling for a steel cylindrical shell with given defect, one could make following conclusions:

Installation of a composite wrap on a cylindrical shell with the defect leads to decreasing of axial and circumferential strains inside of area of the defect (points 1a, 2a, 3a, 4a, 5a, 1b, 2b, 3b, 4b, 5b) and also near exterior sides of the defect, which are transverse to axis of shell (points 6b, 7b). All of these indicate the efficiency of methodology of wrapping with using of composite materials for reinforcement of cylindrical thin-walled constructions with defects.

After installation of the wrap, the decreasing of axial strains (points 8a, 10a) and increasing of circumferential strains (points 9b, 10b) are observed near exterior sides of the defect, which are parallel to axis of shell. As we can see, the influence of the wrap on strain level at these points has ambiguous trend, while it does not doubt the efficiency of the wrap. The results of finite-element modeling confirm increasing of equivalent stresses in these points after installation of the wrap, but level of stresses in them is lower than in the case, when shell is free from the defect at all (see Fig. 12).

The procedure developed for calculating the stressed state of a repair joint allows one to obtain well-grounded rational solutions already at the stage of design and choice of materials and parameters of technological process for the structure in view.

Table 7 Comparison of results of the experiment and finite-element analysis for vessel without wrap

Point	Direction of strain	Experiment	ANSYS	Difference, %	Point	Direction of strain	Experiment	ANSYS	Difference, %
1a	Axial	8.11E-05	9.28E-05	12.61	1b	circum	4.55E-04	5.10E-04	10.80
2a	Axial	1.06E-04	1.10E-04	3.27	2b	circum	4.02E-04	5.00E-04	19.53
3a	Axial	1.29E-04	1.60E-04	19.54	3b	circum	3.93E-04	4.61E-04	14.73
4a	Axial	1.08E-04	1.29E-04	16.46	4b	circum	4.20E-04	3.93E-04	6.88
5a	Axial	1.34E-04	1.95E-04	31.33	5b	circum	4.14E-04	3.78E-04	9.47
6a	Axial	1.95E-04	4.96E-05	292.8	6b	circum	2.54E-04	2.78E-04	8.75
7a	Axial	1.55E-05	5.37E-05	71.12	7b	circum	2.88E-04	2.89E-04	0.35
8a	Axial	6.18E-05	6.14E-05	0.61	8b	circum	^a	4.67E-05	100
9a	Axial	5.31E-05	7.20E-05	26.30	9b	circum	1.36E-04	5.35E-05	153.8
10a	Axial	5.55E-05	8.07E-05	31.21	10b	circum	1.43E-04	7.20E-05	99.20

^aThe strain gage was broken

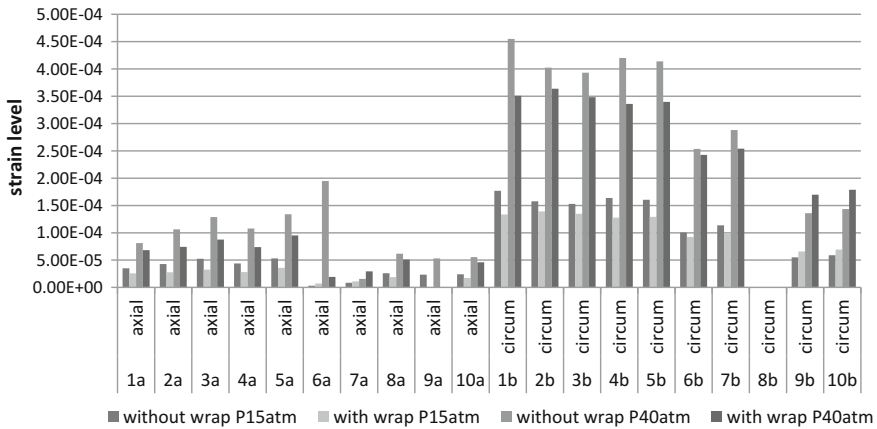


Fig. 12 General diagram of all obtained experimental results

References

1. H. Altenbach, D. Beschtnikov, G. Lvov, K. Naumenko, V. Sukiasov, Kontakt Wechselwirkungeiner Rohrleitungmit der Reparatur Bandage Auseinem Komposit Werkstoff, Forschungim. Ingenieurwesen. **78**(1–2), 59 (2014)
2. E. Barkanov, D. Beschtnikov, G. Lvov, Effect of technological tensioning on the efficiency of reinforcement of pipelines with composite bands, *Mech. Compos. Mater.* **50**(6), 725 (2015)
3. G. Lvov, Investigation of the contact interaction between nonlinear elastic shells of finite shear rigidity and punches. *Int. Appl. Mech.* **20**, 246 (1984)
4. A.A. Lyapin, M.I. Chebakov, A. Dumitrescu, Gh. Zecheru, Finite element modeling of pipeline with volumetric defect, in *Proceedings of Universities of North Caucasus Region*, Nat. Sci. 2, 24 (2014)
5. A.A. Lyapin, M.I. Chebakov, A. Dumitrescu, G. Zecheru, Finite element modeling of damaged pipeline including polymer filler and composite wrap, *Mech. Compos. Mater.* **51**(3), 333 (2015)

Analytical Modeling of the Damaged Zone of Pipelines Repaired with Composite Materials Systems

A.S. Skaliukh, M.I. Chebakov and Andrei Dumitrescu

Abstract The present chapter describes an applied mathematical model aimed at assessing the strength properties of a damaged area of a transmission pipeline after repair works were performed using a composite material system. In the two-dimensional case, the problem of the stress–strain state in a pipe area with a long volumetric surface defect (VSD) has been considered. We have assumed that the repair work in the damaged area of the pipeline consisted of applying polymeric filler (in order to reconstruct the external configuration of the pipe in the VSD area) and then wrapping several layers of polymeric composite material, bonded with the help of a polymeric adhesive. We have also assumed that the VSD length (longitudinal extent) is considerably greater than its width (circumferential extent), which allows us to develop a two-dimensional analytical model. In our model, the effect of the composite material was taken into account by applying, on the pipeline outside surface, an additional normal stress, which is proportional to the tensile stresses from the composite wrap. These tensile stresses, in their turn, consist first of a pretension of the wounded composite layers, and second of the stresses arising from the circumferential deformation of the pipe. Such deformation, in the simplest case, can be described using Hooke’s law, as the product between the modulus of elasticity of the composite material in the circumferential direction and the circumferential strain of the pipe at its surface. Additional studies were conducted to evaluate the stress concentration effect at the corner points of the surface. To solve this problem, the whole area of the pipe cross-section has been divided into two subareas, each of which had its own stress function. Taking into account the symmetry of the field and external loads in each area, one stress function has been built in each subregion. All boundary conditions on the inner and outer surfaces of the pipe and on the symmetry axis are satisfied exactly. To obtain a closed system of equations, it was necessary to add two equations, including the condition of

A.S. Skaliukh (✉) · M.I. Chebakov
I.I. Vorovich Institute of Mathematics Mechanics and Computer Science,
Southern Federal University, Rostov-on-Don, Russia
e-mail: a.s.skaliukh@gmail.com

A. Dumitrescu
Petroleum-Gas University of Ploiesti, Ploiești, Romania

equality of the bending moment in the coupling zone and the proportionality condition of the radial and tangential displacements in the vertical direction for a solid body. Finally, we have obtained a closed system of 12 linear algebraic equations whose solution allowed us to obtain all the relevant characteristics of the problem. Numerical calculations have been conducted and von Mises combined stresses analyzed in the damaged pipe area as function of the VSD depth and compared with results obtained using a finite elements model.

Keywords Transmission pipeline · Volumetric surface defect (VSD) · Composite material · Stress function · Plane strain model · Elasticity theory · von Mises combined stress

1 Introduction

The problem of adequately repairing an area with volumetric surface defects (VSDs), generated by corrosion and/or erosion on the surface of a transmission pipeline in order to restore the pipe strength, is very important from both technical and economic points of view. There are several methods to repair such defects, among which a composite material system is often used. Such method consists of machining by grinding the damaged pipe area (in order to round the flaw geometry and consequently to diminish the mechanical stress concentration effects), followed by the application of a wrap or sleeve made of a composite material reinforced with glass fibers. This repair procedure is conducted without the use of welding, and on the in-service pipeline (without turning off the fluid supply), but normally with a decrease in the internal operating pressure not greater than 70%. It has been proven that by using composite wraps, the damaged pipe can be repaired even if the entire pipe wall is affected (the VSD depth is almost equal to the steel wall thickness). However, in our model, we have considered that the pipe wall is only partially damaged, i.e., the maximum depth of the defect is not greater than 60% of the pipe thickness. Otherwise, the pipe stresses in the damaged area would be comparable to or even exceed the pipe steel specified yield strength, which is unacceptable for the normal operation of the damaged pipeline.

To build the model, a section of a transmission pipeline affected by corrosion defects has been considered. The VSD area has been machined by grinding and, as a result, an initial defect with the geometry shown in Fig. 1 has been obtained. The machined defect area is then filled with a polymeric material (filler), and a composite material wrap is wounded around the pipe and bonded with the help of a polymeric adhesive (see Fig. 1).

The primary and major objective of such repair activities is to restore the strength properties of the transmission pipeline. Therefore, it is very important for the pipeline users to be able to evaluate the mechanical strength of areas subjected to repair. To that purpose, both experimental and theoretical studies are useful. In the present study, we have developed an analytical model based on the

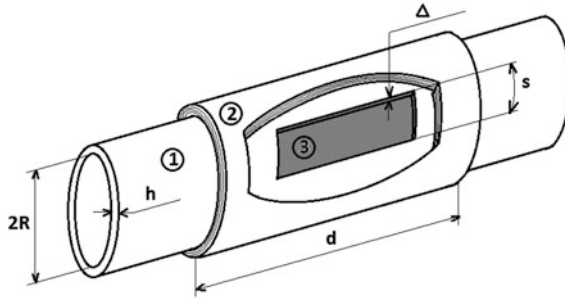


Fig. 1 Scheme of a composite material repair system applied on a transmission pipeline: 1 transmission pipeline; 2 polymeric composite material wrap; 3 VSD filled with polymeric filler; R pipe inner radius; h pipe wall thickness; s machined defect width; Δ defect depth; d composite wrap length

two-dimensional theory of elasticity, which allows quantifying the pipe strength by means of the von Mises combined stresses in the most affected points of pipe cross-section. The limits of applicability of this theory have been evaluated as well.

Obviously, the use of a finite element model, taking into account the full pipe structure with its defect and the composite material, can provide a better approximation of strength characteristics in the VSD area. However, besides the finite element approach, an analytical method could also be of interest even considering its applicability limits for solving such problems. Any analytical method always involves a simplified formulation of the problem. A further generalization, including additional geometric fields and materials, leads to a further complication of the task that, if using finite elements software is inexpedient. Therefore, we have preferred a simpler approach in which, first, a two-dimensional plane strain model of the elasticity theory has been used, and, second, the effect of the composite wrap is reduced to additional normal stresses on the outer surface of the pipe steel.

Details and features of our approach will be discussed in Sect. 3, devoted to the problem statement. In this section, we only note that we have used a well-known analytical formulation, in which the exact solutions for a circular area were obtained and where the field of mechanical stresses was similar to the field of stresses in our problem.

The occurrence of the defect on the surface of the pipe leads to the disruption of the circular symmetry of the pipe cross-section. This leads to the presence in the cross-section of shear stresses with normal stresses. Furthermore, the corner points of the boundary may cause stress concentration effects that certainly affect the strength properties of the pipe. Therefore, we have taken into account and constructed such a stress function that described both normal and shear stresses. In this regard, noteworthy solutions were obtained by X.C. Golovin and described in [2].

There is a well-known solution for a ring subjected to internal stresses applied to its internal and external borders (the task of Lamé). The type of stress function, used for this task, is selected such that the boundary conditions are satisfied exactly.

The additional conditions of uniqueness of displacement at distinct direction gives the possibility to determine the constant related to the angular coordinate. X.C. Golovin presented a solution for the problem of a bending ring with the shear load applied on the butt end of the ring. This problem used a stress function comprising a circumferential coordinate such that the shearing stresses can be determined. In this case, the boundary condition at the butt end of the ring in form of shear stresses is fulfilled in an integral meaning. In order to define the stress functions, which describe both normal and shear stresses, we have used both solutions mentioned above. Our research focused on the construction of a theoretical mathematical model to evaluate the mechanical properties in any region of the pipe area weakened due to the VSD presence, considering also the effect of repair activities.

2 Problem Formulation

We assume that the defect at the pipe external surface is of sufficient length (along the pipe axial coordinate) and placed at a certain distance from the edges so that all edge effects fade away and the average cross-section of the pipe can be considered. It is obvious that the pipe geometry and the loading conditions (internal pressure) give the possibility to apply the plane strain model of the theory of elasticity. We assume that the polymeric composite material fits in a plane stress model and that the filler is a polymeric material in conditions of uniform compression. These assumptions allow us to consider the problem in the framework of a two-dimensional case for the pipe cross-section, a portion of which is shown in Fig. 2.

A further simplification of the problem is connected with the characteristics of the composite material. While wrapping the composite, compressive loads develop in the pipe wall that can be associated with the wrap tension and the number of composite material layers. After repairing the pipe, during its operation under internal pressure, an additional compression stress appears in the contact area with the composite material wrap. It is natural to assume that these additional stresses are proportional to the axial stress in the composite material that, according to Hooke's law, is equal to the elastic modulus of the composite material along the circumferential direction multiplied by the circumferential strain of the pipe. The uniform compression conditions of the filler polymeric material applied inside the defect allow us to conclude that the filler is in state of hydrostatic compression, as it can be seen in Fig. 3.

Fig. 2 Section of the pipe cross-sectional area with the filled VSD and the applied composite material wrap (p_0 is the internal pressure)

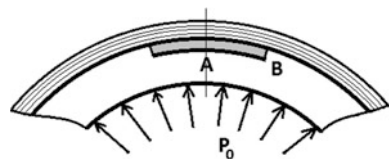


Fig. 3 Cross-sectional area of the pipe with a machined defect

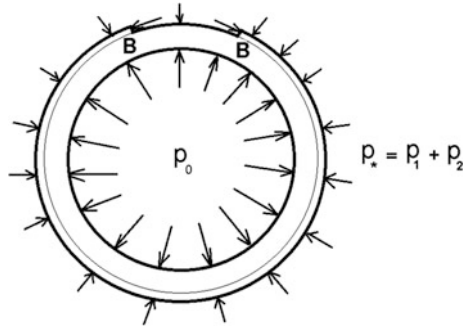
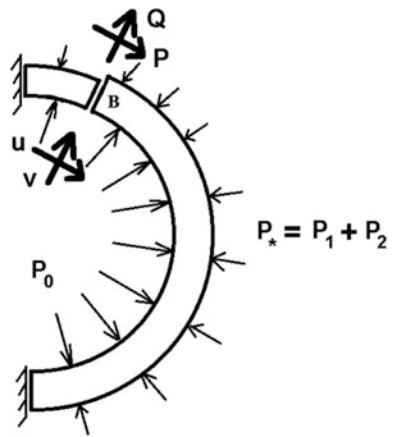


Fig. 4 Areas Ω_1 and Ω_2 , and conditions of solutions conjugation at the border of the areas (P and Q are the average forces, in an integral sense, in the cross-section; u and v are the average displacements, in an integral sense, in the cross-section)



It can be observed that both the region itself and the boundary conditions have properties of symmetry along the vertical axis. This results in the fact that the solution will have the symmetry property with respect to this axis, as shown in Fig. 4.

The following geometrical characteristics have been defined: r_2 is the outer radius of the pipe; r_1 is the inner radius of the pipe; Δ is the depth of the defect, measured from the outer radius. To solve this problem, we have considered half of the pipe cross-section, which is divided into two subregions, Ω_1 and Ω_2 , each of which with its own outer radius:

$$\begin{aligned} \Omega &= \Omega_1 \cup \Omega_2; \\ \Omega_1 &:= \{r_1 \leq r \leq r_2 - \Delta, \quad 0 \leq \theta \leq \beta\}; \\ \Omega_2 &:= \{r_1 \leq r \leq r_2, \quad \beta \leq \theta \leq \pi\}, \end{aligned} \tag{1}$$

in which θ is the current angular coordinate and β is the angle corresponding to half of the width (circumferential extent) of the defect.

It is now necessary to determine the stress functions, $\Phi^{(1)}$ in Ω_1 and $\Phi^{(2)}$ in Ω_2 , which are subjected to the boundary conditions and conjugation conditions on the adjacent areas, as shown in Fig. 4. The well-known formulae relating the stress functions with the stresses that will be needed in the model have been used:

$$\begin{aligned}\sigma_{rr}^{(k)} &= \frac{1}{r} \frac{\partial \Phi^{(k)}}{\partial r} + \frac{1}{r^2} \frac{\partial^2 \Phi^{(k)}}{\partial \theta^2}; & \sigma_{\theta\theta}^{(k)} &= \frac{\partial^2 \Phi^{(k)}}{\partial r^2}; \\ \sigma_{r\theta}^{(k)} &= -\frac{\partial}{\partial r} \left(\frac{1}{r} \frac{\partial \Phi^{(k)}}{\partial \theta} \right), & k &= 1, 2.\end{aligned}\quad (2)$$

In Eq. (2) and further, $k = 1$ refers to the area Ω_1 , and $k = 2$ —to the area Ω_2 . The relationships between strains and stresses are the following:

$$\begin{aligned}\varepsilon_{rr}^{(k)} &= \frac{1}{E^*} \left(\sigma_{rr}^{(k)} - \nu^* \sigma_{\theta\theta}^{(k)} \right); & \varepsilon_{\theta\theta}^{(k)} &= \frac{1}{E^*} \left(\sigma_{\theta\theta}^{(k)} - \nu^* \sigma_{rr}^{(k)} \right); \\ \varepsilon_{r\theta}^{(k)} &= \frac{1 + \nu^*}{E^*} \sigma_{r\theta}^{(k)}; & E^* &= \frac{E}{1 - \nu^2}; & \nu^* &= \frac{\nu}{1 - \nu}.\end{aligned}\quad (3)$$

In addition, the following formulae coupling strains and displacements have been used:

$$\begin{aligned}\varepsilon_{rr}^{(k)} &= \frac{\partial u^{(k)}}{\partial r}; & \varepsilon_{\theta\theta}^{(k)} &= \frac{1}{r} \frac{\partial v^{(k)}}{\partial \theta} + \frac{u^{(k)}}{r}; \\ \varepsilon_{r\theta}^{(k)} &= \frac{1}{2} \left(\frac{1}{r} \frac{\partial u^{(k)}}{\partial \theta} + \frac{\partial v^{(k)}}{\partial r} - \frac{v^{(k)}}{r} \right).\end{aligned}\quad (4)$$

At the border of Ω_1 , the following boundary conditions can be written:

$$\begin{aligned}v^{(1)}|_{\theta=0} &= 0; & \sigma_{r\theta}^{(1)}|_{\theta=0} &= 0, & (r_1 \leq r \leq r_2 - \Delta); \\ \sigma_{rr}^{(1)}|_{r=r_1} &= p_0; & \sigma_{r\theta}^{(1)}|_{r=r_1} &= 0, & (0 \leq \theta \leq +\beta); \\ \sigma_{rr}^{(1)}|_{r=r_2-\Delta} &= p_1 + p_2; & \sigma_{r\theta}^{(1)}|_{r=r_2-\Delta} &= 0, & (0 \leq \theta \leq +\beta); \\ p_1 &= \frac{T}{Ll(r_2-\Delta)}; & p_2 &= \frac{E_c}{Lr_2} \varepsilon_{\theta\theta}.\end{aligned}\quad (5)$$

For the composite material, the following characteristics have been defined: T is the wrap pretension, l is the wrap thickness, L is the wrap length, E_c is the elastic modulus in the circumferential direction of the composite material. At the boundary of Ω_2 , it can be written as follows:

$$\begin{aligned}
 v^{(2)}|_{\theta=\pi} &= 0; & \sigma_{r\theta}^{(2)}|_{\theta=\pi} &= 0, & (r_1 \leq r \leq r_2); \\
 \sigma_{rr}^{(2)}|_{r=r_1} &= p_0; & \sigma_{r\theta}^{(2)}|_{r=r_1} &= 0, & (\beta \leq \theta \leq \pi); \\
 \sigma_{rr}^{(2)}|_{r=r_2} &= p_1 + p_2, & \sigma_{r\theta}^{(2)}|_{r=r_2} &= 0, & (\beta \leq \theta \leq \pi).
 \end{aligned}
 \tag{6}$$

In addition, at the interface, the following conditions regarding the equality of the stresses and displacements must be fulfilled:

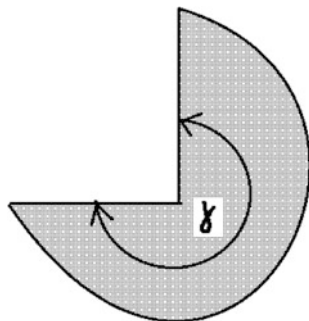
$$\begin{aligned}
 \sigma_{\theta\theta}^{(2)}|_{\theta=\beta} &= \left\{ \begin{aligned} &\sigma_{\theta\theta}^{(1)}|_{\theta=\beta}, & (r_1 \leq r \leq r_2 - \Delta) \\ &p_1 + p_2, & (r_2 - \Delta \leq r \leq r_2) \end{aligned} \right\}; \\
 \sigma_{r\theta}^{(2)}|_{\theta=\beta} &= \left\{ \begin{aligned} &\sigma_{r\theta}^{(1)}|_{\theta=\beta}, & (r_1 \leq r \leq r_2 - \Delta) \\ &0, & (r_2 - \Delta \leq r \leq r_2) \end{aligned} \right\}; \\
 u_{\theta=\beta}^{(2)} &= u_{\theta=\beta}^{(1)}, & (r_1 \leq r \leq r_2 - \Delta); \\
 v_{\theta=\beta}^{(2)} &= v_{\theta=\beta}^{(1)}, & (r_1 \leq r \leq r_2 - \Delta).
 \end{aligned}
 \tag{7}$$

3 Assessment of the Nature of Decision at the Corner Points

In the region of the pipe cross-section, at the corner points (points B from Fig. 3), the property of smoothness of the boundary is disrupted. When approaching this point, an infinitely increasing solution can appear. To answer the question of whether or not there are unlimited growing solutions, we have considered the wedge with the corner angle $\gamma = 3\pi/2$, as shown in Fig. 5. We have introduced polar coordinates, and searched the solution of the equilibrium equations in such coordinates as $u_r = r^2 u(\theta)$, $u_\theta = r^2 v(\theta)$.

These solutions should be subordinated to the boundary conditions at the edges of the wedge. In our case, the stresses are specified at the edges, so the decision

Fig. 5 Wedge-shaped area with the solution angle $\gamma = \frac{3}{2}\pi$



should be subjected to the following boundary conditions: $\sigma_{\theta\theta}|_{\theta=0,\gamma} = 0$, $\sigma_{r\theta}|_{\theta=0,\gamma} = 0$.

After substituting these expressions in the equations of equilibrium, the following system of ordinary differential equations was obtained:

$$\begin{aligned} u'' + (\alpha^2 - 1)(\kappa + 1)u + [(\alpha - 1)\kappa - 2]v' &= 0; \\ (\kappa + 1)v'' + (\alpha^2 - 1)v + [\kappa(\alpha + 1) + 2]u' &= 0. \end{aligned} \quad (8)$$

The solution of the system (8) is written below:

$$\begin{aligned} u &= C_1 \cos(\alpha + 1)\theta + C_2 \sin(\alpha + 1)\theta + C_3[\kappa(1 - \alpha) + 2] \cos(\alpha - 1)\theta \\ &\quad + C_4[\kappa(\alpha - 1) - 2] \sin(\alpha - 1)\theta; \\ v &= -C_1 \sin(\alpha + 1)\theta + C_2 \cos(\alpha + 1)\theta + C_3[\kappa(1 + \alpha) + 2] \sin(\alpha - 1)\theta \\ &\quad + C_4[\kappa(1 + \alpha) + 2] \sin(\alpha - 1)\theta. \end{aligned} \quad (9)$$

The solution of this system should be subordinated to the homogeneous boundary conditions mentioned above. The existence of a nontrivial solution must require that the determinant of the fourth order system would be zero. After some simplifications, the determinant can be written as follows:

$$D(\gamma, \alpha) = [\alpha \sin \gamma - \sin(\alpha\gamma)][\alpha \sin \gamma + \sin(\alpha\gamma)] = 0. \quad (10)$$

It is noteworthy that the roots of the equations are independent from the Poisson's ratio of the material. And since in this case $\gamma = 3\pi/2$, two equations are obtained to determine the ratio α :

$$-\alpha - \sin\left(\alpha\frac{3}{2}\pi\right) = 0; \quad -\alpha + \sin\left(\alpha\frac{3}{2}\pi\right) = 0. \quad (11)$$

These equations have two real roots: $\alpha_1 \approx 0.911$, $\alpha_2 \approx 0.545$. Each of these roots is smaller than 1, so in these points unlimited solutions may appear. Whether or not they are obtained depends on the specific boundary conditions on the edges of the wedge.

4 Method for Solving the Problem

To solve the above-formulated problem, the methods of the plane theory of elasticity in polar coordinates have been used. Considering the condition of symmetry, a biharmonic stress function has been chosen in each of these areas in the form:

$$\Phi^{(k)} = A_0^{(k)} r^2 \ln r + B_0^{(k)} r^2 + C_0^{(k)} \ln r + \left(A_1^{(k)} r^3 + B_1^{(k)} r \ln r + C_1^{(k)} \frac{1}{r} \right) \cos \theta, \quad (12)$$

$k = 1, 2.$

According to (2), the following stresses have been found in each of the areas:

$$\begin{aligned} \sigma_{rr}^{(k)} &= A_0^{(k)} (1 + 2 \ln r) + 2B_0^{(k)} + C_0^{(k)} \frac{1}{r^2} + \left(2A_1^{(k)} r + B_1^{(k)} \frac{1}{r} - 2C_1^{(k)} \frac{1}{r^3} \right) \cos \theta; \\ \sigma_{\theta\theta} &= A_0^{(k)} (3 + 2 \ln r) + 2B_0^{(k)} - C_0^{(k)} \frac{1}{r^2} + \left(6A_1^{(k)} r + B_1^{(k)} \frac{1}{r} + 2C_1^{(k)} \frac{1}{r^3} \right) \cos \theta; \\ \sigma_{r\theta} &= \left(2A_1^{(k)} r + B_1^{(k)} \frac{1}{r} - 2C_1^{(k)} \frac{1}{r^3} \right) \sin \theta. \end{aligned} \quad (13)$$

Using Eqs. (3) and (4), the displacement has been found after integration:

$$\begin{aligned} u^{(k)} &= \frac{1}{E^*} \left[A_0^{(k)} \left((-1 - v^*)r + 2(1 - v^*)r \ln r \right) + 2B_0^{(k)}(1 - v^*)r - C_0^{(k)} \frac{1}{r}(1 + v^*) \right] \\ &\quad + \frac{1}{E^*} \left[A_1^{(k)} (1 - 3v^*)r^2 + B_1^{(k)} (1 - v^*) \ln r + C_1^{(k)} (1 + v^*) \frac{1}{r^2} \right] \cos \theta \\ &\quad + D_1^{(k)} \cos \theta + D_2^{(k)} \sin \theta + 2B_1^{(k)} \frac{1}{E^*} \theta \sin \theta; \\ v^{(k)} &= \frac{4A_0^{(k)} r \theta}{E^*} + \frac{1}{E^*} \left[A_1^{(k)} (5 + v^*)r^2 + B_1^{(k)} (1 - v^*)(r - \ln r) + C_1^{(k)} (1 + v^*) \frac{1}{r^2} \right] \sin \theta \\ &\quad - D_1^{(k)} \sin \theta - D_2^{(k)} \cos \theta + D_3^{(k)} r + 2B_1^{(k)} \frac{1}{E^*} (-\theta \cos \theta + \sin \theta). \end{aligned} \quad (14)$$

It is easy to observe that we have obtained 18 constants. To find them, boundary conditions (5)–(7) have to be used. First, let us turn to the first conditions (5)–(6), i.e., to the conditions on the axis of symmetry:

$$\begin{aligned} -D_2^{(1)} + D_3^{(1)} r &= 0; \\ D_2^{(2)} + \frac{2B_1^{(2)} \pi}{E^*} + \left(D_3^{(2)} + \frac{4A_0^{(2)} \pi}{E^*} \right) r &= 0. \end{aligned} \quad (15)$$

These equations are linearly dependent on r , so they are always met if accepting:

$$D_2^{(1)} = 0; \quad D_3^{(1)} = 0; \quad D_2^{(2)} = -\frac{2B_1^{(2)} \pi}{E^*}; \quad D_3^{(2)} = -\frac{4A_0^{(2)} \pi}{E^*}. \quad (16)$$

A similar situation occurs in the inner section of the border, so also there the boundary conditions can be satisfied exactly:

$$\begin{aligned} A_0^{(1)}(1 + 2 \ln r_1) + 2B_0^{(1)} + C_0^{(1)} \frac{1}{r_1^2} &= -p_0; & 2A_1^{(1)}r_1 + B_1^{(1)} \frac{1}{r_1} - 2C_1^{(1)} \frac{1}{r_1^3} &= 0; \\ A_0^{(2)}(1 + 2 \ln r_1) + 2B_0^{(2)} + C_0^{(2)} \frac{1}{r_1^2} &= -p_0; & 2A_1^{(2)}r_1 + B_1^{(2)} \frac{1}{r_1} - 2C_1^{(2)} \frac{1}{r_1^3} &= 0. \end{aligned} \quad (17)$$

Therefore, as we have replaced the effect of composite material on the outer part of the section by additional normal stresses that are proportional to the circumferential strain, we cannot meet exactly the boundary conditions on the outer part of the section with the selected stress function. We will then assume that the additional normal stresses do not depend on the angular coordinate. This situation can be obtained, if we fix, in the terms of circumferential strain, the angle $\theta = \gamma_k$, $k = 1, 2$, where γ_1 is selected from the interval $0 \leq \gamma_1 \leq \beta$ in the area Ω_1 , while for area Ω_2 : $\beta \leq \gamma_2 \leq \pi$. We have obtained the following conditions:

$$\begin{aligned} &A_0^{(1)}(1 + 2 \ln(r_2 - \Delta)) + 2B_0^{(1)} + C_0^{(1)} \frac{1}{(r_2 - \Delta)^2} \\ &= \frac{nt}{(r_2 - \Delta)} \left\{ \frac{T}{Lt} + \frac{E_c}{E^*} \left[A_0^{(1)}((3 - v^*) + (2 - 2v^*) \ln(r_2 - \Delta)) + B_0^{(1)}(2 - 2v^*) - C_0^{(1)} \frac{1 + v^*}{(r_2 - \Delta)^2} \right] \right\} \\ &\quad + \frac{ntE_c}{(r_2 - \Delta)E^*} \left\{ A_1^{(1)}(6 - 2v^*)(r_2 - \Delta) + B_1^{(1)}(1 - v^*) \frac{1}{r_2 - \Delta} + C_1^{(1)} \frac{2 + 2v^*}{(r_2 - \Delta)^3} \right\} \cos \gamma_1; \\ 2A_1^{(1)}(r_2 - \Delta) + B_1^{(1)} \frac{1}{r_2 - \Delta} - 2C_1^{(1)} \frac{1}{(r_2 - \Delta)^3} &= 0; \end{aligned} \quad (18)$$

$$\begin{aligned} &A_0^{(2)}(1 + 2 \ln r_2) + 2B_0^{(2)} + C_0^{(2)} \frac{1}{r_2^2} \\ &= \frac{nt}{r_2} \left\{ \frac{T}{Lt} + \frac{E_c}{E^*} \left[A_0^{(2)}((3 - v^*) + (2 - 2v^*) \ln r_2) + B_0^{(2)}(2 - 2v^*) - C_0^{(2)} \frac{1 + v^*}{r_2^2} \right] \right\} \\ &\quad + \frac{ntE_c}{r_2E^*} \left\{ A_1^{(2)}(6 - 2v^*)r_2 + B_1^{(2)}(1 - v^*) \frac{1}{r_2} + C_1^{(2)} \frac{2 + 2v^*}{r_2^3} \right\} \cos \gamma_2; \\ 2A_1^{(2)}r_2 + B_1^{(2)} \frac{1}{r_2} - 2C_1^{(2)} \frac{1}{r_2^3} &= 0. \end{aligned} \quad (19)$$

Before writing the conjugation conditions for the displacements and stresses, it should be noted that the expressions contain nonlinear functions of the radial coordinate. Therefore, it is not possible to satisfy exactly these conditions.

Consequently, we can meet these conditions, on average, i.e., using an integral function. For the displacements, it can be written as

$$\begin{aligned}
 & \int_{r_1}^{r_2-\Delta} \left[A_0^{(1)}((-1-v^*)r + 2(1-v^*)r \ln r) + B_0^{(1)}(2-2v^*)r - C_0^{(1)}\frac{1+v^*}{r} + 2B_1^{(1)}\beta \sin \beta \right. \\
 & \quad \left. + \left[A_1^{(1)}(1-3v^*)r^2 + B_1^{(1)}(1-v^*) \ln r + C_1^{(1)}\frac{1+v^*}{r} \right] \cos \beta + E^*D_1^{(1)} \cos \beta + E^*D_2^{(1)} \sin \beta \right] dr \\
 & = \int_{r_1}^{r_2-\Delta} \left[A_0^{(2)}((-1-v^*)r + 2(1-v^*)r \ln r) + B_0^{(2)}(2-2v^*)r - C_0^{(2)}\frac{1+v^*}{r} + 2B_1^{(2)}\beta \sin \beta \right. \\
 & \quad \left. + \left[A_1^{(2)}(1-3v^*)r^2 + B_1^{(2)}(1-v^*) \ln r + C_1^{(2)}\frac{1+v^*}{r} \right] \cos \beta + E^*D_1^{(2)} \cos \beta + E^*D_2^{(2)} \sin \beta \right] dr;
 \end{aligned} \tag{20}$$

$$\begin{aligned}
 & \int_{r_1}^{r_2-\Delta} \left\{ \left[4A_0^{(1)}\beta r - E^*D_1^{(1)} \sin \beta - E^*D_2^{(1)} \cos \beta + 2B_1^{(1)}(-\beta \cos \beta + \sin \beta) + E^*D_3^{(1)}r \right. \right. \\
 & \quad \left. \left. + \left[A_1^{(1)}(5+v^*)r^2 + B_1^{(1)}(1-v^*)(1-\ln r) + C_1^{(1)}\frac{1+v^*}{r^2} \right] \sin \beta \right\} dr \\
 & = \int_{r_1}^{r_2-\Delta} \left\{ \left[4A_0^{(2)}\beta r - E^*D_1^{(2)} \sin \beta - E^*D_2^{(2)} \cos \beta + 2B_1^{(2)}(-\beta \cos \beta + \sin \beta) + E^*D_3^{(2)}r \right. \right. \\
 & \quad \left. \left. + \left[A_1^{(2)}(5+v^*)r^2 + B_1^{(2)}(1-v^*)(1-\ln r) + C_1^{(2)}\frac{1+v^*}{r^2} \right] \sin \beta \right\} dr,
 \end{aligned} \tag{21}$$

while for the stresses as

$$\begin{aligned}
 & \int_{r_1}^{r_2} \left\{ A_0^{(2)}(3+2 \ln r) + 2B_0^{(2)} - C_0^{(2)}\frac{1}{r^2} + \left(6A_1^{(2)}r + B_1^{(2)}\frac{1}{r} + C_1^{(2)}\frac{2}{r^3} \right) \cos \beta \right\} dr \\
 & = \int_{r_1}^{r_2-\Delta} \left\{ A_0^{(1)}(3+2 \ln r) + 2B_0^{(1)} - C_0^{(1)}\frac{1}{r^2} + \left(6A_1^{(1)}r + B_1^{(1)}\frac{1}{r} + C_1^{(1)}\frac{2}{r^3} \right) \cos \beta \right\} dr \\
 & \quad + \int_{r_2-\Delta}^{r_2} \left\{ \frac{nT}{Lr} + \frac{ntE_c}{rE^*} \left[A_0^{(2)}((3-v^*) + (2-2v^*) \ln r) + B_0^{(2)}(2-2v^*) - C_0^{(2)}\frac{1+v^*}{r^2} \right] \right. \\
 & \quad \left. + \frac{ntE_c}{rE^*} \left[A_1^{(2)}(6-2v^*)r + B_1^{(2)}\frac{1-v^*}{r} + C_1^{(2)}\frac{2+2v^*}{r^3} \right] \cos \beta \right\} dr;
 \end{aligned} \tag{22}$$

$$\int_{r_1}^{r_2} \left\{ A_1^{(2)} 2r + B_1^{(2)} \frac{1}{r} - C_1^{(2)} \frac{1}{r^3} \right\} \sin \beta \, dr = \int_{r_1}^{r_2-\Delta} \left\{ A_1^{(1)} 2r + B_1^{(1)} \frac{1}{r} - C_1^{(1)} \frac{1}{r^3} \right\} \sin \beta \, dr. \tag{23}$$

The fulfillment of the boundary conditions for displacements in the integral meaning leads to the satisfaction of the conditions, just as it happens for a movable hinge. In other words, we have not ruled out the rotation of one region relative to the other. Furthermore, it is easy to see that the conditions on the symmetry axis does not exclude the movement of all sections as a whole along a vertical axis, which also results from the Eqs. (20) and (21), if we take into account Eq. (16). That means that the displacements on the axes are proportional to each other and these equations are linearly dependent. If (20) is multiplied by $\sin \beta$, and (21) by $\cos \beta$ and they are added together, this relationship is obtained in the form of a single equation (which is cumbersome and thus not written here).

On the other hand, for a mobile hinge, even if the conditions of equality for the longitudinal and transversal forces are satisfied, this does not mean that the bending moments are also equal. Therefore, we must add the condition of equality for the bending moments in the conjugation areas. Consequently, another equation is obtained:

$$\begin{aligned} & \int_{r_1}^{r_2} \left\{ A_0^{(2)} (3 + 2 \ln r) + 2B_0^{(2)} - C_0^{(2)} \frac{1}{r^2} + \left(6A_1^{(2)} r + B_1^{(2)} \frac{1}{r} + C_1^{(2)} \frac{2}{r^3} \right) \cos \beta \right\} r dr = \\ & \int_{r_1}^{r_2-\Delta} \left\{ A_0^{(1)} (3 + 2 \ln r) + 2B_0^{(1)} - C_0^{(1)} \frac{1}{r^2} + \left(6A_1^{(1)} r + B_1^{(1)} \frac{1}{r} + C_1^{(1)} \frac{2}{r^3} \right) \cos \beta \right\} r dr \\ & + \int_{r_2-\Delta}^{r_2} \left\{ \frac{nT}{Lr} + \frac{nE_c}{rE^*} \left[A_0^{(2)} ((3 - v^*) + (2 - 2v^*) \ln r) + B_0^{(2)} (2 - 2v^*) - C_0^{(2)} \frac{1 + v^*}{r^2} \right] \right. \\ & \left. + \frac{nE_c}{rE^*} \left[A_1^{(2)} (6 - 2v^*) r + B_1^{(2)} \frac{1 - v^*}{r} + C_1^{(2)} \frac{2 + 2v^*}{r^3} \right] \cos \beta \right\} r dr. \end{aligned} \tag{24}$$

As a result, we have a system of 12 linear algebraic equations with 12 unknowns:

$$\mathbf{A} \cdot \mathbf{X} = \mathbf{B}, \tag{25}$$

in which the vector of unknowns is

$$\mathbf{X} = \left\{ A_0^{(1)} B_0^{(1)} C_0^{(1)} A_1^{(1)} B_1^{(1)} C_1^{(1)} A_0^{(2)} B_0^{(2)} C_0^{(2)} A_1^{(2)} B_1^{(2)} C_1^{(2)} \right\}^T \tag{26}$$

and the vector of right parts is

$$\mathbf{B} = \{b_1 \ b_2 \ b_3 \ 0 \ 0 \ 0 \ b_7 \ b_8 \ b_9 \ 0 \ 0 \ 0\}^T, \tag{27}$$

where

$$b_1 = -p_0; \ b_2 = -\frac{nT}{(r_2-\Delta)L}; \ b_3 = -\frac{nT}{L}(\ln r_2 - \ln(r_2 - \Delta));$$

$$b_7 = -p_0; \ b_8 = -\frac{nT}{r_2L}; \ b_9 = -\frac{nT}{L}\Delta.$$

The matrix **A** has the following structure:

$$\mathbf{A} = \begin{pmatrix} a_{11} & a_{12} & a_{13} & 0 & 0 & 0 & 0 & 0 & 0 & 0 & 0 & 0 & 0 \\ a_{21} & a_{22} & a_{23} & 0 & 0 & 0 & 0 & 0 & 0 & 0 & 0 & 0 & 0 \\ a_{31} & a_{32} & a_{33} & a_{34} & a_{35} & a_{36} & a_{37} & a_{38} & a_{39} & a_{3,10} & a_{3,11} & a_{3,12} \\ 0 & 0 & 0 & a_{44} & a_{45} & a_{46} & 0 & 0 & 0 & a_{4,10} & a_{4,11} & a_{4,12} \\ 0 & 0 & 0 & a_{54} & a_{55} & a_{56} & 0 & 0 & 0 & 0 & 0 & 0 \\ 0 & 0 & 0 & a_{64} & a_{65} & a_{66} & 0 & 0 & 0 & 0 & 0 & 0 \\ 0 & 0 & 0 & 0 & 0 & 0 & a_{77} & a_{78} & a_{79} & 0 & 0 & 0 \\ 0 & 0 & 0 & 0 & 0 & 0 & a_{87} & a_{88} & a_{89} & a_{8,10} & a_{8,11} & a_{8,12} \\ a_{91} & a_{92} & a_{93} & a_{94} & a_{95} & a_{96} & a_{97} & a_{98} & a_{99} & a_{9,10} & a_{9,11} & a_{9,12} \\ a_{10,1} & a_{10,2} & a_{10,3} & a_{10,4} & a_{10,5} & a_{10,6} & a_{10,7} & a_{10,8} & a_{10,9} & a_{10,10} & a_{10,11} & a_{10,12} \\ 0 & 0 & 0 & 0 & 0 & 0 & 0 & 0 & 0 & a_{11,10} & a_{11,11} & a_{11,12} \\ 0 & 0 & 0 & 0 & 0 & 0 & 0 & 0 & 0 & a_{12,10} & a_{12,11} & a_{12,12} \end{pmatrix} \tag{28}$$

After solving the system of algebraic equations, all unknown quantities will be determined. These values will allow us to define all the characteristics of interest in the pipe volume and on the surface. In particular, we can calculate the von Mises combined stress intensity, as follows [3]:

$$\sigma_M = \frac{1}{\sqrt{2}} \sqrt{(\sigma_{rr} - \sigma_{\theta\theta})^2 + (\sigma_{\theta\theta} - \sigma_{zz})^2 + (\sigma_{zz} - \sigma_{rr})^2 + 6(\sigma_{r\theta}^2 + \sigma_{\theta z}^2 + \sigma_{rz}^2)}. \tag{29}$$

5 Computational Experiments

Before analyzing the obtained stress state of the repaired pipeline, we have to evaluate the results of the proposed model qualitatively and quantitatively. To this purpose, we have conducted a series of numerical experiments and compared the results with similar ones obtained using the finite elements method. As an example,

we have used the finite element model presented in [4], which allows for the determination of the stress–strain state in the damaged area of a pipe in a three-dimensional case. In particular, we compared the von Mises combined stress at the outer side of the pipe along the entire length of the defect.

The following values have been used for the problem parameters of our numerical experiments, in accordance with [4]: $E = 210$ GPa and $\nu = 0.31$ are the elastic characteristics of the pipe material, $\sigma_T = 360$ MPa is the specified yield strength of the pipe material (corresponding to a X52 steel), $p_0 = 7$ MPa is the internal pressure, Δ is the VSD depth (varying between 0 and 6 mm), $\beta = 26.96^\circ$ is the angle corresponding to half of the VSD width, s (equal to 152.4 mm, see Fig. 1). The geometrical dimensions selected for the pipe are: an external diameter of 323.9 mm; a pipe wall thickness of 8 mm, i.e. $r_2 = 161.95$ mm, $r_1 = 153.95$ mm. For the composite material, the following parameters were adopted: $t = 0.75$ mm is the thickness of a composite layer (including the adhesive layers used for bonding), $n = 4$ is the number of composite layers, $T = 100$ N is the tensile force on one layer of composite wrap during winding, $L = 440$ mm is the composite wrap length, $E_c = 30$ GPa is the elastic modulus of the composite materials in the circumferential direction.

It should be also noted that, the angles γ_1 and γ_2 were introduced into Eqs. (18) and (19), and they must be set for the numerical analysis. Following the physical sense, we can observe that, for a small section of the damaged zone in the circumferential direction, the strains in the composite wrap will be maximized. They will be approximately equal to the greatest deformation that occurs in middle of the defect. Therefore, it is necessary to set $\gamma_1 = 0$. The greatest circumferential strain of the composite wrap should be fully encountered in the stress state from the damaged area. Numerical experiments also confirmed such assumption. The value of γ_2 does not affect the calculation results, which is also consistent with the physical meaning of the problem (beyond the damaged area, a circumferential strain of the composite material wrap is approximately the same). Therefore, we set $\gamma_2 = \beta$.

Before assessing the von Mises stresses, we have verified the accuracy of our model for the simplest problem of a ring affected by an internal stress (the task of Lamé). This problem has an exact solution, expressed by the circumferential normal stresses within the ring, $\sigma_{\theta\theta}|_{r_1} = \frac{r_2^2 + r_1^2}{r_2^2 - r_1^2} p_0$, and at the outside, $\sigma_{\theta\theta}|_{r_2} = \frac{2r_1^2}{r_2^2 - r_1^2} p_0$. If, in our model, we accept $\Delta = 0$, $T = 0$, $E_c = 0$, then we obtain $\sigma_{\theta\theta}|_{r_1} = 357.784$ MPa, $\sigma_{\theta\theta}|_{r_2} = 324.68$ MPa that coincide with the exact solution. Then, considering the case when the pipe has no defect, but the composite material is attached to the pipe, we have obtained $\sigma_{\theta\theta}|_{r_1} = 132.044$ MPa, $\sigma_{\theta\theta}|_{r_2} = 125.345$ MPa. It is clear that the stresses are smaller by almost two and half times, which indicate that the program takes into account the effect of the coupling between the composite material and the pipe steel.

The next step for the verification of our model was to compare it with the numerical calculations of von Mises combined stress, σ_M . For this purpose, we have used the data from [4], where these stresses are studied in detail on the surface of the damaged area with a VSD depth $\Delta = 6$ mm. In particular, we have considered

the von Mises combined stress distribution in the circumferential direction from the middle region of the damaged area, as presented in [4], and shown in Fig. 6 (which include also the case of the unrepaired pipe). In order to assess the qualitative behavior of the unknown functions and to quantify the results of the research, we have carried out a similar numerical experiment and compared the calculations result. The von Mises stress distribution obtained by using our model is present in Fig. 7.

In the considered case, as also observed in other cases, the maximum stress is reached at the edge. The numerical values of maximum stress, as obtained in [4], are as follows: $\sigma_{M \max} = 347.42 \text{ MPa}$ or $\sigma_{M \max} = 348.03 \text{ MPa}$. Application of our model defines $\sigma_M / \sigma_T = 0.954092$. Taking into account that $\sigma_T = 360 \text{ MPa}$, we find that $\sigma_{M \max} = 343.47 \text{ MPa}$. Comparing these results, we can state that the difference does not exceed 1.2%. However, the stress distribution in circumferential direction differs significantly. While in [4], the stress underneath the composite

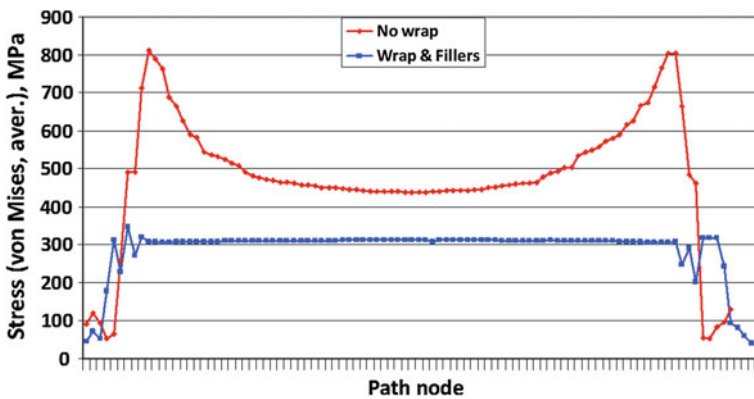
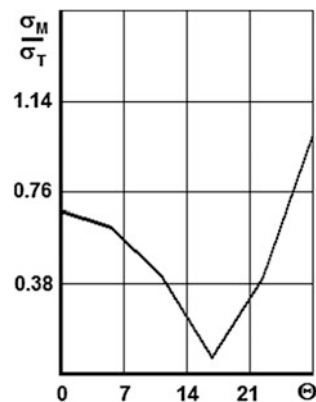


Fig. 6 FEM analysis results

Fig. 7 Analytical results



material is found almost constant, in our model, such constancy is not observed. In the central area, a difference between the results of more than 22% is observed. Furthermore, our calculations indicate a conspicuous minimum, which is not observed by using the finite element approach.

However, it is necessary to make the following remark. The calculation results have been compared for a defect depth $\Delta = 6$ mm. Both in our calculations and in the calculations from [4], the maximum stress is almost equal to the yield strength. Obviously, in numerical experiments, this circumstance does not play a significant role. However, in a real situation, such a stress is not acceptable from the viewpoint of the structural strength and the normal pipe operation. By virtue of this, our further investigations were carried out for such values of the geometric parameter Δ selected so the stresses are within the allowable values.

The following numerical experiments are connected with the study of the influence of the defect depth on von Mises stress. Obviously, for a full pipe without defects, the major stresses affecting its strength are the circumferential and axial normal stresses. These stresses are larger on the inner surface of the pipe. The occurrence of the defect breaks the uniform axial solutions, causing stress concentration effects in the corner points. After that, we will examine the impact of the defect on the same strength characteristic. In literature, there is quite a wide variation in the data regarding the strength properties of the pipe materials. As mentioned above, we have selected the yield strength of $\sigma_T = 360$ MPa. In addition, as already shown in Fig. 7, we have introduced the relative expression of von Mises stress, σ_M/σ_T .

Therefore, it is quite normal to define first the relative von Mises stress for the pipe without defect, but with composite wrap applied on it. We have obtained $\sigma_M/\sigma_T = 0.169834$ at the inner surface of the pipe, and $\sigma_M/\sigma_T = 0.154108$ on the outer surface, for the geometrical and physical parameters mentioned above. Figure 8 shows the dependence of the relative von Mises stress along the circumferential coordinates inside the pipe for different values of the defect depth. The value of the circumferential coordinate varies from 0 to the half angle of the defect, $\beta = 26.96^\circ$.

Figure 9 shows the same dependencies, but on the outer surface of the pipe. It is interesting to note that the maximum von Mises combined stress on the inside

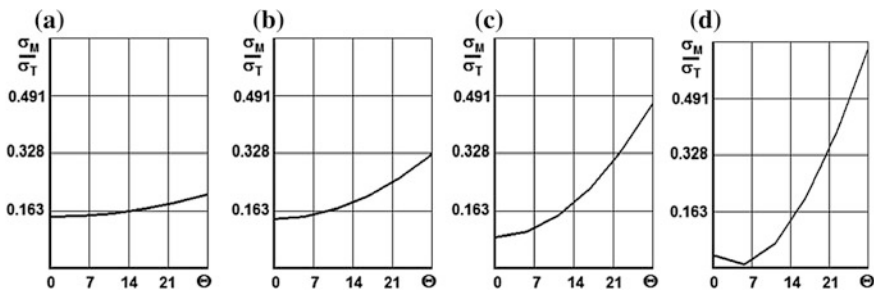


Fig. 8 Relative von Mises stress distribution on the inner surface of the pipe for various defect depths: **a** $\Delta = 1$ mm; **b** $\Delta = 2$ mm; **c** $\Delta = 3$ mm; **d** $\Delta = 4$ mm

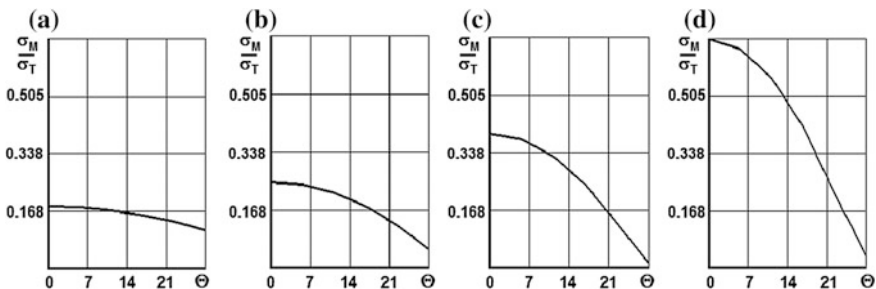


Fig. 9 Relative von Mises stress distribution on the outer surface of the pipe for various defect depths: **a** $\Delta = 1$ mm; **b** $\Delta = 2$ mm; **c** $\Delta = 3$ mm; **d** $\Delta = 4$ mm

surface of the pipe cross-section appears in the axis of symmetry. However, the maximum values of von Mises stresses on the outer surface of the pipe appear at the corner point. Obviously, the larger is the defect, the greater are the von Mises stresses.

Another interesting remark is that the numerical values of the maximum stresses inside and outside of the pipe sections are virtually identical. Thus, it can be noted that the occurrence of the concentrator at a corner point on the outer contour of the pipe cross-section leads to a stress concentration effect that is not less than the maximum stress on the inner surface.

6 Conclusions

The given chapter presents one of the simplest approaches, using an analytical method, for solving the problem of stress concentration in a damaged pipeline area with a VSD, repaired with a composite material wrap. A mathematical model based on the theory of elasticity for the two-dimensional case has been built to assess the strength characteristics in the cross-section of the pipe. The influence of the composite wrap has been modeled by defining two additional normal stresses, the first one proportional to the pretension of the composite wrap, and the second one connected with the circumferential strain of the pipe. In the latter case, a value for the modulus of elasticity along the circumferential coordinate of the composite material was used. We have made assumptions that allowed us to apply the equations of the plane theory of elasticity. Using the symmetry of the cross-section and of the external loads, we have introduced in the model only half of the section of the pipeline from the damage zone. This area is divided into two subregions by a radial cross-section. To solve the problem, we have chosen one stress function for each of the two areas. The type of stress functions was selected so that it was possible to find both normal and shear stresses.

The main difficulty of solving this problem is to satisfy the boundary conditions at the interfacing line of the boundaries areas. This problem was solved only in

integral meaning. The latter circumstance has inevitably led to the fact that the displacements of areas as absolutely rigid body in the coupling zone, both in radial and circumferential direction, are proportional to each other. In addition, it was necessary to introduce an additional equation of the equality of the moments in the interface areas. As a result, the problem is reduced to solving a system of linear algebraic equations of twelfth order. The strength characteristics such as von Mises combined stresses were numerically investigated on both the inside and the outside surfaces of the pipe. It is shown that in the concentration areas, stresses are comparable with the maximum stresses on the pipe inner surface.

The proposed model can be used to assess the pipeline remaining strength in the area, where repair works have been carried out using a composite material system to reduce the effect of a VSD placed on the external surface of the pipe.

Acknowledgements This research was supported by the Russian Ministry of Education and Science, project No. 0110-11/2017-48 (9.4726.2017) and the Russian Foundation for Basic Research, project No. 16-08-00852.

References

1. *Repair Guide for Defective Pipes of Main Gas Pipelines of Polymer Composite Materials*. VSN 39-1.10-001-99. Moscow (2000) (In Russian)
2. S.P. Demidov, *Theory of Elasticity: A Textbook for Institutions* (High School, Moscow, 1979). (In Russian)
3. G.S. Pisarenko, N.S. Mozharovsky, *Equations and Boundary Value Problems of the Theory of Plasticity and Creep. Reference Manual* (Naukova Dumka, Kiev, 1981). (In Russian)
4. M.I. Chebakov, A. Dumitrescu, I. Lambrescu, R. Nedin, ed. by E. Barkanov, M. Mikovski and V. Sergienko, *Innovative Solutions in Repair of Gas and Oil Pipelines*. Bulgarian Society for Non-destructive Testing Publishers, Sofia, vol. 228 (2016)

Optimal Design of Composite Repair Systems of Transmission Pipelines

Evgeny N. Barkanov, I. Lvov and P. Akishin

Abstract Optimisation methodology for composite repair systems of transmission pipelines with volumetric surface defects is presented. Due to large dimension of the numerical tasks to be solved, this methodology is developed employing the method of experimental design and response surface technique. To bring an efficiency of damaged section up to the level of undamaged pipeline, two optimisation problems based on equivalently resistant (equiresistant) and minimum weight designs are formulated and solved in the present study. Features, advantages and limitations of both approaches are discussed in their applicability for the optimal design of composite repair systems of transmission pipelines.

Keywords Pipe · Volumetric surface defect · Composite repair · Optimisation

1 Introduction

Transmission pipelines have supreme significance for an effective functioning of industry providing European markets with energy resources: crude oil, natural gas and liquid petroleum products. For this reason, provision of their continuous work and accident-free operation is very important. Unfortunately, the volumetric surface defects arising in the result of corrosion or erosion–corrosion processes considerably decrease the pipeline strength. Likely, application of composite materials in the advanced repair systems of damaged pipelines gives the possibility to make the repair more effective and does not require a stop of the pipeline operation.

The original version of the book was revised: Incorrect author names have been corrected. The erratum to the book is available at https://doi.org/10.1007/978-3-319-56579-8_28

E.N. Barkanov (✉) · P. Akishin
Riga Technical University, Riga, Latvia
e-mail: barkanov@latnet.lv

I. Lvov
National Technical University, Kharkiv Polytechnical Institute, Kharkiv, Ukraine

© Springer International Publishing AG 2018
E.N. Barkanov et al. (eds.), *Non-destructive Testing and Repair of Pipelines*,
Engineering Materials, DOI 10.1007/978-3-319-56579-8_24

To obtain an effective repair of transmission pipelines with volumetric surface defects, two parameters of composite repair systems are mostly examined: thickness and width of the applied composite bandage. These values could be determined by using the following standards [1, 2]. An application of these standards for the design of composite repair systems of damaged pipelines is demonstrated in papers [3, 4]. Additionally, the thickness of composite bandage could be estimated using the results of parametric studies carried out for different pipe diameters [5], defect dimensions [6] and inner pressures [7]. Since the width of composite bandage has negligible influence on the stress state in the damaged area, it is estimated mostly by the developed standards [1, 2].

It is necessary to note that only investigation of the joint influence of both geometrical parameters of the composite bandage on the strength properties of repair system could provide an optimal solution. For this reason, an optimisation methodology based on the planning of experiments and response surface technique is developed for the optimal design of composite repair systems of transmission pipelines. Two optimisation problems based on equiresistant and minimum weight designs are formulated and solved in the present study to bring an efficiency of damaged section up to the level of undamaged pipeline. Finally, two approaches are compared and their advantages and limitations are discussed in applicability for the optimal design of composite repair systems of transmission pipelines.

2 Optimisation Methodology

Due to large dimension of the numerical problems solved, an optimisation methodology is developed employing the method of experimental design [8] and response surface technique [9]. This methodology is a collection of mathematical and statistical techniques that are useful for the modelling and analysis of problems in which a response of interest is influenced by several variables and the objective is to optimise this response. Optimisation procedure based on experimental design is not only an effective tool for the optimum design of different systems and processes requiring computationally expensive analyses but it also easily combines modelling and optimisation stages and requires less intervention from an analyst in comparison with other approaches. Moreover, this approach is general in the sense that it permits to optimise any systems or processes under arbitrary conditions with respect to any objective function (e.g. performance, durability, integrity, reliability and cost) taking into account all practical requirements [10–12]. An engineering approach of optimisation based on experimental design and response surface technique is presented in Fig. 1. It is necessary to note that in each of these stages it is possible to solve a problem by different methods.

2.1 Experimental Design

The plan of experiments can be obtained by different methods: Factorial, D-Optimal, Latin Hypercube, Central Composite, Box–Behnken, Orthogonal

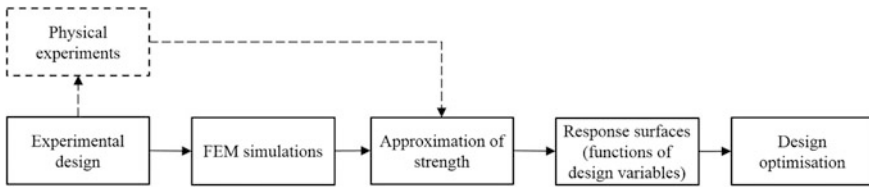


Fig. 1 Optimisation process

Array, Uniform Design, Orthogonal Latin Hypercube, Minimal MSD, MMSD Latin Hypercube, Combined Latin Hypercube D-Optimal, etc. [8]. Then numerical calculations and/or physical experiments are carried out in these points. It is well known that, if for global approximations it is planned to use the second-order polynomial functions, the D-Optimal experimental design is the most suitable, and if an optimisation problem contains the discrete and continuous design variables, the Combined Latin Hypercube D-Optimal experimental design should be chosen [13]. The minimal number of design experiments in the optimisation problem is determined in this case as $n = 2L$, where $L = (k + 1)(k + 2)/2$ and k is the number of design parameters.

2.2 Response Surface Technique

Different approximation technique can be applied for the numerical and/or physical experiments carried out in the points of the developed plan of experiments. There are Polynomial (Global), Neural Networks, Radial Basis Functions, Kriging, Splines, Rational Functions, etc. [9]. Approximations can be obtained using a conventional un-weighted least square estimation with an elimination of some points and can be performed by the second-order polynomials:

$$\bar{F}(x) = \beta_0 + \sum_{i=1}^K \beta_i x_i + \sum_{i=1}^K \sum_{j=i}^K \beta_{ij} x_i x_j \tag{1}$$

The error of approximation is calculated by the following expressions:

$$\sigma_{\text{err}} = \frac{\sum_{i=1}^N (F(x^i) - \bar{F}(x^i))^2}{N}, \quad \sigma_{\text{err}}^0 = \sqrt{\frac{\sum_{i=1}^N (F(x^i) - \bar{F}(x^i))^2}{N - L}} \tag{2}$$

where σ_{err} is the mean squared error, σ_{err}^0 is the standard deviation, $F(x^i)$ and $\bar{F}(x^i)$ are the values of original and approximating functions in the sample point x^i of experimental design, and N is the number of points used for an approximation. The

relative error is determined relatively to a diapason of the approximating function in the domain of interests:

$$\sigma_{\text{err}}^r = \frac{100\sigma}{A_F} \quad (3)$$

where $A_F = \max_{i=1,2,\dots,N} F(x_i) - \min_{i=1,2,\dots,N} F(x_i)$.

2.3 Nonlinear Optimisation

The constrained nonlinear optimisation problem can be written in the following form:

$$\begin{aligned} \min F(x); \quad H_i(x) \geq 0; \quad G_j(x) = 0 \\ i = 1, 2, \dots, I; \quad j = 1, 2, \dots, J \end{aligned} \quad (4)$$

where I and J are the numbers of inequality and equality constraints. This problem is replaced with the unconstrained minimisation problem, where constraints are taken into account with the penalty functions. New version of random search method [14] is used for a solution of the formulated optimisation problems.

3 Finite Element Modelling

An optimal design of composite repair systems is demonstrated on the corroded section of gas transmission pipe with outer diameter of 220 mm, wall thickness of 6 mm and length of 953 mm ramped from both sides with a cap as presented in Fig. 2. The repaired pipe was made of Steel 20 with the mechanical properties given in Table 1. The volumetric surface defect locates on the outer surface of pipe (Fig. 2) and has the following dimensions: 102 (in annular) \times 130 (in axial) \times 3.3 (in depth) mm. The pipe with defect is repaired to bring an efficiency of damaged section up to the level of undamaged pipe without any plastic deformations. For this purpose, the defect is filled by the filler and covered by the composite bandage with the mechanical material properties, presented in Tables 2 and 3, respectively. Finally, the repaired pipe section is subjected to the inner pressure of 3.34 MPa.

To define stress field in the examined pipe section under applied inner pressure, the finite element linear static analysis is applied in the points of the developed plan of experiments. 3D finite-element model of the repaired pipe (Fig. 3) is built using ANSYS code [15], where all the components of the composite repair system are modelled by the 3D 8 nodes structural solid-elements SOLID185. Due to the large difference between material moduli of different components, rigorous convergence

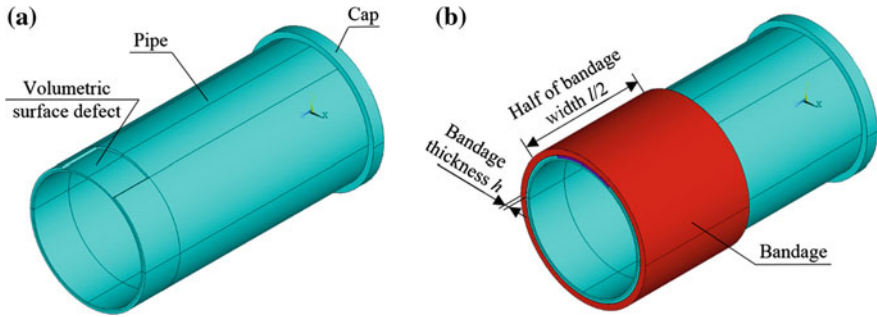


Fig. 2 Half of pipe section: **a** with volumetric surface defect, **b** with composite bandage

Table 1 Mechanical properties of steel 20

Yield strength σ_Y (MPa)		Ultimate tensile strength σ_T (MPa)		Relative extension δ (%)		Young modulus E (MPa)	Poisson ratio ν
Annular	Axial	Annular	Axial	Annular	Axial		
305	314	474.76	461.40	33.13	40.97	2.0×10^5	0.3

Table 2 Mechanical properties of filler

Ultimate tensile strength σ_T (MPa)	Young modulus E (MPa)	Poisson ratio ν
80	4500	0.5

Table 3 Mechanical properties of the separate layer of composite bandage

Ultimate tensile strength σ_T (MPa)		Young modulus E (MPa)		Poisson ratio ν
Annular	Axial	Annular	Axial	
678.5	75	48,465.21	3000	0.17

study was performed. From this study (Fig. 4) and following to the multiplicity of the bandage width, the element edge size of 2 mm was chosen. This value gives the possibility to carry out the linear static analysis with regular finite element mesh for all the points from the plan of experiments.

4 Formulation of Optimisation Problems

Two optimisation problems based on equiresistant and minimum weight designs are formulated for the composite repair systems of transmission pipelines. Both of them have two design parameters: thickness h and width l of the applied composite bandage. Moreover, one design parameter (width) is examined as continuous, but

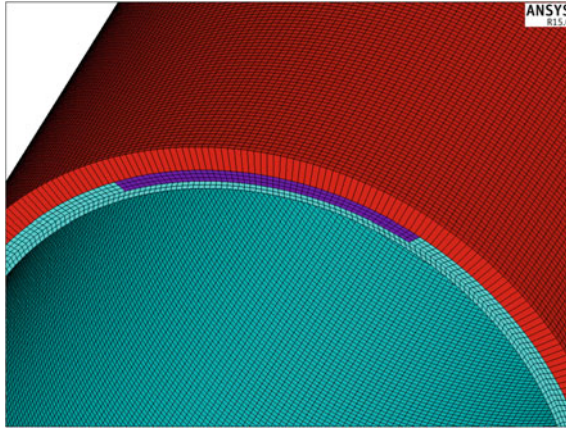


Fig. 3 Finite element model

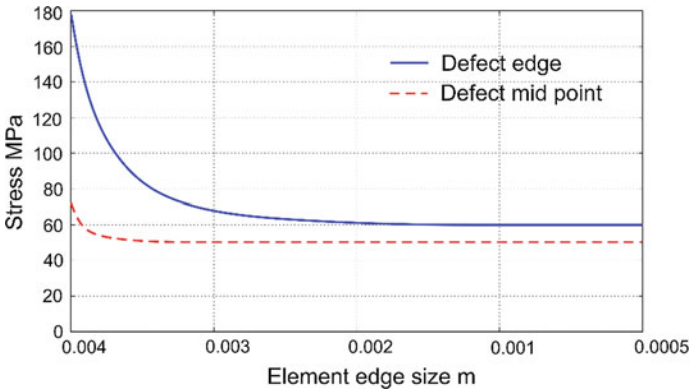


Fig. 4 Solution convergence

another (thickness)—as discrete value due to the layered nature of composite. These design parameters are searched in the following limits:

$$\begin{aligned} 15 \leq k \leq 34 \\ 140 \leq l \leq 400 \text{ mm} \end{aligned} \quad (5)$$

where $k = h/t$ is the number of layers in composite bandage and $t = 0.39$ mm is the thickness of separate layer.

In the first optimisation problem, the objective function is defined by the following way to provide the same strength of the repaired part and undamaged area of the pipeline:

$$Q = \left(\frac{\sigma_{\max} - \sigma_0}{\sigma_0} \right)^2 \Rightarrow \min \tag{6}$$

where σ_{\max} is the maximal stress in the zone of volumetric surface defect and $\sigma_0 = 61.2$ MPa is the stress of undamaged area under applied inner pressure of 3.34 MPa.

The second optimisation problem is formulated as the minimum weight design problem in term of bandage volume:

$$V = \pi lh(h + d) \Rightarrow \min \tag{7}$$

where d is the outer diameter of pipe. For the second examined problem, the following constraint should be also satisfied:

$$\sigma_{\max} \leq \sigma_0 \tag{8}$$

5 Solution of Optimisation Problems

At the beginning of optimisation process, the stress field is calculated in 20 points of experimental design generated by the minimal square distance Latin Hypercube sampling method [16] since the formulated optimisation problems contain the discrete and continuous design variables. The minimal number of sampling points for the second-order polynomial with n variables (design parameters) is $(n + 1)(n + 2)/2$. It is common practice to use more than two times greater number of points. Because the finite element calculations in the linear static analysis are not

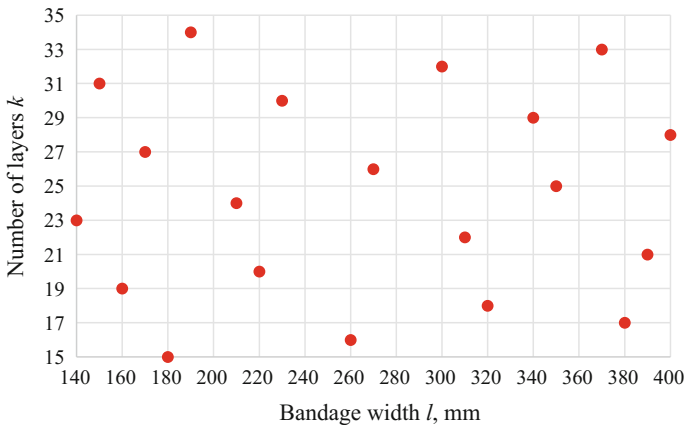


Fig. 5 Plan of experiments

time consuming, 20 sampling points were used. The corresponding plan of experiments is presented in Fig. 5.

5.1 Equiresistant Design

Using results of the finite element analysis and the conventional un-weighted least square method [9], the second-order polynomial was obtained with the standard deviation of $\sigma_{\text{err}}^0 = 0.009121$ for an approximation of the objective function described by Eq. (6):

$$Q = 0.755 + 0.885 \times 10^{-3}k^2 + 0.504 \times 10^{-9}l^2 + 0.572 \times 10^{-5}kl - 0.0513k - 0.186 \times 10^{-3}l \quad (9)$$

The corresponding response surface is presented in Fig. 6a, where it is seen that the bandage width has no significant influence on the objective function especially in the points closed to the optimal solution.

Then optimisation problem is solved by the random search method [17], using EDAOpt optimisation software [18] with the purpose of minimising the objective function presented by Eq. (9). The applied algorithm is an improved multi-start algorithm with a generation of new start points by exchange of randomly selected point coordinates from the previously found best solution. The EDAOpt optimisation algorithm utilises only Latin Hypercube type sample calculations with a sequential reduction of the neighbourhood size (nearly feasible region). In reality,

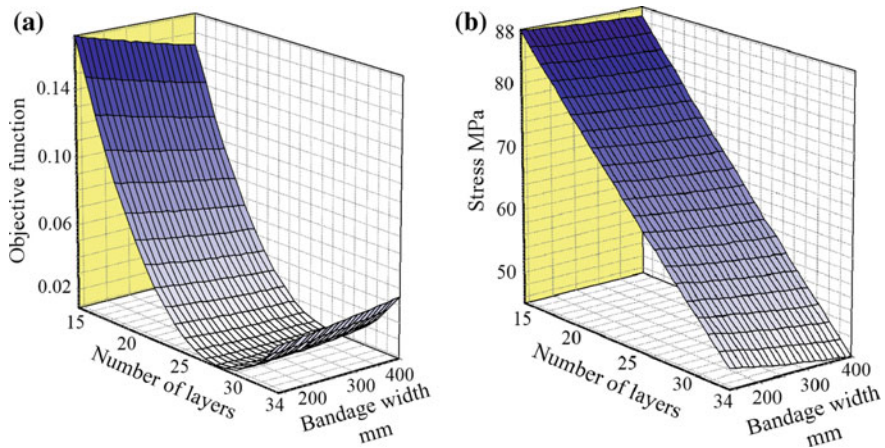


Fig. 6 Response surfaces: **a** dependence of objective function on bandage thickness and width, **b** dependence of maximal stresses on bandage thickness and width

Table 4 Optimal results

Optimisation problem	Bandage parameters		Bandage volume V (cm ³)	Stress in pipe with repair		Stress in pipe without damage σ_0 (MPa)
	Width l (mm)	Number of layers k		Approximation σ_{max} (MPa)	FEM σ_{max} (MPa)	
Equirestant design	260	28	2060	61.2	54.7	61.2
Minimum weight design	140	28	1109	60.4	55.3	

the search region is moved after each improvement of the objective function and its size is decreased after unsuccessful calculation of the given number of testing points. The treatment values for discrete variables are obtained as a nearest discrete level of Latin Hypercube sample. It is necessary to note that there are not any considerable differences between continuous and discrete variables in this algorithm. Practically, it may be assumed that the continuous variable is the same discrete variable with a large number of levels. In practice, 1001 levels are used as the number of levels for continuous variables. However, the optimisation process is organised in such a way that even for the continuous variables the initial number of levels is set as 3 or 5, the optimum is found and then the number of levels is increased. More information on the Latin Hypercube sampling and applied random search method used in the present study is given in [18]. The paper [14] presents a short review of the global optimisation methods and comparison of the appropriate software by solving a set of recognised optimisation test problems.

The optimisation results, bandage thickness and width, are given in Table 4. Since the response surfaces are used instead of the original functions, optimal results are checked using ANSYS finite element solution. Good coincidence of results is observed for the finite element analysis and developed approximations. The stress field obtained for the present optimal design of composite repair system of the examined pipe section is presented in Fig. 7a.

5.2 Minimum Weight Design

After finite element calculations, the second-order polynomial function was obtained with the standard deviation of $\sigma_{err}^0 = 2.5460$ MPa for the maximal stresses determined at the edge points of the defect using the conventional un-weighted least square method [9]:

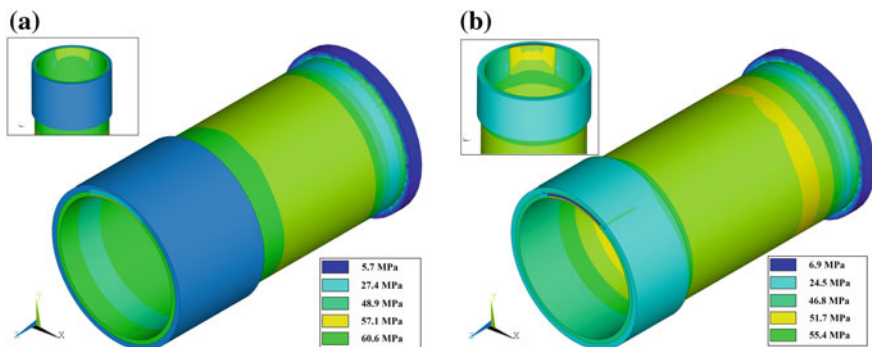


Fig. 7 Stress fields obtained by using: **a** equirestant design, **b** minimum weight design

$$\sigma_{\max} = 123.61 - 2.357k + 0.00604l + 0.00636k^2 - 0.000408kl - 0.0000133l^2 \quad (10)$$

The corresponding response surface is presented in Fig. 6b. It is seen that the bandage thickness has more significant influence on the maximal stresses than the bandage width.

Then the minimum weight optimisation problem Eqs. (7) and (8) is solved by the same way as described in paragraph 5.1 using the random search method [17] and EDAOpt optimisation software [18]. The optimal results are presented in Table 4 together with the results of equirestant design. Since the response surfaces are used instead of the original functions, optimal results are checked using ANSYS finite element solution. It is seen from Table 4 that good coincidence between finite element and approximation results was obtained. The stress field determined for the minimum weight optimal design of composite repair system of the examined pipe section is presented in Fig. 7b.

5.3 Comparison of Optimal Results

Table 4 shows that optimal solution obtained with the minimum weight design formulation is considerably more effective (85.8%) than solution, obtained with the equirestant design, since it requires less composite material for the repair system. This could be explained by an insensitivity of the objective function from the bandage width in the area closed to the optimal solution in the equirestant design (see Eq. 9; Fig. 6a). At the same time, the bandage width enters directly into the objective function presenting the bandage volume, Eq. (7), which is minimised in the minimum weight design problem that gives the possibility to estimate the bandage width more accurately. It is necessary to note that the obtained bandage thickness is the same for both formulated optimisation problems and maximal

stresses in the repaired pipe do not exceed corresponding values of the undamaged pipe.

Since only linear behaviour of construction is examined, optimal solutions obtained for the applied inner pressure (3.34 MPa) could be used also for other values of pressure. The highest level of pressure in this case is limited by the arising stresses in the undamaged pipe, which should be lower than the yield strength of steel material (Table 1). In other words, obtained optimal solutions remain in force for the inner pressure levels less than 16.64 MPa.

6 Conclusion

Two optimisation problems based on equiresistant and minimum weight designs were formulated and solved to bring an efficiency of damaged section up to the level of undamaged pipeline. It was demonstrated that minimum weight design gives more effective and accurate repair solution since the bandage width, which has insignificant impact on the stress state in the damaged zone, enters directly into the objective function in the second optimisation problem. For this reason, the minimum weight design formulation is recommended for the optimal design problems of composite repair systems of transmission pipelines with volumetric surface defects.

References

1. ISO 24817:2015: *Petroleum, Petrochemical and Natural Gas Industries—Composite Repairs for Pipeworks—Qualification and Design, Installation, Testing and Inspection* (2015)
2. ASME PCC-2-2015: *Repair of Pressure Equipment and Piping* (2015)
3. P.H. Chan, K.Y. Tshai, M. Johnson, S. Li, *Compos. Struct.* **133**, 312 (2015)
4. A. Chris, J. Souza, C. Whalen, in *Proceedings of the ASME 2014 Pressure Vessels & Piping Conference*. Anaheim, California (2014)
5. V. Orlov, *Procedia Eng.* **165**, 1168 (2016)
6. A. Kovalska, M. Eiduks, in *Proceedings of the 9th International DAAAM Baltic Conference Industrial Engineering*. Tallinn, Estonia (2014)
7. A. Chris, L. Cercone, J. Lockwood, in *Proceedings of the 27th International Conference on Offshore Mechanics and Arctic Engineering*. Estoril, Portugal (2008)
8. C.F.J. Wu, M. Hamada, *Experiments: Planning, Analysis, and Parameter Design Optimisation* (Wiley, New York, 2000)
9. R.H. Myers, D.C. Montgomery, *Response Surface Methodology: Process and Product Optimisation Using Designed Experiments* (Wiley, New York, 2002)
10. E.N. Barkanov, R.B. Rikards, A.K. Chate, *Mech. Compos. Mat.* **1**, 485 (1993)
11. E. Barkanov, S. Gluhih, A. Kovalov, *Mech. Adv. Mat. Struct.* **15**(3–4), 325 (2008)
12. E. Barkanov, E. Eglitis, F. Almeida, M.C. Bowering, G. Watson, *Eng. Optim.* **48**(9), 1618 (2016)
13. J. Auzins, in *Proceedings of the 10th AIAA/ISSMO Multidisciplinary Analysis and Optimisation Conference*. Albany, New York, AIAA 2004–4578 (2004)

14. A. Janushevskis, T. Akinfiev, J. Auzins, A. Boyko, Proc. Est. Acad. Sci. Eng. **10**(4), 236 (2004)
15. *ANSYS User's Manual*. ANSYS, Inc. (2016)
16. J.C. Helton, F.J. Davis, Reliab. Eng. Syst. Saf. **81**, 23 (2003)
17. S.S. Rao, *Engineering Optimisation: Theory and Practice* (Wiley, New York, 2009)
18. J. Auzins, A. Janushevskis, J. Janushevskis, E. Skukis, in *Proceedings of the International Conference on Engineering and Applied Sciences Optimisation*. Kos Island, Greece (2014)

Part VI
Testing of Advanced Composite Repair
Systems of Transmission Pipelines

Development of an Experimental Programme for Industrial Approbation

Gh. Zecheru, Andrei Dumitrescu, P. Yukhymets
and R.I. Dmytriienko

Abstract This chapter describes the planning and development of an experimental programme performed by the authors, with the aim of studying the reinforcement (consolidation) effects of a given repair system using composite material wraps for damaged transmission pipelines (intended for petroleum, liquid petroleum products or natural gas), with defects of the type metal loss (also named volumetric surface defects, VSDs). Such programme could be applied to any type of advanced pipeline repair system with composite wraps in view of its qualification and industrial approbation. The results (briefly described in Sect. 2) of experimental tests executed within previous research activities together with the necessity to validate numerical methods developed for the simulation of composite repair systems have emphasized the need to define and perform a new set of tests for such repair systems. The selection of the materials (pipe steel, composite) to be tested, the testing conditions and their parameters are detailed in this chapter and the plan and objectives of such experimental programme are also explained. The results of our experimental programme will be described in Chapter “[Inner Pressure Testing of Full-Scale Pipe Specimens](#)”, while Chapter “[Effectiveness Assessment of Composite Repair Systems](#)” will present the efficiency assessment of the investigated composite repair system, performed on the base of our experimental data.

Keywords Transmission pipelines · Composite repair system · Volumetric surface defect (VSD) · Composite material wrap · Qualification

Gh. Zecheru · A. Dumitrescu (✉)
Petroleum-Gas University of Ploiesti, Ploiești, Romania
e-mail: andrei.upg@gmail.com

P. Yukhymets · R.I. Dmytriienko
E.O. Paton Electric Welding Institute, Ukrainian National Academy
of Sciences, Kiev, Ukraine

1 Introduction

The transmission pipelines (normally made of steel) used to transport natural gas, petroleum or liquid petroleum products are providing services of great importance and therefore their maintenance and repair activities need special attention. Among the most common defects that might be detected on these pipelines are the ones of the metal loss type (also called volumetric surface defect, VSD), due to corrosion and/or erosion processes.

In the last years, the repair of the transmission pipeline areas with such defects was frequently performed by means of applying composite materials sleeves/wraps, because this repair technology did not require welding operations and could be applied without removing the pipelines from service. However, even if such repair procedure (described in Chapter “[Comparative Analysis of Existing Technologies for Composite Repair Systems](#)”) has been used from some time, the problems regarding its application did not found yet technical solutions fully underlain and unanimously accepted.

For this reason, we have carried out an extended research programme (which we plan to continue in the near future) that studies both theoretically and experimentally the transmission pipeline repair systems using composite materials. One of the main goals of our research programme is to investigate experimentally the efficiency of the repair systems using composite materials applied on transmission pipelines with VSDs, under various loading conditions (internal pressure, low cycle loading). The main objectives of our past and future experimental work are the following:

- (i) to evaluate the consolidation effect, considered as a measure of their effectiveness, for some composite repair systems used for damaged pipelines, by investigating the stress–strain state in the damaged area under the operational (internal) pressure, and also by determining the burst pressure value (such evaluation is described in Chapter “[Effectiveness Assessment of Composite Repair Systems](#)”);
- (ii) to validate numerical and analytical models developed by the authors of this book for the assessment of the remaining strength of a pipeline with VSDs reinforced using composite repair systems (these models have been described in Part 5) and also the design procedures defined in Chapter “[Design of Composite Repair Systems](#)” for the composite wraps applied for pipelines repair;
- (iii) to compare, in the future, the obtained experimental data and results with similar investigations performed by other research teams.

The development of our research programme has also considered the requirements of international standards dealing with the pipeline repair methods using composite materials, including their qualification procedures. Currently, two standards involving such issues are in use, ASME PCC-2 [1] and ISO/TS 24817 [2]. Article 4.1 from [1] provides the requirements for pipeline repair using a qualified

Table 1 Repair system required material and performance properties, according to [1]

Material property	International test method	ASTM test method
Tensile strength, Young's modulus and Poisson's ratio	ISO 527	ASTM D 3039
In-plane shear modulus	NA	ASTM D 5379
Thermal expansion coefficient	ISO 11359-2	ASTM E 831
Glass transition temperature of polymer	ISO 11357-2	ASTM E 1640, ASTM D 6604 or ASTM E 831
Heat distortion temperature (HDT)	ISO 75	ASTM D 648
Barcol hardness	BS EN 5	ASTM D 2583
Shore hardness	ISO 868	ASTM D 2240
Lap shear adhesion strength (of composite bond to substrate)	EN 1465	ASTM D 3165, ASTM D 5868
Long-term strength (creep-rupture) (optional)	ASME PCC-2 mandatory appendix V	ASTM D2990, ASTM D2992
Toughness parameter, energy release rate (optional)	ASME PCC-2 mandatory appendix IV	NA
Structural strengthening (optional)	ASME PCC-2 mandatory appendix III	NA

non-metallic repair system, while the standard [2] covers the requirements and recommendations for the design, installation, testing, and inspection for the external application of composite repairs to pipes affected by corrosion or other sources of damage. Both standards require the determination of the characteristics summarised in Table 1 for the qualification of a composite repair system intended for pipelines.

The use of the standards [1] or [2] is limited to those composite repair systems for which the qualification testing has been completed. Any change to any element of the repair system constitutes a different and therefore new repair system that shall require qualification in view of its industrial approbation.

In the followings, after a brief description of the experimental results previously obtained by the authors (in Sect. 2), the definition of the parameters for the future tests (pipe material and geometry, VSD geometry, loading conditions etc.) is detailed and the plan for the experiments carried out jointly is described.

2 Previous Experimental Tests on Pipelines Repaired with Composite Wraps

The authors have been involved in several testing programmes regarding pipeline repair systems with composite materials. These tests constituted the starting point for the development of the experimental programme described in the followings

and whose results are included in Chapter “[Inner Pressure Testing of Full-Scale Pipe Specimens](#)”. A brief description of the results of some tests previously executed is included below.

Among the analyses regarding the repair methods intended for transmission pipelines, a repair system using composite materials conceived by ICECHIM Bucharest, named IWR (ICHECHIM Wrap Repair) has been the object of investigations under an extensive research programme carried out within the University of Ploiesti. The IWR material is made of a multilayer composite material, in which the reinforcement component consists of layers of fibreglass fabric, while the matrix is the polymeric material used to impregnate the fabric. This polymeric resin has been conceived as a modified polymeric system having flexibilization components with small molecular weight and with mineral fillings.

The IWR mechanical properties (E_C is the elastic modulus, R_{mC} is the tensile strength, A_C is the elongation at fracture) are compared in Table 2 with the ones of other composite repair systems developed for transmission pipelines (for other details, see Chapter “[Review on Materials for Composite Repair Systems](#)”).

The IWR repair has the structure shown in Fig. 1, and its achievement requires the following three steps: (i) pipeline preparation for repair (cleaning its surface using an appropriate procedure; polishing, grinding or sand blasting in order to round the edges and smooth the VSD profile, eliminating the possible micro-cracks initiated by the defect and transforming the VSD in long-radius curvature groove, with reduced mechanical stress concentration effects); (ii) rehabilitation of the pipe external configuration, by filling the VSD using a polymeric filler; (iii) rehabilitation of the pipe mechanical strength, applying the reinforcing composite wrap in the defects area.

The IWR research programme was included, but not limited to the experimental testing of the IWR system, applied to three full-scale pipe specimens, all made of steel grade L245/B (with the yield strength $R_{0.5} = 245$ MPa, and the tensile strength $R_m = 415$ MPa) and with one or several VSDs, obtained by machining,

Table 2 Comparison between the mechanical characteristics of IWR, KPB and other composite materials intended for transmission pipelines repair

Composite material	Reinforcement material	Mechanical characteristics of the composite material ^a		
		E_C (GPa)	R_{mC} (MPa)	A_C (%)
IWR	Fibreglass	17.5–22.7	265–315	1.32–1.60
KPB	Fibreglass	2.8–3.1	30–31	0.90–1.10
EC 10 1680	Fibreglass	25.5–34.6	403.2–503.6	1.36–1.58
Perma Wrap	Fibreglass	34.0–38.0	580–620	1.00–1.10
Fiba Roll	Fibreglass	7.9–8.7	72–86	2.60–3.10
Clock Spring	Fibreglass	33.8–34.5	630–650	1.06–1.36
TDW RES-Q	Carbon fibre	68.8	1028	–

^aMeasured in the direction corresponding to the composite wrap circumference, when applied on the pipeline

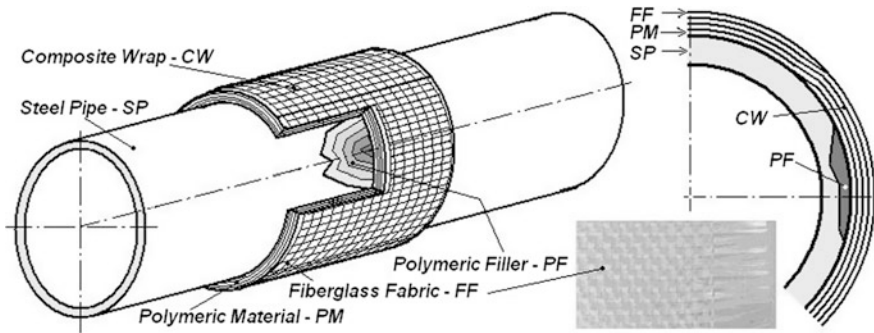


Fig. 1 Structure of IWR composite repair system for pipelines

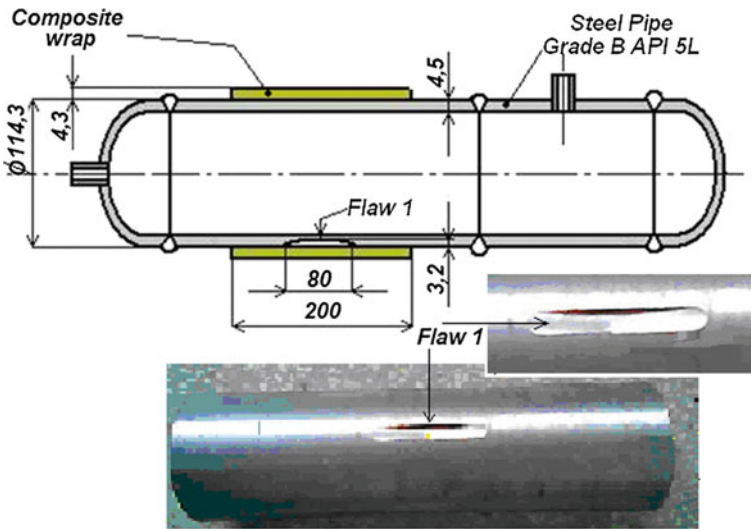


Fig. 2 Geometry of specimen P1 (with only one flaw/VSD)

subjected to internal pressure loading (maximum allowable operating pressure $MAOP = 5.5$ MPa). Figures 2–7 illustrate the test method applied and the behaviour of specimens, reinforced with composite wraps, after being subjected to bursting tests.

An important research programme regarding the KPB composite repair system has been carried out within E.O. Paton Institute in Kiev, including the experimental testing of two full-scale pipe specimens after repair. The KPB material, provided by Kailas Ltd., was made of a multilayer composite material, in which the reinforcement component consists of layers of fibreglass fabric, and the matrix is the polymeric resin used to impregnate the fabric.

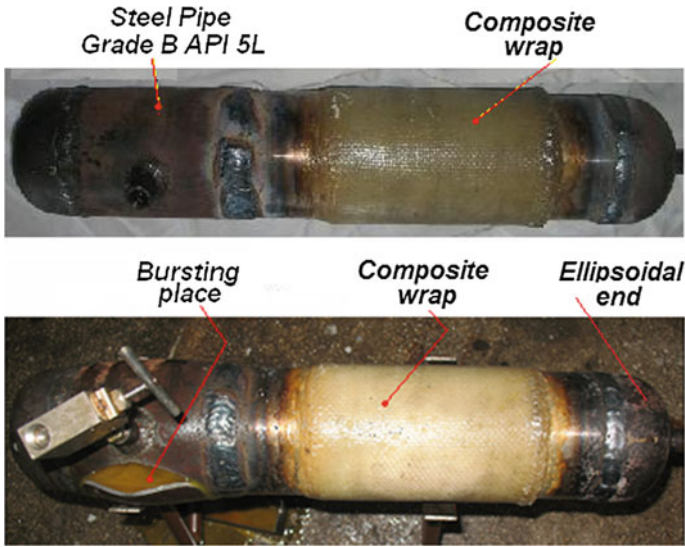


Fig. 3 Specimen P1 before and after testing

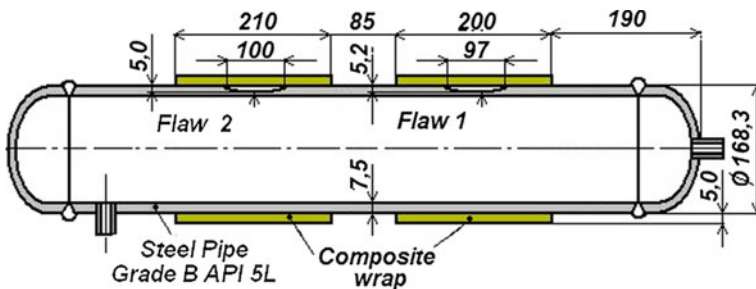


Fig. 4 Geometry of specimen P2 (with two flaws/VSDs)

KPB wrap repair has the structure shown in Fig. 8, and its achievement requires four steps: (i) pipeline preparation (cleaning, etc.); (ii) rehabilitation of the pipe external configuration, by filling the VSD using REM-stal filler; (iii) covering the pipeline surface using a polymeric primer (MB); (iv) rehabilitation of the pipe mechanical strength, applying the composite wrap (KPB) for reinforcement in the defects area.

The testing method and parameters are illustrated in Figs. 9–12 for both specimens (made of the same steel grade, similar to L360/X52), while the mechanical behaviour of the pipes, reinforced with KPB composite wraps, during the bursting test, is summarised in Fig. 13.

Table 3 includes a brief summary of all tests described above. In the table, the estimated value of the burst pressure for the steel pipe (without defects), p_b , has

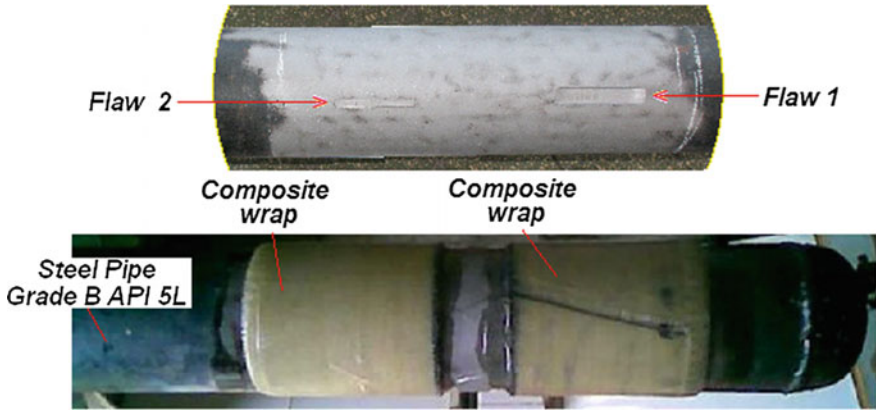


Fig. 5 Specimen P2 before and after repairing

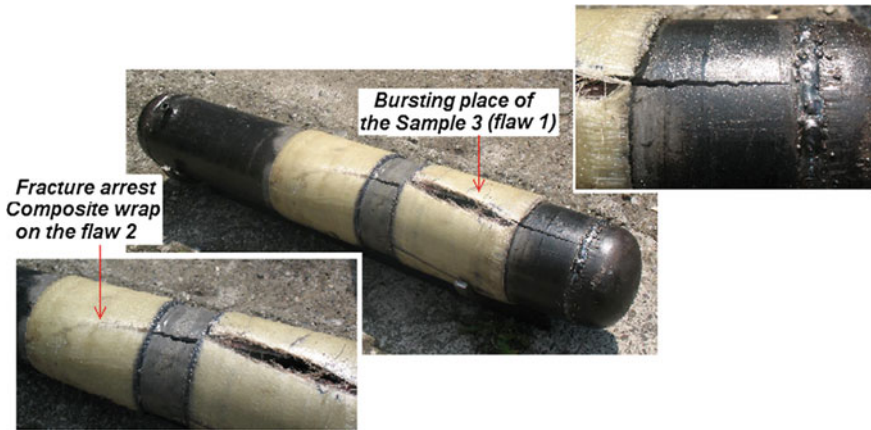


Fig. 6 Specimen P2 after testing

been calculated using the equation from DNV RP-F 101 [3], Sect. 2.1, while the same estimated value for the repaired pipe (with the composite wrap applied), p_{br} , has been calculated with as follows [4]:

$$p_{br} = \frac{2}{D_e} (R_{m,p}t_{mm} + R_{m,c}t_c) \tag{1}$$

where D_e is the pipe outside diameter, $R_{m,p}$ is the tensile strength of steel pipe, $R_{m,c}$ is the tensile strength of composite wrap, t_c is the composite wrap thickness, t_{mm} is the minimum remaining thickness of the pipe in the defect area.

The main conclusion on the previous tests (summarised in Table 3) is that the use of wraps made of composite material of the IWR type (or other similar materials

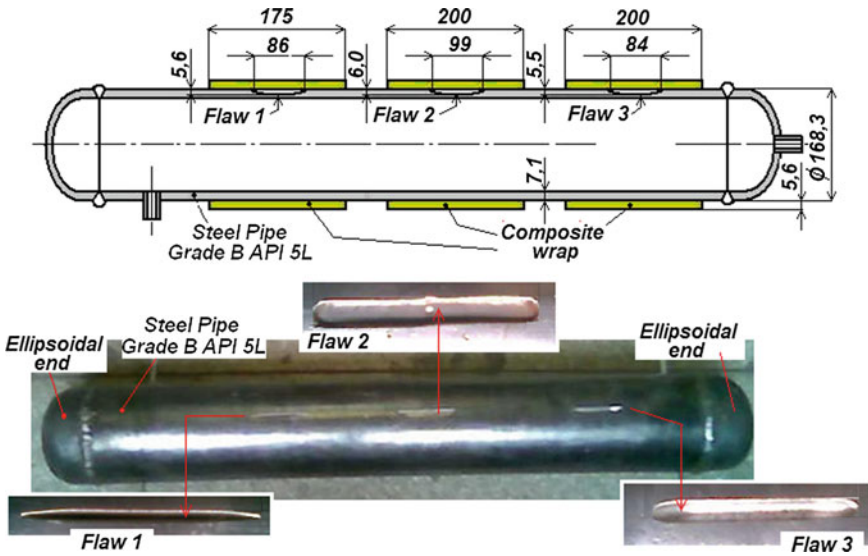


Fig. 7 Geometry of specimen P3, with three flaws/VSDs

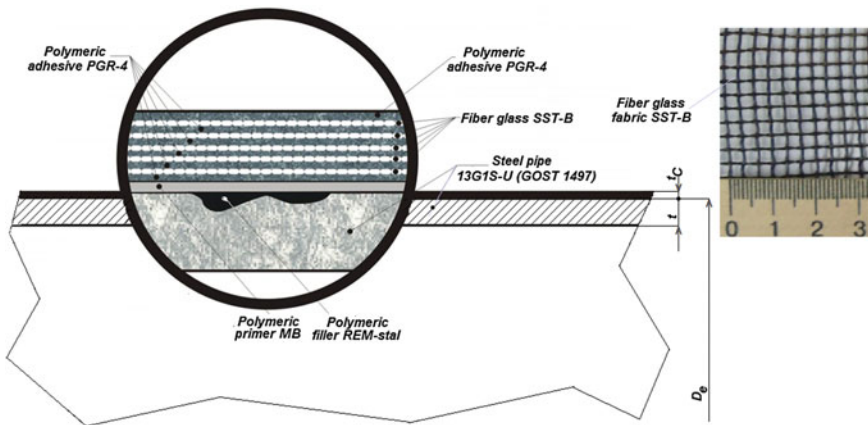


Fig. 8 Structure of KPB composite repair system for pipelines

—see Table 2), is suitable, because it can guarantee levels of the burst pressure in the repaired area superior to the burst pressure of the pipe without defects. At the same time, the use of composite wraps made of KPB type materials is not convenient, because a reinforcement effect similar to the one of IWR type wraps requires a very thick wrap (more than 50 mm), inappropriate due to high costs and technological implementation problems.

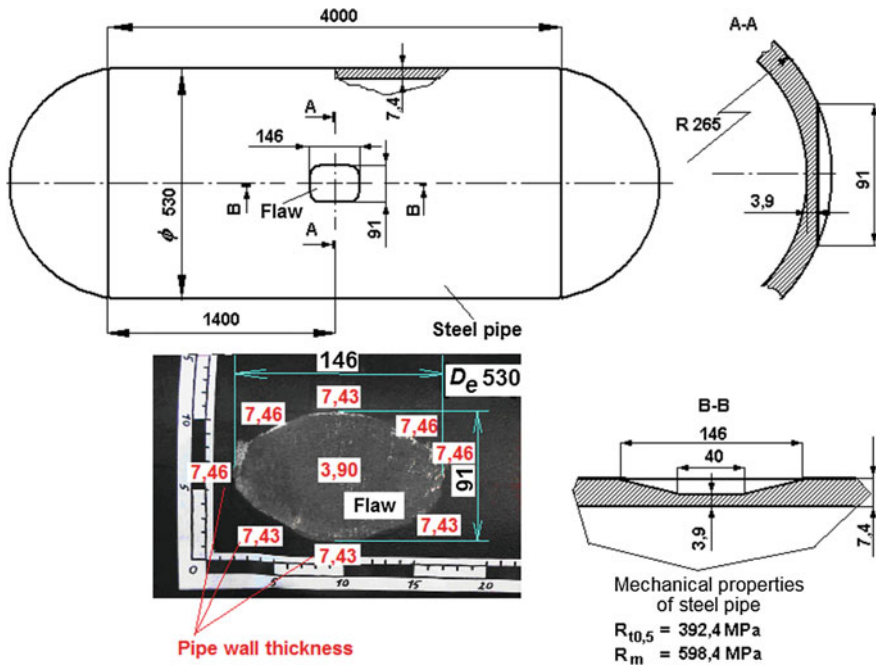


Fig. 9 Geometry of specimen K1 before repair, with VSD details

3 Definition of the Experimental Parameters and Planned Experimental Programme

First, the most adequate pipe materials to be tested were considered the steel grades L290/X42 and L360/X52 (or equivalent) [5], because they ranged among the most frequently used steel grades in European natural gas transmission pipelines systems, especially in the older ones that usually present VSDs and therefore require repair systems. For the same reason, the most suited values for the outside diameter of the pipes tested were considered $D_e = 219.1; 323.9; 508.0; 711.0$ mm.

The pipe specimens finally selected for testing, based also on available pipe materials and dimensions, are manufactured of Steel 20 (according to GOST 550-75 [6]). They are very similar to L290 and have the outside diameter $D_e = 219.0$ mm. Table 4 compares the mechanical properties of steels L290, L360, Steel 20 given in their standards [5, 6] with the ones determined by performing tensile testing on samples cut in the axial and circumferential direction for the specimens material.

In order to compare the results of our research work with those of other similar researches, we select a pipe wall thickness and define a defect geometry equivalent to the values, used within an extensive experimental programme currently underway. It investigates the long-term performance of composite repair systems, and it is organized by Pipeline Research Council International—PRCI [7] and sponsored

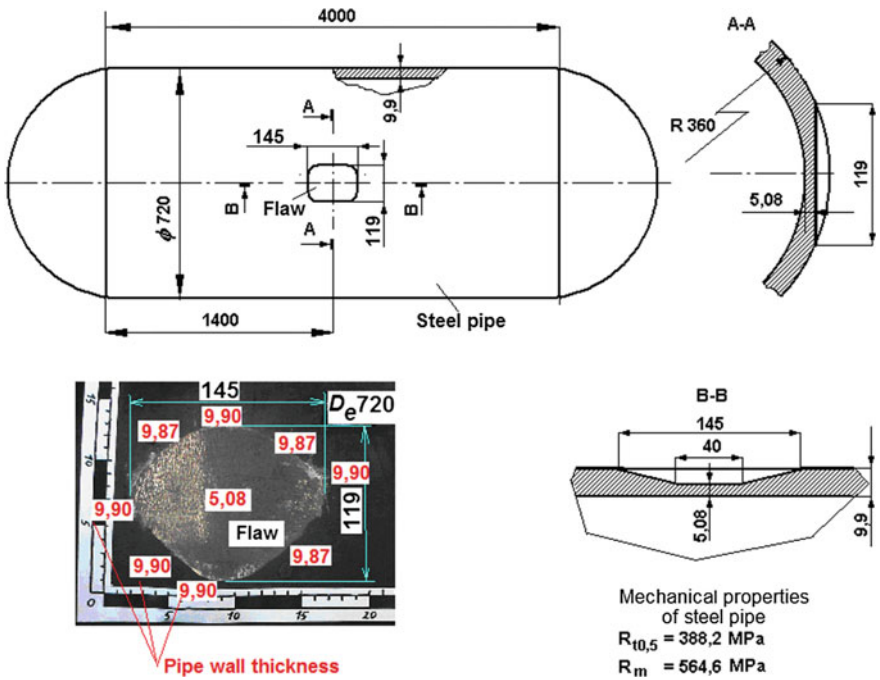


Fig. 10 Geometry of specimen K2 before repair, with VSD details

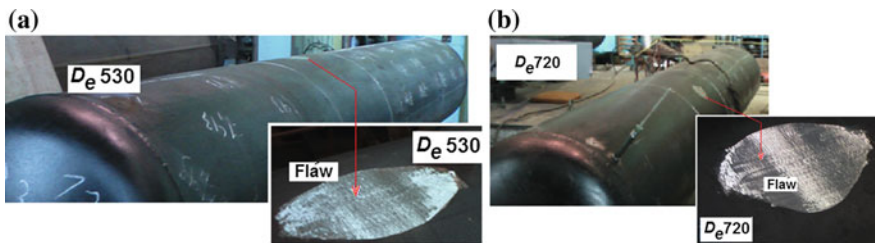


Fig. 11 Photos of the specimens before repairing: a specimen K1; b specimen K2

by 13 composite manufacturers from around the world, among which we mention: Armor Plate, T.D. Williamson, Clock Spring Company, Pipe Wrap. The programme consists of the preparation of grade L290/X42 test specimens with welded end caps and machined VSDs having the geometry as shown in Fig. 14, repaired by the participating manufacturers.

Burst tests were planned for all the repaired specimens at 0, 1, 2, 3, 5, 7.5, and 10 years. While 36 samples were burst immediately after repair, 144 samples were buried in the ground and continuously pressurized at 36% SMYS, then cycled 75

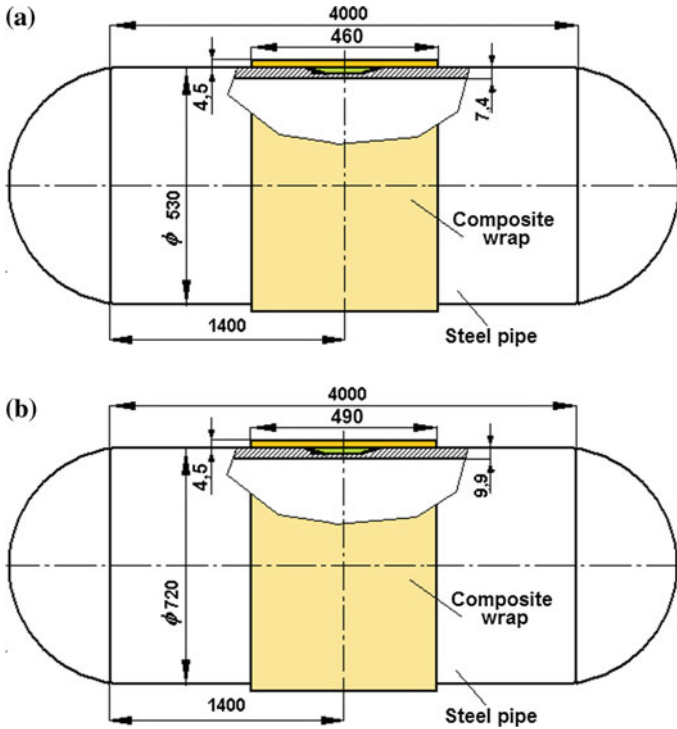


Fig. 12 Geometry of specimens after repairing (with KPB wrap): a specimen K1, b specimen K2

times once per month at 36% SMYS and once per quarter at 72% SMYS. Burst test samples are being removed from the buried trenches at the designated test periods. During the testing period, strain gauges are used to monitor strain in the corroded steel beneath the composite repair systems.

The nominal wall thickness of the pipe specimens, t_n , has been selected such that to obtain approximately the same *SDR* (Standard Dimensional Ratio— $SDR = D_e/t_n$) as the PRCI pipes. As these pipes have $SDR = 34.09$, the resulting value for the nominal wall thickness has been $t_n = 6.0$ mm. The defect dimensions have been determined to obtain the same values as per the PRCI experimental programme (including three different values for the defect depth corresponding to 40, 60, and 75%, respectively, of the nominal thickness t_n) for the non-dimensional parameters of the defect defined in the API 579 standard [8], characterizing its depth, length and width, respectively

$$h_d = \frac{d_m}{t_n}, \quad \lambda = \frac{1.285 \cdot s_p}{\sqrt{D_e \cdot t_n}}, \quad \lambda_c = \frac{1.285 \cdot c_p}{\sqrt{D_e \cdot t_n}}, \quad (2)$$

where d_m is the maximum defect depth, s_p is the axial extent (length) of the defect, c_p is the circumferential extent (width) of the defect.

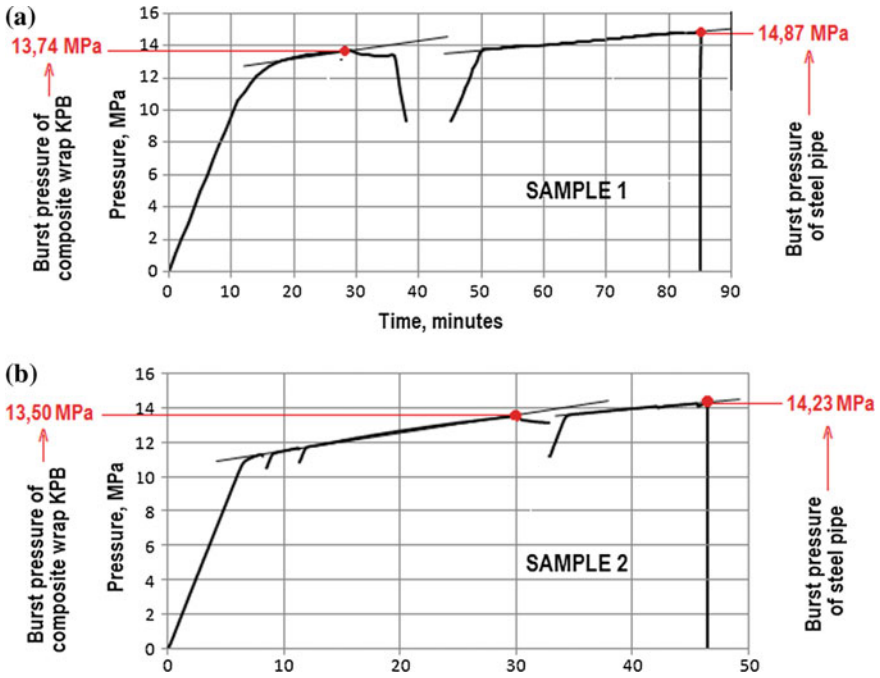


Fig. 13 Test results for both specimens: **a** specimen K1, **b** specimen K2

Table 3 Summary of the results of previously performed composite repair system tests

Specimen/pipe material	Pipe outside diameter, D_e (mm)	Pipe wall thickness, t_n (mm)	Burst pressure, p_b (MPa)	Burst location/composite wrap behaviour	Estimated burst pressures (MPa)	
					p_b (steel pipe)	p_{br} (with wrap)
P1/L245	114.3	4.5	39.5	Steel pipe/wrap unbroken	35.7	37.6
P2/L245	168.3	7.5	31.5	Flaw 1/wrap broken with crack propagation	40.6	26.1
P3/L245	168.3	7.1	29.5	Flaw 2/wrap unbroken, but tightness loss under it	38.4	23.4
K1/L360	530	7.4	14.9	Flaw area/full wrap rupture	15.2	8.0
K2/L360	720	9.9	14.2	Flaw area/full wrap rupture	15.8	8.0

Table 4 Mechanical properties comparison

Pipe grade/sample direction		SMYS ^a , $R_{t0.5}$ (MPa)	Tensile strength, R_m (MPa)
L290/X42		290	415
L360/X52		360	460
Steel 20	GOST	240 ^b	431
	Axial sample	314	461
	Circumferential, straightened	323 ^b	474
	Circumferential, not straightened	305 ^b	475

^aSpecified minimum yield strength

^b $R_{c0.2}$ (corresponds to residual elongation 0.2%)

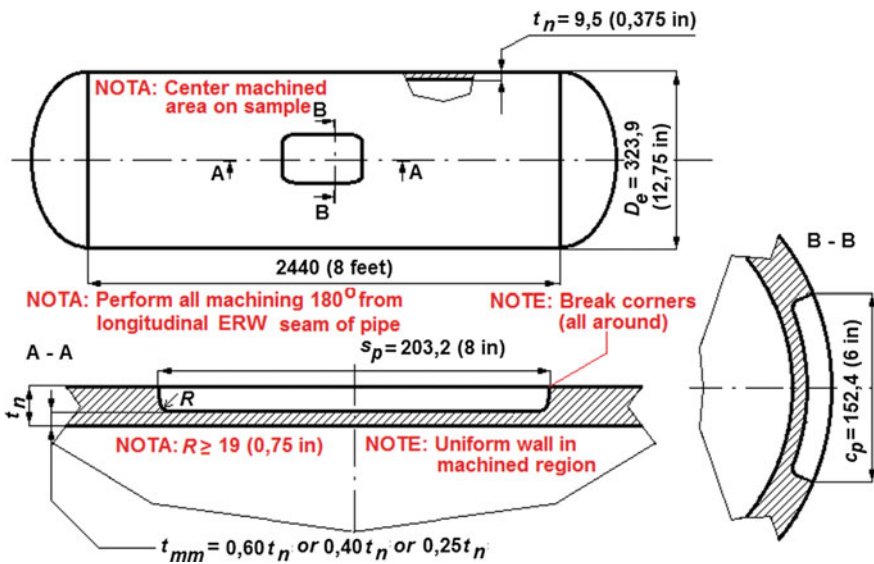


Fig. 14 PRCI full-scale test specimen [7]

Applying Eq. (2) for the PRCI pipes (with the defect dimensions shown in Fig. 14) and then for our pipes, we have obtained the following defect dimensions values: $s_p = 133$ mm; $c_p = 103$ mm; $d = 2.4, 3.6, 4.5$ mm. The pipes used as specimens are shown in Fig. 15a before machining the VSDs and in Fig. 15b after machining the defects. The specimen geometry is the same as the one used by PRCI (see Fig. 14).

Two composite repair systems were initially intended for investigation in our experiments, the ICECHIM wrap repair (was described in Sect. 2, while its main properties are indicated in Table 2) and a system using fibreglass EC 10 1680 N-U10(168), combined with the polymeric resin KDA-HI (its properties are also

Fig. 15 **a** Blank pipes used for specimens; **b** VSDs machined on two specimens



shown in Table 2). It was decided to use this system instead of KBP as its properties are more suitable for pipeline repair. Up to now, only the second system mentioned above has been investigated, while the IWR system will be tested in a future research programme. The composite wrap thickness has been defined according to the recommendations of ISO/TS 24817 [2] and the design procedure used was the one presented in Chapter “[Design of Composite Repair Systems](#)”.

The test planned have comprised hydraulic bursting tests performed on four specimens, as follows: (i) a bare pipe specimen without defect; (ii) a specimen without defect, but with a composite wrap applied on it; (iii) a specimen with a machined VSD, but without composite repair applied; (iv) a specimen having a VSD and repaired with composite wrap. The composite repair system applied has been the one using EC 10 1680 fibreglass.

During the first stage of pressure loading (from zero up to the strain limit of gauge), the measurement of pipe strains has been done using strain gauges preliminary installed on each specimen surface. Two gauges (one in the axial direction and one in circumferential direction) were placed outside the repaired area of the specimen and another two in the VSD area, before applying the filler and composite wrap. Strain measurement of repaired specimens were done before (in the elastic region) and after applying the wrap. The detailed description of the tests performed and their main results are included in Chapter “[Inner Pressure Testing of Full-Scale Pipe Specimens](#)”.

Within upcoming research programmes, we are considering the possibility to apply a composite wrap on a specimen with a VSD while subjected to internal pressure (thus simulating an in-service pipeline repair) and to analyse the effect of a pressure decrease on the system pipe wrap. In the future, we plan to execute also experimental tests under cyclic pressure loading due to the reasons briefly explained below.

In the most cases, the main load of a transmission pipeline is the internal pressure, that is not constant in service and changes very significantly during pumping starts/stops and periodical hydraulic tests. This creates the prerequisites for low cycle failure in the zones of stress concentration, among which VSDs areas. Furthermore, any cyclic loading could adversely influence the reinforcement effect of composite wraps applied in the damaged zone. Therefore, we regard the cyclic testing of full-scale specimens with composite wrap repair system as another important direction of our future experimental activity, which could develop the experience in this field accumulated by E.O. Paton Institute [9].

In the end, we mention that recent testing has shown fatigue lives for pipelines repaired with composite wraps ranging from 20,000 to 500,000 cycles, at a pressure level equivalent to 36% SMYS and VSDs with a depth equal to 75% of the wall thickness [7].

4 Conclusions

This chapter described the plan developed to perform an experimental programme with the aim of studying the reinforcement effects of composite materials repair systems designed for transmission pipelines. This joint research programme has completed previous results obtained separately by the authors and presented in Sect. 2. The results of our programme are described in Chapter “[Inner Pressure Testing of Full-Scale Pipe Specimens](#)”, while their application in order to assess the efficiency of the investigated repair system is shown in Chapter “[Effectiveness Assessment of Composite Repair Systems](#)”. Our programme could constitute an example of how to test a newly developed composite repair system in view of its industrial approbation.

The reasons for which we decided to execute new tests has been to validate the numerical methods developed for the simulation of composite repair systems (described in Part 5) and the composite wrap design method proposed in Chapter “[Design of Composite Repair Systems](#)” (as the wrap thickness used in our tests was calculated accordingly), and also to enrich our database of experimental results. In the near future, additional tests are planned to investigate other important issues regarding composite wrap repair systems, such as the behaviour under low cycle internal pressure loading and testing of specimens repaired while the pipe is subjected to internal pressure (simulating the repair of an in-service transmission pipeline).

References

1. ASME PCC-2, *Repair of Pressure Equipment and Piping* (2015)
2. ISO/TS 24817, *Petroleum, Petrochemical and Natural Gas Industries—Composite Repairs for Pipework—Qualification and Design, Installation, Testing and Inspection* (2006)
3. DNV RP-F 101 *Corroded pipelines, Recommended Practice* (2015)

4. C. Alexander, S.Mishael, *19th Biennial JTM (Joint Technical Meeting) on Pipeline Research*, APIA-EPRC-PRCI, Sydney, Australia, Paper 36 (2013)
5. ISO 3183/API Spec. 5L, *Specification for Line Pipe* (2007)
6. GOST 550-75, *Seamless Steel Tubes for the Oil Refining and Petrochemical Industries*
7. C.R. Alexander, in *NACE International 2007 Corrosion Conference & Exposition*, Nashville, Paper No. 07144 (2007)
8. API 579-1/ASME FFS-1, *Fitness for Service* (2007)
9. P.S. Yukhymets, A.A. Rybakov, V.A. Nehotyaschy, T.N. Filipchuk, XXVII International Conference "Defectoscopy 2013". XXI 2(139), 75 (2013)

Inner Pressure Testing of Full-Scale Pipe Samples

R.I. Dmytriienko, S.M. Prokopchuk and O.L. Paliienko

Abstract This chapter describes the experimental tests performed with the aim of studying the reinforcement effects of a given repair system using composite material wraps intended for a damaged transmission pipeline (for petroleum, liquid petroleum products or natural gas), with defects of the metal loss type (also named volumetric surface defects). These tests have been defined based on the considerations presented in Chapter “[Development of an Experimental Programme for Industrial Approbation](#)”, which details the material selection, the testing conditions and the objectives of our experiments. The sequence of the comparative hydraulic inner pressure tests, performed on full-scale samples, is detailed below. Our experiments were aimed on simulation of a pipeline under the following four conditions: as-delivered, damaged, repaired using a composite material wrap and reinforced on its entire length with composite materials. All samples have been loaded up to fracture. The properties of material used for the pipe manufacturing and the main results of hydraulic tests are also present. Based on the experimental results, presented in this chapter, an efficiency assessment (including numerical simulations using finite element method) of the investigated composite repair system has been also performed and it will be presented in Chapter “[Effectiveness Assessment of Composite Repair Systems](#)”.

Keywords Hydraulic tests · Inner pressure · Pipe · Wrap

1 Preparation of Samples

Four full-scale samples, simulating the pipeline in as-delivered condition as well as in the conditions damaged, repaired and reinforced with composite wraps, were subjected to the comparative static hydraulic inner pressure tests. The reference designations of the samples are I1, I2, I3, I4, respectively. The samples were made

R.I. Dmytriienko (✉) · S.M. Prokopchuk · O.L. Paliienko
E.O. Paton Electric Welding Institute, Kiev, Ukraine
e-mail: dril@ukr.net

© Springer International Publishing AG 2018
E.N. Barkanov et al. (eds.), *Non-destructive Testing and Repair of Pipelines*,
Engineering Materials, DOI 10.1007/978-3-319-56579-8_26

417

from hollow billets, cut out from one seamless hot-worked pipe 219x6 (steel 20 [1]), produced in accordance with [2, 3 i.1.2B] at OJSC „Interpipe NTZ”, Dnepropetrovsk, Ukraine. The pipe was produced with standardization of its mechanical properties and composition. All samples were equipped with flat steel bottoms of 32 mm thickness. They were manually welded-up to the hollow billets, at the edges of which a technological bevel was preliminary done. Geometry of the bottom and weld provided for the fracture of each of the samples to occur in its middle part. The bottoms were used for samples sealing.

Samples I2 and I3 included milled similar defects (see Fig. 1), simulating erosion–corrosion damage with the depth equal to 60% of the pipe thickness. Geometry of the defects was defined as described in Chapter “[Development of an Experimental Programme for Industrial Approval](#)”. The defect shapes were provided for uniform plastic deformation in the defect middle zone that simplified measurements. The relative parameters of the sample I2 defect, according to [4], are the following: depth: $\lambda_c = \frac{S_o - t_o}{S_o} = 0.60$, length: $\lambda_a = 1.258 \frac{a}{\sqrt{D_H S_o}} = 4.34$, width $\lambda_b = 1.258 \frac{b}{\sqrt{D_H S_o}} = 3.33$. These parameters are smaller by about 1.75% for the defect in sample I3.

The composite wraps were installed on samples I3 and I4 employing machine winding of direct roving ES 10 1680N-U10(168). It consists of elementary fiber-glass filaments “E” [5], being wetted in hot curing epoxy binder KDA-KhI [6]. Winding was carried out on the rotating hollow billets with welded-up bottoms fixed in a special device of turning machine. The wraps were formed layer-by-layer: roving was fed through a machine support, which was moved along the sample axis with fixed step. Laying of roving was carried out under $\approx 90^\circ$ angle to pipe axis. The average value of roving tension force for samples I3, I4 was 45 and 41N, respectively, and its oscillation due to axis misalignment of outer surface of hollow billet and machine axis ± 6 N. After laying the necessary amount of layers, the wraps were subjected to polymerization at 120–150 °C temperature. Actual thickness of wraps was determined after their polymerization by means of measurement of the wrap and pipe parameters. On sample I3 the wrap was installed with overlapping of the defect in axial direction. A cone transfer to pipe metal was formed at one side. On sample I4 winding covered all cylindrical surface including tack welds. Before wrap setting on sample I3 the defect cavity was filled with a compound (sections of roving of ~ 15 mm length), mixed with epoxy binder of cold curing [7] for uniform transfer of force from defect surface to inner wrap surface.

Tension diagrams were obtained for the calculation of necessary amount of the wrap layers (see below) and mechanical properties of pipe material, composite material and roving were determined, samples perimeters were measured. The wrap set on sample I3 should provide for elastic behavior of metal in the defect up to test pressure as well as strength no worse than in as-delivered pipe (sample I1).

Determination of strengthening effect of the wrap depending on number of layers was carried out from the condition of mutual deformation of pipe and wrap. Description of mutual work of pipe and wrap up to fracture based on

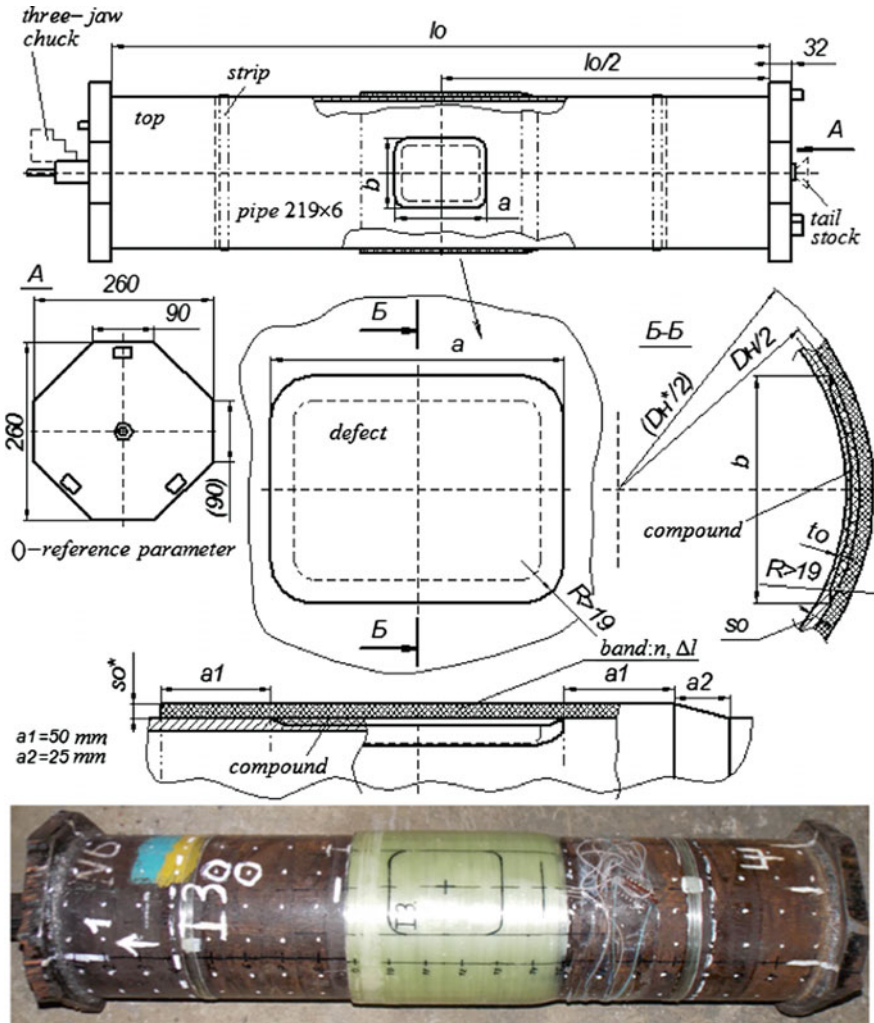


Fig. 1 Basic diagram by the example of sample I3 and its photo

deformation plasticity theory for simple loading is shown by the example of sample I4. Regardless the fact that relationship of axial and circumferential stresses in the pipe in this case is not constant, i.e., loading is not simple, nevertheless the experimental data showed the possibility of such approximation that significantly simplifies a problem [8]. With some complements, this approach can be used for the calculation of composite wrap on a pipeline damaged section.

Let us consider the main provisions of calculation. Since the ultimate deformations of the wrap are insignificant, the calculation is carried out on the initial geometry and tensile diagram. Effect of preliminary tension of the wrap is also

insignificant and it can be neglected. Making equal circumferential deformations of pipe middle surface and wrap, an equation of mutual deformation is obtained as

$$\varepsilon_t = \varepsilon_{t^*} \frac{r^*}{r} = \frac{\sigma_{t^*}}{E_*} \cdot \frac{r^*}{r} = \frac{1}{E} (\sigma_t - \mu \sigma_z) + \left(\frac{1}{E_C} - \frac{1}{E} \right) (\sigma_t - 0.5 \sigma_z) \quad (1)$$

where σ_t , σ_z are the circumferential and axial stresses in the pipe; r , s are the radius of middle surface and thickness of the pipe, respectively; ε_t is the circumferential deformations of middle surface of the pipe; E , μ is the elasticity modulus and Poisson's ratio of pipe material. A star (*) shows corresponding parameters for the wrap. $E_C = \sigma_i / \varepsilon_i$ is the secant modulus determined on curve connecting stress intensity σ_i with deformation intensity ε_i (diagram of pipe material tension in circumferential direction).

Stresses in the pipe are expressed by the following equations:

$$\sigma_z = \frac{Pr}{2s}, \quad \sigma_t = \frac{r}{s} (P - P_*) \quad \text{and} \quad \sigma_t = \frac{Pr - \sigma_{t^*} s_*}{s}, \quad (2)$$

where P , P_* are the inner pressure in the pipe and the pressure between pipe and wrap.

Expression (2) are obtained from the equilibrium condition of the part of structure cut with axial plane: $\sigma_t s + \sigma_{t^*} s_* = Pr$. The radial stresses are taken equal zero.

Inserting stresses (2) into Eq. (1) provides

$$\sigma_{t^*} = \frac{Pr \left(\frac{3E}{E_C} + 1 - 2\mu \right)}{\frac{r_*}{r} \cdot \frac{E}{E_*} + \frac{s_*}{s} \cdot \frac{E}{E_C}}, \quad P_* = P \frac{\frac{r}{4s} \left(\frac{1-2\mu}{E} + \frac{3}{E_C} \right)}{\frac{r_*}{s_* E_*} + \frac{r}{s E_C}}. \quad (3)$$

Making the secant modulus equal to the elasticity modulus, we obtain a solution for elastic pipe deformations. As it can be seen, circumferential stresses in the wrap and outer pressure on the pipe in the elastic area are directly proportional to inner pressure.

Equation (3) is solved using a method of incremental motion on ε_i , σ_i curve set by discrete values. Employing stress intensity in the pipe $\sigma_i = \sqrt{\sigma_t^2 - \sigma_t \sigma_z + \sigma_z^2}$, corresponding to it deformation intensity, and value of the secant modulus in a previous point allows determining a current value of the secant modulus. The calculation is performed up to the moment when the wrap circumferential deformations $\varepsilon_{t^*} = \sigma_{t^*} / E_*$ will not reach the limit values.

The increase of number of the wrap layers promotes for increase of value of inner pressure, at which intensity in the pipe reaches a proportionality limit and conventional yield strength, and circumferential deformations in the wrap, compared with the limiting values. Corresponding calculated dependencies for sample I4 without preliminary wrap tension are given in Fig. 2, lines P, Y and B. As it follows from the figure, the increase of the number of the wrap layers has more

significant effect on serviceability of the wrap (curve B) than on elastic deformation ability of the pipe metal (curves Y, P). It should be noted that these dependencies are not strictly linear, each following layer increases the limit pressure by a smaller value, than the previous one.

Close correspondence of experimental data (indicated by bold marks) and calculated values (curves P, Y, B) show sufficiently high accuracy of SSS prediction for selected number of the wrap layers (8).

Detailed ultrasonic thickness measurement of cylinder metallic part of the samples, including defects, was carried out before tests and after their finishing. The values of thickness were measured at the points equally distributed over the surface. Working and calibrating pressures (similar for all samples) were assigned in accordance with [9–12] taking into account the results of determination of mechanical properties of pipe material and thickness measurement.

The wire strain gauges of 10 mm base were glued on outer metallic surface of the samples (except for sample I1) in regular (distant from the effect of defect and bottoms) zone in circumferential and axial directions for the measurement of elasto-plastic deformations. The strain gauges were also set in the defect central zone and on the wraps after their assembly. Deformation was measured under load and after its rejection. Complete deformations under loading were determined considering accumulated residual deformations. All strain gauges were duplicated. The strain gauges on wraps of samples I3 and I4 were located over the strain gauges glued to pipe metal.

Measuring bases were applied in the regular part and in the defect using punching in circumferential and axial directions. They were used for determination of residual plastic deformation after the next stage of loading as well as fracture. Measurements under the wrap on samples I3 and I4 were carried out only after

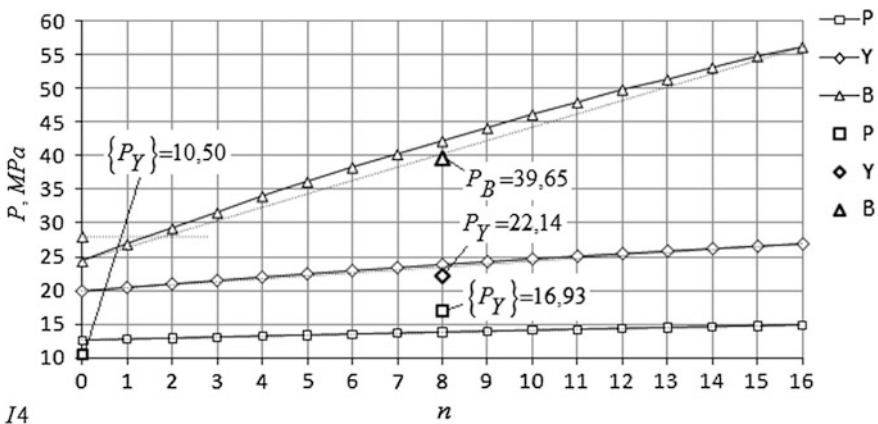


Fig. 2 Effect of the number of wrap layers on critical pressure value determined by: stress in a vessel wall, corresponding to a limit of proportionality of stress intensity (line P); stress in a vessel wall corresponding to conventional yield strength (line Y); limiting circumferential deformations in the wrap (line B); bold marks indicate the experimental data

fracture and wrap removal. Three circumferential sections were determined on each of samples I1 and I4, on which 16 measuring bases were made, for detection of the dependence of residual deformation on thickness difference. The same sections were used to control the residual deformations in axial direction. The difference between punching points on the defect surface in circumferential and axial directions was ~ 45 mm. The distance between points was measured with the help of flexible metallic ruler by means of its mating with metal surface.

2 Peculiarities of Full-Scale Samples Testing

Tests of the samples were carried out in a hydraulic bench. Moreover, tests of samples I1 and I4 at the initial stage took place in a water jacket (WJ), which allowed determining the increase of sample volume in process of inner pressure loading as well as after its release [13]. The minimum pressure, applying of which provoked residual increase of sample volume, was taken as a yield start pressure $\{P_T\}$. Inner pressure in the sample was created using “Hofer” pump of 50 l/h efficiency. Loading was carried out in few steps. Pressure in each stage rose from zero to a set value, which exceeded the maximum pressure of the previous stage. Exposure under pressure was used after reaching the set value. At the initial stages, this time was used for taking the readings of the strain gauges, at the next stages for complete realization of plastic deformations. Digital manometer Metran 100-DI was used for pressure recording. Weight of the sample and outer perimeters of several sections of the pipe and the wrap were measured after finishing each stage (except for steps performed in the water jacket). Loading in the hydraulic bench was carried out to fracture (depressurizing) of the sample. Two receivers were embedded in a serial hydraulic circuit between the pump and test object in order to increase hydraulic system volume. This allowed reducing a pressure growth rate and provide for smoother loading. The testing water temperature was into 10–23 °C range. A diagram of sample loading, simulating pipe in as-delivered condition, is shown in Fig. 3 as an example.

Below are given the main peculiarities of sample testing.

I1: *Pipe in as-delivered condition.* Loading was carried out in the water jacket and at plastic deformations close to the limit strains; it was performed in the hydraulic bench (HB). After full-scale sample fracture, it was used for cutting out the samples, which were subjected to uniaxial tension tests. The samples were cut in circumferential and axial directions from the zones with residual plastic deformation set on punched base measurement. The samples for hardness measurement were cut out close to previous specimens.

I2: *Simulation of damaged section of the pipeline.* Loading was carried out in HB with simultaneous measurement of deformations with the help of strain gauges.

I3: *Model of damaged section of the pipeline repaired using composite wrap.* After the stain gauges, mounted on the defect in circumferential direction, start

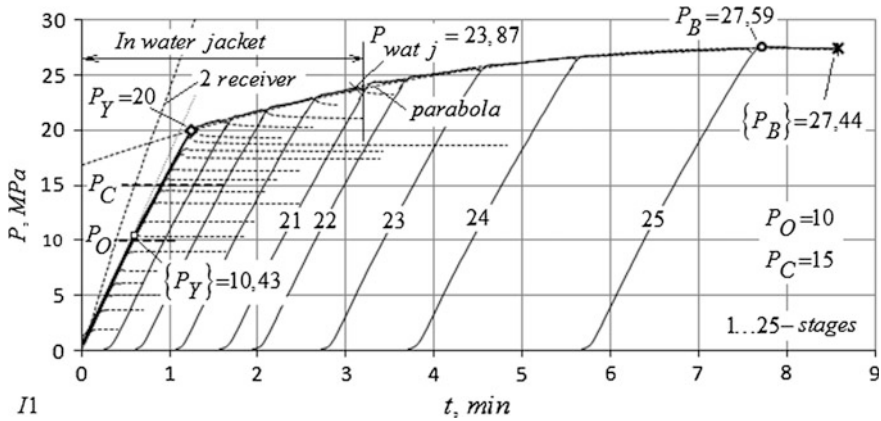


Fig. 3 Stages of loading with inner pressure to sample fracture I1: $P_{wat,j}$ is the pressure to which the sample was loaded in water jacket; 2 receiver is the diagram of loading of two twin receivers without testing object; parabola is the line of approximation of diagram of sample loading in plastic area by second-degree equation with a peak in P_B point; fine dashed lines are the exposure at loading stages; other designations see in Table 3

registering residual deformations, a wrap was installed on the sample and pressure loading was renewed.

I4: Model of strengthened part of the pipeline. Loading was carried out in the water jacket before residual volume increase. Then, the strain gauges were mounted on the pipe surface and the sample was subjected to secondary loading to a pressure $\leq \{P_T\}$ in HB. After wrap winding and setting the strain gauge on its surface the sample was ones more subjected to loading to a pressure $\leq \{P_T\}$ in HB. Then, the tests were continued in WJ. The tests in HB were finished at deformations close to the limit strains.

Manufacture and testing of the full-scale samples was carried out in the I1-I2-I4-I3 order. This sequence allows correcting the parameters of current tests, based on the test results of previous samples. For example, the wrap of sample I3 was manufactured considering the results of testing of composite material in I4 sample, behavior of non-strengthened defect of sample I2 as well as fracture pressure of sample I1, which was set as a fracture required pressure.

Figure 4 shows the equipment used for hydraulic tests.

3 Main Test Results

The results of the determination of the mechanical properties, composition of material and other main parameters of the pipes are given in Tables 1 and 2.

Table 1 gives the results of tension of the samples with minimum values of ultimate strength. It should be noted that the group of the samples cut out in

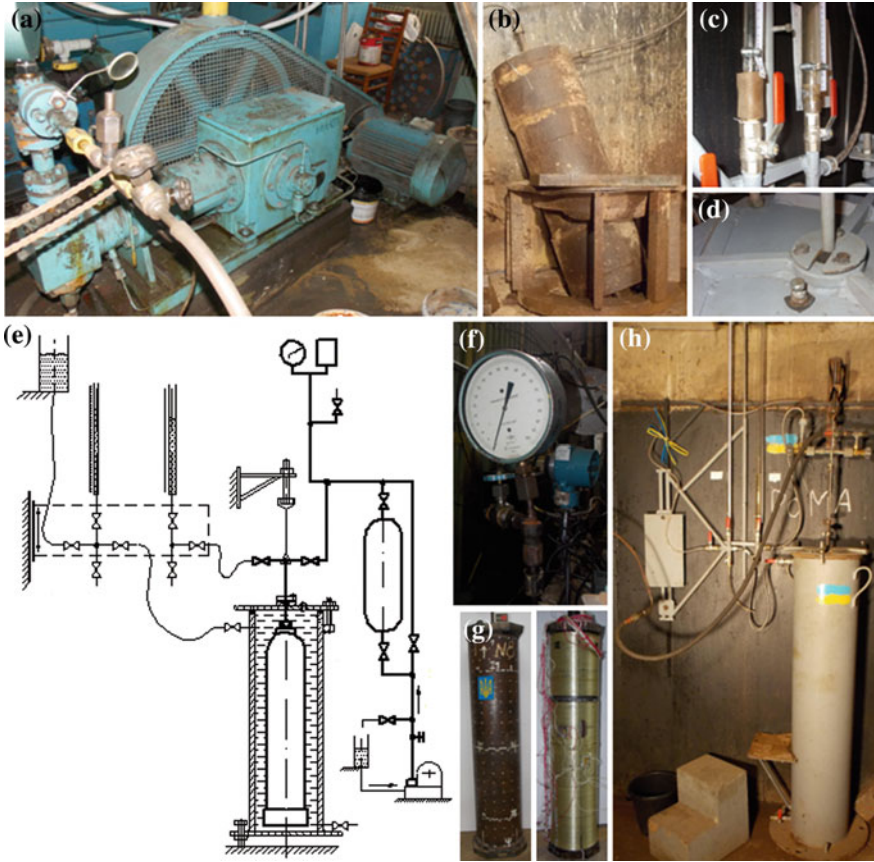


Fig. 4 Equipment for hydraulic tests of vessels (PWI): **a** “Hofer” pump; **b** receiver; **c** burette connection; **d** system of air made from “water jacket”; **e** basic diagram of test system; **f** manometer and Metran 100-DI pressure probe; **g** samples tested by inner hydraulic pressure; **h** “water jacket” installation

Table 1 Mechanical properties of pipe material

According to	σ_t (MPa)	σ_y, σ_{02} (MPa)	δ (%)	
GOST 8731-74, п.1.2. B	412.00	24.00	21.0	
Manufacturer’s certificate	475.78	323.73	32.0	
	480.69	328.64	33.0	
Mechanical tests ^a	C	474.76	305.00	33.1
	A	461.40	314.00	41.0

^aC, A are the samples cut out in circumferential and axial directions of the pipe, respectively

Table 2 Pipe material composition

According to	Weight fraction of elements (%)							
	C	Mn	Si	S	P	Cr	Ni	Cu
GOST 1050-88	0.17–0.24	0.35–0.65	0.17–0.37	<0.040	<0.035	<0.25	<0.30	<0.30
Manufacturer's certificate	0.19	0.54	0.29	0.02	0.011	0.07	0.05	0.08
Chemical analysis	0.177	0.55	0.289	0.018	0.008	0.078	0.065	0.070

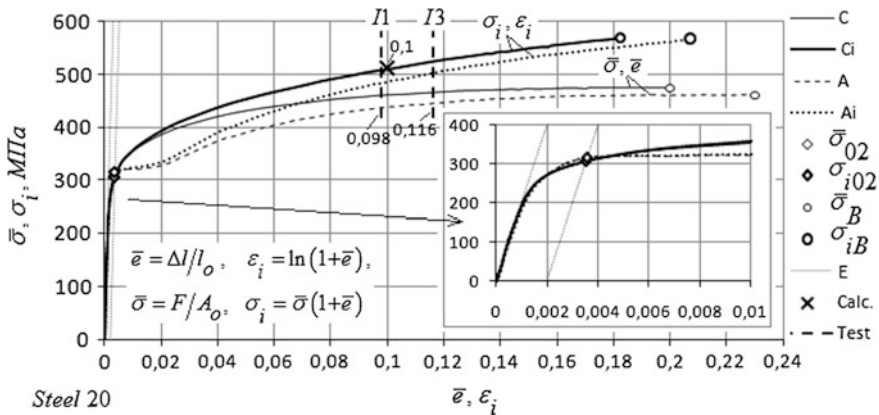


Fig. 5 Diagrams of tension $\bar{\sigma}, \bar{\epsilon}$ of samples cut out in circumferential and axial directions of pipe in initial condition, and actual deformation diagrams plotted on them: C, A are the diagrams of sample tension in circumferential and axial directions; C_i, O_i are the actual diagrams of deformation, respectively; $\bar{\sigma}_{02}, \bar{\epsilon}_B$ are the conventional stresses; $\sigma_{i02}, \sigma_{iB}$ are the actual stresses; E is the dependence of stresses on deformations in elastic area ($E = 2 \times 10^5$ MPa)

circumferential direction were subjected to complete leveling in a press by four-point bend test, the other group was leveled only in the grip places, a test portion remaining non-deformed. Obtained results showed that the values of conventional yield strength of completely leveled samples are ~5% higher, the rest of parameters are not different. The samples, cut out in axial direction, were not leveled, the places for grips the same as in circumferential samples were polished. The sides of all samples, corresponding to inner and outer pipe surface, were not mechanically treated.

Figure 5 shows conventional and actual tension diagrams to the moment of start of formation of neck of the samples cut out from the pipe at initial condition, in circumferential and axial directions. The following dependencies were used for plotting an actual diagram of deformation:

$$\varepsilon_i = \ln(1 + \bar{\varepsilon}), \quad \sigma_i = \bar{\sigma}(1 + \bar{\varepsilon}), \tag{4}$$

where ε_i and σ_i are the intensity of logarithmic deformations and actual stresses, respectively, $\bar{\varepsilon}$ and $\bar{\sigma}$ are the deformations and stresses determined from conventional tension diagram. The actual deformation diagram is invariant in relation to type and sequence of loading that is also verified by the results of present investigations.

Figure 5 also indicates the calculation and experimental values of deformation intensity corresponding to limiting state of the full-scale samples I1 and I3.

The conducted investigations showed that the pipe taken for manufacture of the full-scale samples had significant thickness difference that is caused by hot-worked production technology. Wall thickness distributions before and after tests are characterized by left-side asymmetry (Fig. 6). After fracture, the average thickness is reduced by 4.3% and standard deviation due to more intensive deformation in thinner areas rises 1.5 times.

The performed statistical processing of thickness measurements ($n = 352$) allowed making some observations useful for practical application

- (i) an average value, based on 16 measurements in a random cross-section, differs not more than 0.75% from average thickness value, determined on the results of all carried measurements; the deviation becomes <1.2% in the case of eight measurements.
- (ii) cross-section of hot-worked pipe is sufficiently well described by two eccentric circumferences of different diameter.

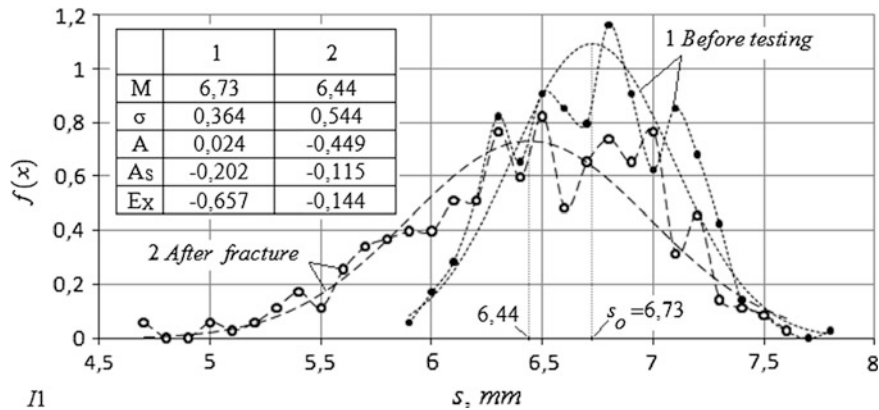


Fig. 6 Distribution of wall thickness in sample I1 before and after hydraulic tests with inner pressure to fracture: $f(x)$ density distribution; M average value; σ standard deviation; A third central moment (asymmetry); A_s asymmetry relative index; E_x fourth central moment (excess); *fine lines* show distributions under the assumption of their normality; *pointed points* correspond to thickness range 0.1 mm

Table 3 Generalized data on full-scale samples I1, I2, I3 and I4

Parameter		Unit of measurement	Sample designation			
			I1	I2	I3	I4
<i>Hollow billet</i>						
Outer diameter, D_O		mm	220.15	219.77	220.15	219.99
Wall thickness of hollow billet	Average, s_O	mm	6.73	6.76	6.89	6.55
	Minimum, s_{min}	mm	5.9	6.1		5.7
Internal volume, W_o		l	32.0	31.9		31.,8
Length between bottom inner surfaces, l_o		mm	953.00	953.25	954.50	956.50
ΔW_{evc} , per 1 MPa, to pressure $\{P_Y\}$; method of least squares		cm ³	5.329	–	–	5.702
Yield pressure, $\{P_Y\}$		MPa	10.43	–	–	10.50
<i>Defect</i>						
Wall thickness in defect	Average, t_o	mm	–	2.70	2.82	–
	Minimum, t_{min}	mm	–	2.4	2.3	–
Linear dimensions, [length (a) \times width (b)]			–	133 \times 102		–
Design factor of strength reduction				0.499	0.493	
Yield pressure, $\{P_Y\}$		MPa	–	5.83	5.93	–
<i>Composite wrap</i>						
Wrap outer diameter, $D_{O'}$		mm	–	–	232.59	225.02
Number of wrap layers, n		psc	–	–	16	8
Wrap thickness, $s_{O'}$		mm	–	–	6.22	2.52
Thickness of wrap layer, Δr		mm	–	–	0.389	0.315
Winding step Δl		mm/rev	–	–	2.36	2.36
ΔW_{evc} , per 1 MPa, to pressure $\{P_Y\}$; method of least squares		cm ³	–	–	–	5.024
Yield pressure, $\{P_Y\}$		MPa	–	–	16.65	16.93
<i>Loading diagram</i>						
Yield pressure, $\{P_Y\}$		MPa	20.00	–	19.60	22.14
Maximum pressure, P_B		MPa	27.59	13.83	29.06	39.65
Fracture pressure, $\{P_B\}$		MPa	27.44	13.83	29.03	33.87
Safety factor n_B		–	2.76	1.38	2.91	3.97
Safety reduction/increase factor, ϕ		–	1	0.501	1.053	1.437
<i>Measured operating and check pressure</i>						
Operating pressure, P_O		MPa	10			
Check pressure, P_C		MPa	15			

Note $\{P_Y\}$ is the yield pressure determined on water jacket for samples I1 and I4, and on circumferential stress gauges in the defect for samples I2 and I3; P_Y is the yield pressure determined as a culminating point of diagram of inner pressure loading; ΔW_{evc} is the elastic volume change



Fig. 7 Full-scale samples I1, I2, I3 and I4 after fracture by hydraulic inner pressure

Combined data on geometry parameters of the samples and the main results of their hydraulic testing are shown in Table 3. Figure 7 gives the photos of the samples tested to fracture. Absence of chips, peculiarities of fracture surface and fracture line trajectory indicate ductile fracture of metal of the full-scale samples [14].

References

1. GOST 1050-88. *Rolled Section, Calibrated with Special Surface Finishing from Carbon Quality Structural Steel. General Specification* (1988) (in Russian)
2. GOST 8732-78. *Hot-Rolled Seamless Steel Pipes. Assortment* (1978) (in Russian)
3. GOST 8731-74. *Hot-Rolled Seamless Steel Pipes. Specification* (1974) (in Russian)
4. API 579-1/ASME FFS-1. *Fitness for Service*
5. GOST 17139-2000. *Glass Fiber. Roving. Specification*. Minsk (2000) (in Russian)
6. TU-U 24.6-0030314547-002-2004. *Epoxy Binder of KDA-KhI Grade* (2004) (in Russian)
7. *Versatile Epoxy Glue of "Khimkontakt - Epoxy"*, TU-U 24.6-2558309112-006-2006 (2006) (in Russian)
8. I.F. Obraztsov, V.V. Vasilev, Bunakov V. A. *Optimum Armoring of Rotational Shells of Composite Materials*. Moscow, Mashinostroenie, 144 (1977) (in Russian)
9. GOST 8731-74. *Metallic Pipes. Hydraulic Pressure Testing Method* (1974) (in Russian)
10. GOST 3845-75. *Metallic Pipes. Hydraulic Pressure Test Method* (1975) (in Russian)

11. V.M. Belayev, V.M. Mironov. *Design and Calculation of Elements of Branch Equipment. P. I: Thin Wall Vessels and Apparatuses of Chemical Industry* (Tomsk Polytechnic University Press, Tomsk, 2003), p. 168 (in Russian)
12. GOST 14249-89. *Vessels and Apparatuses. Norms and Methods of Strength Calculation*
13. R.I. Dmytriienko, E.F. Garf, V.P. Chizhenko. *Technical Diagnostics and Non-destructive Testing*. **1**, 23 (2014) (in Russian)
14. ISO 9809-1:2010(E). *Gas Cylinders—Refillable Seamless Steel Gas Cylinders—Design, Construction and Testing. Part 1: Quenched and Tempered Steel Cylinders with Tensile Strength Less than 1100 MPa* (2010) (in Russian)

Effectiveness Assessment of Composite Repair Systems

R.I. Dmytriienko, O.L. Paliienko, P. Yukhymets, I. Lvov
and O. Marusenko

Abstract This chapter is dedicated to the analysis of the efficiency of a given repair system using composite material wraps intended for damaged sections with volumetric surface defects of transmission pipelines (for petroleum, liquid petroleum products or natural gas). The analysis refers to the composite repair system investigated in Chapter “[Inner Pressure Testing of Full-Scale Pipe Samples](#)” and it has used the experimental data presented in Chapter “[Inner Pressure Testing of Full-Scale Pipe Samples](#)”. The tests performed were defined based on the considerations in Chapter “[Development of an Experimental Programme for Industrial Approbation](#)”. The efficiency assessment has been made, in the first place, considering the change of volume and the yield pressure, then taking into account the changes observed in the samples perimeter. The effect of the composite wrap on the deformations recorded for each defect and the loading diagrams have also been investigated. Finally, the efficiency has been assessed using a numerical finite-element model.

Keywords Hydrottest · Inner pressure · Pipe · Defect · Wrap

1 Evaluation Based on Change of Volume and Yield Pressure

The measurements, carried with the help of “water jacket” in the process of hydraulic loading by inner pressure of a sample, allowed sufficiently accurate registration of its volume change. Figure 1 shows the dependencies of volume

The original version of the book was revised: Incorrect author names have been corrected. The erratum to the book is available at https://doi.org/10.1007/978-3-319-56579-8_28

R.I. Dmytriienko (✉) · O.L. Paliienko · P. Yukhymets
E.O. Paton Electric Welding Institute, Kiev, Ukraine
e-mail: dril@ukr.net

I. Lvov · O. Marusenko
National Technical University, Kharkiv Polytechnical Institute, Kharkiv, Ukraine

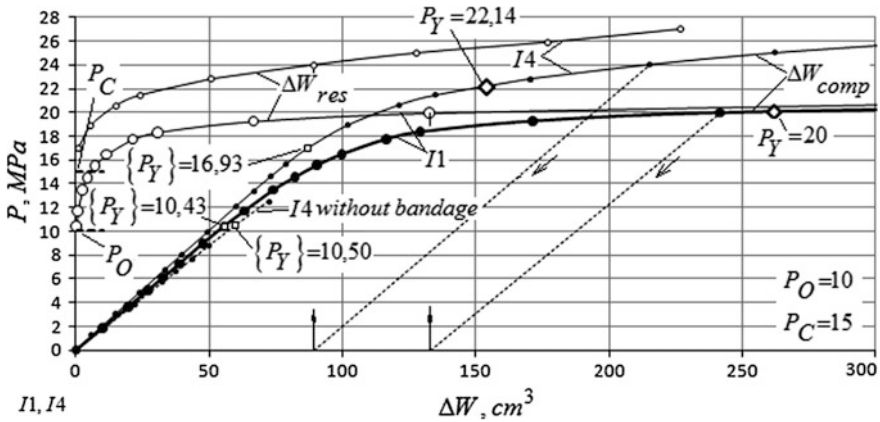


Fig. 1 Complete (ΔW_{comp}) and residual (ΔW_{res}) values of volume change of samples I1 and I4 at initial stages of loading in water jacket: $\{P_Y\}$ is the yield pressure, determined in water jacket; P_Y is the yield pressure, determined as a breaking point of inner pressure loading diagram; ΔW_{comp} , ΔW_{res} are the complete and residual volume changes

change in samples I1 and I4 at initial stages of loading. It can be seen from the figure that yield start pressure $\{P_Y\}$ (volume of sample after unloading does not come back to initial state) increases 1.61 times after the wrap installation on sample I4. By this P_T pressure (determined from a hydraulic loading diagram, Fig. 6) shows a slight increase 1.1 times. It is a pressure, at which a significant part of the cylinder shell has already come to plastic deformation area. Due to the variation of pipe wall thickness and the deviation of geometry of its cross-section from circular ring, plastic deformations propagate to wider areas with pressure growth. These deformations localize in the zones of reduced cylindrical stiffness, where combination of thinning and larger curvature is observed. Diagram of hydraulic loading $P = f(T)$, as a result of reflection of the dynamic process, is not so susceptible, therefore difference between $\{P_Y\}$ and P_Y pressures can be a measure of the deviation of pipe geometry from the ideal one. Noticeable increase of $\{P_Y\} - P_Y$ difference in the case of sample I4 can indicate inclusion of the wrap in the process of plastic deformation propagation within pipe cross-section.

The increase of volume in the process of plastic deformation of cylinder sample with bottoms takes place due to reduction of the wall thickness and increase of the middle surface radius. The dependence of volume change on inner pressure, in this case, can be determined using actual deformation diagrams as

$$P = \frac{2\sigma_i s_o}{\sqrt{3}r_o e^{\sqrt{3}\epsilon_i}}, \quad \Delta W_{comp} = \pi l_o r_o^2 (e^{\sqrt{3}\epsilon_i} - 1), \quad (1)$$

where s_o, r_o are the wall thickness and radius of middle surface in the initial state, l_o is the length of cylinder part, which does not change at plastic deformations,

σ_i, ε_i are the stress and deformation intensity on actual deformation diagram, respectively.

The residual value of deformation intensity ε_{res} is inserted in formula (1) when ΔW_{res} is determined.

Since Poisson’s ratio $\mu = 0.5$ under plastic deformation conditions, then current values of wall thickness s and middle surface radius r can be related with initial values through logarithmic deformations ε_i or deformation intensity

$$\varepsilon_i = \frac{2}{\sqrt{3}} \varepsilon_t = \frac{2}{\sqrt{3}} \ln \frac{r}{r_0} = - \frac{2}{\sqrt{3}} \ln \frac{s}{s_0} \tag{2}$$

The results of calculations using Eqs. (1) and (2) showed close correspondence with data of sample I1 testing.

In a whole, the strengthening effect of the composite wrap in the elastic deformation area can be sufficient extent characterized by the absolute value of P_Y pressure.

Dependencies (1) and (2) can be used to determine the residual expansion coefficient (ratio of residual change of vessel volume to full one, characterizing plastic deformation level) and the current safety margin (ratio of maximum pressure, which was carried by the sample, to maximum pressure at the stage). Figure 2 gives the dependence of current safety margin and residual expansion coefficient by the example of samples I1 and I4. The inclination angle of dependence in the central part for sample I4, corresponding to stable plastic deformation (Fig. 2), is more than for sample I1. This indicates that at the same increment of pressure in this area, the sample with wrap changes in volume for a smaller value than the sample without wrap, that shows a possibility of application of indicated index for evaluation of the efficiency of installed wrap.

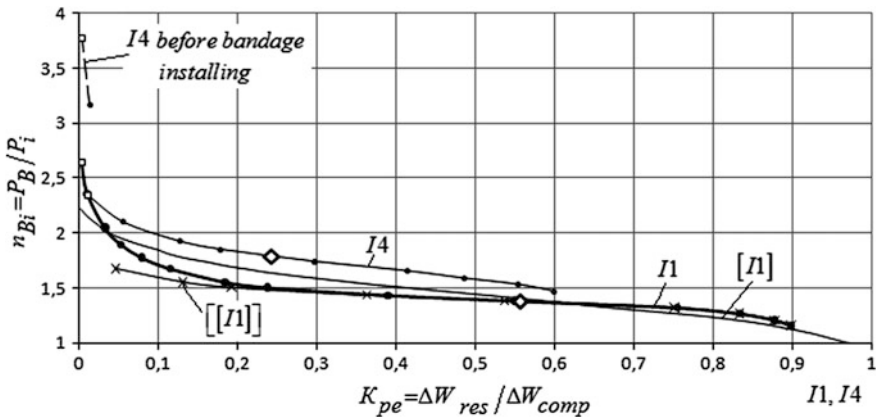


Fig. 2 Relationship of the inner pressure and safety margin on the plastic deformation level by the example of samples I1 and I4: [I1] theoretical dependence for sample I1 being calculated on actual deformation diagram; [[I1]] dependence for sample I1, if we did not take into account residual change of volume in its loading up to calibrating pressure; for other designations see Fig. 1

2 Evaluation Based on Change of Sample Perimeter

The wrap remains in elastic deformed state after fracture of sample I4 due to pipe plastic deformation. Its perimeter change along the pipe generator, out of fracture zone, is of 0.90–1.04%. It cracked at small mechanical influence, unloading took place and its perimeter was reduced. After wrap removal, residual changes of the perimeters of pipe sample I4 were 1.05–1.47%, in the case of I1 perimeter the increase was 6.8–8.6% (the maximum changes were registered in the fracture zone and the minimum ones close to the bottoms). Thus, the installation of the wraps resulted to significant (6–8 times) decrease of the circumferential residual deformations. It is necessary to note that circumferential residual deformations, obtained by measuring the distances between sample I1 punching points, were 3.3–16.4%. Considerably larger spread in deformations in comparison with the results, obtained in perimeters' measurement, is observed with variation of pipe wall thickness.

Since the value calculated for the elastic deformation is of about 0.2% at the joint work of wrap and pipe in the process of pressure release from maximum value to zero in sample I4, then carried perimeter measurements can indicate virtually complete exhaust of a deformation capability of composite material ($\sim 1.4\%$) at sample fracture.

3 Effect of Composite Wrap on Change of Deformations in a Defect

Figure 3 gives the results of deformation measurement in the defect and regular part of sample I3 before and after wrap installation. Loading without wrap was carried out before the occurrence of circumferential residual deformations in the defect. There are also deformation data on the wrap surface. Figure 3 also presents deformations of sample I2 for comparison.

As it can be seen, circumferential deformations in the defect area significantly decrease after some initial deformation that can be related with the removal of discontinuity flaws inside the composite and defect filling compound as well as on their mating surfaces. Installation of wraps on sample I3 does not influence the initial part of axial deformations in the defect. Axial deformations of the wrap over the defect completely match with the defect axial deformations.

Buckling resulted in a reduction of stresses in the central part of the defect, and fracture of the sample I2 took place along genetratrix with minimum thickness at the end of the defect (indicated by arrow in Fig. 4d). By this, average wall thickness in the defect zone decreased by 9%, and the wall thickness is without variations in the pipe regular part. A change of length of a measuring base in axial direction was not registered.

Fracture of the sample I3 took place in the uncoated section of the pipe. After wrap removal, residual circumferential deformations in the defect were 1.33% that

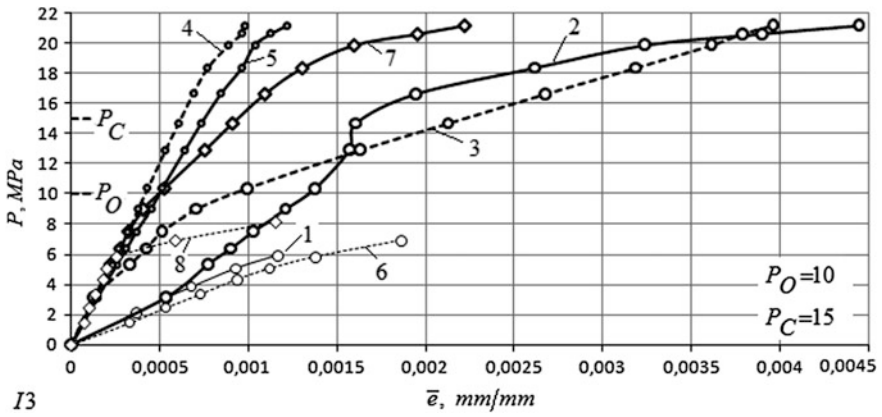


Fig. 3 Deformations of sample I3 at the initial loading stages: circumferential deformations in defect before (1) and after (2) wrap installation; at wrap in defect zone (3), in regular zone (4); for pipes in regular zone (5); in defect of I2 sample (6); axial deformations in defect after wrap installation (7) and in defect of sample I2 (8)

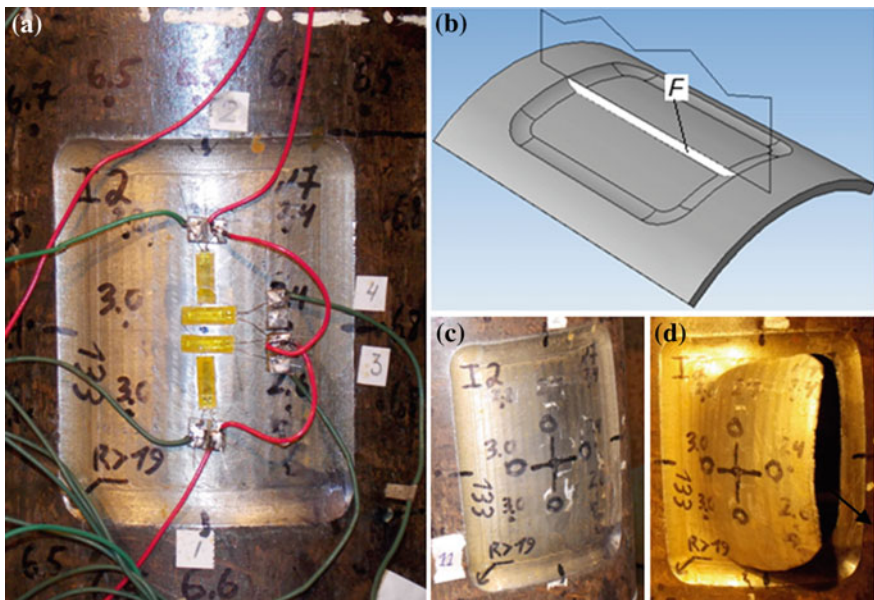


Fig. 4 Defect in sample I2: **a** with installation of resistance strain gauge; **b** area of defect in pipe axial section; **c** after penultimate stage; **d** after failure; **d** shows punching points circled by marker

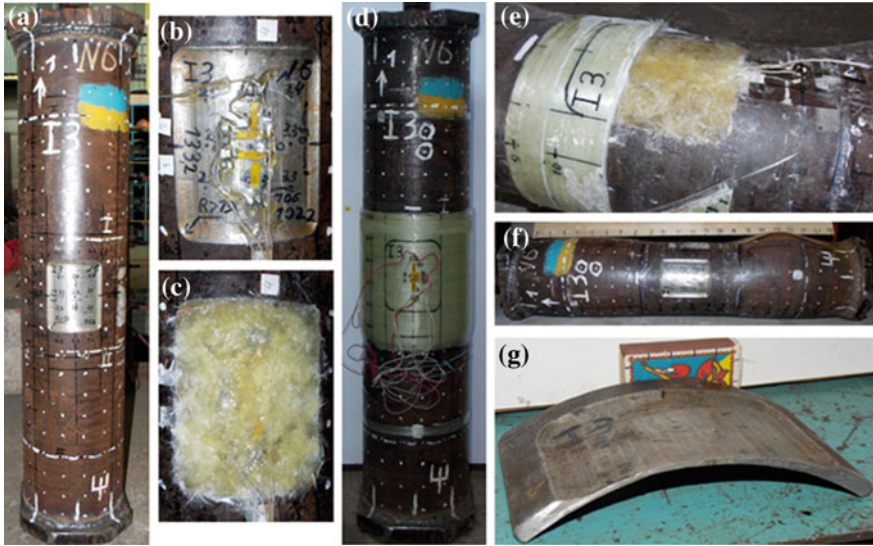


Fig. 5 Full-scale sample I3 before and after testing: **a** sample before installation of resistance strain gauge and wrap; **b** positioning of resistance strain gauge in defect; **c** compound-filled defects with resistance strain gauges; **d** sample before testing; **e** defect after testing; **f** sample after wrap removal, **g** cut out part of defect

verifies proportion of the selected wrap thickness and fracture pressure. Residual circumferential deformations of defect-free section of the pipe under the wrap were $\approx 0.2\%$ and outside the wrap $\approx 11\%$. It is noted that residual circumferential deformations in the defect after fracture of the sample without wrap (I2) was equal to 5.36% (Fig. 5).

4 Matching of Loading Diagram

Figure 6 shows the loading diagrams before fracture of samples I1-I4, made in “pressure-time” coordinates.

Diagram of sample I1 was used as a reference. Areas of elastic and plastic deformation are well seen on the diagrams; moreover the latter corresponds to transfer in plastic state of all or main part of metal of the cylinder part of sample.

Diagram of sample I2 proves that, due to relatively small defect surface and corresponding to it plastic deformation zone, the main, non-deformed part of the pipe was subjected to elastic deformation up to fracture, which took place at a pressure two times lower than in sample I1. It should be noted that the difference of elastic parts’ inclination angles in the loading diagram was not taken into account in this investigation, since it was a consequence of a series of difficult-to-consider factors, such as, for example, possible leakages in the hydraulic system.

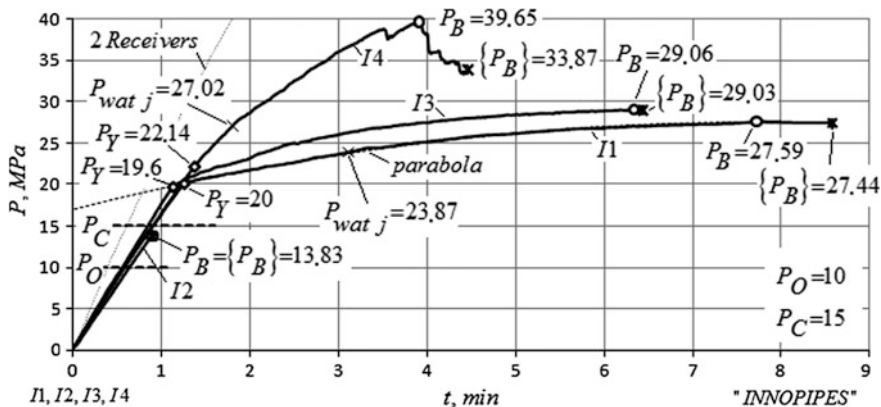


Fig. 6 Diagrams of inner pressure loading before fracture of I1, I2, I3 and I4 samples: $P_{wat,j}$ pressure to which the samples were loaded in water jacket; P_B maximum pressure; $\{P_B\}$ fracture pressure; 2 Receivers—diagram of loading of two twinned receivers without testing object; other designations see in Fig. 1

The increase of yield pressure and significant growth of fracture pressure (1.44 time) taking place simultaneously with the decrease of loading time, due to constraint of the radial movements, characterize the loading diagram of the sample simulating the strengthened part of the pipeline (I4). The rapid drop of pressure, anticipating its maximum value, obviously matches with the start of fracture of the fiberglass wraps on the boundary with a circular cutout.

The diagram of repaired sample (I3) is the closest to the reference. As it was mentioned earlier, part of the pipe under the wrap had virtually elastic deformations due to the wrap strengthening effect, except for defects. Total increase of volume, which was observed, first of all, due to plastic deformation of the non-strengthened part, significantly reduced, that, respectively, resulted to a decrease of the time of pump work before fracture. Typical points of the loading diagram, corresponding to yield and fracture pressure as well as its location (out of the wrap) clearly indicate repair efficiency.

5 Efficiency Assessment by Numerical Calculations

5.1 Selection of Finite-Element Mesh

Models of experimental pipes were built in the software package SolidWorks (Figs. 7 and 8). It is possible to execute the construction of the models close to real structures. Further models have been exporting to program complex ANSYS Workbench (WB).

Fig. 7 Solid model I2

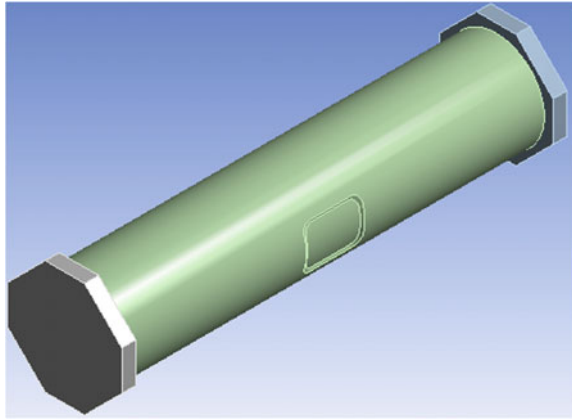


Fig. 8 Solid model I3

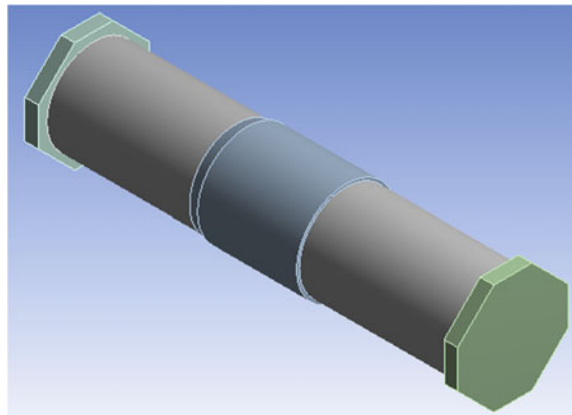


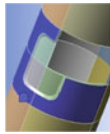
Table 1 Mechanical properties of composite material

Experiment	E (MPa)		σ_B (MPa)		ν
	Annular	Axial	Annular	Axial	
I3	48,465.21	3000	678.51	75	0.17
I4	59,850.69	3000	837.91	75	

The composite wrap was built in SolidWorks and exported to ANSYS Workbench. After that, properties of the composite were applied, and properties of anisotropy have been set. The composite material properties are present in Table 1.

The selection of finite-element mesh was conducted for I2 model. The mesh size was reduced by two times with each subsequent calculation. Mesh size was changed in the pipe plane, in the defect area and through thickness of the pipe. Example of mesh size selection is given in Table 2. Size of finite element was

Table 2 Selection of finite element mesh on the defect (axial strain)

<i>P</i> (MPa)	Defect, mesh size (m)			I2 model defect strain		
	Axial strain			Axial strain		
				T1	T2	WB T1_2
5.04	0.006 	0.012 		0.000193	0.000211	0.000176
5.04	0.003 	0.006 		0.000193	0.000211	0.000182
5.04	0.0015 	0.003 		0.000193	0.000211	0.000202

selected from comparison of experimental (T1, T2) and calculated (WB T1_2) strains in axial and annular directions. The selected size of the elements is highlighted in the table.

5.2 Solution of the Models and Analysis of Results

After selecting the mesh size of finite elements, series of calculations were performed for each of the models I2, I3, I4. Internal pressure loading was carried out stepwise. Pressure was reset to zero after each step, bringing the pressure values on the plots with strain calculation results that were put here together with experimental data (Figs. 9, 10, 11, 12, 13, 14, 15, 16, 17 and 18).

Analytical results for undamaged and unrepaired zone for I2 model in elastic state (Figs. 19 and 20) have been found as follows [1]:

$$\sigma_{axial} = \frac{Pr}{2s} \tag{3}$$

$$\sigma_{annular} = \frac{Pr}{s} \tag{4}$$

$$\varepsilon = \sigma/E \tag{5}$$

where P is the internal pressure; r is the radius of the pipe; s is the pipe thickness; E is the Young's modulus.

General charts of analytical and WorckBench calculations for I2, I3, I4 models, annular strain are shown in Figs. 21 and 22.

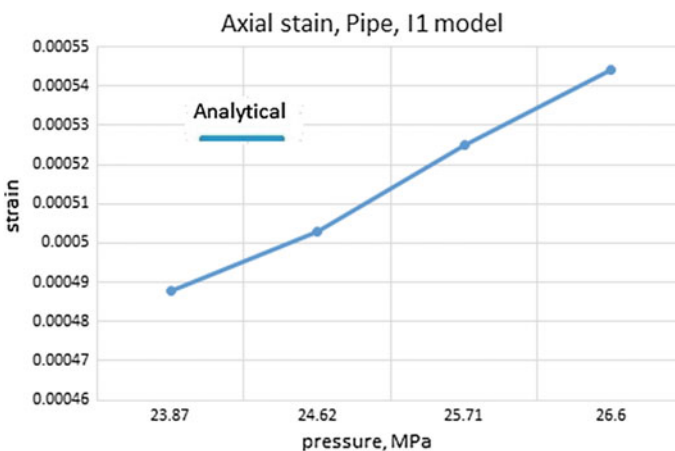


Fig. 9 Curves of axial strain and pressure (Pipe), I1 model

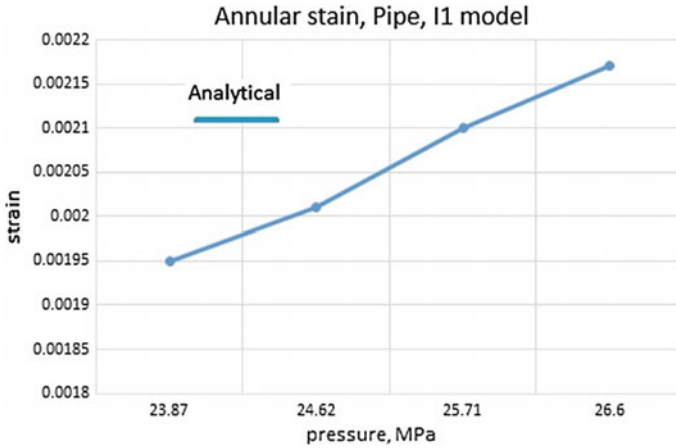


Fig. 10 Curves of annular strain and pressure (Pipe), I1 model

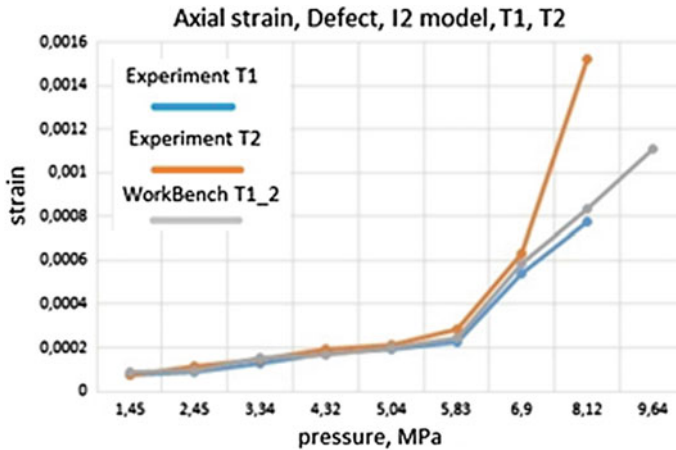


Fig. 11 Curves of axial strain and pressure (Defect), I2 model

Obtained results showed that the calculation models in the defect zone are close to the experimental data. The difference of the results for model I2 in the defect zone was from 3.87 to 9.84% in axial strain (Fig. 11) and from 5.81 to 12.79% in annular strain (Fig. 10). For the pipe far from the defect zone, the difference was from 3.53 to 7.52% in axial strain (Fig. 11) and from 4.16 to 11.4% in annular strain (Fig. 12).

The difference for model I3 in the defect zone was from 1.56 to 16.8% in axial strain (Fig. 13) and from 1.35 to 10.33% in annular strain (Fig. 14). For the pipe, the difference was from 0.73 to 6.27% in axial strain. On the wrap, difference was

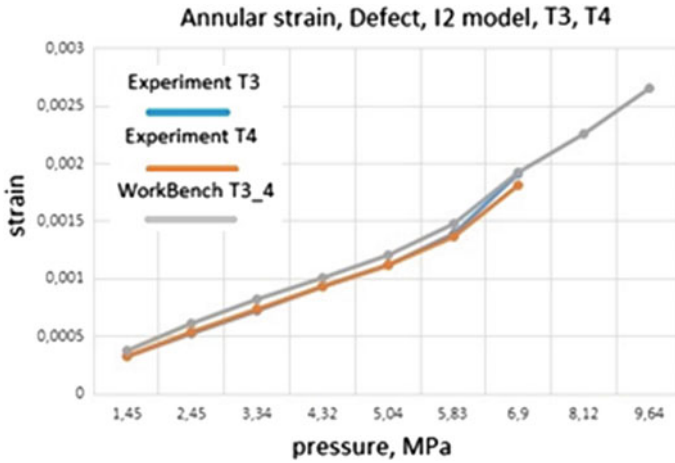


Fig. 12 Curves of annular strain and pressure (Defect), I2 model

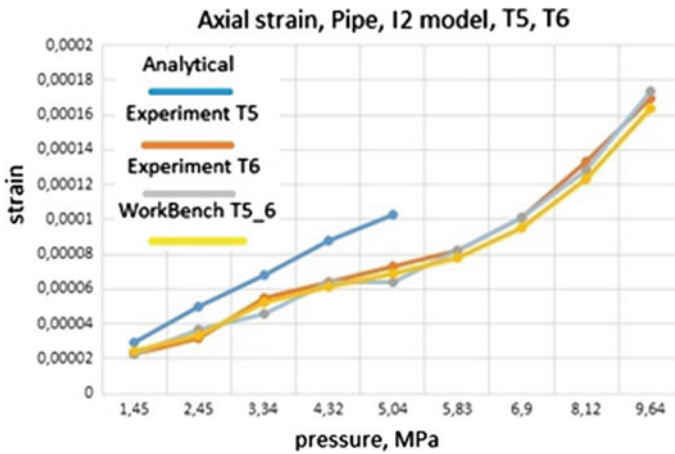


Fig. 13 Curves of axial strain and pressure (Pipe), I2 model

from 8.0 to 15.39% in axial strain (Fig. 15) and from 3.02 to 10.57% in annular strain (Fig. 16).

The difference for model I4 of the pipe was from 5.26 to 8.7% in axial strain (Fig. 17) and from 1.83 to 9.5% in annular strain (Fig. 18).

Probable reasons of difference between calculated and experimental strains are inaccuracy of data receiving from sensors in the experiments in some sections of the pipe and also the fact that a decision with the help of programs makes certain idealization calculations.

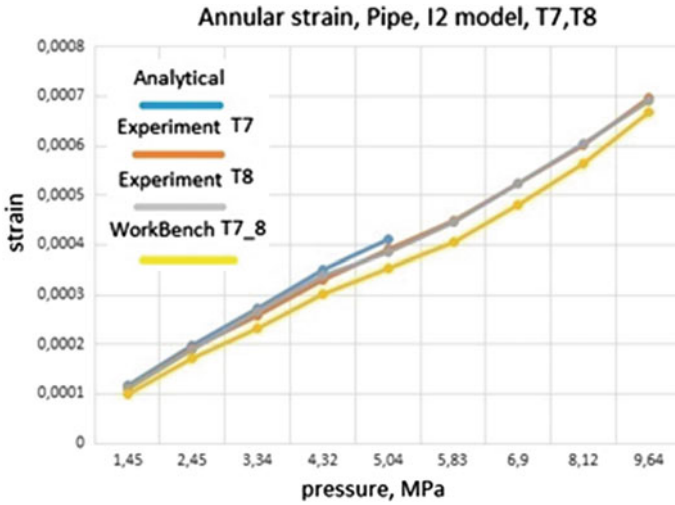


Fig. 14 Curves of annular strain and pressure (Pipe), I2 model

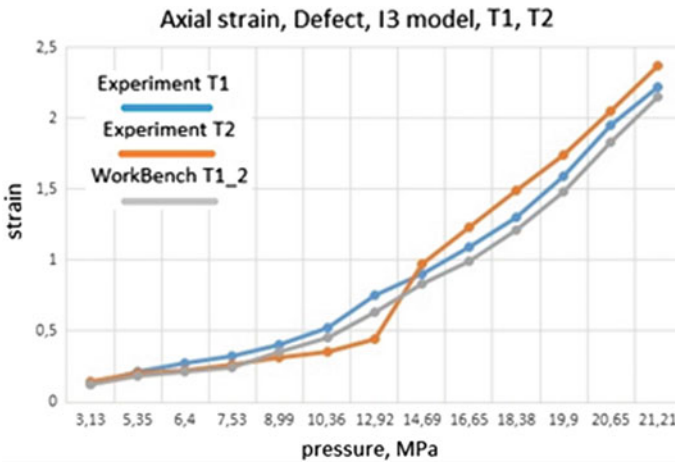


Fig. 15 Curves of axial strain and pressure (Defect), I3 model

Enough close agreement between experimental and calculated data can serve, on one hand, as confirmation of the authenticity of performed numerical calculations and, at the same time, as another indication of the efficiency of used composite repair system (Figs. 23 and 24).

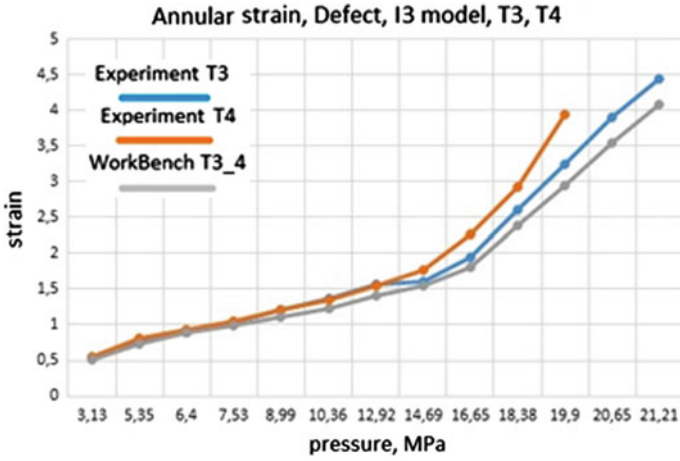


Fig. 16 Curves of annular strain and pressure (Defect), I3 model

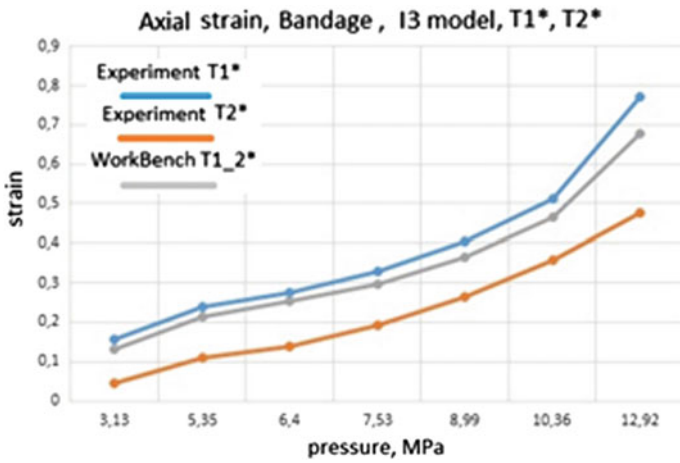


Fig. 17 Curves of axial strain and pressure (Wrap), I3 model

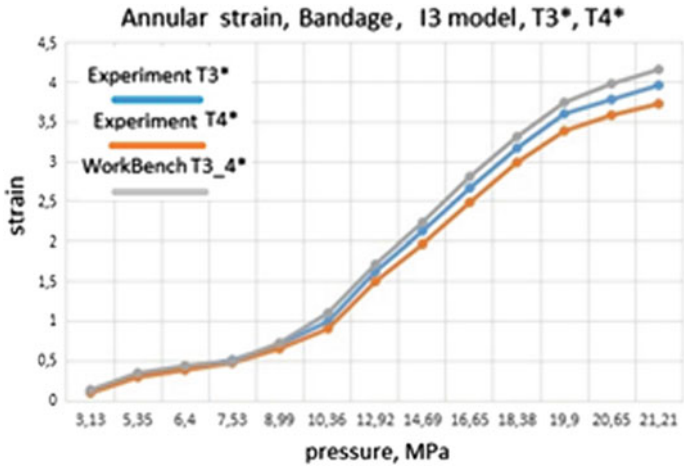


Fig. 18 Curves of annular strain and pressure (Wrap), I3 model

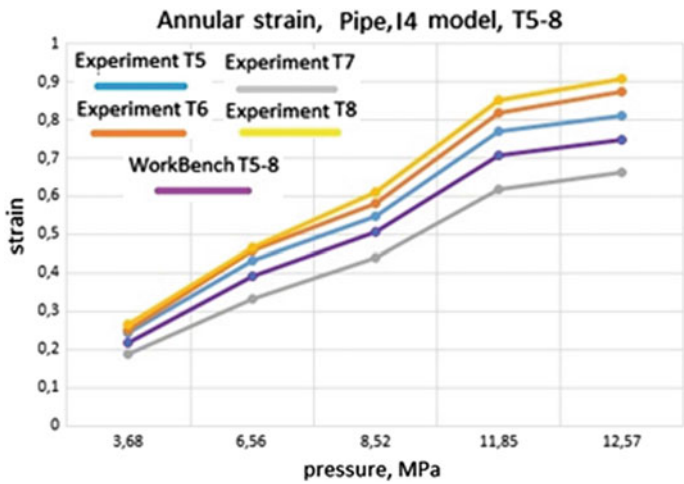


Fig. 19 Curves of annular strain and pressure (Pipe), I4 model

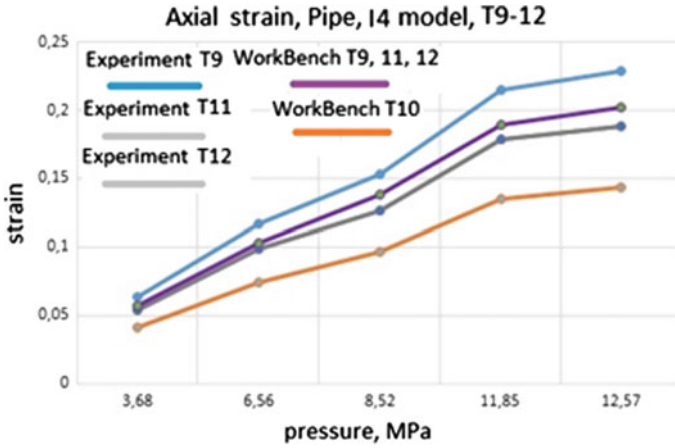


Fig. 20 Curves of axial strain and pressure (Pipe), I4 model

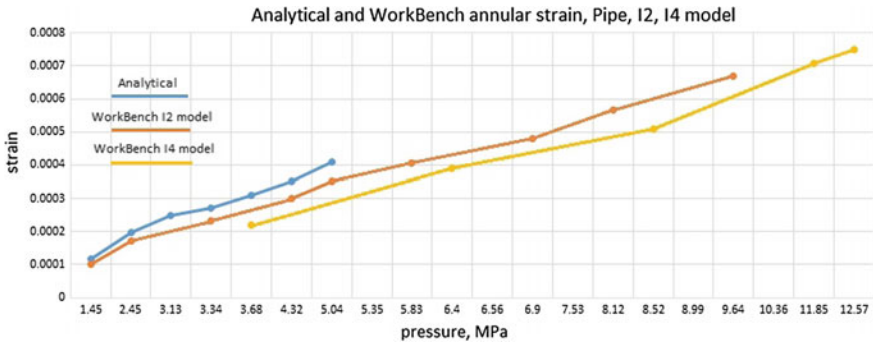


Fig. 21 General chart of analytical and WorkBench calculations for I2, I4 models, annular strain

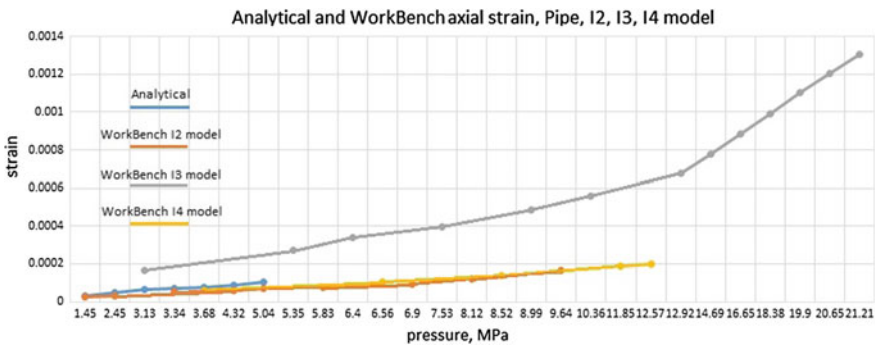


Fig. 22 General chart of analytical and WorkBench calculations for I2, I3, I4 models, axial strain

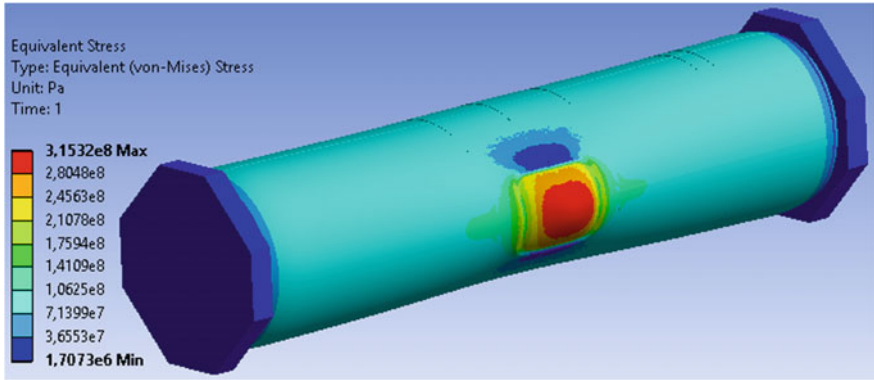


Fig. 23 Area of the defect zone of I2 and I3 models

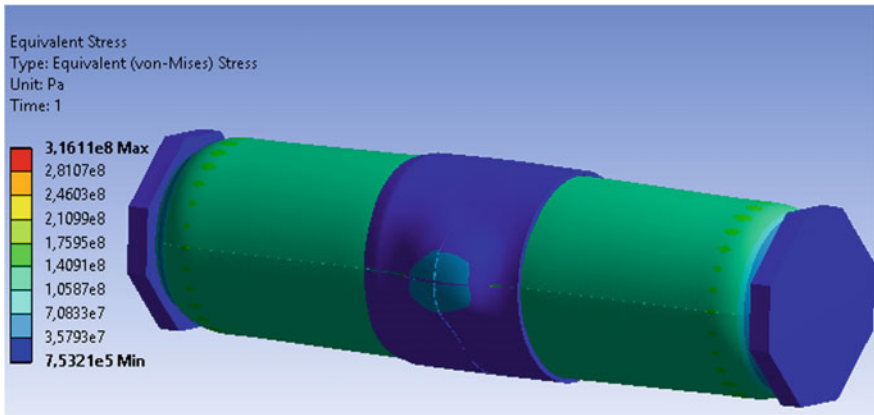


Fig. 24 Curves of annular strain and pressure (models I1-I4)

6 Conclusions

Comparative analysis of changes in the volume, yield pressure, perimeter, deformations in the defect and loading diagrams of natural samples during their hydraulic tests as well as results of numerical modeling have demonstrated the efficiency of the used technology of the repair of a damaged pipeline section using composite material wraps.

References

1. V.M. Belayev, V.M. Mironov, *Design and calculation of elements of branch equipment. P.I: Thin wall vessels and apparatuses of chemical industry: Manual*. Tomsk, Tomsk Polytechnic University,(2003), 168 p

Errata to: Non-destructive Testing and Repair of Pipelines

Evgeny N. Barkanov, Andrei Dumitrescu and Ivan A. Parinov

Errata to:

E.N. Barkanov et al. (eds.), *Non-destructive Testing and Repair of Pipelines, Engineering Materials*, <https://doi.org/10.1007/978-3-319-56579-8>

The original version of the book was inadvertently published with incorrect author names “A.A. Lyapin and Y.Y. Shatilov” which have to be corrected as “A.A. Lyapin, Y.Y. Shatilov and A.A. Lyapin Jr.” in Chapter 5 and “G.I. Lvov” has to be corrected as “I. Lvov” throughout the book. The erratum book has been updated with the changes.

The updated online version of this book can be found at <https://doi.org/10.1007/978-3-319-56579-8>

https://doi.org/10.1007/978-3-319-56579-8_5

https://doi.org/10.1007/978-3-319-56579-8_21

https://doi.org/10.1007/978-3-319-56579-8_22

https://doi.org/10.1007/978-3-319-56579-8_24

https://doi.org/10.1007/978-3-319-56579-8_27

© Springer International Publishing AG 2018

E.N. Barkanov et al. (eds.), *Non-destructive Testing and Repair of Pipelines, Engineering Materials*, https://doi.org/10.1007/978-3-319-56579-8_28

Index

A

Acoustic waves, 91
Active focusing, 5, 32, 37
Adhesive, 170, 175, 177, 179–186, 250, 254, 255, 257–262, 265, 289, 298, 300, 304, 305, 312, 319, 369, 370
Amplitude–Time Response (ATR), 91
ANSYS, 46, 49, 50, 52, 60, 66, 92, 93, 96, 197, 293, 305, 324, 390, 395, 437
Artificial Neural Network (ANN), 92, 96, 106

B

Bursting, 139, 144, 145, 151, 158, 275, 405, 406, 414

C

Circumferential amplitude curves, 43
Colony of flaws, 154, 155, 158, 164
Composite, 64, 65, 73–75, 170, 172, 173, 175–177, 182, 183, 186, 191, 200, 220, 245, 250, 252, 308, 313
Composite bandage, 340, 344, 348, 349, 353, 387, 388, 390, 391
Composite material, 73, 169–172, 175–177, 179–181, 183, 184, 186, 187, 191, 192, 218, 227, 228, 231, 233, 234, 237, 242, 244–247, 249, 251, 252, 254–256, 260, 261, 263–265, 269, 270, 272, 273, 340, 366, 369, 370, 372, 374, 378, 382, 384–387, 396, 402, 403, 405, 407, 417, 418, 423, 434
Composite repair, 244, 245, 249, 274, 302, 354, 403, 414
Composite repair system, 171, 186, 244–246, 270, 273, 289, 387, 388, 390, 391, 395, 396, 402–405, 409, 412, 413, 415, 443
Composite wrap, 270–282, 284, 290, 293, 296, 298, 299, 301–303, 305, 311, 312, 314, 318, 319, 322, 325, 354, 356–366,

369–371, 382, 384, 385, 401, 402, 404, 406–408, 414, 415, 417, 418, 422, 433, 438

Composite wrap design, 283, 415
Contact problem, 339–341, 354
Correlation, 65, 73, 75, 79, 81, 82, 84, 85, 88, 180, 199, 204, 261
Corrosion, 3, 10–12, 15, 21, 24–26, 46, 73, 92, 117–120, 122, 125, 128, 138, 154, 155, 159, 169, 171–173, 175, 179, 185, 186, 242, 245, 249, 251, 254, 256, 259, 264, 265, 311, 321, 329, 355, 370, 387, 402, 403, 418
Crack, 26, 27, 74, 75, 91, 93–96, 100, 101, 104, 105, 118, 172, 179, 184, 254, 321, 404
Cylindrical shell, 340, 344, 348, 353, 366

D

Damage, 5, 10, 11, 63–68, 70, 71, 74, 75, 77–82, 84–87, 92, 148, 150, 175, 186, 192, 214, 245, 251, 260, 355, 385, 403, 418
Damage detection, 46, 63, 64, 66, 68
Defect, 17, 20, 22–29, 49, 53–57, 59, 60, 63, 64, 91–93, 95–98, 100–105, 120, 122, 125, 126, 131, 134, 138, 140, 141, 143, 145–147, 149, 151, 154, 155, 158–160, 162–164, 171, 248, 272, 281, 289, 304, 308, 312, 315, 322, 324, 326, 327, 334, 353–357, 366, 370–373, 382, 384, 388, 390, 395, 401, 402, 404, 406–409, 411, 414, 418, 421, 422, 434, 436, 438, 441, 447
Defect detection, 46
Deflection shape, 74–77, 82, 87
Disperse filler, 233, 234
Dispersion curves, 7, 8, 17

- Distance, 4, 5, 9, 13, 16, 17, 19–21, 23, 24, 33, 36, 38–41, 43, 53, 68, 71, 92, 95, 96, 100, 105, 110, 123, 128, 146, 149, 150, 154, 162, 164, 198, 211, 213–215, 217–219, 221–224, 276, 315, 316, 318, 322, 326, 327, 334, 372, 393, 422, 434
- Dynamic Distance Focusing (DDF), 33
- Dynamic modulus, 234, 236, 237
- E**
- Elasticity theory, 46, 47, 92, 93, 371
- Elastic material properties, 193, 200, 206
- Elastic moduli, 218
- Elastic plate, 107
- F**
- Filler, 170–175, 180, 181, 183, 185, 186, 233, 234, 236, 246, 249, 289, 293, 296, 298, 302, 304, 307, 308, 312, 313, 318, 319, 329, 337, 357, 362, 371, 372, 390, 404, 406, 414
- Finite element, 50, 52, 54, 60, 66, 93, 96, 121, 159, 161, 164, 198, 204, 279–282, 312, 354, 371, 381, 384, 390, 392, 393, 395, 437, 439
- Finite Element Analysis (FEA), 127, 197, 204, 290, 322, 324, 328, 330, 394, 395
- Finite Element Method (FEM), 46, 48, 64, 105, 130, 197, 312, 383, 417
- Fitness-For-Service (FFS), 127
- Flaw, 118–120, 122–131, 134, 138–141, 143, 145, 151, 154, 252, 408, 434
- Flexural mode, 7, 12, 28
- Focal law, 32–34, 36–38
- Full Width at Half Maximum (FWHM), 38–43
- H**
- Harmonic oscillation, 107
- Hydraulic tests, 151, 415, 423, 424, 426, 447
- I**
- Identification, 64, 74, 75, 77, 79, 80, 92–94, 96, 99–101, 103–105, 193, 196–198, 200, 204–207, 224
- Impact, 11, 32, 61, 74, 75, 77, 78, 83, 86, 87, 122, 149, 171, 175, 176, 181, 185, 186, 227, 237, 258, 259, 273, 321, 384, 397
- Impulse excitation method, 193, 194, 202, 207
- Incompressible fluid, 107, 108, 255
- Inner pressure, 138, 147, 160, 175, 251, 254, 299, 311, 319, 388, 390, 393, 397, 420, 422, 423, 426, 427, 431–433, 437
- In-service repair, 159, 242, 252, 255
- Integral equation, 109, 110
- Interacting flaws, 124, 127
- Inverse problems, 92–94, 105
- Inverse technique, 192, 193, 196, 197, 203–207
- L**
- Laminated composites, 200, 205, 206
- Laser-induced, 211, 214, 216, 219, 222–224
- Local metal loss, 118, 119, 123, 134, 243, 269, 289
- Longitudinal mode, 7, 52, 54–56, 60
- Longitudinal wave (L-wave), 49, 54, 56, 57, 61, 211, 219, 220
- Long Range Ultrasonic Technique (LRUT), 16, 32
- Long range ultrasonic testing, 15, 16
- Low-cyclic fatigue, 146, 147
- Low-frequency guided wave, 45, 46
- M**
- Magnetostrictive transducers, 24, 27
- Mechanical properties, 122, 147, 151, 153, 173, 175, 176, 183, 186, 192, 206, 227, 228, 231, 233, 234, 237, 245, 265, 271–274, 277, 279, 296, 298, 301, 302, 362, 372, 390, 391, 404, 409, 413, 418, 421, 423, 424, 438
- Modeling, 18, 24, 26, 36, 159, 160, 164, 224, 324, 341, 358, 362, 364, 366, 447
- Mode shapes, 65–68, 71, 75, 79, 202
- N**
- Non-destructive characterisation, 193
- Non-destructive testing, 16, 210, 224
- NX, 159, 312, 319, 324
- O**
- Optimisation, 196, 198, 200, 388–391, 393, 396
- Optoacoustics, 211, 212
- P**
- Perforated metal tape, 236, 237
- Phased antenna array, 32–35, 37, 38, 42
- Phased array technology, 4
- Piezoactuator, 95, 96
- Piezosensor, 95, 96, 98, 105
- Pipe, 4, 5, 7–9, 11, 13, 16, 17, 20, 28, 31–36, 38–40, 46, 49, 52, 54, 56, 57, 59, 60, 67, 68, 95–98, 100, 103, 118–120, 122, 125, 140, 144, 146, 151, 162, 172, 179, 245–248, 251, 255, 258, 261, 264, 274, 281, 289, 290, 293, 296, 299, 302, 305, 307, 311, 312, 315, 318, 319, 322, 324,

- 355, 369–373, 382, 384, 385, 390,
395–397, 404, 406, 409, 418, 420, 423,
425, 426, 432, 434, 436, 440–442
- Pipeline systems, 64, 402, 409, 415
- Plane strain model, 371, 372
- Plate, 7, 34, 74–79, 81, 82, 86, 87, 107, 108,
112, 113, 192, 204, 206, 410
- Polymeric Composite Material (PCM), 170,
172, 249, 369, 371, 372
- Pretension, 369, 374, 385
- Q**
- Qualification, 120, 122, 130, 246, 247, 270,
302, 401–403
- R**
- Reinforcing fibres, 176, 187, 245, 270, 273,
279, 404
- Remaining Strength Factor (RSF), 124, 138
- Repair system, 169, 170, 176, 186, 192,
244–247, 249, 251, 254, 255, 264, 270,
272, 279, 371, 387, 396, 401–403, 409,
415, 417
- Repair technology, 186, 242, 252, 264, 402
- Residual life, 146, 151
- S**
- Safe working pressure, 154
- Scale, 17, 18, 21, 28, 66, 67, 75, 79–81, 87,
146, 149–151, 228, 313, 354, 404, 405,
422, 426, 428, 436
- Scalogram, 75, 80, 82, 84, 86, 87
- Scattering, 24, 37, 211, 218, 219, 222–224
- Serviceability, 138–140, 144, 151, 421
- Sleeves, 172, 173, 242, 244, 245, 251, 263,
284, 402
- Stress, 26, 47, 54–57, 59, 60, 93, 122,
125–127, 129, 138–140, 146, 147, 150,
151, 154, 155, 158–160, 163, 173, 177,
179, 254, 271, 278, 280, 282, 290, 296,
298, 302, 305, 306, 308, 311, 313, 315,
316, 318, 319, 322, 354, 356, 369, 370,
372, 381–383, 385, 390, 395, 404, 415,
420, 421, 427, 432
- Stress function, 369, 371, 374, 378, 385
- Stress-strain state, 46, 57, 59–61, 146, 319,
354, 356, 369, 382, 402
- Structural health monitoring, 16, 64, 74
- Synthetic focusing, 6, 32–34
- T**
- Tensile test, 147, 230, 232, 409
- Three-points-bending test, 192, 193, 201, 202,
206
- Timoshenko-type shell theory, 348
- Torsional mode, 5, 9, 14, 19, 26, 32, 36, 52–55,
57, 60
- Torsional wave (T-wave), 19, 27, 46, 54–58,
60, 61
- Transmission pipeline, 117, 118, 120, 122,
124, 127, 130, 131, 134, 138, 139, 146,
151, 154, 169–172, 175, 180, 186,
241–247, 249, 251, 255, 256, 263, 264,
271–274, 277, 282, 284, 319, 369, 370,
387, 391
- Two defects, 21, 159, 161–164, 322–324, 326,
330, 334
- U**
- Ultimate limit state, 139, 144, 151, 154, 284
- Ultrasonic guided wave, 11, 46, 52, 54
- Ultrasound, 4, 5, 9, 10, 12, 18, 19, 27,
210–212, 214–218, 222–224
- Universal threshold, 75, 86, 88
- V**
- Variance, 75, 81, 82, 84, 86, 87
- Vibration test, 75, 82, 87, 193, 194, 196–198,
205, 206
- Volumetric Surface Defect (VSD), 119, 122,
134, 146, 154, 159, 179, 243, 282, 290,
293, 311, 319, 322, 369
- Von Mises combined stress, 325, 326, 328,
370, 371, 381, 382, 384, 386
- W**
- Wavelet, 74, 75, 78–81, 84–87
- Wraps, 176, 178, 242, 244–247, 249, 259, 260,
263, 265, 270, 273, 274, 276, 282, 284,
298, 312, 330, 402, 407, 417, 418, 421,
434, 437